TECHNICAL REPORT 1904
September 2003

VLF/LF High-Voltage Design and Testing

. .

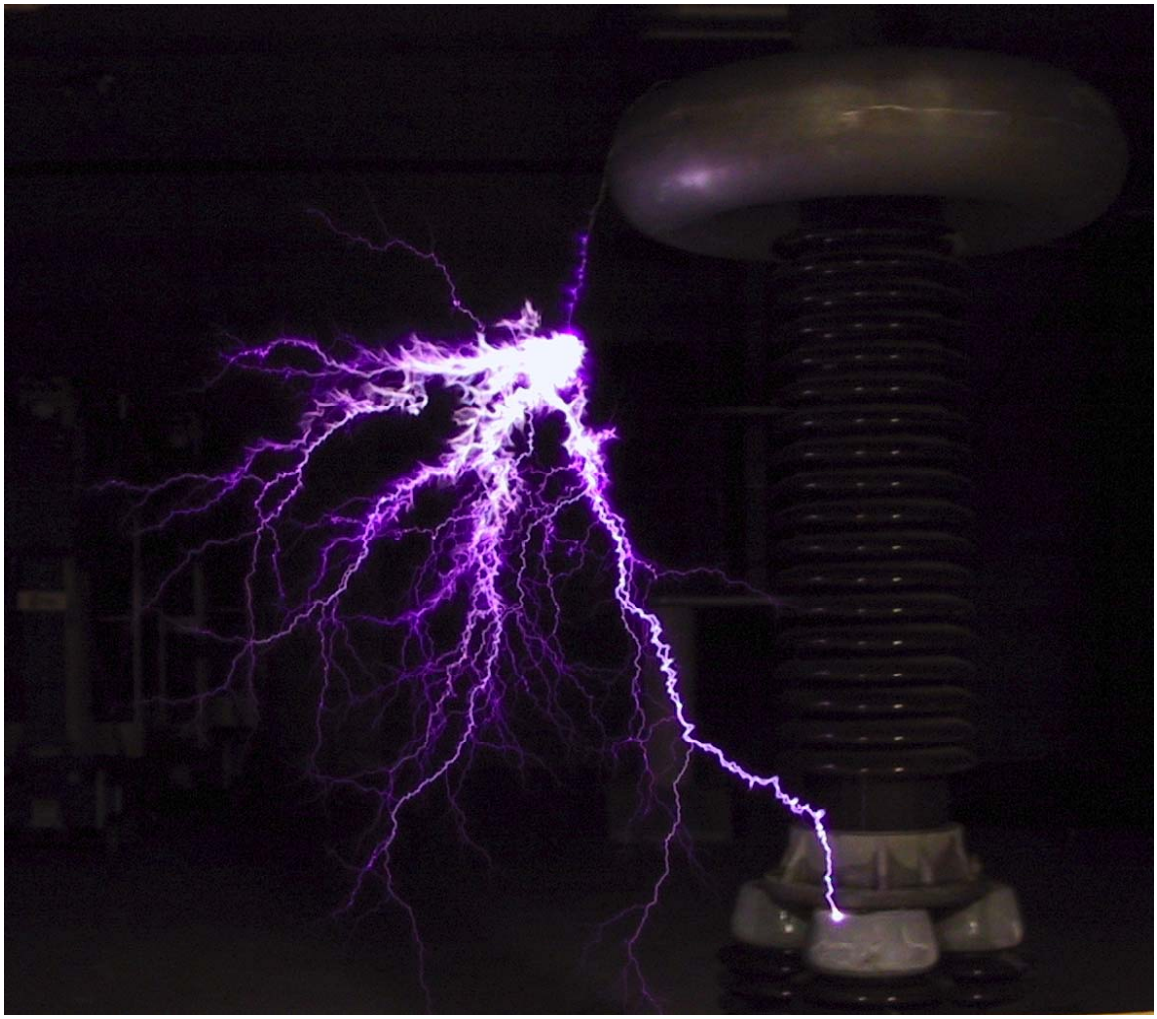

SSC San Diego

Report Documentation Page

Form Approved
OMB No. 0704-0188

1. REPORT DATE	2. REPORT TYPE	3. DATES COVERED
SEP 2003		**00-00-2003 to 00-00-2003**

4. TITLE AND SUBTITLE	5a. CONTRACT NUMBER
VLF/LF High-Voltage Design and Testing	5b. GRANT NUMBER
	5c. PROGRAM ELEMENT NUMBER
6. AUTHOR(S)	5d. PROJECT NUMBER
	5e. TASK NUMBER
	5f. WORK UNIT NUMBER
7. PERFORMING ORGANIZATION NAME(S) AND ADDRESS(ES) **SPAWAR Systems Center ,SSC San Diego,San Diego ,CA,92152-5001**	8. PERFORMING ORGANIZATION REPORT NUMBER
9. SPONSORING/MONITORING AGENCY NAME(S) AND ADDRESS(ES)	10. SPONSOR/MONITOR'S ACRONYM(S)
	11. SPONSOR/MONITOR'S REPORT NUMBER(S)

12. DISTRIBUTION/AVAILABILITY STATEMENT
Approved for public release; distribution unlimited

13. SUPPLEMENTARY NOTES

14. ABSTRACT

15. SUBJECT TERMS

16. SECURITY CLASSIFICATION OF:			17. LIMITATION OF ABSTRACT	18. NUMBER OF PAGES	19a. NAME OF RESPONSIBLE PERSON
a. REPORT **unclassified**	b. ABSTRACT **unclassified**	c. THIS PAGE **unclassified**	**Same as Report (SAR)**	**485**	

TECHNICAL REPORT 1904
September 2003

VLF/LF High-Voltage Design and Testing

P. M. Hansen
A. D. Watt

SSC San Diego
San Diego, CA 92152-5001

SSC SAN DIEGO
San Diego, California 92152-5001

USN
Commanding Officer

Executive Director

ADMINISTRATIVE INFORMATION

This report was prepared for Space and Naval Warfare Systems Command by the Adaptive Systems Branch (Code 28505) of the RF Communication Systems Division (Code 284), SSC San Diego.

Front Cover Photo by David Phillips.

LH

Acknowledgments

The authors gratefully acknowledge the assistance of our many friends. The work described in this document took place over many years and it is impossible to acknowledge all who have helped. If you are not on the list and you have helped in any way, please pardon our oversight and know that we also thank you.

Much of the Forestport data was generated under the watchful eye of Jim Brooks, who also provided us with helpful information about the data during the development of this document. Others who helped in obtaining the data include: Goeffrey Dann of the Naval Civil Engineering Laboratory (NCEL), and Donald Mangold of the USAF/Rome Air Development Center (RADC). We owe much to Bill Cheyne who ran the Forestport facility. His expertise greatly facilitated the construction and operation of the tests.

Those of us working in VLF recognize the great contribution of our friend Andy Smith, who did much of the pioneering work in VLF/LF corona. He did much of the work during the 1985 tests. Some of these results are included in the material presented here. Thanks are also due to our friend Charles Smith of Raytheon E Systems for his encouragement and help in the computer analysis.

Of special note are those personnel of the Navy Technical Facility in San Diego, now known as SSC San Diego. This includes Jose Chavez who participated in the experimental work and analysis. Jim Ward, Paul Pelland, Jim Birkett, Linda Poff, and Mabel Vares took care of administrative aspects. Jim Birkett and Karl Cain performed many tedious computer calculations required to generate some of the data. Jim Birkett also made many of the drawings. Special thanks go to the reviewers James Bond and David Phillips, Lee Hood our diligent editor, and Chris Billingsly, who created the illustrations.

Much of the information regarding the history of the Navy's VLF insulators has come from Mr. A. N. Smith, retired from NCCOSC (now SSC San Diego). In addition, the authors have been privileged to associate with many of the people involved in the development of the Navy's LF frequency shore transmitting system: W. Alberts, E. Devany, W. Gustafson, B. Hagaman, L. Hice, W. Hopkins, N. Matlock, R. Nash, and A. N. Smith. Some of the information in the background section has come from them either by personal communication or from publications not available in the open literature.

Finally, this document would not have been possible were it not for the insight and vision of the sponsor Paul Singer PEO (C4I-Space), formerly of SSC San Diego, who provided the wherewithal to complete and publish this document.

CONTENTS

FIGURES

TABLES

CHAPTER 1 INTRODUCTION

NAVY INTEREST

The U.S. Navy has had a requirement for long-distance communications from the beginning and it is natural that their interest in high-power wireless transmitting systems dates back to the beginning of radio. Until only recently, the Navy was still operating some of the very-low-frequency and low-frequency (VLF/LF) antennas that were constructed not long after the beginning of radio. For example, the LF transmitting antenna at Chollas Heights in San Diego, torn down in 1997, dated back to 1915. Three of the towers in the VLF antenna at Annapolis are identical to towers in the original VLF antenna constructed in 1917. They were added to the original antenna between 1934 and 1937 as part of an upgrade. The Annapolis antenna was modified in 1969, keeping those three towers. The VLF station was closed in late 1997 and the antenna has been demolished. The design of high-power VLF/LF antennas has evolved over the years, but the design of the modern antennas still leans heavily on the early antenna designs. The existing VLF/LF system is the only visible remnant of the Navy's original radio system constructed at the beginning of this century, and it is appropriate that this report begin with a brief review of the history of the Navy's involvement in radio communications.

A U.S. Navy Lieutenant, Bradly A. Fisk, demonstrated wireless communication in the early 1890s, purportedly before Marconi's famous experiments. He communicated between two ships over a short range by winding a coil around the USS *Atlanta*, making a large electromagnet, and generating a signal using interrupted current (Howeth, 1963). The first official Navy message was sent via wireless telegraph from a ship to shore in 1899 with Marconi as the operator, and by 1900 the Navy had installed Marconi wireless systems on three ships. The same year, after the successful resolution of a patent dispute with Tesla, Lt. Fisk was granted an underlying patent to Tesla's patent describing radio control.

By 1902, the Navy's first serious wireless broadcast system consisted of a series of shore stations established along the East Coast and Caribbean. By 1903, a "Wireless Division" existed in the Bureau of Equipment, and by 1906 the Navy had completed a West Coast chain of radio stations. Stations were soon established at 23 locations on the East and West Coasts, including Panama, Cuba, Puerto Rico, Hawaii, the Philippines, Guam, and the Marianas, providing the world's first global radio broadcasting network (Law, 1985).

In 1912, the Navy was the first to change the name of its stations from wireless to radio, a term later adopted by the entire communications industry (DTIC, 1958). Fisk was a strong proponent of radio communication in the early days. Later, however, strong political opposition to the Navy's use of radio for communication arose within the ranking senior officers, and even Fisk as a commander joined this large group of senior officers in opposition to wireless[1]. Nevertheless, the utility of radio proved itself, and when World War I erupted, the Navy's use of radio increased dramatically.

In the beginning, many of the Navy shore stations were designed to operate in the VLF (10 to 30 kHz) and LF (30- to 300-kHz) bands, together called the long-wave band at that time. These stations used spark gap or arc transmitters, sending hand-keyed telegraphy. The locations and operating power rating of the early long-wave stations are provided in Table 1. Several high-power stations were built during World War I. Surprisingly, the Navy's first 1-million-watt long-wave station was

[1] Fisk eventually retired as a rear admiral.

built in France after the war and commissioned in 1920. The Navy started to build a 4-million-watt transmitting system in North Carolina during the war, but did not complete the project until after the war (Howeth, 1963).

Table 1-1. Early U.S. Navy high-power long-wave stations.

Year	Site	Call Sign	Transmitter Type	Power (kW)
1913	Arlington, VA	NAA	Rotary Spark	100 kW
1914	Colon, Canal Zone		Rotary Spark	100 kW
1915	Darien, Panama Canal Zone	NBA	Arc	200 kW
1916	Pearl Harbor, HI	NPM	Arc	300 kW
1917	San Diego, CA	NPL	Arc	100 kW
1917	Cavite Philippines	NPO	Arc	350 kW
1917	San Francisco, CA	NPG	Spark	100 kW
1918	New Brunswick, NJ	NFF	Alexanderson Alternator	200 kW
1918	Annapolis, MD	NSS	Arc	2-500 kW
1920	Bordeaux, France	Radio Lafayette	Arc	2-1000 kW

The power stated in Table 1 is the input power to the transmitter, not the power to the antenna. The actual radiated power was much less, being reduced by both the transmitter and antenna efficiencies. Thus, the transmitters limited the radiated power achieved by the early transmitting systems and the simple insulators available at the time were adequate. As time went on, the technology developed for higher power transmitters and the amount of power that could be radiated began to be limited by the capacity of high-voltage insulators in the antenna systems.

Most of the early long-distance communication and broadcast systems operated in the VLF and LF bands. For example, in 1920 the Dutch built a rather famous large VLF facility (PKX) in the Dutch East Indies at Malabar, on Java, for communication back to Holland (De Groot, 1924). The antenna was a large valley span type and had both arc type and alternator type transmitters. The U.S. Navy later built similar valley span antennas at Haiku, HI, Trinidad Island (for the Omega navigation system), and Jim Creek, WA. The site at Jim Creek was constructed in the early 1950s and is still operational today. In 1924, the British opened a large VLF station at Rugby capable of worldwide communication by radiotelegraph.

The Navy originally used VLF/LF transmitters to communicate with ships at sea. However, with the development of submarines, VLF/LF communications provided a capability to communicate with submerged submarines because the attenuation of VLF/LF radio waves by seawater supports underwater reception to moderate depths. VLF/LF also supports long-range communications because the earth and ionosphere form a waveguide for propagation in this frequency range. The refraction height for VLF/LF waves is in the middle to upper-D region of the ionosphere, 70 to 90 km above the earth. Solar flares and nuclear events increase the conductivity of the D region. VLF/LF propagation is not affected much by solar flares or nuclear events, which do affect communications

in the HF range. In fact, when these events occur, the propagation in the VLF/LF range actually improves, whereas for higher frequencies the waves must pass through the D region, and the increased conductivity resulting from nuclear or solar events greatly increases the signal attenuation.

Prior to World War II, the U.S. Navy had built a large VLF transmitting system at Annapolis MD and a valley span VLF transmitting system at Haiku on the Hawaiian Island of Oahu. These VLF systems provided reliable long-range communications to ships and submarines. Following the war, the VLF/LF system was expanded to support worldwide communications. During the 1950s, a set of LF stations was developed to fill in the communications gap (skip zone) that often occurs at HF when a ship is within 300 miles of a shore broadcasting station. During the same period, the Navy built a large valley span VLF antenna at Jim Creek, WA, just north of Seattle, to expand the communication capability to submarines.

As the Cold War began to heat up in the early 1960s, the Navy built huge, nearly antipodal, 2-megawatt VLF stations at Cutler, ME, and the Great Northwest Cape in Western Australia. In the late 1960s to early 1970s, the Navy undertook to upgrade the existing VLF stations at Annapolis and Lualualei, Hawaii, replacing the antennas. In both cases the antenna system was cut back due to financial pressures resulting from the conflict in Viet Nam. All these stations are still in operation, even though the available bandwidth is limited, because VLF/LF is still the only affordable technique for long-range communications to submerged submarines. Bandwidth is limited because VLF/LF antennas are necessarily electrically small antennas due to the long-wavelengths of VLF and LF signals. In the late 1980s and early 1990s, the U.S. Navy investigated blue-green optical communication from satellites to submarines, but an operational system was never developed due to the high projected operating cost.

At one time, the U.S. Navy operated over 30 LF and VLF transmitting stations around the world. The insulators used in many of these antennas were modified power distribution insulators. As time went on some manufacturers provided special-purpose radio frequency insulators because there was a significant market composed of the many commercial high-power broadcast stations. For example, the replacement antennas at both Annapolis and Lualualei had base insulators, fail-safe guy insulators and feed-through bushings manufactured by Lapp Insulator Company of Leroy, NY. However, not long after going operational the base insulator at Annapolis cracked leading to concern that the 1200’ tower might collapse, either there or at Lualualei, which has 2-1500’ towers. Both systems were turned off and a High Voltage Test Facility was constructed at Lualualei using the transmitter and helix augmented by two outside coils and an air capacitor. This facility was designed and operated by Andy Smith who had returned to the Navy Electronics Laboratory (now SSC San Diego) (Smith, 1973). Continental designed and built a new base insulator assembly which was tested at the facility at Lualualei and then used to replace the base insulators there. It was difficult to get access for testing once Lualualei went operational and the test facility was eventually dismantled.

As new communication systems developed, the market for costly high-power broadcast systems decreased, reducing the number of commercial suppliers of high-power broadcast components. At the same time, problems started to develop with the Navy’s VLF/LF insulators, cables, and other high-voltage hardware that had been operating continuously for 20 to 30 years. Thus, the supplies of adaptable commercial components for use with Navy high-power transmitters decreased at the same time that the components in Navy systems needed to be replaced. Direct replacements were not available for much of the hardware because most of the manufacturers were either out of business or no longer making the same materials. This was a serious problem because the Cold War was in full swing and the VLF/LF system was the main link to submarines deployed as a component of the strategic triad.

Because of these issues, the Navy started a VLF/LF high-voltage research program in the early 1980s. The goal of the research program was to develop replacement parts and identify a way to increase the reliability of the VLF/LF transmitting stations. During the same period, the Air Force operated its own LF system for fail-safe communication to strategic bombers and agreed to a joint program with the Navy to fund the research. The program involved setting up a High-Voltage Test Facility (HVTF) at the site of the original Omega navigation system test station, Forestport, NY, and operated by the Air Force's Rome Air Development Center. The new test facility was designed by Andy Smith based on his experience with the Lualualei test facility (Smith 1980, 1981, 1982, 1986). A description of the Forestport HVTF is given in Chapter 5, with additional background and history provided in Appendices 5A and 5B.

At the same time, the U.S. was being forced by politics and financial pressure to close many foreign bases. Many of our overseas communications stations were closed and some of the remaining ones were upgraded to make up for the loss of coverage. Transmitter technology improved and older transmitters were sometimes replaced with newer, higher power ones without upgrading the antennas. This led to some serious insulator problems. Because of these and other problems caused by the aging of high-voltage components, a large portion of the Navy's VLF/LF high-voltage program was dedicated to solving operational problems.

Nevertheless, over the course of the several years of operation of the high-voltage program, the Navy conducted fundamental research on high-voltage design, with a focus on nuances associated with VLF/LF. It soon became clear that in the early days of radio and the Navy's VLF/LF system, designers primarily used information available from the power distribution industry. Computers were not available and extensive use was made of rules of thumb, simplified formulas, and large safety factors to ensure that the antennas would operate at high voltage. At some sites, the transmitters were replaced with new, higher power transmitters, and often the voltage limits of the antenna insulators were exceeded. It became obvious there was a need for more accurate knowledge of the voltage limits for insulators and other high-voltage hardware.

Professor Kreuger of Delft University of Technology in the Netherlands, in his book *Industrial High Voltage* (Kreuger, 1991) states that there are two things needed for high-voltage design. One is an accurate knowledge of the electromagnetic fields around an object, and the second is accurate information of critical field levels that cannot be exceeded. He states that "nowadays the first is readily available with the advent of modern computer technology but the second is not so easy to find." When the Navy's High Voltage project began, neither was readily available. As a first step to improve high-voltage design, the Navy funded a Canadian group to develop a computer program to calculate electrostatic fields. That group has now become one of the world's leading suppliers of electromagnetic solver computer programs.

So as time passed, tools were developed to identify the important parameters governing high-voltage designs for VLF/LF. Many fundamental experiments were conducted at Forestport, usually piggybacked on some other research effort, to try to understand the high-voltage design problem and develop design techniques. Additional data were obtained from measurements on specific pieces of hardware during testing prior to installation at some station. During this period, knowledge gained from the high-voltage program was used in the design of several new high-power LF stations. The knowledge developed by the high-voltage design facility led to the successful design of numerous pieces of high-voltage hardware. These are now in use at the Navy's remaining VLF/LF stations (10 in all). These hardware items include base insulator assemblies (BIA), tower lighting isolation transformers (TLIT), guy insulators, span insulators, feed through bushings, tuning inductors (helices), and interconnecting bus systems.

The method defining the design process is conceptually simple in that we determine the voltage limit experimentally for a given hardware component. This is not as easy as it sounds because there are many failure mechanisms and test conditions under which high-voltage tests must be conducted. The critical electric field strength that results in each kind of failure is determined from the measured breakdown voltage and the calculated electric field strengths. We have found that the corona onset voltage for VLF/LF is nearly the same as for 60 Hz, but the wet flashover voltage can be drastically different. In addition, we have found that there is much more power in corona, or any other breakdown phenomena, at VLF/LF than at 60 Hz. In general, due to these findings, the design principle for VLF operation is to operate without corona, unlike at 60 Hz where operation in corona is often tolerated. Consequently, many of the efforts described below concentrate on the determination of the critical electric field for corona onset under specific conditions.

The Air Force completely closed down its LF system in 1995 and had terminated all research work several years earlier (see Appendix 5A and 5B for background and history of the Forestport site). The Navy closed the test facility at Forestport in September 1996 but has recently completed a similar facility at the Naval Radio Transmitting Facility at Dixon, CA. Much of the high-voltage design work mentioned above was done under pressure to solve operational problems, and there was little time or funding available for documenting results. Therefore, during the interim, while the new facility was being developed, we have undertaken to document the findings and high-voltage design concepts obtained at Forestport.

ELECTRICAL BREAKDOWN OF AIR

Description

The electrical breakdown of air is caused by the presence of high electrical field strengths between charged conducting surfaces separated by air. When the electric field becomes strong enough, the molecules of air become ionized, forming plasma resulting in an electrical discharge. During electrical discharges, the plasma (ionized air) becomes a good conductor and produces heat, visible light and often audible noise.

For the case of a uniform electric field such as occurs in the gap between parallel plates, as the voltage between the plates is increased, eventually a voltage level will be reached such that a sudden spark will jump across the gap without any preliminary discharge; this is called breakdown of the gap. For this case, since the field is the same all the way across the gap, the ionized plasma (spark) propagates all the way across the gap (flashover), forming a conductor, which in effect shorts out the gap.

When the electric field is highly non-uniform, such as the field around a wire above ground, the field around the center conductor for co-axial geometry or the field at the top of a pole above a plane, a different effect occurs. In this case, the strong localized field causes the air to breakdown in a constrained region near the electrode. However, the field falls off away from the electrode and a spark cannot propagate across and short out the gap. This localized breakdown or discharge is called corona, after the bright ring of light around the sun, and can be observed visually as a faint bluish-white glow given off by the ionized gases. A sizzling or hissing noise and the distinctive odor of ozone often accompany corona. The magnitude of the voltage when corona is first observed is called the critical or onset level. As the voltage is increased above that level, the intensity of the observable effects increases.

Man-made electrical discharge often occurs in high-voltage systems, such as power distribution systems and high-power radio transmission systems. For most of these high-voltage systems, corona is undesirable for a number of reasons. Corona consumes power. Corona causes ultraviolet radiation and produces chemical byproducts (formed in corona and bombardment by energetic ions) that cause the deterioration of nearby materials (e.g., insulation and conductors). Corona discharge induces nonlinear currents in the antenna, which generate radio frequency interference. Corona generates sounds that can be irritating. It follows that knowledge of the factors involved in corona formation and how to prevent it are important high-voltage electrical equipment design considerations.

History

Electrical breakdown of air has been observed since early times, in the form of lightning and Saint Elmo's Fire, which is a glow that sometimes appears about ships' masts, flagpoles, and other high structures, most often during stormy conditions. Saint Elmo's fire is corona that forms about the sharp objects in the large electrical field that naturally occurs beneath charged clouds. It is rare, but such high fields and the resulting corona can occur even when there are no visible clouds.

Ben Franklin's experiments with electricity culminated in the famous kite-key experiment said to "discover" electricity in June 1752. Coulomb was probably the first to record the fact that air itself is conductive in about 1795. He proposed that all materials have a limit above which they will conduct electricity (Lyubimov, 1983). Not until around 100 years later was it discovered that particles of molecular size carrying charge, i.e., ions, were the source of this conductivity. J.J. Thomson at Maxwell's Cavendish laboratory measured the charge-to-mass ratio for an electron. This helped make it clear electrical current is mostly carried by electrons in a gas. Beginning in 1900, J. S. Townsend, a student of J.J. Thomson, discovered the laws pertaining to ionization and electric discharge in a uniform electric field. This work developed the foundations of our understanding of electrical discharges in gases.

Much of the early work on electrical breakdown and corona was motivated by the development of the electric power industry. Early in that development, it became clear that high-voltage transmission lines were desirable because line losses were inversely proportional to voltage. Consequently, there is a large body of literature describing observed corona and arc-over phenomena at 50 to 60 Hz, including many proposed theories of corona formation. There is much less information available for the VLF/LF range. Much of the VLF/LF information was gathered just after the turn of the century, driven by the desire to build very high-power radio stations. The earliest investigations in the VLF/LF frequency range noted the greatly increased power dissipated in corona and the other breakdown phenomena over that at power line frequencies of 50 to 60 Hz. Because of this, the deleterious effects of corona increase at higher frequencies.

DC and 60-Hz Investigations

The nature of the electrical breakdown of air is very complicated, and the study of it has resulted in a very large body of literature. The references used directly in the text are given in a Reference section at the end of the book. The literature in this area is extensive and there are many other references that we reviewed in the process of this effort. Most them are listed in a bibliography section also at the end of the book. In particular, there have been extensive investigations of corona and flashover at DC and 50 to 60 Hz in support of power distribution.

Townsend (1915), one of J.J. Thomson's students, made some of the early contributions to the understanding of electrical discharges in gases. This was followed by Loeb (1939, 1941, 1961, 1965),

Llewellyn-Jones (1957), and Cobine (1958). All these writers contributed materially to the understanding of the processes of electrical breakdown. Morgan and Morrow (1978) of the Commonwealth Scientific and Industrial Research Organization (CSIRO) at Sydney, Australia, provide a description of the effects of positive and negative DC, as well as 25- to 60-Hz AC potentials on corona onset and power loss. Meek and Craggs (1978) give an excellent summary of the important results included in the extensive literature on the investigation of electrical breakdown of gases up to that time.

F. W. Peek of the General Electric Company did early practical work leading to practical high-voltage design formulas. Peek produced a series of papers, (1911, 1922, 1927) on the law of corona and the dielectric strength of air. Most of his work was at power distribution frequencies near 60 Hz. He made measurements of the power dissipated in corona as a function of frequency in this range. He presents a formula for power dissipated in corona indicating it is proportional to frequency (Peek, 1929).

Fundamental work was also done in the former Soviet Union. For example, Aleksandrov (1957) provided a detailed account of observations and theoretical models to describe DC and AC corona at 50 Hz in cylindrical test facilities over a range of conductor diameters. Bogdanova and Popkov (1959, 1960) used a stroboscopic camera and radio noise sampler to investigate the details of corona within the cycle period at 50 Hz as the voltage is increased above corona onset. Similar to the earlier work of Peek (1929), they found a distinct difference between the character of the corona on wires during the positive and negative half-cycles. The negative corona consists of small tufts scattered along the wire, and positive corona consists of a dim uniform sheath as well as positive streamers. Negative corona has the lowest onset voltage for the wire diameters used and generates very little radio noise. As the voltage is increased above onset, the position of dominant corona current flow shifts toward and then into the positive half-cycle, similar to the effect of moving into the high-frequency region discovered by Kolechitskii (1967).

Bogdanova and Popkov found that the interfering radio emission on conductors of practical dimensions is created mainly during the positive half-cycle, when the positive corona has the form of local streamers. They also discovered that the positive streamers and hence radio noise can be drastically reduced by increasing the negative corona currents. This is done by putting smaller radii of curvature objects such as small bumps, hemispheres, or spheres on or near the surface, causing negative corona current to flow. The flow of negative corona current results in a sheath of positive ions, which shields the surface during the positive half-cycle, reducing or eliminating positive streamers. They suggest that a practical method for the application of this technique to power distribution systems would be to wind a thin wire in a spiral around the main current carrying conductor.

The impact of atmospheric humidity and wire surface moisture on corona onset and gap breakdown has been a difficult problem, with experimental data at times giving apparently conflicting results. Kuffel (1961b) has provided additional insight into this problem at power line frequencies. Normally, one might expect that the corona onset potential would decrease with humidity because the density of water vapor is less than that of air. However, the onset potential has been observed to increase for many conditions. For example, Kuffel shows a breakdown voltage increase of about 5% for gaps of 0.5 to 2 cm when the humidity was increased from 0 to 18 mm Hg.

The effect of humidity seems to vary with gap length. There have been unexpected variations noted for gap lengths in the region of 1 to 2 cm. Abdel-Salam (1985) has added further information on the impact of humidity. He shows significant increase in the ionization coefficients as well as

electron attachment coefficients as humidity increases. These two coefficients are key factors in determining the electrical breakdown fields. Calculations based on his model show that the corona inception voltage decreases with increasing relative humidity for thin wires (0.004 cm radius) while it increases for thick wires (1.4 cm radius). The effect of humidity on non-uniform field gaps is also discussed in Meek and Craggs (1978, p. 420).

The increase in corona onset voltage obtainable from bundled conductors has been treated by Miller (1956). More recent treatments of bundled conductors are given by Trinh et al. (1973), who consider voltages of up to 1100 kV. Hansen (1992) developed an accurate approximate formula to give the gradient on bundles (cages) of conductors.

Radio Frequency Investigations

There have been many investigations of both gap breakdown and corona formation at power distribution frequencies. A lot less literature exists on RF breakdown and corona, though some work has been done, primarily to develop design data for high-power transmitting systems. Heinrich Hertz was possibly the first to generate RF discharges, which occurred during his pioneering experiment to demonstrate the transmission and reception of radio waves. He discharged a spark gap connected across a resonant dipole antenna. Current flows through the discharge when the gap fires. This current exponentially rings down at the resonant frequency of the antenna. Later, continuously driven RF discharges were produced by Nicolai Tesla shortly before the beginning of the 20th century, using the self-resonant coil circuit that bears his name. The first investigations into radio frequency breakdown date back to the early days of radio. Algermissen (1906) measured spark voltages for ball gaps at frequencies in the megahertz (MHz) range using damped oscillations and found that the flashover voltage increased for frequencies above 1 MHz. Whitehead and Gorton (1914) investigated corona between 60 and 3000 Hz and found that the critical voltage decreased by as much as 3 to 4 percent at 2 kHz from that at 60 Hz. They also found some significant differences in the nature of the corona. For example, they found that thin wires would oscillate physically when in corona at the higher frequencies but not at 60 Hz.

Alexanderson (1914) also did some measurements at 100 kHz as did Clark and Ryan (1914). Ryan and Marx (1915), of Stanford University, studied RF corona at frequencies from 50 to 200 kHz. They found little if any frequency effect for the breakdown of a uniform field gap, but for non-uniform field gaps they found the breakdown (flashover) voltage to be much less at RF than at 60 Hz. They also found a large difference in the appearance of the corona at RF versus 60 Hz: “The radio frequency corona appeared to be very active, it was quite brilliant and noisy and gave off an appreciable amount of heat.” (Ibid. p 354) They also observed that a needle-point was rapidly melted and burned by RF discharge. These differences between 60 Hz and RF corona are due to the much larger power dissipated in corona at RF.

In the early 1920s, W.W. Brown (1923) used a 200-kW Alexanderson alternator to develop design criteria for high-voltage insulators at VLF frequencies (18 to 28 kHz). Peek did most of his work at power distribution frequencies near 60 Hz but he reports one test at 100 kHz, using the Alexanderson alternator, where corona losses were measured (Peek, 1929, p. 211). Of note is the early work on the power dissipated in corona done by Ryan and Henline (1924). They describe the hysteresis characteristics of corona and present some of the early work on calculating corona power. They investigated the frequency effect, although only in the range of power line frequencies, and found the power dissipation in corona increased approximately proportional to frequency. Schuman (1923) also published valuable measured breakdown data at power distribution frequencies. Goebler (1925)

measured the breakdown voltage in air between plate and ball electrodes at frequencies between 86 kHz and 120 kHz and found no frequency dependence.

Several investigators in the late 1920s and 1930s pushed the frequencies for corona experiments up to a few MHz (Meek & Craggs, 1978, chapter 8). Reukema (1928) provided data showing that the flashover voltage for ball gaps reduces with frequency up to about 15% at 60 kHz and then increases again at higher frequencies. Kampschulte (1930) and Lassen (1931) made measurements on the breakdown of non-uniform field gaps in the frequency range 50 Hz to 100 kHz.

As time went on, the technology for generating higher frequencies developed, and the investigation of electrical discharge at these frequencies followed. Seward (1939**)** presents data on electrical breakdown of air for frequencies from 50 to 900 kHz measured at the University of Liverpool. In this study, a reduction of up to 10% in the flashover voltage between spherical electrodes was observed. The reduction was approximately proportional to frequency for the lower frequencies, and flattened out as 1 MHz was approached. For needle points, ionization in the form of brush discharge always occurs before flashover, and a much larger frequency effect was observed, again flattening out as the frequency approached 1 MHz. In this case, the ratio of the flashover voltage at 900 MHz to that at 60 Hz was approximately 3.2. Seward suggests that this reduction in breakdown voltage is due to space charge buildup caused by slow-moving positive ions and suggests that the mechanism causing the buildup should be proportional to frequency.

In general, all these investigators found that the breakdown voltage is lowered more for non-uniform field gaps than for uniform field gaps. For breakdown between spheres or plates, several investigators reported a critical gap length below which the breakdown voltage was independent of frequency. The critical gap length is shorter for increasing frequency and corresponds roughly to the travel time for a positive ion across the gap during a half-cycle. Thus, the reduction at higher frequencies is assumed to be due to space charge buildup and the resulting field enhancement.

Other important contributions to the effect of frequency on corona in the VLF and LF frequency range were made by Smith and Gustafson (1961) at the Navy Electronics Laboratory**,** and Watt (1962) and A.N. Smith (1963) at DECO Electronics in Bolder, CO. These contributions were made in support of the development of the expanded U.S. Navy's VLF/LF broadcast system. Smith (1963) made extensive measurements of corona on wires at VLF and LF at various elevations from 5,000 feet to 14,000 feet. These measurements indicated that negative corona started first for small wires ($\leq$ No. 18 AWG) and positive corona started first for larger wires ($\geq$ No. 10 AWG). Smith's data shows that phase of the initial discharge pulses depends upon whether the discharge is positive or negative and how much the voltage is above the onset level. The reduction in corona onset voltage as a function of frequency reported by Smith (1963) is 5% for 15 to 20 kHz, 9% for 25 to 30 kHz and 14% for 45 to 60 kHz, consistent with Reukema (1928).

Of special interest is the work by Kolechitskii (1967), who made extensive, well-instrumented, measurements of corona on wires at frequencies between 10 and 100 kHz, with a few measurements at higher frequencies (probably in support of upgrading the USSR's VLF/LF transmitting systems). Kolechitskii also made measurements at 50 Hz using the same test setup. Corona onset was determined by monitoring the waveform of the current flowing through the gap and noting when corona current pulses started to flow. At VLF/LF the glow of the corona jacket at onset was observed to be much brighter than at 50 Hz and corresponded with corona current initiation. Koletchitskii said that ". . . at high frequencies the corona onset voltages can be determined quite reliably from the glow around the conductor." We have found this to be true as well.

Several interesting findings of Kolechitskii are described below:

1. He states that the onset voltage is practically independent of frequency up to 67 kHz and that Peek's formula applies for clean, smooth dry conductors. However, his data show a decrease in the critical surface electric field for VLF/LF of up to 5 % from that at 50 Hz, depending upon frequency and wire diameter. The difference was greater for larger wire diameters and lower frequencies. Some of the reduction was attributed to surface irregularities due to imperfect grinding. It was also observed that contamination such as dust or oil deposits decreases the onset voltage by 10 to 15%.
2. He found that the corona extinction voltage at VLF/LF was lower than at 60 Hz, and the difference was greater at higher frequencies.
3. He notes a difference in the visible nature of the corona at onset, and correspondingly the corona current waveform, as frequency increases. The phenomena can be divided into a low-frequency effect, a high-frequency effect, and a transition region. It is important to note that the frequency where this transition takes place is a function of the wire diameter, starting at lower frequency for larger wires.
   a. In the low-frequency effect region, the corona appears as a thin sheath near the wire, corresponding to the corona observed at DC for negative polarity (negative corona). When the voltage and current waveforms are examined, it is observed that the corona current flows for a small portion of the cycle near the peak of the negative half-cycle.
   b. In the high-frequency effect region, the initial corona consists of individual or clusters of thin branching channels having a length much greater than the wire diameter. These correspond to the corona streamers observed at DC for positive polarity (positive corona). In this case, examination of the voltage and current waveforms indicate that corona currents flow for a small portion of the cycle just after the point where the voltage crosses from negative to positive. These channels or clusters have an intact base on the wire and are spaced along the wire a distance somewhat greater than their length. They also tend to move about, around, and along the wire.
   c. In the transition region between the low-frequency region and the high-frequency region, both types of corona can be seen to some degree.

   Thus, when the frequency is well below the critical frequency, the negative onset voltage has a magnitude less than the positive onset voltage, and corona first starts to appear near the peak of the negative half-cycle. The corona observed in this case is similar to the corona observed with negative DC voltages. When the frequency is well above the critical frequency, the positive onset voltage is less than the magnitude of the negative onset voltage, and positive corona appears first.

   As the frequency is increased toward the critical frequency, a point is reached where both the positive and negative corona has the same onset voltage and both types appear. As the frequency is increased further, positive corona starts to form at a slightly lower voltage than negative corona. When this happens, the positive corona current starts after the voltage goes positive, at a point between the positive going zero crossing and the maximum positive voltage. As frequency is increased, this point moves toward the zero crossing. When it reaches the zero crossing, this marks the critical frequency and the transition to the high-frequency region.
4. Kolechitskii has empirically determined a critical frequency, dependent upon wire size, that defines the start of the high-frequency region, given by

$$f_{cr} = \frac{7.56}{r + .298 \cdot \sqrt{r}} \quad \text{kHz},$$

where r is the wire diameter in cm.

5. Kolechitskii determined that when operating in the high-frequency region, the corona region around the wire was at a distinctly higher temperature than when operating in the low-frequency region.

The most recent work at VLF/LF has been done at the Navy's Forestport HVTF. (Smith, 1986) including measurements of corona power loss (Watt & Hansen, 1992). There has also been recent work where the partial discharge technique has been applied to RF applications. In this work partial discharge was found to initiate at lower voltages at RF and caused considerably more damage than at 60 Hz, again due to the increased energy in the discharge at RF (Plessow & Pfeiffer, 1987).

There are many references to work done at higher frequencies than VLF/LF given in Meek and Craggs (1978, chapter 8). Of particular note is the work by Pim (1949**),** giving breakdown in air versus gap length for parallel plates at frequencies from 300 kHz to 100 MHz. For small gaps, the breakdown voltage is nearly the same as at 60 Hz. However, as the gap is lengthened, a critical length is encountered at which the breakdown voltage decreases somewhat with increasing gap length. This is believed to be due to ion mobility being slow enough to allow space charge buildup within the gap. For a given gap length, the amount of space charge buildup is greater at higher frequencies. The presence of water is known to decrease positive ion mobility (Chalmers, 1967, p 86). Thus, the presence of moisture would tend to decrease the frequency at which a given gap experiences space charge buildup. This effect is believed to be part of the explanation for the variability and general decrease in observed corona onset voltage at VLF/LF.

MacDonald (1966) gives a good history and summary of the work on breakdown at microwave frequencies. Olsen and Stimpson (1988) treat the RF radiation produced by corona, with particular emphasis in the VHF/UHF range.

SUMMARY

Unfortunately, the data given in the literature describing the frequency effects of electrical breakdown are often confusing and sometimes misleading. Some of the problems with the data stem from difficulties with measuring environmental factors in the early days. Some are caused by not accounting for humidity. Some are due to voltmeter calibration errors. For example, the earlier measurements used ball gaps to measure the voltage, and these are subject to numerous environmental factors and frequency effects unknown at the time. Some inconsistencies resulted from the proximity of other conductors, which cause the actual onset field in the experiment to be different than that calculated by simple geometry. Anomalies also are caused when the air is contaminated with blowing snow in the winter or dust and pollen in the summer.

All these factors can change the apparent corona onset values, and some of them are frequency dependent. For example, small wire diameters (1 cm and above) appear to be much less sensitive to surface and whether conditions than larger cables. The effect of humidity at the higher frequencies is not the same as at power line frequencies, which has led to much of the confusion about the frequency effect. In addition, residual ionizing sources or materials can appear to reduce onset values at higher frequencies. Another source of confusion is that the frequency variation of corona onset is very different than it is for flashover due to space charge buildup at the higher frequencies.

Most available data indicate that VLF/LF corona onset occurs at nearly the same, or within a few percent of, the voltage at power distribution frequencies. However, the RF flashover voltages are quite often greatly reduced over that at power distribution frequencies. This has led to much confusion about the differences between 60 Hz and VLF/LF high-voltage effects.

There were no data indicating the effect of humidity on the corona onset levels at VLF/LF. A limited amount of data on the corona onset levels for rain or spray wet conditions had been developed in conjunction with insulator tests over several years at the Navy's Forestport HVTF. Although humidity investigations were not a specific part of these tests, we observed that "dry" measurements could not be made accurately following wet tests. If the test cell was wet, even though the test piece was dry, the onset voltages were significantly reduced, indicating that increased humidity decreases the onset of breakdown at VLF/LF. This is the opposite of the effect at DC and 50 to 60 Hz.

CHAPTER 2 THEORY OF ELECTRICAL BREAKDOWN

INTRODUCTION

Simple Geometric Configurations

Electrical breakdown of air or other gases occurs when the electric field exceeds the breakdown (dielectric) strength of the gas. Accurate knowledge of the electric field is required to analyze and understand the levels at which breakdown phenomena occur. The original experiments were done before the advent of the computer. The experimenters used simple geometric configurations having analytic solutions for the electric field to determine the breakdown strength of gases.

This chapter discusses the original experiments and the theories that were derived from them. In order to understand the results and implications of these experiments, it is important to understand the electric fields for these configurations. This chapter starts with a discussion of the electric fields for simple electrode configurations. Chapter 4 has a more thorough discussion of the calculation of electric fields, including more complicated configurations for which analytic expressions for the fields exist and the use of computers to calculate the fields for configurations for which analytic solutions do not exits.

It is important to understand that the electric fields are all calculated assuming no space charge. Thus, these fields apply to the condition before breakdown or where no charged particles are present. After breakdown, space charge is generated, which can significantly modify these fields.

Uniform Field Gap

The simplest configuration is that of parallel plates. For locations not near the edges, the field is uniform between the plates. An example of this configuration is shown in Figure 2-1A. The critical dimension is the distance between the plates, sometimes referred to as the gap length, denoted by l. The electric field within the gap is given by the voltage difference between the plates V, divided by the gap length l:

$$E = \frac{V}{l} \quad \text{Volts/meter.} \tag{2-1}$$

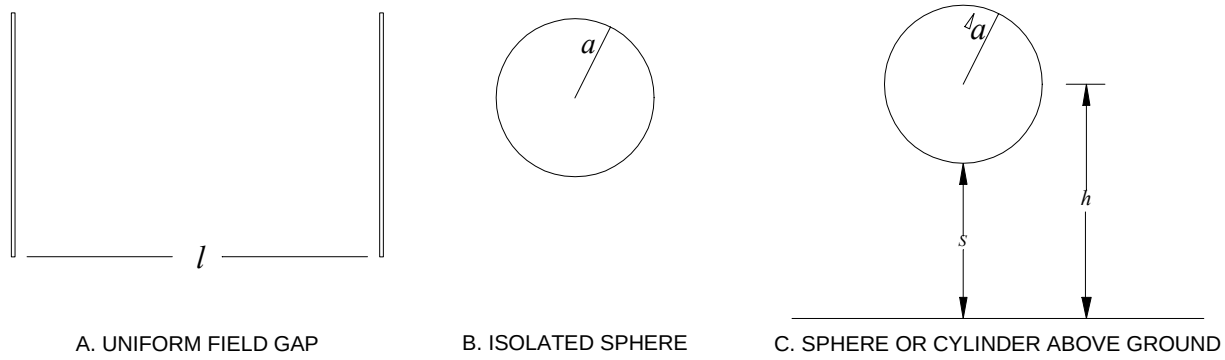

Figure 2-1. Canonical configurations. Simple geometric configurations.

Isolated Sphere

Most configurations do not have uniform fields. For these configurations, the maximum electric field is the most important parameter for determining the breakdown limit. Breakdown is also a function of the rate at which the fields fall off away from the electrode. Note that the maximum field always occurs on the surface of the electrode. The simplest configuration having non-uniform fields is a charged sphere in free space. A drawing of this configuration is shown in Figure 2-1B. For this configuration, the electric field outside the sphere is given everywhere by:

$$E = \frac{V}{R} \qquad \text{volts/meter for R} \geq a$$

where V is the potential on the sphere relative to free space,
R is the distance from the center of the sphere and
a is the radius of the sphere.

Substituting the radius of the sphere into the above equation gives the electric field on the surface of the sphere:

$$E = \frac{V}{a} \tag{2-2}$$

Sphere above Ground

The configuration of a sphere above ground is shown in Figure 2-1C. Two dimensions define this configuration, the radius of the sphere, *a*, and the height above ground, *h*. The dimension *S*, the separation between the ground and the sphere, *S*, is sometimes used instead of *h*. The formula for this case is given in Equation 2-3. The form of the equation is similar to Equation 2-2, although the solution is not so simple because the function *G* (*h*/*a*) is an infinite series. The method of calculating the charges and fields for a sphere above a ground plane is derived in Chapter 4 and the results are plotted in Figure 4-3.

$$E = \frac{V}{a} \cdot \frac{1}{G(h/a)} \qquad \text{volts/meter, for R = a} \tag{2-3}$$

Infinite Cylinder above Ground

The configuration of an infinitely long cylinder, parallel to and above a ground plane, has a simple expression for the field on the surface of the cylinder. This configuration is also illustrated in Figure 2-1C. Similar to the sphere, the important dimensions are the radius of the cylinder, *a*, and the height of the center of the cylinder above the ground, *h*. The maximum field occurs on the bottom of the cylinder, and when the cylinder is well above ground, it is given by Equation 2-4.

$$E = \frac{V}{a} \cdot \frac{1}{\ln(2h/a)} \tag{2-4}$$

The general fields for this configuration are also derived in Chapter 4.

Summary

The maximum electric field on the electrode is summarized for the four simple geometric configurations in Table 2-1. The last two cases, the sphere and cylinder above a ground plane, are respectively equivalent by image theory to opposing spheres or cylinders in free space, with equal and opposite voltages on them.

The examples given above illustrate the fact that the general expression for the electric field at a point on the surface of any object can be written as (see Chapter 4):

$$E = \frac{V}{b} \cdot \frac{1}{G(h/b)}, \tag{2-5}$$

where b is a dimension that defines the size of the object such as the radius of the sphere or cylinder in Equations 2-2, 2-3, and 2-4.

The units for the electric field are volts per unit length, which arise due to the first term in Equation 2-4. The second term in Equation 2-4, the function G (h/b), has no units and depends only on the ratio of the dimensions defining the configuration.

Table 2-1. Electric field formulas for simple geometric configurations.

Configuration	Important Dimensions	Electric Field Formula	Figure
Uniform Field Gap	Length l	$E = \frac{V}{l}$	2-1 A
Isolated Sphere	Radius a	$E = \frac{V}{a}$	2-1 B
Sphere above ground	Radius a Height h	$E = \frac{V}{a} \cdot \frac{1}{G(h/a)}$	2-1 C
Cylinder above ground	Radius a Height h	$E = \frac{V}{a} \cdot \frac{1}{\ln(2h/a)}$	2-1 C

There are two cases shown in Table 2-1 where there is only one defining dimension. The first is the uniform field gap, defined by the length of the gap, l, and the second is the isolated sphere, defined by the sphere radius, a. For both of these cases, the function G is a constant equal to 1.

In the other two examples shown in Table 2-1, the sphere above ground and the cylinder above ground, there are two defining dimensions. In such a case, G is strictly a function of the ratio of those two dimensions.

The results are similar if there are more than two defining dimensions. For example, a toroid above ground has three defining dimensions, which are the major and minor radii of the toroid (a and b) and the height (h). For this case, the function will be a function of two ratios G (h/a, h/b). For other cases, with n defining dimensions, G will be a function of n-1 ratios.

For any configuration, the field at a point can be written in the form of Equation 2-5. This is a very useful result, because it means that the field is known when the dimensions are scaled. For example, suppose configuration one has a field E_1 for a given voltage V_1. Configuration two is the same except that all the dimensions have been multiplied by a scale factor S and has an applied voltage V_2. The following derivation uses the fact that the field at any point is given by Equation 2-5.

$$E_1 = \frac{V_1}{b} \cdot \frac{1}{f(h/b)}$$

$$E_2 = \frac{V_2}{S \cdot b} \cdot \frac{1}{f(h/b)}$$

Taking the ratio of these two equations, it follows that

$$\frac{E_2}{E_1} = \frac{V_2}{V_1 \cdot S} \tag{2-6}$$

This knowledge of how the field changes as the dimensions are scaled, expressed in Equation 2-6, is important and will be applied later on in this chapter.

BREAKDOWN IN UNIFORM FIELDS

Paschen's Law

One of the earliest discoveries regarding the electrical breakdown of gases is Paschen's law, discovered by Paschen (1889). This law, in its simplest form, states that for a given gas the breakdown voltage across a uniform field gap is a function of the product of gas density times gap length. For convenience we use the relative gas density δ, which is the absolute gas density divided by the absolute gas density at a standard pressure and temperature (STP). For dry air and STP of 20° C and 760 mm Hg, the absolute air density is 1.205 kilograms/cubic meter, while for STP of 25° C and 760 mm Hg, absolute air density is 1.185 kilograms/cubic meter. At STP, $\delta = 1$ (Chapter 3, esp. Equation 3-1).

Using relative gas density, Paschen's law can be written as:

$$V_s = f(\delta \cdot l) \tag{2-7}$$

where V_s is the breakdown or sparking voltage,
δ is the relative gas density, and
l is the gap length (Figure 2-1A).

The function f depends on the particular gas and must be determined empirically. Plots of f are called Paschen curves. However, because f is a function only of $\delta \cdot l$, a single series of measurements with varying gap spacing, taken at one density, defines the breakdown strength of the gas for a wide range of densities and gap lengths. Similarly, a single series of measurements with one gap length but varying density defines the breakdown strength of the gas for a wide range of densities and gap lengths. Paschen's law has been verified experimentally, over wide ranges of temperature and pressure for many gases, including air. There are gases where Paschen's law is not strictly obeyed, but they are unusual exceptions.

For most gases, the deviation from Paschen's law occurs at very high and very low density. In air, Paschen's law has been shown to be true over a range of density far wider than occurs in the earth's atmosphere. The upper limit of Paschen's law in air is approximately 10 atmospheres. The lower limit occurs when the pressure is so low that the probability of collision between an electron and an air molecule within the gap is small. This corresponds to a vacuum and means that most electrons cross the gap without colliding with anything. Thus, the lower limit is a function of pressure and gap length. For practical gap lengths, Paschen's law remains valid until the pressure reaches a vacuum with pressures less than 1 torr (1 mm Hg).

The breakdown voltage for gases is generally plotted as a function of $\delta \cdot l$. Figure 2-2 shows measured data for the uniform field breakdown strength of air (Paschen curve) plotted in this manner. The Paschen curves for most gases are similarly shaped and include a minimum, which for air is 327 volts. The presence of this minimum has unusual consequences. When the voltage is less than this minimum, a spark cannot form in a uniform field gap, no matter how small the gap or what the air

density. When $\delta \cdot l$ is less than the minimum the spark discharge will take place over the longer of two paths because the breakdown voltage is less for the longer path (see Figure 2-2). The reason for the minimum is discussed in the section on Townsend's Theory below.

Even a few parts per million of impurities, such as aerosol water droplets, dust, or pollen can significantly reduce the effective dielectric strength of a gas because of field distortion caused by the particles or by charge buildup on the particles. The addition of small amounts of other gases such as water vapor, sulfur hexa-fluoride, or freon can also significantly alter the dielectric strength of a gas. For example, the addition of 5% sulfur hexa-fluoride increases the dielectric strength by 10%, while the addition of 30% sulfur hexa-fluoride increases the dielectric strength of air by a factor of two. The addition of other components changes the gas composition, and therefore the function *f* changes. Thus, determination of the function *f* for one gas gives no information about that function for a different gas.

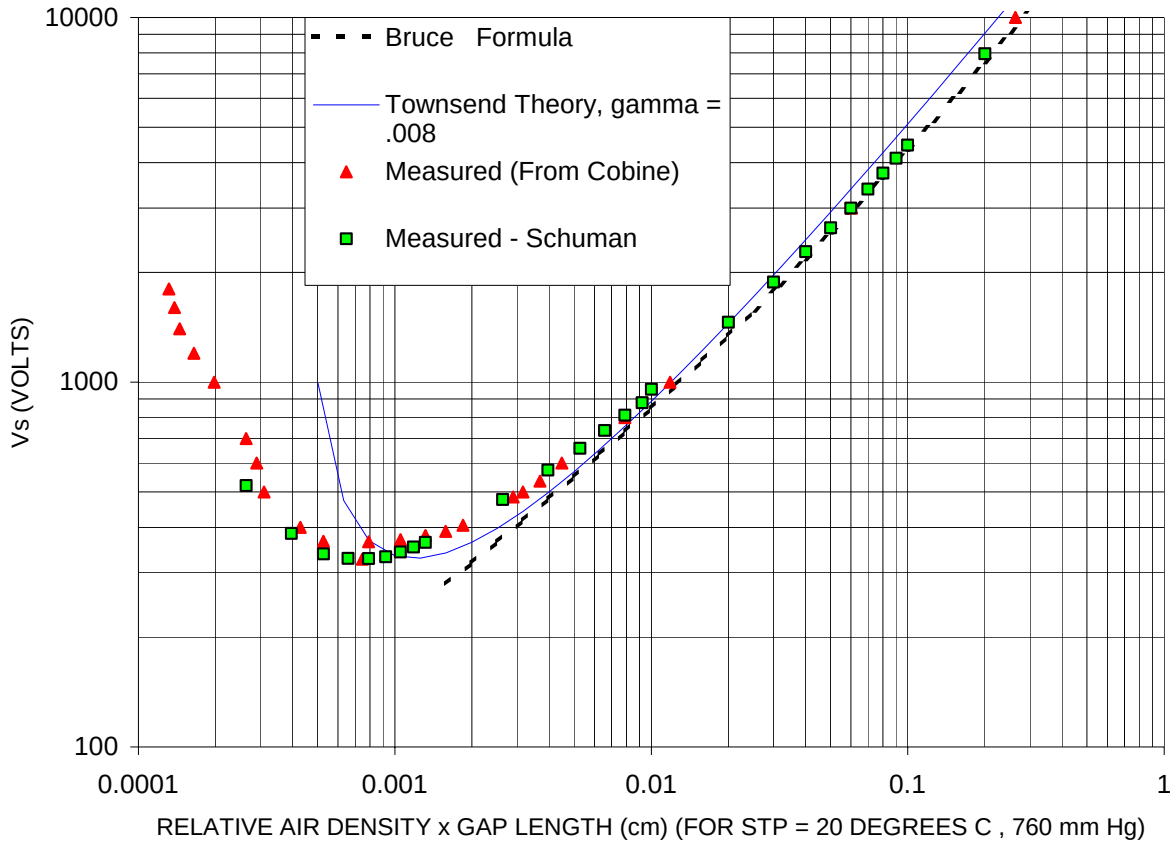

Figure 2-2. Paschen's law, breakdown of air in uniform field gaps.

Similarity

Dimensional analysis often reveals similarity relationships, which are useful in understanding complicated problems having a relatively large number of experimental variables. It is based on the fact that any relationship between physically measurable quantities must have consistent dimensions. It follows that these relationships can be reformulated in terms of non-dimensional quantities over the range of validity. The number of such non-dimensional quantities is smaller than the number of variables, and often experimental or theoretical relationships can be more easily understood when

expressed in terms of these quantities. MacDonald has an excellent description of this theory, including a proof of the reduction in the number of variables (MacDonald, 1966, pp. 7–13).

Paschen's law is an example of a similarity relationship. This law expresses the breakdown voltage between parallel plates as a single curve a function of $\delta \cdot l$ instead of families of curves parametric in δ or l (Figure 2-2). Because f is a function only of $\delta \cdot l$, it defines a similarity relationship (sometimes called similitude). For this application, two situations are "similar," i.e., have the same breakdown voltage, if they have the same value for the parameter air density times gap length ($\delta \cdot l$).

As previously mentioned, this similarity relationship allows one to relate measurements taken at one air density to measurements taken at a different air density. For the case of parallel plates, this relationship is very simple, defined by Equation 2-1, which gives the sparking (or breakdown) voltage as a function of $\delta \cdot l$. For example, a gap of length l_1 was determined to breakdown at a voltage V_1 with relative air density δ_1. The breakdown field is given by $E_{c1} = V_1/l_1$. This can be related to a measurement made at another density using Equation 2-1 as follows.

The sparking or breakdown voltage is unchanged when the product $\delta \cdot l$ remains the same. Thus given another density δ_2, then the length of gap l_2 that would breakdown at the same voltage is defined by:

$$\delta_1 \cdot l_1 = \delta_2 \cdot l_2$$

or

$$l_2 = (\delta_1/\delta_2) \cdot l_1.$$

It is important to note that even though the breakdown voltage for these two cases is the same, the gap length, and therefore the electric field at breakdown, is different, given below:

$$E_{c2} = V_1/l_2 = E_{c1} \cdot (\delta_2/\delta_1).$$

For example, if the density were increased by a factor of two, similarity implies that the sparking voltage will be the same if the gap length is half, and therefore the electric field is double the original value.

This relationship is useful for relating measurements of the sparking voltage made at one gas density to the sparking voltage at some other gas density. For example, measurements taken at ambient temperature are often converted to values that would occur at standard temperature and pressure. For this application, the first density (δ_1) is the relative density for the measurement and the second density ($\delta_2 = 1$) is the relative density at standard temperature and pressure.

The similarity relationship derived from Paschen's law applies only to the case of a uniform field. However, it can be generalized, as will be shown later.

Townsend's Theory

Residual Ionization

The electrical breakdown of air is a process that ionizes the air. The amount of ambient ionization present before breakdown is an important part of this process. There are several natural causes of the ionization of air, such as cosmic rays, local radioactivity, and ultraviolet photons. These produce ions and electrons, which cause the air to be slightly conductive, and which can reduce the electrical field strength required for breakdown. Ionization rates versus elevation above the earth's surface are shown in Figure 2-3. The rapid production of ion pairs near the earth's surface is caused by the radioactivity of the earth and can cause the air conductivity to be relatively low there. At about 10

meters above sea level, the ionization rate is about 10 ions per cubic cm per sec and the residual ionization is about 1000 ions per cubic cm (Pierce, 1958).

The magnitude of the atmospheric conductivity at DC varies from about $2 \cdot 10^{-14}$ mhos/meter at the earth's surface to 10^{-4} mhos/meter at heights of 80 km and even greater in the ionosphere, as shown in Figure 2-4 (Clark & Kraakevik 1958, pp. 61 & 75; Watt 1967). The effective conductivity for radio frequency is somewhat different because it is a function of frequency and in some cases the earth's magnetic field.

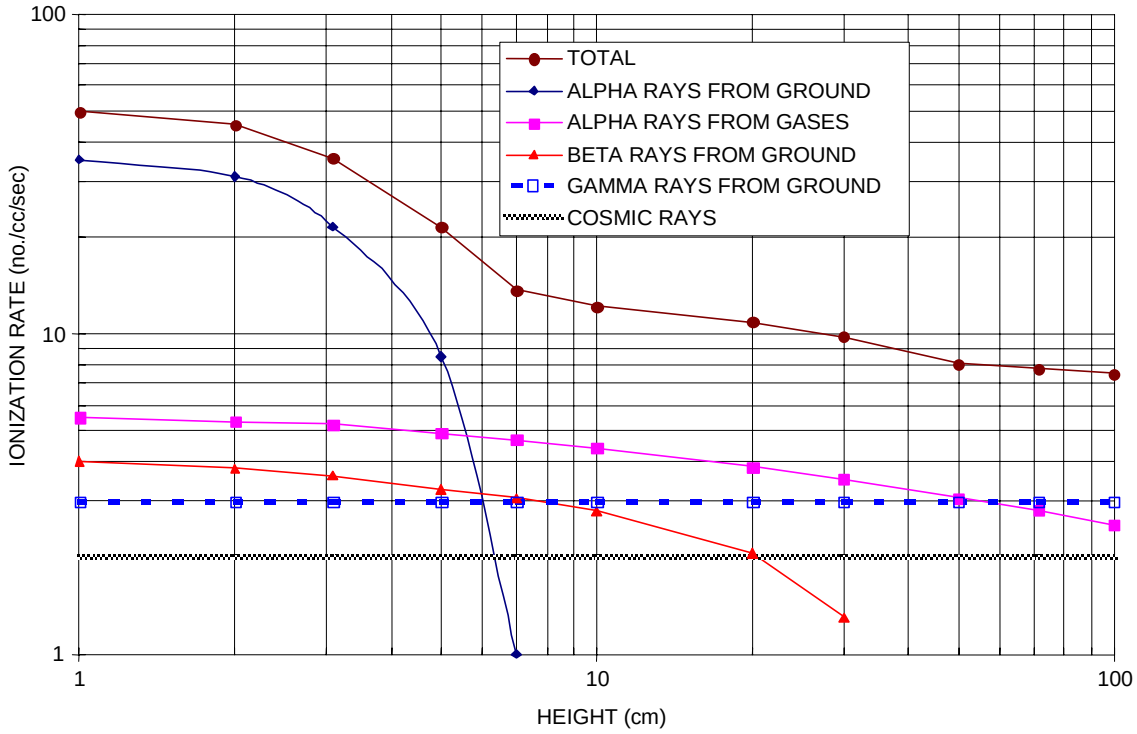

Figure 2-3. Effective conductivity of the earth's atmosphere.

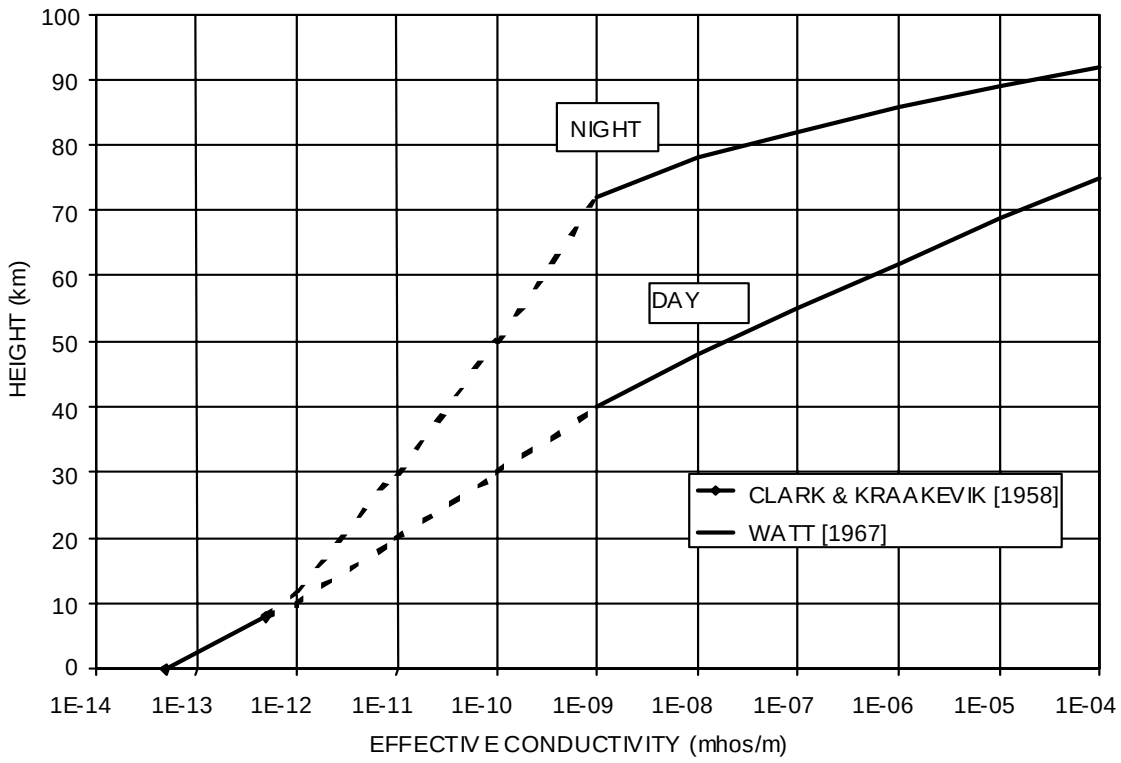

Figure 2-4. Atmospheric ionization rates over land.

Velocity

In a vacuum where there are no collisions, the velocity of a charged particle subjected to the force caused by an electric field increases continuously until relativistic effects take over. In a relatively dense gas, collisions play an important role and limit the velocity the charged particle can achieve. For this case, it has been found that heavy ions acquire a constant mean velocity (sometimes called drag velocity or mobility) that depends on the field, the pressure and the nature of the ions and the gas (Papoular, 1965). The kinetic theory of gases indicates that the collisions cause the velocity to be strictly a function of (E/d), where E is the electric field and d is the density of the gas (often stated as pressure but actually density). This is because the velocity of an ion increases until the drag force equals the accelerating force due to the electric field. The collision rate is proportional to the gas density. For low intensity values of E, the resistance for heavy ions is proportional to the collision rate and the resulting drift velocity is directly proportional to (E/d). At higher values of E, the resistance increases and eventually the asymptotic velocity becomes proportional to $(E/d)^{1/2}$ (Raizer, 1991, Chapter 2). For convenience, these functions can be reformulated in terms of (E/δ), where δ is the relative gas density compared to a standard temperature and pressure.

Electrons have much less mass than ions and therefore have much larger mobility. Nevertheless, their velocity in a gas is also a strict function of (E/δ); but because of their small mass it approaches $(E/\delta)^{1/2}$ at much lower field intensity. Numerous experimental results have confirmed this theory to first order (Papoular, 1965, p. 94; Cobine, 1958, p. 37).

Electrical Breakdown

If the field strength applied to the gas is large enough, the gas begins to ionize and significant current starts to flow. This is called electrical discharge through the gas, or breakdown, which can be

divided into two general types, self-sustained and non-self-sustained. The non-self-sustained discharges are "dark," usually generating no visible light. The transition to a self-sustained discharge is called a spark and usually occurs very suddenly. A non-self-sustained discharge requires that there be continuous residual ionization (free electrons) present in the gas. Normally, this ionization occurs due to radiation or the photoelectric effect from external light sources. A non-self sustained discharge will be eliminated when the source of ionization is removed. A self-sustained discharge generates its own ionization and will continue even when the residual ionizing effect is removed.

Parallel Plate Experiment

If a DC voltage is placed across a set of parallel plates, a uniform electric field is set up between them. When a conductive medium is between the plates, electric current flows between them. For air, this current is carried by the residual ions in the air. The observed current varies in a predictable way, with voltage as shown in Figure 2-5. The upper curve is for a higher level of residual ionization. At very low voltages, the current is linear with voltage. However, as the voltage increases, the current eventually levels off at a constant value, known as saturation, such that further increases in voltage do not increase the current. However, the voltage eventually reaches a point where the current starts to increase exponentially (multiplication). Eventually a voltage is reached where the current starts to increase at a more rapid rate than exponential (meta-exponential). Slightly above this level, sparking (flashover) occurs with corresponding light emission and noise.

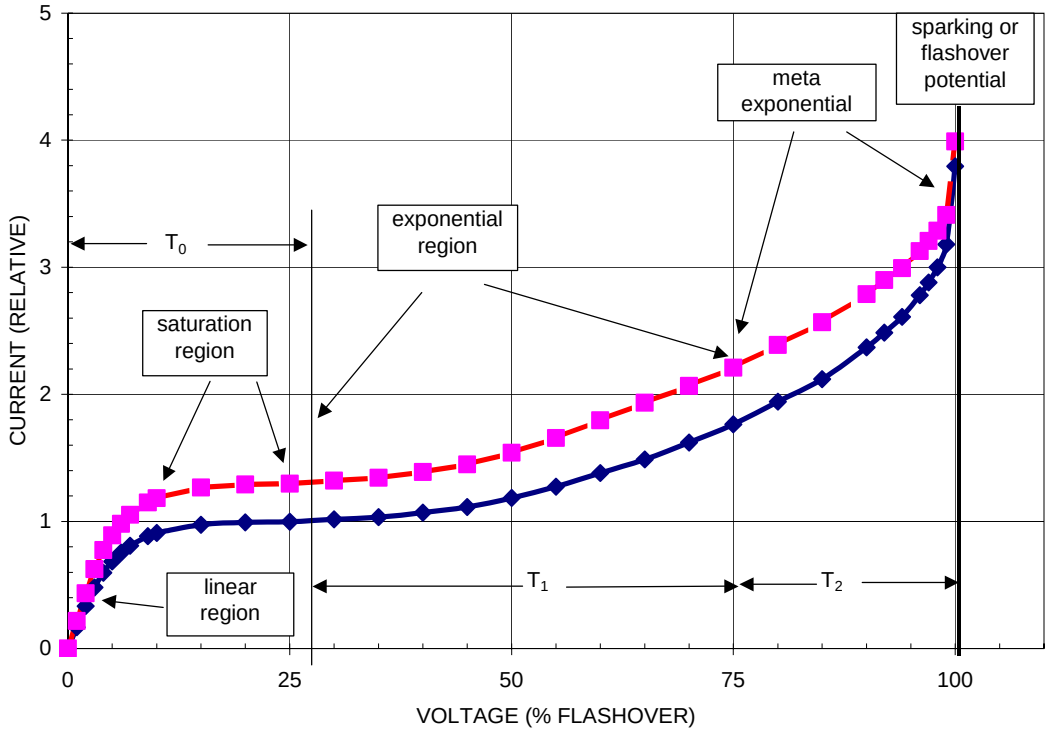

Figure 2-5. Townsend current growth.

The discharge process is generally divided into three regions T0, T1, and T2 after J.S. Townsend, who conducted early and extensive investigations of these phenomena at the Cavendish laboratory. Townsend developed a theory that explains much of the observations. (Cobine,1958, p. 143, Townsend, 1915). We further subdivide these three regions as follows: (T_{0A}) linear, (T_{0B}) saturation, (T_1) exponential, (T_{2A}) meta-exponential, and finally (T_{2B}) breakdown (see Figure 2-5).

It is interesting that if another source of ionization such as ultraviolet or a radioactive source is used to introduce primary electrons, the saturation current increases but the breakdown voltage remains the same. In addition, the current that flows in the Townsend discharge regions, T_1 and T_2, ceases as soon as the external ionizing source is removed and hence is not a self-sustained discharge. When the voltage reaches the critical or sparking voltage, V_s, the current increases very rapidly and a spark occurs followed by one of the types of self-sustaining discharges, such as a glow or arc discharge. The nature of the self-sustained discharge depends on the characteristics of the discharge path and the impedance of the electric circuit.

Linear Region

In the first region, the current is linearly proportional to voltage, which results from the ion velocity being proportional to the E field. Assuming a uniform distribution of residual ionization within the gap, the number of ions reaching an electrode is directly proportional to this velocity, which is proportional to the E field, which is proportional to the voltage across the gap. This remains true as long as the rate of collection of the ions is less than the rate that they are created within the volume of the gap.

Saturation

The second region, saturation, corresponds to the situation where the velocity is fast enough to collect all the ions created within the gap volume. For this case, an equilibrium condition exists such that the ions are collected by the plates at the same rate they are created within the gap volume. The saturation current (i_o) is limited by this rate. Figure 2-5 shows curves for two different saturation currents, corresponding to two different residual ionization rates. For example, when the majority of residual ionization is generated by light striking the plates the current will be proportional to the light intensity. This is the phenomenon that causes the operation of a photoelectric tube. Figure 2-5 shows that the sparking or flashover voltage is the same for the two different cases. Thus, the flashover voltage is independent of the saturation current and hence the residual ionization rate.

Multiplication (Exponential)

As the electrons move across the gap, they collide with the oxygen, nitrogen, and other molecules in the air. Most of these collisions are elastic collisions, and the electron loses only a small part of its kinetic energy in a collision. However, as the field strength increases, the velocity of the electrons increases, causing non-linear reactions during collisions. Occasionally, an electron may strike an atom sufficiently hard that excitation occurs and the atom shifts to a higher energy state, with a corresponding loss of kinetic energy for the electron. The excited atom reverts to its normal state later by releasing one or more photons. Sometimes the atoms are excited into a nearly stable (meta-stable) excited state that lasts considerably longer (10^{-3} sec) than the normal lifetime (10^{-8} sec).

At higher field strengths, the electron velocity can attain a velocity great enough to free another electron during a collision with an atom or molecule. The field strength is strong enough such that between collisions an electron can accumulate energy equal to or greater than the ionization potential of the atoms and molecules in the air. This marks the beginning of the third region, electron multiplication. At this field strength, some collisions “liberate” electrons, resulting in two slow electrons. The field accelerates the liberated electrons, which strike other atoms or molecules, thus repeating the process repeatedly. This results in an exponential growth (avalanche) of electrons (and corresponding positive ions).

Avalanches are the primary mechanisms of electrical breakdowns in gases and have been the object of considerable study (Townsend, 1915). The currents in avalanches can be observed as small impulses with very fast raise times, called Trichel pulses after another of J.J. Thomson's students (Trichel, 1938). Electron avalanches have been photographed using the Wilson cloud-chamber technique, which causes water droplet condensation on the charges in the avalanche (Raether, 1964). They are cone-shaped and, because of electron dispersion, have a hemispherical head similar to an ice cream cone (Raizer, 1991, p. 331). A conceptual diagram of one of these avalanches is shown in Figure 2-6. Note that as the electrons travel across the gap, they leave behind slower positive ions.

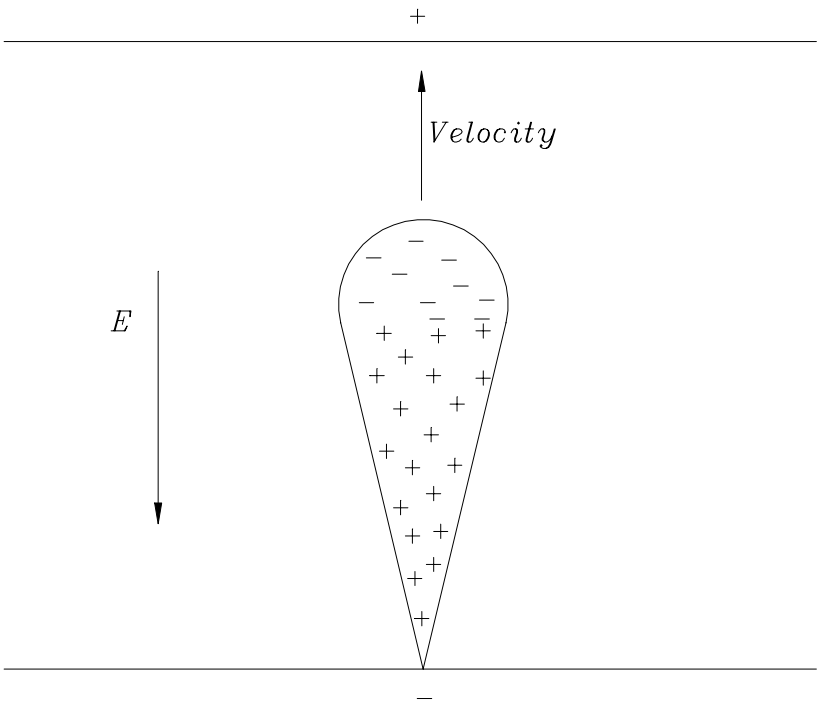

Figure 2-6. Shape and charge distribution of an electron avalanche.

The collisions in the avalanches create new ion-electron pairs. This is known as field-intensified ionization, which enables the current to increase beyond the saturation-level current. In a uniform electric field, the number of ions grows exponentially with the distance the electrons travel. Townsend found it convenient to characterize these phenomena in terms of the number of ions formed per unit path length along the field, as (α cm^{-1}). This is called Townsend's primary, or first, ionization coefficient.

Under these conditions, the average current increases above the saturation level and is given by:

$$i = i_0 \cdot e^{\alpha \cdot l}$$

where i is the total current,
i_0 is the saturation current,
α is the first Townsend coefficient, and
l is length of the gap.

The value of α can be determined from the slope of the curve in the T_1 region on a log-log plot.

This coefficient, α, is proportional to the number of collisions per centimeter of travel of the electron, which is just the inverse of the mean free path length, λ (cm). It is also a function of the energy obtained by the electron in that distance, which is equal to the electric field times the mean free path length:

$$\alpha = \frac{f(E \cdot \lambda)}{\lambda} .$$

Townsend was able to show that the ionization in T_1 region is due to electrons acting alone. He discovered that in intense electric fields, the electrons do not attach themselves to neutral particles to form ions and therefore electrons must be the sole source of ionization in the T_1 region discharge.

Townsend's derivation and most textbook discussions use the parameter pressure, and assume a standard temperature. However, the correct parameter is gas density. For convenience, we have converted these equations into a form that uses normalized or relative gas density.

Since the mean free path is inversely proportional to relative gas density, δ, the ionization coefficient can be expressed as:

$$\frac{\alpha}{\delta} = f\left(\frac{E}{\delta}\right) .$$

Townsend found that a smooth continuous curve was generated when measured values for the ratio α/δ are plotted as a function of E/δ, for a wide range of δ and E. This verified that the equation is true and that all the factors involved are accounted for by the equation (Cobine, 1958, p148). Using the, then newly developed elementary gas theory (Loeb, 1927), Townsend was able to derive a theoretical form for the function $f(E/\delta)$:

$$\alpha = \frac{1}{\lambda} \cdot e^{-\frac{V'_i}{E \cdot \lambda}}$$

where V_i' is the effective electron ionization potential for the gas molecules in electron-volts.

Townsend adjusted the values of the constants so that the values of α/δ fit the experimental results over a limited range. An ionization potential of 25 volts gave the best fit to experimental data for air at STP. This is considerably higher than currently accepted values and is probably due to his assumption that the probability of ionization is zero when electron energy is below V_i' and unity when electron energy is above V_i'. Townsend used several simplifying assumptions in this derivation, including (1) electrons are the sole source of ionization, (2) electrons do not gain energy by collision, (3) the field is strong enough so that electrons always move in the direction of the field, and (4) the probability of ionization is zero for energies less than the ionization energy (eV_i') and unity for greater energies. These assumptions are not correct. However, this simple theory was quite successful giving results that agreed well with measurement over limited ranges. This success is probably due to compensating effects in the assumptions (Cobine, 1958, p. 150).

Townsend's equation is normally rewritten as shown below, where p is pressure in Torr, while A and B are constants that are dependent on the type of gas.

$$\alpha = A \cdot p \cdot e^{-\frac{B \cdot p}{E}} \qquad (2\text{-}8)$$

Measured results are available for the values of A and B in various gases (e.g., Cobine, 1958, p. 149, Raizer, 1991, p. 56). For air at 20° C, they are commonly given as:

$$A = 14.6 \text{ cm}^{-1} \cdot \text{Torr}^{-1} \text{ and } B = 365 \text{ V} \cdot \text{cm}^{-1} \cdot \text{Torr}^{-1}.$$

The equation for α can be converted into terms of relative density, δ, for standard conditions. Assuming STP, defined by T = 20° C, and p = 760 Torr, and substituting for pressure gives:

$$\alpha = A \cdot 760 \cdot \delta \cdot e^{-\frac{B \cdot 760 \cdot \delta}{E}} .$$

Figure 2-7 shows a plot of α versus δ using the above values of A and B in air, for two fixed values of E. Note when E is fixed, there is an optimum density at which α is maximum. This occurs because at high density the mean free path is short and therefore only a little energy can be absorbed between collisions. As a result, little ionization takes place. At low density, the mean free path is large and an electron can absorb adequate energy for ionization, but the probability of striking a gas molecule becomes small and little ionization takes place. In between, the ionization rate increases and reaches a maximum where the energy absorbed and the probability of collision balance out to maximize ionization.

Stoletow (1890) had observed this effect at about the same time as Paschen's law was discovered. Stoletov found that if the gas pressure in a photoelectric tube is varied, there is a pressure for which the current reaches a maximum. His experiments resulted in the following expression for the optimum pressure:

$$P_m = \frac{E}{372} .$$

This expression can be derived from Townsend's equation for α by setting the first derivative equal to zero, giving:

$$P_m = \frac{E}{B} .$$

The theoretical derivation of this expression was one of the early successes of the Townsend theory (Cobine, 1958, p. 152).

The value of E/δ at the minimum of the Paschen curve corresponds to Stoletov's point, where the electron multiplication factor, α, is maximum (Raizer, 1991, p. 134).

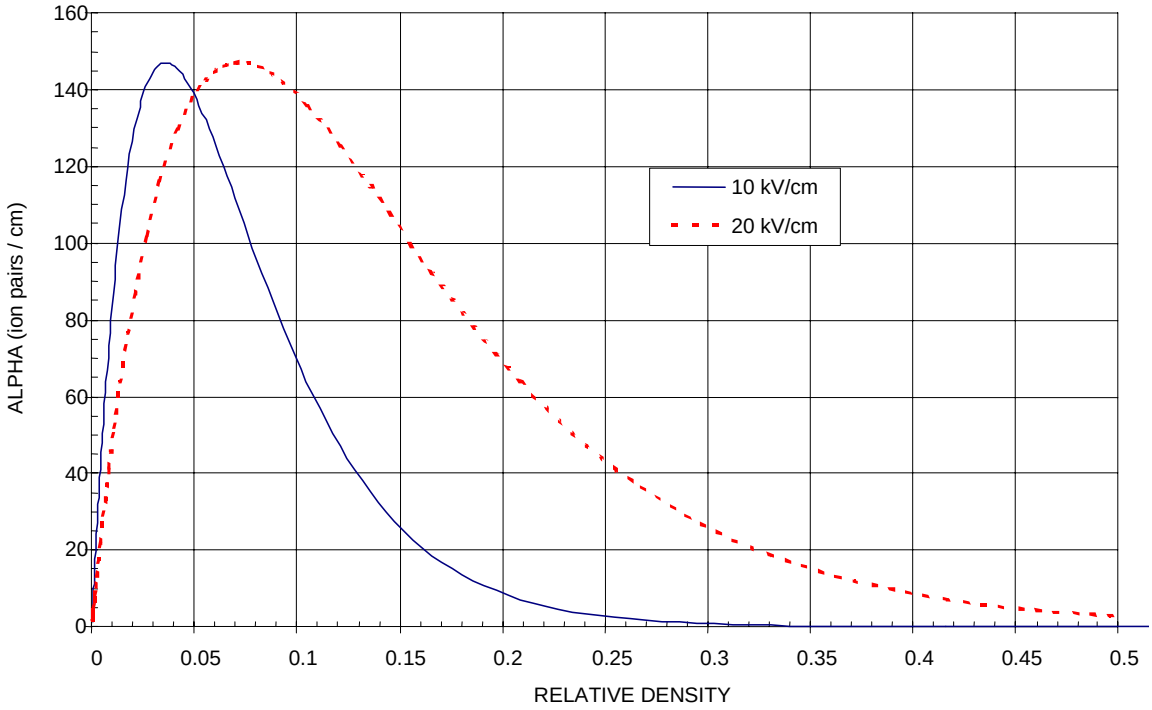

Figure 2-7. Theoretical value of Townsend's first coefficient versus relative air density.

The Townsend equation for the primary ionization coefficient is usually written in a form showing that α/δ is a function of only E/δ as follows:

$$\frac{\alpha}{\delta} = 760 \cdot A \cdot e^{-\frac{760 \cdot B}{E/\delta}} .$$

So far, we have only talked about the processes that cause additional free electrons to occur in the gas. There are processes that remove electrons from an avalanche as it travels across the gap (capture). An electron can collide with a positive ion and recombine, converting the ion to a neutral atom. There are atoms and molecules that have an affinity for electrons and can easily form negative ions. A gas containing these types of particles is termed electronegative. Several types of atoms and molecules found in air, including oxygen, hydrogen, water vapor, the halogens and their compounds, are electronegative (Raizer, 1991, p. 63, Naidu & Kamaraju, 1995, p. 15). The negative ions, thus formed, cannot obtain enough velocity to contribute to the avalanche, except in extremely high fields; therefore, any electrons captured by such ions are effectively removed from the avalanche.

The rate of capture (η) is small in air. For example, in normal atmospheric conditions, an electron might make 2 x 10^5 collisions before capture (EPRI, 1982, p. 170). The capture rate is only weakly dependent on the electric field.

For electronegative gases, like air, where absorption is important, the effective primary Townsend coefficient is the difference between the multiplication rate and the capture rate:

$$\alpha_{eff} = \alpha - \eta .$$

The parameter α is a strong function of the magnitude of the electric field, increasing rapidly with the field strength. It has been shown experimentally that for a given gas, α/δ depends only on E/δ

(similarity) (Papoular, 1965, p. 111). The absorption rate (η) obeys the same similarity law (Raizer, 1991, p. 64). Both can be determined empirically and a plot of them for air at STP is given in Figure 2-8 (Sarma & Janischewskyj, 1969). Note that below a certain value of E/δ, α is less than η. For this case, α_{eff} is negative and electron multiplication does not occur, hence breakdown cannot occur. For air at STP, this corresponds to about 24.4 kV/cm, as seen in Figure 2-8, which defines the true fundamental dielectric strength of air. Various authors give slightly different values (24.1 to 24.6) for this parameter. Some of the variation of this parameter is due to differences in the definition of STP.

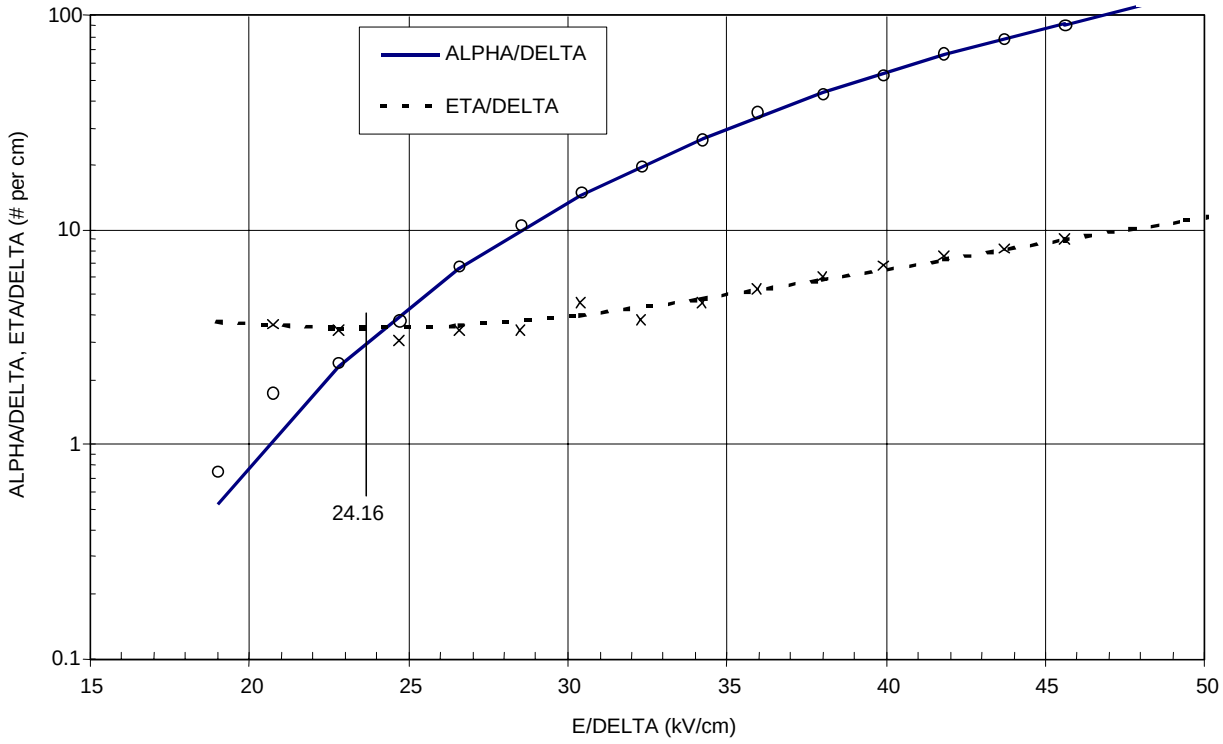

Figure 2-8. Ionization and attachment coefficients of dry air at 20° C.

Meta-exponential

As the voltage increases further, the current starts to increase more rapidly than exponential, soon becoming self-sustaining, i.e., not depending on the residual ionization. Townsend reasoned that this occurred when the field became strong enough so that the residual positive ions obtained enough velocity to free an occasional electron from the cathode on impact. This provides an additional or secondary source of electrons to avalanche.

Processes that create more free electrons as a result of the primary avalanche process are called secondary processes. It turns out that secondary processes are more complicated than Townsend originally thought, and occur throughout the gas. However, they are most important at the cathode, since free electrons created there can avalanche across the entire gap. When secondary emission at the cathode is taken into account, the steady discharge current is given by:

$$i = \frac{i_0 \cdot e^{\alpha \cdot l}}{\left\{1 - \gamma \cdot \left(e^{\alpha \cdot l} - 1\right)\right\}}$$

where γ is the number of secondary electrons created at the cathode per ionizing collision in the gap.

The parameter γ can be interpreted as the probability that a free electron occurs in the vicinity of the cathode due to the secondary processes resulting from any given ionizing collision. The emission of an electrode at the cathode, secondary emission, arises in several ways, including positive ions colliding with the cathode, photons impacting the cathode, and meta-stable atoms interacting at the cathode. All of these are produced in the gas by electron collisions. The coefficient, γ, is known as Townsend's second or secondary ionization coefficient, and can be thought of as the combination of the three respective components (positive ion, photons, and meta-stable atoms):

$$\gamma = \gamma_i + \gamma_p + \gamma_m \ .$$

It can be shown that the secondary ionization coefficient obeys the same kind of similarity relationship as the primary ionization coefficient, namely that it is a function of E/δ.

Breakdown

As long as the denominator of the above equation for discharge current is positive, the current is not self-sustaining. That is, the current only exists because of the fundamental ionization source of electrons and is limited by that process. Setting the numerator equal to zero results in:

$$\gamma\left(e^{\alpha \cdot l} - 1\right) = 1 \tag{2-9}$$

or since $e^{\alpha \cdot l} >> 1$ the equation is sometimes rewritten as

$$\gamma \cdot e^{\alpha \cdot l} = 1 \ .$$

This is known as Townsend's criteria for spark breakdown. It corresponds to the electric field reaching a level for which any electron released by the cathode produces enough primary ionization so that the resulting secondary processes result in at least one additional electron being released by the cathode. When this condition persists, the discharge is self-sustaining, no longer requiring an outside source of ionization. The current can increase until a limit is reached, which is determined by the impedance of the circuit and the power dissipated in the plasma (Alston, 1968, p. 26).

From physical considerations, the secondary-ionization coefficient is a function of a number of factors, including the material, the surface condition, contamination, and the electric field in the immediate vicinity of the surface. However, the breakdown voltage is relatively insensitive to the value of gamma (Sarma & Janischewskyj, 1969, p. 164). Thus, the breakdown voltage varies only slightly for various materials at atmospheric pressures (Alston, 1968, p. 46).

The breakdown mechanism described above is called the Townsend process. Three stages are required to initiate a Townsend breakdown:

1. The existence of residual ambient free electrons and ions created by light, cosmic rays, or some other form of radiation.
2. Field-enhanced multiplication of electrons leading to an avalanche.
3. Feedback by secondary processes that results in new free electrons at the cathode.

Application to Paschen's Law

Since both α and γ are functions of E/δ, the Townsend breakdown criteria is also a function of E/δ, as was determined experimentally by Paschen before the turn of the century. The factor γ is weakly dependent on the field and can be assumed to be a constant for a given gas and cathode material. Townsend substituted his expression for the ionization constant Equation 2-2 into Equation 2-3 above and developed a universal equation for the breakdown voltage in uniform field gaps:

$$V_s = \frac{B \cdot p \cdot l}{\ln \frac{A \cdot p \cdot l}{\ln\left(1 + \frac{1}{\gamma}\right)}}.$$

This equation can be recast in terms of the relative air density, δ, as follows:

$$V_s = \frac{B \cdot 760 \cdot \delta \cdot l}{\ln \frac{A \cdot 760 \cdot \delta \cdot l}{\ln\left(1 + \frac{1}{\gamma}\right)}}.$$

This equation explicitly shows that the critical voltage for breakdown is a function of the product $\delta \cdot l$. This equation, using the values of A and B, as determined in air is plotted in Figure 2-2 (labeled Townsend theory), along with the measured data for Paschen's curve. As can be seen in the figure, the theoretical curve has the same characteristics as the measured data, including the minimum. In fact, the theoretical curve fits the measured data fairly well in certain regions.

The coefficients $\alpha(E/\delta)$ and $\gamma(E/\delta)$ have been determined empirically by many (e.g., Raizer, 1991, pp. 54–55). By making appropriate analytic approximations to these functions, various formulas for Paschen's law can be derived analytically (Gary et al., 1972, Sarma & Janischewskyj 1969, Olsen, et al. 1997)**.** An equation that quite accurately fits the right-hand (high-pressure, $\delta \cdot l > .01$) portion of Paschen's curve is given by the following (Alston, 1968, p. 48, after Bruce, 1953) (see Figure 2-2):

$$V_s = 24.22 \cdot \delta \cdot l + 6.08 \cdot \sqrt{\delta \cdot l} \quad \text{kV/cm.}$$

where V_s is the sparking or breakdown voltage,
δ is the relative air density with respect to STP (20° C for this case) and
l is the gap length in centimeters.

This equation satisfies similarity because V_s is a function of the ratio $\delta \cdot l$. When $\delta \approx 1$, $V_s \approx 6\sqrt{l}$ for values of l around 0.01 centimeter. When $l > 10$ centimeters, $V_s \approx 24.4 \cdot l$.

Dividing both sides of this equation by the gap length gives an equation for the electric field required for sparking or breakdown that satisfies the similarity relationship.

$$E_s = 24.22 \cdot \delta \cdot \left(1 + \frac{0.251}{\sqrt{\delta \cdot l}}\right) \quad \text{kV/cm.} \tag{2-10}$$

There are some interesting conclusions that follow from the above equation. Firstly, somewhat surprisingly, the electric field strength required to break down air depends on the length of the gap. For small gaps, this field strength can be very large. The reason for this is that longer gaps allow the avalanches to propagate farther, creating more ions, which increase the probability of emission of secondary electrons from the cathode.

In fact, it is a well-known consequence of Paschen's law that the flashover voltage for a large gap can be greatly increased if it is divided into several smaller gaps by several conducting plates. This is because the lengths of the individual avalanche regions are reduced and, as a result, the electric field required for breakdown in each gap increases. Lately there has been a resurgence of interest in the application of this design principle to stacked insulators, primarily for ultra high-voltage particle accelerators. The layered design has been demonstrated to significantly increase both the bulk and surface breakdown voltages for an insulator by factors varying from 1.5 to 4 (Houck, et al. 1997).

Secondly, there is a minimum field strength below which breakdown will not occur, regardless of the gap length. This is called the fundamental breakdown strength of the gas. In air at STP, the fundamental breakdown strength is 24.22 kV/cm. The reason for this is that air is electronegative, primarily due to the oxygen content, and below that level, the effective Townsend coefficient is negative implying that electron avalanches cannot occur.

Thirdly, the similarity law appears in Townsend's theory, and this law can be used to compare measurements made with different air density.

As instrumentation improved and high-speed photographs were obtained of the breakdown process, it was discovered that for longer gaps the breakdown process occurred too rapidly to be explained by Townsend's theory. In fact, for long gaps and fast wavefront impulses, the resulting peak breakdown voltages are in excess of the normal breakdown voltage for the gap. For these cases, the breakdown time is sometimes considerably less than the time required for an electron to transit the gap. Because of this, a new theory was developed to explain the breakdown of longer gaps, called streamer (or Kanal) theory (Loeb, 1965; Meek & Craggs, 1978, p. 322; Alston, 1968, p. 28). This theory invokes the development of the spark discharge from an individual avalanche that contains enough electrons ($\sim 10^8$) so that the field strength in front of the avalanche is enhanced enough to continuously break down the air. Thus, a single avalanche can propagate across the entire gap without depending on secondary emission from the cathode. This type of breakdown usually occurs in a single narrow channel, much like lightning. A similar theory has been developed for positive streamers. The mathematical description of breakdown conditions for streamers is more complicated than that of the Townsend theory.

The Townsend process is believed to adequately explain breakdown for small gaps in gases at relatively high pressure. Townsend breakdown channels are wider than those for streamers. In air at normal conditions, it is reported that the Townsend process dominates for gap lengths less than 5 cm or so (Alston, 1968, p. 33, Raizer, 1991, p. 340). A transition region is probable, where both processes operate. It will be shown below, for the case of corona onset on wires, that the equivalent active gap length is small, and thus the Townsend process dominates, even for large wires.

NON-UNIFORM FIELDS

Most high-voltage applications involve insulator configurations having non-uniform electric fields. Examples include spheres, rods, toroids, and cylinders above ground. For these cases, the fields are strongest on the surface of the energized object and fall off with distance away from the object. If the maximum field in the gap is less than about five times the average field, the breakdown behavior is similar to that for a uniform field in that complete breakdown (flashover) occurs before any other phenomena. However, when the maximum field is greater than about five times the average field, ionization can be maintained locally in the high field region without breakdown of the entire gap (Raizer, 1991 p. 345; Alston, 1968, p49). This localized breakdown is known as corona. For example, the electric field around power distribution lines is very non-uniform and corona forms

around the wires when the voltage is high enough. It will be shown below that the electric field required to initiate the formation of corona depends on the radius of curvature of the object.

Generalized Similarity

The similarity relationship given by Paschen's law applies to the one-dimensional geometry of a parallel plate gap. Similarity strictly means that the Townsend currents illustrated in Figure 2-5 remain constant as long as the gap length times gas density remains constant. Thus, the breakdown voltage remains constant for the same conditions. Two cases are similar (i.e., have the same breakdown voltage) when the gap length for one case is multiplied by a scale factor while the gas density is divided by the same scale factor (Cobine, 1958, p. 160).

Similarity can be extended to any configuration as long it has a short active region so that Townsend's theory applies (Llewellyn-Jones, 1957, Alston, 1968, p. 50). The extension involves the assumption that the critical voltage at breakdown is constant when the product of scale factor times gas density remains constant. The scale factor is applied to all dimensions of the configuration. Thus, two cases are similar (i.e., have the same breakdown voltage) when the dimensions for the second case are the same as for the first case multiplied by a scale factor while the gas density is divided by the same scale factor.

The case of a sphere above ground is defined by the dimensions a, the radius of the sphere, and S, the spacing between the surface of the sphere and ground. The breakdown voltage will be the same for cases with different dimensions as long as the dimensions are directly related by a scale factor, s, and the gas density is inversely related by the scale factor. Table 2-2 gives the explicit relationships for similar cases of a sphere above ground.

Table 2-2. Similarity extension to a sphere above ground.
Scale factor, s.

	Case 1	Case 2
Radius, a	a_1	$s \cdot a_1$
Separation, S	S_1	$s \cdot S_1$
Relative density, δ	δ_1	δ_1/s
Breakdown Voltage, V	V_1	V_1

This extension of the Paschen's similarity law to two and three dimensions has been validated empirically for many configurations and over wide ranges of density for most gases.

In a non-uniform field, where corona forms before flashover, the voltage at which corona forms is called the critical voltage (V_c) or sometimes the onset voltage (V_o). A simple formula for V_c that satisfies the similarity relationship is given below.

$$V_c = \left\{ E_0 \cdot (\delta \cdot b) + k \cdot (\delta \cdot b)^m \right\} \cdot G \tag{2-11}$$

where E_0, k, and m are constants,
b is a dimension of the object used to calculate the electric field, and
G is a dimensionless function of the ratio of the defining dimensions.

For the case of a uniform field gap, *b* is the gap length. For the case of a sphere or cylinder above ground, *b* will be the radius. It will be shown that the function *G* is the same dimensionless function defined at the beginning of the chapter used to calculate the electric field. As previously stated, *G* is strictly a function of ratios of dimensions of the configuration.

The term inside the brackets of Equation 2-11 is strictly a function of δd and thus has a constant value when the product δd is constant. This product remains constant when the dimensions of the configuration are multiplied by a scale factor, while the gas density is divided by the same scale factor. Since *G* is a function of the ratio of dimensions, it does not change when the dimensions are multiplied by a scale factor. Equation 2-11 satisfies the extended similarity relationship in that two cases have the same breakdown voltage as long as their dimensions relate directly by a scale factor and their gas density relates inversely as the same scale factor.

Equation 2-11 can be inverted to solve for the critical electric field at breakdown by using the relationship between voltage and electric field discussed at the beginning of this chapter. This relationship, repeated below (Equation 2-5), depends on the geometry involved; but in general it can be shown to follow the relationship:

$$E = \frac{V}{b} \cdot \frac{1}{G(h/b)} \tag{2-5}$$

where *b* is a dimension that defines the size of the object such as the radius of the sphere or cylinder in equations.

In Equation 2-5, *G* and *b* are selected for the particular configuration involved and the equation has the dimensions for electric field (i.e., volts/unit length). Multiplying Equation 2-5 by the factor *1/(b·G)* gives the following:

$$\frac{V_c}{b \cdot G} = E_c = E_0 \cdot \delta + k \cdot \frac{(\delta \cdot b)^m}{b},$$

which can be simplified as follows:

$$E_c = E_0 \cdot \delta \cdot \left\{ 1 + \frac{k / E_0}{(\delta \cdot b)^{1-m}} \right\} . \tag{2-12}$$

Because it is derived from Equation 2-11, Equation 2-12 must also satisfy the generalized similarity relationship, where the breakdown voltage remains constant when the product of the dimensional scale factor times relative gas density is fixed.

Equation 2-12 indicates that as the dimension *b* goes to infinity, E_c approaches $E_0 \cdot \delta$, thus E_0 defines the fundamental breakdown strength of the gas (i.e., the asymptotic breakdown strength for very large gaps when the gas density is 1).

The breakdown strength for a uniform field air gap (Equation 2-10), derived from Bruce's (1953) formula for the breakdown voltage on the right-hand side of Paschen's law, is in the form of Equation 2-12, with $E_0 = 24.22$, $k/E_0 = 6.08$ and $m = 1/2$.

Peek's Law

As the power industry developed early in this century, much attention was focused on high-voltage phenomena. Peek did extensive studies of the formation of corona on wires (Peek, 1929, Chapter IV, 1922, 1927). For his measurements, he used both coaxial and parallel wire geometry, for which the electric fields could be easily calculated at that time. He discovered that the onset of visible corona

on the wires could be accurately predicted from the magnitude of the electric field on the surface of the wires. The electric field on the surface of the wire when corona starts is called the critical electric field or critical gradient.

Peek found this critical gradient to be a function of wire diameter. He also found the critical gradient to be independent on the outer diameter for the coaxial geometry and wire separation for the parallel wire geometry. It turns out that the variation of the electric field near the wire is independent of wire spacing for both of these configurations (Chapter 4).

He investigated the effect of temperature and pressure and determined that air density was the appropriate parameter to use to correct for variation of these parameters. He was able to accurately fit analytic functions to his data, a rather remarkable feat for the time. These functions are good fits to his data and are known as Peek's Laws, given below. The voltage in these formulas is in terms of the crest (peak) value.

The critical field for coaxial geometry is given by:

$$E_c = 31 \cdot \delta \cdot \left(1 + \frac{0.436}{\sqrt{\delta \cdot d}}\right) \quad \text{kVp/cm}$$

and the critical field for parallel wires is given by:

$$E_c = 30 \cdot \delta \cdot \left(1 + \frac{0.426}{\sqrt{\delta \cdot d}}\right) \quad \text{kVp/cm}$$

where E_c is the critical surface electric field for the onset of corona,
d is the wire diameter in centimeters, and
δ is the relative air density.

Note that the above equations are in terms of diameter instead of radius as given by Peek (1929, p66).

Peek called the first term in these equations (30 or 31, respectively) the dielectric strength of air (g_0).

Both of these equations are of the form of Equation 2-12 and satisfy the generalized similarity law. They are very similar to Bruce's (1953) fit to the high-pressure side of Paschen's law (Equation 2-4), including the effect of air density. The main difference is that as the fundamental breakdown strength of air (g_0 in Peek's equations) is 30 kV/cm, vice 24.22 kV/cm for Bruce's fit to the parallel plate case. Also, Peek's equations weight the effect of changing wire diameter about twice as much as the effect of changing gap length in Bruce's equation.

Peek's measured data for wires is shown in Figure 2-9, along with plots of his equations. There is some scatter in his data, as might be expected from the usual measurement error limitations and the statistical nature of the breakdown process. The data appear to be taken from two slightly different distributions. The parallel wire measurements and some of the mid-range coaxial measurements appear to come from a lower distribution. He also made separate measurements on larger (parallel) wires having diameters of up to 8 cm, using voltages exceeding 1 million volts (EHV on Figure 2-9) (Peek, 1929 p. 61, p. 396). The larger diameter coaxial measurements and the EHV parallel measurements appear to come from the higher distribution. There could be a number of reasons for the differences, including (1) lack of knowledge of the geometric correction factors, (2) calibration difficulties associated with very large voltages, (3) the measurements may have been taken in a high-

humidity environment, which increases the critical gradient at 60 Hz, and (4) surface roughness, or dust and pollen in the air, either of which decreases the critical gradient.

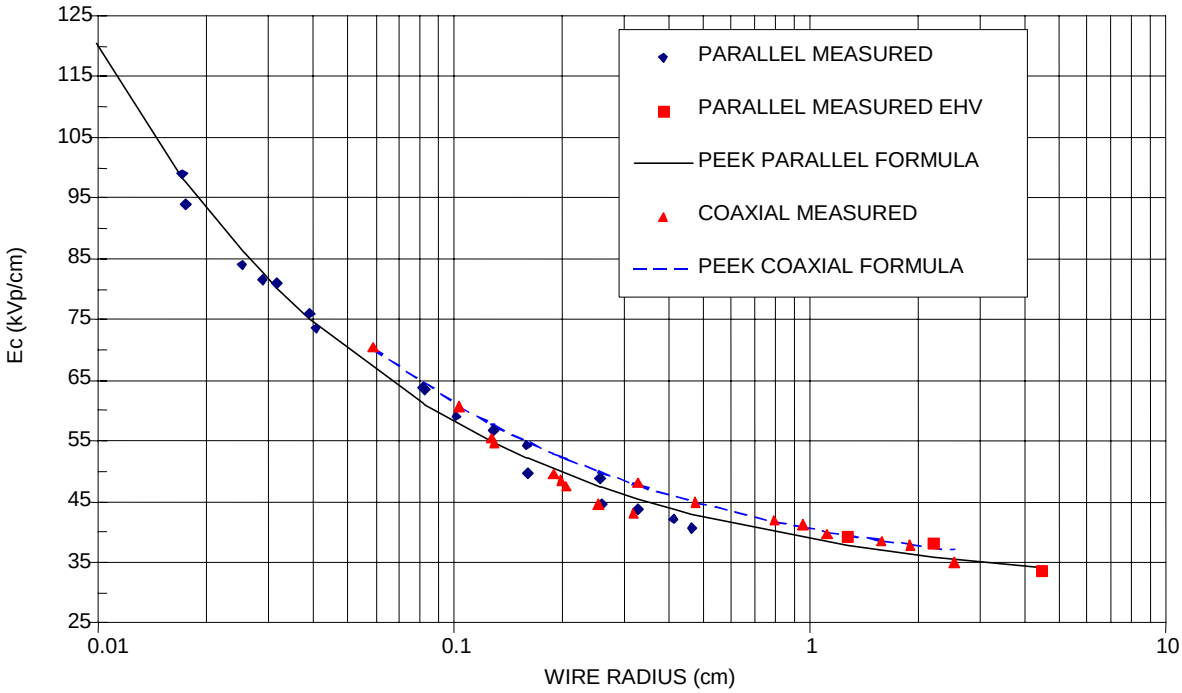

Figure 2-9. Measured critical gradient for corona onset, wires at 60 Hz.

For Peek's coaxial measurements, only the larger wires had the slightly higher critical gradient, which led to his using $g_0 = 31$ for that case. From Figure 2-9, it is seen that Peek's coaxial formula fits the data from the higher distribution well, while the parallel formula falls between the two distributions.

Schuman (1923) also gives measured data for wires, including wires with radii up to 15 centimeters. His measurements are shown in Figure 2-10, along with Peek's measured data. Schuman's data appears to come from the higher distribution and has a lot less scatter than Peek's. Schuman gives formulas similar to Peek's, as does Whitehead & Gorton (1914). All of these formulas are asymptotic to approximately 30 kV/cm. However, as will be shown in the next section, the true function should be asymptotic to a value near 24 kVp/cm, based on Townsend's theory. Peek did obtain a slightly smaller value of g_0 from measurements using large diameter spheres, but this value was still considerably greater than 24 kVp/cm.

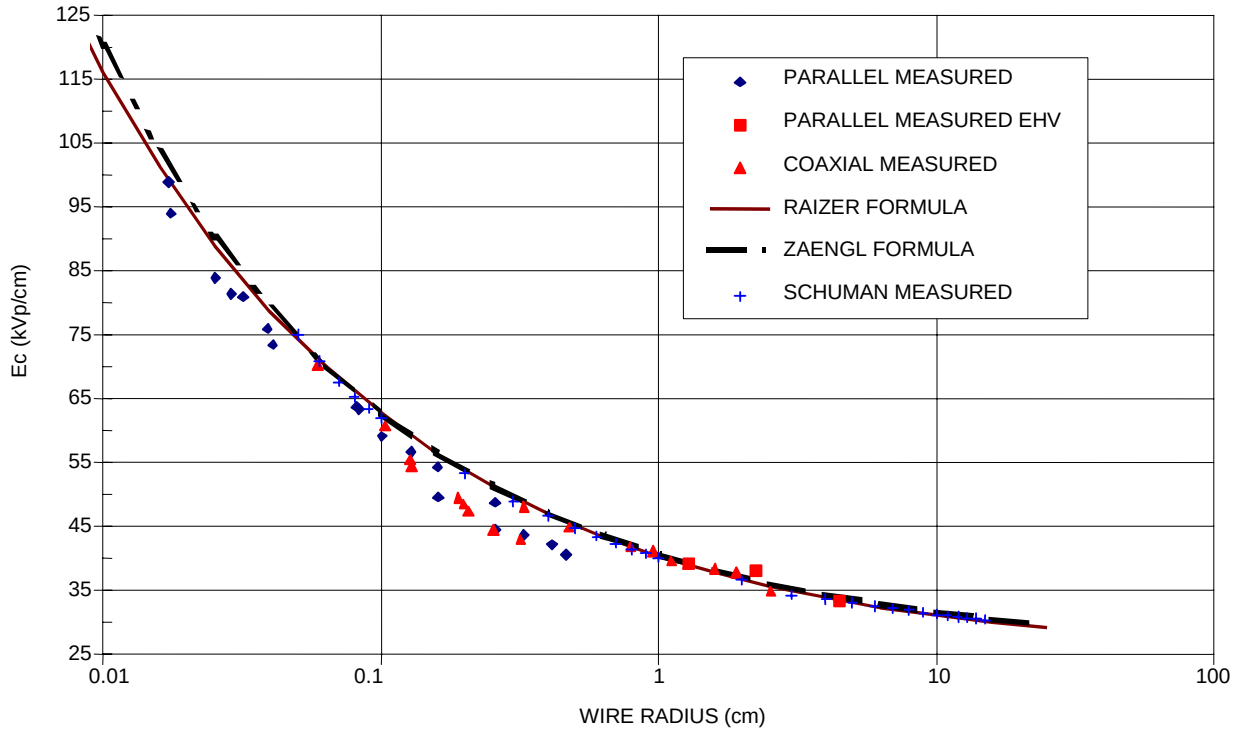

Figure 2-10. Comparison of 60-Hz corona onset data and formulas for wires including Schuman's measurements.

One reason that the formulas derived from the early data were not asymptotic to 24 kVp/cm is because the most of the measurements used relatively small diameter wires, less than 1 cm, and the equations fit that data well (Sarma & Janischewskyj, 1969, p. 164). There are other possible reasons involving errors that could have crept into the measured data. Another reason could be the obvious calibration problem for high-voltage measurements. In addition, our experience has been that the analytic formula often overestimates the actual surface field strengths for practical configurations of larger diameter wires. This is because the analytic formulas do not account for shielding from the end fittings and feed lines used to support and feed the wires. Peek did not have access to computer programs such as we used to determine the actual fields for our measurement configurations (see Chapter 4), and it may be that this type of error affects some of his results, especially for the larger diameter wires. Another possible reason for error is that the effect of humidity was not taken into account. If the larger wires were measured in a high-humidity environment, the humidity effect would increase the critical gradient at power distribution frequency.

Comparison of Peek's data to Schuman's data indicates that Peek's data may have low values of the critical gradient for wires with radii between 0.1 and 0.5 cm. One reason for this could be that some of those samples had surface scratches, roughness, or surface contamination, which can cause a reduction in critical gradient. This is not too likely because Peek indicates that he used highly polished wires in a clean, dry, laboratory environment. Another possible cause is aerosol dust particles or pollen in the air since these are invisible and can also reduce the critical gradient.

Most of Peek's data was measured at 60 Hz. He did vary frequency for a few measurements within the realm of power distribution systems but found no appreciable frequency effect on the critical gradient for corona onset over the range of 25 to 60 Hz. He also found no effect due to increased ionization, increased humidity, different conductor materials, or current in the wires.

Peek also made measurements on wires that were not clean, smooth, or dry, and found that weathering, oxidation, or other surface irregularities reduced the critical gradient for corona formation. He accounted for these effects by using a surface irregularity factor *m* that in effect reduces g_0. The effect of stranding is also included in *m*. He also found that surface contamination with water and oil reduces g_0. Oil decreases g_0 but not as much as water. For small wires, the effective increase in diameter, due to the oil, more than compensates for the lowering effect of the oil, resulting in slightly increased g_0. This may also be true for water. When water or oil is present, there is considerable variability and Peek's formulas, given below, are specifically noted to be approximations and do not include the effect of temperature or air density.

For water surfaces wetted by a fine spray or fog, Peek's equation is:

$$E_c \cong 9 \cdot \left(1 + \frac{1.15}{\sqrt{d}}\right) \text{ kVp/cm}$$

and for oil film surfaces, the equation is:

$$E_c \cong 19 \cdot \left(1 + \frac{0.92}{\sqrt{d}}\right) \text{ kVp/cm.}$$

Application of Townsend's Theory

Assuming clean, dry conditions and a smooth wire, the maximum electric field on the surface of a wire above ground occurs on the bottom of the wire. The field at this point falls off as 1/r, even when the wire is close to the ground (see Chapter 4). Based on Townsend's theory, field-enhanced ionization can take place in the region around the wire out to the point where the field is equal to 24.4 kVp/cm. Beyond that point, the field is too small to support ionization, and no ionization or breakdown processes occur beyond that point. The region between the wire and the point where the field reaches 24.4 kVp/cm is called the active region.

If the field on the surface of the wire is less than 24.4 kVp/cm, there will be no active region. As the voltage is increased, eventually the surface field will reach 24.4 kVp/cm. From this point on, as the voltage increases, the location of the point where the field equals 24.4 kVp/cm field moves out away from the wire, and both the surface field and the thickness of the active region increase.

Since the field is non-uniform, application of Townsend's theory requires integration of the Townsend ionization coefficient, across the active region, to determine the total number of ionization pairs created. For a wire of radius *a*, the equation for the number of electrons in an avalanche $n(\tau)$ is given by:

$$n(\tau) = \exp\left[\int_a^{a+\tau} (\alpha - n) \cdot d\delta\right] = \left(\frac{1}{\gamma} - 1\right)$$

where τ is the thickness of the active region, i.e., the distance from the surface of the wire to the point where the field drops below 24.4 kV/cm.

The Townsend breakdown criterion is applied by setting the number of electrons equal to:

$$1/\gamma - 1 \approx 1/\gamma \ .$$

Using the above equation, a formula for Peek's law can be derived from Townsend's theory, given that appropriate analytical functions are assumed for the Townsend coefficients and appropriate limits are used for the integral (Gary et al. 1972). As previously pointed out, Peak's law for wires is very similar to the equation fitting Paschen's law for parallel plates. This is somewhat surprising

since, for the case of the wire, the field falls off non-uniformly (1/*r*) and therefore the thickness of the active region increases with voltage. One might expect the variation for this case to be quite different than for a uniform field (Paschen's law). However, the ionization rate is much greater in the high field region and much lower, going to zero, near the outside of the active region. It happens that the average of the ionization rate over the active region gives a function very similar to that for Paschen's law on the right-hand side of the minimum (high-density region).

From Townsend's theory, it is clear that the critical field for very large wires should approach that same value for large gaps between parallel plates, namely 24.4 kVp/cm, the field below which electron multiplication cannot occur. Thus, Peek's law cannot be correct for larger diameter wires since it is asymptotic to 30 or 31 kVp/cm. This has been known for some time. For example, Zaengl and Nyffenegger (1974) applied Townsend's formula to cylindrical geometry. Using an appropriate formula for the effective Townsend coefficient, they derived the following transcendental equation for E_c.

$$\left(\frac{E_c}{\delta}\right)^2 - 2\left(\frac{E_c}{\delta}\right)\cdot E_0 \cdot 1n\left[\frac{1}{E_0}\cdot\frac{E_c}{\delta}\right] - E_0^2 = \frac{K/C}{\delta \cdot r} \ . \qquad (2\text{-}13)$$

The constant E_0 corresponds to the dielectric strength of air. They found that the best fit for this formula, to what they considered to be "very precise" measured values (Shost, 1962; Schroder, 1961), occurred with $E_0 = 24.36$ kV/cm, and $K/C = 42$ (kV)^2/cm.

We found another example in the Russian literature, given by (Raizer, 1991, p. 350), who stated that "the formula used nowadays in electrical engineering," is given by:

$$E_c = 24.5 \cdot \delta \cdot [1 + 0.65 \cdot (\delta \cdot r)^{-0.38}] \ . \qquad (2\text{-}14)$$

For both Equations 2-13 and 2-14, the value of E_0 corresponds closely to that predicted by Townsend's theory. Also, both of these formulas explicitly include the effect of air density on both the fundamental breakdown strength and the wire size.

The above two formulas have been plotted on Figure 2-10, along with Peek's data and Schuman's data. Note that since Peek's formulas are not asymptotic to 24.4 kVp they give values that are too large for the breakdown field as the wire diameter becomes large. It turns out that Peek's formulas also give values that are too large for small wires. Both Raizer's (1991) and Zaengle and Nyfenneger's (1974) formulas give results larger than Peek's data for wires with radii in the range from 0.1 cm to 0.4 cm, which is the range where Peek's data have the most scatter and disagree most with Schuman's data. Both Raizer's and Zaengle and Nyfenneger's formulas give results that agree very well with Schuman's data and are both asymptotic to 24.4 kVp. They should give good results for larger diameter wires.

Raizer's formula is simple and can be used to develop a formula for the thickness of the active region around the wire at breakdown (corona onset). In the immediate vicinity of a cylinder above ground, the electric field, at the location of the maximum, falls off away from the cylinder as 1/r, independent of the height (Chapter 4). The field near the wire is given by:

$$E(r) = \frac{E_s \cdot a}{r}$$

where $E(r)$ is the field in the vicinity of the wire,
r is the radius from the center of the wire,
E_s is the field on the surface of the wire, and
a is the radius of the wire.

The radius of the active region (r_a) can be determined by setting E_s equal to E_c, the critical surface field for corona onset, and $E(r)$ equal to 24.4 kVp/cm. Solving for r gives

$$r_a = \frac{E_c \cdot a}{24.4} \ .$$

The thickness of the active region, τ, is the distance from the wire surface to the edge of the active region.

$$\tau = r_a - a = \left(\frac{E_c}{24.4} - 1 \right) \cdot a$$

Substituting Raizer's Equation 2-3 for E_c ($\delta = 1$) and simplifying gives:

$$\tau = 0.65 \cdot a^{0.62} \ .$$

Converting to diameter (d) gives:

$$\tau = 0.423 \cdot d^{0.62} \ .$$

This equation has been plotted in Figure 2-11. From the figure, it can be shown that for a wire of diameter 50 centimeters (19.7 inches), the thickness of the active region is 4.8 centimeters. Townsend's theory applies to gaps having a length of 5 centimeters or less (Alston, 1968, p. 33; Raizer, 1991, p. 340). Since the thickness of the active region around the cylinder decreases with diameter, Townsend's theory applies to breakdown around cylinders with a diameter of 50 centimeters or less, which includes most practical cases. The fact that Townsend's theory applies means that the similarity law also applies. Thus, similarity applies to most practical cases involving corona breakdown around pipes, cables, or wires.

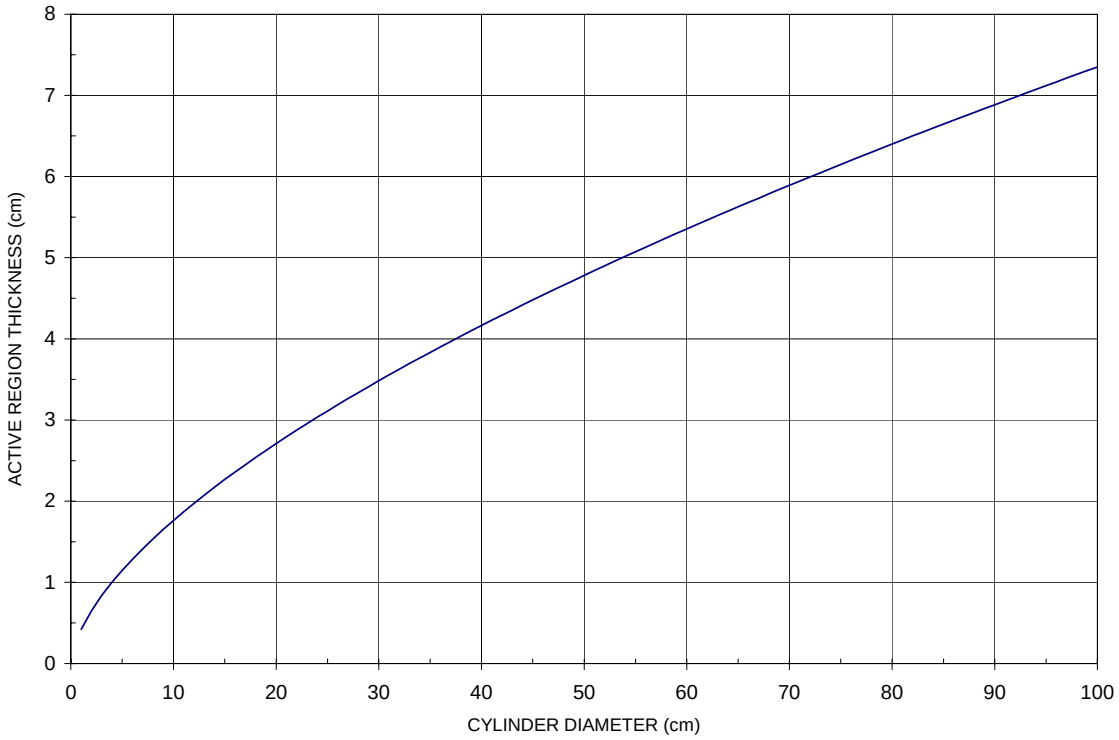

Figure 2-11. Thickness of the active region around a cylinder..

CHAPTER 3 ATMOSPHERIC EFFECTS

From the discussion of Paschen's and Peek's Laws, it is clear that gas density has a strong effect on the electrical field at which electrical breakdown occurs. For breakdown in air, the amount of water vapor also strongly affects the breakdown process. In this chapter, we will discuss how atmospheric density and humidity are determined, the variation expected, and the application of these parameters to the measurement of breakdown and corona onset in air.

AIR COMPOSITION

The major constituents of the atmosphere are gases and water vapor. The gases consist (by volume) of 78% nitrogen, 21% oxygen, 0.9% argon, and 0.03% CO_2. There are numerous other gases present, including ozone with a concentration on the order of 0.000,005%.

The average amount of water vapor is about 0.2% (by weight) for the total atmosphere. The actual amount at a specific site varies greatly with time and location, and is frequently reported in terms of relative humidity.

The ratio of the major gases remains essentially fixed up to the top of the mixing layer at a height of about 100 km, while most of the water vapor is concentrated in the first 1 to 2 km above sea level.

The atmosphere also contains significant amounts of dust, pollen, and spores as shown in Figures 3-1 and 3-2. In some locations, salts and other chemical pollutants are significant and sometimes insects are included. The concentration of these atmospheric particles varies greatly with time and geographic location. The sizes range in diameter from 0.1 to 10 μm (ASHRAE, 1977, chapter 10). In some cases, the particles play an important role in the breakdown and corona formation processes and may cause frequency dependency of the processes.

IDEAL GAS LAW

Air acts like an ideal gas at normally encountered pressures and temperatures. It obeys the ideal gas law, relating pressure, volume, and temperature.

$$P \cdot V = n \cdot R \cdot T = \frac{M}{w} \cdot R \cdot T$$

where P is the total atmospheric pressure in atmospheres
V is the volume of the gas in m^3
n is the number of moles of the gas contained in the volume = M/w
M is the mass of the gas in the volume V in kg
w is the molecular weight of the gas
R is the universal gas constant = 0.08208 $(m^3 \cdot Atm) / (kg \cdot mole \cdot °K)$
T is the absolute temperature in °K.

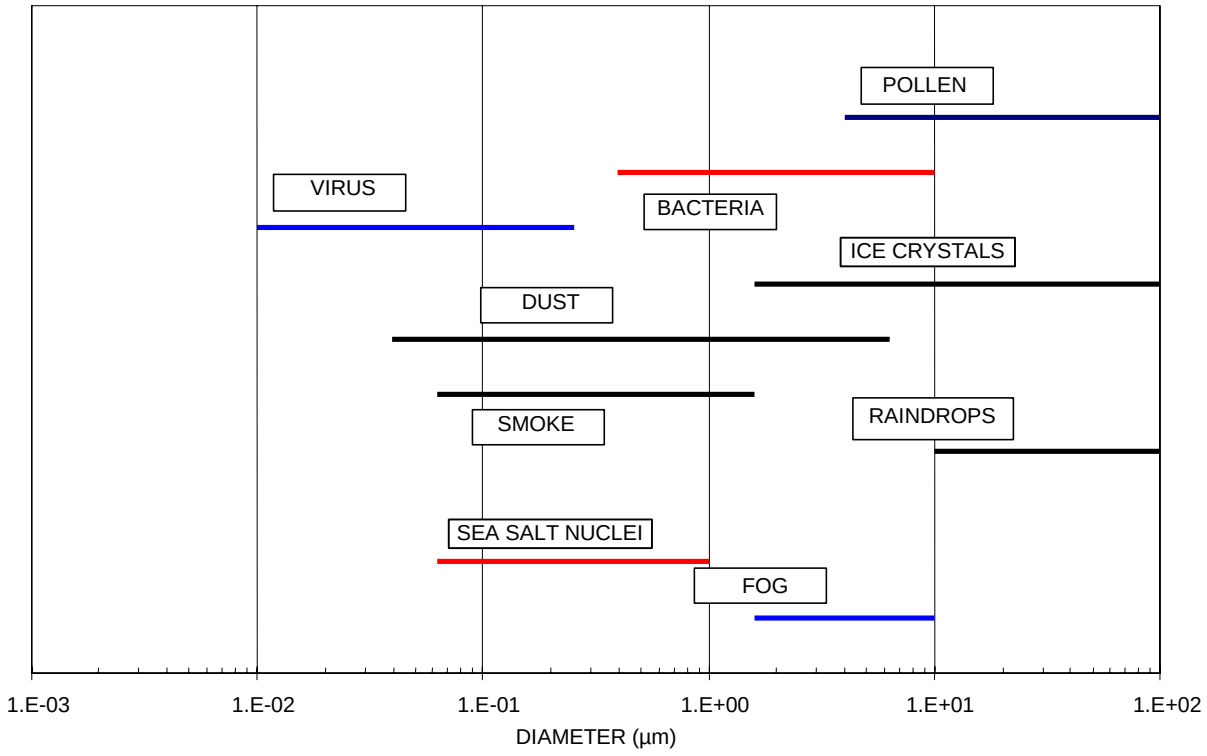

Figure 3-1. Atmospheric particle size and composition.

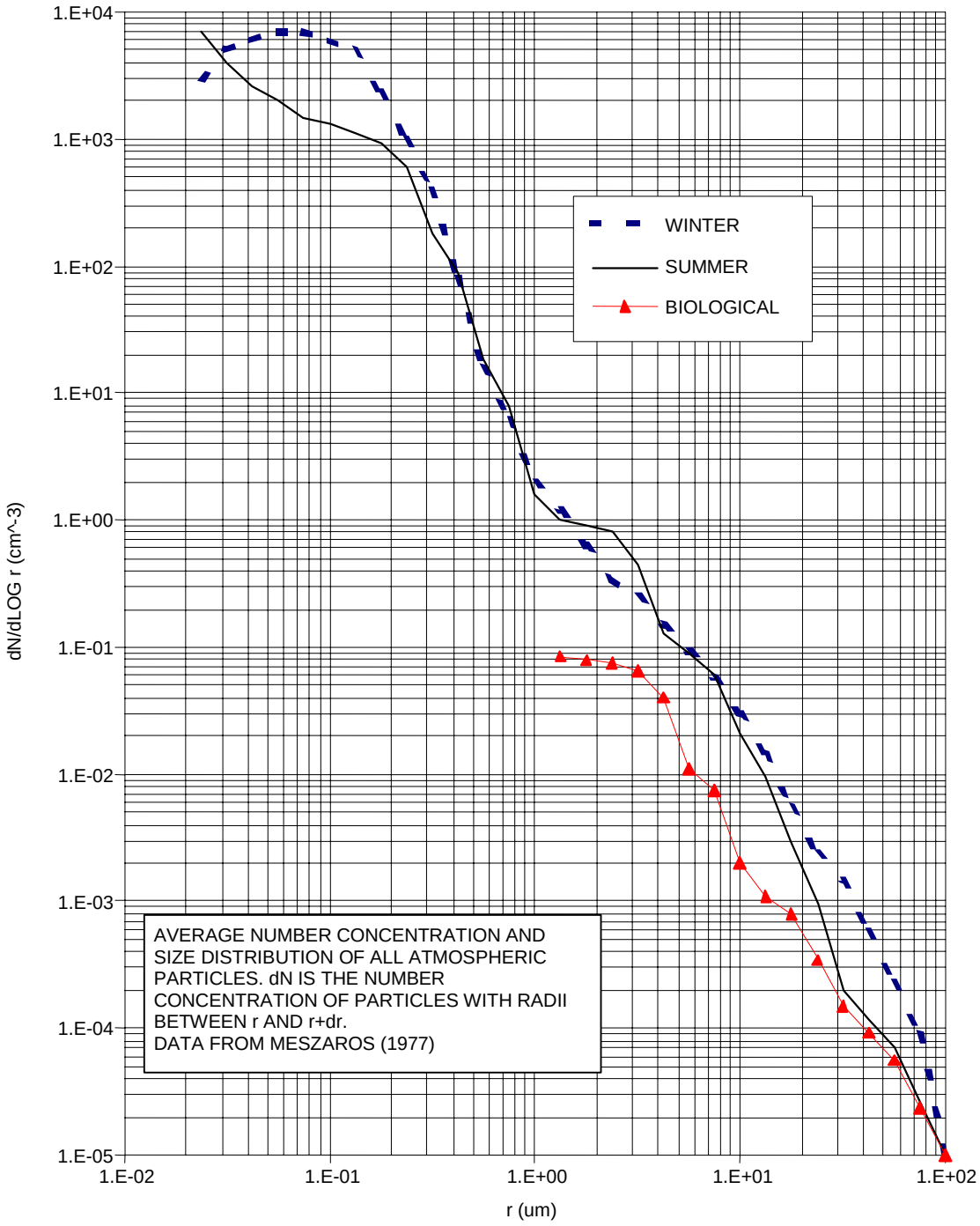

Figure 3-2. Size distribution of atmospheric particles.

The gas density, d, is the mass per unit volume. The ideal gas law equation can be used to solve for density.

$$d = \frac{M}{V} = \frac{P \cdot w}{R \cdot T}$$

where d is the gas density in kg/m^3.

It can be seen from this equation that the density of any gas varies directly with pressure and inversely with absolute temperature. The density of the gas at a defined standard temperature, T_0, and pressure, P_0, is found by substituting these values into the above equation and the result given in Equation 3-1.

$$d_0 = \frac{M}{V} = \frac{P_0 \cdot w}{R \cdot T_0} \tag{3-1}$$

The relative density of a gas, δ, is defined as the ratio of the gas density at some pressure, P, and absolute temperature, T, to the density the same gas would have at Standard Temperature and Pressure (STP).

$$\delta = \frac{d}{d_0} = \frac{P_0 \cdot T}{P \cdot T_0} \tag{3-2}$$

For a mixed gas, the total number of moles, n, is the sum of the moles of each individual component.

$$n = \left(n_1 + n_2 + \cdots n_n\right) = \left(\frac{M_1}{w_1} + \frac{M_2}{w_2} + \cdots + \frac{M_n}{w_n}\right)$$

Since each individual component follows the ideal gas law, it follows that the overall gas mixture also obeys the ideal gas law as shown below.

$$\left(P_1 + P_2 + \cdots P_n\right) \cdot V = \left(n_1 + n_2 + \cdots + n_n\right) \cdot R \cdot T$$

The total pressure is the sum of the partial pressures of the constituent gases (Dalton's Law).

$$P = \left(P_1 + P_2 + \cdots + P_n\right) = \left(\frac{n_1}{n} + \frac{n_2}{n} + \cdots + \frac{n_3}{n}\right) \cdot P$$

In a closed volume, the partial pressure of one of the gases is the pressure that it would assume if all the other gases were removed and the remaining gas allowed to expand to fill the volume, while remaining at the same temperature.

The mass of the individual components of the gas contained in the volume can be determined from the ideal gas law as follows:

$$M_i = \frac{P_i \cdot V \cdot w_i}{R \cdot T}$$

The total mass is the sum of the individual components.

$$M = M_1 + M_2 + \cdots + M_3 = \left(P_1 \cdot w_1 + P_2 \cdot w_2 + \cdots + P_n \cdot w_n\right)\frac{V}{R \cdot T}$$

The total density follows.

$$d = \frac{M}{V} = \frac{P_1 \cdot w_1 + P_2 \cdot w_2 + \cdots + P_n \cdot w_n}{R \cdot T} = d_1 + d_2 + \cdots + d_n \tag{3-3}$$

The total density is sum of the individual density components, which are equal to the density of each constituent weighted by its partial pressure.

This equation can be rewritten as follows:

$$d = \frac{M}{V} = \frac{(P_1 + P_2 + \cdots + P_n) \cdot w_{av}}{R \cdot T} = \frac{P \cdot w_{av}}{R \cdot T}$$

where w_{av} is the average molecular weight of the mixed gas, defined as follows:

$$w_{av} = \frac{P_1 \cdot w_1 + P_2 \cdot w_2 + \cdots + P_n \cdot w_n}{P}$$

The average molecular weight for mixed gases is the average of the molecular weights of the constituents weighted by the ratio of the partial pressure to total pressure. For mixed gases, the ratio of the partial pressures to the total pressure defines the gas mixture. As long as the gas mixture is fixed, any change to the gas in terms of temperature or pressure will not change the ratios of the partial pressures. Therefore, all the individual partial pressures change by the same factor as the total pressure. As long as the gas mixture is fixed, the relative density for any mixed gas is given by Equation 3-2. If the mixture changes, Equation 3-2 does not hold.

WATER VAPOR

In the natural state, air always contains some water vapor, known as humidity. At normally encountered temperatures and pressures, water can be in any of the three states (solid, liquid, gas). The amount of water vapor that the air can hold depends upon temperature, and for this reason it varies from almost none in cold arctic conditions to a maximum in hot tropical conditions. Because of the variability of the humidity, atmospheric air is best treated as a binary mixture of two gases, "dry air" and water vapor. The well-developed science of psychrometrics involves the determination of the thermodynamic properties of moist air and is useful for determining the amount of water vapor in the air for high-voltage applications.

The amount of water vapor in the air affects the absolute density. Any specified air–water mixture will have a certain absolute density. The average molecular weight of dry air is 28.9645 while the molecular weight of water is 18.01534. Since the density of water vapor is less than that of dry air, humid air is less dense than dry air.

The parameters required to determine the density of humid air are atmospheric (barometric) pressure, temperature, and the partial pressure of the water vapor. Instrumentation for the determination of atmospheric pressure and temperature are readily available. The partial pressure of water vapor can be determined as described below.

Saturation Vapor Pressure

Every fluid has a parameter known as the saturation vapor pressure. This is the pressure of the vapor form of the fluid, measured just above the surface of the fluid. The vapor form of the fluid above the surface is the result of thermal motion of the molecules in the liquid, which causes some of them to break away from the surface. The saturation vapor pressure of a liquid is only a function of the liquid temperature.

By definition, a gas is saturated with the vapor of a fluid when the partial pressure of the gaseous form of the fluid equals the saturation vapor pressure. At saturation, condensation forms at the same rate as the fluid evaporates. For water vapor in air, this condition is called 100% relative humidity. Thus, when the relative humidity is 100%, the partial pressure of the water vapor in the air equals the saturation vapor pressure of water. The relative humidity is given as a percentage of the saturation level of water vapor actually present. Boiling occurs when the saturation vapor pressure of the water

equals the pressure of the atmosphere above it. Thus at 100° C, the saturation vapor pressure of water is equal to the standard atmospheric pressure at sea level, 760 mm Hg.

The saturation vapor pressure of water has been studied extensively and a very accurate equation has been developed, giving the variation with temperature (ASHRAE, 1977, Chapter 5). The formula is given below.

$$\begin{aligned} B_1 &= 647.27 - T_A \\ P_V &= (218.167) \cdot 10^{-E_2} \\ E_2 &= \frac{B_1}{T_A} \cdot \frac{A + B \cdot B_1 + C \cdot B_1^3}{1 + D \cdot B_1} \end{aligned} \tag{3-4}$$

where $T_A = T_c + 273.1$ = Atmospheric temperature, degrees Kelvin
T_c= Atmospheric temperature, degrees Celsius
P_V = Saturation vapor Pressure of H_2O, atmospheres
A = 3.2437814
B = 0.00586826
C = 1.1702379 x 10^{-8}
D = 0.0021878462.

This equation is plotted in Figure 3-3 and accurately fits the measured vapor pressure data (Sears & Zemansky, 1955).

A psychrometric chart is a graphical representation of the thermodynamic properties of moist air and provides for convenient graphical solutions of many types of moist air problems. The properties of the moist air are a function of atmospheric pressure. Psychrometric charts and tables are available for atmospheric pressures corresponding to sea level, 5000 ft. altitude and 10,000 ft. altitude in (ASHRAE, 1977, Chapter 5). Equation 3-4 corresponds to the 100% relative humidity curve on the psychrometric charts. (ASHRAE, 1977, Chapter 5, IEEE Std 4-1995). A simplified formula that fits fairly well from 0 to 60° C, as shown in Figure 3-3, is given in Equation 3-5.

$$P_V = 0.00623 \cdot \left(1 + 0.01457 \cdot T^{1.833}\right) \tag{3-5}$$

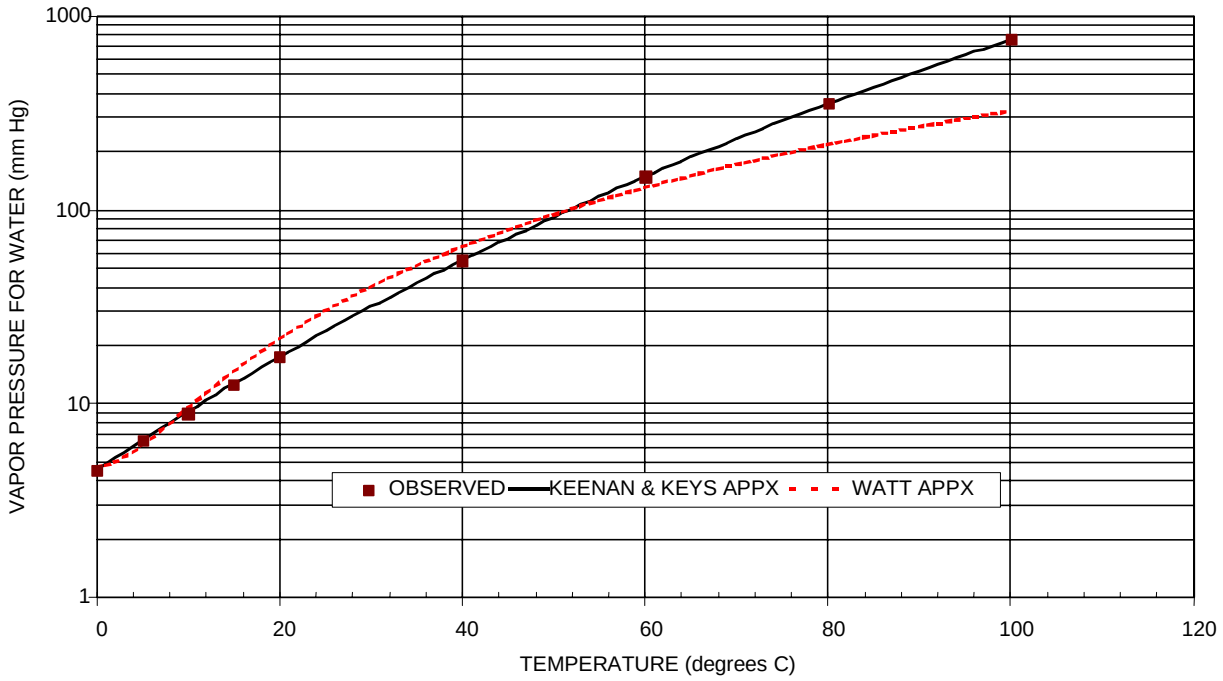

Figure 3-3. Vapor pressure of water at saturation.

Humidity Measurements

There are several ways of determining the partial pressure of water vapor present in the air (P_w), but all of them require that P_V be known. At the Forestport HVTF, the humidity measurements are now taken as relative humidity. The hygrometer used has a specified accuracy of $\pm$2%. Given relative humidity, the partial pressure of H_2O can be determined as follows.

Relative humidity (*RH*) is defined by the following equation (Sears & Zemansky, 1955).

$$RH = \frac{P_w}{P_V} \times 100\% \tag{3-6}$$

where P_w = Partial pressure of H_2O in air
P_V = Saturated vapor pressure of H_2O for ambient air temperature.

P_w is determined by substituting the measured value of *RH* and the calculated value of P_V into the above equation and solving.

Another common method of measuring the condition of moist air is to use wet and dry bulb temperature measurements. Often this is done using a sling psychrometer. This type of measurement was used in the past at the HVTF. The IEEE Std 4-1995, section 16.3, points out that wet and dry bulb measurements are somewhat complicated and require careful measurement techniques to avoid excessive errors. These measurements are usually reduced using psychrometric charts or tables. However, the relationships involved are a function of atmospheric pressure. To do the reduction correctly requires a chart or table for the existing atmospheric pressure, or error is introduced. We have found at the HVTF that the wet and dry bulb measurements are time-consuming, and give erroneous results if not made carefully and reduced correctly. We now believe that wet and dry bulb measurements are often less accurate than measurements with the modern relative humidity

instruments available, and for this reason have essentially abandoned wet and dry bulb measurements at the HVTF.

However, prior to abandoning wet and dry bulb measurements, we did work out a procedure to determine P_V from wet and dry bulb measurements, included below.

The relationship of P_V to the wet and dry bulb temperature measurements depends upon barometric pressure and is given below (ANSI C29.1-1998).

$$P_w = P_V' - 0.00367 \cdot b \cdot (t - t') \cdot \left\{ 1 + \frac{t' - 32}{1571} \right\} \tag{3-7}$$

where P_w = Partial Pressure H_2O, inches Hg,
P_V' = saturated vapor pressure of H_2O at temperature t',
b = Barometric Pressure, inches Hg,
t = air temperature, degrees F, and
t' = wet bulb temperature, degrees F.

Given the wet bulb and dry bulb temperatures, the above formula is used to find P_w .

Another method of determining humidity is to measure the dew point temperature. This method is thought to be quite accurate, especially at high values of relative humidity. The dew point temperature (T_d) is defined as the temperature at which the given mixture of air and water vapor becomes saturated, meaning the partial pressure the water vapor equals the saturated water vapor pressure. For a given mixture of air, as the temperature is lowered, when the dew point temperature (T_d) is reached, condensation starts to form. At the dew point temperature, $P_w = P_V$. The dew point temperature is often measured by cooling down a mirror and measuring the temperature at which fog starts to form. Given the dew point temperature T_d, the saturation vapor pressure P_V can be determined by substituting T_d into Equation 3-4 or 3-5. Multiplying this value for P_V by the ratio of the absolute temperatures gives the value of P_w at the actual air temperature.

$$P_w = P_V(T_d) \cdot \frac{T_d}{T}$$

There are methods to convert between the various parameters describing moist air. For example, if P_w is known, the dew point can be calculated by solving Equation 3-4 or 3-5 (by iteration) for the temperature at which the P_V equals P_w. Relationships between the various parameters of moist air and recommended procedures for their numerical calculation are given in the ASHRAE handbook (ASHRAE, 1977, Chapter 5).

Mixing Ratio

The humidity ratio or mixing ratio (W) of air with water vapor is an important parameter because it defines the mixture of "dry air" and water. The mixing ratio is defined as the ratio of the mass of water vapor divided by the mass of the dry air contained in a sample of the atmosphere.

$$W = \frac{M_w}{M_a} = \frac{d_w}{d_a} = \frac{w_w}{w_a} \cdot \frac{P_w}{P_a} = 0.62198 \cdot \frac{P_w}{P_a} = 0.62198 \cdot \frac{P_w}{P - P_w}$$

The partial pressure of water vapor is given in terms of the mixing ratio below.

$$P_w = \frac{W \cdot P}{W + \frac{w_w}{w_a}} = \frac{W \cdot P}{W + 0.62198}$$

The mixture of air and water vapor is defined by the mixing ratio. For a given mixture of air and water vapor, the mixing ratio is independent of changes in pressure and temperature. Thus, if a sample of air were changed from ambient temperature and pressure to STP, the mixing ratio does not change. Of course, if in this process the temperature falls below the dew point, the humidity of the air would exceed 100%, in which case the air must shed some water, changing the mixture. In such cases, converting the sample to STP does not make sense.

AIR DENSITY

Obviously, the amount of water vapor in the air affects the absolute density. This section discusses how to calculate the density of air containing water vapor. In order to do so, atmospheric air will be treated as a binary mixture of "dry air" and water vapor using the mixed gas formulas developed above. The average molecular weight of dry air is 28.9645 while the molecular weight of water is 18.01534. Note that the density of water vapor is less than that of air.

For the binary mixture of air and water, the total atmospheric pressure is given by the sum of the two partial pressures.

$$P = P_a + P_w$$

where P is the total atmospheric pressure in atmospheres
P_a is the partial pressure of dry air in atmospheres
P_w is the partial pressure of the water vapor in atmospheres

Substituting the appropriate parameters for an air–water vapor mix into Equation 3-3 gives the following equation for density. The total density of the air is equal to the sum of the constituent densities.

$$d = d_a + d_w = \frac{w_a \cdot P_a + w_w \cdot P_w}{R \cdot T}$$

where d is the absolute density of the air in kg/m^3
d_a is the density of the dry air in kg/m^3
d_w is the density of water vapor in kg/m^3
P_a is the partial pressure of dry air in atmospheres
P_w is the partial pressure of the water vapor in atmospheres
w_a is the molecular weight of dry air = 28.9645 kg/mole
w_w is the molecular weight of water vapor = 18.01534 kg/mole

This equation can be put in different forms, depending upon the parameters known. For example, a convenient form, when the total atmospheric pressure and the partial pressure of the water vapor are known, is given below.

$$d = 1.29213 \cdot \left(\frac{273.1}{T}\right) \cdot \left(\frac{P - 0.378 \cdot P_w}{760}\right) \text{kg/m3,}$$

where d = Atmospheric density, kg/m^3
T = Atmospheric temperature, degrees Kelvin,

P = Atmospheric pressure, mm Hg, and
P_w = partial pressure of H_2O, mm Hg.

It can be seen from this equation that the absolute density of the atmosphere decreases with increased water vapor content (contrary to common belief). This occurs because water vapor has less molecular weight than dry air.

It is convenient to obtain a formula for air density explicit in the parameter, mixing ratio.

$$d = 1.29213 \cdot \left(\frac{273.1}{T} \right) \cdot \left(\frac{P}{760} \right) \cdot \left(\frac{0.62198 \cdot (W+1)}{W + 0.62198} \right) \text{ kg/m3 ,}$$

where W = humidity mixing ratio.

STANDARD ATMOSPHERE

The U.S. standard atmosphere used for heating and air conditioning, based on STP condition of 15 °C and 760 mm Hg = 1013.25 mbar. For completely dry conditions, ($P_w = W = 0$) at these STP conditions, the calculated air density is 1.2257 kg/m^3. The density quoted for the U.S. standard atmosphere is 1.22486 kg/m^3, slightly less than the value calculated for dry conditions.

For high-voltage applications, other reference temperatures are sometimes used, for example, Cobine (1958, p 171) quotes a reference of 25^o C and 760 mm Hg for a relative density of 1. This is also the standard used by much of the power industry (ANSI C29.1-1998, IEC Publication 60 1979). However, the IEEE standard uses 20^o C (IEEE Std 4-1998). Also, the amount of water vapor present is not always made clear when specifying standard conditions. As a result, care must be taken in comparing reported measured results.

VARIABILITY

The range of atmospheric density encountered in nature is of interest in determining the effect it may have on corona onset and high-voltage breakdown. The expected variability caused by various phenomena is discussed below.

Elevation

Atmospheric density decreases with altitude. Figure 3-4 shows the density variation with altitude for average conditions. It should be noted that near the surface, the density is greater in the winter than in the summer. The variation with altitude is considerable. For example, at 10,000 feet the expected air density is 30% less than at sea level. Thus, the corona onset voltages are considerably reduced with altitude. Note that this variation is primarily due to a reduction in pressure and is reflected in the barometric pressure reading.

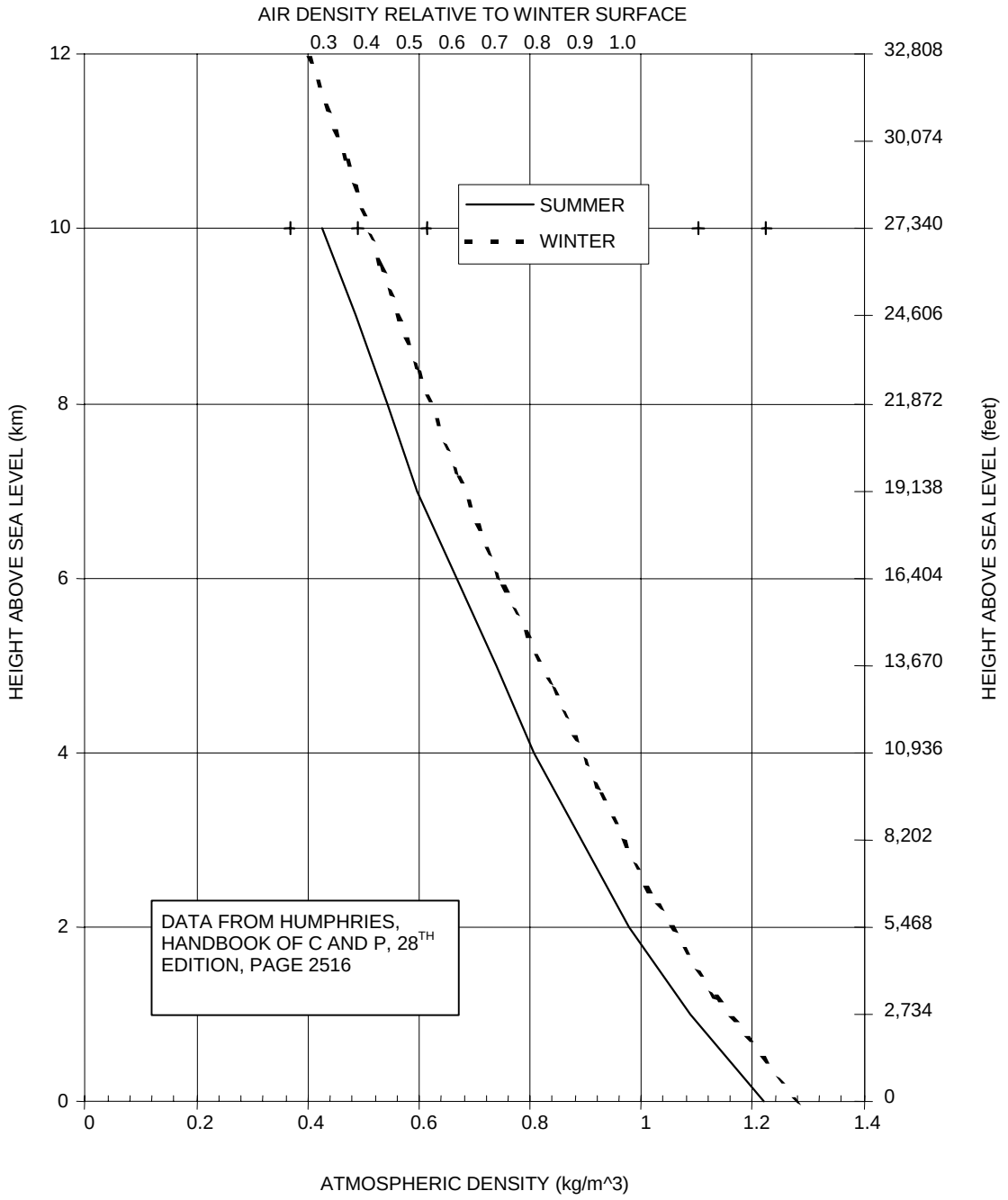

Figure 3-4. Variation of atmospheric density with height.

Temperature

The air density equation indicates that the density is inversely proportional to absolute temperature. It is denser when cold and less dense when hot. A nominal range of temperature variation, say from 0° to 45° C, translates into a 16% density variation.

Barometric Pressure

Atmospheric (barometric) pressure is given in a number of different units as shown in Table 3-1.

Table 3-1. Atmospheric pressure units.

1 atmosphere = 760 mm of Hg
760 Torr
29.92 inches of Hg
1013.25 milli-bars
101.325 kPa, kilo Pascals
10332 kg/m^2
14.66 Lbs/in^2

The highest values of atmospheric pressure occur under cold dry masses of air, usually in Arctic regions, and the lowest values of atmospheric pressure occur in hurricanes at lower latitudes. The extreme pressures recorded vary from 31.75 inches of Hg (806 mm Hg) in Siberia to 26.35 inches of Hg (669 mm Hg) in Florida (Valley, 1965, pp. 3-40). This extreme pressure ratio is 1.2 to 1 or a 20% range. Typical pressure variations at a dry mid-latitude location are much less; for example, an examination of monthly averages at Grand Junction, CO, show a variation of 0.5% for the year 1986. At the same location, the spread of daily values for the month of January was 2%. The total variation in atmospheric density is much greater since it includes the pressure effects plus temperature and humidity variations.

Humidity

The air density equation has been used to generate a set of curves of air density versus relative humidity, parametric in temperature (Figure 3-5). From the figure, it is seen that the air density variation with relative humidity, over the possible range of variation, is much less than 5%, unless it is very warm. This may be part of the reason that the air density correction factors in the IEEE and ANSI test standards ignore the effect of humidity on air density. The water vapor in the air changes the gas constituents and therefore affects electrical breakdown in a different way than just the density variation. The test standards attempt to account for this with a separate correction factor, discussed later in this chapter.

Combination

The air density equation has been used to generate curves of relative air density versus temperature, parametric in atmospheric pressure for 50% relative humidity (Figure 3-6).

From Figure 3-6 it is seen that variation of temperature over a temperature range of 15^o to 30^o C results in the air density changing by about 5%. The nominal range of atmospheric pressure variation, say 720 mm to 800 mm, results in a similar density variation.

An important parameter for high-voltage design turns out to be the expected amount of reduction in atmospheric density from the density at STP. At sea level and mid latitude, an expected reduction of 15% seems reasonable. However, in a tropical depression where hot temperature, high humidity, and very low atmospheric pressure can be experienced, the air density can be considerably reduced from that at STP. It is estimated that under those conditions, the temperature factor could be about 5% (40^o C), the pressure factor could be 12% (669 mm Hg). Humidity would account for another

5%, or a total of 22%, implying a similar reduction in electrical breakdown voltage. An even greater reduction in air density and hence breakdown voltage can result from increased elevation.

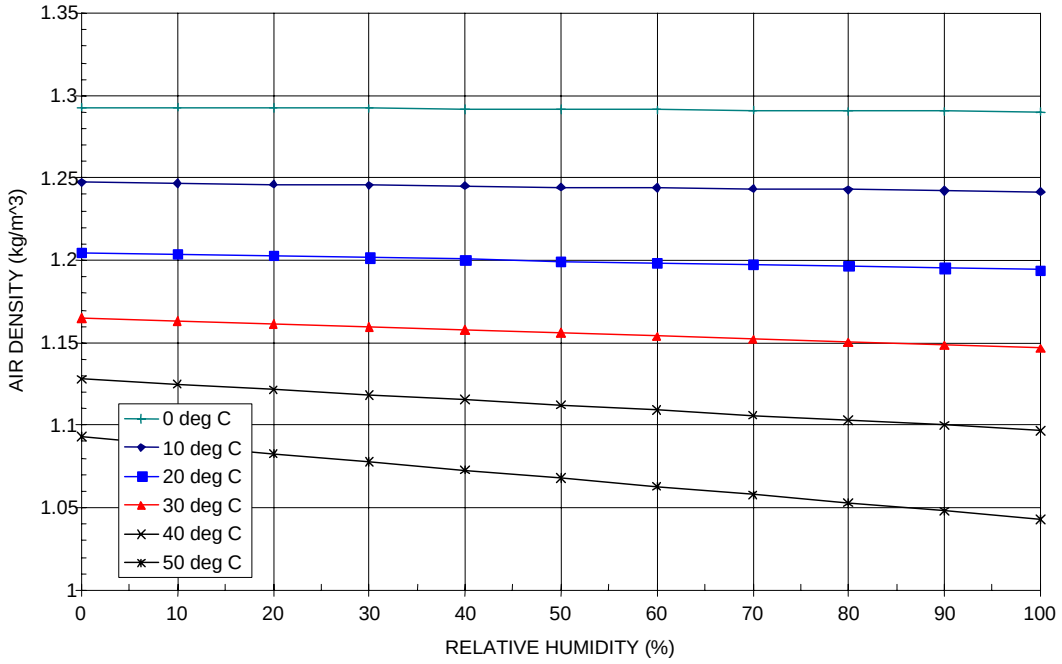

Figure 3-5. Air density versus relative humidity and temperature for standard pressure.

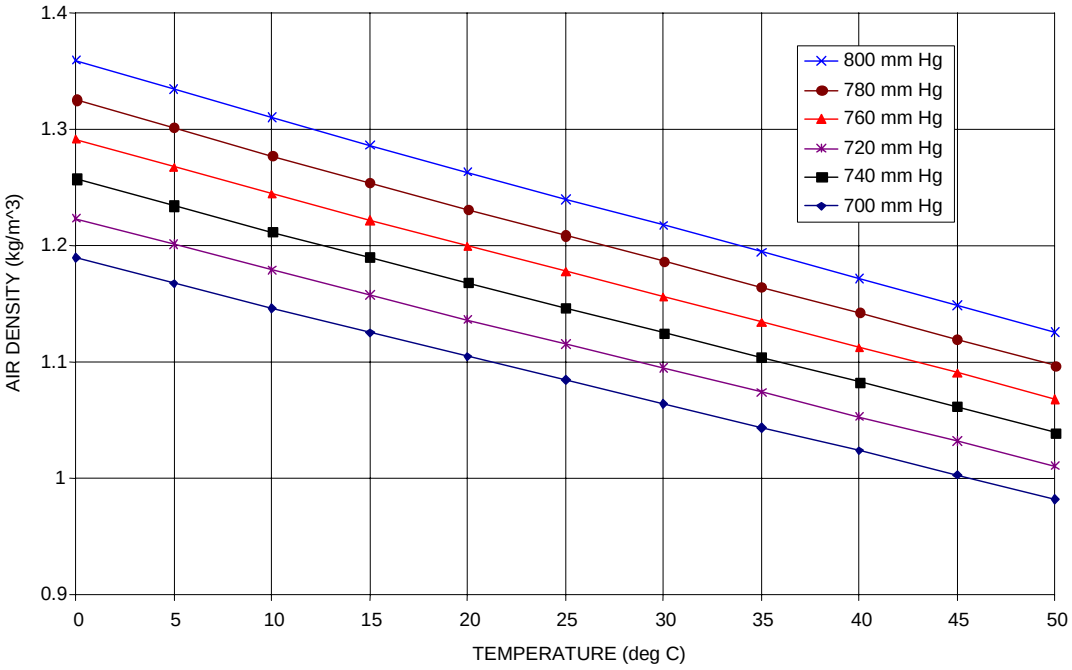

Figure 3-6. Air density versus temperature and pressure for 50% humidity.

ENVIRONMENTAL CORRECTION FACTORS

The electrical power industry has developed standards for testing high-voltage insulators and hardware. They are documented in IEC publication 60-1 (1979), "High Voltage Test Techniques," ANSI C.29-1998 "American National Standard for Electrical Power Insulators – Test Methods" and IEEE Std 4-1995, "IEEE Standard Techniques for High-Voltage Testing." The origin of these standards is not completely disclosed. However, the IEEE standard gives an extensive bibliography and appears to rely heavily on IEC 60. The 1998 ANSI standard relies heavily on the IEEE standard. According to Rizk (1992), the recommendations of Kucera (1970) form the basis for the earlier version, IEC publication 60 (1968).

These standards define testing techniques for various conditions, including AC and DC voltages, lightning and switching impulses, wet and dry, as well as defining the methods for measuring voltage, and current and the power requirements for these types of tests. The environmental conditions of air pressure, temperature, and humidity affect the flashover and withstand voltage test results. Because of this, the electrical power industry has developed empirical correction factors to translate measurements made at one environment to the value they would have for the standard environment. Thus, measurements made under different conditions and at different laboratories can be compared and adjusted to estimate performance for other environments.

These correction factors are not based on the similarity laws developed previously (Chapter 2). They have been empirically developed for application to flashover voltage, not corona onset field. In fact, similarity may not strictly apply to flashover phenomena across large gaps, since it is not really a Townsend process. The similarity relations lead to an environmental correction factor that corrects the air density and geometry to a situation that will have exactly the same breakdown voltage. This correction factor changes the fields but not the voltage. In the original development of standard test procedures for VLF/LF high-voltage hardware at the HVTF, we leaned heavily on the use of the existing industry standards and applied the correction factors obtained from these standards. However, when we discovered that the important phenomena at VLF/LF are highly correlated to corona, which is a Townsend process for most practical situations, we switched to an air density correction factor based on similarity. Chapter 6 contains measurements validating this approach. The humidity correction factor is more complicated and will be discussed later.

The following is a description of the environmental correction factors used by the power industry. Each of the standards uses two separate correction factors, one for atmospheric density and one for humidity. The atmospheric density correction factor is a function of the relative atmospheric density, which can be determined from atmospheric pressure and temperature. The humidity correction factor is given as a function of the amount of water vapor in the air. For wet tests, the humidity correction factor is ignored. The correction factors given in these three standards are similar but not exactly the same. For example, the IEC and ANSI humidity correction factor is in terms of the partial pressure of the water vapor, while the IEEE standard uses absolute humidity of the air in terms of density. Also, the IEC and ANSI standards use 25° C for the standard temperature, versus 20° C for the IEEE standard. In all of these standards, the correction factor is applied directly to the flashover voltage, not to fields, as Townsend's theory would suggest.

Standard Conditions

The standard atmosphere reference for the correction factors is given in terms of barometric pressure, (P_0), absolute temperature, (T_0), and humidity in terms of the partial pressure of the water vapor in the air, (P_w), in Table 3-2 below.

Table 3-2. Standard atmospheric conditions.

Parameter	ANSI C29.1-1998 & IEC 60	IEEE 4-1995
P_0	29.92 inches Hg = 760 mm Hg	760 mm Hg
T_0	77° F (25° C) = 298.1° K	20° C (69° F) = 293.1° K
P_w	0.6085 inches Hg (15.46 mm Hg)	N/A
d_w	N/A	11 grams/m^3
W	13.07 grams/kg	9.29 grams/kg
RH	65.3%	63.9%

Both W and relative humidity have been calculated from the given parameters.

Relative Air Density

The relative air density, δ, is defined the same in all the standards, although different units are used in the equations. The relative air density is a ratio: absolute density of the air–water mixture for a given set of conditions divided by the absolute density of the same air–water mixture at standard conditions. The formula used by all the standards to calculate the relative air density given by the following:

$$\delta = \frac{P}{P_0} \cdot \frac{T_0}{T}$$

where P = total atmospheric pressure in absolute units (mm or inches Hg, or psi)
P_0 = standard pressure in the same units
T = ambient temperature in degrees Kelvin
T_0 = standard temperature in degrees Kelvin.

This equation gives the density ratio for a fixed air–water mixture at a given temperature and pressure to what it would be at STP. Using this relative density factor ignores the fact that different air–water mixtures have different absolute densities. Thus, the absolute density at STP will be different for different air–water mixtures, although this effect is fairly small as previously shown. It is not mentioned in the standards, but this density correction factor does not strictly apply when the correction to STP would transcend the dew point. In this case, the test sample air would have a relative humidity greater than 100% at STP, and this mixture could not exist normally. The effect of this loss of moisture on the air density is normally quite small. The effect on the humidity correction factor is more complicated and will be discussed below.

Humidity

At low frequency, it is well known that the presence of humidity results in increased breakdown voltage for air. Unfortunately, there is no concise theory available that can be used to help develop a correction factor for humidity. Similarity does not apply directly, because changing the vapor content changes the gas mixture. Different gases behave differently, meaning they have different Paschen's curves. As a result, the humidity correction factor has to be based entirely on empirical data.

Both the IEEE and ANSI high-voltage test standards have similar humidity correction factors. In order to determine the humidity correction factor, both of these standards require the determination

of an appropriate humidity parameter by measurement, which is then used to obtain the correction factor from a graphical plot, originally developed from empirical data. The standards specify the humidity parameter differently.

The IEEE standard humidity correction factor is based on the ratio of the absolute humidity, in terms of the mass density of water in the air, to the relative air density (d_w/δ) in units of grams/m^3. The mass density of water vapor is given by Equation 3-3. Division by the relative air density, δ, corrects this parameter to STP. In other words, (d_w/δ) is the mass density of the water vapor for the sample air–water mixture if it were converted to STP.

The ANSI humidity correction factor is given in terms of the partial pressure of the water vapor in the air. The ANSI standard calls this partial pressure the "vapor pressure," P_h. This is calculated from the relative humidity by using Equation 3-6. For a given air–water mixture, this parameter is a function of pressure and temperature. The standard does not specify, but it seems logical that this parameter should be adjusted by relative density, similar to the method used by the IEEE standard. If the partial pressure of water vapor is adjusted in that manner, the parameters of the two standards have a simple linear relationship between them. In this case, any given value of the parameter has a one-to-one correspondence to a particular air–water mixture. If the partial pressure of water vapor is not adjusted, it will not be directly related to the air–water mixture and inconsistencies will occur. For example, the uncorrected parameter is measured at ambient conditions and different air–water mixtures could have the same value for the partial pressure of water vapor, depending upon the temperature and pressure of the air measured. Similarly, the same air–water mixture measured at conditions other than STP could have different values for the partial pressure of the water vapor.

Both of these correction factors have a problem, not mentioned in the standards, if when correcting to STP the dew point is transcended. As previously mentioned, this would correspond to the air sample having a relative humidity greater than 100% at STP, which could not exist normally. This situation can arise when the conditions are warm and humid, as might occur in the tropics. Also, the cooler and denser the standard conditions, the more likely this is to happen. This may be part of the reason that the ANSI standard chose a higher reference temperature.

Correction Factors

The standards use a separate factor to correct for air density and humidity. These factors are applied directly to the standard flashover voltage to determine the actual flashover voltage for the prevailing atmospheric conditions. The formulas are inverted to correct actual measured flashover voltages to the standard flashover voltage. The correction factors are described below. For all of these standards, the humidity correction factor is assumed equal to 1 for wet conditions.

ANSI C-29.1998

The correction factors are applied to the breakdown voltage at standard conditions, V_0, to yield the breakdown voltage at the existing conditions as follows.

$$V = \frac{V_s \cdot \delta}{H} \tag{3-8}$$

where V = flashover voltage for existing atmosphere
V_s = flashover voltage for standard atmosphere
δ = relative atmospheric density
H = humidity correction factor.

The air density correction factor is equal to the relative air density and is applied directly to the flashover voltage. IEC publication 60 uses an air density correction factor, which diverges slightly from relative air density (see Figure 3-7).

The humidity correction factor for ANSI C29-1998 is specified by a pair of curves that give correction factor versus vapor pressure in inches of Hg (Figure 3-8). From the figure, it is seen that the correction factor is equal to 1 when the vapor pressure is 0.6085 inches of Hg, representing standard humidity for ANSI C29-1998. The slope of these curves is negative. Since the breakdown voltage is inversely proportional to the ANSI humidity correction factor (Equation 3-8), the negative slope implies that increased humidity increases breakdown voltage. At the standard humidity, the slope is approximately -35% per inch Hg water vapor pressure, indicating humidity increases the flashover voltage by 35% per inch Hg water vapor pressure. For wet tests, the humidity correction factor is not used, i.e., H = 1.

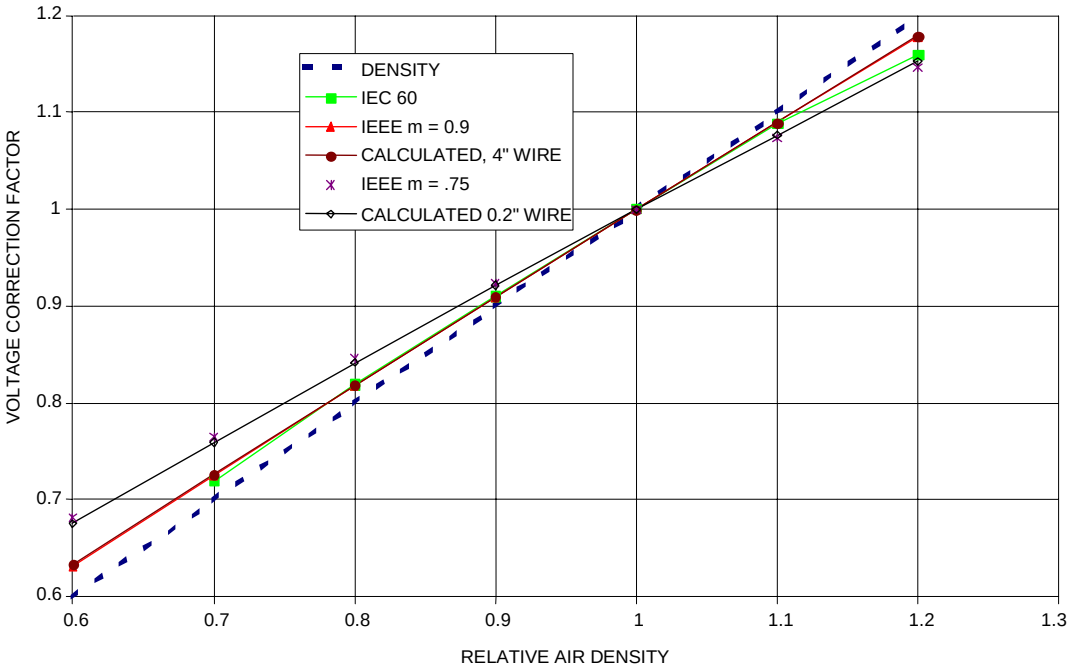

Figure 3-7. Air density correction factor comparison.

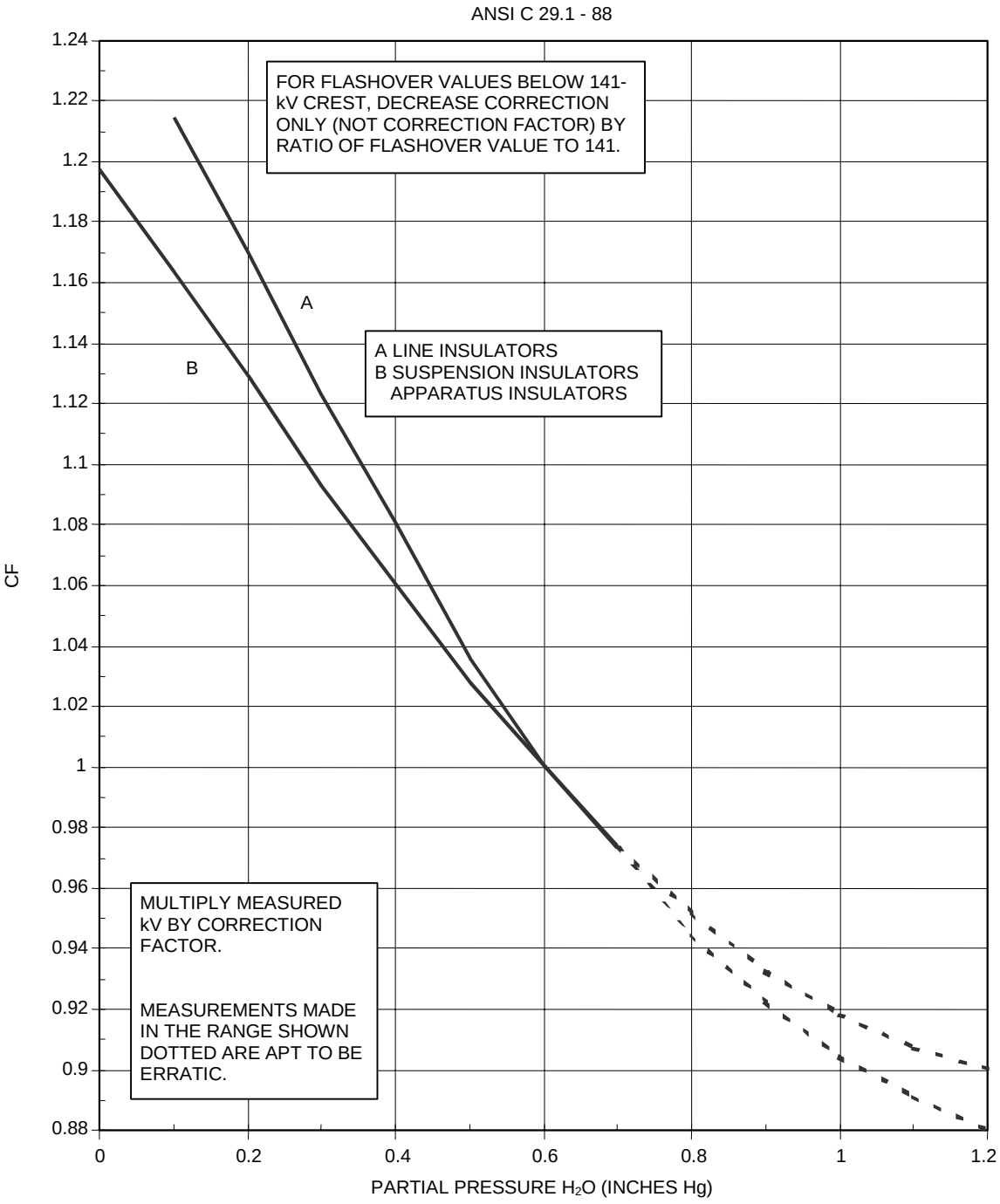

Figure 3-8. ANSI low-frequency humidity correction factor.

IEEE 4-1998

The IEEE standard is more complicated. It defines a correction factor, *K,* given below.

$$k = k_1 \cdot k_2$$

where k_1 is the air density correction factor and
k_2 is the humidity correction factor.

Note the humidity correction factor is not used for wet tests, i.e., $k_2 = 1$.

The correction factor is applied to the breakdown voltage at standard conditions, $V_{0,}$ to yield the breakdown voltage at the existing conditions as follows.

$$V = V_0 \cdot k \tag{3-9}$$

The inverse equation is applied to correct measured discharge voltages to standard reference atmosphere by dividing by k.

$$V_0 = \frac{V}{k}$$

Air Density

The air density correction factor, k_1, depends upon relative air density as follows.

$$k_1 = \delta^m$$

where m is given by a graphical function of the parameter g.

The standard indicates that the exponent m is a function of the test object and the waveform.

The function g is given by:

$$g = \frac{V_b}{500 \cdot L \cdot \delta \cdot k}$$

where V_b is the 50% breakdown voltage in kV, at actual atmospheric conditions,
L is the minimum discharge path in meters.

Note that the ratio of V_b/L is the average field across the gap at breakdown.

This is somewhat of a circular function since g depends upon k, which affects the breakdown voltage and hence g. However, for most practical cases, both δ and k are near 1 and g is approximately the average field in the gap at flashover, normalized by 500 kV/m.

The exponent m is given graphically in Figure 3-9. The rule for m is that if $g \geq 1$, then $m = 1$. In this case, the air density correction factor is just equal to the air density. However if $g \leq 1$, then m is reduced from 1 until it reaches 0 at $g = 0.2$. Thus, for some conditions the air density correction factor is equal to the air density with an exponent less than 1. Increasing m has the effect of decreasing the slope of the air density correction factor. The air density correction factor is plotted for two different values of the exponent m in Figure 3-7. Note that the IEC 60 air density correction factor, plotted in the figure, is almost the same as the curve for $m = 0.9$. All of the curves pass through 1 at the standard humidity. All the curves except for the straight-line plot of relative air density have a slope less than 1. For this reason, the curves deviate from straight relative air density more when the relative air density is farther from the standard value.

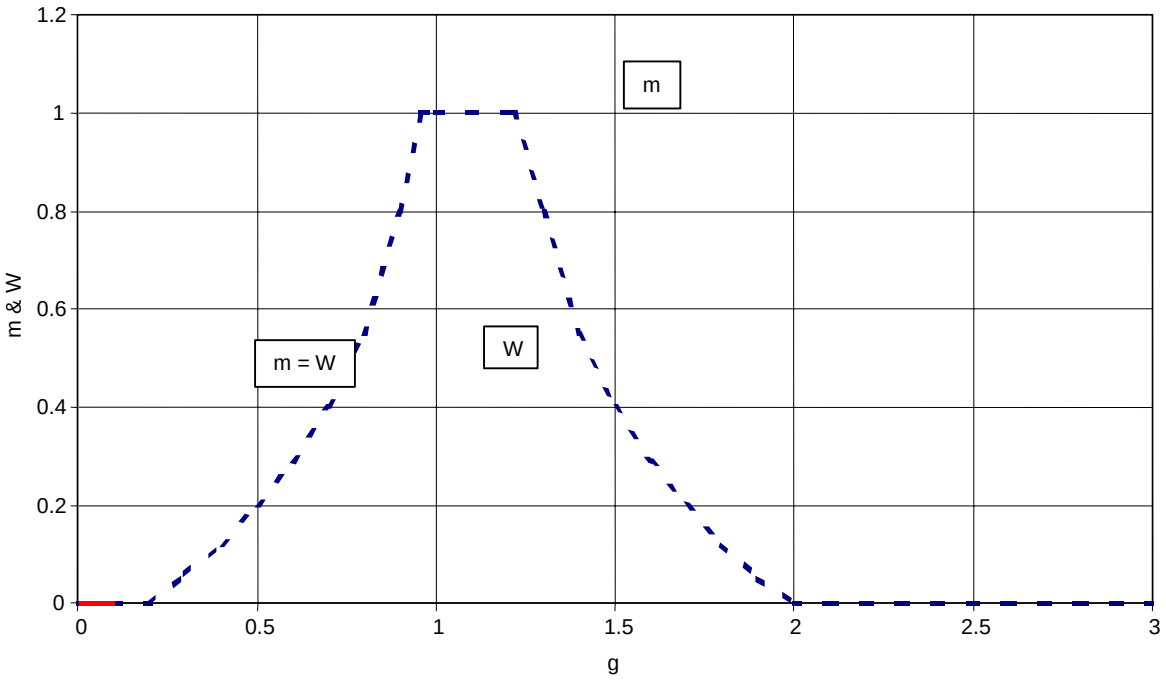

Figure 3-9. Exponents *m* and *w* for IEEE air density and humidity correction factors.

Humidity Correction Factor

The humidity correction factor, k_2, depends upon K_h, which is a function of the ratio of absolute humidity to relative air density as follows.

$$k_2 = k_h^w$$

where w is given by a graphical function of the same parameter g used for the air density correction factor.

Th factor w is also plotted in Figure 3-9. From the figure it is seen that w is equal to 1 only when $1 \geq g \geq 1.2$. Otherwise, it is less than 1.

The factor K_h is described by a set of graphical curves. These curves are equal to 1 when the water vapor density is equal to 11 grams/m^3, which is the standard humidity condition for the IEEE standard. Plots of these curves are given in the standard. For engineering purposes, the standard indicates that these curves can be approximated by straight lines with the following formulas:

Alternating voltage $$k_h = 1 + 0.012 \cdot \left(\frac{d_w}{\delta} - 11 \right)$$

Impulse voltage $$k_h = 1 + 0.010 \cdot \left(\frac{d_w}{\delta} - 11 \right)$$

Direct voltage $$k_h = 1 + 0.014 \cdot \left(\frac{d_w}{\delta} - 11 \right)$$

where d_w is in grams/m^3.

The IEEE standard indicates that errors as much as negative 14% may occur when the value of d_w exceeds 15 grams/m^3 and that in this region the humidity correction factor is still under investigation.

Comparison with ANSI

The IEEE humidity correction factor is applied inversely to the ANSI humidity correction factor (compare Equations 3-8 and 3-9) and the positive slope implies that humidity increases the flashover voltage, which is in agreement with the ANSI standard.

The IEEE humidity correction factor is centered on a water vapor density of 11 g/m3, where it has the value of 1. This corresponds to a mixing ratio, *w*, of approximately 0.01. The ANSI standard humidity correction factor is centered on a water vapor pressure of 0.6 inches of Hg, which corresponding to 15 grams/m^3, considerably higher than that used by IEEE.

The slope of the humidity correction factor k_h of the IEEE standard is approximately 1.2% per gram/m^3, which converts to 54% per inch Hg. From the equation for the humidity correction factor, $k_2 = \left(k_h\right)^w$, the slope is equal to *w* times 54% per inch Hg. Since *w* is mostly less than 1, this compares favorably with the 35% per inch Hg slope of the ANSI humidity correction factor curves. In fact, they both have the same slope when $w = 0.65$.

Similarity-based Air Density Correction Factor

The generalized similarity law can be used to develop a theoretical basis for correcting for air density variation. This correction factor is applied to the electric fields and the geometry and not directly to the voltage. The use of the generalized similarity relationship to develop a density correction factor will be illustrated by application to the case of a single wire above ground. In this case, the field is non-uniform and the beginning of breakdown corresponds to corona onset. As has been shown in Chapter 2, the equivalent gap for this geometry is small and Townsend's theory applies.

Let the geometry be defined by the diameter of the wire d_1, the height of the wire h_1. The breakdown voltage measured for this case is V_1 and the air density during the measurement is δ_1. For a wire well above ground, the maximum surface electric field is given by the following equation.

$$E_1 \approx \frac{2 \cdot V_1}{d_1 \cdot \ln\left(\frac{4 \cdot h_1}{d_1}\right)}$$

For any geometry, the electric field is similarly a function of the voltage divided by a linear distance (hence the units volts per meter for *E*) and a dimensionless function of the ratio of geometric distances (see Chapter 4).

The generalized similarity relationship can be used to convert the parameters in the above equation to those for a different air density, δ_2, as follows. Similarity implies, just as in the case of a uniform field, the gap times the air density must remain a constant. This will be true if all the dimensions are changed such that:

$$\delta_1 \cdot (d_1, h_1) = \delta_2 \cdot (d_2, h_2)$$

or

$$(d_2, h_2) = (\delta_1/\delta_2) \cdot (d_1, h_1) .$$

Thus the appropriate scale factor is (δ_1/δ_2). When $\delta_2 = 1$, standard density, the result becomes:

$$(d_2, h_2) = \delta_1 \cdot (d_1, h_1) .$$

Similarity requires that the breakdown voltage remain constant for the new density and spacing; but since the dimensions changed, the electric field at breakdown changes as given below.

$$E_2 = \frac{2 \cdot V_1}{d_2 \cdot \ln\left(\frac{4 \cdot h_2}{d_2}\right)} .$$

Note that since d_2 and h_2 are equal to d_1 and h_1 multiplied respectively by the same factor, the dimensionless function of the ratio of distances remains unchanged. However, the remaining distance factor $d_2 = d_1 \cdot \delta_1$. Substituting this in the equation for the maximum surface field gives the following for E_2:

$$E_2 = E_1 / \delta_1 \quad .$$

Thus, adjusting a measurement made at any air density to the value it would have at STP amounts to dividing the electric field by the relative air density present during the measurement. It is important to remember that the geometric distances are also changed. This is important because the effective radius of curvature for the test object is changed as the air density changes. In this case, the wire diameter changes. This is important because the critical field for corona onset is a function of wire diameter. Similarly, for objects other than wires, such as corona rings, the critical gradient is expected to be a function of the radius of curvature. For the example of the wire above ground, the corrected value of E applies to a wire that has the corrected diameter (i.e., $d_2 = \delta_1 \cdot d_1$).

The correction factors developed by the power industry are applied directly to voltage and not to the field and the dimensions suggested by the similarity law. For a comparison, we have used Raizer's formula for the corona onset gradient on smooth wires (Equation 2-3) combined with the similarity law, to calculate the voltage air density correction factor for a wire above ground. Two examples have been selected. One has a 4-inch diameter wire and the other has a 0.2-inch diameter wire. Both are located 48 inches above the ground. The relative air density was varied from 0.6 to 1.2. The two calculated voltage correction factors are plotted in Figure 3-7 along with the IEC and IEEE (m = 0.9 and 0.75) air density correction factors. Note that IEEE m = 0.9 corresponds closely to the IEC curve except at the highest relative density of 1.2, where the IEC curve falls below, closer to the IEEE 0.75 curve.

The calculated correction factor deviates from air density because the critical gradient is a function of the radius of the wire. From similarity, changing the air density changes the effective wire diameter. The deviation is greater for the smaller diameter wire because the slope of the breakdown gradient versus diameter curve is less for larger diameter wires (see Figure 2-9). This same effect will occur with any Townsend process, including uniform field gaps, where the deviation from air density will be greater for smaller gaps.

Based on this analysis, it is expected that the voltage air density correction factor is a function of the object's shape, especially the radii of curvature of the electrodes. We believe that most, if not all, of the deviation of the observed voltage correction factors from those associated with a linear relationship to air density is due to this effect. For normal high-voltage hardware, the magnitude of this effect will depend mostly upon the radii of curvature of the electrodes. The IEEE standard uses air density to the exponent, m, (δ^m) to account for this effect. It may be possible to estimate the value of the exponent, m, from the geometry of the object. In Figure 3-7, the three curves, IEEE m = 0.9, IEC, and calculated 4-inch diameter wire correspond very closely. The two curves, m = 0.75 and the one calculated for the 0.2-inch diameter, are almost exactly the same. Thus, objects with larger radii

of curvature correspond to IEEE voltage correction factors with larger values of m. The IEC density correction factor corresponds to objects with radii of curvature of 2 inches.

From the above analysis, it is clear that the voltage air density correction factor is different for differently shaped objects. For wires and other simple geometrical shapes with identifiable radii of curvature, we believe that it is better to use the true air density correction factor based on the generalized similarity law, which applies to the electric field and the geometry, not to the voltage.

Humidity Correction Factor and Paschen's Law

For the application to high-voltage breakdown, it is important to understand that air mixed with water is a different gas than air alone. Changing the amount of water vapor in air amounts to changing gas constituency, which not only changes the density but the mixture. In general, each specific mixture has a different Paschen curve function, f (Equation 2-1). One can imagine a family of Paschen's curves parametric in the mixing ratio, each curve representing a different air–water mixture. Changing the density of a given air–water vapor mixture amounts to sliding up or down on the appropriate Paschen's curve. Changing the air–water vapor mix corresponds to changing from one curve to another curve. The humidity correction factor is derived from the spacing between the curves. It is a function of the air–water mix at STP. It is likely that a humidity correction factor would be best applied to the electric field and dimensions geometry as was the similarity based air density correction factor, instead of directly to the voltage.

It is unlikely that this family of Paschen's curves would be everywhere parallel. Thus, the humidity correction factor for uniform field gaps will probably be a function of the gap length times the air density. Because of the correspondence between gap length and radii of curvature, it is likely that the humidity correction factor for curved objects is a function of the radii of curvature. Thus, the humidity correction factor for wires is quite likely a function of the wire diameter. It seems probable that the humidity correction factors presented in the standards would correspond to objects with relatively large radii of curvature, similar to the case for the air density correction factors.

In order to understand the real effect of humidity, a set of measured Paschen's curves parametric in the mixing ratio is needed. A second set of similar data should be measured for corona onset on wires. Based on the limited data available, we believe the frequency effect is a strong function of both humidity and radii of curvature (see Chapter 6). In order to help sort out these effects, data for both the parallel plate and wire geometry should be measured at several frequencies up through the LF band.

CHAPTER 4 CALCULATING ELECTRIC FIELDS

BACKGROUND

Electrical breakdown of the air in the vicinity of high-voltage hardware occurs when the voltage reaches some critical value. Based on Townsend's theory and Paschen's measurements, the breakdown is the result of strong electric fields in the immediate vicinity of the surface of the electrode. Breakdown is actually a function of the integral of the electric field from the surface out over the active ionization region. For this reason the field on the surface at breakdown is a function of the radius of curvature and other surrounding objects. However, for a given radius of curvature breakdown is essentially a function of the surface field on the electrode. For most cases, breakdown occurs where the surface field is a maximum. Thus for a given object the maximum surface field closely tracks breakdown and is the single parameter best used to estimate the breakdown level.

Professor Kreuger of Delft University of Technology in the Netherlands states that there are two things needed for successful high-voltage design (Kreuger, 1991). One is an accurate knowledge of the electromagnetic fields around the design object and the second is accurate information about the critical field level at which breakdown occurs. He states that "nowadays with the advent of modern computer technology, the first is readily available but the second is not so easy to find." When we began the Navy's VLF/LF High-Voltage project, neither was readily available. In fact, the Navy funded a Canadian group to develop an electrostatic field calculation computer program, and that group has since become one of the world's leading suppliers of such software.

The electrical breakdown process is highly non-linear, and the breakdown voltage of any complicated object can only be determined empirically. From Townsend's theory, it is clear that the most important parameter directly involved in breakdown is the electric field on the surface and how it decreases with distance from the surface. The determination of the electric field strength is often not easy, especially when the field is highly non-uniform. In general, direct measurement of the electric fields is impractical. However, it is usually easy to measure the voltage on the object. The time-honored technique for determining the electric field at breakdown is to measure the breakdown voltage and then calculate the electric field that results from the measured voltage and the shape of the object. This is the process used to determine the critical breakdown fields. Once the critical field has been determined for a given radius of curvature and atmospheric conditions, this information can be used in design or analysis. Consequently, calculation of electric field is an essential part of the science and engineering associated with high-voltage design.

In early studies of electrical discharge in gases, experimenters did not have the luxury of computers to provide numerical solutions for electric field strengths. As such, they were forced to limit their measurements to simple geometric configurations for which field strength could be calculated analytically. Often the objects investigated had a two-dimensional or rotationally symmetric geometry so that the electrostatic problems could be solved by the use of images or conformal transformations. These configurations include two parallel plates: a cylinder parallel to and above a ground plane and a sphere above a ground plane. These configurations are briefly discussed in Chapter 3 and illustrated in Figure 3-1. Maxwell himself worked out many of these solutions. The case of the cylinder above ground is equivalent by image theory to the case of two parallel wires. Similarly, the case of the sphere above ground is equivalent by image theory to the case of two separated spheres. Approximate solution can be obtained for some more complicated configurations; for example, the case of a cage or bundle of parallel wires, parallel to and well above a ground plane.

The initial empirical investigations of breakdown focused on the simple geometric configurations of parallel plates and a wire above a ground plane. The fields for these cases are quite easy to calculate and values of the critical electric fields were inferred by calculation from the voltage measurements. With few exceptions, real-world high-voltage hardware is more complicated than hardware corresponding to the above simple geometric configurations. Before field computation software became readily available, the design approach was to obtain estimates derived from simple geometric configurations similar to the actual configuration and then design with large safety factors to compensate for uncertainties in the estimation process.

These days the computers and software necessary to make calculations of electromagnetic fields are readily available. It is common knowledge that is unwise to use computer-generated data for engineering purposes without some form of validation.. This is especially true for computer programs that calculate electromagnetic fields. There is still considerable art involved with the application of these programs for obtaining calculations with the required accuracy. This is particularly true for three-dimensional cases. In this chapter, we discuss the process that we used to validate the computer calculations. The computer programs have been applied to the simple geometric configurations that have analytic solutions. In this way, we can try various techniques and develop an appropriate method that yields answers of acceptable accuracy. As it turns out, this requires considerable effort, and we felt that what we learned in this process may be valuable to others.

The chapter includes the discussion of the analytic solution for a few simple geometric configurations, previously discussed in Chapter 2 but included here for completeness, followed by a discussion and examples of the application of the computer programs to treat both the simple configurations and more complicated configurations.

SIMPLE GEOMETRIC CONFIGURATIONS

Parallel Plates

The simplest geometry for which the field can be calculated involves parallel plates. The calculation of the electric field strength for this case is trivial. This was the geometry investigated by the first experimenters. The electric field strength, E, throughout the gap is given by the voltage, V, divided by the gap length, l.

$$E = \frac{V}{l}$$

Any practical parallel plate configuration has finite-sized plates. There tends to be a charge concentration on the edge of the plates that depends on their shape. This can result in breakdown occurring near the edges of the plate and not in the field in the gap, leading to results significantly different from those for infinite plates. Consequently, the plates used for uniform field breakdown measurements should have rounded edges, so that breakdown occurs in the uniform field region of the gap. Rogowski (see Cobine, 1958, p. 177), using conformal transformation theory for the case of two-dimensional electrodes, discovered a way to design the plates such that the field on the edges of the gap is less than the field at the center. He found an analytic solution for the appropriate shape, now called a Rogowski surface. Although this shape is based on a two-dimensional solution, it is truncated and used to make rotationally symmetric electrodes for testing the dielectric strength of materials such as oil.

There is no analytic solution for the rotationally symmetric case, but shapes based on the Rogowski concept work very well. It is now possible to adaptively find the “optimum” shape of

electrodes for most any application by using the computer (Kato & Okubo, 1997; Okubo et al., 1997).

Coaxial

Peek and others made measurements for coaxial configurations. Again for this case, the calculation of the electric field strength is trivial. The field anywhere in the gap between the center conductor and the outer conductor is in the radial direction and given by

$$E = \frac{V}{r} \frac{1}{\ln\left(\frac{b}{a}\right)} .$$

where r is the radius to the field point,
a is the radius of the inner conductor, and
b is the radius of the outer conductor.

For this configuration, the maximum field occurs on the center conductor and is given by

$$E = \frac{V}{a} \frac{1}{\ln\left(\frac{b}{a}\right)} .$$

Both of the above expressions for the electric fields are exact. However, in actual practice it is important to consider the field modifying effects of guard rings at the ends of the center contuctor.

Isolated Conducting Sphere

An isolated conducting sphere in free space can be treated as if it had a point charge at the center. By Gauss' theorem, the electric field from a point charge at the origin in free space is given by

$$\overline{E} = \frac{q}{4\pi\varepsilon_0 r^2} \hat{r} \tag{4-1}$$

where q is the charge,
ε_0 is the permeability of free space, and
r is the distance from the charge.

Surfaces having equal potential are defined by $\overline{E} \cdot \hat{n} = 0$ on the surface. Since the field is radial, the equipotential surfaces are spheres centered on the point charge. Thus, the fields outside of a charged conducting sphere (an equipotential surface) in free space are same as the fields due to a point charge at the center of the sphere. By Gauss' theorem, the magnitude of that point charge is equal to the total charge on the sphere.

The potential (voltage) at any point in space around a point charge can be determined by integrating the force on a sample charge moved in from infinity (zero voltage). For the case of a charge located at the origin, the voltage (V) at any point can be expressed by the following integral:

$$V = \frac{q}{4\pi\varepsilon_0} \int_{\infty}^{r_1} -\frac{dr}{r^2} = \frac{q}{4\pi\varepsilon_0 r_1} \tag{4-2}$$

where r_1 is the distance from the charge to the point where the voltage is calculated.

If the sphere has a radius, *a*, the voltage on the sphere is given by the following:

$$V = \frac{q}{4\pi\varepsilon_0 a} \quad . \tag{4-3}$$

Solving for *q* and substituting into the Equation 4-1 for the electric field around the point charge gives

$$\overline{E} = \frac{V \cdot a}{r^2}\hat{r} \quad . \tag{4-4}$$

On the sphere surface the magnitude of the electric field is given by

$$E = \frac{V}{a} \quad .$$

Point or Line Charge above a Ground Plane

Both these problems can be solved exactly by image theory. Figure 4-1 illustrates the geometry where the charge in the upper part of the figure represents either a point charge or a line charge above an infinite perfectly conducting ground plane. The image is given opposite charge and is placed an equal distance below the ground plane. The component of the electric field parallel to the ground plane is equal and opposite for the source and image. Thus this component is zero, satisfying the boundary condition for a perfectly conducting ground plane. The uniqueness theorem says that there is only one solution for the electromagnetic fields that satisfies the boundary conditions. Therefore, the configuration consisting of the charge plus the ground plane is equivalent to the configuration consisting of the charge and its image. Of course, this solution is valid only in the region above the ground plane. For the case of a point charge, the electric field above the ground plane can be simply calculated by using Equation 4-1 and superimposing the field from both charges.

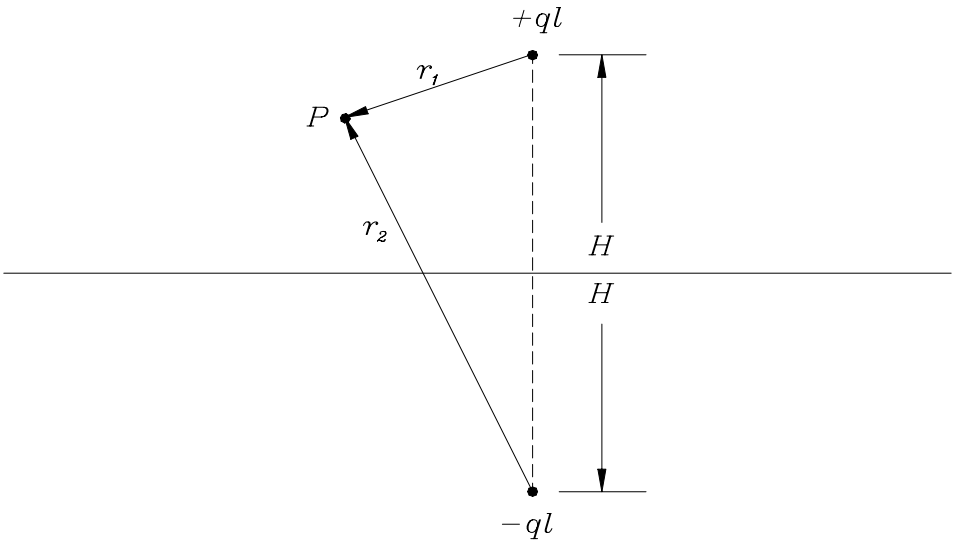

Figure 4-1. Line charge or point charge above a perfectly conducting plane.

Point Charge Near Conducting Sphere

This problem consists of a point source charge located outside of a conducting sphere. It can also be solved exactly by image theory. In this case, the conducting sphere is replaced by an image charge. Figure 4-2 illustrates the geometry. The source charge is located a distance, *d*, away from the center of the sphere. The image charge is offset from the center of the sphere by the distance, O. The field from the charge and its image are given by superposition using Equation 4-1, with suitable transformations for the location of each charge.

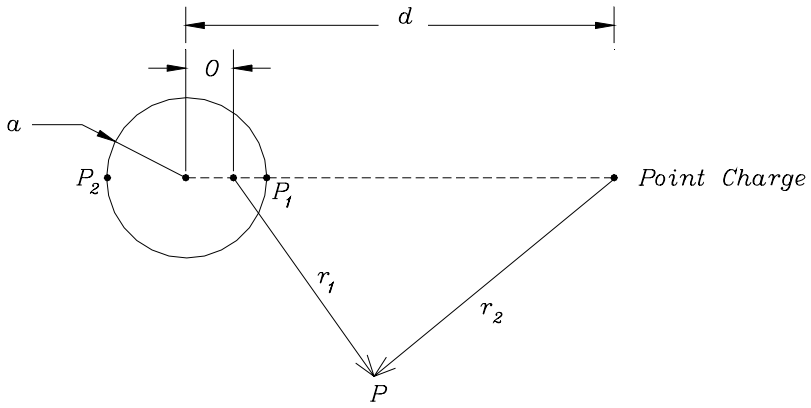

Figure 4-2. Point charge near a sphere.

The potential (voltage) at any point in space can be determined by application of Equation 4-2. Superposition holds and the voltage at a point due to a group of charges is equal to the sum of the voltages from each charge. The voltage at any point is given by the following equation:

$$V = \frac{q}{4\pi\varepsilon_0 r} \cdot \left\{ \frac{q_1}{r_1} + \frac{q_2}{r_2} \right\}$$

where r_1 is the distance from the charge and,
r_2 is the distance from the image.

The magnitude of the image charge and the offset can be determined by setting the voltage at points P_1 and P_2 equal to zero (Figure 4-2). For this condition, it can also be shown that the voltage is zero everywhere on the sphere (Lorrain and Corson, 1970, p. 147). The resulting image charge and offset are given by the two equations below.

$$q_2 = -\frac{a}{d} \cdot q_1 \ , \ O = \frac{a^2}{d}$$

These two charges can be used to calculate the exact field and voltage (potential) everywhere outside of the sphere, given the sphere surface is at zero voltage.

The sphere can have a voltage other than zero by simply adding a charge at the center. The fields from the center charge are perpendicular to the surface of the sphere, and therefore it remains an equipotential surface. The voltage on the surface of the sphere due to the external charge, and its image is zero since the net charge on the sphere is zero. The voltage on the sphere's surface is determined only by the charge at the center, which is given by Equation 4-3.

Charged Sphere above Ground Plane

This problem can also be solved exactly using image theory to generate an infinite series of images that amount to successive approximations. This series converges rather rapidly. The series of images is started by placing a charge at the center of the sphere, located a height, *h*, above a perfectly conducting ground plane. The charge at the center of the sphere results in a negative image located at a distance, *h*, below the ground plane. This image then results in a positive image in the sphere, with a magnitude *a*/*2* times the first charge, offset from the sphere center by the distance $a^2/2h$. This results in another negative image below the ground plane, etc. This series of images converges rapidly and can be used to accurately calculate the capacitance for the sphere above ground and the potential (voltage) and electric field everywhere outside of the sphere and above the ground. A spreadsheet can be set up to calculate these charges and their fields. Table 4-1 shows the first seven charges that appear in the sphere and their images. Note that the seventh charge has a value less than 0.00005, which illustrates how fast the series converges. For the example given in Table 4-1, the separation between the bottom of the sphere and ground, *S*, (see Figure 2-1C), is equal to two sphere radii. An increasing number of terms are required as the value of *S* approaches zero.

The voltage on the sphere is determined only by the first charge, which in Table 4-1 was assumed equal to 1. The capacitance is determined by the total charge on the sphere. Thus, the capacitance of the sphere, normalized to the capacitance it would have in free space, is equal to the converged value of the total charge (bottom of the fourth column of Table 4-1), in this case about 1.2. Thus, for the case of the sphere separated from ground by two radii, the capacitance is 20% higher than it would be for free space.

Table 4-1. Charged sphere above ground.

	h =	3	Height of sphere center		
	a =	1	Radius of sphere		
	S =	2	Separation of sphere from ground		
Sphere side of plane				Image side of plane	
Charge Number	Individual Charge	Distance from center	Total Charge on Sphere	Image Charge	Distance from Center
1	1.0000	0	1	-1	6
2	0.1667	0.1667	1.1667	-0.1667	5.8333
3	0.0286	0.1714	1.1952	-0.0286	5.8286
4	0.0049	0.1716	1.2001	-0.0049	5.8284
5	0.0008	0.1716	1.2010	-0.0008	5.8284
6	0.0001	0.1716	1.2011	-0.0001	5.8284

7	0.0000	0.1716	1.2012	0.0000	5.8284

Given the charges, the corresponding electric fields can be calculated simply using Equation 4-1 and superposition. Figure 4-3 gives the calculated results for the capacitance and electric fields associated with a sphere above ground using this technique. In Figure 4-3, the capacitance and fields are normalized to the value they would have in free space. For example, *C/Co* represents the capacitance of the sphere divided by the capacitance it would have in free space. Similarly *Es/Eso* represents the field on the sphere divided by the field that would be on the sphere (for the same voltage) in free space. As shown in Figure 4-3, the capacitance and the fields are increased by the presence of the ground. As the sphere is moved farther away from ground, the values of both C/Co and *Es/Eso* are asymptotic to 1, indicating that they approach the value they would have in free space. The term *Eg/Ego* represents the field at ground plane divided by the field that would be present at that point if there were no ground plane. This term has value asymptotic to 2 because the boundary condition at the conducting ground plane doubles the field. Note that both *Es/Eso* and *Eg/Ego* are asymptotic to 1/*S* when *S*/*a* becomes small.

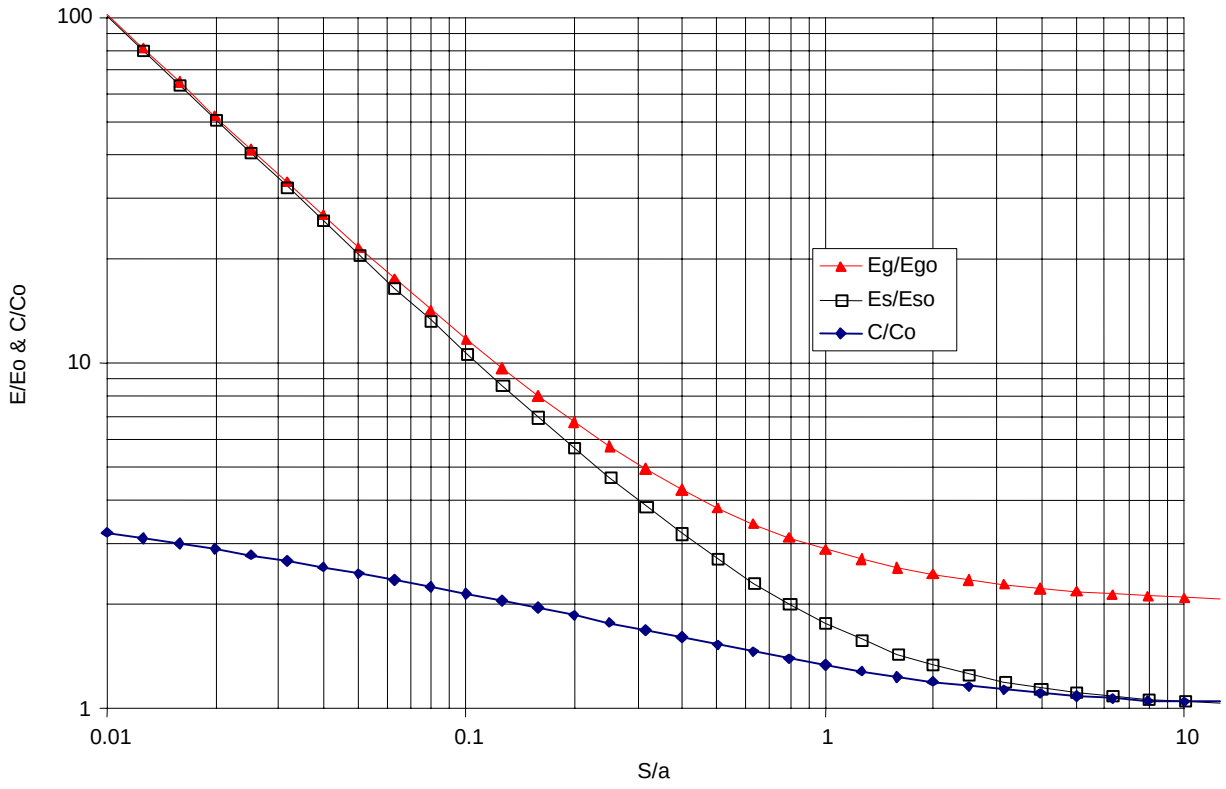

Figure 4-3. Capacitance and fields from a charged sphere above ground.

As previously discussed, the voltage on the sphere is determined only by the charge at the center. This charge can be adjusted to give any desired value for the voltage. The case of a sphere above ground is exactly analogous to two spheres, one at the positive voltage and the other at the negative voltage. The voltage on each sphere can be individually adjusted by changing the charge at the center. For the case of two spheres, one charged but the other floating (i.e., not connected to anything), the net charge on the floating sphere must be zero. This is accomplished by setting the

charge at its center equal to the sum of all the image charges. This center charge defines the voltage that the floating sphere takes on. The second sphere could also be forced to some other voltage by connecting it to a voltage source. It turns out that the electric fields around that sphere are at a minimum when the voltage on the sphere is the same as it assumes when it is floating. This is because there is no net charge on the sphere at this voltage.

Voltage for a Line Charge Above Ground

Figure 4-1 illustrates the geometry involved. Note that the line charge above ground has a linear charge density of q_l coulombs/meter. The effect of the ground plane can be taken into account exactly by removing the ground plane and the introduction of an image charge of opposite sign ($-q_l$) at twice the distance to the ground. Two cylindrical coordinate systems have been assigned, one centered on the charge above the ground, denoted by r, and θ and the second centered on the image charge denoted by r' and θ'.

Gauss' law gives the electric field around a line charge by the following equation:

$$\overline{E} = \frac{q_l}{2\pi\varepsilon_0 r} \cdot \hat{r}$$

The voltage (potential) at a point in space can be determined by integrating the force on a point charge moved in from infinity (presumably at zero voltage). Superposition holds and the voltage from a group of charges is equal to the sum of the voltages from each charge. For the situation shown in Figure 4-1, the voltage at the point, P, a distance, r_1, from the original charge and a distance, r_2, from the image charge can be expressed by the following integral:

$$V = \frac{q_l}{2\pi\varepsilon_0}\left(\int_{\infty}^{r_1} -\frac{dr}{r} - \int_{\infty}^{r_2} -\frac{dr'}{r'}\right)$$

The first term in the above integral represents the voltage due to the original charge while the second term, using primed coordinates, represents the voltage due to the image charge. Note that each integral results in a natural logarithm. The limit at infinity results in what appears to be two singularities. However, these singularities can be eliminated as follows. First, rewrite the first integral, separating it into two parts:

$$\int_{\infty}^{r_1} = \int_{\infty}^{r_2} + \int_{r_2}^{r_1}$$

Substituting this into the first equation, the overall integral becomes:

$$\Phi = \frac{q_l}{2\pi\varepsilon_0}\left(\int_{\infty}^{r_2} + \int_{r_1}^{r_2} - \int_{\infty}^{r_2}\right)\cdot\left(-\frac{dr}{r}\right)$$

The two semi-infinite integrals can be combined, and the result is a semi-infinite integral with an integrand of zero that can be shown to be equal to zero, leaving the following result:

$$\Phi = \frac{q_l}{2\pi\varepsilon_0}\int_{r_1}^{r_2}\frac{dr}{r} = \frac{q_l}{2\pi\varepsilon_0}\ln\left(\frac{r_2}{r_1}\right)$$

The above equation can be used to calculate the voltage due to a line charge (parallel to ground) at any point above the ground. By image theory, the same equation applies to two parallel line charges of opposite sign. The log term on the right-hand side is sometimes referred to as the Gaussian potential or the Gaussian coefficient.

From the above equation, it is seen that equipotential surfaces are defined by the loci given by r_2/r_1 = constant. These equal potential surfaces can be shown to be circles around both the line charge and its image. The centers of these circles are offset from the charge location by an amount that depends on the charge height and the radius of the equipotential surface. When the charge is very far away from the ground, the offset approaches zero.

Line Charge Near a Cylinder

Image theory can be used to solve the case of a line charge near a cylinder. The geometry looks the same as for the case of the point charge near a sphere, shown in Figure 4-2, except the circle represents an infinite cylinder. For this case, the image charge is equal and opposite to the source charge, and the Gaussian potentials can be used. Setting the voltage (potential) at points P_1 and P_2 equal gives the equation for the offset.

$$V_1 = \frac{q_1}{2\pi\varepsilon_0} \ln\left(\frac{d-a}{a-o}\right)$$

$$V_2 = \frac{q_1}{2\pi\varepsilon_0} \ln\left(\frac{d+a}{a+o}\right)$$

Setting these two expressions equal gives

$$\left(\frac{d-a}{a-o}\right) = \left(\frac{d+a}{a+o}\right)$$

Solving for the offset gives $O = \frac{a^2}{d}$.

Single Wire above Ground

Voltage on Conducting Cylinder above Ground

Figure 4-4 illustrates the case of a conducting circular cylinder parallel to and above ground. The cylinder has radius, a, and the center is located at a height, h, above ground. The surface is assumed to be at voltage (V) and, because it is a good conductor, the entire cylinder surface is at this voltage, defining an equipotential surface. As shown above, the equipotential surfaces for a line charge above a ground are circular cylinders. Thus, an equipotential surface corresponding to the surface of the cylinder can be generated by a line charge and its image. To match the equipotential surface to the cylinder the location of the line charge is offset from the center of the cylinder by a distance O (see Figure 4-4). The magnitude of the offset (O) can be determined by solving the equations resulting when the voltages at two points on the cylinder are set to be equal as follows.

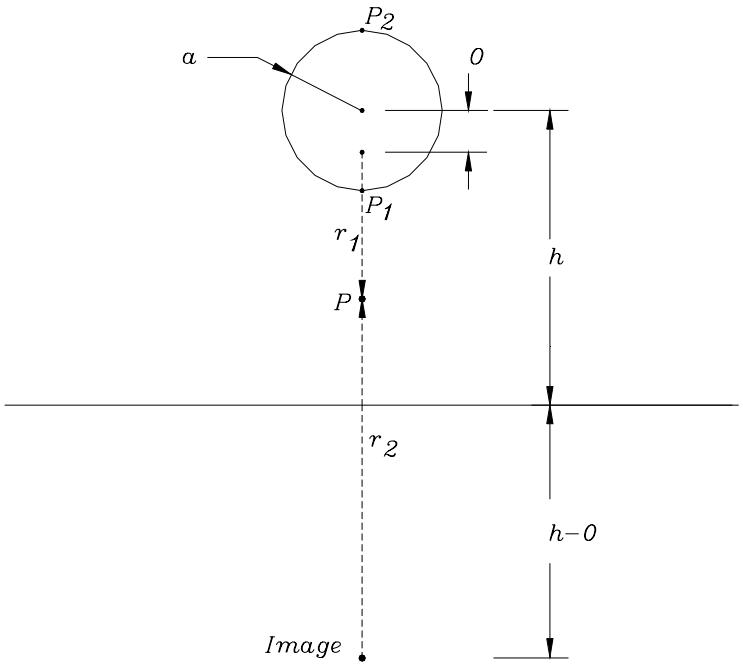

Figure 4-4. Charged cylinder above ground.

The voltage of the two points at the top and bottom of the cylinder, P_1 and P_2, respectively, can be expressed using the Gaussian potentials.

$$V_1 = \frac{q_1}{2\pi\varepsilon_0} \ln\left(\frac{2h-a-o}{a-o}\right)$$

$$V_2 = \frac{q_l}{2\pi\varepsilon_0} \ln\left(\frac{2h+a-o}{a+o}\right)$$

Since the voltage at these two points must be equal ($V_1 = V_2 = V$), it follows that

$$\frac{2h-a-o}{a-o} = \frac{2h+a-o}{a+o}$$

Solving for O leads to the quadratic equation:

$$o^2 + 2 \cdot h \cdot o + a^2 = 0$$

with solutions

$$o = h \pm \sqrt{h^2 + a^2}$$

The negative sign for the square root is chosen so that the offset is less than the radius of the cylinder, and hence that line charge is inside of the cylinder. The offset resulting from selecting the opposite sign for the square root corresponds to the offset to the image charge on the other side of the ground plane. Thus, selection of either sign results in the two line charges being located in the same place.

The offset can be substituted into the voltage equations to solve for the voltage on the cylinder as follows. Substituting for *O* in the argument of the logarithm for either of the equations for the voltages at P_1 or P_2 gives the same result.

$$\frac{2h+a-o}{a+o}=\frac{2h+a-h+\sqrt{h^2+a^2}}{a+h-\sqrt{h^2-a^2}}=\frac{(h+a)+\sqrt{h^2+a^2}}{(h+a)-\sqrt{h^2+a^2}}$$

Dividing the numerator and denominator by $\sqrt{h^2+a^2}$ leads to

$$\frac{2h+a-o}{a+o}=\frac{\sqrt{h+a}+\sqrt{h-a}}{\sqrt{h+a}-\sqrt{h-a}}$$

Substituting this into the equation for the voltage on the cylinder gives

$$V=\frac{q_l}{2\pi\varepsilon_0}\ln\left(\frac{\sqrt{h+a}+\sqrt{h-a}}{\sqrt{h+a}-\sqrt{h-a}}\right)$$

This can also be rewritten

$$\Phi=\frac{q_l}{2\pi\varepsilon_0}\ln\left(\frac{1+\sqrt{\frac{h+a}{h-a}}}{1-\sqrt{\frac{h+a}{h-a}}}\right)$$

This equation is the exact solution for the two parallel wires, or for a wire parallel to and above a ground plane, based on image theory.

If $h >> a$, the expression inside the log term approaches (2h/a) and

$$\Phi\cong\frac{q_l}{2\cdot\pi\cdot\varepsilon_0}\ln\left(\frac{2h}{a}\right)$$

Note that these equations can be inverted to solve for the charge density, given the voltage on the cylinder. For example, solving for the charge density in the simplified equation

$$q_l\cong\frac{2\cdot\pi\cdot\varepsilon_0\cdot V}{\ln\left(\frac{2h}{a}\right)}$$

The exact solution can be simplified by using

$$\tanh^{-1}(x)=\frac{1}{2}\ln\left(\frac{1+x}{1-x}\right)$$

By using the above identity an expression for the voltage on the cylinder can be obtained as follows.

$$V=\frac{q_l}{\pi\cdot\varepsilon_0}\tanh^{-1}\left(\frac{\sqrt{h-a}}{\sqrt{h+a}}\right)$$

When x is small $\tanh^{-1}(x)$ is approximately equal to x and

$$V \approx \frac{q_l}{\pi \cdot \varepsilon_0}\sqrt{\frac{h-a}{h+a}} \qquad (\lim h => a)$$

Field on Line between Charge and Image

General Field Expression

The field on the surface of the cylinder is maximum where it is nearest to ground (i.e., P_1 in Figure 4-4). The fields can be calculated as the superposition of the field from the line charge at the offset location inside of the cylinder and its image. Note that this field is a vector, and the direction from each charge must be taken into account. However, for any point along the line between the two charges, the direction of the fields from each charge are in-line and add directly with angle dependency reduced to sign. In Figure 4-4, a field point, P, is shown located on the line between the offset charge and its image. The distance from the center of the cylinder to the field point is r. Note that the offset is also on the line between the charge and its image. The distance from P to the offset charge is equal to (r-O), while the distance to the image charge is ($2h$-r-O). The field at P is given by

$$\frac{2\pi\varepsilon_0}{q_1}E = \frac{1}{r-o} + \frac{1}{2h-r-o}$$

Substituting for the offset (O) gives

$$\frac{2\pi\varepsilon_0}{q_l}E = \frac{1}{\sqrt{h^2-a^2}-(h-r)} + \frac{1}{\sqrt{h^2-a^2}+(h-r)}$$

Consolidating terms yields

$$\frac{2\pi\varepsilon_0}{q_1}E = \frac{2\sqrt{h^2-a^2}}{2hr-r^2-a^2}$$

Substituting for q_l gives the following

$$E = 2V\frac{\sqrt{h^2+a^2}}{2hr-r-a^2}\cdot\frac{1}{1\mathrm{n}\left(\dfrac{\sqrt{h+a}+\sqrt{h-a}}{\sqrt{h+a}-\sqrt{h-a}}\right)}$$

Substituting the identity two times the hyperbolic tangent for the log term gives another equivalent form

$$E = 2V\frac{\sqrt{h^2+a^2}}{2hr-r^2-a^2}\cdot\frac{1}{\tanh^{-1}\left(\dfrac{\sqrt{h-a}}{\sqrt{h+a}}\right)}$$

*Field on Cylinder Surface (*r = a*)*

Exact Expression

At the surface of the cylinder, the radius is (a). Making this substitution in the above equation gives the maximum field on the cylinder surface at the location closest to ground.

$$E = \frac{V}{a}\sqrt{\frac{h+a}{h-a}} \cdot \frac{1}{Tanh^{-1}\left(\sqrt{\frac{h-a}{h+a}}\right)}$$

Note that the above equation can be converted to the logarithmic form by substituting the identity for $\tanh^{-1}$.

Asymptotic Expressions (r = a)

There are two limiting cases where asymptotic expressions can be derived. The first is when the cylinder is far above the ground (i.e., $h >> a$). For this case, the above equation can be written as follows.

Approximation 1 for $r = a, h >> a$

$$E \approx \frac{V}{a} \cdot \sqrt{\frac{h+a}{h-a}} \cdot \frac{1}{1n\left(\frac{2h}{a}\right)}$$

This equation is easy to remember and accurate even fairly close to the ground.

At greater heights, this equation can be further refined as follows.

Approximation 2 for $r = a, h >> a$

$$E \approx \frac{V}{a} \cdot \frac{1}{1n\left(\frac{2h}{a}\right)}$$

This is a classic, often-used equation, which can be derived by ignoring the offset.

Similarly, another set of asymptotic formulas can be developed for the case of the cylinder very close to the ground (i.e., $h => a$). In this case, the approximation for the inverse hyperbolic tangent of a small argument is used.

Near Approximation 1 for $r = a, h => a$

$$E = \frac{V}{2a} \cdot \left(\frac{h+a}{h-a}\right)$$

This expression can be further reduced as follows.

Near Approximation 2 for $r = a, h => a$

$$E = \frac{V}{S}$$

where S is the separation between the cylinder surface and the ground (i.e., $S = h–a$).

*Field on Ground Surface (*r = h*)*

General Expression

The field on the ground directly under the cylinder is given by substituting h for r in the general expression.

$$E = \frac{V}{\sqrt{h^2 - a^2}} \cdot \frac{1}{Tanh^{-1}\left(\sqrt{\frac{h-a}{h+a}}\right)}$$

This is an exact result and again the identity for two times $\tanh^{-1}$ can used to obtain the form using the logarithmic expression.

Asymptotic Expressions (r = h)

Asymptotic formulas can also be developed for this case as follows. The same two limiting cases are examined. The first is when the cylinder is far above the ground (i.e., $h >> a$). For this case, the above equation can be written as follows.

Approximation 1 for $r = h,\ h >> a$

$$E = 2 \cdot \frac{V}{S} \cdot \sqrt{\frac{h+a}{h-a}} \cdot \frac{1}{\ln\left(\frac{2h}{a}\right)}$$

where S is the distance between the cylinder surface and the ground plane.

For greater heights, this can be further reduced to the following.

Approximation 2 for $r = a,\ h >> a$

$$E = 2 \cdot \frac{V}{S} \cdot \frac{1}{\ln\left(\frac{2h}{a}\right)}$$

Note that this is the same equation that is derived by ignoring the offset.

When the cylinder approaches ground (i.e., $h => a$), the approximation for the inverse hyperbolic tangent of a small argument is used and gives the following approximate form.

Near Approximation 1 for $r = a,\ h => a$

$$E = \frac{V}{S}$$

where S is the separation between the cylinder surface and the ground (i.e., $S = h–a$).

Note that there is only one approximate form in this case and it is asymptotic to the same value as the field on the cylinder.

Limits of Validity

We have made calculations comparing results of the exact formula with results from the approximate formulas to determine their limits of validity, which are given in the table below. Approximation 1 is very useful, since it is easy to remember and calculate, and it gives excellent results as long as $h/a \geq 3.5$. The simple logarithmic approximation (2) has considerable error unless h/a is quite large.

Table 4-2. Error bounds of the approximate formulas for the maximum electric field on a cylinder above ground.

r = *a*	Error ≤ 1 %	Error ≤ 5 %	Error ≤ 10 %
Approx 1	*h*/*a* ≥ 3.5	*h*/*a* ≥ 2.0	*h*/*a* ≥ 1.6
Approx 2	*h*/*a* ≥ 100	*h*/*a* ≥ 20	*h*/*a* ≥ 10
Near Approx 1	*h*/*a* ≤ 1.06	*h*/*a* ≤ 1.35	*h*/*a* ≤ 1.70
Near Approx 2	*h*/*a* ≤ 1.03	*h*/*a* ≤ 1.17	*h*/*a* ≤ 1.35
r = *h*	Error ≤ 1 %	Error ≤ 5 %	Error ≤ 10 %
Approx 1	h/a ≥ 3.5	h/a ≥ 2.0	h/a ≥ 1.6
Approx 2	h/a ≥ 100	h/a ≥ 20	h/a ≥ 10
Near Approx 1	h/a ≤ 1.06	h/a ≤ 1.35	h/a ≤ 1.70

Derivative of Field

In the section above, the general expression for the field on a line between a charged cylinder above ground and its image was derived. The field, as a function of the distance from the center of the cylinder, is given by

$$\frac{2\cdot\pi\cdot\varepsilon_0}{q_1}E=\frac{2\sqrt{h^2-a^2}}{2hr-r^2-a^2}$$

Taking the first derivative with respect to *r* yields

$$\frac{2\cdot\pi\cdot\varepsilon_0}{q_1}\frac{\partial E}{\partial r}=\frac{\partial}{\partial r}\frac{2\sqrt{h^2-a^2}}{2hr-r^2-a^2}$$

$$\frac{2\cdot\pi\cdot\varepsilon_0}{q_1}\frac{\partial E}{\partial r}=(2r-2h)\frac{2\sqrt{h^2-a^2}}{2hr-r^2-a^2}$$

It follows that

$$E'(r)=\frac{q_l}{2\cdot\pi\cdot\varepsilon_0}4(r-h)\frac{2\sqrt{h^2-a^2}}{\left(2hr-r^2-a^2\right)^2}$$

A useful formula is obtained when the derivative of the field at *r* is normalized to the value of the electric field at *r*.

$$\frac{E'(r)}{E(r)}=\frac{2(r-h)}{\left(2hr-r^2-a^2\right)^2}$$

The value of this normalized derivative has been evaluated at three locations of interest.

(1) At the ground, *r* = *h*, and the derivative is zero.

(2) At the surface of the cylinder, *r* = *a*, and the normalized derivative has the surprising value:

$$\frac{E'(r)}{E(r)} = \frac{-2(h-a)}{2a(h-a)} = -\frac{1}{a}$$

Thus, at the cylinder surface, the magnitude of the normalized derivative is always equal to one over the radius of the cylinder (*1/a*), independent of cylinder height.

(3) The normalized derivative becomes singular when the denominator equals zero. It is easy to show that this occurs when the radius equals the charge offset, which implies that the singularity occurs at the location of the charge.

Multiple Wires (Cages) above Ground

When several parallel energized conductors are near each other, the surface electric field on the conductors is reduced over what it would be on a single wire. The configuration of parallel conductors is known as a bundle or sometimes as a cage. The application of multi-wire cages to high-voltage antennas and power distribution systems goes back many years. Early workers found that several wires together could carry more voltage than a single wire without corona (Clark, 1932; Temoshok, 1948; Adams, 1955; Miller, 1956, 1957).

These early workers developed approximate formulas to calculate the surface electric fields on the wires in a cage. Now it is simple to use a computer and calculate the fields on cage configurations consisting of parallel wires above ground. By using modern computer techniques and extensive calculations, we have discovered a modification to the simple formula that provides more accurate results. The formula is a very good approximation and useful for design.

Definitions/Geometry

The geometry for a general *n*-wire cage is illustrated in Figure 4-5. The cage center height above ground is (*h*), the radius of the cage is (*b*), and the radius of the individual wires is (*a*). MKS units are used.

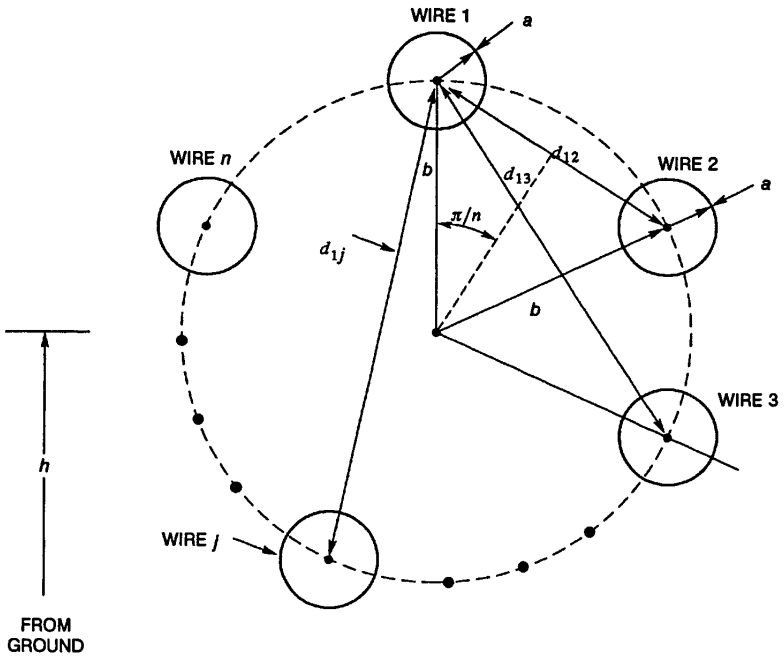

Figure 4-5. n-wire cage geometry.

Assumptions

There are several assumptions needed for the derivation:

1. The wires are parallel to each other and to ground.
2. The wires are perfectly smooth circular cylinders.
3. The wires and the ground are perfect conductors.
4. All the wires are at the same voltage V.
5. The wires all have the same radius.
6. The wires are uniformly separated on a circle of radius b.
7. The wires are much farther above ground than the cage radius b (i.e., $h >> b$).

The last assumption results in the simplifications:

1. The charge is the same on all wires.
2. The electric field in the vicinity of the wires is not affected by the presence of the ground. However, the charge magnitude is affected.

Theory

Matrix Equations

The charge on each wire is assumed to be a filament located at the center of the wire. This is a valid approximation if the wires are separated far from ground and from each other relative to their

diameter. As the wires come closer together, this approximation breaks down. This effect will be examined in the following section and a correction term developed.

Following the notation and method of Miller (1956) and assuming a charge at the center of the wires, the Gaussian potentials define the relationship between voltages and charges:

$$\text{Self potential} \qquad P_{ii} = \frac{\ln(2h / a_i)}{2 \cdot \pi \cdot \varepsilon_0}$$

$$\text{Mutual potential} \quad P_{ij} = \frac{\ln(D_{ij} / d_{ij})}{2 \cdot \pi \cdot \varepsilon_0}$$

where a_i is the radius of the *i*-th wire,
d_{ij} is the distance between wires *i* and *j*, while
D_{ij}, is the distance between wire *i* and the image of wire *j* reflected in the ground plane.

The relationships between voltage and charges are given by

$$V_1 = q_1 \cdot P_{11} + q_2 \cdot P_{12} + \cdots + q_n \cdot P_{1n}$$
$$V_2 = q_2 \cdot P_{12} + q_2 \cdot P_{22} + \cdots + q_n \cdot P_{2n}$$
$$\cdots$$
$$V_n = q_1 \cdot P_{n1} + q_2 \cdot P_{n2} + \cdots + q_n \cdot P_{nn}$$

where q_i is the charge and
V_i the voltage on the *i*-th wire.

These equations can be rewritten in matrix notation.

$$[V] = [P] \cdot [q]$$

where q is a column vector corresponding to the charge on each individual wire.

Simplified Equations

The above equations can be solved for the general case of different voltages, wire diameters, and locations. This may be required in some cases; for example, to obtain charge densities on multiphase power lines in proximity to each other and ground. See, for example, Doyle et al. (1982) as well as Miller (1956) and Adams (1955). However, for complicated cases, it is simpler to use the two-dimensional electrostatic computer programs now available.

The formulas can be greatly simplified for a single bundle composed of wires all having the same radius (a), the same voltage (V), and located at a large distance above ground with respect to bundle dimensions:

$$V_1 = V_2 = \cdots = V_n = V$$
$$a_1 = a_2 = \cdots = a_n = a$$

The fact that $h >> b$ leads to the approximation that

$$D_{ij} \cong 2 \cdot h = D \quad \text{for all values of } i, j \text{ and}$$
$$q_1 = q_2 = \cdots = q_n = q$$

Substituting the above into the matrix equation and using reciprocity ($P_{ij} = P_{ji}$), leads to a single equation that can be solved for the charge density on the individual wires:

$$a = V/(P_{11} + P_{12} + \cdots + P_{nn})$$

Capacitance – Equivalent Radius

The total charge on the bundle (per unit length) is given by

$$Q = n \cdot q$$

The total capacitance (per unit length) of the bundle is

$$C = Q/V = n/(P_{11} + P_{12} + \cdots + P_{1n}) \tag{4-5}$$

For a single wire, the capacitance is

$$C_1 = \frac{2 \cdot \pi \cdot \varepsilon_0}{\ln(2h/a)}$$

Using Gauss' law for the field around the single wire gives

$$E_1 = V\left\{\frac{1}{a}\right\} \cdot \left[\frac{1}{\ln(2h/a)}\right] \tag{4-6}$$

In general, the formula for the surface electric field on the wires of a cage contains one term related to geometry (enclosed in { }) and another term related to capacitance (enclosed in [ ]).

*General Case (*n*-wires)*

The general case of n wires uniformly spaced on a circle of radius b is illustrated in Figure 4-5. The spacing between the centers of wires 1 and j (d_{1j}) is

$$d_{1j} = 2 \cdot b \cdot \sin(j\pi/n)$$

Substituting into Equation 4-5 gives

$$C_n = 2n\pi\varepsilon_0/\{\ln(2h/a) + \ln(2h/(2b\sin(\pi/n)) + \ln(2h/(b\sin(2\pi/n)) + \cdots + \ln(2h/(2b\sin((n-1)\pi/n))\}$$

The log terms in the denominator can be combined to give

$$C_n = 2n\pi\varepsilon_0/\{\ln((2h)^n/[a(2b)^{(n-1)}\sin(\pi/n)\cdot\sin(2\pi/n)\cdots \cdots \sin(j\pi/n)\cdots\sin((n-1)\pi/n])\}$$

This equation can be further reduced using the following identity (Appendix 4A).

$$2\sin(\pi/n)\cdot 2\sin(2\pi/n)\cdots 2\sin(j\pi/n)\cdots 2\sin((n-1)\pi/n) = n$$

The approximate equation for the capacitance (per unit length) of a cage becomes

$$C_n = 2n\pi\varepsilon_0/[n\ln(2h/a_{eqC})] \tag{4-7}$$

where $a_{eqC} = (nab^{(n-1)})^{(1/n)}$ is the cage equivalent radius for capacitance.

The cage equivalent radius for capacitance corresponds to the radius of a single wire that has the same capacitance per unit length as the cage. Note that Equation 4-7 has the same form as Equation 4-6.

This simple expression for the capacitance per unit length is quite accurate as will be shown later. This result is equivalent to one given by Grover (1928), although he did not obtain the closed form. The closed form expression is included in gradient formulations given by Crary (1932) and Chaudhari's comment in (Miller, 1956). The above expression for equivalent radius is the same as the geometric mean radius of the cage (Grover, 1928) and gives the correct inductance for the cage in the high-frequency limit. Schelkunoff (1952, p. 110) has derived the same expression for equivalent radius by a completely different method and shows that it gives the correct value for the transmission line impedance of a multiple wire cage.

Cylindrical Geometry

If the cage of wires is located at the center of a cylinder of radius R instead of at a height h above ground, the formula for capacitance uses the same equivalent cage radius a_{eqC} except that the factor $2h$ is replaced by R.

Capacitance in the Presence of Other Wires

Two-wire Case

Often it is desirable to design a multi-wire cage for each of two or more separated wires carrying a high voltage. The presence of the other wires modifies the capacitance of each wire. For certain conditions, the effect of this modification can be accounted for by changing the apparent height of the wire.

The equations for the two-wire case are

$$2\pi\varepsilon_0 V_1 = q_1 1 \ln\left(\frac{2h}{a}\right) + q_2 \ln\left(\frac{D}{S}\right)$$

and

$$2\pi\varepsilon_0 V_2 = q_1 1 \ln\left(\frac{D}{S}\right) + q_2 \ln\left(\frac{2h}{a}\right)$$

where D is the slant distance between one wire and the image of the other wire, and
S is the separation distance between the wires.

If each of the two wires were caged, the radius a should be replaced by a_{eqC} .

If both wires have the same radius a (or a_{eqC}) and the same voltage, by symmetry they have the same charge, and the equations can be reduced to

$$V = \frac{q}{2\pi\varepsilon_0} = \ln\left(\frac{2h}{a}\right) + \ln\left(\frac{D}{S}\right)$$

For this case, the capacitance of each individual wire (cage) is given by

$$C = \frac{q}{V} = \frac{2\pi\varepsilon_0}{\ln\left(\frac{2h}{a}\cdot\frac{D}{S}\right)}$$

From the above equation, it can be seen that the capacitance of each wire is the same as that of a single isolated wire, but at a different height. This new height is defined to be the apparent height given by $h_a = h \cdot \frac{D}{S}$. For this case, each wire can be treated as a single isolated wire at a new

apparent height. The conditions required are that both wires have the same radius, height above ground, and voltage. For the case of caged wires, a is replaced with a_{eqC}, which must be the same for both wires.

Infinite Wire Grid

Another interesting configuration that lends itself to an analytical solution is an infinite number of parallel wires separated by the distance S and located at the same height above the ground. This problem can be treated in the same manner. The capacitance per unit length of each wire is derived in Appendix 4B and is given below.

$$C_{\infty} = \frac{2\pi\varepsilon_0}{\ln(2h/a) + \ln(X)}$$

where X is given by

$$X = \left(\frac{Sinh(2 \cdot \pi \cdot h / S)}{2 \cdot \pi \cdot h / S} \right)^{1/2}$$

This equation is similar to the two-wire case, and the concept of an apparent height is also valid for this case. The apparent height is given by

$$h_a = h \cdot \left(\frac{Sinh(2 \cdot \pi \cdot h / S)}{2 \cdot \pi \cdot h / S} \right)^{1/2}$$

For the two cases considered, the apparent height is considerably higher than the actual height. This means that the capacitance per unit length is reduced over what it would be if the wire were isolated. Less capacitance implies less charge and therefore reduced fields. The reason for the reduced capacitance is that the wires at the same voltage partially shield each other. The two cases presented have nice solutions for apparent height. Other cases with different configurations for the shielding objects may not have such nice solutions. Nevertheless, the effect of such shielding will always cause an increase in the apparent height.

Surface Electric Field – Theory

Simple Geometric Theory

The electric field on the surface of a wire in the cage configuration is calculated by superimposing fields caused by the charges on each wire. From symmetry it can be shown that the location of the maximum electric field on the surface of one of the cage wires will be at the point on the wire that is directly away from the center of the cage. For example, Figure 4-6 shows a three-wire cage and illustrates the method of calculation of the maximum field on one wire by vector addition of the fields due to the charge on that wire, plus the radial component of the fields due to the charges on the other wires. Assumptions operating here are that the fields from the images (below the ground plane) are negligible and the charges on each wire act as a filament located at the center of the wire.

The field due to the charge on the wire itself is radial and from Gauss' law is given by $E = q/(2\pi \cdot \varepsilon_0 \cdot a)$, where q is the charge on the individual wires, given by $q = C_n V / n$. The fields due to the charges on the other wires must be vectorally added to the self-field to obtain the total field. The magnitude of the fields from the other wires can be approximated by calculating them at the point corresponding to the center of the wire in question, as if the wire were not there, and then modifying that result due to the presence of the cylinder. The effect of the wire (cylinder) can be approximated by assuming that the field is uniform and therefore is twice the free space value at the

point where the field is perpendicular to the surface (Morse & Feshback, 1953). Crary (1932) seems to be the first to have suggested this approximation. This factor of two can also be derived using image theory. The uniform field approximation is accurate when the wires are well separated but becomes less accurate when the wires are closer together.

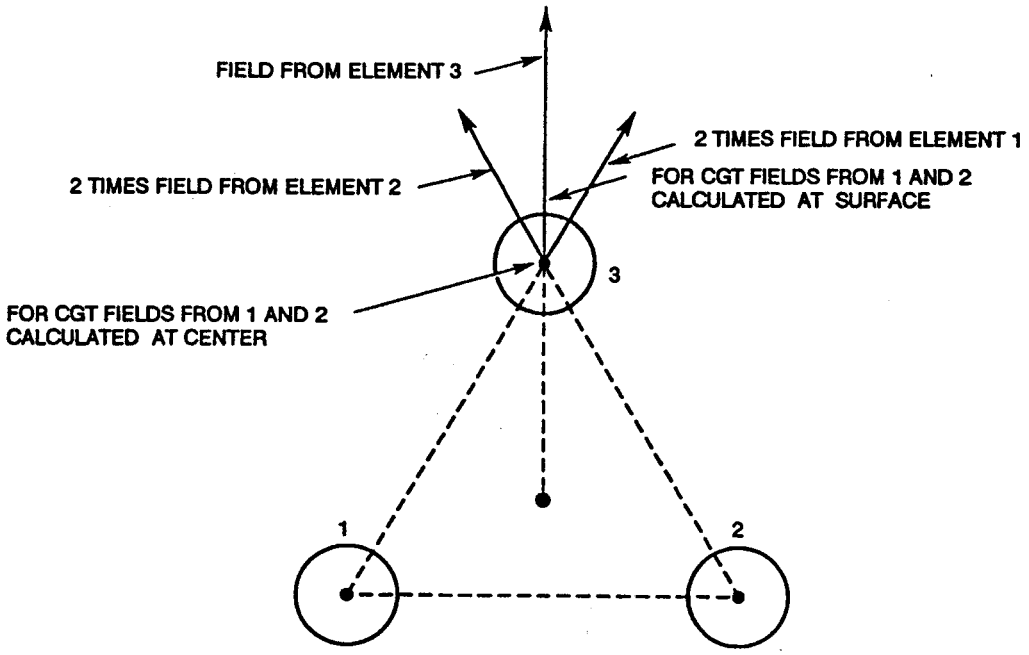

Figure 4-6. Field calculation for three-wire cage.

Using the method illustrated in Figure 4-6 and the geometry of Figure 4-5, it can be shown that the field at the location of the center of wire 1 due to the charge on the *j*-th wire is given by

$$E_{1j} = q/(2\pi \cdot \varepsilon_0 d_{ij}) = q/\{2\pi \cdot \varepsilon_0 \cdot 2b \cdot \sin(j\pi/n)\}$$

To determine the radial component the above term is multiplied by $\cos(x_j)$ which cancels out the $\sin(j\pi/n)$ term (see Appendix 4C, Figure C-1). Thus, at the center of any wire, the radial component of the electric field due to the charge on each of the other wires is identical and given by the following:

$$E = q/(4\pi \cdot \varepsilon_0 \cdot b)$$

The maximum surface electric field on a cage wire is then approximated by the sum of the field from the wire itself plus twice the sum of the contributions from the other wires.

$$E_n = \frac{q}{2\pi \cdot \varepsilon_0}\left\{\frac{1}{a} + \frac{n-1}{b}\right\}$$

The charge *q* in the equation above is the charge on an individual wire, which can be determined from the total cage capacitance and the voltage.

$$q = \frac{V \cdot C_n}{n}$$

Substituting for *q* gives

$$E_n = \frac{C_n V}{2\pi\varepsilon_0}\left(\frac{1}{n}\right)\left\{\frac{1}{a}+\frac{n-1}{b}\right\} \tag{4-8}$$

Further substituting for C_n gives

$$E_n = \frac{V}{n}\left\{\frac{1}{a}+\frac{n-1}{b}\right\}\left[\frac{1}{\ln(2h/a_{eqC}}\right] \tag{4-9}$$

Note that the brackets {} contain the geometry term and the square brackets [ ] contain the capacitance term. Equations 4-8 and 4-9 are derived from the simple geometric theory (SGT). This formula appears in Chaudhari's comment on Miller's (1956) paper and also in (Smith, 1985).

Complete Geometric Theory

The basis of simple geometric theory is that the electric fields on one wire due to the charges on the other wires are estimated by calculating the field at the center of the wire as if the wire was not present. The field is then doubled to account for the effect of the cylinder. This approach is valid when the wires are separated far enough so that the fields from the charges on the other wires are approximately uniform over the space occupied by the wire on which the field is being calculated. This assumption is invalid when the wires are close to one another. For the latter case, a better approximation is to use twice the field strength calculated at the surface of the cylinder instead of the center of the cylinder. This is the basis of the complete geometric theory (CGT). Details of the derivation are presented in Appendix 4C. The formula for capacitance is the same for both of these theories. The resulting equation for the maximum surface field strength is similar to but more complicated than that for the SGT. The geometric factor for the two-wire cage is

$$\{\ \} = \left\{\frac{1}{a}+\frac{1}{b+a/2}\right\}$$

The complexity of the expression for the geometric factor increases as the number of wires in the cage increase. Explicit expressions are derived in Appendix 4C for the three- and four-wire cages. The general expression for the CGT term involves a finite sum, also given in Appendix 4C.

Modified Simple Geometric Theory

For the two-wire cage, the difference between the SGT and CGT expressions for field strength is that $a/2$ has been added to the denominator of the second term in the geometric factor. This suggests a modification to the SGT formula using a geometric factor of the form given below.

$$\{\ \} = \left\{\frac{1}{a}+\frac{n-1}{b+a/2}\right\}$$

The complete modified simple geometric theory (MSGT) formula follows from this and is given below.

$$E_n = \frac{V}{n}\left\{\frac{1}{a}+\frac{n-1}{b+a/2}\right\}\left[\frac{1}{\ln(2h/a_{eqC}}\right] \tag{4-10}$$

It turns out that this formula provides surprisingly good fits to field strength estimates determined by using the two-dimensional computer programs, for the cases we considered.

Computer Calculations

Calculations for several multi-wire cage configurations have been done using the two-dimensional computer program (Electro, 2003). The calculations were done for $2h/a$ equal to 300 and 5000. The case of $2h/a = 5000$ corresponds to a 1-inch-diameter wire approximately 10 feet above ground. These calculations were done for the number of wires $n = 2, 3, 4, 5, 6$, and 12. The results of the capacitance and surface electric field strength are given in Figures 4-7 and 4-8, respectively. The results are normalized to the value for a single wire with the same diameter and at the same height above ground.

The capacitance shown in Figure 4-7 is the total capacitance per unit length of the cage divided by the capacitance per unit length of a single isolated wire at the same height. Due to the geometry and the exact nature of the computer solution, the charge on each wire is not the same. The charge on the wires nearest to ground is slightly greater than the charge on wires further away from ground. Thus, the electric field strength and capacitance are slightly different, depending on which wire is examined. For this reason, the plots in the figures include a maximum, minimum, and average value for both capacitance and surface electric field strength. The difference between the maximum and minimum value increases with increased separation between the wires in the cage. In general, the difference is less than 1% for all values of b/a between 1 and 50.

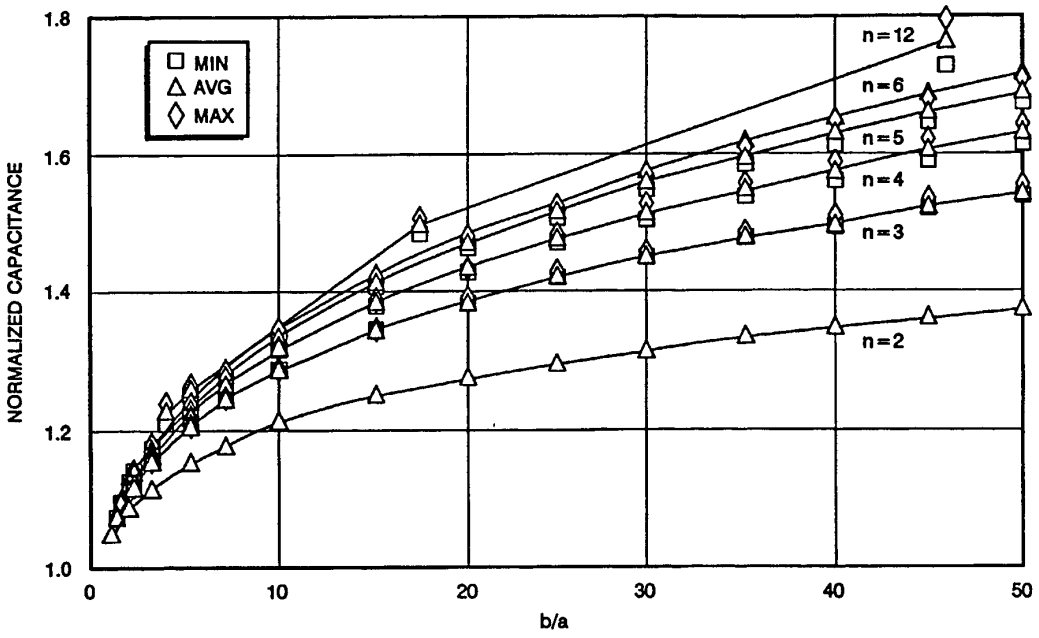

Figure 4-7. Capacitance of an n wire cage for several values of n, normalized to the capacitance of a single wire, where b = cage radius, a = wire radius, h = height above ground, $2h/a = 5000$.

Note that for the two-wire case both wires are at the same height above ground. At large values of separation the wires become independent and the total capacitance is asymptotic to twice the capacitance of a single wire.

The surface electric fields curves (Figure 4-8) decrease rapidly at first with increasing separation, then more slowly, and then pass through a broad minimum after which they slowly increase. They

exhibit a minimum for a particular value of b/a. This implies that there is an optimum cage spacing that results in a minimum value for surface electric field strength. The minimum results from the fact that the surface electric field strength is the product of the two terms, one related to the geometry and the other capacitance. The capacitance term increases approximately logarithmically with separation.

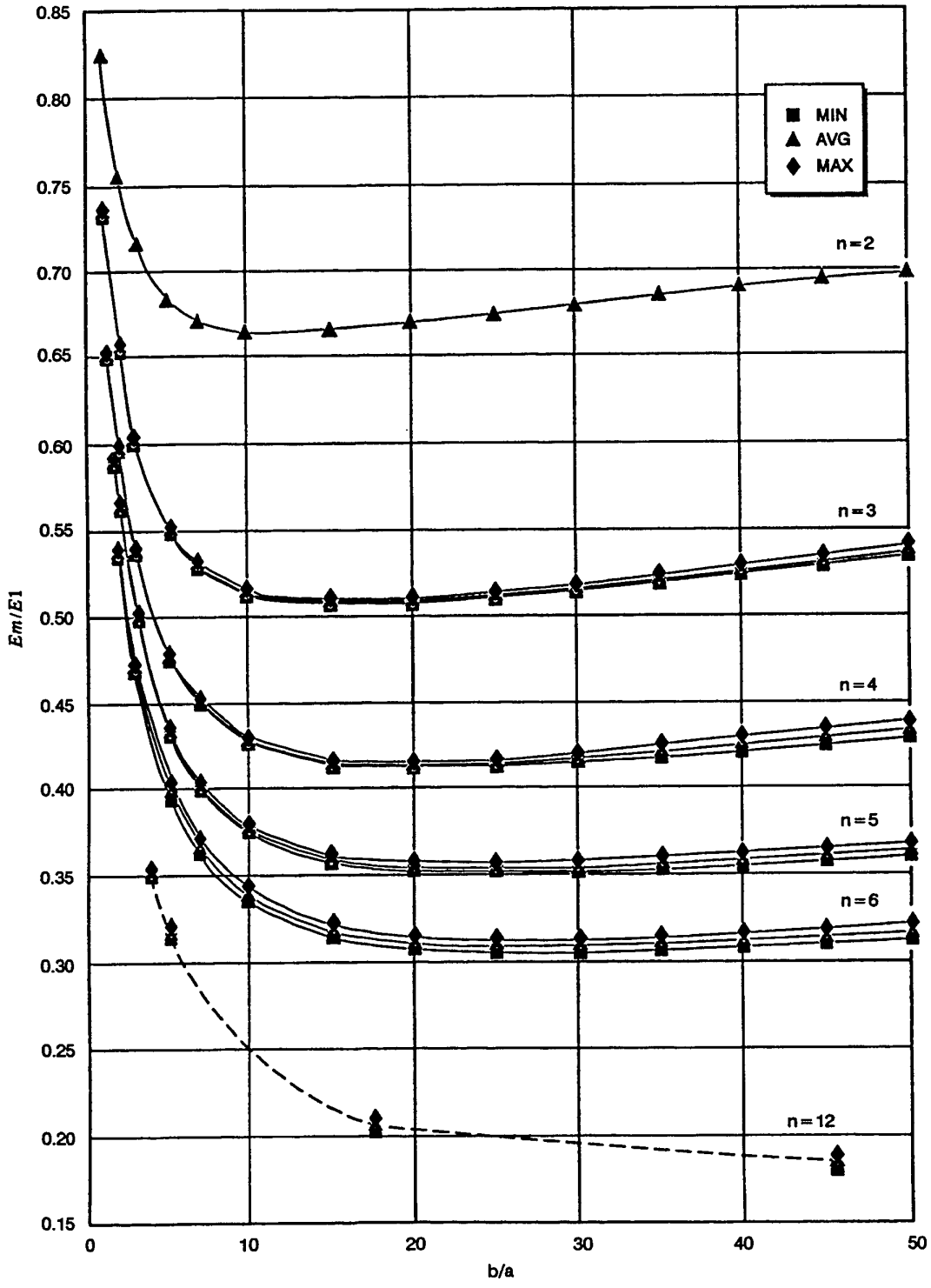

Figure 4-8. Maximum surface electric field on wires in an n-wire cage, normalized to that for a single wire, for several values of *n*, where *b* = cage radius, *a* = wire radius, *h* = height above ground, 2*h*/*a* = 5000 (2D BEM).

This term is less than the value for a single isolated wire provided that $b << h$. The geometry term decreases rapidly with wire separation at first, and then less rapidly, asymptotically approaching the value for a single wire. When the wires are less than one wire radius apart, the product of these factors is somewhat less than the value for a single isolated wire. At large separation, the product is asymptotic to a value less than that for a single isolated wire. For wires near to one another, the geometry term decreases faster than the capacitance increases. However, eventually the capacitance term dominates so that the product exhibits a minimum value.

The capacitance term is a logarithmic function of height. The rate increase of the capacitance is reduced as height increases. The rate decrease for the geometric term is independent of height. Thus, the location of the minimum is a function of height, with the minimum occurring at wider wire spacing for greater cage heights.

Comparison: Theory versus Computer Calculations

Capacitance

An extensive comparison of the results obtained using the above formulas for the field strengths for wire cages with those obtained by computer calculations has been undertaken (Hansen, 1992). The simple capacitance formula (Equation 4-7) was found to be quite accurate over a wide range of spacing (b/a). For example, for the case of a two-wire cage with $2h/a = 5000$, the simple capacitance formula yields results that are within 1.5% of each other when the wires are touching and within 0.5% when $b/a > 2$. Calculations for the case of $2h/a = 300$ showed that the accuracy of the simple capacitance formula begins to decrease if $h/b < 5$, because the approximation that $D_{ij} \approx 2h$ is poor.

For the cases examined, number of cage wires $n = 2, 3, 4, 5, 6$, and 12 with ($2h/a > 300$), the value of capacitance estimated by the simple formula was always within 2.5% of the average value obtained by the computer calculations. For values of $b/a > 3$, the formula gives values that are within 1% of those given by the computer calculations.

Surface Electric Field

The formulas for surface electric field strength derived from the expressions given by SGT, CGT, and MSGT were compared to the computer-calculated field strengths. The comparison consisted of taking the ratio of the results calculated by the formula to the value calculated by the computer program. It was found that the SGT formula had large errors for small values of b/a, with the error decreasing as b/a becomes larger. For example, the three-wire cage with $b/a = 1.5$, the SGT error was in excess of 30%. Because of large errors for small wire spacing, the SGT formula does not give the correct values or wire heights for the minimum surface electric field strength.

The CGT results were calculated for $n = 3$ and $n = 4$. The error for the CGT formula is significant at small spacing but less than for the SGT formula.

The MSGT formula turned out to be the best for all spacing. It has less than a 6% error at very small values of b/a and less than 2% error when $b/a > 3$. The MSGT formula gives the most accurate results of the simple formulas tried. Also, important for design, the MSGT formula does give the correct value and height for the minimum surface electric field. This formula, equation 4-10, should be adopted as the standard formula for cage calculations.

Design

The MSGT formula has been used to develop design procedures for high-voltage cages. The fact that there is a wire separation that results in a minimum value of surface electric field strength leads to optimum design procedures. The geometry for the minimum is denoted by b_{min}/a. The value of b_{min}/a is a function of the height of the cage above ground. This value is plotted in Figure 4-9. Note that the presence of other wires or shielding increases the effective height of the cage, and this increases the wire separation for minimum field strength.

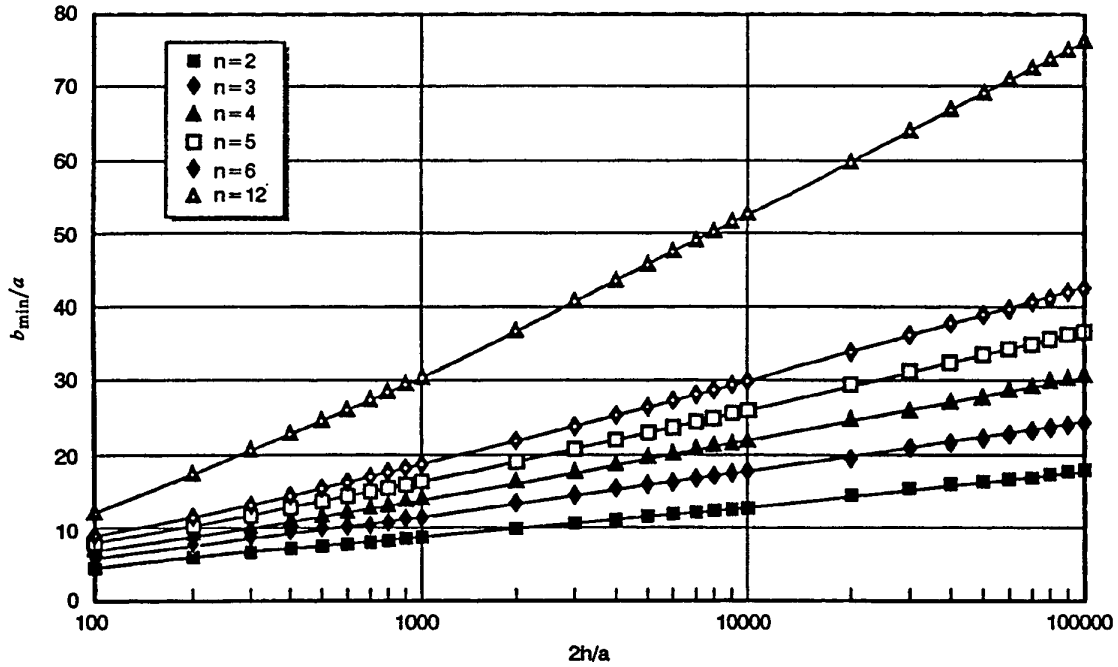

Figure 4-9. *n*-wire cage – b_{min}/a versus height, where b_{min} = cage radius when surface field is minimum, a = wire radius, h = height above ground.

It is convenient to convert the optimum wire separation to wire-to-wire spacing S, which is equal to d_{12} in Figure 4-5. This conversion is a simple geometric function of the number of wires and the cage radius. The wire-to-wire spacing at the minimum denoted by S_{min}, is plotted in Figure 4-10. From this figure it is seen that S_{min} is nearly the same for n equals 3 to 6. S_{min}/a varies logarithmically with height and for n equals 3 to 6 is given by the following formula.

$$\frac{S_{min}}{a} = 10 \cdot Log\left(\frac{2h/a}{10}\right)$$

Note that the slope of S_{min}/a is different for the two-wire case, but nearly the same for three or more wires. For larger values of n, the curves move down slightly, as illustrated by the curve for $n = 12$.

Table 4-3 gives the values of S_{min} in terms of wire diameters ($2a$) for practical heights. For 1-inch-diameter wires, the values of $2h/a$ in the table correspond to heights of 20.8, 208, and 2083 feet, respectively. For practical cage heights, Table 4-3 shows that the wire-to-wire spacing needed to achieve the minimum surface electric field need not be more than 9 to 15 wire diameters for the two-wire case and 10 to 20 wire diameters for three or more wires.

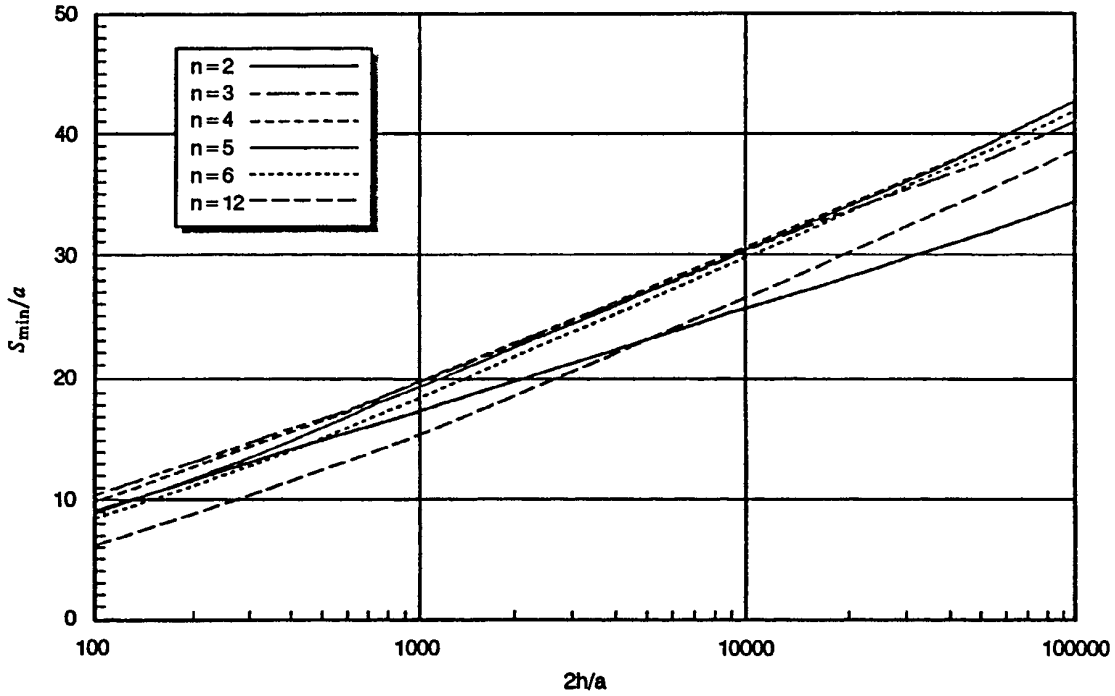

Figure 4-10. *n*-wire cage – S_{min}/a versus height.

Table 4-3. $S_{min}/2a$ for practical values of $2h/a$.

n	$2h/a$ = 1000	$2h/a$ = 10,000	$2h/a$ = 100,000
2	8.86	13.11	17.5
3-6	9.75	15.5	21.5

There are several different design methods that can be developed using the MSGT formula depending on the design criteria. For example, given (1) the voltage, (2) wire diameter, and (3) the critical gradient for that size wire, a design procedure has been developed that finds the minimum number of wires required and the minimum wire spacing required (Hansen, 1992).

Another interesting design approach that can be implemented using the MSGT is to pick the number of wires in the cage and find the minimum wire diameter that will meet the surface electric field criteria at the spacing for minimum surface electric field strength. This technique is more complicated and requires iteration, since the critical gradient is a function of wire diameter. However, it results in a cage that has the minimum total cross sectional conductor area that is able to operate at the required voltage. It turns out that the total cross-sectional area and hence the weight (ignoring spacing hardware) is less as *n* increases. Thus, for very high-voltage applications, cages become a very useful and practical solution to minimize weight of the transmission system.

TOROID IN FREE SPACE

Laplace's equation can be solved in toroidal coordinates. A toroid in free space would be a useful simple geometric configuration to check out computer programs, especially for objects with toroidal

geometry. Thomas (1954) and Hicks (1881) give formulas for the capacitance of a toroidal corona ring in free space. Hobson (1931) discusses the solutions and the toroidal or ring functions used for the solution.

COMPUTER CALCULATIONS

For high-voltage design, there are two applications that require computer-calculated field strengths. The first involves processing measured breakdown voltage data for configurations that do not have analytic solutions for the electric fields. In this case, the objective is to determine the critical surface field at breakdown to develop design data. An example of a configuration having no analytic solution is a conducting toroid above ground. This configuration is similar in shape to several types of insulators used in high-voltage applications. For that reason, we have made extensive measurements of this configuration to develop empirical curves of the breakdown field that can be used for design. To develop these curves, it was necessary to accurately determine the surface field strength on the surface of the measured objects (toroids). It is desirable to have very high accuracy when using the computer results to process measured voltage breakdown data to develop design curves.

The second application is that of using the empirically developed critical field curves to design high-voltage hardware. In this case, a safety factor is usually adopted in the design to reduce the effects of the various uncertainties, including errors in the calculation of the fields on the object and uncertainty in the critical breakdown field strength. The safety factor increases the confidence that the design will operate at the required voltage. For this case, the required accuracy for the field strength calculations can be relaxed depending on the safety factor adopted for the design.

Among people versed in using computer programs to generate engineering data, there is always the question of the validity of computer-generated results. The first application described above requires unusual accuracy because the computer-generated results are used to process measured data to determine critical breakdown field strength. The goal for the voltage measurement accuracy was to be within 1%. While we probably did not achieve that, we believe that the actual error is less than 5%. We desired that conversion from voltage to electric field would not reduce this accuracy. Consequently, the goal for field calculation accuracy was to be within 1%. To achieve and verify this level of accuracy, we had to develop our own techniques for application of the available computer programs. We did this by testing the computer programs against exact solutions for simple geometrical configurations having analytic solutions.

There are two types of electrostatic computer programs available. The first type uses elements on the surface of a conducting object and solves for the surface charge distribution using the method of moments. These are called Boundary Element Methods (BEM). We have experience with some commercial computer programs that use the BEM, including “Electro” by IES for two-dimensional and rotationally symmetric electrostatic problems, and “Coulomb,” also by IES, for three-dimensional electrostatic problems.

The second type of program uses the finite element method (FEM), which solves for the field in space. The commercially available FEM electrostatic program for which we have experience is “Maxwell” by ANSOFT. There are advantages and disadvantages to use of either the BEM or the FEM. The FEM solves for fields in the space around an object. The space must be finite to limit the computational resources required for solution. As a consequence, a finite size “box” must be placed around the object in question and a “free space” boundary condition imposed on the surface. This

requires some “art” to be sure that the box is big enough to give accurate results. However, the larger the box, the more computation time and memory required to calculate field strengths.

The BEM solves for the charges on the surfaces, and therefore the problem formulated is finite. However, the BEM does not have a proof of uniqueness for the solution of the surface charge, and the solution is not guaranteed to converge as the number of elements is increased. Thus, there is art involved in the application of the BEM programs that involves the location and number of the boundary elements.

The boundary element methods require the assignment of boundary elements or segments. The programs typically allow the specification of an “accuracy” parameter. Usually the programs have several different methods available for “looking at” or “measuring” the resulting field strengths. Typically, we obtain a series of computer solutions for a simple geometric configuration that is similar to the case we want to solve and that has an analytic solution. To obtain these solutions, we develop a segmentation method, a solution technique, which may involve an error specification, and a method of “measuring” the field strength at the desired location. We work with all of the variations until we find a method that yields solutions with the desired accuracy. Typically, in this process we discover that a certain minimum number of segments per inch, or per degree, along with a certain accuracy specification yields acceptable results when combined with an appropriate “measurement” technique.

The computer program is used to calculate the field strength on the surface. The maximum field on the surface at breakdown is the single parameter that is most strongly correlated with breakdown and which can be used to estimate breakdown. The calculated field strength on or near the surface can have discontinuities depending on the functions used to describe charge density. For example, if a uniform charge is assumed on each element, there will be a discontinuity in the charge level at the edge of the element and a corresponding discontinuity in the field on the surface of the object. Generally, we find that for two-dimensional cases the boundary element technique requires less art to give accurate results. The two-dimensional and rotationally symmetric programs that we have found useful use charge distribution functions that are smoothly continuous across element boundaries. For these programs, the preferred method of measurement is to plot the surface field strength (either normal or maximum) along the surface. Typically, we are looking for the maximum field strength, and as long as the field plot appears normal, the value can be taken directly off the curve.

For the three-dimensional programs examined, neither the FEM program nor the BEM programs provide solutions that are smoothly continuous at the element boundaries. As a result, a plot of surface electric field strength calculated by these programs exhibits perturbations about some average level**.** The magnitude of the perturbations is less for smaller elements. We have been able to find segmentation techniques for the BEM programs that reduce this variation to less than 1%. However, for the FEM programs we could not reduce the elements enough to achieve that performance and still fit the problem in the available computer memory and have reasonable computer run times. This is because the FEM solution is for all space, and considerably more elements are needed for solution than for the BEM programs. Thus, more effort is required to find a “measurement” technique that gives acceptable accuracy for the FEM programs. With considerable effort, we have found some methods that can be used to give acceptable accuracy.

For all these computer programs, we have found that verification of the results using simple geometric configurations having analytic solutions is essential. As will be shown by an example, the computer results can look reasonable even when they are incorrect, and therefore they cannot be used without verification. The simple geometric configurations used for verification are selected to have

parameters similar to cases of interest. This type of verification is useful to develop techniques for determining the required fields and at the same time giving indications of the expected accuracy. The assumption underlying this technique is that the simple geometrical and actual problems are similar and the accuracy of their computer solutions will also be similar. These verifications can take considerable time, effort, and resources. It is tempting to skip verifications and blindly accept the results of the computer program, especially if the commercial program is expensive and supposedly sound. However, our experience has led us to conclude that verification is required in every case to ensure accurate results.

Two Dimensional

For the two-dimensional and rotationally symmetric situations, the BEM programs typically give very good answers. A typical example of a test is an infinite cylinder parallel to and above an infinite ground plane. A test example is shown below, illustrating the method used to ensure accurate results. In this example, typical segmentation and measurement techniques are used. Also, we examine ground plane size and show that the best way to simulate an infinite ground plane is to use an image of the object instead of the ground plane. When an image is used, the number of segments required and/or the solution volume are usually much less than they would be if the ground plane were included.

Cylinder above Ground

Segmentation

As a typical example, we have examined the case of an 8-inch diameter cylinder placed above ground at heights of 6, 12, 24, and 48 inches. A BEM computer program was used for this example and the ground plane eliminated by use of an image. The calculated results for the maximum electric field strength on the bottom of the cylinder were compared with the exact solution. The test consists of changing the number of segments on the pipe to determine how many segments are required to give the desired accuracy. The measurement technique consists of plotting the normal *E* field on the surface of the cylinder and recording the maximum field strength (See Figure 4-11). In this example, field strength was determined for several cases with increasing numbers of segments and compared to the field strengths given by an exact solution. The results are shown in Figure 4-12. Note that the accuracy is better when the pipe is farther away from ground, but 16 segments gave answers with errors less than 1/4% for all cases considered. We typically use 16 segments for this type of problem.

For this example, note that the error is less than 1/8% when 32 segments are used, except for the case of the cylinder located 12 inches above the ground, where the error increased when the number of segments exceeded 24. BEM solutions are known to demonstrate this type of behavior, in that as the number of segments is increased the answer converges for a while but eventually starts to diverge again. This behavior can have several causes but is usually attributed to round-off error or numerical instability of the matrix solution. In this particular case, something caused the apparent field on the surface of the cylinder to have a discontinuity, as shown in Figure 4-13. This example is shown to provide a caution against blindly accepting the computer output. In particular, it is not wise to use the field strength “measured” at a single point. It is much better to examine the fields over some area, by plotting them if possible to help spot anomalies. Another helpful method is to run several cases, changing one parameter, and checking the trend to be sure it appears correct. In the case presented, both the field plot (Figure 4-13) and the trend plot (Figure 4-12) are anomalous when the cylinder is 12 inches above the ground and there are more than 26 segments.

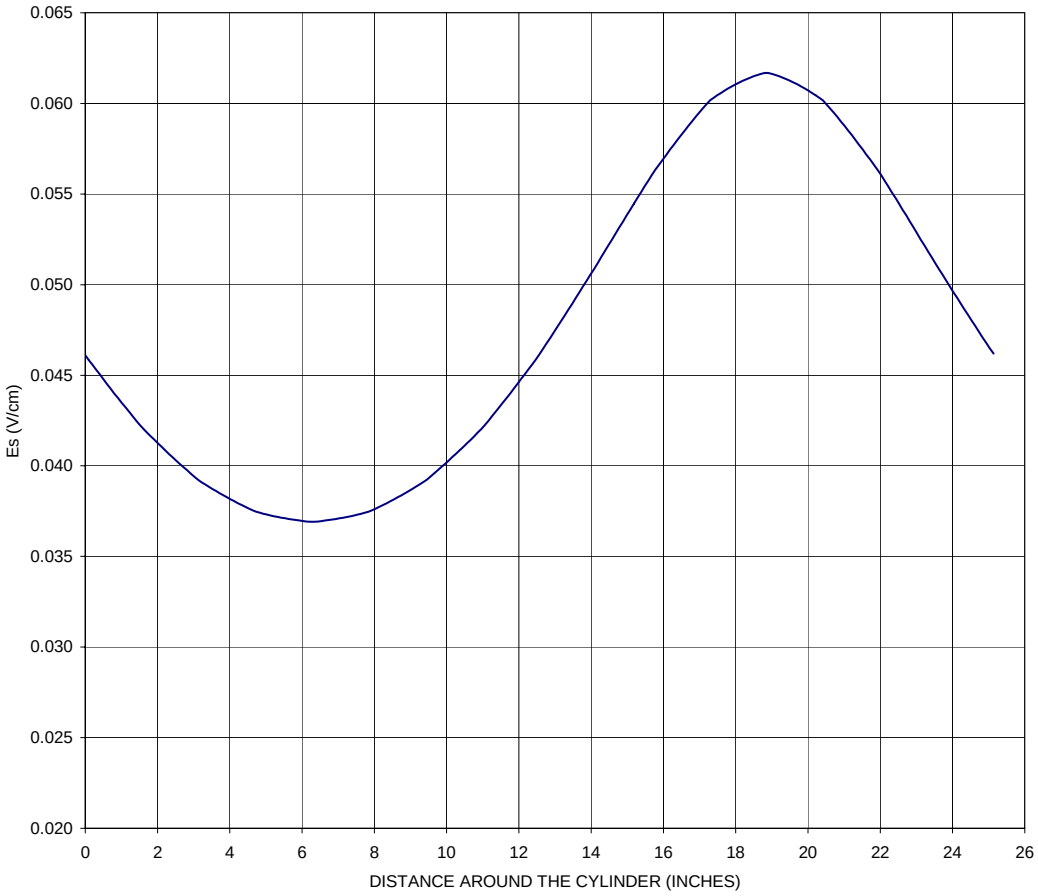

Figure 4-11. Surface electric field on cylinder, 8-inch diameter tube, 12-inch height to bottom, 16 elements, 2-D BEM program.

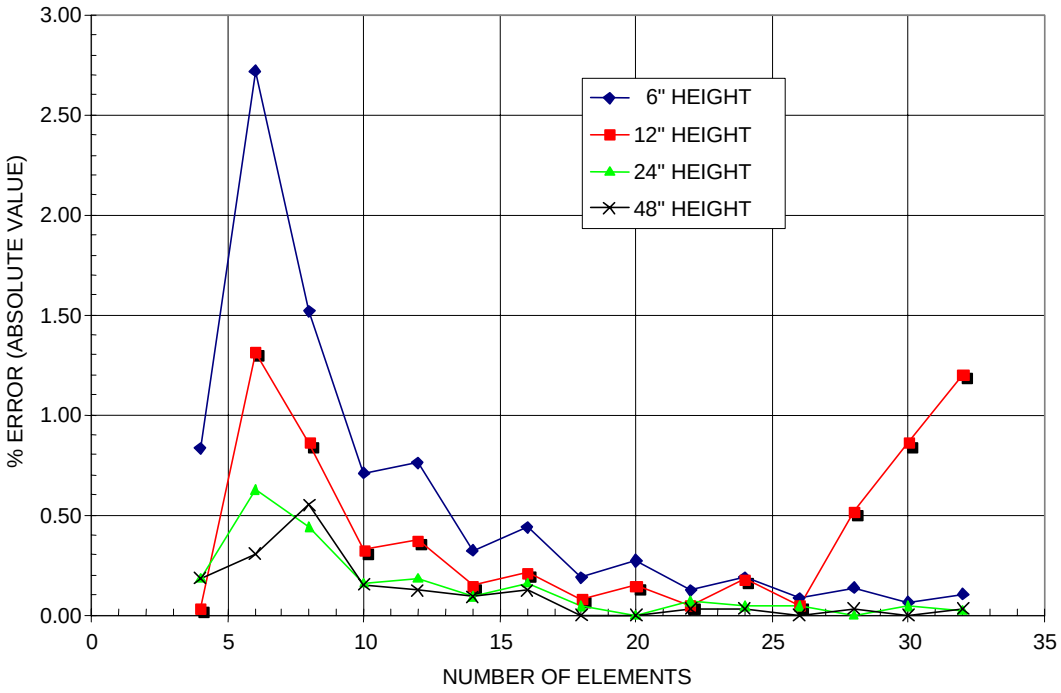

Figure 4-12. Error in Calculated Maximum Surface electric field on cylinder, 2-D BEM Calibration, 8-inch cylinder above ground.

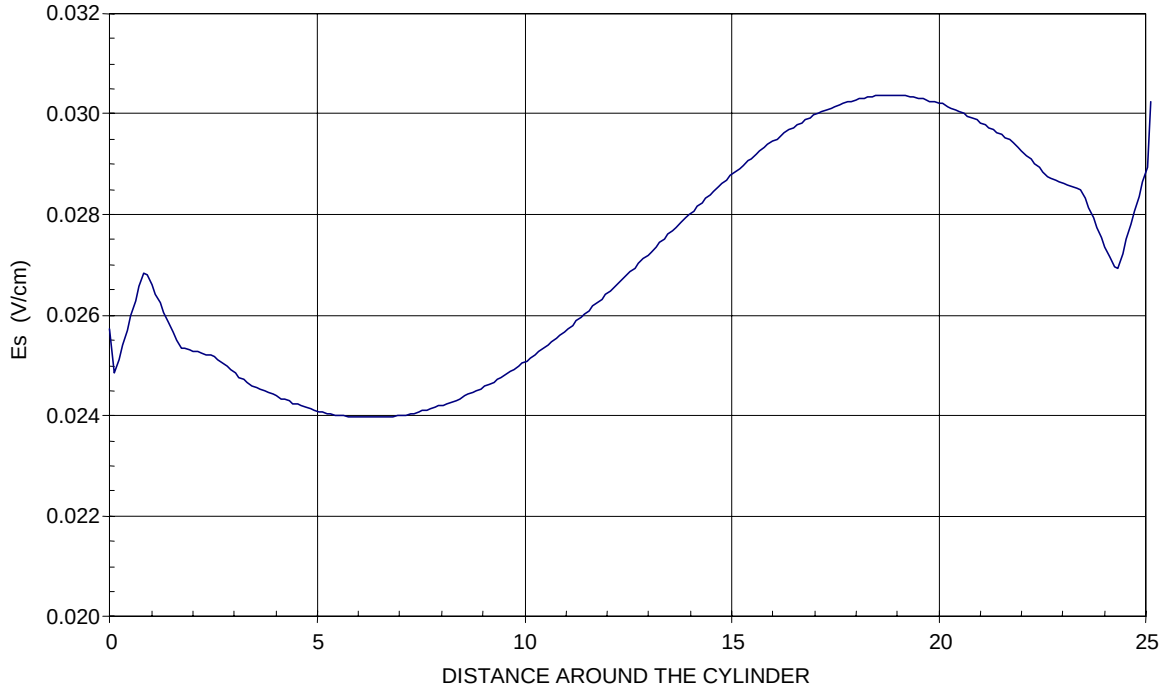

Figure 4-13. Surface electric field on cylinder above ground, 2-D BEM, 8-inch diameter tube, 48-inch height to bottom of tube, 30 elements on tube.

Ground Plane Size

Using the same 8-inch cylinder above ground, we ran an example to illustrate the effect of a finite ground plane. In this example, a pipe was placed 48 inches above the ground and the solution accuracy tracked versus the total width of the ground plane. We first ran a convergence sequence to determine the segmentation density required on the ground plane for convergence. We found that to be six elements per inch for this case. If the cylinder were closer to the ground, more elements would be required. Then, using that segment density, we determined the percentage error between the calculated maximum field strength on the cylinder as a function of ground plane width and the exact solution for an infinite ground plane. The results are plotted in Figure 4-14, which shows that the to obtain an error of less than ½% requires a ground screen width on the order of 10 times the height of the pipe. A ground screen of this size usually takes a lot more segments than the image object, and for that reason we prefer to use the image instead of a ground plane.

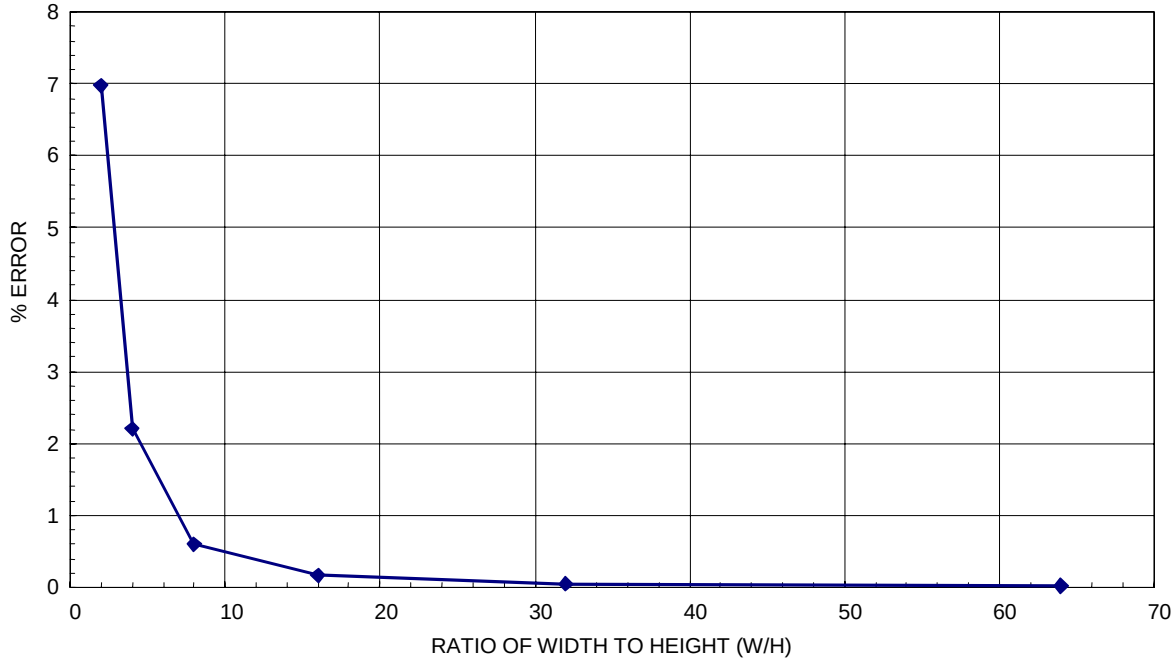

Figure 4-14. Error versus ground size for 2-D BEM program, 8-inch diameter cylinder, bottom 48 inches above ground.

Rotationally Symmetric Objects

The toroid is a rotationally symmetric object that is commonly used for high-voltage hardware and in this context they are commonly called corona rings or grading rings. They are often used on feed-through bushings, base insulator assemblies (BIA), guy insulators, and tower lighting isolation transformers (TLIT) and other high voltage hardware. These types of insulators always have some dielectric material associated with them, typically porcelain, which must be included in the model to accurately determine the fields.

The approach to finding an acceptable method of segmentation, solution accuracy, and measurement technique is similar to that described above for wires, namely using simple geometric

configurations similar to the object in question. For example, for feed-through bushing calculations, we use simple coaxial geometry as the test case.

For horizontal toroids (corona rings), we used the two-dimensional computer program in the rotationally symmetric mode. The segmentation and measurement technique that we applied was the same as we developed for cylinders in the two-dimensional mode of the program. As a further check, we tested with a rotationally symmetrical toroid having a very large minor diameter and placed above ground. For this case, when the minor diameter is large enough, the solution approaches that for a straight cylinder above ground.

The case of an on-axis rotational object, such as a sphere gap, or finite-sized parallel plate, can be treated using rotational symmetry. There is one pitfall here in that the computer programs require that the surface of the object be exactly perpendicular to the axis of symmetry; otherwise there will be a discontinuity at that point. If this is not the case, there will be a slope discontinuity in the surface at the axis of symmetry. This will result in either highly enhanced or decreased field strength at the point defined by the axis of symmetry, depending on whether the surface at that location forms a point or a depression.

Three-dimensional Computer Calculations

The geometry of real-world situations often requires modeling in three dimensions. We have used two different commercially available three-dimensional computer programs, one using the BEM and another using the FEM. Neither of these programs uses functions that are smoothly continuous across the element boundaries. A discontinuity at the boundary results in the field near the surface having significant perturbations about some average value. To diminish these perturbations requires additional processing. We have found that plotting the fields along a line on or very near the surface and averaging provides acceptable results. For programs that allow the user access to the location of the elements, the field strength measured at the center of a surface element often gives accurate answers. Unfortunately, the commercially available FEM programs that we have used do not provide access to the element locations.

A brief description of the application of these programs to some configurations we used to make measurements at the Forestport HVTF is given below. The first step is to apply the programs to analytic solutions for similar simple geometric configurations and develop techniques that give acceptably accurate answers for the problems. There are many details involving the setup and running of the computer programs that are not discussed. However, we describe procedures that enabled us to obtain acceptable solutions for simple geometric configurations similar to the real problem. We suggest that a similar approach be used for validation whenever computed fields are used for engineering purposes.

Finite Length Wire above Ground

Several configurations were used at the Forestport HVTF for measuring corona onset on horizontal wires or cylinders. The geometry varied from vertical wires in a large coaxial cylinder, to outside measurements on horizontal wires 10 feet above ground. We also made measurements on slanted wires above ground. Many measurements were taken inside, using horizontal wire samples 10 to 15 feet long, supported on each end by insulators. In all cases, the test object was connected to the high-voltage source on one end via a 6-inch pipe coming in at an angle. In addition, corona rings shielded the ends of the test object. For the inside measurements, a pair of corona rings stacked on top of the insulators shielded each end of the pipe or wire. There are pictures of these setups in chapter 3. A typical computer-generated line drawing of the indoor horizontal wire configuration is given in

Figure 4-15. The actual configuration is pictured in Figure 6-3 showing the corona rings, which are supported by insulators. The feed pipe is shown on the right of the figure. For this case, the larger cable samples had a natural bend and had to be set up with a slight curve, as shown in the figure. The smaller cable and the pipe samples went straight across between the corona rings. The critical dimension for this setup was the height at the wire center, between the supports, where the wire was closest to the ground.

Figure 4-15. Line drawing of indoor test setup with a horizontal wire above ground.

We obtained a large amount of corona onset data using setups similar to that shown in the figure. Physical measurements were taken for each individual test setup and used to calculate the actual field strengths for processing the data. Accurate three-dimensional calculations were required to be sure that the shielding effect of the feed pipe, end rings, and other objects were taken into account. We developed what we call the "geometric correction factor" for these measurements. The geometric correction factor is the ratio of the actual field (as calculated by the three-dimensional program) to the field calculated using the exact formula for the simple geometric configuration of an infinite wire with the same diameter and height above ground. One reason for using the geometric correction factor is that the dimensions of each individual test setup could not be predicted exactly ahead of time, and thus we could not use the computer program to provide the exact fields prior to the measurements. Since the exact fields were not available, we used the simple analytic formula to provide a partial check on the data at the time of measurement. After the measurements, we ran the three-dimensional program and corrected the data. It is interesting to note that most of these geometric correction factors indicate the field on the finite length wires is somewhat less than the field for the infinite geometry. We attribute this to the shielding effect of the feed and corona hardware on the end of the wires.

Figure 4-16 shows a line drawing of the outdoor sloping wire test setup. For this case, we used an initial field estimate given by the field at the center of the span using the analytic formula for an infinite wire at the same height. The geometric correction factor was the ratio of the maximum field along the wire calculated using the three-dimensional BEM program to the field for the simple analytic formula.

Horizontal Cylinder

The three-dimensional BEM electrostatic program was used to obtain the field strengths for the various cylinders or wires above ground. The corresponding simple geometric configuration used for verification involved a 30-foot length of pipe above ground. As previously mentioned, the desired accuracy was at least 1%. Considerable effort is involved to develop a satisfactory calculation technique to yield this accuracy for the three-dimensional programs.

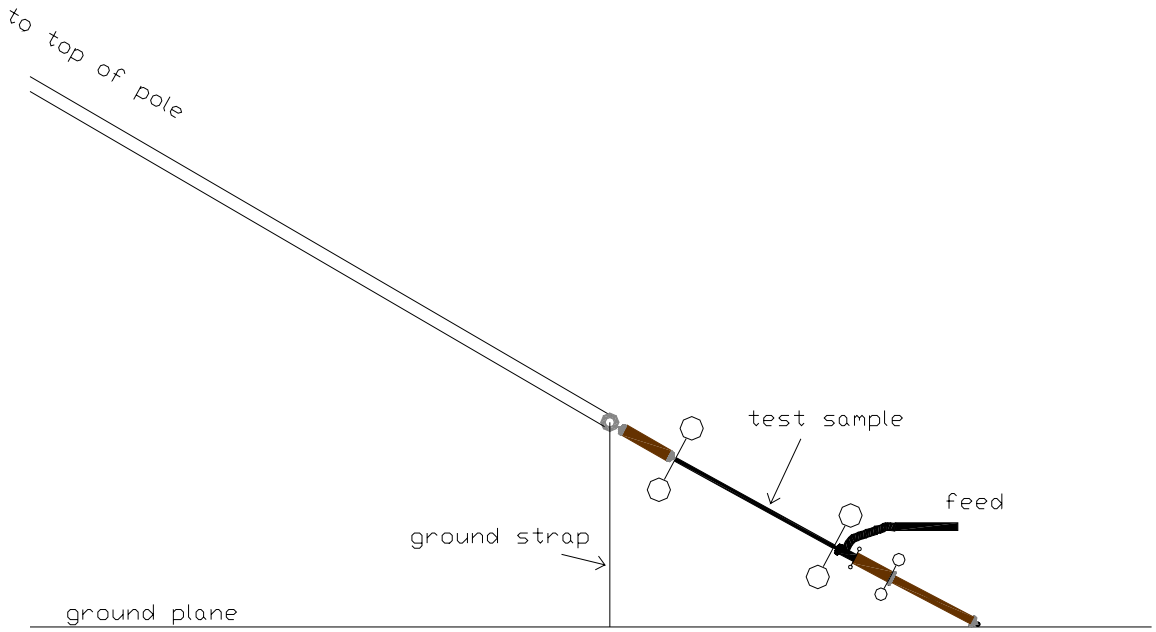

Figure 4-16a. Side view of sloped wire.

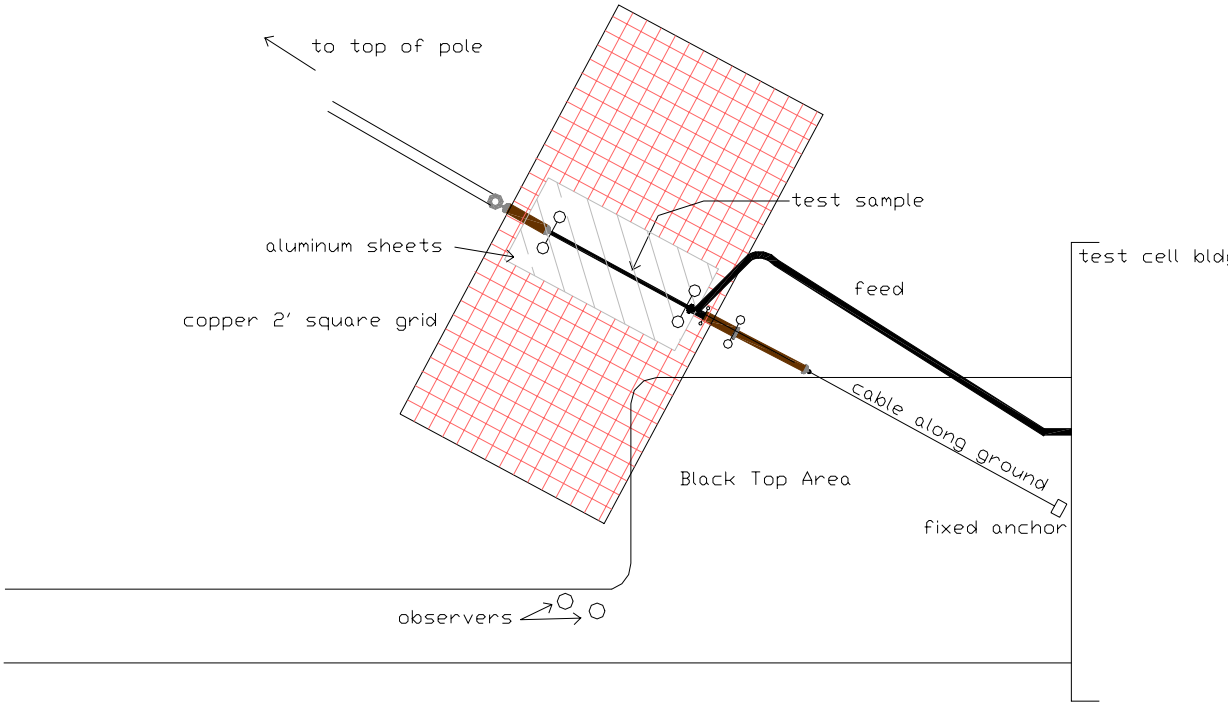

Figure 4-16b. Top view of sloped wire.

Corona onset measurements were made using several different diameter test objects, located at various heights above the ground. The test configurations with wires or pipes close to the ground were located indoors. These samples were approximately 30 inches above ground. We focused our validation tests on this case because the computer programs generally require more elements when the energized object is close to ground.

The technique developed for accurately calculating the fields consisted of the following steps. First, the circle defining the horizontal cylinder was created. It consisted of four segments around. This was rotated in such a way to ensure that there was not a segment boundary on the bottom of the cylinder. This is because the maximum field in this case occurs on the bottom of the cylinder and, if there is a segment boundary at that point, the calculated fields might be significantly perturbed.

This circle was then linearly swept to form the long portion of the cylinder. This particular program has a limitation of 49 horizontal elements for an object. It turned out that for a 15-foot cylinder this resulted in an element density that was too small. After considerable experimentation, it was determined that any given linear object needed to be shorter than 6 feet in order to obtain an element density providing the required accuracy. For the simple geometric configuration, a cylinder consisting of five contiguous sections was selected. The two end sections were 7.5 feet long and the three sections in the center were 5 feet long. All of them had 49 segments along the axis of the cylinder. The center section segments were 1.22 inches long.

The four segments around the cylinder were further divided into four segments to give 16 segments around the cylinder. Note this is the same segmentation requirement that was determined for the two-dimensional program. Figure 4-17 illustrates the segmentation scheme around the center of the cylinder.

Because of the field variation across element boundaries, the fields on the surface have considerable variation, and we had to develop a technique to accurately determine the surface electric field at the center of the cylinder. The technique we eventually settled on was to form a fictitious cylinder, 0.00005 inches outside of the conducting cylinder. A line was drawn along the fictitious cylinder just below the conducting cylinder, and the vertical electric field on this line was plotted. The fictitious cylinder and line were 50 inches long, centered on the 5-foot-long center section of the total cylinder. A plot of this field is shown in Figure 4-18. The plot shows that the vertical electric field oscillates along this line. For this example, the variation is about ±1%. Coarser segmentation results in considerably more variation. Averaging reduced this variation. The figure includes a plot of the 10-inch moving window average, which reduces the variation. We determined that a very good answer could be derived by taking the rms value within a 10-inch window located at the center of the cylinder. Using this technique, the error in the calculated value was less than 0.6% for cylinders with diameters ranging from 0.262 to 8 inches and less than 1.2% for cylinders up to 20 inches in diameter (see Figure 4-19).

The BEM computer program, using the parameters and techniques determined by the use of the simple geometric configuration as described above, was applied to determine the fields for the actual measurement case. Based on the results with the simple geometric configuration problem, we believe the calculated fields to be accurate to within about 1%.

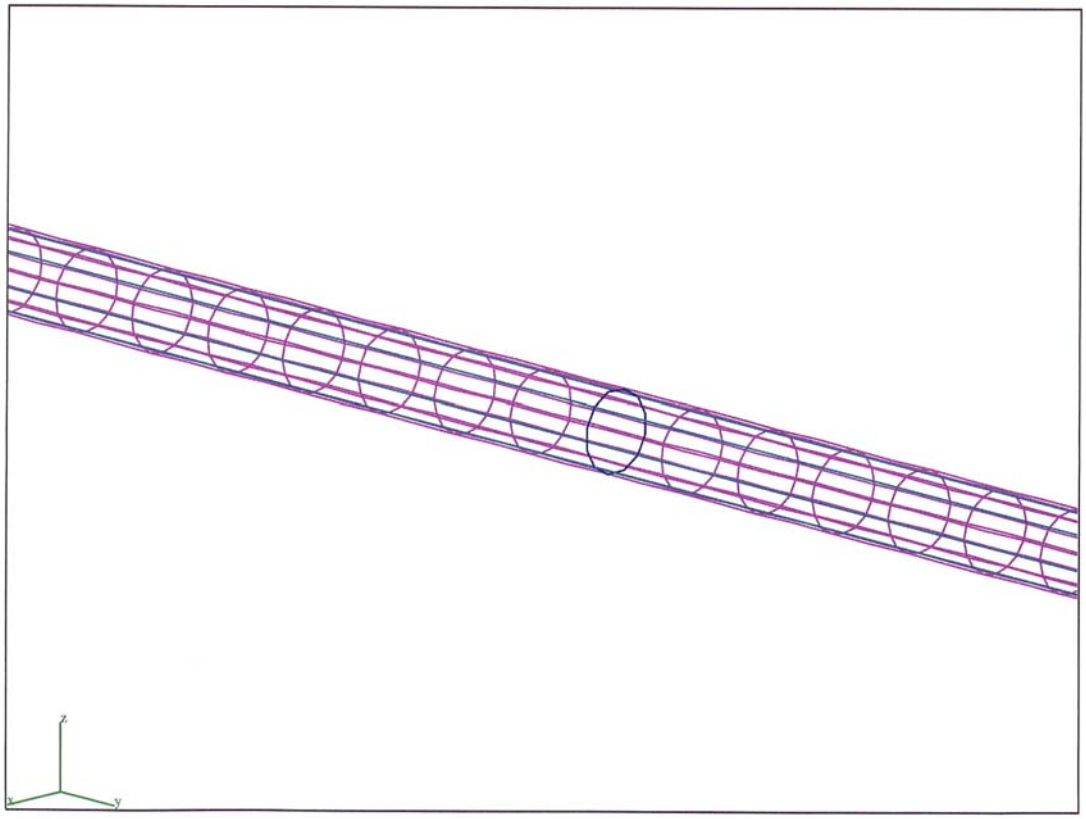

Figure 4-17. 30-foot pipe, 6-inch diameter, with elements for BEM.

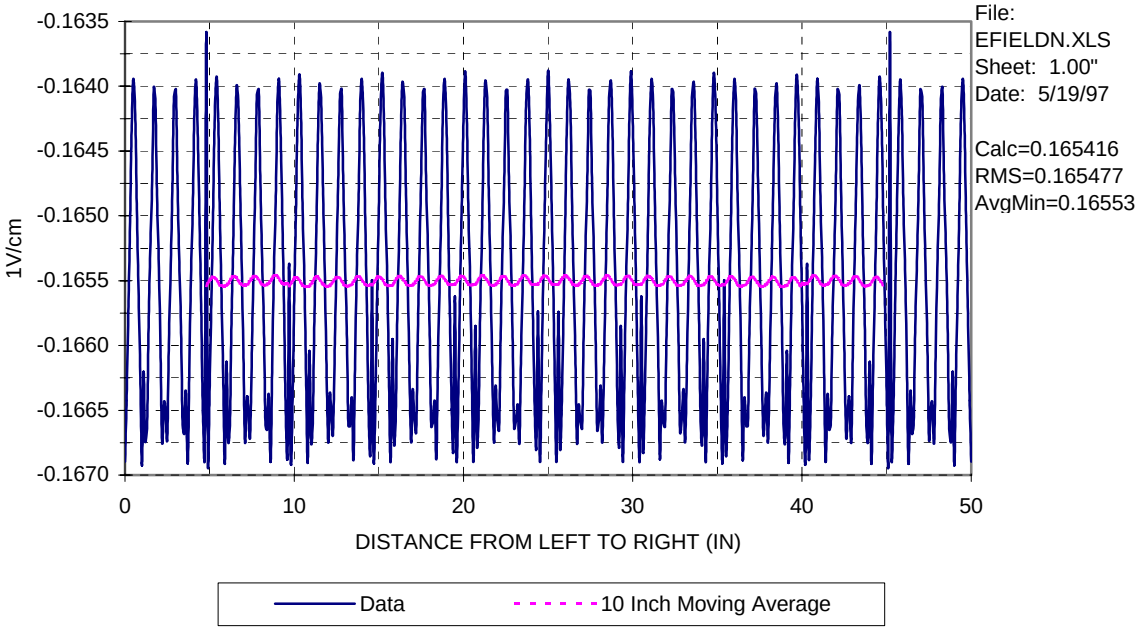

Figure 4-18. E-field at center of 30-foot wire, BEM program, 31-inch height, diameter 1 inch, 500 samples.

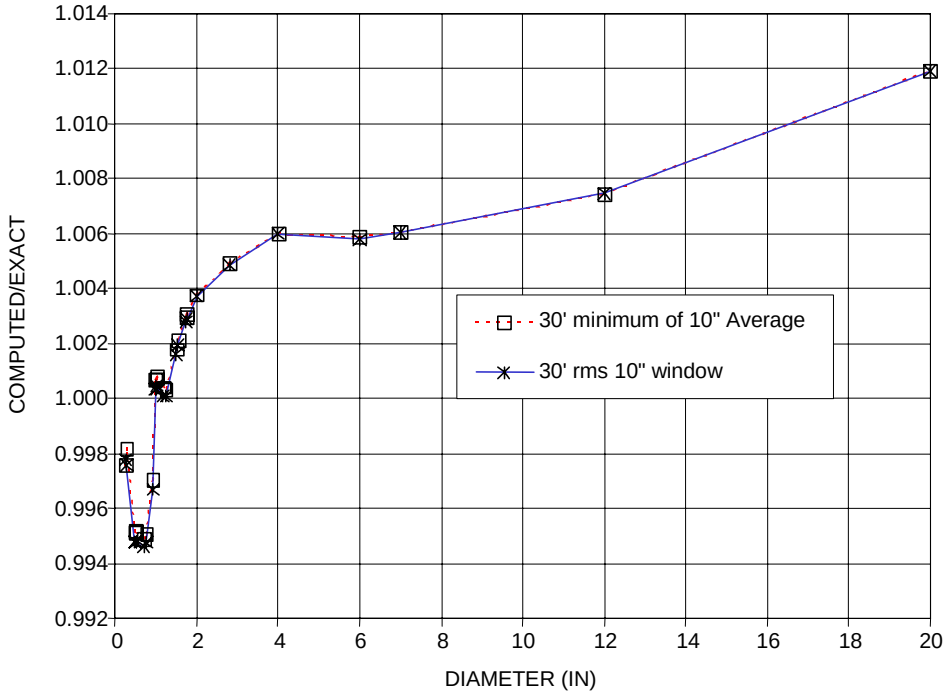

Figure 4-19. 30-ft cylinder calibration data, 3-D BEM program, 31 inches above ground.

Vertical Toroids

This problem is illustrated in Figure 4-20. We made a series of flashover/flare measurements on vertical toroids at different heights above the ground. These toroids were suspended by a vertical cylinder. This configuration requires a three-dimensional program to calculate the fields on the toroid. The critical location for the field is on the bottom of the toroid closest to the ground. A somewhat similar configuration consists of a horizontal cylinder above the ground having the same diameter as the minor diameter of the toroid located at the same height above ground. For an isolated toroid, without any supporting members, the field on the bottom of the toroid will be greater than the field on the bottom of the horizontal cylinder. We started by applying the BEM program to this problem, using an 8-inch minor diameter toroid located 6 inches above ground, without vertical support. For this case, the BEM program gave values of electric field on the bottom of the toroid less than that for a horizontal cylinder having the same diameter as the toroid minor diameter and at the same height. This is incorrect and therefore the BEM program results were suspect. The field on the toroid must be greater than the field on the cylinder because the charge concentrates on the low part of the toroid. The values obtained from the program for a horizontal cylinder were very accurate, but obviously the values for the vertical toroid were incorrect. Considerable effort was put into refining our approach using this program without success. We never determined the source of the errors, and as a result turned to a commercially available FEM program to solve for fields on the vertical toroids.

Finite Element Method

As a result of the failure of the BEM program for our vertical toroidal configuration test case, we tested a commercially available FEM program and found that it gave results with approximately the correct field strength magnitudes for that problem. We then proceeded to test this program on similar

simple geometrical configurations having analytic solutions to develop a method giving the required accuracy.

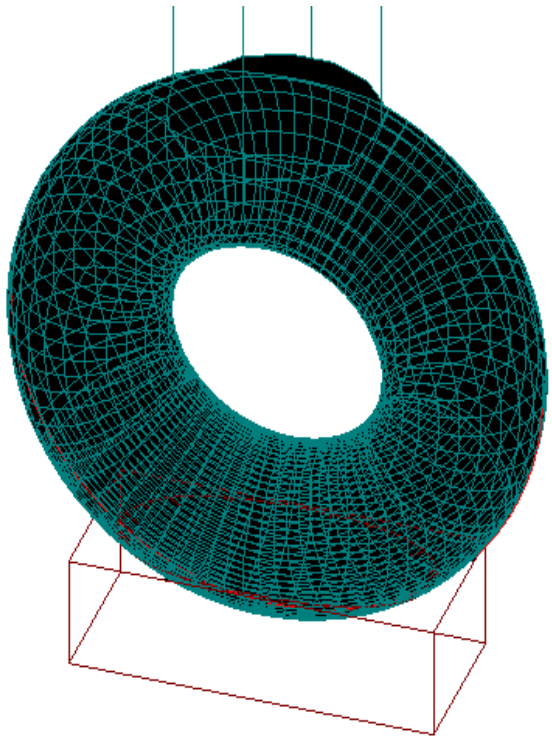

Figure 4-20. Vertical toroid.

Horizontal Cylinder

The applications of the FEM and BEM programs to horizontal cylinders differed. FEM calculates the fields in a specified volume and applies “free space” boundary conditions on the boundaries of the volume. The first step is to specify the dimensions of this volume. A rule of thumb is to use a volume with sides that extend five times the width of the object being modeled in any given direction. This resulted in a large number of unknowns for the 30-foot-long, 3-inch-diameter pipe, and the available computers were not capable of developing the solution. To get around this difficulty, we reduced the size of the simple geometric configuration problem to fit the available computer memory. The result was 6-foot-long, 3-inch-diameter cylinder with the center located 7.5 inches above ground. The geometry for the horizontal cylinder configuration illustrating the solution space boundary is shown in Figure 4-21. The FEM program models the ground screen by the use of anti-symmetry with respect to the ground plane. This is the same as image theory.

The FEM program allows the definition of a dummy box within which an accuracy parameter can be specified. The program enhances the mesh in this box to get more accurate answers within the dummy box. The program also allows the specification of a maximum number of enhancement passes for reduction of error within the box. We used a 24-inch-long dummy box on the bottom of the cylinder near the center (Figure 4-22). A similar box was specified for the toroid calculations, as shown in Figure 4-20.

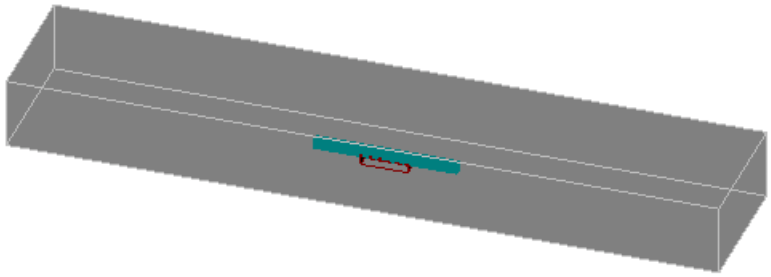

Figure 4-21. Three-inch wire with dummy box and background space.

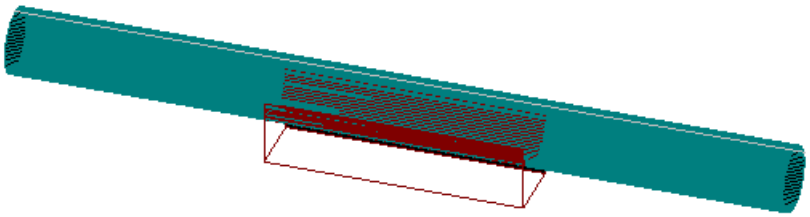

Figure 4-22 . Six-foot length of 3-inch diameter pipe with dummy box.

The tests modeling the cylinder above a ground plane revealed that using a smoothly varying curved surface boundary for the cylinder resulted in a prohibitive number of elements to achieve the desired accuracy within the dummy box. As a result, we switched to using a polygon approximation to a circle for generating the cylinder. Using this approach, we were able to get an acceptable result by using a 72-sided polygon, when we specified the accuracy parameter at 0.1% and limited the number of enhancement passes to 30.

The FEM program assigns the location and sizes of the elements and enhances the size of the elements to reduce the error parameter. Unfortunately it does not allow the user to determine the location of the elements. Thus, we could not look at the field at the center of elements, and we naturally applied a similar approach to what we had developed for the BEM programs by sampling the field along a line on the bottom of the cylinder.

An example of the magnitude of the electric field plotted along a 24-inch line on the bottom of the cylinder surface is given in Figure 4-23. The field is continuous at these locations but the slope is not continuous. Note that the sharp points where the slope is discontinuous correspond to the edges of the finite element domains. There are many ways to use the data to get an average value to estimate the field at the surface. One way would be to use the field at the center of the each element (in the direction of the line). Unfortunately, that may not be the center of the element in the perpendicular direction. Partly for that reason, we elected to use two points from each element, each halfway between the sharp discontinuity and the peak. For this example, we have selected six data points from the three elements closest to the center of the cylinder, and they are marked in figure 4-23. Note, that if the next element to the left were included, the average level would be raised somewhat. However, for this case, a smooth cylinder having a uniform surface, the field should be uniform and the field strength on this one element appears to be anomalously high. This is a good example how the plot can be used to spot anomalous behavior and why using any single data point is not acceptable. We have found that in every case it is useful to plot the field strength and check for anomalous behavior.

A summary of the data taken at the points marked in Figure 4-23 is given in Table 4-4 below. Note that the accuracy of this result is well within the desired 1%.

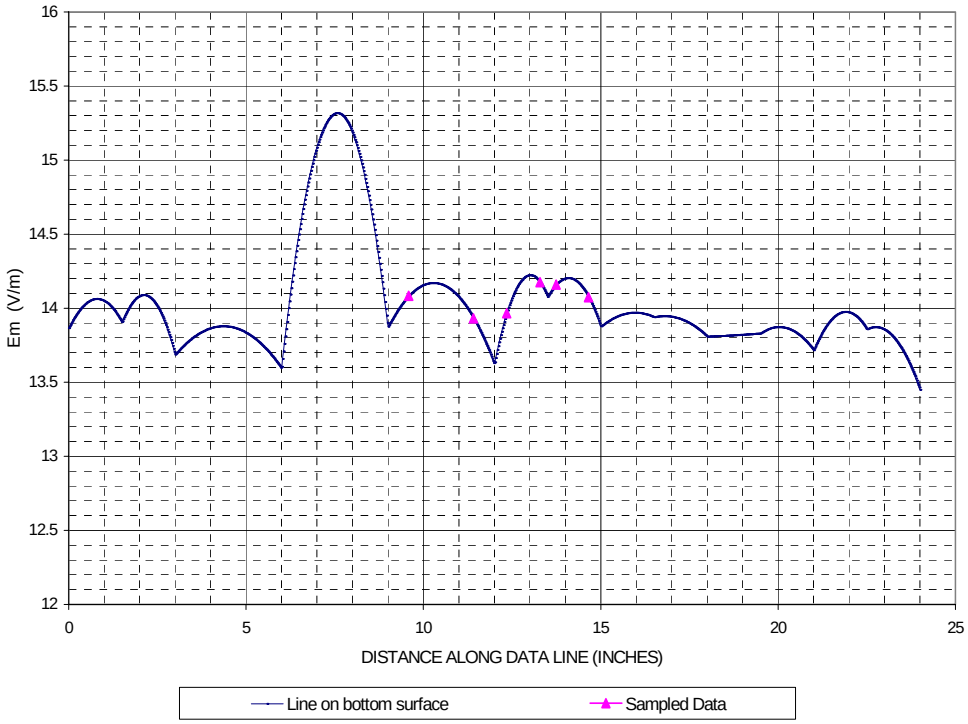

Figure 4-23. Sample field along horizontal 3-inch pipe, bottom at 6 inches, FEM program.

Table 4-4. Sample field points for 3-inch pipe example.

Data Sample Points	Data Line on Surface
1	14.082
2	13.931
3	13.965
4	14.174
5	14.158
6	14.073
Average (V/m)	14.063
Exact Value (V/m)	14.022

Sphere above Ground

As a further check, we decided to exercise the program using an 8-inch sphere located 6 inches above ground. The geometry is shown in Figure 4-24: a sphere approximated by a multi-sided polyhedron with the dummy box located beneath the sphere. The solution space is not shown in this figure. The magnitude of the electric field has been calculated along a curved line on the surface of the sphere passing under the bottom of the sphere. The plot of this field is shown in Figure 4-25. Again, data were taken at six locations closest to the exact bottom of the sphere in the manner previously specified. These points are marked on the figure.

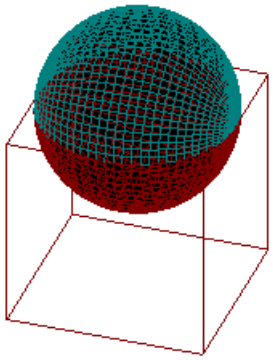

Figure 4-24. Eight-inch diameter sphere and dummy box.

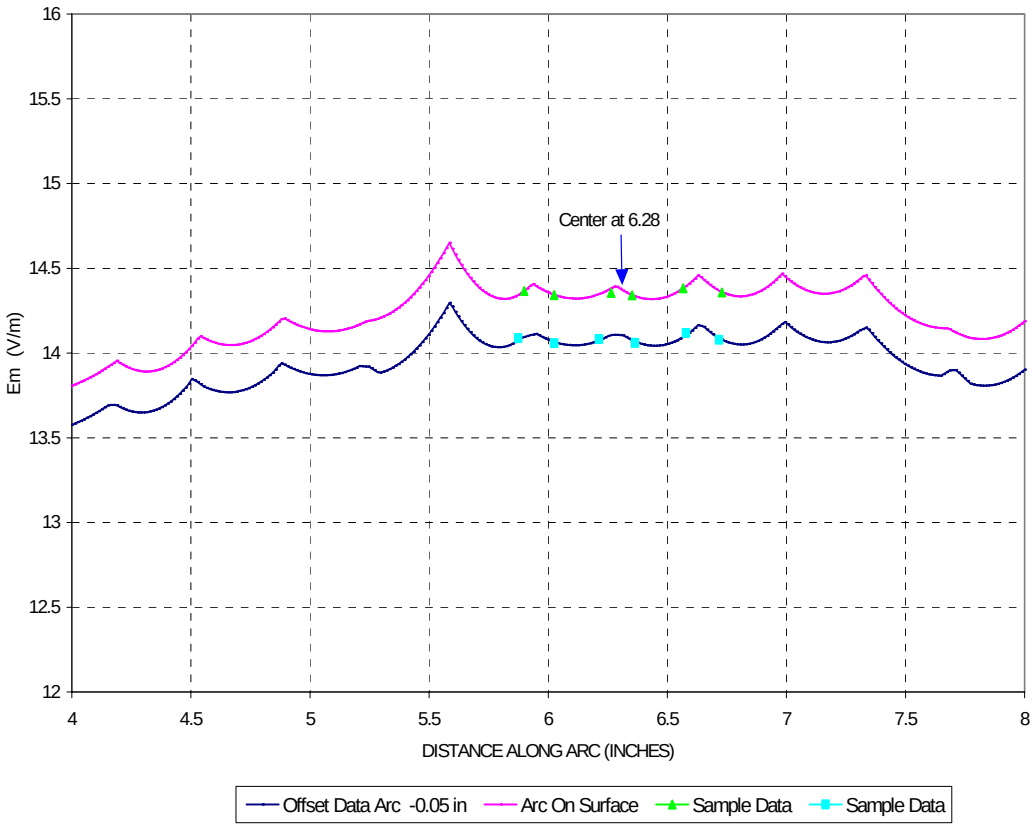

Figure 4-25. Magnitude of electric field for 8-inch sphere, 6-inch height above ground.

For the case of the toroid, the curve for plotting the field strength had to be located slightly below the cylinder to avoid getting several points having zero fields, which corresponded to those points being inside the cylinder. Use of a curve separated from the surface by a distance of 0.05 inches below the toroid avoided this problem. However, the fields fall off with distance and the value at 0.05 inches is somewhat less than the value at the surface. A correction factor was used to translate the value taken at 0.05 inches to an estimated value on the surface. The correction factor is based on an approximate formula for the field at a distance away from a charged surface given by (Olsen et al, 1997).

$$\frac{E_s R_1 R_2}{(R_1 + \delta)(R_2 + \delta)} = E_\delta$$

where R_1 and R_2 are the Gaussian radii of curvature that define the surface at that point,
E_s is the surface electric field at that point,
δ is the distance from the surface to the field point, and
E_δ is the electric field at this point.

This formula is general and applies to any surface where both radii of curvature are positive. The formula is exact at the surface, with increased possibility of error as the distance from the surface increases. If the charge is uniform, such as for a sphere in free space, it gives exact results everywhere. For the sphere, both radii of curvature are equal.

Inverting the above formula and substituting the known values for E_δ, δ, R_1 and R_2, E_s can be calculated:

$$E_s = \frac{E_\delta (R_1 + \delta)(R_2 + \delta)}{R_1 R_2}$$

For the case of the sphere, the offset was not necessary, but we used it to test use of the offset since the offset was required for the vertical toroid. Figure 4-25 shows a plot of the magnitude of the field along the surface of the sphere and along a curve parallel to the sphere surface but offset by 0.05 inches. Six data points have been taken from that curve using the method previously described. The data from both the curves is included in Table 4-5 below. Note that the variation of the field around the average is about 3.0% for this example.

Table 4-5. Magnitude of electric field for 8-inch sphere, 6-inches above ground.

Data Points	Data Arc on Surface	Data Arc Offset 0.05 inches	Data Arc Offset Corrected
1	14.366	14.089	14.443
2	14.343	14.059	14.413
3	14.355	14.083	14.437
4	14.341	14.060	14.414
5	14.382	14.119	14.474
6	14.358	14.078	14.432
Average (V/m)	14.356	14.081	14.435
Exact Solution	14.533	14.177	14.533

The six data points are averaged to give the computer-generated estimate of the surface electric field. The table contains a comparison between this average and the exact solution for the sphere above ground and shows that the desired accuracy has been achieved by using this technique.

The computer-calculated data for the 8-inch and 2-inch vertical toroid have been plotted in Figures 4-26 and 4-27. In these figures, both the BEM and FEM data are included as well as the exact calculations for a cylinder having the same diameter as the minor diameter of the toroid. Note that the curve for the FEM data and the cylinder are parallel but the BEM curve has a different variation with height. In fact, at the shortest height, the BEM value is less than that for the cylinder. This is clearly incorrect and was a clue that the BEM data for other heights may not be correct. As an alternative, we applied a commercially available FEM program to this problem. As a further check, we used a completely different FEM program known as EIGER 3-D, which is under development (Johnson, 2003), to calculate the fields on a 2-inch cylinder and a 2-inch toroid, both 6 inches above ground. A comparison of that data with our calculations is given in Table 4-6 below. For this comparison the 2-inch toroid did not have the vertical support, and therefore the field strength is somewhat greater than when the vertical support is included (see Figure 27). The results of the EIGER 3-D agree closely with the results of the 3-D BEM program, which increased our confidence in the results.

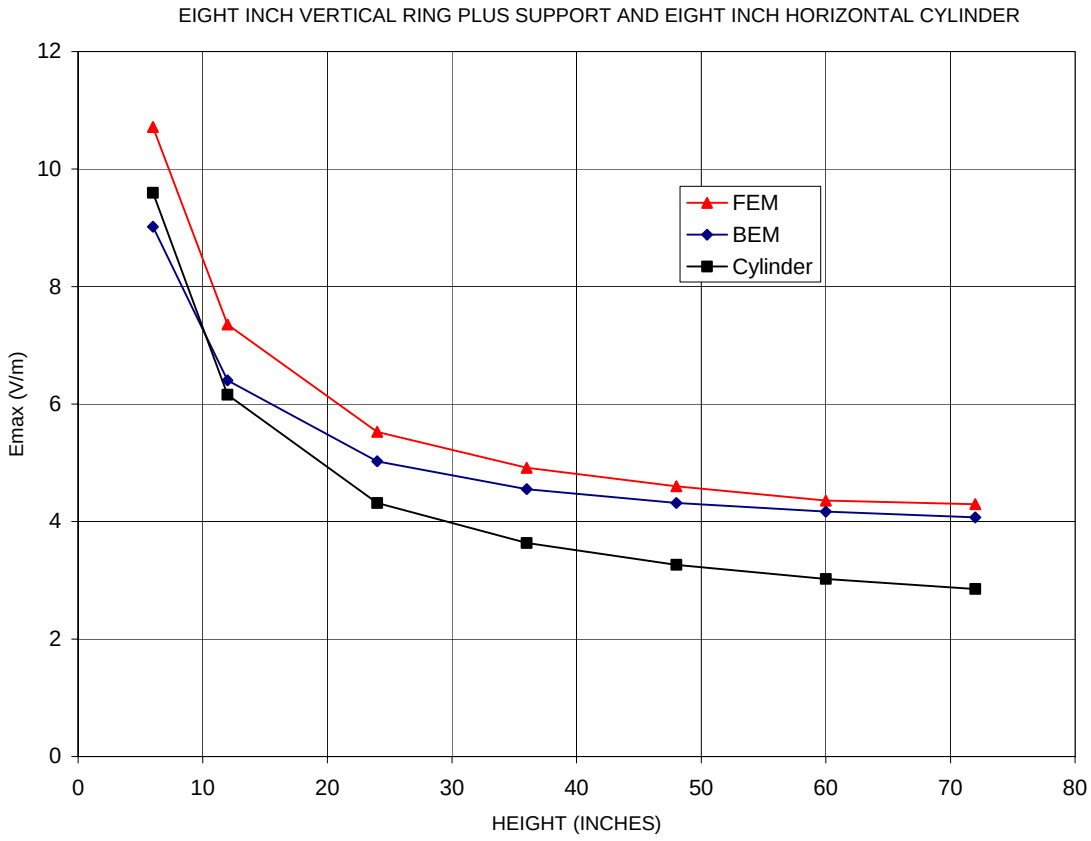

Figure 4-26. Emax versus height for 8-inch vertical toroid with support and 8-inch horizontal cylinder, 3-D FEM.

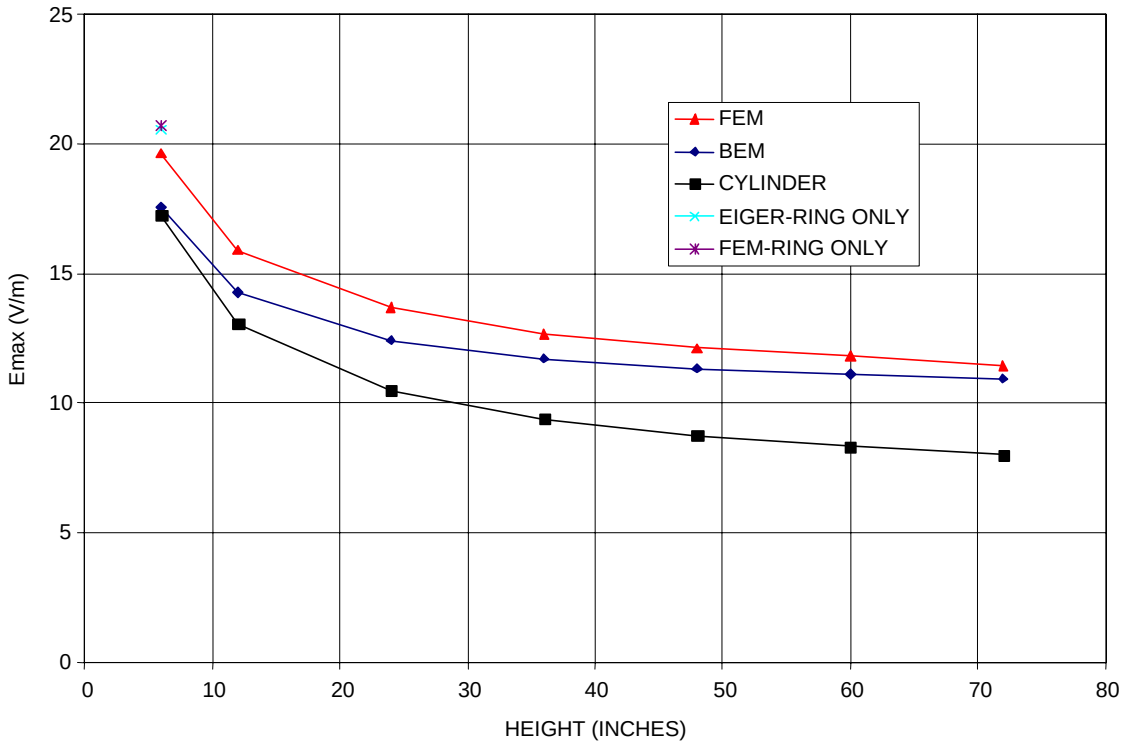

Figure 4-27. Emax versus height for 2-inch vertical cylinder plus support and 2-inch horizontal cylinder, 3-D FEM.

Table 4-6. Comparison of data from different programs cylinder and toroid 6 inches above ground Emax V/m, 1 volt applied.

	Exact	3-D BEM	3-D FEM	EIGER 3-D
2” Cylinder	17.26	–	17.39	17.10
2” toroid w/o support	–	–	20.72	20.56
2” toroid + support	–	17.55	19.65	–

Appendix 4A Sine Product Identity

The sine product identity to be proven is given below,

$$\prod_{k=1}^{N-1}\left[2Sin(k\pi / N\right] = N \tag{A-1}$$

Euler's identity for Sin(x) is given by

$$Sin(x) = \left\{e^{ix} - e^{-ix}\right\} / \left(2i\right)$$

where $i = \sqrt{-1}$.

Substituting Euler's identity into the left-hand side of Equation A-1 and letting $k\pi / N = x$ gives the following.

$$\prod_{k=1}^{N-1}\left[2\left\{e^{ix} - e^{-ix}\right\}/2i\right]$$

Operating on this result gives the following.

$$= (1/i)^{N-1}\prod_{k=1}^{N-1}\left\{e^{ix} - e^{-ix}\right\}$$

$$= (1/i)^{N-1}\prod_{k=1}^{N-1} e^{ix}\left\{e^{2ix} - 1\right\}$$

$$= (1/i)^{N-1}\exp\left\{\sum_{k=1}^{N-1}(-ix)\right\}\cdot\prod_{k=1}^{N-1}\left\{e^{2ix} - 1\right\}$$

$$= (1/i)^{N-1}\exp\left\{\sum_{k=1}^{N-1}(-ik\pi / N)\right\}\cdot\prod_{k=1}^{N-1}\left\{e^{2ix} - 1\right\}$$

$$= (-i)^{N-1}\exp\left\{(-i\pi / N)(N)(N-1)/2)\right\}\cdot\prod_{k=1}^{N-1}\left\{e^{2ix} - 1\right\}$$

$$= (-i)^{N-1}\exp\left\{(-i\pi)(N-1)/2)\right\}\cdot\prod_{k=1}^{N-1}\left\{e^{2ix} - 1\right\}$$

$$= (-i)^{N-1}\left(\exp\left\{i\pi/2\right\}\right)^{N-1}\cdot\prod_{k=1}^{N-1}\left\{e^{2ix} - 1\right\}$$

$$= (-i)^{N-1}\left(-i\right)^{N-1}\cdot\prod_{k=1}^{N-1}\left\{e^{2ix} - 1\right\}$$

$$= (-1)^{N-1}\cdot\prod_{k=1}^{N-1}\left\{e^{2ix} - 1\right\}$$

$$= (-1)^{N-1}\cdot(-1)^{N-1}\cdot\prod_{k=1}^{N-1}\left\{1 - e^{2ix}\right\}$$

and finally,

$$= \prod_{k=1}^{N-1} \left\{1 - e^{2ix}\right\} = \prod_{k=1}^{N-1} \left\{1 - e^{2ik\pi/N}\right\} \quad . \tag{A-2}$$

The set of exponentials, $e^{2ik\pi}$, for k = 1 to N-1, are the Nth roots of 1 (except for 1 itself). These roots are sometimes called the cyclotomic numbers. The other Nth root of 1, is 1 itself. This can be demonstrated as follows.

$$1 = e^{ik2\pi} \quad \text{for k = integer.}$$

Taking the Nth root gives $1^{1/N} = e^{(ik2\pi)/N}$.

These roots are represented on the complex plane by points on the unit circle, at angles of 2kπ/N. There are a total of N unique roots (angles), because as k increases, the angle rotates around to a unique angle. When k = N, the angle is 2π, and the value of the root is 1. For k > N, the roots (angles) repeat.

These roots are solutions of the equation $Z^N - 1 = 0$. Using these roots to construct the equivalent polynomial gives the following.

$$Z^N - 1 = (Z - e^{i2\pi/N}) \cdot (Z - e^{i4\pi/N}) \cdots (Z - e^{i(N-1)2\pi/N}) \cdot (Z - 1)$$

Rearranging terms gives the following.

$$(Z^N - 1) / (Z - 1) = (Z - e^{i2\pi/N}) \cdot (Z - e^{i4\pi/N}) \cdots (Z - e^{i(N-1)2\pi/N})$$

or

$$\prod_{k=1}^{N-1} (Z - e^{i2\pi/N}) = \cdot (Z^N - 1) / (Z - 1)$$

Note that the polynomial $(Z^N - 1)$ can be factored as follows.

$$Z^N - 1 = (Z - 1)(Z^{N-1} + Z^{N-2} + \cdots + Z + 1)$$

Substituting this into the previous equation gives the following.

$$\prod_{k=1}^{N-1} (Z - e^{i2\pi/N}) = Z^{N-1} + Z^{N-1} + \cdots + Z + 1$$

Substitution of this result into Equation A-2 completes the proof.

Appendix 4B Infinite Wire Grid

The geometry consists of an infinite set of parallel wires, which are also parallel to the ground. They all have the same radius, a, and height, h, above ground. They are spaced apart a distance S. The geometry is illustrated in Figure B-1. In the figure, D_k denotes the slant range between the image of one wire and other wires, where the subscript refers to the number of spaces of length S between the wires. D_k is given by the following equation.

$$D_k = \sqrt{(2h)^2 + (kS)^2}$$

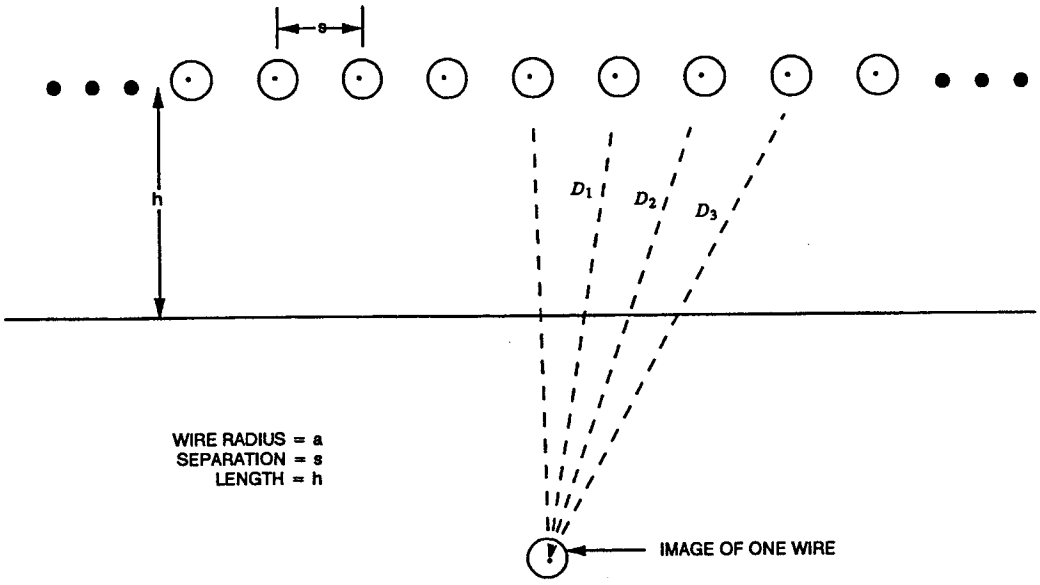

Figure 4B-1. Geometry for an infinite wire grid above ground.

The wires all have the same voltage V and by symmetry the same charge q. The potential at one wire is the sum of the potential from the charge on that wire plus the potentials due to the charge on all the other wires. This potential is given by the following equations.

$$\frac{2\pi\varepsilon_0 V}{q} = \ln(2h/a) + \sum_{k=1}^{\infty} \ln(D_k / kS)$$

or

$$\frac{2\pi\varepsilon_0 V}{q} = \ln(2h/a) + \sum_{k=1}^{\infty} \ln\left[\sqrt{\frac{(2h)^2 + (kS)^2}{(kS)^2}}\right]$$

and finally

$$\frac{2\pi\varepsilon_0 V}{q} = \ln(2h/a) + \frac{1}{2}\sum_{k=1}^{\infty} \ln\left[1 + (2h/kS)^2\right]$$

The summation term can be rewritten as a product.

$$\frac{2\pi\varepsilon_0 V}{q} = \ln(2h/a) + \frac{1}{2}\ln\left[\prod_{k=1}^{\infty}\left(1+(2h/kS)^2\right)\right]$$

The infinite product in the above equation has a closed form. The derivation starts with the following series (Jolley, 1961)

$$\prod_{i=0}^{\infty}\left(1-(\theta/i)^2\right) \tag{B-1}$$

Solving for θ to make the products equal,

$$-\left(\frac{\theta}{\pi}\right)^2 = \left(\frac{2h}{S}\right)^2$$

$$\theta = \sqrt{-1}\cdot\frac{2\pi\cdot h}{S}$$

Substituting for θ in equation B-1, gives the following closed form.

$$\prod_{i=1}^{\infty}\left(1+(\theta/i)^2\right) = \frac{Sin(\sqrt{-1}\cdot 2\cdot\pi\cdot h/S)}{\sqrt{-1}\cdot 2\cdot\pi\cdot h/S} = \frac{Sinh(2\cdot\pi\cdot h/S)}{2\cdot\pi\cdot h/S}$$

Using this closed form gives the equation for the capacitance per unit length of one wire.

$$C_1 = \frac{2\pi\cdot\varepsilon_0}{\ln(2h/a) + \frac{1}{2}\ln\left(\frac{Sinh(2\pi\cdot h/S)}{2\pi\cdot h/S}\right)}$$

From this equation, it can be seen that each wire has the same capacitance that it would have if it were a single isolated wire at the height h_a.

$$h_a = h\cdot\left(\frac{Sinh(2\pi\cdot h/S)}{2\pi\cdot h/S}\right).$$

Appendix 4C Geometric Theory Derivation

The derivation for the complete geometric theory is the same as for the simple geometric theory, except that the fields from the other wires are calculated on the surface of the wire instead of at the center of the wire. This leads to a more complicated geometric factor.

The assumptions used in this derivation are summarized below:

The charge on each wire is the same and acts as a filament located at the center.

The fields from the images of the wires in the ground plane are negligible.

The fields in the vicinity of the wire, where the field is being calculated, are approximately uniform, and therefore the effect of the wire can be accounted for by doubling the fields calculated as if the wire were not there.

The geometry for the general wire cage is shown in Figure C-1. For convenience, only the first and jth wire are shown. The various angles involved are defined in the figure.

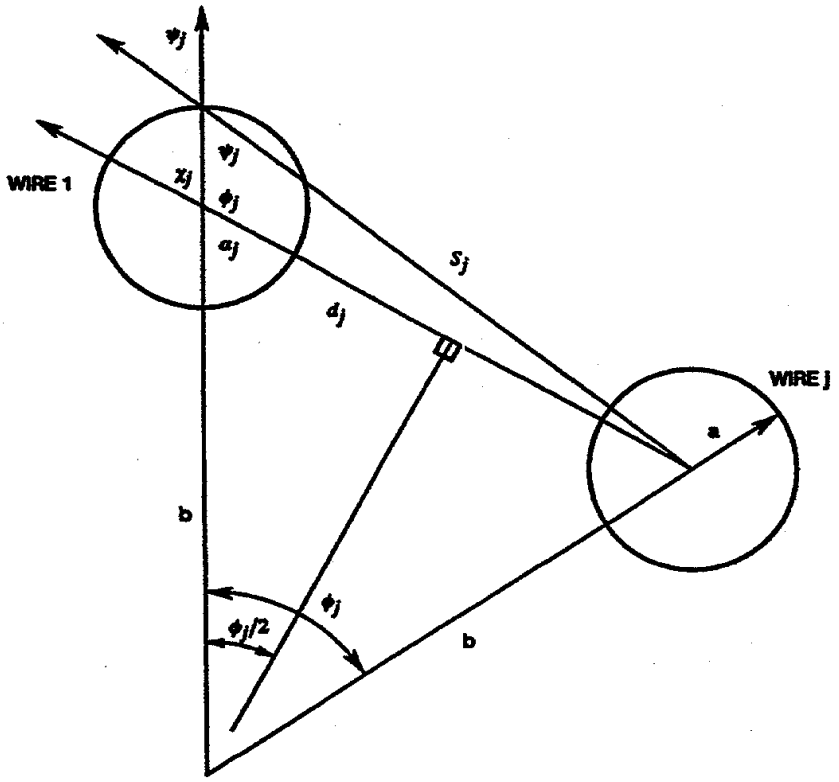

Figure 4C-1. General cage geometry and angle definitions. (needs new orig)

The field normal to wire 1 at the point opposite the cage center is given by

$$E_m = q\left[\frac{1}{a} + 2\sum_{j-2}^{N}\frac{Cos(\alpha_j)}{\rho_j}\right]$$

where ρ_j is the distance from the center of the jth wire to the field calculation point, and α_j is the angle between ρ_j and the radial from the cage center at the field calculation point.

The $1/a$ term represents the field on wire 1 from the charge on wire 1, and the summation term represents the field on wire 1 from each of the other wires. The factor of 2 in front of the summation accounts for the effect of wire 1 on the fields from all the other wires.

For this example, the fields are calculated on wire 1 but by symmetry, all wires have the same field.

Simple Geometric Theory (SGT)

For this theory, the fields are calculated at the center of the wire, i.e.,

$$\rho_j = d_j$$

$$\alpha_j = \sigma_j$$

(See Figure C-1)

$$\frac{Cos(\alpha_j)}{\rho_j} = \frac{Cos(x_j)}{d_j}$$

Solving for each factor gives the following equations.

$$\frac{d_j}{2} = b \cdot Sin(\theta_j / 2)$$

or

$$\frac{d_j}{2} = 2 \cdot b \cdot Sin(\theta_j / 2)$$

and

$$Cos(x_j) = Cos\left(\frac{\pi}{2} - \frac{\theta_j}{2}\right).$$

Thus, each term in the series is the same

$$\frac{Cos(x_j)}{d_j} = \frac{1}{2b}$$

and the series sums to the following simple closed form

$$2\sum_{j-2}^{N}\frac{1}{2b} = \frac{N-1}{2b}$$

The final form of the equation is given below.

$$E_m = \frac{q}{2\pi\varepsilon_0}\left\{\frac{1}{a} + \frac{N-1}{b}\right\}$$

Substitution of the total cage capacitance C_n gives the result.

$$E_m = \frac{VC_n}{2\pi\varepsilon_0 n}\left\{\frac{1}{a}+\frac{N-1}{b}\right\}$$

or finally

$$E_m = \frac{V}{n}\left\{\frac{1}{a}+\frac{N-1}{b}\right\}\left[\frac{1}{\ln(2h/a_{eqC}}\right].$$

This is called the Simple Geometric Theory (SGT) formula.

Complete Geometric Theory (CGT)

For the complete geometric theory, the fields are calculated at the surface of wire 1, i.e.,

$$\rho_j = S_j$$
$$\alpha_j = \psi_j$$

The summation becomes the following.

$$\sum_{j-1}^{n}\frac{Cos(\psi_j)}{S_j}$$

By using the definitions of Figure C-1 and the law of cosines, we can solve for S_j

$$S_j^2 = d_j^2 + a^2 - 2ad_jCos(\varphi_j)\ .$$

Substitution of the following

$$Cos(\varphi_j) = Cos\left(\frac{\pi}{2}+\frac{\theta_j}{2}\right) = -Sin(\theta_j/2)$$
$$d_j = 2bSin(\theta_j/2)$$

gives

$$S_j^2 = 4d^2Cos(\theta_j/2)+a^2+4adSin^2(\theta_j/2)$$

which reduces to

$$S_j^2 = a^2+4b(b+a)Sin^2(\theta_j/2)$$

similarly solving for $Cos(\psi_j)$.

$$d_j^2 = S_j^2+a^2-2aS_jCos(\psi_j)$$
$$Cos(\psi_j) = \frac{S_j^2+a^2-d_j^2}{2aS_j}$$

The summation terms are

$$\frac{Cos(\psi_j)}{S_j} = \frac{S_j^2+a^2-d_j^2}{2aS_j^2} = \frac{a+2bSin^2(\theta_j/2)}{S_j^2}$$

$$\frac{Cos(\psi_j)}{S_j} == \frac{a + 2bSin^2(\theta_j/2)}{a^2 + (4b)(b+a)Sin^2(\theta_j/2)}$$

For n = 2, $\theta_j / 2 = \pi$ and the equation for maximum surface field becomes

$$E_m = \frac{V}{2}\left\{\frac{1}{a} + \frac{1}{b + a/2}\right\}\left[\frac{1}{\ln(2h/a_{eqC}}\right]$$

For n = 3, $\theta_j / 2 = \pi/3$ and $2\pi/3$, and the equation for maximum surface field becomes

$$E_m = \frac{V}{3}\left\{\frac{1}{a} + 4\frac{a+1.5b}{a^2+3ab+3b^2}\right\}\left[\frac{1}{\ln(2h/a_{eqC}}\right]$$

For n = 4, $\theta_j / 2 = \pi/4$, $\pi/2$ and $3\pi/4$, and the equation for maximum surface field becomes

$$E_m = \frac{V}{4}\left\{\frac{1}{a} + \frac{1}{b+a/2} + 4\frac{a+b}{a^2+2ab+2b^2}\right\}\left[\frac{1}{\ln(2h/a_{eqC}}\right]$$

The terms of the summation can be rewritten in the following form.

$$2\sum\frac{Cos(x_j)}{d_j} = \sum\frac{1}{b + \frac{a}{2} + \frac{ab\cdot\left(Sin^2(\theta_j/2)-1\right)}{a+2bSin^2(\theta_j/2)}}$$

Modified Simple Geometric Theory

The terms of the summation above are all of the form

$$\frac{1}{b + a/2 + CF(\theta)} .$$

where $CF(\theta)$ is a correction term. If this term is neglected, then the series has a simple closed form and gives the following equation for the maximum surface field.

$$E_m = \frac{V}{n}\left\{\frac{1}{a} + \frac{n-1}{b+a/2}\right\}\left[\frac{1}{\ln(2h/a_{eqC}}\right]$$

This equation is similar to the simple geometric theory result and will be called the Modified Simple Geometric Theory (MSGT).

CHAPTER 5 TEST FACILITY AND MEASUREMENT METHODS

BACKGROUND

This chapter marks a transition from theoretical considerations to measurements. The objective of this chapter is to describe the test facility and the measurement methods used to develop the data presented in the chapters following. The requirements for a high-voltage test facility are outlined, followed by a description of the Forestport High-Voltage Test Facility (HVTF). Although this facility has been closed and moved to Dixon, CA, the description is included for the following reasons. First, it provides necessary background material for the test setup descriptions in following chapters. Second, it gives an overview of the design of a successful high-voltage test facility, which could serve as a guide for the construction of other similar test facilities, and as such, it includes some discussion of design alternatives. The Dixon facility is very similar to Forestport, using the same transmitter and almost exactly the same high-voltage resonant circuit, which is the heart of the HVTF, and this circuit is described in detail. Previously unpublished techniques for design of the circuit elements are included in appendices 5C and 5D**.** This chapter also contains descriptions of the measurement techniques, including detailed descriptions of the high-voltage phenomena. These are also referred to in later chapters containing measured test results.

TEST FACILITY REQUIREMENTS

Tests

The main requirement for a Navy VLF/LF test facility derives from a requirement to test large insulators that are used in large antenna systems under normal environmental conditions. The insulators must be tested at full voltage under conditions that adequately simulate their operational environment. Some insulators are used indoors in the helix house, but most of the insulators are located outdoors and experience ambient weather conditions. Inclement weather turns out to provide worst-case conditions, and therefore the most important tests are those that determine the acceptability of an insulator operating under actual environmental conditions including: dry, rain (with or without wind), snow, and ice.

Most of the procedures used for the VLF/LF high-voltage measurement were developed by modifying U.S. power industry standard high-voltage test procedures (ANSI C29.1 1998, IEEE Std 4-1995, and ANSI C68.1 1968). The Canadian and European standards also provided useful references (CEA 1991, CEI/IEC 60-1 1989, and CEI/IEC 60-1 1994). Early in the testing program, it was discovered that the “drip dry” wet measurements specified in the 60-Hz standards did not adequately characterize insulator performance for VLF/LF applications. Realistic performance determination for outdoor VLF/LF insulators required simulated windblown rain.

To accurately determine the acceptability of a VLF/LF insulator assembly, the HVTF facility must be capable of generating enough voltage and power to simulate the actual high-voltage phenomena experienced at the high-power transmitting stations. These phenomena include corona, power dissipation, heat rise, and flashover or flaring for both wet and dry conditions. The data for high-voltage design curves presented in later chapters were developed primarily from flashover/flare and corona inception data measured on generic forms.

Test Frequencies

The primary VLF/LF frequencies currently used by the Navy are 14 kHz to 60 kHz. Some of the LF stations still operate at frequencies up to 150 kHz, but their transmitter power and operating voltages are low. Thus, a realistic test frequency range for the VLF/LF HVTF is from 15 to 60 kHz. In addition, it is desirable to have some high-voltage test capability at 60 Hz as a research tool to compare with VLF/LF measurements to help determine frequency effects.

Test Voltages

The typical maximum operating voltage is 250 kV rms for the Navy's VLF/LF stations. For testing, it is desirable to have a source capable of operation at voltages higher than the required test voltage. This is required in order to obtain consistent measurements. For that reason, the design goal for the Forestport facility was 300 kV rms. However, during construction, there were two reasons for concern that this voltage level might not be adequate. The first involved mounting financial and political pressure to reduce the number of foreign U.S. bases, which pointed to the possibility that larger transmitters would be need to provide coverage and/or smaller antennas would be needed to fit into existing U.S. facilities. Both would require operation at higher voltages. This turned out not to be the case, in part due to improved receiver performance. The second concern was that a 300-kV high-Q source might not adequately simulate high-voltage phenomena at 250 kV. Another concern was that there would not be enough voltage to determine dry flashover voltages for large insulators. However, "it is well known that corona and flashover, especially self-propagating arcs or streamers extending to ground or to other wires of the system, depend upon the energy of the system as well as the voltage" (LaPort, 1952). So, as we discovered at Forestport, it turns out that the high-voltage phenomena, particularly flashover, was more dependent on the transmitter power than the maximum voltage. In addition, since the worst case (lowest flashover voltage) for these insulators is windblown rain, it was not necessary to determine the VLF/LF dry flashover voltage as long as it was above the system operating voltage. Thus, for testing 250-kV system components, a test facility with capability to achieve 300 kV is adequate if it has a powerful transmitter.

The high voltage is generated by a high-Q, high-voltage resonant circuit. The nature of these circuits results in frequency-dependent voltage limits. The voltage limits typically have a maximum at a certain frequency and fall off for higher or lower frequencies. Thus, the first part of the design process is to select the frequency where it is desired to develop the greatest voltage. For VLF/LF testing, the design frequency for maximum voltage was selected to be 30 kHz based on the following rationale.

The U.S. Navy VLF/LF antennas are all electrically small monopoles. Assuming a constant radiated power, there is a strong frequency dependence on voltage for such antennas. The maximum voltage occurs at the lowest operating frequency. There is also a weak frequency dependence (frequency effect) on the breakdown voltage for insulators, which is discussed in later chapters. For a given insulator, this effect leads to slightly lower breakdown voltages at higher frequencies. The Navy's VLF antennas (14 to 30 kHz) are designed for a 250 kV rms maximum operating voltage. Thus, testing for full voltage at 30 kHz ensures operation over the Navy's VLF band. The operating voltages at the new LF stations (30 to 160 kHz) approach 250 kV rms but only at the low end of the band (30 kHz). The operating voltage falls off rapidly with frequency, so the frequency effect does not dominate, and it turns out that 30 kHz is the worst case for LF stations also. Thus, testing at full voltage at 30 kHz satisfies both the VLF and LF requirements and was selected as the design frequency for maximum voltage at the HVTF. Nevertheless, it is desirable to generate voltages approaching that level over the frequency range from 15 to 60 kHz to verify the frequency effect and

adequately test insulators used in the new higher power LF stations; this is the design frequency range for the VLF/LF test facility.

Test Objects

The insulators at VLF/LF stations include base insulator assemblies (BIA), guy insulators (single and combination), halyard insulators (including large grading rings), tower lighting isolation transformers (TLIT), and feed-through bushings. Other high-voltage hardware that requires testing includes wires, cables (including bundles of cables) and protective gaps. In addition, special research tests are sometimes required such as those used to develop design curves for generic hardware (corona rings) or radiation hazard measurements exposing a phantom (dummy simulating a human) to VLF/LF electric fields.

Some of these objects such as the large BIAs and TLITs are large enough that outdoor testing is required. Testing guy and halyard insulators requires suspending them some distance above ground to adequately simulate their actual installation, which also requires an outdoor facility. Thus, a high-voltage test facility requires both indoor and outdoor test areas.

Test Facility Components

A VLF/LF high-voltage test facility contains the following components:

1. RF power source
2. Control console
3. Transmission line connection to the high-voltage circuit
4. Impedance match to the high-voltage circuit
5. Tunable High-Q resonant high-voltage circuit
6. Test cell (inside and outside)
7. Observation area
8. Water spray system
9. Instrumentation (calibrated high-voltage measurement equipment)
10. Workshop, tools, and equipment for constructing test configurations
11. Equipment for moving large, heavy insulator assemblies
12. Storage for large insulators

A brief description of each of these components as they existed at Forestport is provided in the following section. This section will be referred to in the later chapters about measurements. It also provides a guide for constructing a high-voltage test facility. Other references for construction of a high-voltage test facility include Smith (1982), which has a good description of the requirements for a VLF/LF high-voltage test facility and Hylten-Cavallius (1988)**,** which includes information on designing and operating a high-voltage test facility, although primarily directed at power system frequencies.

FORESTPORT TEST FACILITY

Introduction

The facility was located in a rural area on the edge of Adirondacks National Park, near Forestport, NY, about 40 miles north of Rome, NY. The site had a 1200-foot tower that could be configured to transmit VLF or LF and had a long history as a research site for various systems using that frequency range. The site is now closed and demolished. A brief history and background is given in Appendices 5A and 5B. A similar high-voltage test facility has been constructed at the Navy's transmitting station in Dixon, CA.

An aerial view of the Forestport site is shown in Figure 5-1. There are two main areas. The area at the base of the tower on the left side of the picture shows the helix house, which contains the coil for tuning the antenna, with the indoor test cell located adjacent. The transmitter is located in the building on the right side of Figure 5-1 and is connected to the high-voltage test area by an underground transmission line. A drawing of the overall layout of the site is shown in Figure 5-2.

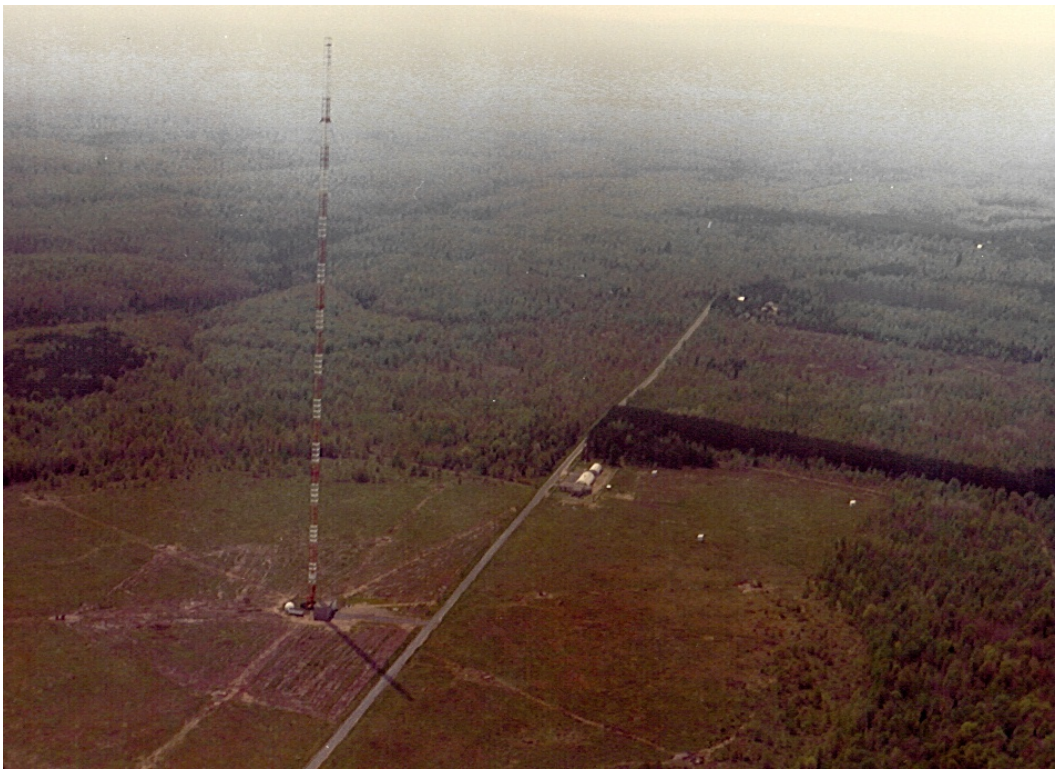

Figure 5-1. Aerial view of Forestport test facility.

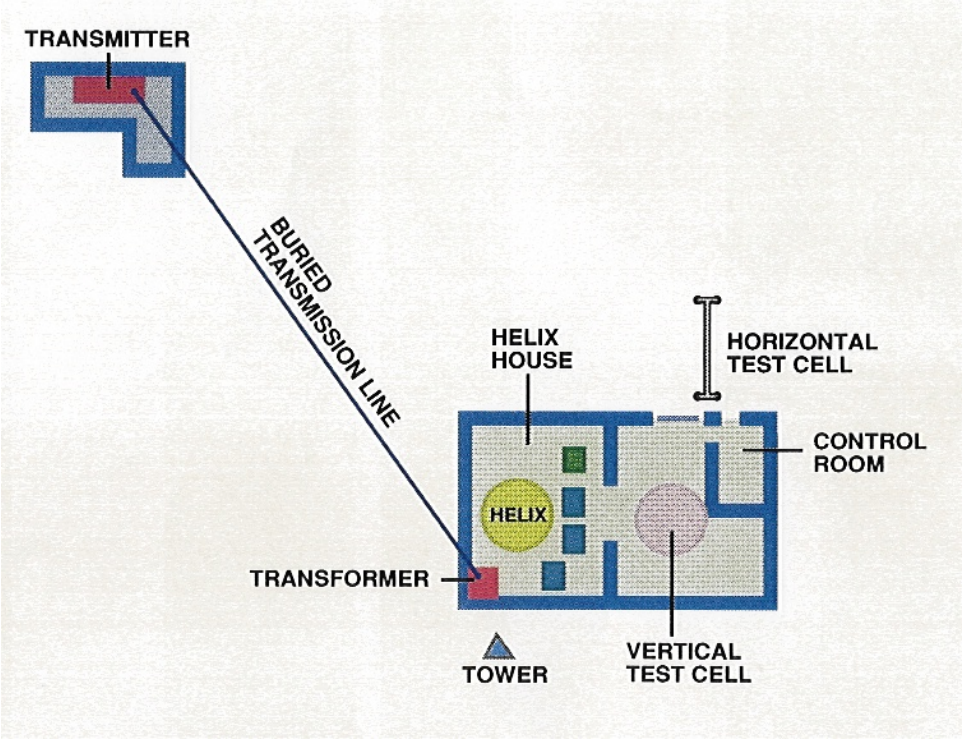

Figure 5-2. Forestport HVTF overall layout.

A drawing of the test area layout is given in Figure 5-3 and a picture given in Figure 5-4. The blacktop area in front of the test cell was used for outdoor testing of the larger insulators. There was a small storage-workshop also located in this area, seen on the right of Figure 5-4.

A drawing showing the detailed layout of the indoor test cell and the helix house is given in Figure 5-5. The helix house contains the components of the high-Q tuned circuit that generates the high voltages. The layout of the helix house shows the location of the matching transformer, the small tuning variometer, the large solenoidal helix, the capacitor stacks, and the voltage divider. The figure also shows the test cell and observation areas. Note that the tower was located immediately next to the helix house. A schematic diagram of the high-voltage circuit is given in Figure 5-6. For VLF transmitting operations, the helix was disconnected from the capacitor stack and instead connected to the tower via a feed-through opening in the wall.

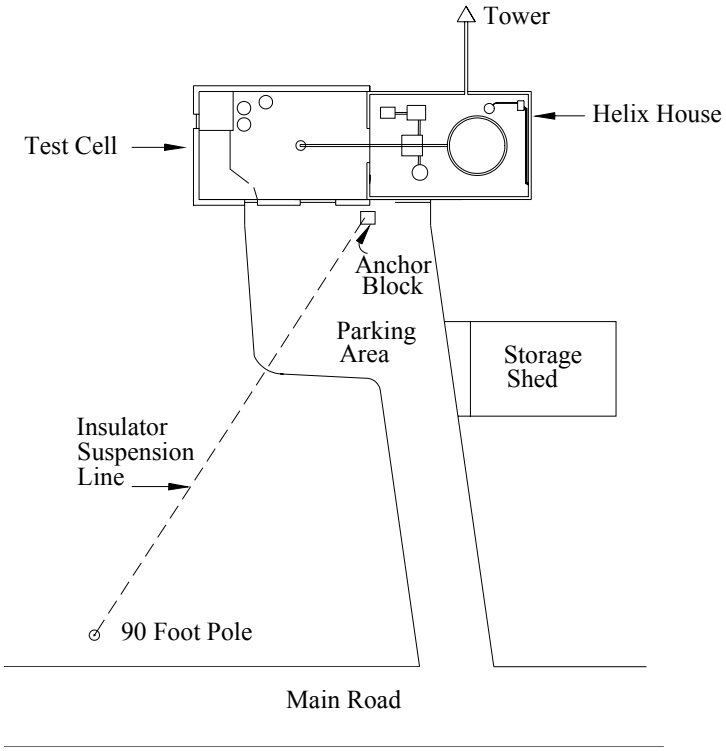

Figure 5-3. Layout of high-voltage test area.

Figure 5-4. High-voltage test area.

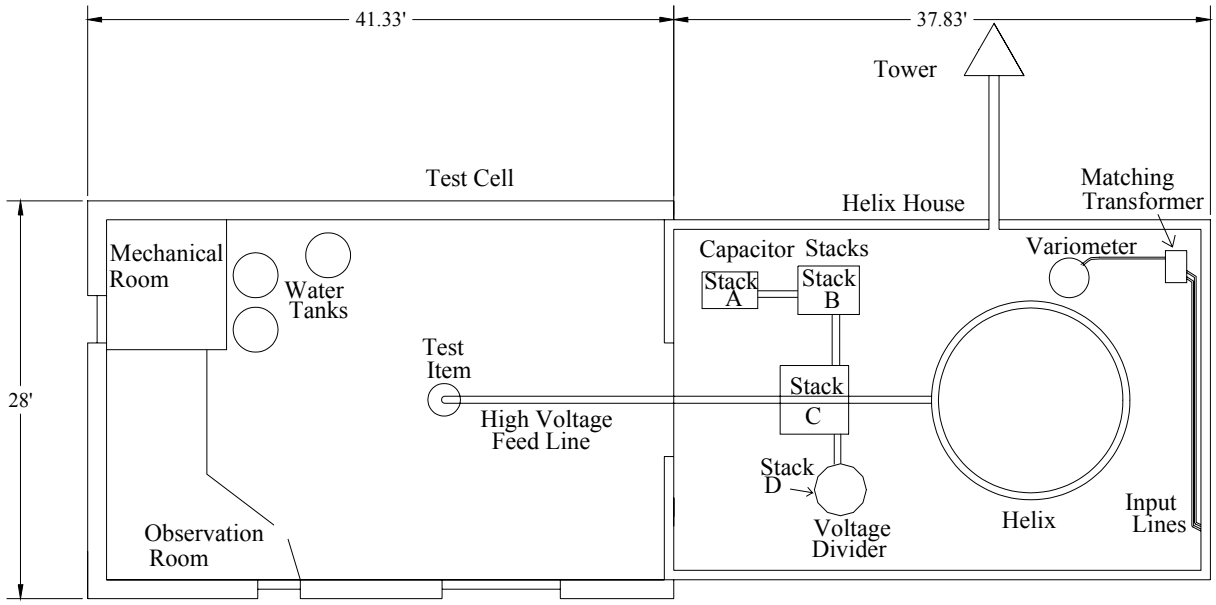

Figure 5-5. Layout of inside test cell and helix house.

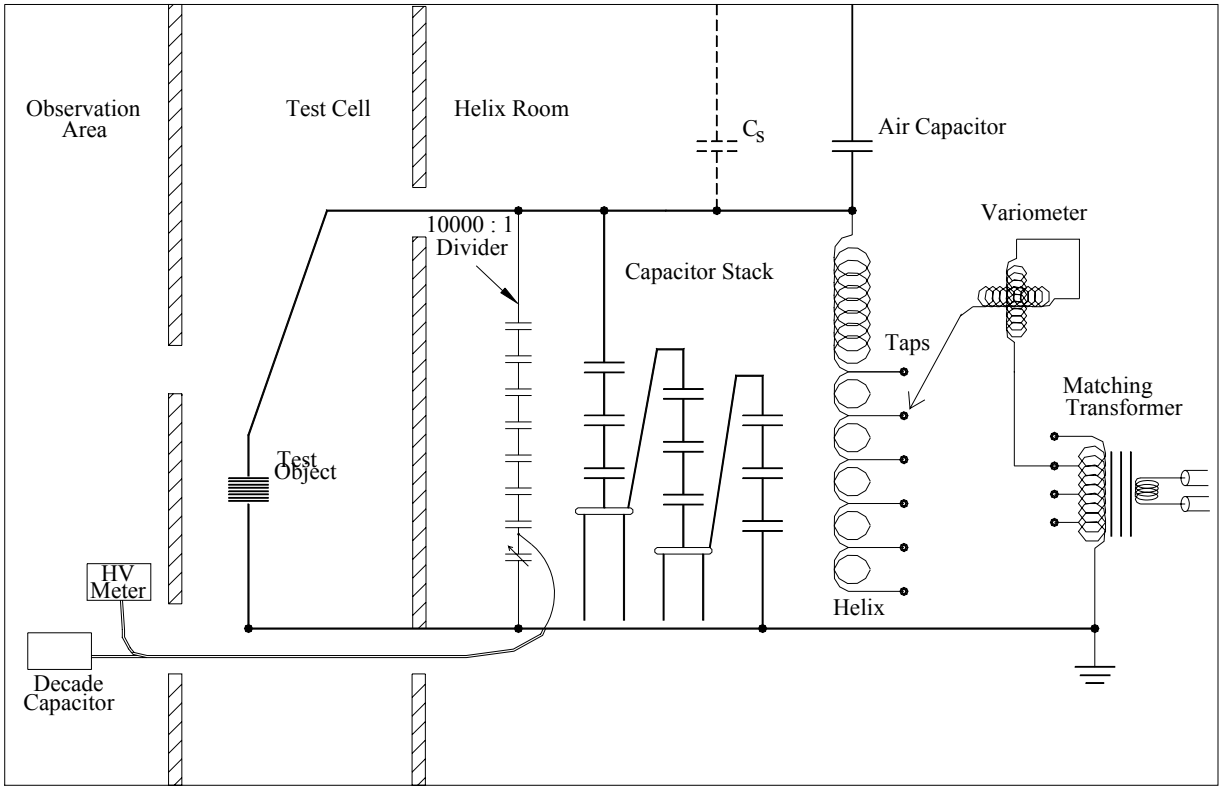

Figure 5-6. Schematic of Forestport high-voltage circuit.

RF Power Source

A transmitter is used as the source of RF power. The high voltage is generated in the resonant circuit formed by the helix and the capacitor stack described later in this section. The resonant frequency of this circuit varies somewhat depending on the test object since the capacitance of the object is in parallel with the capacitor stack. Heating of the circuit components as well as the formation of corona can cause the resonant frequency to drift during the course of a test, requiring constant adjustment to maintain resonance. One technique used to maintain resonance involved small frequency adjustments during a test. Often the tests required measurements at a few widely different frequencies and, as a result, it was necessary to change the tuned circuit and operating frequency several times a day. Because of the frequency change requirement, a wide-band high-power transmitter is the best source of RF power for a VLF/LF high-voltage test facility. Typically, this is an untuned class A, AB, or B power amplifier having a transformer coupled output.

The required transmitter power depends on the Q of the high-voltage circuit and on the test objects and test conditions. Experience at Forestport indicates that under heavy spray-wet conditions or heavy icing conditions, the resistance of an insulator can drop well below 1 million ohms. The lower the resistance, the more power is required to maintain a given voltage. Insulator breakdown tests, especially during wet conditions, involve the sustaining of flares or arcs that dissipate significant amounts of power. All of these effects require increased power from the transmitter. Thus, the transmitter power required for adequate VLF/LF high-voltage testing is well above that needed to reach a given voltage with the high-voltage circuit alone. In addition, for low-power sources, it turns out that the flashover voltage is a function of the available power. This is because a low-power source can limit the current inhibiting flashover. Thus, accurate determination of breakdown voltage requires a powerful transmitter. Our experience indicates that the Forestport 100-kW transmitter was barely adequate to support testing for Navy applications, especially under wet conditions.

The Forestport transmitter (now at Dixon) is the AN/FRA-31, which was constructed by Westinghouse as the commercial prototype for the Omega transmitter (pictured in Figure 5-7). The final amplifier of this transmitter operates class B and has a transformer coupled output. The amplifier has two sides operating push-pull, each containing two Machlett ML-6697 air-cooled tubes, each having a maximum plate dissipation rating of 35 kW. Each side has space available for a third tube. The low-frequency limit for this transmitter corresponds to the Omega requirement of 9 kHz. The high-frequency limit for this transmitter was specified to correspond to the RADUX operating frequency of 40 kHz, although it has been operated at frequencies in excess of 60 kHz. The output power available is less at the low end of the frequency range. The transmitter specifications state that an output power of 14 kW can be achieved from 9 kHz to 14 kHz and full power (100 kW) from 34 kHz to 40 kHz. We have operated this transmitter at nearly full power at frequencies as high as 60 kHz.

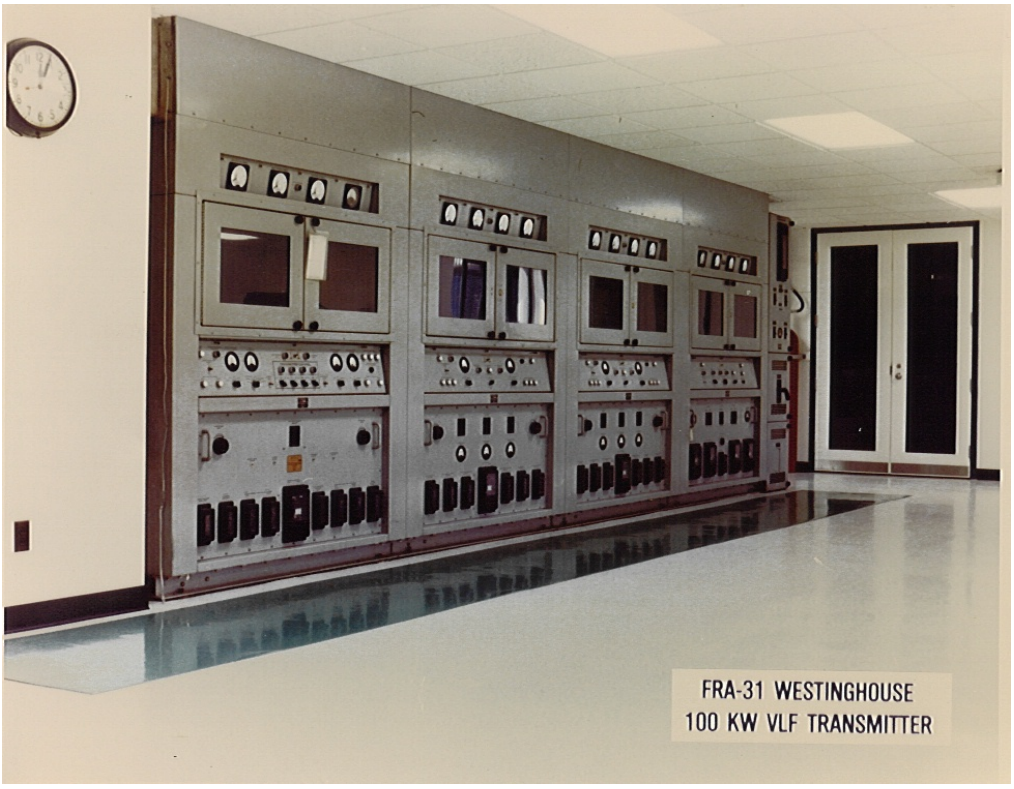

Figure 5-7. Westinghouse AN/FRA-31 100-kW VLF transmitter.

Control Console

The Forestport control console has also been moved to Dixon. At Forestport (and Dixon), the transmitter was located in a separate building some distance away from the antenna with a transmission line connecting the transmitter to the antenna. The control console is located directly in front of the transmitter, so that the operator can monitor transmitter status, record data if necessary, and react accordingly if something goes wrong at the transmit end.

One of the requirements for high-voltage testing, particularly flashover tests, is that the RF voltage increase (ramp) at a specified rate. The control console has the capability of providing these rates. Initially this function was provided by the internal capability of a Hewlett-Packard frequency synthesizer, but later a computer-based controller was developed that does this automatically.

An intercom provides communications from the test and observation area to the control console. In this way, the tests are in effect controlled from the observation area, but there is an operator near to the transmitter.

One essential requirement for a high-voltage test facility is a safety switch. This switch is located in the observation space and provides the test director positive control over the transmitter. The safety switch interfaces with the control console and prevents the RF from being activated unless the safety switch is off. The safety switch is activated when necessary to protect the observers, the test object, or the high-voltage circuit. The test director uses the safety switch as a precaution to deactivate the transmitter whenever personnel enter the test area to make observations or adjustments. The safety switches also allow the test director to cut off the transmitter quickly in the event that some high-voltage phenomena occurs that might damage the test object or the high-voltage

circuit. It is important that the safety switch operates reliably and should always be tested prior to a test sequence.

Transmission Line

A transmission line is required for connecting the power source (transmitter) to the high-voltage circuit. At Forestport, the transmitter was located in a building about 1/4 mile from the helix house and connected by two buried 5/8-inch coax lines in parallel; together these made up a 100-ohm balanced transmission line.

The requirement on the transmission line is that it can carry a specified amount of power. It is important to remember that the tuning and matching conditions may not be optimum and, depending on the load, there may be a high SWR on the line. Almost any type of transmission line can be used. For example, the original installation at Forestport made use of an elevated 600-ohm, balanced open-air transmission line. However, now the Navy favors using a large coaxial line that can be buried or placed in a trench. A 4-inch coaxial line will be used at Dixon. Coaxial lines are usually pressurized with dry air to avoid moisture entering the line.

Impedance Match

The resistance of the high-voltage circuit at resonance depends on frequency. The high-voltage circuit used at the HVTF has a resistance on the order of 1 ohm over the frequency range. Thus, an impedance matching device is required to couple power from the 100-ohm transmission line to the lower impedance of the high-voltage circuit. This is typically done using a ferrite core transformer. These transformers have many taps to accommodate the wide range of impedance encountered over the operating frequency range. The transformer is usually located in the helix house.

Forestport had (Dixon has) the capability to do both high-voltage testing or transmit using the adjacent antenna. At Forestport, a single transformer located in the helix house provided the impedance matching for both of these functions. The primary of the transformer was connected to the center conductor of the two 50-ohm coaxial cables. One side of the secondary was connected to the copper ground of the helix house, and the other side was connected to the tuning inductor. The Forestport transformer was custom made for the AN-FRA-31 and is pictured on the left side of Figure 7-7 (Chapter 7).

The resistance of the antenna or high-voltage circuit increases with operating frequency. VLF antenna resistance values are usually much less than 1 ohm, but at LF they are typically about 1 ohm. The transformer must match the resistance over the entire frequency range. The usual solution is to use a transformer tapped to accommodate the expected range of impedance. The tap is selected that most nearly matches the impedance for the operating frequency. The Forestport transformer had taps for matching resistances between 0.47 ohms and 1.16 ohms to the 100-ohm balanced line.

Forestport was (Dixon is) capable of being quickly reconfigured between transmitting from the antenna and high-voltage testing. For high-voltage testing, the top of the inductor is disconnected from the antenna and connected to the top of a capacitor stack. The capacitors can withstand higher voltages than the Forestport or Dixon antennas. The circuit characteristics for high-voltage testing are similar to those for transmitting except that the resistance is usually less, and often the transformer tap must be changed when switching between transmitting and testing.

VLF/LF antennas are designed such that the resistance of the antenna does not significantly change with time, even during inclement weather. Thus, while transmitting, transformer tap changes are not

normally required. One of the differences between high-voltage testing and normal transmitter operation is that for high-voltage testing the load resistance can change considerably during a single test. For example, once corona forms on the test object, the extra power dissipated by the corona increases the effective series circuit resistance considerably. Similarly, the effective resistance increases dramatically during flashover, flaring, and when the insulators are wet.

For maximum test effectiveness, it is desirable to be able to change the impedance matching to track resistance changes. However, this is not possible with a fixed-tapped transformer. The approach used to deal with this problem at Forestport was to set the transformer one or two tap settings higher than the circuit resistance with no corona or water losses. A trial run was then made and if the transmitter could not deliver enough power into the circuit, the tests would be discontinued and the transformer tap adjusted. This process is inconvenient, but effective.

Another method to match the load impedance to the transmission line is a coupling coil used in place of the transformer. The coupling coil is placed in shunt between the transmission line and the series tuned circuit. The impedance of this circuit at the transmission line is the parallel combination of the resonant circuit and the coupling coil. This impedance is effectively the inverse of the series resonant circuit. This inversion converts the series resonance response to a parallel resonance response. For this circuit, the resistance seen by the transmission line at resonance is given by:

$$R_T = \frac{X_c^2}{R_a}$$

where R_T is the resistance seen by the transmission line,
X_c is the reactance of the coupling coil at resonance, and
R_a is the antenna or high-voltage circuit resistance.

Making the coupling coil a variable inductor, such as a variometer, allows real-time adjustment of the impedance match to the transmission line and hence can accommodate variable circuit resistance. This is the preferred approach for impedance matching. However, it is difficult to know how to adjust the impedance without some form of instrumentation. At Forestport, a power meter was used to measure the circuit resistance at the secondary of the matching transformer. This enables accurate adjustment of coupling coil impedance. This power meter was also used for corona power measurements (Chapter 7).

High-Voltage Tuned Circuit

A high-Q resonant circuit consisting of an inductor and capacitor is used to develop the high voltage. This inductor is large high-Q air wound solenoidal coil, termed a helix. The capacitor consists of a series parallel combination of high-Q capacitors known as the capacitor stack. Both of these elements must withstand the full design voltage. The resonant circuit is tuned using a spherical variometer or by changing frequency. Each of these elements is described below.

Variometer

Two techniques were used at Forestport to maintain the high-voltage circuit resonance. It was easy to change the frequency of the transmitter to generate maximum voltage because the transmitter is broadband. The test objects were connected across the capacitor stack and the resonant frequency changed slightly when a new test object was connected. When testing a new object, the first step is to find the resonant frequency. During the test, as the components of the high-voltage circuit heated up and/or corona formed, the resonant frequency would drift. One method of compensating for this is to

change the frequency to track the drift. These frequency changes amounted to only a few percent, which is not enough to change the phenomena being measured for the test object.

During a set of measurements designed to determine the power dissipated by wet insulators, it was discovered that changing the frequency decreased the accuracy of the power meter. Therefore, for tests requiring accurate power dissipation measurements, a small spherical variometer (as pictured in Figure 5-8) was connected in the circuit. The variometer could be remotely controlled from the observation area. Changing the inductance of the variometer compensates for the changes in the high-voltage circuit and keeps the circuit resonant at the initial operating frequency. The variometer has a small tuning range, but it is able to maintain resonance for most tests.

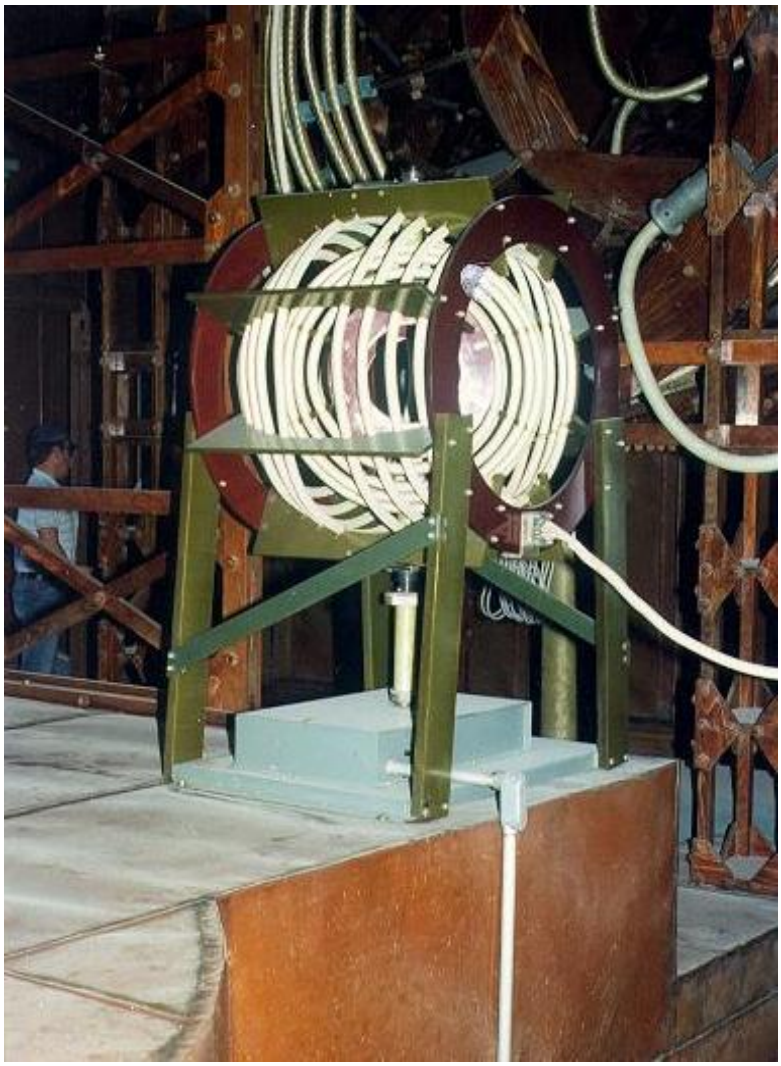

Figure 5-8. Spherical variometer at Forestport.

Helix

Structure

The inductor for the Forestport high-voltage circuit is a large air-wound solenoidal coil (helix). The helix structure was approximately 12 feet in diameter by 18 feet tall. The coil had a total of 72 turns of 7/8-inch Litz wire wound on a cylindrical fiberglass (G-10) form approximately 12 feet long. The G-10 form is mounted on 48-inch-tall porcelain insulators so that the bottom turn was approximately 5 feet above ground. The turns were double wound, with 3-inch axial and radial pitches. The radius of the outer turns was 72 inches, and the radius of the inner turns was 69 inches. The top six turns of Litz wire are single wound with the same turn-to-turn spacing. The topmost turn is fabricated from 6-inch diameter aluminum tube, which serves as a corona ring to provide adequate electric field grading. The helix is pictured in Figures 5-9 and 5-10.

The self-inductance of the Forestport helix was measured to be 14,600 μH. The self-resonant frequency of the helix was 76 kHz. The helix is tapped to allow configurations with less inductance. A tapping tree was used with the turns available in groups of 32, 16, 8, 8, 4, 2, 1, and 1 turns from the top. A pictographic representation of the helix configuration is given in Figure 5-11.

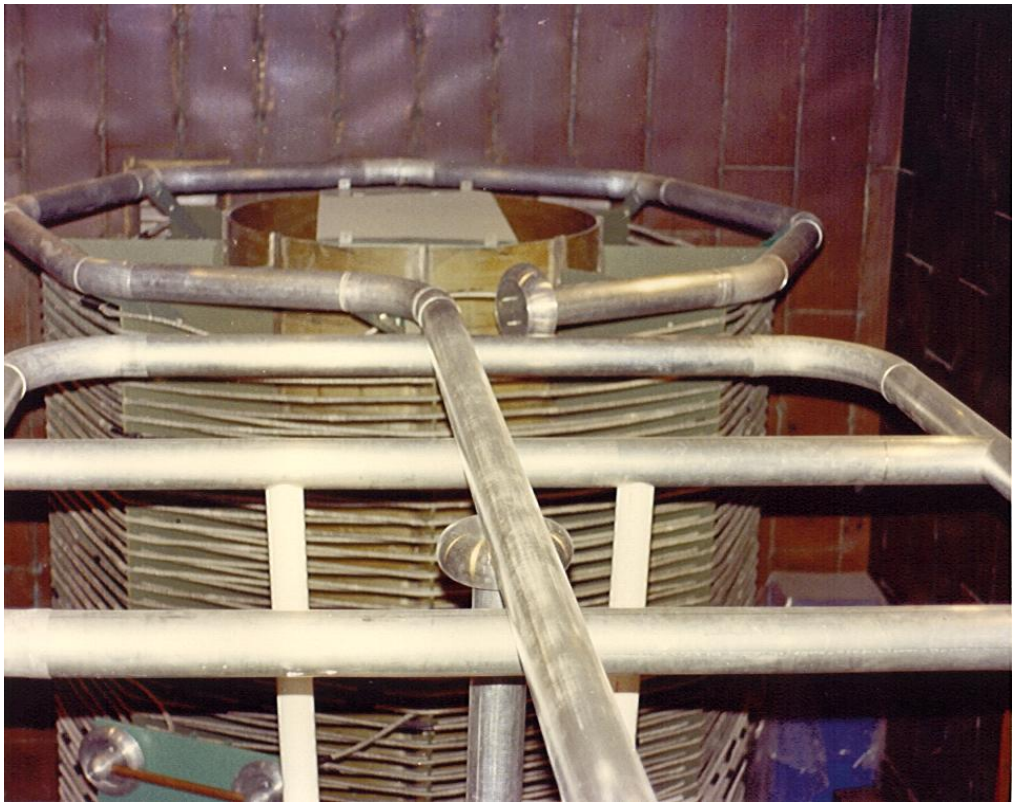

Figure 5-9. Top of Forestport helix.

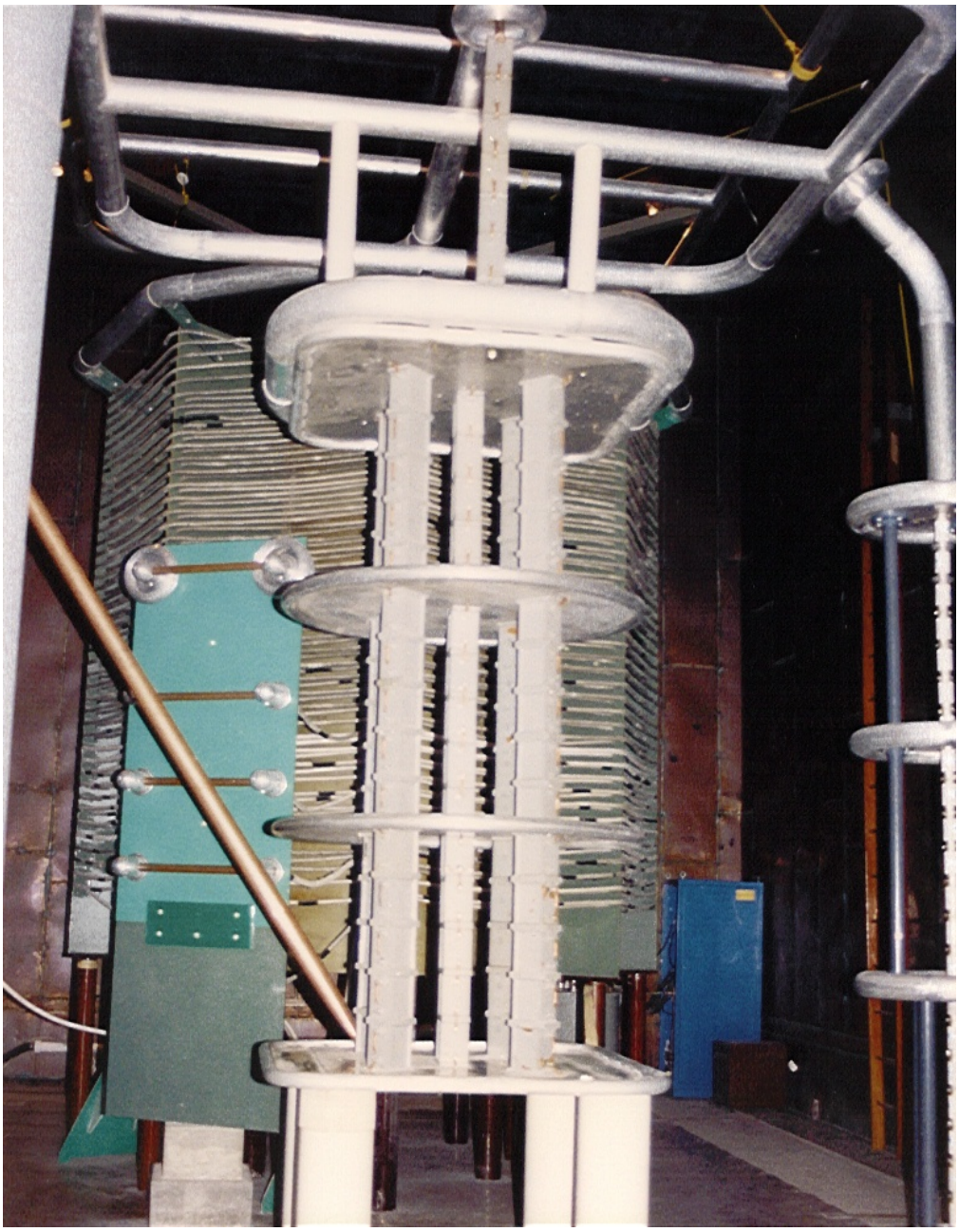

Figure 5-10. Forestport high-voltage tuned circuit.

Current Limit (Litz Cable)

The use of Litz cable in the coil enables the construction of a very high-Q inductor. Litz cable is composed of a large number of fine strands of insulated wire. The strands are woven in such a way that each strand occupies all possible positions within the cable with nearly equal probability. The flux linkages are the same for every strand, and therefore the inductance of each strand is the same, which results in equal current flowing in each strand. The use of Litz wire reduces the losses due to

both skin effect and proximity effect so that the resistance of the cable at RF is nearly the same as its DC resistance. Litz wire is used to make low-loss coils for applications at frequencies up to 500 kHz. At VLF/LF, carefully constructed Litz wire coils can be made to have Q on the order of 3500.

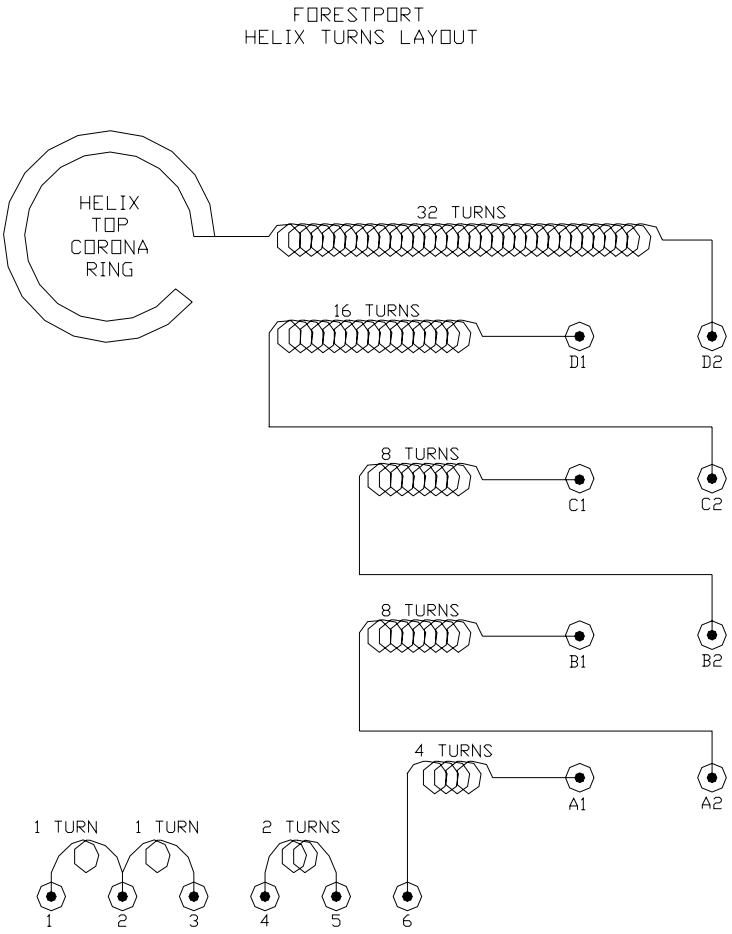

Figure 5-11. Forestport helix configuration.

Current-carrying capability is a critical design parameter for the high-Q circuit. The Litz cable used for the Forestport helix was 7/8-inches in diameter and consisted of 5,672 strands of #36 copper wire (28,360 circular mills). A rule of thumb for the current carrying-capability of Litz wire used by early designers of the Navy's VLF/LF system is that it can be safely operated with 1 amp of current for each 1000 circular mills of copper. According to that rule, the safe current operational limit for the Forestport helix would be about 28 amps. Restricting the current to this level at Forestport would have severely reduced the maximum voltages that could be reached, and we exceeded this limit. It turns out that the rule of thumb is very conservative; a better method for estimating the current limit is discussed below.

The fundamental limit for Litz wire is temperature. A varnish-like coating is used to insulate the individual wires. If the insulating coating gets hot enough to melt, the individual wires come in contact and the cable is no longer Litz wire. When this happens, the current concentrates on the outside, heating the copper even more, and thermal runaway develops, which can completely destroy

the cable. The rule of 1000 circular mills/amp does not take into account many of the critical factors that affect the current-carrying capability of Litz wire. This rule significantly underestimates the current rating, especially for smaller diameter cables.

A design technique has been developed to more accurately determine the rating of Litz cable itself, which includes the effects of frequency, strand diameter, cable diameter, shape of the winding, and the temperature rise allowable. This design technique is described in Appendix 5C. The temperature rise is taken into account by using an allowable dissipation of ¼ watt per square inch. It turns out that this is also conservative, since it leads to a temperature rise usually less than 5 to 10° C. Nevertheless, this technique gives higher ratings than the 1000 circular mills/amp, especially for the smaller cables, and also explicitly accounts for the effect of the various parameters.

The design procedure uses the concept of a breakpoint frequency that depends on the construction of the Litz wire and the shape of the coil. Below the breakpoint frequency, the long-term current heating limit for the Litz wire is given by

$$I_{\max} = 600 \cdot d \cdot (n \cdot d_0)^{1/2}$$

where $I_{\max}$ is the long-term current limit due to heating in amps rms,
d is the diameter of the individual Litz strands in inches,
n is the number of individual Litz strands, and
d_0 is the diameter of the copper portion of the Litz cable in inches.

The breakpoint frequency for the Forestport helix and Litz wire construction is 82.6 kHz. For frequencies below the breakpoint frequency, the long-term current limit calculated using the above equation is 211 amps.

Our experience with Litz wire inductors indicates that the highest temperature occurs at the cable ends or terminations. The type of termination, known as “elephant’s foot,” is common at the Navy’s VLF/LF installations. This type of termination operates at much higher temperatures than the cable. If a termination gets hot enough, the heat can propagate to the cable, melt the insulation, and destroy the cable. Thus, for installations with elephant’s feet, the maximum long-term current is limited by temperature rise of the elephant’s feet, which is less than that of the Litz wire by itself.

There is a better termination used at some Navy VLF/LF sites. These terminations have the individual bundles of Litz wire separated and soldered to a copper tab. The tabs are connected onto the perimeter of a circular connector. This type of connection operates with little or no increase in temperature over that of the Litz cable by itself. For installations with this type of connector, the Litz wire itself usually determines the current limit. However, unusual heating can arise where the Litz cable has sharp turns, and each installation must be carefully heat tested after construction to be sure that the temperature limit is not exceeded. The excessive heating at the terminations and sharp bends may have influenced the original designers of the VLF/LF system to base their design on a very conservative rule of thumb. It is important to keep in mind that the temperature rise in a cable or connection depends on the power input minus the power removed by conduction, convection, and radiation. Careful design to minimize thermal power input and maximize thermal power removal can increase the current carrying capacity of coils and other elements.

The Forestport coil contains elephant’s feet terminations and splices. Thus, even though all operations at Forestport were below the breakpoint frequency of 82.6 kHz, the long-term rating for the coil will be somewhat less than the 211 amps given above due to heating at the end connections and splices in the Litz wire. The actual long-term rating for any helix must be determined experimentally by determining the actual temperature rise. At Forestport, we often operated for

extended periods of time (hours) at currents around 100 amps without excessive heating of the Litz wire or the connections. Thus, the long-term current rating of the Forestport helix coil is greater than 100 amps, possibly around 150 amps. This is true of the Dixon helix as well since it uses the Litz wire salvaged from the Forestport helix.

Voltage Limit

Electrical breakdown occurs when the surface electric fields on an electrode exceed the critical level for breakdown. The electric field is greatest at the locations of the maximum voltage in the circuit, which is at the top of the helix and capacitor stack. If breakdown occurs, it can damage the organic insulating materials in the Litz wire and helix frame. Consequently, it is important to operate without breakdown occurring on or close to the high-voltage circuit components that are vulnerable to damage. There are many locations where breakdown could occur, and each one implies a different limit for the maximum operating voltage.

One set of voltage limits involves corona formation on the surface of the Litz wires, corona rings, and feed line at or near the top of the helix and capacitor stack. The Forestport helix is mounted vertically and fed at the bottom. The voltage on each turn increases approximately linearly with height. The top turn has the greatest voltage and surface field. The field is greatest there because it has the highest voltage, and because it is not shielded by any turns above it. For these reasons, the top turn of a high-voltage helix is usually constructed from metal tubing having a significantly larger diameter than the Litz wire. This greatly increases the withstand voltage of the top turn (tubing) and reduces the surface field on the next few turns of Litz wire by partially shielding them.

When the top turns of Litz wire are adequately shielded, the top corona ring limits the breakdown voltage for the helix. In this case, breakdown occurs first from the corona ring at the top of the coil, limiting the voltage. The breakdown voltage depends on the minor diameter of the ring and the distance from it to the nearest grounded object (walls or ceiling). Because it is made from metal, the corona ring is not damaged when corona, flashover, or flare occurs and, in effect, the corona ring protects the rest of the coil.

The maximum turn-to-turn voltage can become the limiting parameter depending on the spacing (pitch) of the coil. This is undesirable for two reasons. First, if corona or flashover occurs between the turns, it damages the Litz. Second, if the coil is turn-to-turn voltage limited, the maximum voltage must be reduced when the number of turns is reduced (for example by changing the tap). However, a coil can usually be designed, using one or more layers to have enough pitch such that turn-to turn voltage is not the limiting parameter.

The voltage limit for the bottom turn of the inductor can also become the limit depending on the operating voltage of the circuit and its distance to ground. This is undesirable for the same reasons mentioned above, and consequently the bottom turn is usually somewhat elevated. The elevation height of the bottom turn is one of the important design parameters for a helix.

For a well-designed helix, the top corona ring should limit the voltage. Changing taps in a way that eliminates turns from the bottom of the helix reduces the inductance and moves the bottom turn farther from the ground. For this case, as long as the helix is not turn-to-turn limited, the top corona ring limits the voltage, and the rating for the helix remains fixed for different configurations. The voltage rating for a well-designed helix is essentially independent of the tap configuration (i.e., inductance), and this was the case for the Forestport inductor.

At Forestport, the top corona ring of the helix and the bus work connecting the helix to the capacitor stack and to the test cell set the voltage limit for the helix. This limit depended somewhat on environmental conditions, but the helix could usually operate at more than 300 kV rms after a few conditioning flashovers to burn off moisture, dust, and insects.

KVA Rating

The reactive power rating for a given component is equal to the product of the maximum voltage times the maximum current. The Forestport inductor has a short-term reactive power rating of 200 amps times 300 kV or 60 MVA, independent of the number of turns. The long-term rating is estimated to be 150 amps times 300 kV or 45 MVA.

Capacitor Stack

The high-Q inductance of the helix is resonated by a capacitor, which forms the resonant circuit. This capacitor is formed by a series-parallel combination of smaller capacitors, known as a stack, because capacitors are only available in units smaller than needed for the HVTF requirement. The design of the capacitor stack configuration requires consideration of the interrelationship of several parameters, including the capacitance of the individual capacitors, their voltage and current ratings, the total value of capacitance needed to resonate the helix at the desired frequency, and the voltage rating of the helix. Stack design is described briefly below and is treated more thoroughly in Appendix 5D.

The Forestport stack was moved without modification to Dixon. The capacitor units used in the stack are oil-filled capacitors manufactured by Plastic Capacitors Inc., model BNZ 540-143A. These individual capacitors have 0.0145 μF capacitance and ratings of 5.4 kV rms and 12 amps rms. At Forestport, these capacitors were routinely operated at voltages of nearly 6 kV, with currents sometimes exceeding 20 amps. However, when operated at these levels for very long, individual capacitors sometimes failed spectacularly by exploding. The nominal VA rating of each individual capacitor is 64.8 kVA, but the extended VA rating approaches 120 kVA, at least for short periods of time.

Structure

The capacitor stack at Forestport (Dixon) consists of three separate sections labeled (A), (B), and (C). These sections were connected in series with A being the low-voltage section, grounded at one end, (B) being connected between the top of (A) and the bottom of the high-voltage section (C). The location of each of the three capacitor stack sections at Forestport is shown in Figure 5-5.

Each of the sections consisted of three layers. Each layer had five stacks of individual capacitors in parallel. Each layer of the low-voltage section (A) had the capacitors stacked six high. Grading plates separated the layers to minimize the effect of stray capacitance on the voltage distribution. (The grading plates for the high-voltage section can be seen in Figure 5-10). Each layer of 5 x 6 capacitors has 5/6 the capacitance of an individual capacitor, with six times the voltage rating and five times the current rating. The bottom of this section sits on the floor and is connected to ground.

Section (B), the middle section, is configured the same as the bottom section (A), in that it has three layers of capacitors, five in parallel by six high, separated by grading plates. The bottom of this section is insulated above ground using porcelain post insulators that are approximately 20 inches tall.

The high-voltage section (C), pictured in Figure 5-10, consists of three layers. In this case, each layer is only five capacitors high. The bottom of this stack is elevated above ground by porcelain station post insulators that are approximately 40 inches long.

Voltage Limit

Normal Configuration

The "normal" capacitor stack configuration was designed to achieve maximum voltage at 30 kHz. This configuration has all three sections (A, B, and C) connected in series. The voltage limit for the stack is equal to the combined voltage limits of the individual capacitors. In this case, it is equal to the individual capacitor voltage limit multiplied by the height of the stack (i.e., number of capacitors in series). The total height of the "normal" configuration is 51 capacitors, which has a nominal rating of 221 kV rms and an extended rating of 306 kV. The total capacitance of this configuration, including estimated strays is 1.922 nF, which resonates the full helix at approximately 30 kHz rms.

Low-Frequency Configurations

There are some practical ways to quickly change the capacitor stack to change the operating frequency. It is simple to short out one or both of the two lower voltage sections in order to lower the resonant frequency. This increases the capacitance but reduces the voltage rating of the stack. With only the bottom section shorted out, the calculated operating frequency is approximately 28 kHz and the voltage limit is about 180 kV. When the bottom two sections were shorted, the calculated operating frequency is approximately 20 kHz and the voltage limit is about 90 kV. For both of these cases, the actual test frequency is reduced because of test object capacitance.

High-Frequency Configuration

The high-frequency stack configuration, used to achieve frequencies above 30 kHz, consisted of 1 x 59 capacitors. For this configuration, four of the five parallel stacks were disconnected and a 1 x 8 capacitor extension was added to the top (top of Figure 5-10). The capacitance for this configuration, including strays, is approximately 0.625 nF, which resonated at frequencies around 60 kHz, using only a portion of the helix. The 59-capacitor-high stack has a nominal voltage rating greater than the normal configuration. However, at the higher frequencies, the dissipation limit of the capacitors, evidenced by the spectacular failures previously mentioned, limited the voltage to 200 kV or less.

An air capacitor was constructed at Forestport in an attempt to exceed the dissipation limit of the oil-filled capacitors. The idea was to use an adjustable air capacitor in place of the capacitor stack for operation at the higher frequencies. The air capacitor consisted of a grounded aluminum frame suspended from the ceiling above the helix and the capacitor stacks. A sketch of this frame is shown in Figure 5-12, and it can be seen in the top of Figure 5-10, suspended by the yellow polypropylene rope. This capacitance could be adjusted somewhat by moving the frame up or down (Smith, 1981). W.W. Brown (1923) used a similar technique.

Several problems occurred when the air capacitor was the only capacitor in the circuit. These problems included difficulties with tuning for the desired frequency, maintaining the tuned condition, and inadequate reproduction of high-voltage phenomena, especially flashover. These problems, which are discussed below, were all the result of not having enough capacitance in the circuit. As a consequence, the air capacitor was not useful for measurements at Forestport and is not implemented at Dixon.

One problem results from the fact that corona on the test object changes the capacitance. If the circuit has too little capacitance, the additional corona capacitance causes the resonant frequency to fluctuate. This makes it difficult or impossible to maintain resonance, which has the effect of changing the high-voltage phenomena, often making it difficult to obtain flashover. A related problem affecting the high-voltage phenomena is due to the fact that the initial current pulses for breakdown have very fast rise times, and the charge for these pulses must come from the capacitors. If the capacitance is too small, this current is limited and normal flashover does not occur. The energy dissipated by a flashover also comes from the capacitors. Thus, for a given flashover voltage, the maximum current, heating, sound level, and damage are determined by the total circuit capacitance.

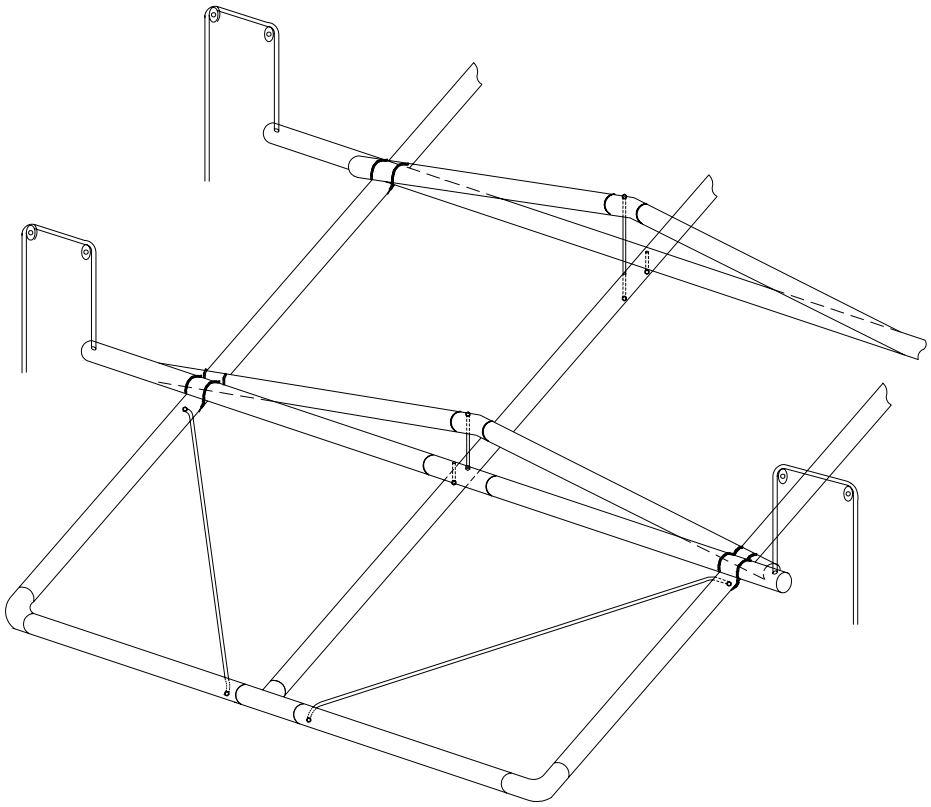

Figure 5-12. Adjustable air capacitor at Forestport.

Experience with the air capacitor at Forestport indicates that there is a minimum capacitance required for adequately reproducing the high-voltage phenomena, especially flashover. The magnitude of the required capacitance is probably a function of the length of the gap. The Navy's VLF/LF antennas have relatively large values of capacitance varying from a few nF up to a few hundred nF (Hansen, 1990). A true simulation of the expected high-voltage phenomena for these antennas would require similar capacitance, but this is not practical for a high-voltage test facility. The capacitance of the normal configuration was 1.922 nF, including strays, and this seemed to provide adequate simulation of high-voltage phenomena for most cases. The problems described above were sometimes experienced when testing larger insulators using the high-frequency configuration, which had a total capacitance of only about 0.746 nF, including strays.

Current Limit

The current limit for the stack is equal to the current limit of the individual capacitors multiplied by the number of capacitors in parallel. The corresponding voltage limit is calculated by multiplying the maximum allowable capacitor stack current plus the current in the shunt capacitance by the inductive reactance of the helix at resonance. This limit is frequency dependent since the reactance varies with frequency. The normal stack configuration and the two low-frequency stack configurations have five capacitors in parallel. Ignoring shunt current, the maximum current for this case has a nominal value of 60 amps rms and an extended value of 100 amps rms.

KVA Rating

An important design parameter for the capacitor stack is its overall VA rating because this determines the number of capacitors required. Each individual capacitor has a fixed voltage and current rating. The VA rating of a series-parallel combination of capacitors with equal ratings is equal to the sum of their VA ratings. Thus, the required VA rating determines the number of capacitors in the stack.

For example, by putting two capacitors in parallel, the capacitance doubles, as does the current rating, but the voltage rating remains unchanged. Thus, the VA rating is doubled. For two capacitors in series, the capacitance is halved but the voltage rating doubles, while the current rating remains unchanged. Again the VA rating is doubled. This relationship can be generalized to apply to combinations of capacitors having the same voltage and current ratings.

The three sections of the capacitor stack are connected in series for typical operation. This results in a composite capacitor consisting of five parallel arrays of 51 capacitors for a total of 255 capacitors. The capacitance of this configuration is 1.422 nF, and it has a nominal VA rating of

$$(255)(77.22 \text{ kVA}) = 19.7 \text{ MVA}$$

and an extended rating of

$$(255)(120 \text{ kVA}) = 30.6 \text{ MVA}.$$

This is less than the helix VA rating of 45 MVA nominal and 60 MVA extended. Thus, as will be seen in the next section, the capacitor stack was the overall limiting factor for the high-voltage circuit at Forestport.

Operating Limits

The overall voltage limit is determined by the lowest of the limiting values for each of the circuit elements. There are four limits to consider. The first two are the overall voltage limits of the helix and the capacitor stack. The other two limits are voltages that occur for the maximum allowable currents of the capacitor stack and the helix respectively. The helix voltage limit is approximately 300 kV rms, independent of tap setting and capacitor distribution. The extended voltage rating for the capacitor stack in the normal configuration is 306 kV. The extended rating for the low-frequency configuration with the bottom section of the capacitor stack shorted out is 190 kV rms, and it is 90 kV rms when both lower sections are shorted out.

The maximum voltages as determined by the current limits are also frequency dependent. These limits are calculated as the limit for the total helix current times its reactance at resonance. The helix current limit is nominally 150 amps. The extended current limit is 100 amps for the normal stack configuration and 20 amps for the high-frequency configuration. The leakage currents must be added

to these values to obtain the total current through the inductor. These voltage limits are summarized in Table 5-1.

Table 5-1. Forestport tuned circuit voltage limits at resonance.

Limiting Parameter	Parameter Value Forestport	Calculated Voltage Limit	Voltage Limit at Forestport
Helix Voltage	300 kV	300 kV	300 kV
Helix Current	150 amps	$V = 150 \cdot X_l$	Freq dependent
Capacitor Voltage	6 kV/cap	$V = 6 \cdot m$ *	306 kV
Capacitor Current	20 amps/cap	$V = 20 \cdot n \cdot X_l$ **	Freq dependent

* *m* = stack height number of capacitors

** *n* = number of capacitors in parallel

The operating voltage limits for the Forestport high-voltage tuned circuit have been calculated and are shown in Figure 5-13. The values shown in the figure closely correspond to the actual limits observed at Forestport. The figure plots maximum voltage capability as a function of resonant frequency for the three different helix configurations and three different capacitor configurations used at Forestport. The helix configurations are labeled Max *L* (all 72 turns), Mid *L* (64 turns) and Min *L* (32 turns). The description for the capacitor stack configurations and the associated designation used in the figure are given in Table 5-2.

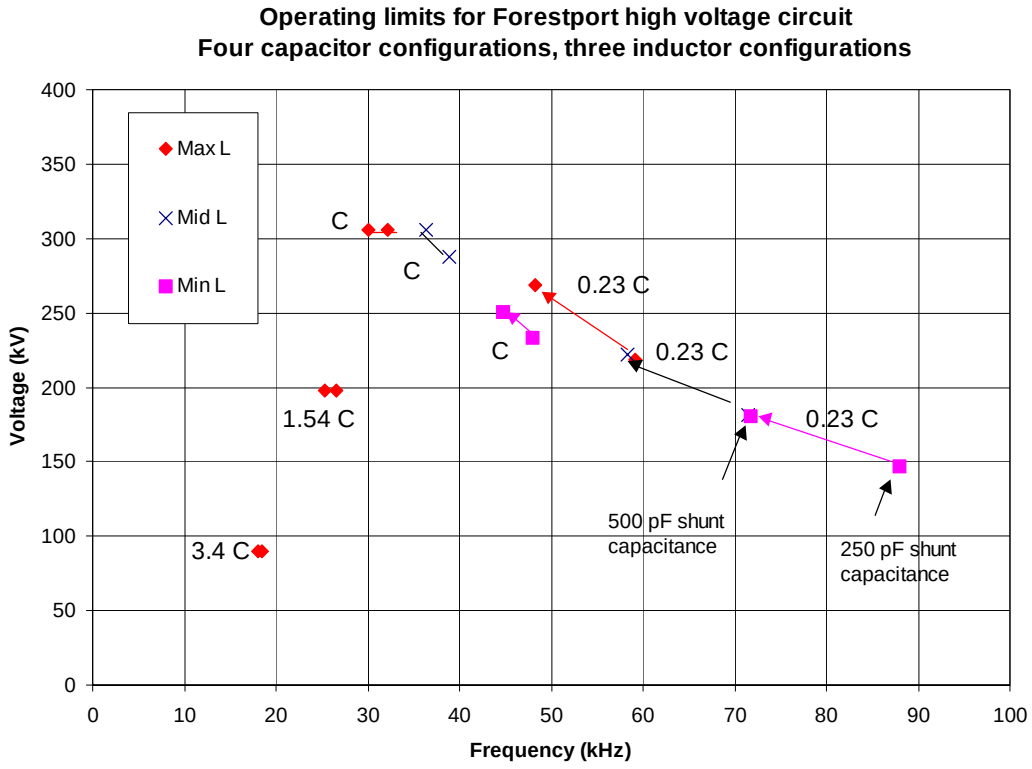

Figure 5-13. Forestport operating voltage limits.

Table 5-2. Capacitor stack configuration labels.

Designation	Stack Configuration
C	The normal 5 x 51 stack,
1.54 C	The 5 x 33 configuration; section A shorted,
3.4 C	The 5 x 15 configuration; sections A and B shorted, and
0.23C	The 1 x 59 high-frequency stack configuration.

The voltage limits given in Figure 5-13 were calculated for shunt capacitance values of 250 pF and 500 pF. The smaller value is an estimate of the stray capacitance of the high-voltage circuit alone, and the larger value is an estimate for a typical indoor test setup. For each configuration of the helix and stack, Figure 5-13 shows two values of resonant frequency and a voltage limit corresponding to the two values of shunt capacitance. The two values are connected by a line, which includes an arrowhead when the separation allows. The arrowhead indicates the direction of increasing shunt capacitance. The high-frequency end of these lines corresponds to the lower value of shunt capacitance (250 pF). The low-frequency (higher voltage) end of the line corresponds to the larger value of shunt capacitance (500 pF). For example, the end points for the 0.23 C – Min L curve on the right-hand side of the figure have the end points labeled. This curve shows the reduction in resonance for the larger value of shunt capacitance. The other curves show similar but smaller shifts. The stray capacitance values for the points on the ends of the other curves are the same but not labeled.

The resonant frequency shifts somewhat depending on the amount of stray capacitance. The stray and test object capacitance will normally be between 250 pF and 500 pF and so the resonant frequency for any test setup should fall between the frequencies shown in the figure. For indoor tests, the observed resonant frequency agreed well with the calculations. However, when configured for outdoor testing, the resonant frequency was often lower than that calculated for 500 pF, indicating the added stray capacitance of the bus-work carrying the high-voltage outside was more than 500 pF. As previously mentioned, the presence of the stray capacitance increases the capacitor current-limited voltage, and this effect has been included in the results shown in Figure 5-13.

Figure 5-13 shows that the maximum operating voltage is 300 kV rms and it occurs at approximately 30 kHz for configuration C with Max L and Mid L. The maximum operating voltage falls off above and below that frequency. For a given capacitor configuration, the capacitor current-limited voltage is inversely proportional to frequency because the capacitive reactance is inversely proportional to frequency. This limit is lower than the capacitor voltage limit at higher frequencies. As the frequency decreases this limit increases until it equals the capacitor voltage limit. Below that frequency the capacitor voltage limit is lower. The normal configuration for the capacitor stack was designed to resonate the full helix (Max L) at 30 kHz and to have its voltage rating at 30 kHz equal to that of the helix (Appendix 5D). Thus, at a frequency near 30 kHz (depending on the amount of shunt capacitance), the capacitor voltage limit and current-limited voltage are equal and nearly equal to the helix voltage limit.

The voltage limits fall off above 30 kHz because of the capacitor current-limited voltage, which is inversely proportional to frequency. The reduced voltage limit below 30 kHz is due to the capacitor voltage limit of the stack, which is reduced because the stack is reconfigured to have more capacitance and it has a lower voltage rating.

Note that for the capacitor current-limited cases (above 33 kHz), increasing the shunt capacitance increases the voltage limit. The main reason for this is that the resonant frequency decreases. However, it is also partly because the shunt capacitance carries some of the current, reducing the current flowing in the capacitor stack. The amount that shunt capacitance increases the voltage depends on the capacitance of the stack. It is greatest when the stack capacitance is a minimum (0.23C). For capacitor voltage-limited cases (frequencies below 33 kHz), the overall voltage limit is not affected by shunt capacitance.

Test Cell

Inside

The Forestport test cell was 38 feet long by 25 feet wide by 25 feet high, including the space for the observation and control area and the water tanks. There was a large doorway between the helix house containing the high-voltage circuit and the test cell. The top of the high-voltage circuit has a suspended bus made of 6-inch-diameter aluminum pipe, which brings the high voltage through the door into the test cell. The high-voltage bus has a universal joint suspended from an insulator at a location just inside the test cell. A sliding trombone section of bus hangs down into the test cell from the universal joint enabling connection of the high-voltage circuit to inside test objects. Figure 5-14 is a picture of a typical indoor test setup showing the feed with the universal joint and the trombone section.

Many high-voltage phenomena are only visible in the dark. Thus, the test cell and helix house are designed without windows to allow testing in the dark even during the daytime. Both the helix house and the test cell had overhead lighting in zones that could be individually controlled from the observation room.

The test cell had two rolling overhead electric winches that were used to move or suspend test objects.

The test cell floor had a drain to collect the water during wet tests.

At Forestport, a heater was required in order to maintain an inside temperature above freezing. In addition, there were plenty of electric power outlets for tools and instrumentation.

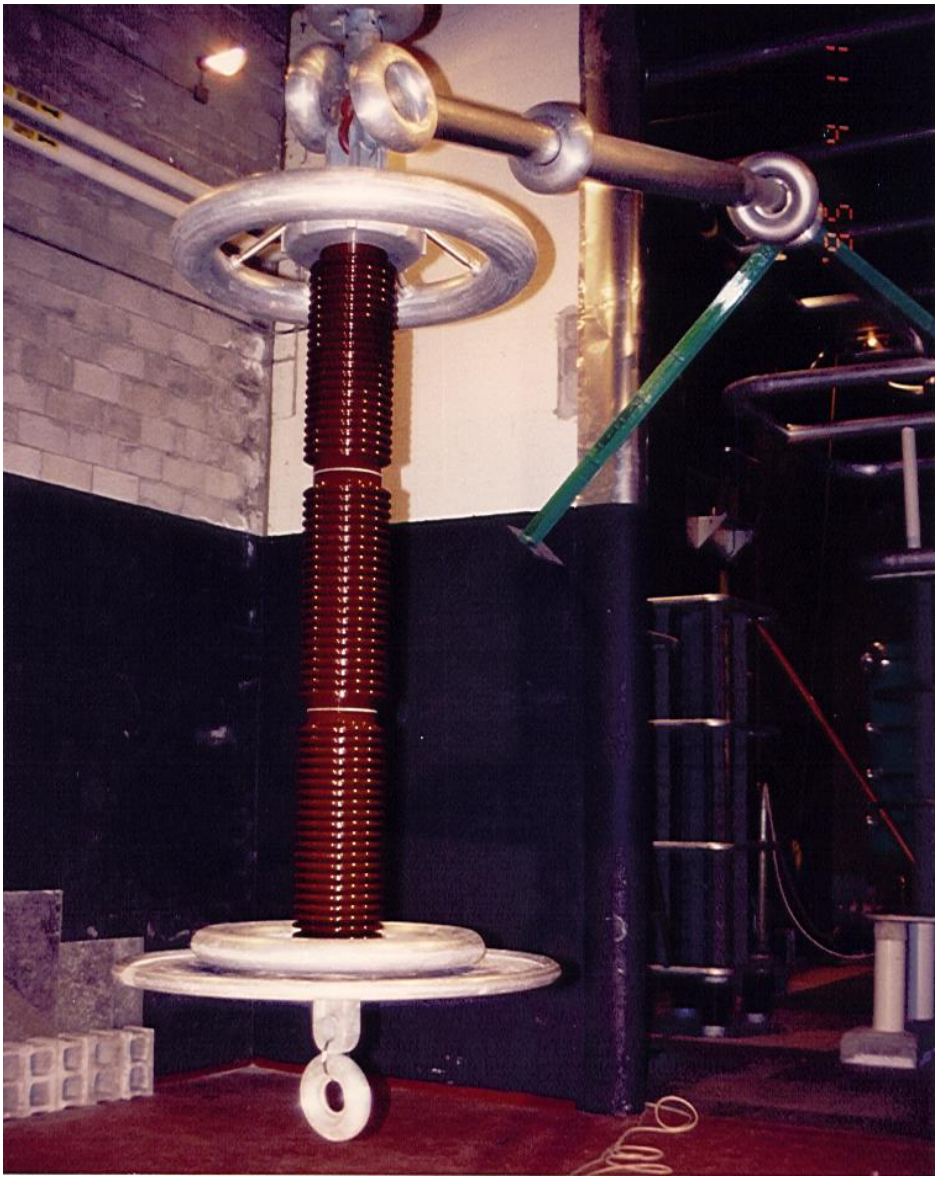

Figure 5-14. Forestport inside test cell.

Outside

The outside tests were primarily centered on the cement pad that was just outside the roll-up door (Figures 5-3 and 5-4). This door allows the extension of the bus work outside for testing of objects too large to fit into the test cell. Large test objects were often placed on this pad and connected by an extension of the bus through the roll-up door. Figure 5-15 shows the inside configuration typically used to feed outside test objects. The bus extension on the right of the figure feeds through the large roll-up door to the outside test pad. Figure 5-16 shows a typical outdoor test configuration.

Figure 5-15. Forestport high-voltage feed from helix house.

The outside test area included the capability to suspend insulators and cables. This was accomplished in several ways. The insulators and cables were usually attached to an anchor block, which was placed outside just next to the roll-up door. There was a 90-foot utility pole located about 100 feet away from the anchor block, such that a line between the anchor block and the pole diagonally crossed the outside test pad near its center (Figure 5-17). A cable or insulator could be suspended from the pole at a location approximately near the center of the outside test pad. Another method used when a nearly horizontal configuration was needed was to suspend the test object on a cable between the utility pole and the top of the helix house as shown in Figure 5-18.

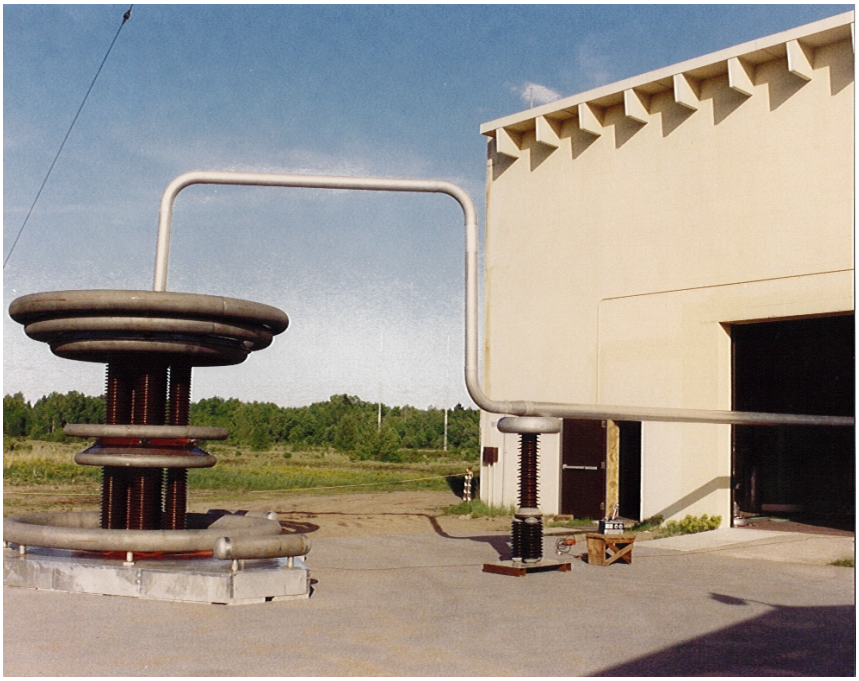

Figure 5-16. Forestport outside test setup.

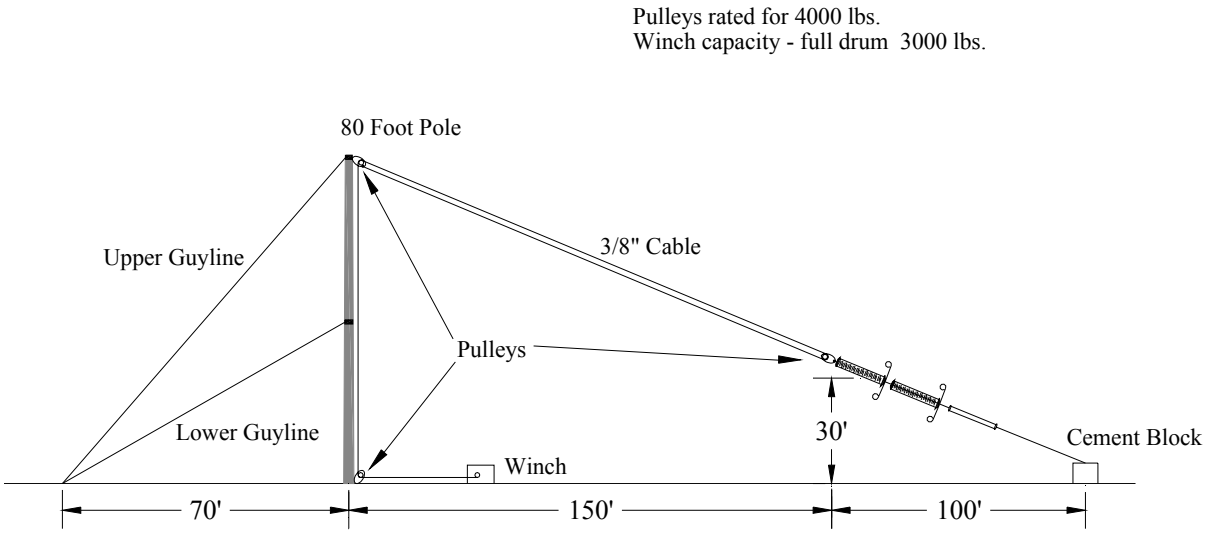

Figure 5-17. Forestport outside, hoisting pole and winch.

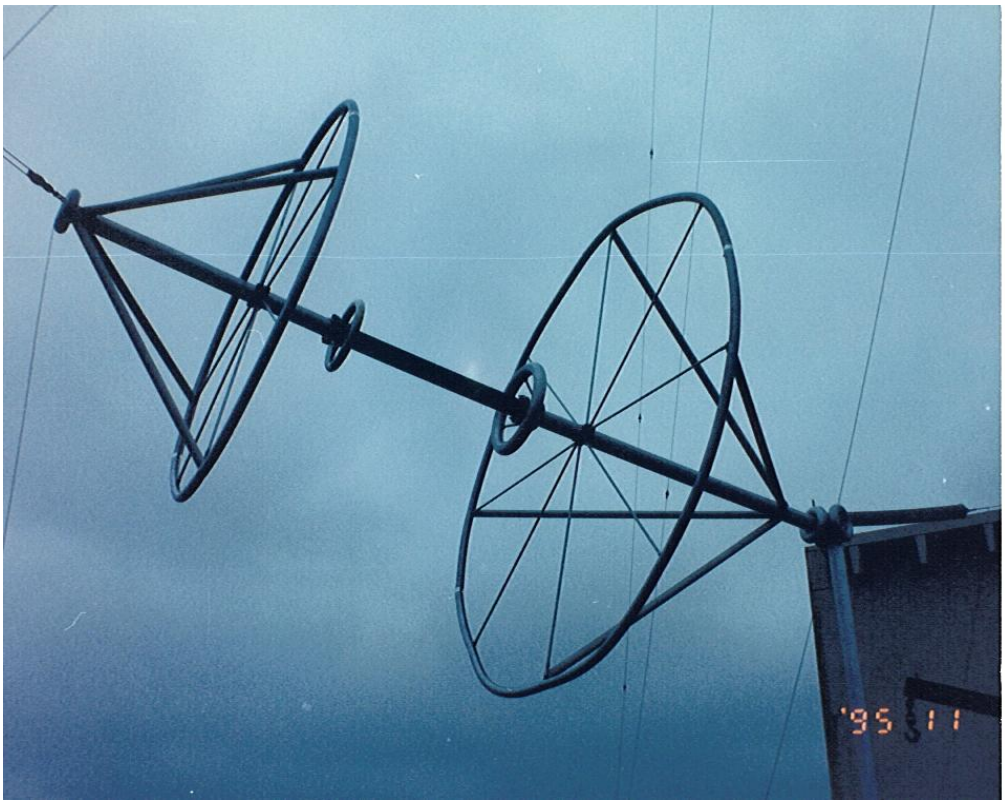

Figure 5-18. Cutler failsafe insulator mock-up suspended from top of helix house.

Observation Area

Inside

The inside observation area at Forestport consisted of a 10-foot-wide screened area across the end of the test cell. The outside door to the test cell enters into the observation area to ensure that someone does not inadvertently walk into the energized high-voltage area.

The wall separating the observation area from the test cell was formed by a 2-by-4 frame covered with a fine copper mesh on each side. The wall had two rows of open spaces (windows) for observation. One row of the windows was at a height convenient for standing observers and the other at a height convenient for sitting observers. There is one door between the observation area and the test cell. The safety switch was mounted next to this door, and during a test the safety director activated this switch whenever someone went into the test cell area. With a few rare exceptions, everyone was located inside the observation area during tests. The control and observation area is pictured in Figure 5-19.

Control of the transmitter was maintained through voice commands to the transmitter operator by the use of an intercom. The intercom speaker was mounted in the observation area and operated such that the channel from the observation area to the transmitter was normally open. The transmitter operator had to manually operate a switch in order to communicate back to the observation area. Sometimes the test required recording transmitter parameters, which the transmitter operator reported over the intercom. The weather station readout was located at the transmitter console, and that data, including barometric pressure, was passed to the test cell area via the intercom.

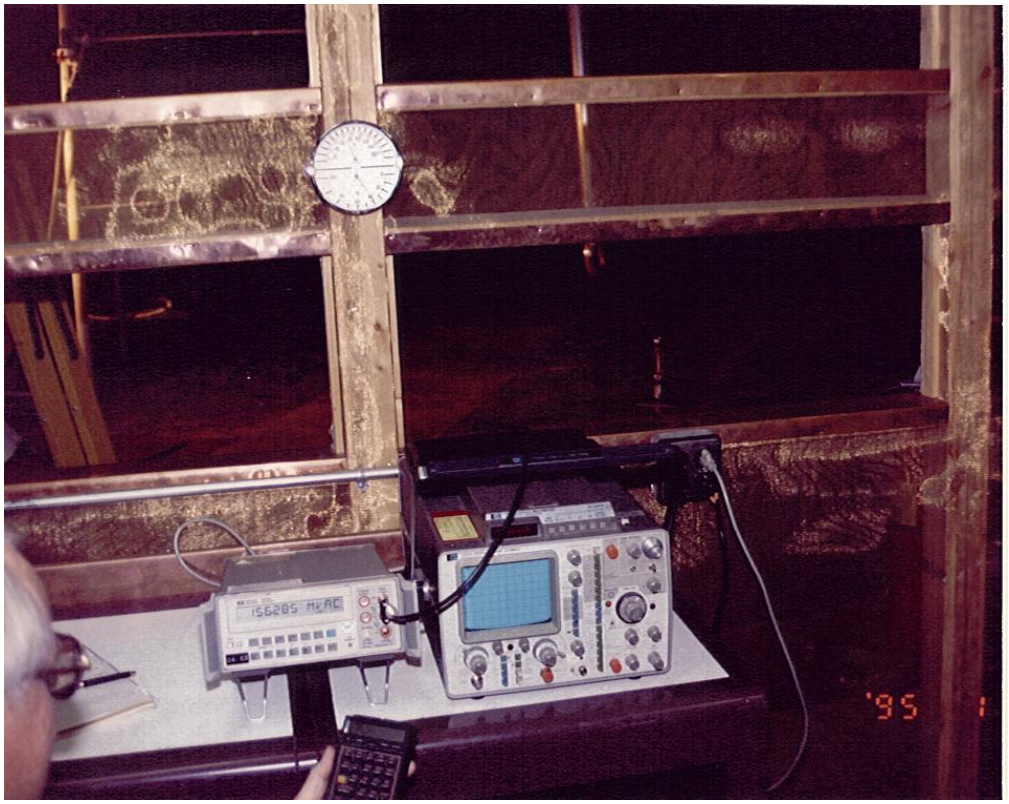

Figure 5-19. Inside test cell observation area.

The observation area also contained the instrumentation for measuring the high voltage and frequency. Additionally, there was storage for tools and other instruments for observing temperature, humidity, cameras, binoculars, etc. There were built-in tables for mounting instruments and for recording data. A small, red table lamp was used to enable the data recorder to see the data without the observers losing their night vision.

Usually, the only variable recorded during testing was the high voltage. The voltmeter had an LED display that could be read in the dark. Normally, one person was given the job of observing and calling out the voltmeter readings for the data recorder to log.

Outside

Most of the outside tests were done at night to facilitate observation of the high-voltage phenomena. Visual observation of certain high-voltage phenomena, such as corona onset and extinction, require it to be quite dark. Thus, testing outside required the outside lighting be turned off. At Forestport we could turn out all the lights except for the tower strobe lights. The strobe lights were sometimes irritating but did not materially affect observations.

The main outside observation area was located in the storage shed that was along the driveway coming into the test area (see Figures 5-3 and 5-4). For outside testing, the high-voltage meter, intercom, and safety switch were all moved into this shed, as well as the thermometers, humidity meters, and other items used to measure test observables. A portable table was used to accommodate the person recording the data.

The shed had a two-car garage door, which was opened for testing. When operating at high voltage, most of the observers would be located inside the shed, and observations were generally made while sitting or standing in the plane of the garage door. The common practice was to cordon off an area around the test object using PVC stands and plastic ribbon. Sometimes, it was required to have observers outside of the shed. In this case, the usual procedure was to position the observers prior to energizing the circuit. Except for a few rare occasions, the observers would remain outside the cordoned area.

Water Spray System

The withstand voltage of high-voltage hardware used in outdoor applications is usually the most limited during wind-driven rain conditions. For that reason, the spray-wet testing, simulating wind-driven rain, is probably the best single test to define outdoor high-voltage hardware performance. Consequently, a high-voltage test facility needs to have a water spray system.

The water spray system at Forestport was designed to provide test conditions as defined by the IEEE Std 4-1995, "Standard Techniques for High-voltage Testing" and ANSI C29.1-1988, "Test Methods for Electrical Power Insulators." Both of these standards are for 60-Hz testing. The standards indicate that the conventional test procedure in the U.S. is to use water having a resistivity of 178 $\pm$ 27 Ohm-m. This particular number is a holdover from earlier standards in which resistivity was specified to be 7000 Ohm-inches. The rainfall rate for the standard test procedure in the U.S. is specified to fall at an angle of approximately 45^{o} with a vertical component of 5.0 ± 0.5 mm/minute, which corresponds to 11.8 ±1.2 inches/hour. The water temperature for the spray-wet test is required to be at ambient temperature $\pm 15^{o}$ C.

The Forestport test facility was located in a remote area without water utilities, so a well was used to obtain water. The well water was considerably more conductive than called for in the ANSI specifications. Consequently, a deionization system was installed to produce water of the prescribed conductivity.

Three 700-gallon fiberglass tanks were used to process and store the water. Originally, the water was pumped from the well into the first tank through a commercial filter and deionization system supplied by Culligan. This tank was used solely for deionized water. From there the deionized water was pumped into tanks two and three where it was mixed with well water that had been filtered but not deionized. The mixing ratio was determined experimentally to produce water with the conductivity of 0.02 meg-ohm-cm (200 ohm-meters). The Culligan system included two meters for monitoring the conductivity of the water.

The capacity of the two water tanks was 1400 gallons, which provided 7 hours of testing. The well did not have a large flow rate, and it took several days to fill the tanks. To get around this, the Forestport system included a 500-gallon tank fed by the floor drain to recover the water. During extended periods of wet testing, the recovered water was recycled through the filter and deionization system back into tank number one. From there the water was pumped into the empty water tank and mixed with well water while testing was ongoing. Thus, a continuous supply of water could be provided for extended periods of time. A diagram of the water system is shown in Figure 5-20. Note that the 700-gallon tanks were located in the test cell area so that the stored water would equalize to the ambient temperature of the test cell.

The sprayers were specially made using a copper pipe extension with a brass nozzle attached on the end. The nozzles were specially made to meet the specifications defined in the IEEE and ANSI standards. These nozzles can be adjusted to provide the specified rainfall rate. These spray nozzles

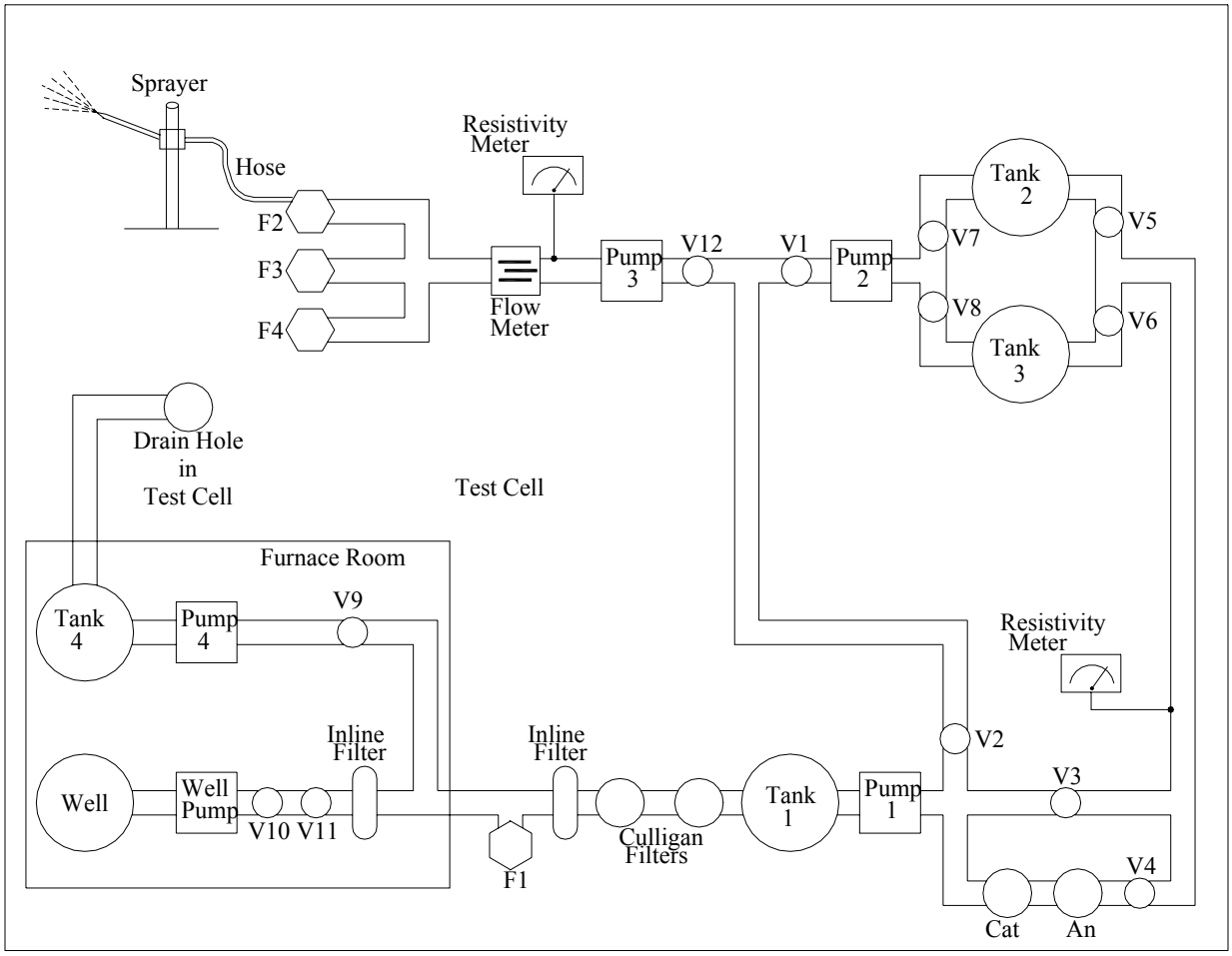

Figure 5-20. Water spray system.

were mounted on a vertical stand made from PVC pipe. The attachment allowed the nozzles to be easily pointed, moved up and down, and the take off angle adjusted. Figure 5-21 illustrates one of the spray nozzles. The pipe shown holding the nozzle is made from PVC pipe. However, we later discovered it was necessary to make this pipe out of copper because the PVC pipes would melt during testing at high voltage when full of water but not flowing. The nozzles at the end were made from brass because during testing they would often go into corona and plastic nozzles melted or burned. The hoses from the pump were attached to the nozzles near the vertical PVC pipe stand. Standard garden hoses were used but care was taken to keep the hoses from touching the ground near the base of the PVC stand to avoid arcing between the hose and ground, which will burn through the hose and quickly ruin it.

Outdoor testing usually involves larger test objects and/or suspended test objects. For these tests, the water has to be sprayed farther and higher. Often there is some wind during outside tests, which blows the spray around. The nozzles specified in the IEEE and ANSI standards are not very effective for throwing water very far or against even a light wind. We found that standard adjustable garden hose nozzles made of brass were much more effective for delivering the specified rainfall rate to the required locations. These nozzles can be located considerably farther away than the standard nozzles and still provide the appropriate water spray. In addition, they are easier to adjust than the standard nozzles and can be adjusted to simulate a driving rain much better than the standard nozzles. Driving

rain is a realistic worst case for the kind of operating conditions experienced at a Navy VLF/LF transmitting station. These nozzles were especially useful for testing insulators installed at operational stations, and we eventually adopted them as our standard.

Figure 5-21. Water spray nozzle.

Instrumentation

High-voltage

Sources

In addition to the VLF/LF high-voltage circuit described above, there were other useful sources of high voltage used at Forestport:

25-kV DC Hipot
150-kV, 60-Hz high-voltage source
300-kV lightning pulser

The DC high-potential test set (Hipot) was useful for checking small insulators for leakage. The 60-Hz high-voltage source was useful for making measurements to compare with other 60-Hz measurements. The lightning pulser was used for simulated lightning measurements.

VLF/LF Divider

The magnitude of the high voltage is the primary observable necessary to determine the performance of high-voltage insulators. The VLF/LF high voltage was measured using a 10,000:1 voltage divider that was constructed on site using a tall stack of capacitors. The divider, shown schematically in Figure 5-6, reduces the maximum high voltage of approximately 300 kV to 30 volts. The capacitors were located in the helix house near the helix and the tuning capacitor stack (stack D in Figure 5-5). One consequence resulting from this location of the voltage divider was that whenever the configuration of the helix or the tuning capacitor stack changed, the stray capacitance to the divider changed, and it was necessary to recalibrate the divider. Since the configuration of the either the helix or the stack, or both, was changed for each frequency, this had the effect of making the division ratio frequency dependent. This was corrected using the adjustable decade capacitor shown in Figure 5-6 and discussed in the section below on divider calibration.

The top of the divider consisted of a stack similar to one of the sections of the tuning capacitor but using much smaller capacitors. It consisted of three sections each having seven 50-pF Jennings model CHFD-50 capacitors rated at 60 kV each. Parallel plates separate these sections to control the stray capacitance and keep a more nearly uniform voltage distribution across the individual capacitors in the stack. The upper part of the divider can be seen on the far right of Figure 5-10. The bottom capacitor in the stack was a Jennings CVFP 1500-355 variable capacitor with a voltage rating of 35 kV that can be adjusted from 500 to 1500 pF. The base of the divider is constructed of an aluminum tube and circular plate that sits on the copper floor at ground. A braided strap was attached to the base and welded to the copper floor (see Figure 5-22).

The divided high-voltage signal was picked up across the bottom capacitor (the variable) in the divider stack, with one side being ground. This signal was routed via a cable trench to the observation space using a double-shielded 50-Ohm coaxial cable where it was connected to the input of the high-voltage meter located in the observation space. The meter used was a Hewlett Packard HP-8903A audio analyzer, which has an LED output for both the voltage and the frequency and can be easily read in the dark.

The voltage divider by itself was designed to have a division ratio of from 210 to 630, considerably less than the factor of 10,000 desired. However, the capacitance of the coax and the meter are in parallel across the bottom capacitor in the stack, which increases the division ratio. The variable capacitor at the bottom of the divider was adjusted so that the division ratio at the end of the coax in the observation area is a little less than 10,000:1. An additional adjustable decade capacitor was placed across the input to the audio analyzer to enable adjustment of the overall division ratio. The calibration procedure, described below, amounts to adjusting this decade capacitor such that the division ratio between the high voltage and that displayed on the HP-9803A was exactly 10,000:1.

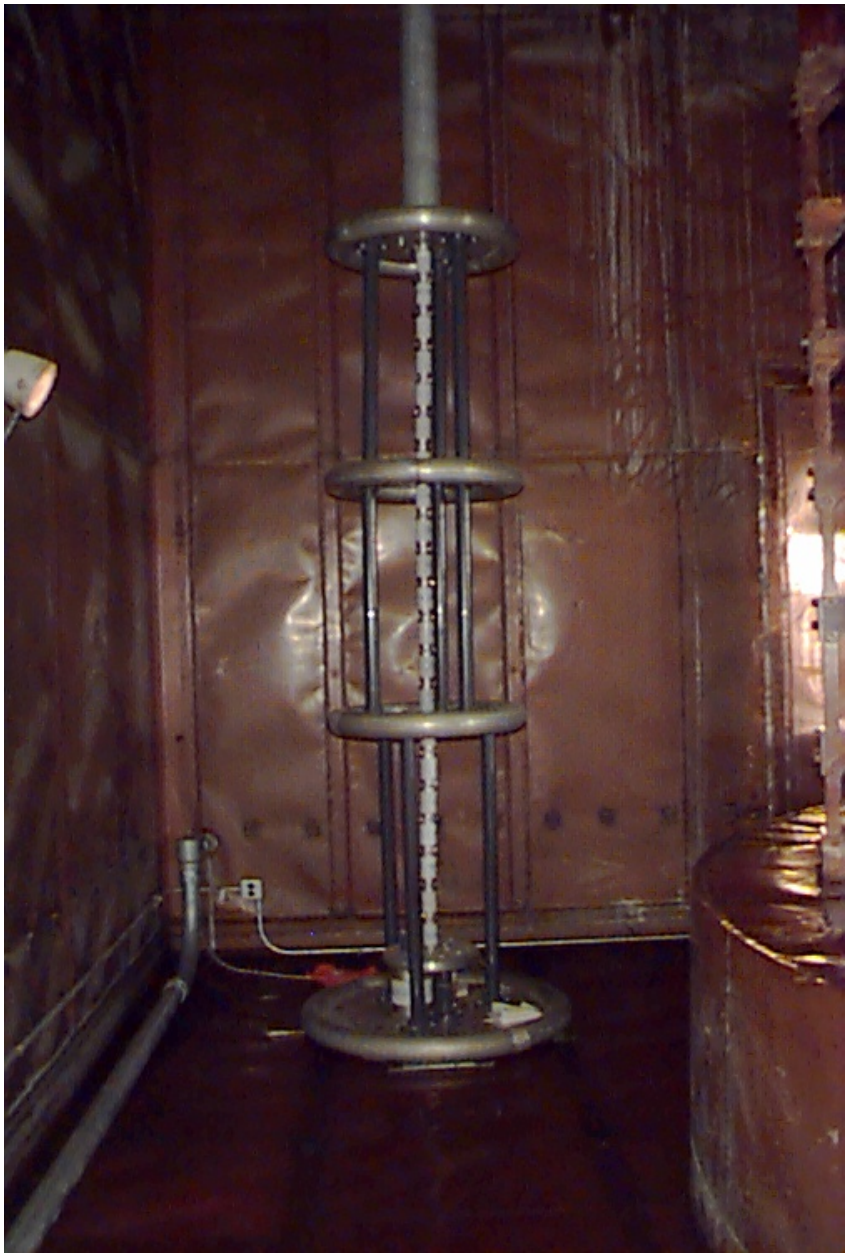

Figure 5-22. 10,000:1 voltage divider.

Calibration

We found that calibrating the high-voltage divider using high-voltage meters or probes that had been calibrated elsewhere led to serious discrepancies in the high-voltage measurements. As a result, a calibration technique was worked out on site that gave consistent and repeatable results that we believe to be quite accurate. The basis of the procedure was to use commercially available calibrated digital multi-meters with high-accuracy specifications in the VLF/LF range. Many of these meters can accurately measure voltages up to 300 Volts rms and some of them 1200 volts rms or higher. These meters were used to accurately calibrate a commercially available capacitance divider with a nominal 1000:1 ratio. The calibrated divider was used in conjunction with one of the multi-meters to

calibrate the 10,000:1 divider. The 1000:1 divider was calibrated in place on the test cell floor so that the stray capacitance was the same for both parts of the procedure.

The procedure to calibrate the 10,000:1 divider requires the following instruments (or equivalents):

Digital Multi-meter, Hewlett-Packard HP 3468A (2 required)
Jennings Voltage Divider model 13200-1000-1 with 1000:1 ratio
Synthesizer/Generator, Hewlett-Packard model 3325B with high-voltage option
Step up transformer (24-volt filament transformer)
Audio Analyzer, Hewlett-Packard model HP 8903B
Decade capacitance box

1000-to-1 Divider Calibration

The test frequency must be first determined by setting up the test object and using the transmitter at low power while adjusting the transmitter frequency until maximum voltage across the high-voltage tuned circuit occurs. The two dividers are then calibrated using that frequency.

The first step is to determine the division ratio of the nominal 1000:1 Jennings bottle voltage divider at the test frequency. The Jennings bottle divider is set up on the floor of the test cell where it can be connected to the high-voltage circuit. However, for the initial calibration of the bottle, it is not connected to the high-voltage circuit. Instead, it is connected across the secondary of a small transformer located next to the divider, shown schematically in Figure 5-23 and pictured in Figure 5-24. An extra length of double-shielded coaxial cable was connected to the short piece of coaxial cable provided with the Jennings divider to connect with meter M1. The extra coaxial cable adds capacitance, which increases the division ratio. We used a specially made up and labeled cable dedicated to that purpose. With this extra cable, the division ratio was about 1182:1.

The high-voltage output of the synthesizer was connected to the secondary of the filament transformer using another piece of double-shielded coaxial cable. The primary is connected across the Jennings divider, providing a stepped-up voltage. The synthesizer is tuned to the test frequency and placed in high-voltage mode, which provides up to 22 volts peak-to-peak output. The output amplitude is adjusted to provide the maximum possible reading without waveform distortion. This voltage must be less than the 300-volt rating of the HP 3468A multi-meter, which is also connected across the transformer secondary (M2 in Figure 5-23, pictured in Figure 5-24).

The meters used for this calibration are wide band, and to obtain accurate results it is important that the calibration waveform is not distorted. At high-output levels, the synthesizer can have a distorted waveform when driving an inductive load like the transformer, and an oscilloscope is necessary to check the waveform. A slight reduction of the synthesizer output level often eliminates distortion.

The output of the Jennings bottle divider is read using another HP 3468A multi-meter, M1 in the schematic (Figure 5-23). The ratio of the voltages from these two meters defines the division ratio of the Jennings bottle divider. These voltages were measured five times by simultaneously triggering both meters and recording the readings. The readings were averaged, the ratio taken and recorded as the division ratio for the Jennings divider. The data sheet used for this procedure is given in Figure 5-23.

Date: _____

Procedure to Determine Division Ratio of Voltage Dividers

1. Connect Equipment as shown in Diagram. Include any extension cables that will be used during calibration.

2. Set synthesizer to approximate test frequency.

   Frequency_____Hz

3. Set synthesizer to 22 vp-p (7.2 vp-p without high voltage option on).

4. Simultaneously single trigger M1 and M2. Take 5 sets of readings.

   M1 ≈ 0.160 V_{RMS}
   M2 ≈ 140 V_{RMS}

5. Calculate division ratio:

   RATIO = M2 avg / M1 avg

   _____=_____/_____

	M1	M2
1		
2		
3		
4		
5		
AVG		

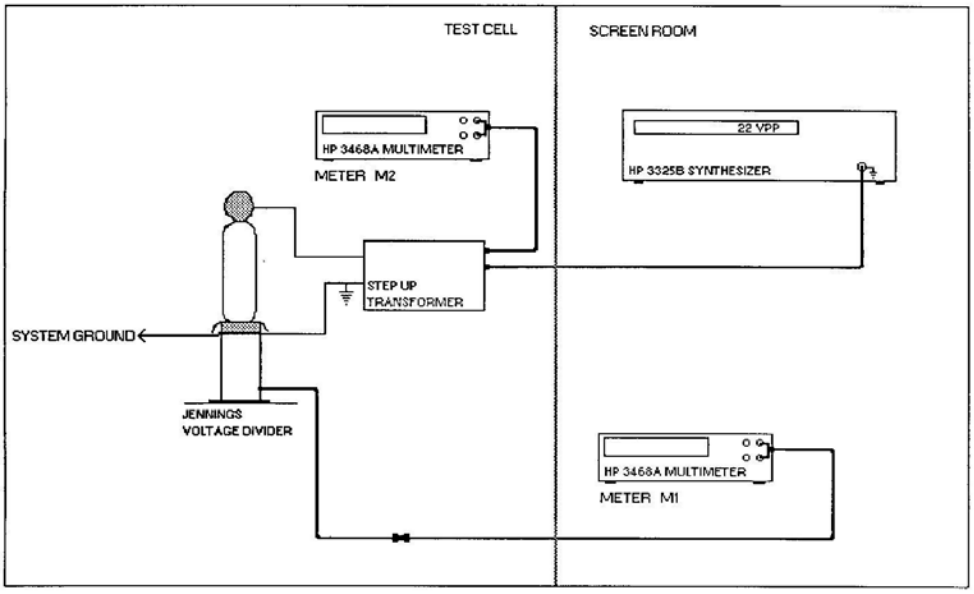

Figure 5-23. Form for determining division ratio of voltage divider bottle.

The calibration of the Jennings divider was regularly checked prior to using it to calibrate the 10,000:1 divider. We found that the division ratio of the Jennings divider measured in this way was repeatable with variability less than 0.5%, and that this ratio was essentially constant over the frequency range used at Forestport.

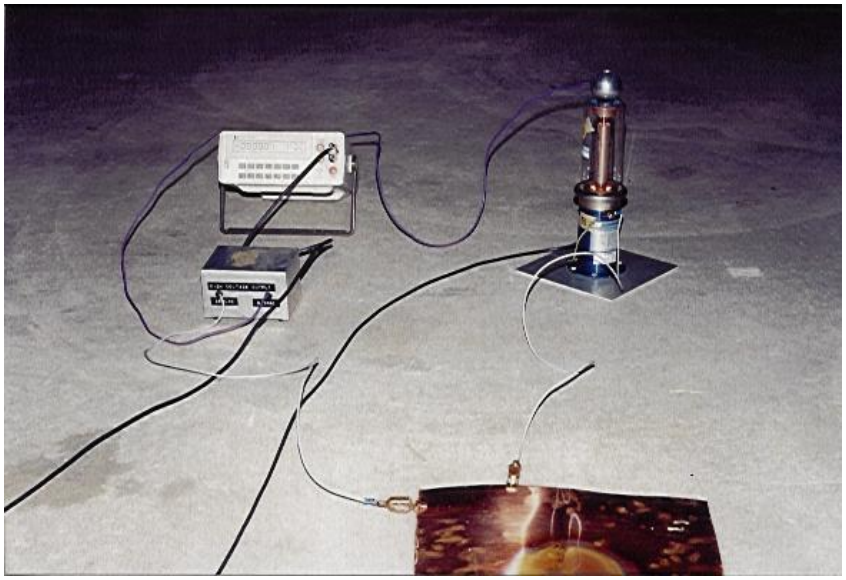

Figure 5-24. Determining the Jennings voltage division ratio.

10,000:1 Divider Calibration

Following calibration, the Jennings 1000:1 divider was used to calibrate the 10,000:1 divider. For this procedure, the Jennings bottle was left in place on the test cell floor. The transformer was disconnected and removed from the test cell area. The top (high-voltage section) of the Jennings divider connected to the high-voltage circuit. The HP 3468A meter (M1) was connected to the output of the Jennings divider to allow measurement of the high voltage using that (now calibrated) divider. This reading is compared to the readings from the 10,000:1 divider taken with the HP 8903B audio analyzer. This setup is shown schematically in Figure 5-25, the data sheet for calibrating the 10,000:1 divider.

The calibration procedure involved slowly increasing the transmitter power on the previously determined test frequency. The meter connected to the Jennings divider was carefully monitored and the transmitter power slowly increased until it read about 28 volts rms, corresponding to a high-voltage of about 31 kV rms or 44 kV peak across the Jennings divider. The rating for the Jennings divider is 50 kV peak, and it is important not to exceed that rating. Flashover across the Jennings divider connects the high-voltage circuit directly to the coaxial cable going to the meter. This would destroy the meter and is dangerous to personnel. To reduce the danger to personnel, the meter should be set outside the observation space in a location where it is easily read but not touched by personnel while the high voltage is activated.

Once the desired level is reached, readings are taken from the meter attached to the Jennings divider. These readings are multiplied by the division ratio of the Jennings divider, and the product is called $HV_{CAL.}$ The audio analyzer measures the 10,000:1 voltage divider signal, which is close to HV_{CAL} /10,000. The final step involves adjusting the decade capacitance box, across the input to the HP audio analyzer (shown in Figures 5-6 and 5-25), until the analyzer reads exactly HV_{CAL} /10,000. When that adjustment is complete, the value of the decade capacitor is recorded in the logbook. The transmitter is taken down and the Jennings voltage divider removed. This procedure resulted in measurements that were often repeatable to within ±1%.

Date: _____

Procedure to Calibrate the 10,000 to 1 Voltage Divider

1. Connect equipment as shown in Diagram.

2. Tune the Transmitter at low power

   Frequency_____Hz

3. Increase power slowly until the meter (M1) reads approximately 18 V_{RMS}.

4. HV_{CAL} = M1 x RATIO *
   * RATIO obtained from division ratio procedure

   _____=_____X_____

5. Adjust decade capacitance box until the voltage reading on the audio analyzer = M1 x RATIO.

   DECADE CAPACITANCE READING _____ _____ _____

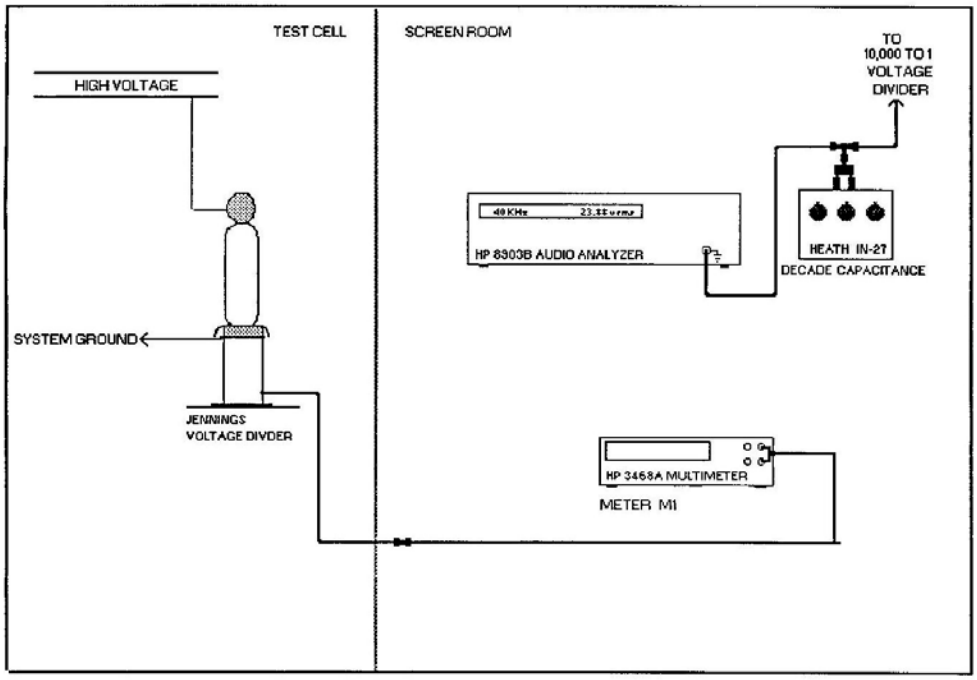

Figure 5-25. Form for calibrating 10,000:1 voltage divider.

Power

The power dissipated in the test circuit was sometimes measured to determine the power dissipated in the high-voltage phenomena such as water heating or corona. The equipment and technique used to measure this power are described in Chapter 7.

Environment

Commercially available instruments were used to measure environmental conditions.

Weather

A weather station is useful for recording general ambient conditions. Accurate barometric pressure is required for making corrections to standard conditions. Consequently, some form of calibration procedure must be used to calibrate the weather station. At Forestport, the calibration of the barometric pressure was done by comparison with accurate data available at the nearby Griffiss Air Force Base.

Temperature

Accurate values for air temperature are required for correcting the test results to standard conditions. This temperature should be measured near the test object because the temperature might depend on location. Surface temperature measurements are required for heat run tests.

Several different types of instruments are useful for temperature measurements, including standard air temperature thermometers, electronic thermometers with probes for measuring surface temperature, hand-held infrared spot thermometers, and infrared imaging scanners that can remotely monitor surface temperature.

Humidity

Accurate values for humidity are required for correcting the test results to standard conditions at 60 Hz. At VLF/LF, this correction factor is not well known, but the humidity must be known accurately for analyzing the results to determine the correction factor. The humidity must be measured near the test object because it can vary considerably within the test and observation areas, especially for outdoor tests. Over the course of operations at Forestport, several methods and instruments were used to measure humidity. We finally settled on relative humidity because it was the easiest, fastest, and most accurate method to determine most values of humidity. The relative humidity can be used to calculate the absolute humidity. The accuracy of absolute humidity determined in this manner is quite high except when the relative humidity is near 100%. This is not an important shortcoming because the high-voltage performance is highly variable when the relative humidity is 90% or greater. We found a commercially available hand-held, wand-type relative humidity meter that was very accurate. This type of instrument is easy to use, has a short settling time, and facilitates measurements close to the test object. There is more discussion on measuring humidity in Chapter 3.

Corona

Visual

VLF/LF corona is such that the dark-adapted eye can see it quite easily, especially when aided by a telescope or binoculars. Consequently, most of the corona measurements at Forestport were done by visual observation. It is important to note the human eye does not fully adapt to the dark for approximately 30 minutes. The U.S. Navy uses dim red lights in the corridors of a ship after dark because the red does not affect dark adaptation. For the same reason, a red light was used at Forestport to facilitate data recording when testing in the dark.

Flashlights with red lenses were useful for the observers to perform various functions without losing dark vision adaptation. They were often used as a light source to briefly illuminate the test

object for focusing binoculars or determining the location of corona. Often it was too dark to determine exactly where a dim corona spot was located on the hardware. Laser pointers can be used as a light source to determine the location of corona spots. The laser is pointed at the corona source while it is dark. Sometimes the laser provides enough light to identify the hardware location. If not, the area is illuminated with a flashlight or overhead lights, providing enough light to see the hardware while the laser pointer pinpoints the corona source.

The observation area was located only on one side of the test cell, and consequently only one side of the test object could be observed directly. Mirrors were used to observe the entire test object. There were four specially constructed mirrors, each approximately 2 feet wide by 3 feet high, which could be placed on the floor at various places around the test object. The vertical angle of the mirrors could be easily adjusted so that the observers in the observation area could see the entire backside of the object.

Night Vision Device

Several night vision devices are available on the market. They work very well for spotting corona. In fact at 60 Hz, where the corona is considerably dimmer than VLF/LF, they are nearly essential. The best night vision devices for corona spotting are wide-aperture devices such as the military surplus starlight scopes. Some much less expensive smaller night vision devices are available on the commercial market, and one of these devices was used successfully at Forestport.

Current

The Trichel pulses that mark the beginning of corona can be observed on the current waveform. This is the basis of the partial discharge technique used for non-destructive testing at 60 Hz. Certain test configurations were constructed at Forestport having an insulated ground plane with a single ground return cable in order to measure the ground return current. For this case, the Trichel pulses can be seen on an oscilloscope given that the current pickup device has enough bandwidth. These pulses were best observed when using current sensing resistor in the ground lead. This configuration has a very wide bandwidth. They were less observable when using a Pearson current transformer, probably due to bandwidth limitations. With the right test setup, corona onset and extinction could be detected by observing Trichel pulses forming in the current waveform. A series of tests resulted in a 100% correlation between visual and oscilloscope observations. Our conclusion was that at VLF/LF visual observations of corona were faster, easier, and usually more reliable than other methods.

Sound

If it is quiet, as is often the case for inside measurements, corona can often be heard. The sound frequency of corona is quite high and it seems that younger observers can better hear corona. This is an excellent technique for locating the source of corona, especially if the test object is large such as a helix and it is not practical to set up mirrors to cover the entire object. Directional ultra-sound microphones are used at power system frequencies to locate the source of corona, and they may also be useful for locating VLF/LF corona. However, they were not tried at Forestport.

Rainfall Rate

A rainfall gauge was constructed to measure the rainfall rate following the suggestion in (IEEE std 4-1995) section 14-2.3. A picture of the gauge used at Forestport is shown in Figure 5-26. Note that the rainfall gauge collects water in the vertical and one horizontal plane. The collection chambers drain into a graduated cylinder shown in the figure.

Figure 5-26. Rain gauge.

Dimensions

Accurate dimensions of the test objects are required for processing the data. At Forestport, we used several commercially available devices to measure dimensions. For accurate measurement of diameters, we had several devices, including micrometers and calipers of various sizes. We also constructed some special large calipers for measuring the major and minor diameter of the larger corona rings and the height of a wire above the ground plane.

Workshops

A good, well-equipped workshop was necessary in order to construct the test fixtures. The performance of insulators depends primarily on the corona hardware. At VLF/LF, the limiting parameter is usually the wet withstand voltage. We found that the performance, particularly wet flashover and wet withstand, did not depend very much on the materials used. For example, flexible corrugated tubing could be used to mock up a grading ring, and even though the dry corona onset voltage was considerably lower than for a smooth corona ring, the wet flashover voltage, which is lower, was essentially the same for both rings. This fact allowed us to easily mock up and test the performance of insulator configurations for design optimization.

A selection of insulators and tubing, both rigid and flexible, was used to mock up insulator configurations to determine the voltage limit for those configurations under wet conditions. The mock-up configuration was easy to change depending on the test results. The mock-ups were an important part of the engineering design process. Often the procedure involved computer design first, then testing of a mock-up, with changes made based on the tests, then construction of a commercial version. The first article commercial version was usually thoroughly tested prior to acceptance and installation.

The ring configurations on some of the larger insulators, such as base insulator assemblies, and tower lighting isolation transformers, and large halyard insulators are expensive and heavy. It would have been impractical to use the actual rings for all the configurations that were tested. In one case, the performance of a large halyard insulator for Cutler, which had a stainless steel ring 20 feet in diameter, was determined using a mock-up made from much lighter flexible pipe. The mock-up, shown in Figure 5-27 (also Figure 5-18), was light enough to enable hoisting it to a height of 25 feet, which would have been impractical with the actual ring.

Figure 5-27. Cutler insulator mock-up.

Special Equipment

Some special equipment was required to effectively maintain and operate the HVTF. One aspect of this is that the test cell and helix house are both high-bay space and often personnel had to access things that were up high for various purposes. For example, reconfiguring the capacitor stack for a frequency change required access to the top of the capacitor stack. The equipment at Forestport included two Genie Man Lifts capable of hoisting 300 pounds up to 25 feet high. These lifts were indispensable and highly recommended components for any high-voltage test facility. They were used for many aspects of the operations. Another example of their use was to elevate the water spray nozzles to provide the proper spray on the Cutler halyard insulator, which was suspended 25 feet in the air.

Another essential piece of equipment for a high-voltage test facility is a 4-ton forklift fitted with pneumatic tires, dual in front, for outdoor operation. At Forestport, the forklift was used for various aspects of operation and maintenance. It provided the normal function for loading and unloading heavy loads (insulators) and moving them around in our outdoor storage area, but it was also used to move around the relative large assemblies that were sometimes tested at Forestport. A 3-ton forklift extension crane was used to provide portable lifting capability. For heavy objects or high lifts, a crane was rented.

A wagon approximately 8 feet wide by 20 feet long was used for moving heavy objects from the workshop to the test cell area. Either the forklift or a ¾-ton pickup truck, also a part of the test area equipment, was used to pull this trailer.

The test cell area had a 2-ton overhead hoist that was on a motor-controlled gantry that could be moved back and forth across the test cell area. This hoist was used to pick up heavy test objects from a truck or trailer and set them down in the center of the test cell area. Often, portions of the test assembly or the feed bus needed to be suspended from an insulator, and there was a separate manual winch with a nylon rope for those functions.

Storage

A large outside storage area was required for the various insulators available at Forestport. Some of the items stored outside are shown in Figure 5-28.

Figure 5-28. Outside storage for insulators.

MEASUREMENT PROCEDURES

The primary objective of high-voltage testing is to establish that insulator assemblies will operate reliably. For that testing, it is necessary to establish the safe operating voltage for the insulator assembly under test. This requires developing knowledge of failure mechanisms for the assembly, determined in part by measurements. Knowledge of the failure mechanisms allows protective mechanisms to be designed that can be tested. Protective mechanisms include spark gaps, which limit the maximum voltage across an insulator and control the path of flashover in the event of a lightning strike. Another objective of high-voltage testing was to develop empirical data useful for design of VLF/LF high-voltage hardware. These data are presented in following chapters.

The dielectric components of the insulators tested at Forestport were made up from various materials. Most were porcelain. However, some insulators were made from fiberglass, Kevlar, and even polymer concrete. There are various failure mechanisms for the insulators. If the insulator is designed well, the wet flashover (or flare) is the limiting phenomena and occurs before any other limit is reached. As long as the flashover occurs from metallic surfaces well away from the dielectric,

it causes no damage. The other limiting phenomenon involves inordinate heating of the insulator dielectric, which does have the potential to cause permanent damage. This heating can result from corona, an arc near or on the surface of the dielectric, internal dielectric heating, or electric field heating of water on the surface of the insulator.

The insulator performance tests performed at the HVTF were based on procedures taken from the IEEE and ANSI standards for 60-Hz insulators. The procedures were sometimes modified to fit the requirements of the Navy's FVLF/LF system and the differences in the high-voltage phenomena at VLF/LF (Brooks, 1982). Not all of the procedures in the standards are relevant to VLF/LF.

For any given insulator assembly, a series of tests is performed to examine each failure mechanism in turn to determine the maximum allowable safe operating voltage. Often the tests would reveal design flaws that unnecessarily limited the performance of the insulator or might allow damage in the event of flashover due to lightning or RF over voltage. The best way to determine and understand these limitations is by observation. Observations provide the information necessary to formulate appropriate modifications for increased performance and/or methods to protect the dielectric portion of the insulator. The on-site workshop enabled the rapid assembly and testing of proposed modifications to determine their effectiveness, which greatly facilitates the design process (see workshop section above for a discussion of mock-ups).

The primary tests necessary to determine insulator performance for high-power VLF/LF applications consists of the following:

For both dry and spray-wet conditions–

RF corona onset/extinction
RF flashover
RF heat rise
Impulse flashover.

The types of insulators and insulator assemblies that require testing include the following:

1. Base insulator assembly (BIA)
2. Guy insulators, single and in combinations
3. Halyard insulators including large grading rings
4. Tower lighting isolation transformers (TLITs)
5. Feed-through bushings
6. Corona inception/extinction on wires
7. Protective arc gaps
8. Special tests of corona hardware (corona rings, etc.)

A brief description of the test methods and techniques follows.

General Procedures

The general procedure for testing an insulator assembly involves first setting up the test object in the test cell and connecting it to the high-voltage tuned circuit. The test object is configured to emulate the intended application. Guy and halyard insulators are usually tested outside where they can be suspended at appropriate angles. For insulators that were to be used in various installations,

the test configurations included the worst-case configuration, if known. For example, guy insulators may hang at various angles and tests should be performed with the insulator hanging with minimum and maximum hang angles. Halyard insulators are often suspended at shallow angles, near horizontal, and should be tested at those angles.

Once the insulator is in place and connected to the high-voltage circuit, the transmitter is brought up at low power and the transmitter frequency is tuned to find resonance in order to establish the test frequency. If required, the capacitor stack, the helix tap, and the variometer settings are changed to obtain the desired frequency. All relevant information about the test is recorded in a lab notebook. This starts with a description of the test object and the setup, including measurements of the physical dimensions of the test object and the feed system. It is important to record the distance between the test object and the floor and walls of the test cell. Those dimensions affect the electric field distribution on the test object and are necessary for calculating correction factors to estimate the performance of the object in the actual installation.

Just prior to each test run, the environmental parameters of temperature and humidity are measured in close proximity to the test object and recorded. For wet testing, the humidity is not recorded. The barometric pressure at the site is also recorded. If the test is a series, involving changing one or more dimensions of the object under test, the dimensions are measured and recorded just prior to the start of each test.

Wet Testing

For wet testing, the water spray system is set up before testing. The nozzles are adjusted to project most of the available spray onto the test object. Typically, the sprayers are adjusted so that the water is falling at approximately a 45^{o} angle per the 60-Hz standards. It is important to adjust the water spray so that there is plenty of water falling onto the high-voltage hardware (corona rings) and also onto the surface of the insulators. Following the adjustment of the sprayers, the waterfall rate is measured using a calibrated measurement device.

The water spray system is provided with a switch so that the water can be turned on and off from inside the control area. The water spray is adjusted and measured without high voltage present. Then the water is turned off until ready for testing. The presence of the water loads the circuit and changes the resonant frequency slightly. Consequently, the high-voltage circuit must be re-tuned with water present. The room is darkened, and while the observer's eyes are adapting, the water is turned on and the transmitter tuned at low power. Then testing proceeds.

Dry Testing

At Forestport, it was discovered for inside measurements that the voltages for the onset of the high-voltage phenomena were greatly reduced when they were measured following wet tests on the same day. This is attributed to the effect of increased humidity in the test cell resulting from the previous water spray. The effect of humidity is the opposite at VLF/LF than at 60 Hz, and the magnitude of the effect is greater (see Chapter 6). To obtain valid measurements for dry conditions, the procedure followed was to perform dry tests before wet tests.

Protective Gaps

Large insulators, such as base insulators, bushings, and tower isolation transformers, often have protective spark gaps. The purpose of these gaps is to limit the maximum voltage that can occur across the insulator and to control the flashover path. These gaps are adjustable by changing their spacing. It is common practice to set these gaps so that they flash over at a voltage just above the

operational voltage to provide maximum protection but not to produce an excessive number of flashovers. This maximizes the protection provided by the gap. The settings for these gaps, especially under wet conditions, must be determined empirically, and the test facility was often used to develop the empirical information required to set the gaps.

It is highly desirable for outdoor gaps to have the wet and dry flashover voltages nearly the same. Rod gaps essentially provide this characteristic (Kotter and Smith, 1983). It is also necessary that the flashover follow the path dictated by the gap, well away from the surface of any insulating material.

Corrections

The withstand voltages are corrected to standard atmospheric density using the following equation, which is the same as used in the 60-Hz standards:

$$V = V_s \cdot \delta$$

where V = the test voltage applied to the test object,
V_s = the rated withstand voltage at STP, and
δ = relative air density.

This correction factor is not strictly accurate, as discussed in Chapter 2 and Chapter 6. However, exact correction factors for complicated objects such as insulator assemblies are not known at this time. For simple objects such as wires and spheres, the exact correction factor is applied. As discussed in Chapter 2, the exact correction factor adjusts both the dimensions of the object and the critical field on the surface.

The 60-Hz standards apply a humidity correction factor for dry tests but not for wet tests. As discussed in Chapter 6, the humidity correction factor at VLF/LF is quite different than that for 60 Hz. The correction factor at VLF/LF depends on the object under test in a fairly complicated manner, being a function of the radius of curvature of the object and test frequency. Since detailed knowledge of the humidity correction factor at VLF/LF is unknown at this time, neither the wet nor dry data were corrected for humidity.

Another correction involves the differences between the configuration in the test cell and the actual installation configuration. This correction factor is developed by calculating the maximum electric field on the surface of the test object for both the test configuration and the installation configuration. Since the high-voltage phenomena of corona, flashover, and flaring can be directly related to the surface field on the object, the correction factor is the ratio of these two calculated fields. For example, the maximum field on the corona rings of a large base insulator assembly for a given voltage is usually greater in the test cell than when installed. This is because the grounded test cell walls and ceiling increase the gradient. Thus, the flashover voltage for the insulator when installed is usually greater than measured in the test cell. However, other details of the installation that are not normally simulated at the HVTF, such as a high mounting pedestal and the tower, tend to reduce the fields at the installation and must be taken into account.

The same type of correction factor, based on the surface electric field, is used for other types of high-voltage hardware. For example, the Cutler halyard insulators were tested at a height such that the bottom of the large corona ring was approximately 17 feet above ground (Figure 5-27), while in the actual installation at Cutler they are suspended 500 feet or more above ground. The corona rings have a 6-inch minor diameter. Computer calculations were used to show that at a height of 500 feet, the surface field on the corona rings is reduced to 62.4% of the field at 17 feet. Thus, the voltage rating at a height of 500 feet is 1.6 times the rating measured at the test height of 17 feet.

Corona Onset/Extinction

Procedure

Visual observation is the primary method of corona detection used at a VLF/LF high-voltage test facility. These observations have to be done in a dark, preferably quiet, environment. Often corona can be heard prior to seeing it, in part due to the time constant for dark adaptation of the eye. Sometimes the corona is hidden and can be detected first by ear, giving an indication that some adjustments, such as position changes of the observers or the mirrors, are needed so the corona can be seen.

For corona onset/extinction measurements, the general procedures described above are followed first. Then, for inside measurements, the doors are closed and the lights turned off to check the test cell for light leaks. Any obvious openings are covered. If needed, the mirrors are adjusted so that the entire insulator can be seen from the various openings in the observation room.

Often four or more observers are necessary. One has responsibility for recording the data, another for reading the high-voltage meter, and two or more for observing the high-voltage phenomena in the test cell. They usually use binoculars, which help to detect small dim spots of corona. The binoculars are focused while the lights were still on. Then the lights are turned off and the transmitter brought up at low level and tuned while the observers were allowing their eyes to adapt to the dark conditions. During this time, the observers can also focus binoculars using a laser pointer or a red flashlight as a light source.

Once the observers are ready and the transmitter tuned, the power is increased in 1-dB steps until corona is observed. The exact location of the corona is determined by use of a laser pointer, a red flashlight, or turning the lights on, and this location is recorded in the data book. If the corona is in a location where it could cause damage, the test stops and the hardware is adjusted so that the initial corona occurs in a location where it cannot cause damage, and the test proceeds. Once this is the case, the transmitter power is cycled up to corona onset and down to extinction. This process is repeated a few times until the observers are confident they are correctly observing the corona.

The corona that first appears is usually very dim, and it is sometimes difficult to differentiate between corona and a reflection from a light leak. In this case, the test director orders the console operator to briefly interrupt the low-level drive signal to the transmitter. This interrupts the high-voltage briefly so that the observers can tell if what they saw is corona or ambient light. The interruption lasts a short time (10 to 20 seconds), and the console operator calls over the intercom when the transmitter goes off, and again when it goes back on.

Once the initial corona has been found and the observers are confident of correctly observing onset and extinction, a data series is recorded. The data consist of observations over a minimum of five cycles of onset and extinction. The onset and extinction voltages are recorded for each cycle. These values are averaged to give the final value for observed corona onset and extinction voltage. To be acceptable, the averages must include at least five measured values that are within ±5% of the average, and they must have been measured within 5 minutes of each other as per the 60-Hz standards.

For wet tests, there are several types of corona phenomena that move or are flickering or turning on and off (see Chapter 6). These corona are noted as the voltage is increased, but since they are not destructive and have little power, they are not of practical importance and onset and extinction voltages are not recorded. As the voltage is increased, eventually stationary corona will appear,

unless flashover or flaring occurs first. The onset and extinction voltages for the stationary corona are recorded.

Failure Mechanisms

For VLF/LF high-voltage operational hardware, small amounts of corona that occurs on metal hardware such as corona rings is acceptable, as it does not cause damage. However, experience at Forestport indicates that at VLF/LF, flashover or flaring will occur at voltages a little above the corona onset voltage. In other words, once corona starts, flashover is not far behind. This is attributed to field enhancements from space charge build-up at VLF/LF. This is not the case at 60 Hz, where there can be a large difference between the corona onset and flashover voltages. Thus, at VLF/LF, corona on the hardware means that the insulator is probably near flashover or flaring and is unlikely to pass a withstand test. This is one reason that at VLF/LF it is desirable to operate with the hardware completely corona free.

Corona is hot plasma, which if touching can destroy most any material over time. Thus, stationary corona on the dielectric (porcelain, fiberglass, Kevlar, etc.) can cause permanent damage to the insulator. Corona has been known to heat porcelain enough to crack it or even melt it down. Fiberglass is easily burned by corona, and once the epoxy carbonizes, it forms a conducting track that will eventually propagate all the way across the insulator.

It is very common for some corona to form on water drops on the surface of an insulator. Often corona will form on a moving water drop and extinguish shortly as the drop either boils away or moves into an area with a lower field. Experience at Forestport indicates this does not cause damage as long as the corona is flickering or moving around.

Acceptance Criteria

To be acceptable, stationary corona must not form on the surface of the dielectric. This must be true at the maximum operational voltage and for the worst-case conditions of wind-driven rainfall. If stationary corona does form, the operating voltage must be limited to a level well below that at which this corona forms.

RF Flashover

The dry flashover voltage for well-designed VLF/LF insulators is considerably greater than the wet flashover voltage. Often the insulators tested at Forestport were quite large, and the 250 to 300 kV available was not enough to determine the dry flashover voltage. Wet flashover could be measured and is an important part of determining the wet withstand voltage, which is the main performance criteria for outdoor insulators.

When considering the RF voltage requirement alone, it is not necessary to determine the flashover voltage but only to determine that the flashover voltage is greater than the maximum required operating voltage. However, as discussed below, it is necessary to determine the location of flashover arcs for both wet and dry conditions because this is involved in the acceptance criteria. If there is insufficient RF voltage for dry flashover testing, impulse testing is substituted.

Procedure

The procedure for flashover testing is the same for both wet and dry conditions. Assuming that no stationary corona spots occur on the insulating material, the voltage is increased in 1- or 2-dB steps until flashover or flare occurs. This is usually done in the dark so that the location of the flashover or flare can be easily seen. When the flashover or flare occurs, the test director activates the safety

switch and the transmitter carrier is cut off. The observer assigned to the high-voltage meter calls out the maximum voltage observed and this value is recorded. The observers assigned to the test object indicate the location of the flare or flashover and this is also recorded. The transmitter drive level is reduced 4 dB and the drive brought up and slowly increased manually until flashover occurs again. This process is repeated until the approximate flashover voltage is established.

Once the approximate flashover voltage has been established, the transmitter drive is reduced 4-dB, which results in a starting voltage of approximately 63% of the flashover voltage. The transmitter power is brought up at this level and the drive ramped up until flashover occurs. This procedure is similar to that specified by in standards (IEEE Std 4-1995, ANSI C29.1 1998). The procedure consists of the following: (1) start the flashover ramp at approximately 75% of the flashover voltage, and (2) ramp at a rate such that the flashover occurs not less than 5 seconds nor more that 30 seconds after reaching 75% of the flashover voltage. At Forestport, the ramp rate was set such that the flashover occurred between 5 and 15 seconds from the start.

The flare or flashover voltage and location are recorded for at least five repetitions. The value of the flashover voltage for the test object is the average of not less than five individual flashovers taken consecutively, all within ±5% of the average value. The average is calculated from consecutive flashovers that occur between 15 seconds and 5 minutes apart.

Failure Mechanisms

There is considerable energy in the form of heat, light, and sound dissipated in a flashover arc. If this arc is near, or on the surface, of the dielectric, it can cause permanent damage. Flashover can be caused by either RF or lightning. Because it is impossible to design insulators that will not break down when hit by lightning, every insulator must be protected during a flashover so that the arc is kept well away from the insulator dielectric. Thus, guy and halyard insulators must be designed to be self-protecting. Protective gaps are used protect the larger insulators such as BIAs, TLITs, bushings, and other insulators inside the helix house by controlling the flashover path. Even so, it is highly desirable for these insulators to be self-protecting in case of a failure of the spark gap.

Acceptance Criteria

Insulator Assembly

An insulator is acceptable if the flashover voltage is greater or equal to the required value and all flashover arcs are well away from the dielectric. If the flashover arc occurs on or near the dielectric materials, the insulator hardware must be redesigned or fitted with permanent protective gaps to keep the arc away from the dielectric materials.

Protective Gaps

The protective gap is acceptable only if the paths of all flashover arcs are well away from the dielectric insulating material. The flashover voltage for each gap setting is determined as described above using five flashovers within 5% of the average.

RF Withstand

The withstand test is intended to develop the service rating for the insulator. The Navy requires a very high level of reliability from the VLF/LF transmitter stations. For that reason, the VLF/LF withstand test is extended over that specified in the IEEE and ANSI standards. The withstand test is done after the flashover voltage has been determined.

The procedures for wet and dry withstand testing are the same. However, dry flashover voltages for VLF/LF insulators are usually much greater than the wet flashover voltages, and for large insulator assemblies there is usually not enough voltage available to determine the dry flashover or withstand voltages. Thus, most of the VLF/LF withstand tests involve spray-wet conditions. The wet withstand voltage is usually 10 to 20% less than the wet flashover voltage. The wet withstand rating is the primary performance factor for insulator applications in VLF/LF antennas.

Procedure

The test cell is darkened, and the observers are positioned comfortably because this is an extended test. The voltage is brought up to a level approximately 5% below the flashover voltage. The voltage is left at this level for 60 minutes. The test object is observed for any signs of corona, hot spots, flare, or flashover. At the same time, the voltage is monitored and adjusted as necessary to maintain the starting level. If any high-voltage breakdown phenomena occur, the voltage is lowered another approximately 5% and the test repeated until 60 minutes of continuous operation without any breakdown phenomena occurs.

The 60-Hz test standards use shorter times for withstand tests, typically 5 minutes. Experience at Forestport indicates that if breakdown is going to occur, it usually happens within the first 5 or 10 minutes, and for that reason we are considering a reduction in the VLF/LF withstand test time.

Acceptance Criteria

The insulator is acceptable if the measured RF withstand voltage is less than the maximum required operating voltage.

Temperature Rise

Temperature rise measurements are done for both dry and wet conditions. The dry test is usually done first. This measures the dielectric heating of the materials in the insulator. The wet temperature-rise test, usually conducted second, examines the field-induced heating of the water on the insulator surface.

Procedure

The insulator is placed in position in the test cell and allowed several hours to reach temperature equilibrium with the ambient air. Prior to beginning the heat run, the temperature on the surface of the insulator is measured at several key locations using a digital surface-probe thermometer. These locations are numbered and if necessary marked on the insulator with a marking pen.

A thermal scanner is useful to give remote readings of the temperature of the test objects while energized. The scanner is set up inside the observation area and calibrated prior to starting the test. It gives a general idea of the location of the hot spots and the rate of temperature rise. This is useful information to help control the test, but it is not sufficiently accurate to use for the measured data.

The primary method for measuring surface temperature is a hand-held surface temperature probe. The measurements using the surface probe can only be taken during periods when the transmitter is down. While the transmitter is operating, the thermal scanner is used to identify hot spots and read the approximate surface temperature. The test director uses the information from the thermal scanner to help determine the times to shut down the transmitter and make the surface temperature measurements.

Dielectric heating is proportional to frequency, and for dry testing a frequency is selected near the upper operating limit for the insulator. The transmitter is brought up to rated voltage, usually the desired wet withstand voltage. The voltage is monitored and adjustments made as necessary to keep the voltage at the rated level. The temperature is monitored using the thermal viewer and recorded periodically (approximately every 10 minutes). The thermal viewer is used to locate the hottest spot on the insulator. After 30 minutes, the transmitter is brought down briefly to allow a rapid measurement of the surface temperature at the previously selected points. At the same time, the observers feel the insulator to locate any other hot spots that should be monitored; when found, these spots are included in the measurements.

After each set of surface temperature measurements, the transmitter is brought back up to the rated voltage for another 30 minutes or more at the discretion of the test director. Then the transmitter is brought down again for another set of surface temperature measurements. This process is repeated at least twice for a minimum test time of 3 hours. The temperature rise (ΔT) of the hottest spot is plotted versus time and is used to determine if enough data has been gathered to accurately estimate the steady state temperature rise ΔT_{∞}. It is not necessary for the temperature to actually reach the steady state value but only to get enough data to accurately fit an exponential curve, which is then used to estimate the steady state value.

Failure Mechanisms

Dry

There are two types of insulator failures caused by dielectric heating. The first is caused by bulk dielectric heating, which leads to thermal runaway. In this case, dielectric heating is produced by the electric field throughout the volume of the material. This heat propagates toward the outer surfaces, where it is dissipated. The internal temperature will rise to the equilibrium point where the heat generated by the electric field equals the heat carried away by the thermal processes. For most materials, the dielectric loss factor increases with temperature. Thus, as the temperature increases, a condition can occur where the rate of heating increase with temperature exceeds the rate of increase with which heat is removed. When this happens, the internal temperature increases without limit until failure of the dielectric occurs. This failure mechanism is a threshold process in that when the field is below the threshold the dielectric does not fail, but when the field is just above the threshold thermal runaway occurs and the dielectric fails.

For porcelain and polymer-concrete, dielectric heating failure usually results in melting, while organic materials usually burn. Often the burning occurs beneath the surface, releasing free carbon. Once the material carbonizes, it becomes semi-conducting and corona can form on the end or edges of the carbon. The carbon forms a track, which propagates slowly and will eventually cross the entire insulator, in effect shorting it out.

The threshold for dielectric heating failure of a material is measured by placing a fairly large piece in a uniform electric field. This configuration corresponds to configuration where some of the dielectric is far enough away from the surface such that the rate that the heat can be carried away is determined solely by the thermal resistivity of the material. In this case, the threshold for thermal runaway is determined solely by the dielectric heating and thermal resistivity characteristics of the material.

For a given insulator, the threshold field for thermal runaway is usually greater than that measured as described above. This is because in a real insulator configuration even the deepest material is close enough to a surface so that there is more cooling than for the bulk case used to measure the threshold.

In addition, in a real insulator configuration, the field is not uniform, and often the deepest (most thermally insulated) part of the dielectric has a lower field than the dielectric near the surface.

The second type of failure involving dielectric heating results in shattering of brittle materials. This type of failure occurs when there is highly non-uniform heating in the dielectric, which results in a significant temperature gradient in the dielectric. In this case, the differential thermal expansion induces mechanical stress. If this stress exceeds the breaking strength of the material (porcelain), it breaks. For porcelain and polymer-concrete, this type of failure results in cracking or even shattering.

For porcelain insulators, the Lapp catalogue gives an allowable temperature rise without risking this type of failure. For insulators that are not structural, such as bushings and tower lighting isolation transformers, Lapp allows a 30° C temperature rise. For insulators that are structural, such as base insulators, guy insulators, etc., only 20° C temperature rise is allowed.

Wet

Under wet conditions, some insulators can have a thin continuous surface coat (film) of water because of their shape and/or their material. This is especially true on insulators with smooth surfaces. When the field parallel to the dielectric surface exceeds about 2.5 kV/inch, the water film heats rapidly and the insulator surface becomes hot. If the field exceeds about 3.0 kV/inches, the water boils within a short time and steam forms. The rate at which this heating occurs depends on the water flow rate. For example, a lot of water flowing carries the heat off with it. If there is too little water, it boils away immediately and the heating stops. For locations with just the right amount of water flowing, the surface temperature of the porcelain can approach 100° C, the boiling temperature of water.

If the Lapp dielectric heating criteria were applied, these insulators would not be acceptable because 100° C is usually greater than 30^{o} above ambient. In fact, at locations that experience winter weather, the temperature rise ΔT can exceed 100^{o} C. Since this heating is localized, a thermal gradient results, which induces mechanical stress, which could break the material. Thus, this type of heating is a concern. However, there is no industry standard to apply as an allowable temperature rise, and informal conversations with Lapp insulator personnel indicated that they feel that surface water heating will not lead to insulator failure.

In an attempt to verify this, some experiments were done at Forestport; boiling water was poured onto a small area of some porcelain insulators that had been stored outside at temperatures well below freezing. These insulators had no structural load. This test was extreme in that the insulators were completely cold and the boiling water was poured onto a small local area. All insulators tested in this way showed no evidence of failure. For that reason, we believe that even in cold climates surface water heating will not damage structurally unloaded insulators.

However, in the past there have been many structurally loaded RF insulator failures attributed to surface water heating. W. W. Brown in 1923 observed and analyzed failures of this type (Brown, 1923). Failures at U.S. Navy sites that may be attributed to surface water heating include the failures of suspension insulators at the Navy's VLF station at Balboa, Canal Zone, and Jim Creek, WA, as well as the failure of the base insulator at the Navy's VLF station at Annapolis, MD. In all of these cases, the failed insulators had heavy structural stresses imposed on them. We believe that the failures were most likely the result of the addition of the stress due to heating to the already existing structural stress. For this reason, we do not recommend using insulators that exhibit significant surface heating in positions having significant structural load. The surface water heating can be

eliminated on most insulators by covering the insulating material with commercially available high-voltage silicon coating.

Acceptance Criteria

Dry

The acceptance criteria for the dry dielectric heating of porcelain have been taken from the Lapp catalogue. For insulators that are not structural, such as bushings and tower lighting isolation transformers, up to 30° C temperature rise is acceptable. For insulators that are structural, such as base insulators, guy insulators, and so forth, up to 20° C temperature rise is acceptable.

Wet

For structural insulators, a temperature rise of up to 20° C is acceptable. Significant surface water heating on structural insulators is not acceptable and if it occurs the insulators must be coated, the hardware modified, or the voltage rating reduced such that this heating does not occur.

For non-structural insulators, significant surface water heating is acceptable.

Impulse Testing

Since VLF/LF antennas will be hit by lightning, the insulators used in them will flash over at times, and they must be designed to be self-protecting from both RF flashover and lightning-induced flashover. The power industry uses impulse-withstand ratings for their insulators. However, we have not adopted them. Instead, use the impulse test to determine the location of flashover, which may be different for impulses than for RF, especially for dry impulse flashover versus wet RF flashover.

The standard lightning pulse (1.2-μs rise time by 50 μs to ½ voltage) (IEEE std 4-1995, p 20) is a good representation of the actual lightning impulse that occurs near the base of a VLF/LF antenna. This is because the antennas are large structures, which filter the waveform, reducing the rise time, similar to power lines. For this reason, the standard-shaped pulse is used to test the large insulators located near the base of the antennas, such as the BIA, TLIT, and bushings.

However, the impulse from a strike close to an insulator can have a much higher rise time than the standard lightning pulse. Power industry tests for lightning tolerance are not standardized, but they approximate a direct hit by using a “fast wavefront” impulse. This type of impulse waveform is used to test the topmost insulators in VLF/LF antennas that are subject to nearby lightning strikes. These insulators include the main top-load insulators of umbrella top-loaded monopoles, suspension insulators for valley span antennas, or halyard insulators for the other types of antennas.

Procedure

The insulator assembly is mounted in the test cell and connected to the lightning simulator. The observers are positioned and mirrors put in place as necessary to enable observation of both sides of the assembly. The room is darkened and a few minutes given for the observers’ eyes to adapt to the dark. The lightning simulator is activated, applying pulses with increasingly greater voltages. Eventually a voltage is reached where the insulator assembly flashes over. The location of each flashover is noted. If the flashovers occur away from insulating material, the impulse voltage is increased further in steps until the maximum voltage available from the simulator is reached. At that level, a minimum of five flashovers were observed and the location of each flashover noted. The locations are documented with sketches and/or photographs.

Failure Mechanisms

One failure mechanism is the same as that described under RF flashover where the arc of the flashover is near or on the surface of the dielectric material. A fast wavefront (high rise time) pulse can lead to a flashover in a different location than RF flashover, and both should be measured.

If the rise time of the pulse is fast enough, there is the possibility of a second failure mechanism involving dielectric breakdown (puncture). The voltage for puncture is usually considerably greater than flashover. However, puncture occurs very fast, and if the voltage is high enough, the puncture can occur before the flashover in air. For this reason, the tests on insulators that could experience a nearby or direct lightning strike are conducted with the highest voltage and rise time that can be simulated.

One other failure mechanism involves the combination of RF and lightning-induced impulses or static discharge. This type of failure only occurs when there is more than one insulator in series, such as guy breakup insulators. In this case, a lightning impulse or static buildup can cause one or more of the insulators in the series to flash over. If all the insulators in the string do not flash over, the transmitter may not kick down and continues to drive the arc(s) that were started by the lightning or static buildup. These arcs do not require much current to sustain them. This current is supplied through the capacitance of the cables attached to the insulators. Once triggered by the lightning, these arcs can go on indefinitely. The amount of power in each arc is a few kilowatts, which is small compared to the normal transmitter power, and the transmitter protective circuits normally do not activate. The arc consists of very hot plasma and will destroy the dielectric if allowed continuous contact.

A true test of this phenomenon involves using the transmitter to generate high RF voltage while at the same time inducing a lightning impulse across the insulator assembly. We have not yet done such a test at VLF/LF. It has been done at 60-Hz test facilities, and we believe it can be done at the VLF/LF HVTF. However, it will take some special rigging, hardware, and more space than we had in the Forestport test cell. Instead, a different test was designed that accomplished the same thing.

For this test, a small wire electrode attached to the insulator hardware was used to trigger flashover at the appropriate location. In order to do this, the location of the flashover initiation must be known. Two insulators were connected in series for this test. One of the insulators was the one under test and was induced to flash over. The capacitance of the second insulator had the function of limiting the arc current; otherwise the transmitter would kick down.

One such test setup is pictured in Figure 5-29 testing a Lapp Compression Cone insulator of the type that failed at the Awase LF transmitting station. In this case, lightning had triggered arcs, which the transmitter drove, resulting in insulator failures. For this test, a very fine wire was used to trigger RF flashover. The wire was placed in an appropriate location to trigger the arc based on observations in the field. The wire was fine enough that it quickly burned away in the arc. For this test, the wire initiated the arc, which was then driven by the transmitter. The arc was contained inside of the porcelain and heated the porcelain so that within a few minutes the porcelain cracked. The same phenomenon at the operational station caused the porcelain in the insulators to melt and fall away from the insulators.

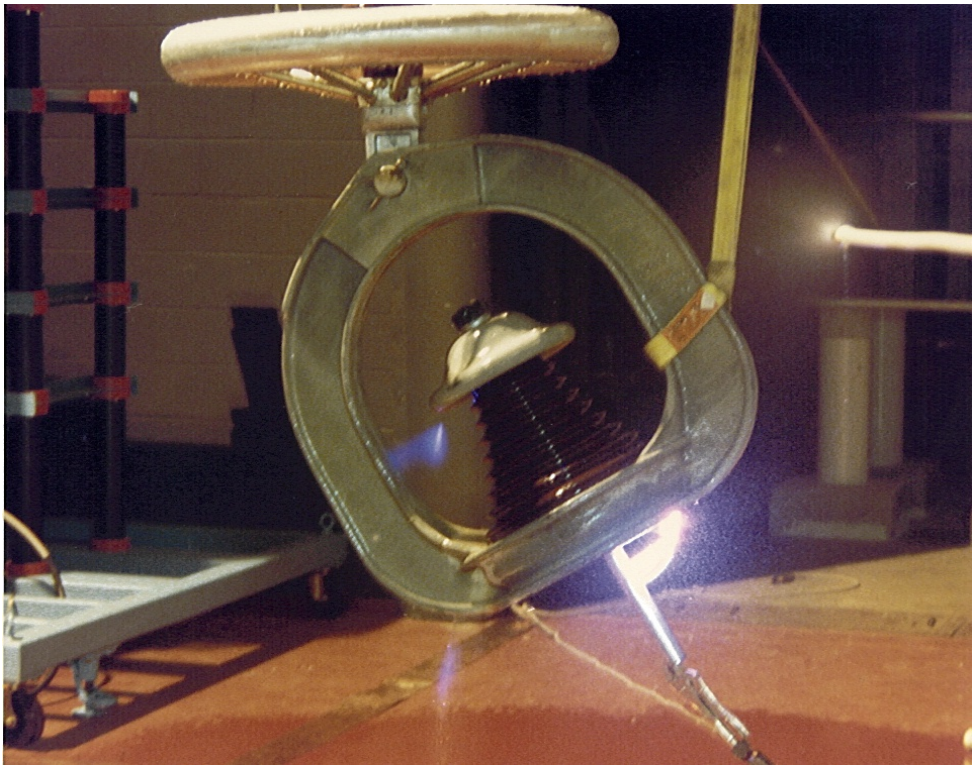

Figure 5-29. Lapp compression cone insulator with arc triggered by wire.

A third form of failure involving lightning has been experienced at operating stations. This type of failure occurred with insulators that have fiberglass bands as strength members. These bands are immersed in oil contained in a porcelain shell between two end caps. An air bubble is included to allow for thermal expansion of the oil. The failure resulted for cases in which the air bubble uncovered the fiberglass band. In that case, lightning impulses caused internal flashover, resulting in some carbonization of the epoxy in the fiberglass band. Then the presence of the high-voltage RF caused the carbonized portion of the dielectric to slowly track across the remainder of the band, causing the insulator to fail. The only real way to test for this is to apply an impulse at the same time the insulator is energized with high-voltage RF. Again, we have not done such a test. An alternative is to test the insulators with a very high-voltage fast-wavefront impulse and then take them apart afterwards to look for burning of the dielectric.

Acceptance Criteria

Insulator Assembly and Protective Gaps

The insulator assembly is acceptable if all flashover paths form well away from the dielectric insulating materials.

Appendix 5A Forestport Background

The VLF/LF high-voltage measurements described in this book were made at the U.S. Navy's VLF/ LF High-Voltage Test Facility (HVTF) located at Forestport, NY. The site, on the edge of Adirondacks National Park, consisted of 183 acres of leased land controlled by the Air Force since 1950. The Air Force constructed this facility in the early 1950s as a test bed for LORAN C and the RADUX/ Omega navigation systems. The facility had a 1200-foot base-insulated tower with a helix house that contained the tuning and matching systems necessary for VLF/LF transmissions. The transmitter (AN/FRA-31) was constructed by Westinghouse and was capable of operation from 10 kHz to over 50 kHz at a nominal power level of 100 kW. The Navy was the primary developer for the Omega navigation system and used Forestport as a test site for its development. Following the development of the Omega system, the facility served as an operational Omega station from 1968 to 1972, when the LaMoure, ND, Omega transmitter replaced it. The Forestport facility then went back to the Air Force for research use. A brief history of the test facility is included as Appendix 5B.

Until about 1972, the Navy and Air Force used 60-Hz standards for specification and acceptance testing of the insulators used in the VLF/LF transmitting antennas. Unfortunately, this approach ignored the difference in performance between 60 Hz and VLF/LF that had been observed experimentally in the early 1920s by Brown (1923) and others. Partly due to this, there was a series of spectacular insulator failures at Navy installations in the early 1970s. These failures involved newly installed insulators at the transmitting stations in Annapolis, MD, Lualualei, HI, and LaMoure, ND. The insulators for these sites had all been accepted based on 60-Hz criteria, but had failed when operated at VLF (Smith, 1982).

The impact of these failures was severe. Annapolis and Lualualei carried the strategic submarine broadcast, and the Cold War was in full swing. The insulator failures took these stations off the air indefinitely, and no solution was readily available. To find a solution, the Navy did an extensive investigation of insulator performance at VLF, using temporary setups at Chollas Heights and Lualualei, both operational transmitters from 1972 to 1976 (Smith 1973). An important conclusion of these investigations was that high-voltage insulators for applications at frequencies at least up to LF should be subjected to acceptance testing at frequencies in the range of application (Smith, 1982).

The use of operational transmitters for testing was not acceptable to the Navy, and it was decided to seek a permanent location for a VLF/LF high-voltage test facility. In late 1977, the Navy, in conjunction with the Air Force, agreed to transform the Forestport facility into a small-scale VLF/LF test facility to support their VLF/LF broadcast systems.

In 1978, to support high-voltage testing at Forestport, a 25-foot-wide by 40-foot-long by 25-foot-high test cell was added beside the existing helix house. A large hole was cut out in the wall between the helix house and the test cell to allow access between them. In addition, the transmitter building was expanded by the addition of a new wing, and the electrical power was upgraded both to the transmitter building and the helix house. The existing 100-kW VLF/LF transmitter was used as the radio frequency (RF) power source. The high-voltage circuit was made up from the original pie-wound helix in conjunction with a series-parallel set of mica capacitors. This tuned circuit was capable of developing voltages on the order of 125 kV rms in the VLF/LF range (Brooks, 1997).

Breakdown is a nonlinear process and one lesson learned from the tests was that direct scaling could not be used to predict the performance of high-voltage insulators. For example, doubling the size of the insulator assembly does not double the breakdown voltage. As a result, full-scale testing

was required, and higher voltages were needed to thoroughly test the insulators to be used at operational sites. That led to a site upgrade that took place during 1980–1981. There were two phases of the upgrade. The goal of the first phase was to achieve 250 kV rms at 30 kHz. The pie-wound helix was replaced with a solenoidal-wound helix designed to operate at higher voltage. The mica capacitor stack was also replaced with a stack made up of oil-filled capacitors designed for the higher voltage. The capacitor stack was configured to allow a rapid change between the connections required for 30-kHz and 60-kHz testing.

The dissipation limit of the capacitors was exceeded as frequency increased above 40 kHz at 250 kV. The goal of the second phase of the upgrade was to increase the frequency range that could be used for 250-kV tests up to 60 kHz. To accomplish this, an indoor air variable capacitor was designed for use at the higher frequencies. This design necessitated enlargement of the archway between the helix room and the test cell to allow the feed line to extend directly from the top of the helix to the test cell. At the same time, a 6-inch feed line with a universal joint and sliding extendable (trombone) section was constructed that allowed the high voltage to be connected anywhere within the test cell (Smith, 1980). Following the completion of this upgrade, a plan was developed for a 500-kV facility, but it was never built (Smith, 1986).

Following the collapse of the Soviet Union and the end of the Cold War, there was a lot of pressure to reduce U.S. military costs. The Air Force had decided to close down their LF broadcast system, which had been used for strategic communications to bombers and buried missile silos. This made it too expensive for the Navy to maintain a high-voltage test facility separate from any other Navy facility. For this reason, it was decided to close down the site at the end of fiscal year 1998 and move it to the Navy's transmitting site at Dixon, CA. Prior to the move, a final series of experiments was done during the winter of 1996–1997. During that time, considerable corona onset data were obtained, including the measurements of the effect of air density and humidity. Following the completion of these tests, the Forestport site was closed and dismantled. The high-voltage generation equipment, including the transmitter, helix, and capacitor stacks, were moved to the Navy's transmitting site at Dixon, CA, where the VLF/LF HVTF is in the process of being reconstructed.

Appendix 5B History of Forestport

The Forestport Research Facility Closes with a Bang

by

Raymond W Tucker, Information Directorate, AFRL
Wayne Bonser, Information Directorate, AFRL
Paul Vanderhoff, Realty Officer, AFRL Rome Research Site
Peder M Hansen, NRaD (Naval Command, Control and Ocean Surveillance Center)*

William Cheyne, Rome Research Corporation
Alfred Paoni (retired), former Rome Air Development Center

The Forestport Research Facility whose history slightly predates Air Force research presence in the Rome, New York, area, was closed and its landmark tower demolished in 1998. The facility consisted of three buildings and a 1200-foot transmitting antenna tower. The final chapter of the "Tower at Forestport" was written by the U.S. Army's 10th Mountain Division on 21 April 1998. At approximately noon, as part of a training exercise, the 41st Engineer Battalion's, 2nd Platoon, Bravo Company, used 320 pounds of C4 explosives to lay the 1200-foot tower on the ground. Thus ended the towers almost 50-year history of navigation and communication research serving the strategic defense of the United States.

Engineers from Watson Labs of Red Bank, NJ, and Truscon Steel Company of Youngstown, OH, designed the tower beginning in 1948. Truscon Steel fabricated the tower's structural steel. The Beasly Construction Company of Muskogee, OK, and Wickes Engineering Company of Camden, NJ, erected the tower, which took 4 months to complete. It reached its full erected height of 1210 feet on 13 December 1950. At that time, only the Empire State Building (1250 feet) exceeded the tower in height. The structural steel weighed 772 tons and 1400 cubic yards of concrete were used for the base foundation and guy wire anchors. There were 18 guy wires holding the tower erect. The top guys were anchored 1100 feet from the tower base and fabricated from 2.5-inch diameter steel cable. The tower was designed to withstand 150 mile per hour winds with only a 7-foot top sway. During construction, on 25 November, a freak hurricane tested the design of the incomplete tower to winds of 105 miles per hour, with no damage. The entire tower sat on three ceramic insulators. The guy wires are also electrically insulated from ground. At the very low frequencies (VLF) transmitted from this facility, the tower itself is the transmitting element of the antenna system.

The tower was somewhat unique in that it had only three guy levels with six guys at each level and no topload. The facility was originally constructed by the Air Force to be used in the development of Long Range Radio Navigation (LORAN C), which was originally to operate at 180 kHz. The operating frequency was later lowered to 100 kHz. The Forestport antenna tower was modified by jumpering the first insulators in the uppermost guy level to provide (in effect) a topload. The antenna then resonated at a frequency slightly above the 100 kHz LORAN C operating frequency. During

* Now called Space and Naval Warfare Systems Center, San Diego (SSC San Diego).

those days, there was no high-power transmitter installed and the facility was used for low-power research operations only.

Later, the facility was to be used as an experimental site for two new navigation systems, Omega and Radux. Omega originally operated at 10.2 kHz and Radux operated at 40 kHz. The U.S. Navy, through the Naval Electronics Laboratory (NEL) (which later became NELC, NOSC, NRaD, NCCOSC and now SPAWAR Systems Center) was the developing agency. A 100-kW transmitter covering 10 to 40 kHz, the AN/FRA-31, was procured from Westinghouse by the Navy and installed at Forestport, commencing operations in November 1959. The procurement included a large (approximately 15 feet in diameter and 30 feet high) “Pi” wound porcelain frame helix loading coil for tuning the antenna down to 10 kHz. The Forestport facility was involved in experimental trials of the Radux-Omega/Omega system along with other sites.

Originally, Omega testing was done with three transmitters, one at Forestport, one in Norway, and one at the Navy's site in Balboa, Panama. As time went on, Balboa was moved to Trinidad, and the Navy's station at Haiku (Oahu, HI) was converted to Omega. Omega went operational in September 1968 with these four stations.

The U.S. Coast Guard became involved with Omega during 1966. The U.S. Navy authorized full-scale implementation of the Omega System in 1968. At that time, the operational responsibility was turned over to the U.S. Coast Guard's specially formed Omega Navigation System Operations Detail (ONSOD), which was first located on the island of Hawaii and later moved to Washington, DC in January 1975.

Over time, other stations were added, Trinidad was moved to Liberia, but Forestport remained on the air as an operational Omega station until October of 1972. It was replaced by the La Moure, ND, site, which had been built by the Navy. At that time, Forestport reverted back to the Air Force for use as an R&D facility. The Omega system in its final configuration consisted of eight sites. They were: La Moure, ND; Haiku, HI; Tushima, Japan; Monrovia, Liberia; Noveken, Norway; Australia; Argentina; and LaReunion Island. With these eight sites, 24-hour, worldwide, all-weather navigation was available. The U.S. Coast Guard Navigation Center terminated Omega operation on 30 September 1997 after 26 years of continuous service.

Meanwhile, the Air Force had developed a VLF communications system known as the 487L Strategic Air Command Survivable Communication System and had installed a transmitting and receiving suite at Forestport during 1969 and 1970. The transmitting system was not used due to Omega operations until after 1972. After that, it was used by the Air Force for various R&D activities related to LF communications, including a system known as BRAVERT for location of downed flyers, tested during 1973-74. The 616 A modem, used for the MEECN (Minimum Essential Emergency Communication Network) system was developed by the then Rome Air Development Center’s Communication Division in the 1970s. MEECN was designed as the last resort communication system for positive force control of our nuclear bombers. Because of its ground wave, it is capable of reaching any point in the world without reliance on ionospheric reflection, which would be disrupted in the event of nuclear war. Forestport was used during the late 1970s for development and testing of dynamic antenna tuning circuitry, which enabled direct sequence, spread spectrum signals to be transmitted, at high powers, using the intrinsically narrow bandwidth (High-Q) VLF tower. Forestport also became the first VLF fixed-location to have its transmissions remotely initiated and controlled via telephone and microwave signals from great distances. The last Air Force use of the tower and VLF transmitter was in support of the Miniature Receive Terminal SPO at Electronic Systems Center, Hanscom AFB, MA.

In approximately 1983, the U.S. Navy and the Air Force worked out a joint agreement to develop and use the Forestport facility as a VLF/LF high-voltage test facility. Following this agreement, a high-voltage test cell was constructed adjacent to the existing helix house. A new helix and capacitor stack was constructed to make a high-Q, high-voltage circuit for generating high voltages for testing. The Navy and Air Force shared in supporting the support the facility and the information gathered, although the Navy primarily supported the high-voltage capability.

In about 1990, the Air Force decided to close their LF sites over a period of time. At that time, they started reducing their support for the Forestport facility; they stopped supporting it around 1992. The last site at Silver Creek, NB, was closed in September 1996. The Navy continued to use the Forestport facility for high-voltage testing, but it became increasingly expensive to operate a separate isolated facility for this purpose. A decision was made to move the HVTF to the Navy's radio transmitter facility at Dixon, CA. Preparations were made at Dixon, and Forestport was operated until February 1997. At that time, the high-voltage portion of the facility was dismantled and transferred to the Navy at Dixon.

The remaining equipment at the facility was redistributed to other Air Force and Navy projects, and the facility was turned over to caretaker status. One large piece of equipment remained, the 1200-foot tower. It required continuous maintenance to assure its mechanical integrity and to maintain the aircraft warning lights needed to prevent collisions. With no future R&D need, the decision was made to sell the tower and have it removed from AFRL property. It had been hoped that the tower, which was in excellent mechanical condition, could be sold, dismantled, and reused at another location, and indeed it was sold at auction to a bidder with that end in mind. Unfortunately, that bidder defaulted on his purchase. No other bidders were interested in removing the standing tower.

It was decided that the tower would be more valuable as scrap steel on the ground than as a standing tower. AFRL's Realty Officer worked with the 10^{th} Mountain Division to conduct a demolition training exercise, using the tower as the target. Coordination with the State of New York, the counties of Herkimer and Oneida, the towns of Forestport and Ohio, Niagara Mohawk Electric Power, police, fire, ambulance and highway departments was accomplished to bring the tower down successfully on 21 April 1998. The 772 tons of scrap steel were sold to CAP Scrap Metal, Frankfort, NY, for recycling.

Appendix 5C Litz Wire Current Limits

BACKGROUND

Litz cable is composed of a large number of fine strands of wire, each of which is insulated. The strands are woven in such a way that any strand can occupy essentially any possible position within the cable with equal probability. Thus, the inductance of each strand is the same and the current is equally distributed. Use of this type of wire reduces skin effect and proximity effect loss so that the resistance is nearly the same as the dc resistance. This type of wire is used at VLF and LF to make very low loss inductors having Qs as high as 3500.

There are several configurations for Litz wire. Usually, several bunches of straight, small-diameter strands are twisted together to make bundles. Then some numbers of bundles are woven to make larger bundles, and the larger bundles are woven to make the final cable. The cable is usually coated with some form of insulation. The designation for Litz usually consists of a series of numbers specifying the size and number of strands per bundle and the number of bundles. For example the notation 3/10/40/38 means

40 no. 38 wires per small bundle,
10 small bundles per larger bundle, and
3 larger bundles make up the cable.

This particular Litz cable has a total of 3 x 10 x 40 = 1200 strands of no. 38 wire. In many cases, the Litz cable is hollow and filled with jute or some other non-conducting fiber. Sometimes the individual bundles are hollow. Figure 5C-1 gives some example Litz cable cross-sections. The New England Electric Wire Corporation catalog shows seven different types of Litz cable construction.

RESISTANCE FORMULAS

Based on formulas given in (Watt, 1967) and assuming that the individual strand diameter is less than four skin depths, the following formula for the ac resistance of a straight isolated piece of Litz cable can be derived

$$R_{ac} = R_{dc}\left\{1+\left(\frac{f}{f_0}\right)^2\right\} \tag{5C-1}$$

where R_{ac} = Resistance of Litz cable at frequency f,
f = frequency,
R_{dc} = dc resistance of Litz cable, and
f_0 = breakpoint frequency for the Litz cable.

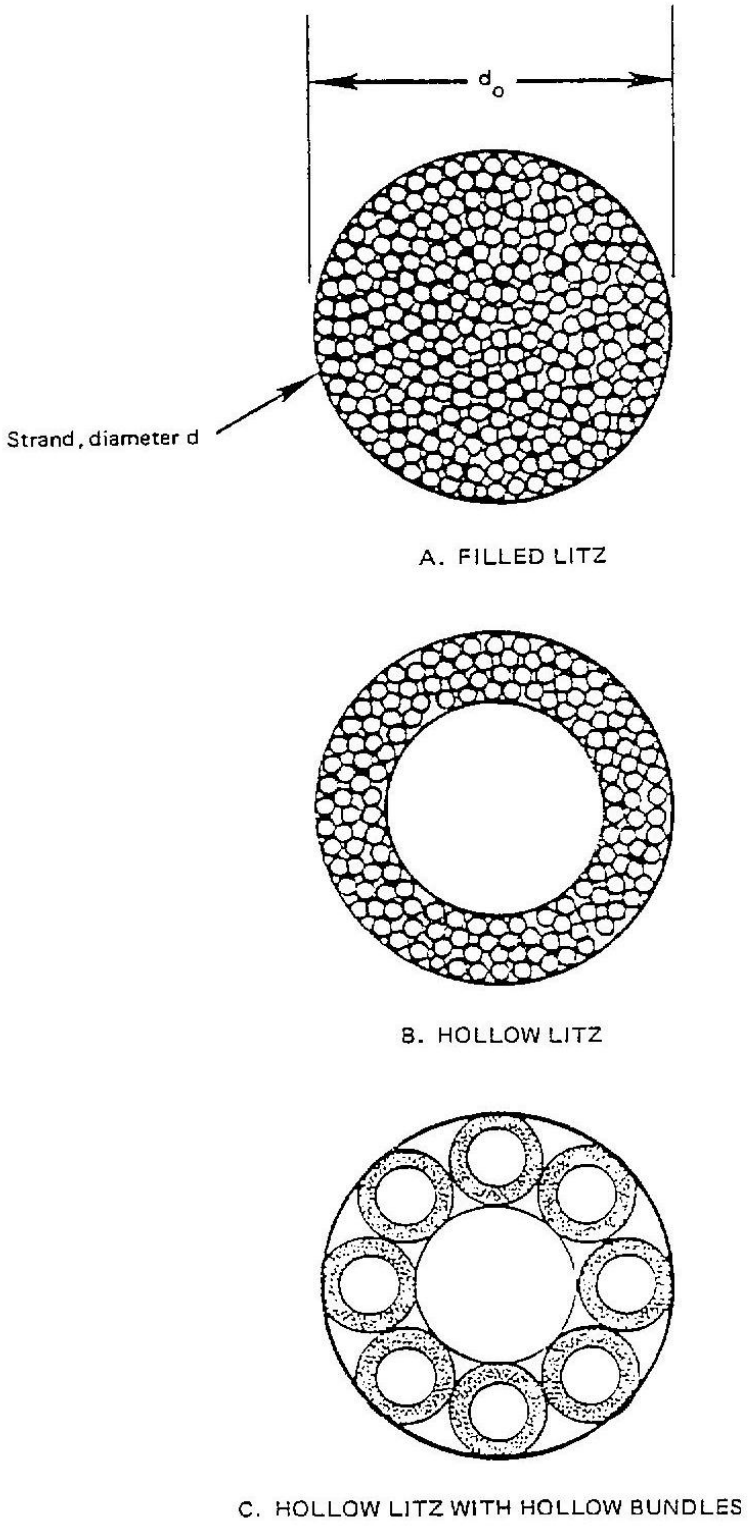

Figure 5C-1. Various litz cable configurations.

The breakpoint frequency for any particular Litz cable is given by

$$f_0 = \frac{76.48 \cdot d_0}{n \cdot d^3} \quad \text{Hz} \tag{5C-2}$$

or

$$f_0 = \frac{76.48}{P \cdot d \cdot d_0} \quad \text{Hz} \tag{5C-3}$$

where f_0 = breakpoint frequency (Hz),
d_0 = outside diameter of copper portion of Litz cable (inches),
d = strand diameter (inches),
n = total number of strands, and
P = Packing factor = area of copper/total area = nd^2 / d_0^2.

Note that the maximum value of the packing factor for filled Litz appears to be about 0.55 based on measurements of a few examples. (See Table 5C-1.)

The value of f_0 given by equations 5C-2 and 5C-3 is for a straight run of Litz cable. The DC resistance R_{dc} of Litz cable must account for the additional length of the copper strands due to spiraling. (Hanselman, 1972) gives a procedure for doing this. The additional length of copper can vary considerable depending upon the Litz construction. The Litz of example 5, Table 5C-1, was chosen for one Omega transmitter helix and has strands about 16% longer than cable length (ibid). A rule of thumb is a 2% increase for the first bundle plus an 8% increase for each additional full wrapping and a 7% increase for each additional hollow wrapping. Note that the first bundle consists of the several twisted bunches.

By this rule of thumb, the extra length of example 5 from Table 5C-1 would be

1st bundle	5/23/33	2%
Plus	6 Hollow	7%
Plus	15 Hollow	7%
Total		16%

Table 5C-1. Example Litz cables and their corresponding parameters.

Cable description	+ d	* d_0	P	f_0 (kHz)	** I_{max}
1. 3/ 10/40/38 full (1 200 strands)	3.965	.203	.4578	207.6	37.1 (18.9)
2. 3/ 10/20/38 full (6 00 strands)	3.965	.131	.5497	267.9	21.1 (9.4)
3. 5/ 3/40/36 full (6 00 strands)	5.0	.176	.4842	179.5	30.8 (15)
4. 2 0/13/60/33 hollow (1 8,200 strands)	7.08	3.0	.1014	35.5	993 (912)
5. 1 5/6/5/32/33 hollow (1 4,400 strands)	7.08	2.4	.125	35.9	887++ (721)

* Inches, not including outer insulation
+ mils
** amps rms
Note the values in parentheses are ratings based on 1000 circular mils per ampere.
++ Using strand length-to-cable length ratio based on calculations of (Watt, 1967). The calculation in (Hanselman, 1972) indicates the value should be 15.9%.

The length increase for Litz no. 3 (Table 5C-1) would be

3/40/36	2%
5 full	8%
Total	10%.

Figure 5C-2 shows a plot of Equation 5C-1 for fixed cable and strand diameter. Below f_0, the Litz resistance is approximately the same as the dc resistance. At f_0, the resistance is equal to twice the dc resistance. Above f_0, the resistance goes up as the square of frequency.

Figure 5C-3 is a plot of equation (5C-1) for various values of packing factor with fixed *d* and d_0. Note that both R_{dc} and f_0 vary inversely with *P*. Given a cable and strand diameter, Figure 5C-3 shows that for frequencies below the filled Litz breakpoint frequency f_{of}, the dc resistance dominates, and the minimum resistance is obtained with filled Litz. This minimum approaches R_{dc} (see f_1, Figure 5C-3). For frequencies above the filled Litz breakpoint frequency, the proximity effect dominates, and the minimum resistance occurs at a packing factor less than 1, such that at that frequency $R_{ac} = 2\ R_{dc}$. (See f_2, Figure 5C-3.)

An example plot of R_{ac} versus P is given in Figure 5C-4. It shows that in the frequency range where dc losses dominate, the minimum R_{ac} occurs when the packing factor is a maximum, corresponding to filled Litz. In the region where proximity losses predominate (above f_0), there is an optimum packing factor giving a minimum for R_{ac}. The minimum value of R_{ac} in this region is twice R_{dc}. The packing factor for minimum R_{ac} in this region is:

$$P_{\min} = .55\left(\frac{f_{of}}{f}\right)$$

where the packing factor for filled Litz has been assumed to be 0.55, and
f_{of} is the filled Litz breakpoint frequency for a given d and d_0.

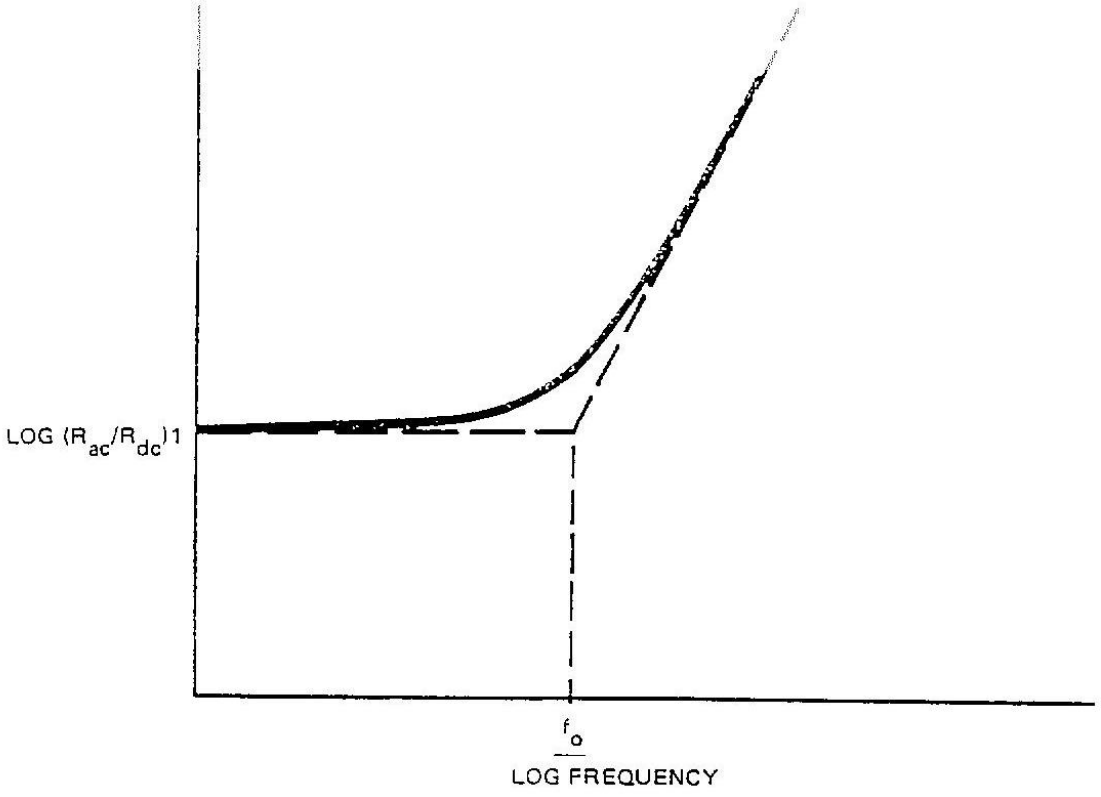

Figure 5C-2. Normalized R_{ac} versus frequency.

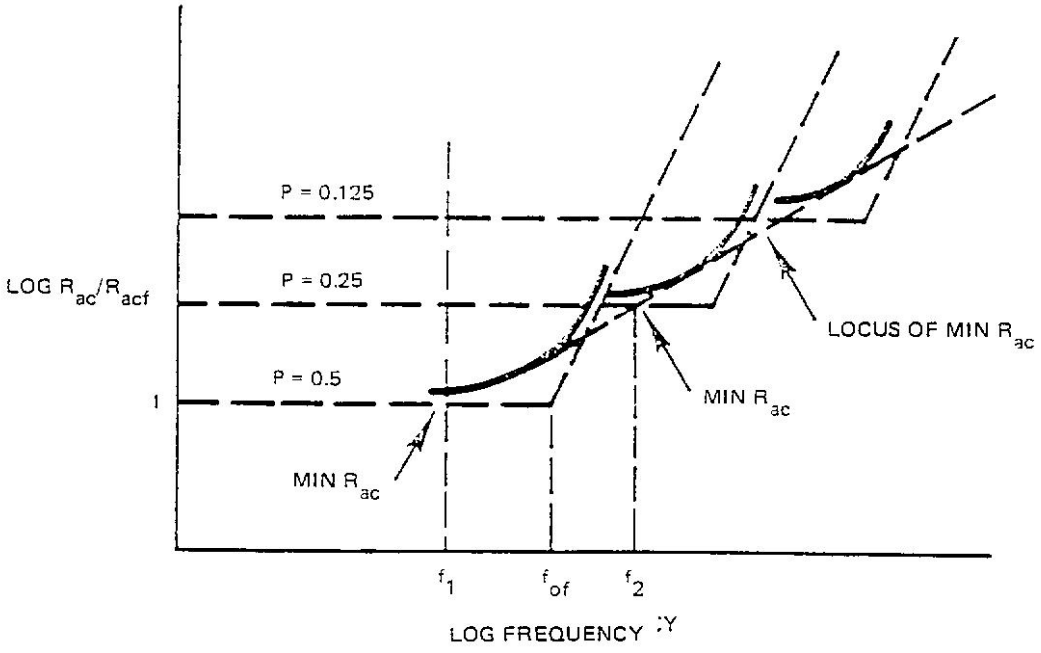

Figure 5C-3. Normalized R_{ac} for various packing factors.

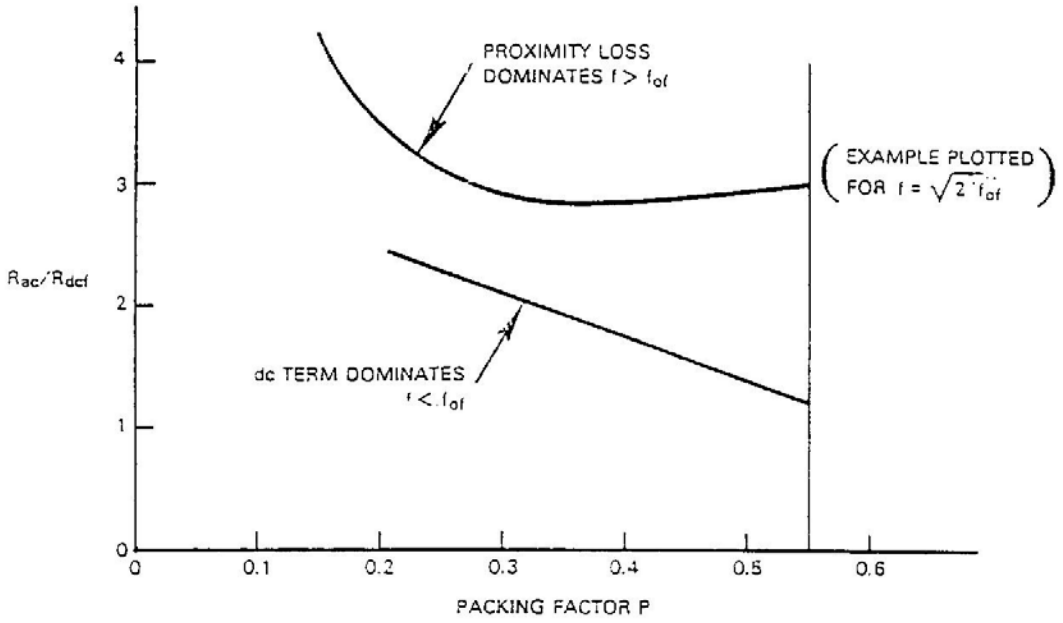

Figure 5C-4. Normalized R_{ac} versus packing factor for both frequency regions.

Similarly, in the proximity effect region, it can be shown that the minimum resistance is given by

$$R_{\min} = 1.1 R_{dcf} \left(\frac{f}{f_{of}} \right)$$

where R_{dcf} is the dc resistance for a filled Litz with diameter d_0.

If the Litz is used to make a solenoidal inductance, Equation 5C-1 still applies, but the breakpoint frequency must be reduced by the appropriate factor R, which depends on the geometry of the solenoid, i.e.,

$$f_b = \mathrm{R}\ f_0$$

where f_0 is breakpoint frequency for straight Litz, and

f_b is breakpoint frequency for Litz in a solenoidal coil

The factor R is given in Figure 5C-5.

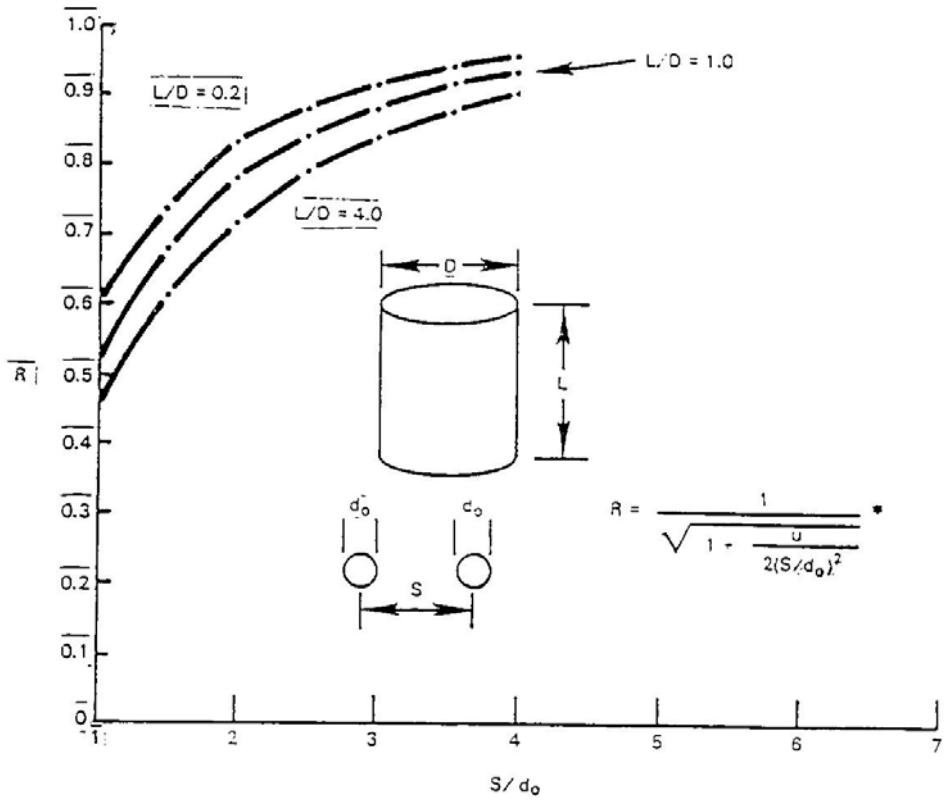

Figure 5C-5. Frequency reduction factor R for solenoidal inductors.
* For values of u see Watt.

EXAMPLES

1. There is a coil at SSC San Diego built by Lloyd Hansen that has the following parameters:

Litz 5/3/40/36 (full), d_0 = 1.176 in., f_0 = 179.5 kHz (Example 3, Table 5C-1)

Coil

N = 220 number of turns
D = 12 1/8 in. avg diameter
L = 55.5 in. length
S = 0.25 in. turn spacing

Measured

l = 3.0 mH inductance
Q = 488 @ 22.5 kHz => R_{ac} = 0.869 ohm
R_{dc} = 0.54 ohm

For this particular coil

$$L/D = 4.6 \qquad S/d_0 = 1.42$$

Hence from Figure 5C-5, R = 0.58 and thus f_b = 104 kHz.

$R_{dc} = 0.539,$ calculated using 10% for strand length increase.

At 22.5 kHz

$$R_{ac} = R_{dc} \left\{1+\left(\frac{22.5}{104}\right)^2\right\}$$

R_{ac} = 0.539 x 1.047 = 0.564 ohm calculated. The difference between calculated and measured resistance is probably due to contact resistance and external eddy currents.

2. The triple deck coupling variometer at Cutler consists of three variometers in parallel. One unit of this variometer uses 242 feet of Litz no. 4 from Table 5C-1, and has an estimated L/D $\cong$ 1 and S/d_0 $\cong$ 2. Thus, by calculation

f_0 = 35.50 kHz

and

f_b = 27 kHz.

R_{dc} for one of the three parallel units is 0.00319 ohm calculated using a 16% strand length increase factor, and the ac resistance is

$$R_{ac} = 0.00319 \left\{1+\left(\frac{17.8}{27}\right)^2\right\} = 0.00458 \text{ ohm}$$

Since all three units are in parallel,

$$R_{ac} = \frac{0.0458}{3} = 0.00153 \text{ ohm.}$$

If this number were doubled, as an outside limit for eddy current losses in the helix house walls and contact resistance, then $R_{ac} \leq$ 0.003 ohm total. A realistic estimate would be R_{ac} = 0.002, which gives a Q on the order of 2000.

CURRENT LIMIT

If the Litz cable configuration and the operating frequency are such that operation is at or below the breakpoint frequency, then $R_{ac} \leq 2R_{dc}$. For this case, a simple formula for the current limit can be derived if by assuming that 0.25 W/sq in. surface area can be dissipated safely [*], and using 12.33% increase of strand length over cable length due to spiraling:

$$I_{\max} = 600 \text{ d } (\text{n } d_0)^{1/2} \quad \text{A rms} \qquad (5C\text{-}4)$$

[*] Private communication with Andy Smith and Jim Hanselman indicates that this is a good design criterion.

or

$$I_{max} = 600 \left(P\right)^{1/2} d_0^{3/2} \text{ A rms} \quad \text{(5C-5)}$$

or

$$I_{max} = 600 \frac{\left(nd^2\right)^{3/2}}{\left(P\right)^{1/2}}$$

where d and d_0 are in inches.

The maximum allowable long-term currents calculated with the above formulas are given in Table 5C-1 for some example Litz cables. Note that these limits apply only below the reduced breakpoint frequency. Above this frequency, the maximum allowable current drops rapidly.

DESIGN FOR MAXIMUM CURRENT

In (Watt, 1967) a design criterion is mentioned whereby 1000 circular mils of copper per ampere are employed. From Table 5C-1, it can be seen that for the five examples given this method would give a very conservative rating, especially for the smaller cables. This rating method does not have universal application since it does not take into account the cable geometry. For example, a filled Litz containing the same amount of copper as no. 4 in Table 5C-1 would have the same rating by this technique. However, from equation 5C-6 it can be seen that the rating should be reduced to less than half, since *P* changes from 0.1 to 0.55.

The actual current limit, using the 0.25-W/sq in. criterion, increases as frequency falls below the breakpoint. This fact can be used to reduce cost of designs where the current requirement decreases with increasing frequency. Antenna current for power-limited operation at the upper end of the VLF band often has this type of variation.

The current rating for the Cutler triple deck variometers using Litz no. 4 from Table 5C-1 would have a current rating of 3 x 993 = 2979 A at 27 kHz (three units in parallel). However, at 17.8 kHz it should handle 1.39 times that amount, or 4141 A rms, considerably more than the 2500 A required for 1 MW antenna input power.

Appendix 5D Capacitor Stack Configuration

INTRODUCTION

This appendix discusses the configuration of the capacitor stack. The high-Q tuned circuit consists of an inductor (helix) and a capacitor. The capacitor must have the appropriate voltage and current ratings matching the helix and the correct capacitance to resonate the helix at the desired frequencies. Since capacitors usually are manufactured as small units, many of them need to be connected together as a series-parallel set to form the required capacitor. This combination of capacitors is sometimes called the capacitor stack.

CAPACITORS

Each individual capacitor has a fixed voltage and current rating. The VA rating of a series-parallel combination of capacitors is equal to the sum of the ratings of the individual capacitors. For example, by putting two capacitors in parallel, the capacitance doubles as does the current rating but the voltage rating remains unchanged. Thus, the VA rating is doubled. For two capacitors in series, the capacitance is half but the voltage rating doubles while the current rating remains unchanged. Again the VA rating is doubled. By using four capacitors, two stacks of two in parallel, the capacitance is the same as an individual unit and both the voltage and current rating are doubled, thus increasing the VA rating by a factor of four.

STACK VA RATING

The VA rating for the capacitor stack is the VA rating of the individual capacitors times the number of capacitors. The VA rating of the capacitor stack should be the same as the rating for the helix, otherwise the one with the smaller rating becomes the limiting component. The Forestport capacitor stack had the smaller VA rating and was the limiting component for most operations at Forestport.

STACK CONFIGURATION

A given number of individual capacitors can be configured in many different ways to provide the overall tuning capacitance for the high-voltage circuit. Selection of the capacitor stack configuration requires consideration of the individual capacitors available, their voltage and current ratings, and the total value of capacitance needed to add to the circuit to resonate with the inductance of the circuit at the desired frequency.

Some insight into the capacitor distribution design problem can be obtained by examining the maximum voltage that can be achieved by the Forestport tuned circuit for various capacitor distributions. In order to do this, we must consider each parameter that limits the voltage. There are four limits to consider. The first two are the overall voltage limits for both the helix and the capacitor stack. The other two limits are voltages that occur at the maximum allowable currents for both the capacitors and the inductor.

The helix voltage limit at Forestport was approximately 300 kV, independent of the capacitor distribution. The capacitor voltage limit is equal to the number of capacitors in series times the rating of the individual capacitors. At Forestport, the stack was 51 high for most configurations, giving an extended rating of 306 kV.

The maximum voltages as determined by the current limits are frequency dependent. These limits are calculated at the resonant frequency (capacitive reactance equals inductive reactance). The helix current limit at Forestport is nominally 150 amps based on the Litz wire. The current limit of the capacitors is determined by the number of capacitors in parallel times the current rating of an individual capacitor. For both these cases, the corresponding maximum voltage due to the current limit is equal to the maximum allowable current times the inductive reactance (equal to the capacitive reactance). The corresponding voltage limits are summarized in Table 5D-1.

Table 5D-1. Forestport tuned circuit voltage limits at resonance.

Limiting Parameter	Parameter Value Forestport	Calculated Voltage Limit	Voltage Limit at Forestport
Helix Voltage	300 kV	300 kV	300 kV
Helix Current	150 amps	$V = 150 \cdot X_c$	Freq dependent
Capacitor Voltage	6 kV/cap	$V = 6 \cdot m$ *	306 kV
Capacitor Current	20 amps/cap	$V = 20 \cdot n \cdot X_c$ **	Freq dependent

* m = stack height number of capacitors
** n = number of capacitors in parallel

One aspect of the design problem for the capacitor distribution can be illustrated by plotting the maximum voltage versus frequency for the various possible capacitor configurations. These voltage limits have been calculated using the Forestport helix and a nominal value of 255 of the plastic capacitors, distributed with from one to eight capacitors in parallel. The stack height is selected such that the total number of capacitors is the integer closest to 255, the actual number of capacitors in the Forestport stack. The calculated voltage limits have been plotted for two different helix configurations. The first helix configuration is when all the turns are included (Max L), and the second is where only the top 39 turns are included (Min L).

A plot of this voltage limit is given in Figure 5D-1. Note that the points on the figure are discrete in that only integer numbers of parallel capacitors are allowed. However, the points have been connected in the figure to facilitate identification of the different cases. In the figure, the integer next to the data points indicates the number of parallel capacitors for that data point. For example, the data points with the “5” next to them correspond to the actual case at Forestport, where the stack consists of five capacitors in parallel.

All four voltage limits are represented in Figure 5D-1, but it is important to understand that the actual limit is the lowest of the four calculated limits. The four limits for the case of maximum helix inductance are represented by the four upper leftmost curves in the figure. For this case, the figure shows that the capacitor voltage limit is lowest for small numbers of parallel capacitors. When the number of parallel capacitors reaches five, the capacitor voltage limit and the helix voltage limits are approximately equal at about 300 kV. For configurations with five or more capacitors in parallel, the helix voltage limit determines the maximum achievable voltage of 300 kV rms.

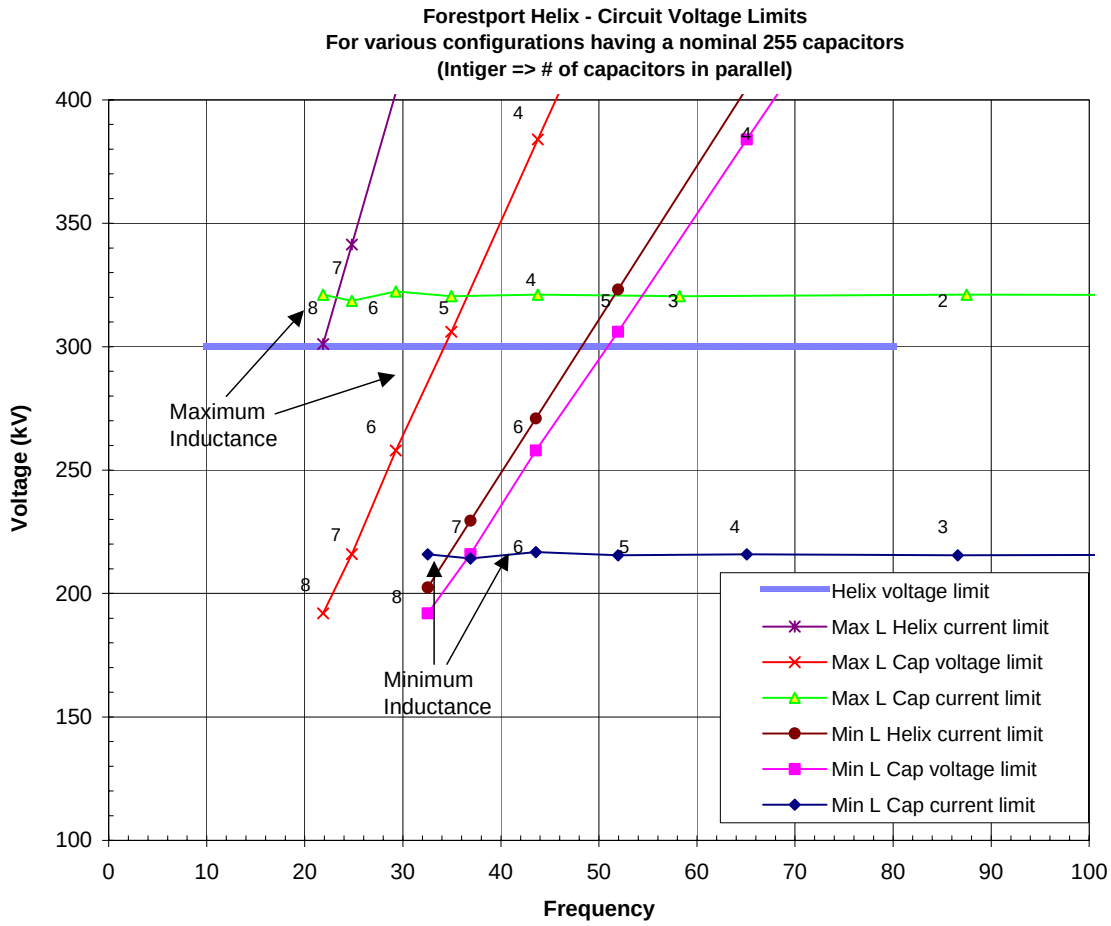

Figure 5D-1. Voltage limitations for various capacitor configurations, Forestport helix.

For a fixed total number of capacitors of the same size, the total capacitance of the stack increases as the number of parallel capacitors squared (n^2). The resonant frequency of the circuit is inversely proportional to the square root of capacitance. The combination of these two things results in the resonant frequency being approximately proportional to the inverse of the number of parallel capacitors. Thus, for a fixed number of capacitors, lower resonant frequencies can be achieved by placing more capacitors in parallel. However, this reduces the height of the stack and thus the maximum voltage the capacitors can support.

It can be seen from figure 5D-1 that for the lowest frequency, the highest voltage that can be developed for the Forestport helix occurs when the inductance is maximum. The corresponding configuration of the 255 capacitors has five capacitors in parallel. This is an optimum design in the sense that the voltage limits for both the helix and capacitor stack are nearly equal. This is the reason that capacitor configuration was chosen for the Forestport high-voltage circuit. The calculated resonant frequency for this configuration is approximately 35 kHz. The actual resonant frequency was closer to 30 kHz when testing due to the additional capacitance of the high-voltage circuit components and the test object.

Additional design considerations for the capacitor configuration involve the physical placement of the configuration. These considerations led us to build the 51-high capacitor stack as three separate stacks.

The minimum helix inductance voltage limits have also been plotted in Figure 5D-1. The four limits for this case are represented by the four lower right-most curves in the figure. Note that the helix voltage limit (300 kV) is common to both cases. The plots are similar to the plots for maximum inductance except that the frequencies are higher and the capacitor current-limited voltages are significantly lower. These latter limits dominate for most frequencies. The capacitor current-limited voltage determines the rating for all configurations with seven or fewer capacitors in parallel.

The figure shows that for a fixed number of capacitors, the capacitor current-limited voltage is nearly independent of the number of capacitors in parallel. This is because the total capacitance for a stack with a fixed number of capacitors is proportional to the square of the number of capacitors in parallel (m). This results in the resonant frequency being proportional to $1/m$. For this case, the reactance of the capacitor stack at resonance is proportional to $1/m$, while the current limit is proportional to m. The product of maximum allowable current times the reactance gives the current-limited voltage, which is constant. The analysis above assumes no external capacitance. Following through with this analysis gives the following equation:

$$V_{IC} = I_0 \cdot \sqrt{\frac{n \cdot L}{C_0}}$$

where V_{IC} is the current limited voltage for the stack,
I_0 is the current limit for an individual capacitor,
L is the inductance of the helix,
C_0 is the capacitance of an individual capacitor, and
n is the total number of individual capacitors in the stack.

The equation indicates the current-limited voltage is independent of m, the number of individual capacitors in parallel. It is proportional to the square root of the total inductance and the total number of capacitors. It is inversely proportional to the square root of the capacitance of each individual capacitor given the capacitors have the same voltage limit. The actual limit differs slightly from this due to the effect of the added stray capacitance and the capacitance of the test object.

Examination of the voltage limits for the maximum inductance case in figure 5D-1 shows that the voltage limit could be 300 kV (helix voltage limit) for frequencies up to 80 kHz or higher if the stack were reconfigured to have one, two, three, or four capacitors in parallel. Reconfiguration of the stack from five in parallel to two or three capacitors in parallel in order to change frequency was not practical and this was not done at Forestport. Thus, with the stack consisting of five capacitors in parallel, the maximum voltage was somewhat less for frequencies higher and lower than 30 kHz. For example, Figure 5D-1 shows that with the stack of five capacitors in parallel (Imax = 20 amps), and changing frequency by using the minimum helix inductance, the voltage limit is slightly in excess of 200 kV at a frequency of about 52 kHz.

LOWER FREQUENCY OPERATION

There were some practical reconfigurations for the Forestport capacitor stack that could be used to change the operating frequency. For example, shorting out one or two of the three-capacitor stacks lowers the resonant frequency. This was simple and could be accomplished in a few minutes. The bottom and middle sections consisted of 5 x 18 capacitors. The top section consisted of 5 x 15

capacitors. Denote the total capacitance of the 5- x 51-capacitor stack by *C*, then the capacitance of the stack with the bottom section shorted is $(51/33)\cdot C \cong 1.54\cdot C$. The maximum voltage for this configuration is reduced by the factor 33/51. With both the bottom and middle sections shorted, the total capacitance is $(51/15)\cdot C \cong 3.4\cdot C$. The maximum voltage for this configuration is reduced by the factor 15/51. The resonant frequency is inversely proportional to the square root of the capacitance. With only the bottom stack shorted out, the calculated operating frequency is approximately 28 kHz and the voltage limit is about 180 kV. When the bottom two stacks were shorted, the calculated operating frequency is approximately 20 kHz and the voltage limit is about 90 kV. For both of these cases, the test resonant frequency is lower because of the capacitance of the test object.

HIGHER FREQUENCY OPERATION

Another practical capacitor reconfiguration for Forestport involved disconnecting four of the five parallel stacks of capacitors. This leaves the stack in a configuration having 1 x 51 capacitors. A 1 x 8 extension was usually added to the top to create a configuration of 1 x 59 capacitors. This extension can be seen at the top of the high-voltage stack shown in Figure 5-10. This configuration has a calculated capacitance of $(59/51)\cdot(1/5) \cong 0.23\cdot C$. This configuration was used for measurements at frequencies in the neighborhood of 60 kHz, using a portion of the helix inductance.

CHAPTER 6 CORONA ON WIRES, PIPES, AND CABLES

INTRODUCTION

This chapter presents measurements of the corona onset level on cylinders (wires, pipes, and cables) at VLF/LF made at Forestport over a several-year period. The measured data have been processed and analyzed and design curves developed. These are presented in later sections of this chapter.

There is a considerable body of literature addressing corona onset at power system frequencies. The literature indicates that the critical voltage and surface electric field at corona onset are dependent on many variables. These include the physical configuration of the object and surroundings, atmospheric environment parameters, and the frequency. We have investigated these effects at VLF/LF. Measured data directed at determining the effect of each parameter are presented along with a discussion of the results in this chapter. The discussion includes comparison to 50/60-Hz data where possible. The data from the VLF/LF measurements have been processed to develop formulas and curves that can be used for the practical design of high-power VLF/LF transmitting systems.

Many, but not all of the effects observed at power system frequencies are the same or similar at VLF/LF. For example, for cylindrical conductors the most important parameter is the cylinder diameter (see Chapter 2). The experimental results and comparison to 50/60-Hz data verified that the effect of both diameter and air density are the similar but not always identically the same at VLF/LF as at power system frequencies. The measurements also showed that effects of surface conditions (roughness and/or coating of oil, water, or ice) are important and similar in both frequency ranges. Under some conditions, the type of material can also have a limited effect.

The atmospheric environmental factors that affect corona onset include atmospheric density and composition, as well as residual or local ionizing sources. Materials in the atmosphere often have an important effect, typically considerably reducing the voltage level for corona onset. These materials include water vapor, raindrops, snowflakes, pollen, molds, large complex ions, salt particles, insects, and blowing dust and sand. Details of typical atmospheric parameters are described in Chapter 3. As mentioned above, the VLF/LF data indicate that the air density effect is the same as that observed at power system frequencies (50/60 Hz). Our measurements did not specifically address the effect of airborne impurities. However, when these were present at Forestport, the effect was similar to that observed at power system frequencies in that their presence reduces the corona onset voltage significantly.

One series of measurements was directed toward determining the effect of humidity at VLF/LF. This effect was found to be quite different at VLF/LF than at power system frequencies. The presence of humidity increases the corona onset voltage at power system frequencies while humidity decreases the corona onset voltage at VLF/LF. The magnitude of the effect depends on frequency and diameter as well as the amount of humidity present. There is a different mode of breakdown at higher frequencies and it is likely that there is a diameter-dependent critical frequency at which the breakdown phenomena changes from low-frequency mode to high-frequency mode, but we do not have enough data to quantify this effect.

PARAMETERS AND CONFIGURATIONS MEASURED

The primary parameters that were examined are:

- Wire Diameter
- Atmosphere – Environment
  - Air Density
  - Humidity
  - Dry - Spray-wet (Simulated Rain) and Rate of Fall
- Frequency
- Surface Conditions
  - Stranded
  - Smooth
  - Rough
  - Wet - Dry - Ice
- Wire Slope
  - Horizontal
  - Vertical
  - Cages (Bundles)

The measurements to investigate these parameters were made over a several-year period at the Forestport HVTF. The test facility, calibration procedures, and test methods are described in Chapter 5.

The test configurations consisted of wires, pipes, and cables configured and located as follows: (1) horizontal outside, (2) horizontal inside, (3) sloped outside, and (4) vertical inside. A brief description of these test configurations is given below.

Horizontal Outside

The outside corona testing on cables and pipes was done using variations on a simple test setup. The horizontal test configuration used in the 1989 tests is shown in Figure 6-1. A top view of the layout is shown in Figure 6-2. The outside test samples were fed through the open roll-up door as shown in the picture. The samples were all about 20 feet (6.1 m) long and about 8 feet (2.4 m) above the ground plane. The feed trunk, shown on the left side of Figure 6-2, can be seen coming through the roll-up door on the right side of Figure 6-1. Vertical insulators were used to support the cable at one or both ends. The large cement anchor block located beside the test cell door was used to anchor one end of the cable with an insulator between it and the cable. The cable was pulled taut by an insulated halyard, shown extending off to the right in Figure 6-2, (left in Figure 6-1). It connected to a utility pole located about 100 yards from the test cell door. The electric winch is located near the base of the utility pole. Figure 5-3 provides an overview of the outside test area including the anchor block, utility pole, and winch.

The outdoor ground system consisted of the buried ground system associated with the Forestport tower, augmented by aluminum sheets and a hardware cloth extension. The antenna ground system consisted of 360 buried wires radial to the tower base located just behind the helix house. The 4-foot by 8-foot aluminum sheets were placed directly under the wire for the horizontal-wire tests and are shown Figure 6-1. This ground was extended using a hardware cloth wire screen illustrated in Figure 6-2 (not in place at the time of the picture shown in Figure 6-1). This screen was approximately 30 feet wide, centered on the test sample. The aluminum sheets were laid directly under the wire on top of the hardware cloth.

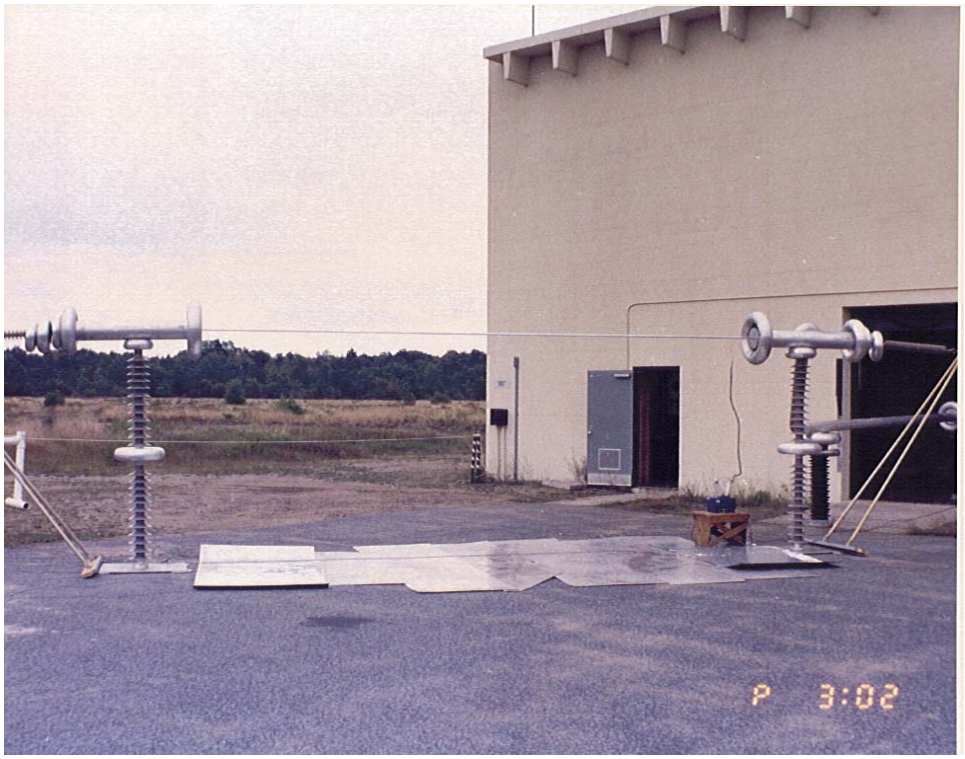

Figure 6-1. Forestport outside horizontal test cell.

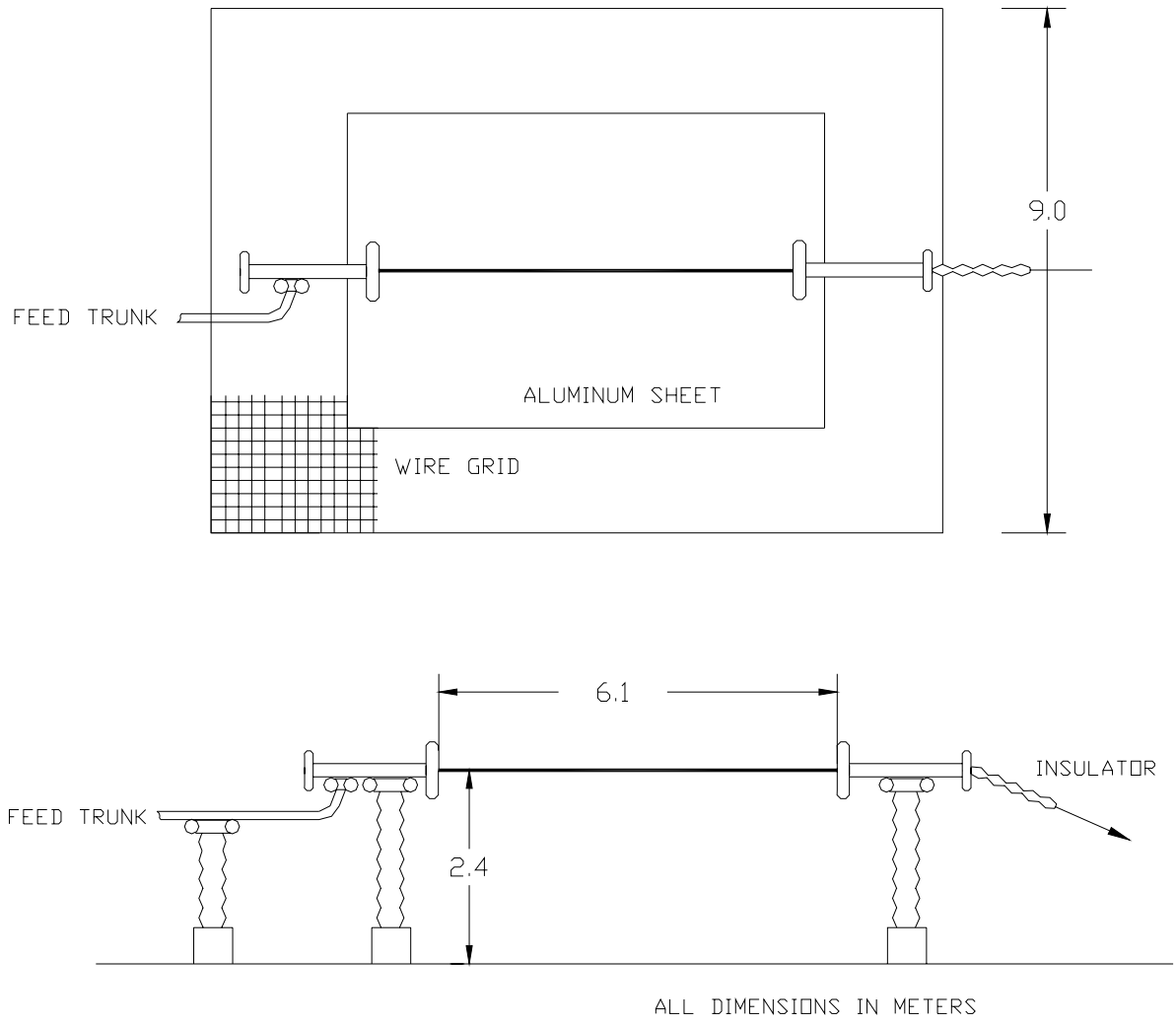

Figure 6-2. Forestport outdoor horizontal test cell.

Corona rings (4-inch minor diameter by 8-inch major diameter) were used at the ends of the test samples to keep the shackles and other mounting hardware from going into corona. The high voltage was fed through the test cell door and connected to the test sample at the corona ring nearest the helix house. The corona rings and the feed connection tend to reduce the field at the center of the test sample, while the grounded building walls and halyard tend to increase the field. These effects complicate the use of computer programs to accurately determine the surface electric field at the center of the test sample. For some of the measurements, a 10-foot extension of 1-inch pipe was added to the ends of the test sample in order to reduce the complicating effects and increase the accuracy of the calculations.

Horizontal Inside

Horizontal outside tests allowed the best geometry to expedite calculation of the exact value of the electric field on the cable or pipe and also allow operation at higher voltages, approaching levels expected in operational antenna systems. However, outside testing does not allow control of the environment. For example, visual corona onset detection requires operation at night. In upstate New

York, dew usually forms during the summer evenings, and the humidity is at or near 100%. In that case, condensation often forms on the surface of the test sample, greatly reducing the corona onset voltage. Thus, it is virtually impossible to measure corona onset voltages outside for dry conditions at Forestport, except in winter.

An inside test setup using horizontal test samples was developed to check the effects of air density and humidity for dry conditions. Most of the inside measurements were made with a set of horizontal test samples 15 feet long, supported on the ends by vertical insulators approximately 48 inches high. The ends of the test samples and insulators were shielded by a double set of corona rings stacked on top of the insulators. The high-voltage source was connected to the top of the corona ring closest to the helix house using a 6-inch diameter aluminum pipe. This pipe was oriented in the plane perpendicular to the test sample and entered the helix house at 45^{o} with respect to ground. A few measurements were made with a similar test configuration using 10-foot samples and slightly lower insulators. The inside horizontal test setup is shown in Figure 6-3, and a drawing of the geometry used for the computer analysis is given in Figure 4-15.

Figure 6-3. Forestport inside horizontal test cell.

The samples tested consisted of a set of smooth pipes with diameters varying from 0.5 to 2.0 inches and stranded cables with diameters varying from 0.25 to 1.25 inches. All samples had minor surface irregularities and scratches due to handling, but all protrusions were polished off prior to testing. The remaining scratches and irregularities were actually intrusions, which do not greatly increase the surface field.

Sloped Outside

Many of the U.S. Navy VLF/LF antennas are umbrella top-loaded monopoles. The top load for this type of antenna consists of cables suspended at angles around 45° from the vertical. The formation and falling of water drops from a cable is a function of the suspension angle. For U.S. Navy VLF/LF applications, it is important to determine the effect of the suspension angle on the corona onset level. This outside test configuration could suspend 20-foot samples at angles adjustable around 45° from horizontal. A drawing of the sloping wire test setup is given in Figure 4-16. The 20-foot test samples used for the outside horizontal tests were used for the sloping wire tests. The configuration was similar to the horizontal test configuration, but the suspension point was moved higher on the utility pole to give the desired angles. The ground system was the same as used for the horizontal outdoor tests.

Vertical Inside

The vertical inside tests were done using vertical coaxial geometry having an outer grounded cylinder and with the energized test sample in the center. A diagram of the vertical test cell is shown in Figure 6-4. The high voltage was applied to the cell via a large cylindrical feed line shown in the upper right-hand portion of the figure. The large cylindrical cage surrounding the sample consisted of 0.25-inch hardware cloth supported on a PVC pipe frame. The outer diameter of this coaxial cell was 3.2 meters, its height was 3.6 meters, and the test sample was 1.98 meters long.

The vertical test cell is shown in Figure 6-5. One of the sprayers for wet testing can be seen on the right-hand side of the figure. During the 1985 tests, the shield ring at the upper end of the sample was 0.61 meter in diameter and was made of aluminum pipe 0.15 meters in diameter. The lower end had a similar ring plus a larger, 0.81 by 0.2-meter, shield immediately below it. For the 1989 tests these rings were replaced with single smaller 0.36- by 0.064-meter rings; one at the top and one at the bottom. These rings were too large and the test cell was too short for the field at the center to be accurately given by the simple coaxial formula. Correction factors were developed using the computer program and verified by neon light field sensor measurements as described in Chapter 7.

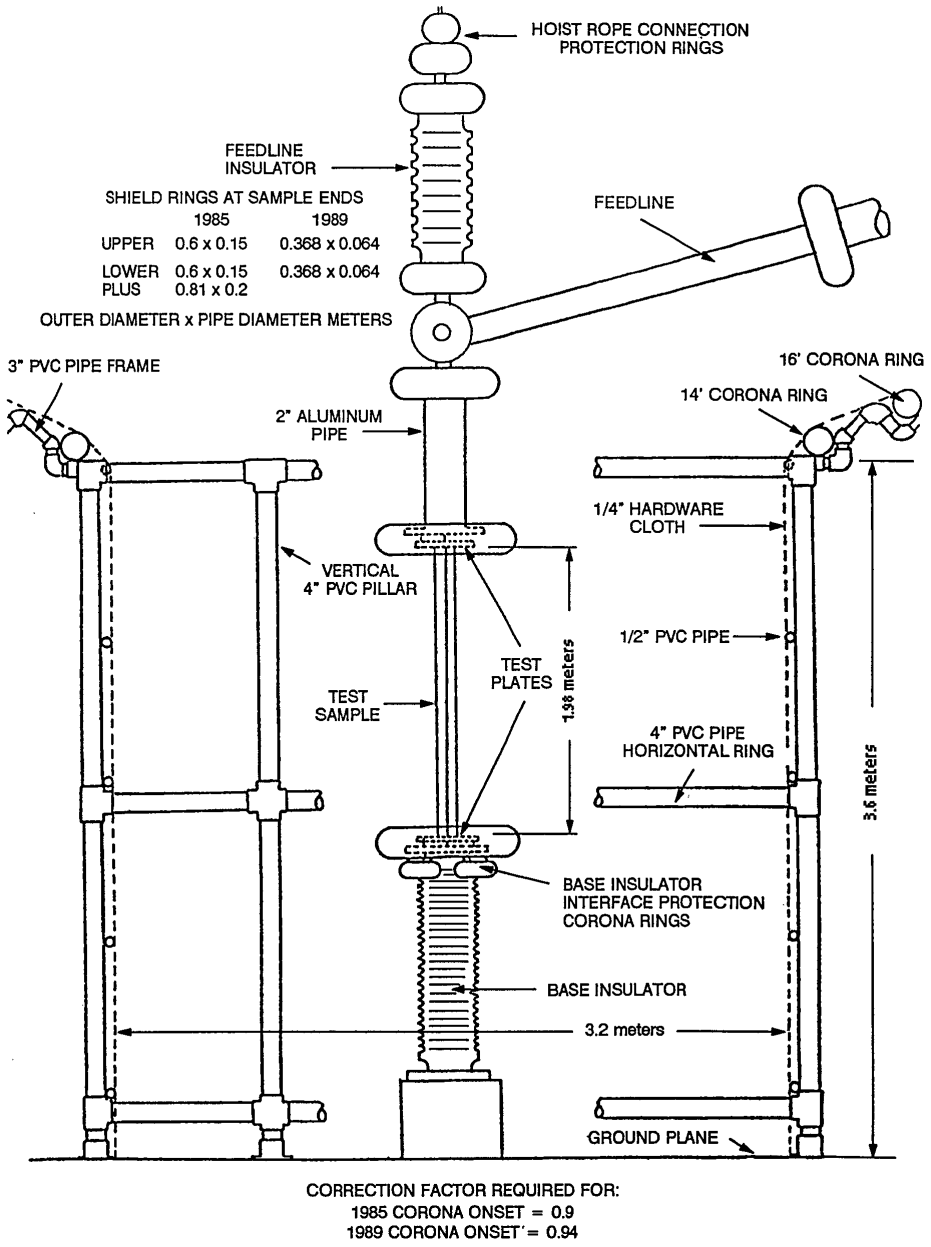

Figure 6-4. Vertical high-voltage corona test cell.

Figure 6-5. Forestport vertical test cell.

VISUAL CORONA PHENOMENA – CYLINDRICAL CONDUCTORS

Corona Detection Method

Visual observation was the method of corona detection used for all measurements on cylindrical conductors. A description of the corona phenomena observed on cylindrical conductors is given in the next section. For spray-wet conditions, several observable phenomena could be called corona onset. For the measurements at Forestport, we used the point at which the purple streaks contacted the conductor and became continuous as the definition of wet corona onset. The continuous purple streaks starting from the conductor were named purple mini-flares and are described in the section on wet corona.

As discussed in Chapter 1, it has been known since the early days of radio that there are differences in the nature of RF corona at VLF/LF compared to that at power system frequencies (Whitehead & Gorton, 1914, p. 972). For example, RF corona causes vibration in smaller wires while this does not occur at 60 Hz (ibid, p. 971). In particular, RF corona contains considerably more power than at power system frequencies (Ryan & Marx, 1915). For example, at 60-Hz, continuous corona was observed on needle points without damage, whereas at RF the points melt (Clark & Ryan, 1914, p. 987). However, at the onset level, there is little difference in the visible phenomena between power system frequencies and RF, especially for smaller diameter wires, except that at RF the corona is brighter. At levels well above onset, there are significant differences in the corona phenomena for RF and power system frequencies.

Dry

The visible phenomena of dc corona for wires depend on the polarity. The convention in the literature is that the polarity of dc corona refers to the polarity (positive or negative) of the electrode on which the corona occurs. At levels not greatly exceeding onset, positive corona forms a continuous bluish white sheath along the wire. Negative corona forms small reddish purple white beads that are regularly spaced along the wires.

The voltage level at which the corona appears depends on the polarity and wire size. There is evidence that negative corona forms first (lower voltage than positive corona) on intermediate sized wires having diameters between 7 $x10^{-3}$ cm and a diameter on the order of 0.1 cm, with positive corona forming first for wires with diameters smaller and larger than that (Watt, 1967, p. 103). Recent dc measurements made on smaller wires, all having diameters less than 0.6 cm indicated that negative corona forms first for dry conditions (Schukantz, 1993).

At 60 Hz, the corona phenomena observed is the same as at dc. However, since both positive and negative voltages are present, the polarity of corona observed at onset depends on the wire diameter. For example, Smith (1963) observed at 60 Hz that negative corona forms first on smaller wires but positive corona forms first on larger wires. When the voltage is above onset level, corona of both polarities is observed. The eye integrates both phenomena and sees a superposition but they can be observed individually by taking pictures with a stroboscope synchronized to the voltage waveform (Peek, 1929).

At VLF/LF, the corona phenomena observed at onset depends on wire size similar to 60 Hz but there is frequency dependence. For example, Smith (1963) observed at VLF that small wires (< # 18 AWG) exhibited negative corona similar to that at 60 Hz, but larger wires (> # 10 AWG) exhibited positive corona. However, the positive corona at VLF/LF was different from that at dc or 60 Hz in that at onset it immediately formed reddish “purple streamers, which had a tendency to branch.” This is consistent with observations at Forestport. Figure 6-6 shows the Forestport inside test cell setup for horizontal testing with a sample exhibiting dry purple streamers. In addition, observations indicate that this type of positive corona forms first on larger diameter wires at higher frequencies (consistent with Kolechitskii, 1967*)*

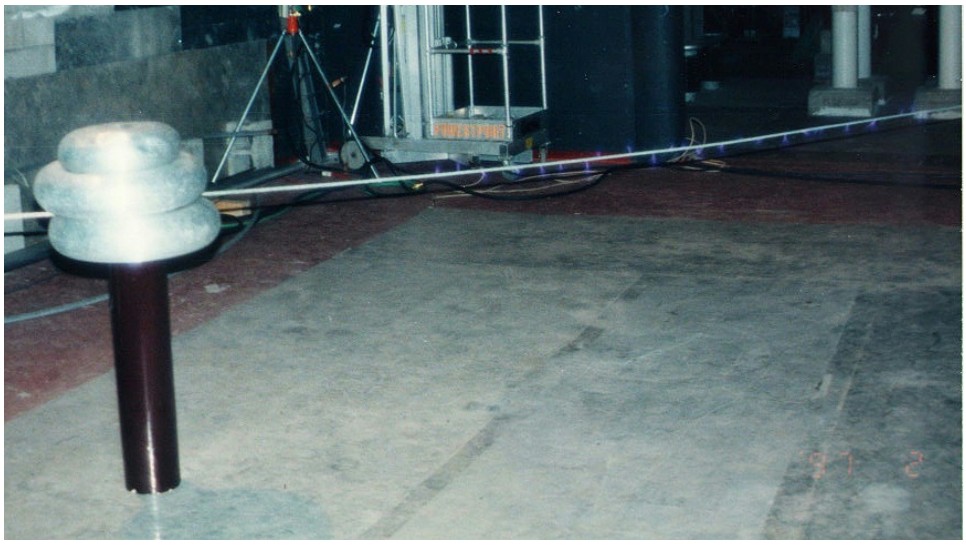

Figure 6-6. Purple streamers (dry).

At the VLF/LF frequencies tested and with practical wire sizes for antennas (>0.25- inch diameter), corona onset (dry) always consisted of the purple streamers corresponding to positive corona. These streamers have a bright whitish purple base on the wire that is slightly wider than the streamer. The streamers have lengths several times the wire diameter when they first form. Typically, streamers are spaced regularly along the wire at distances somewhat greater than their length. A sizzling or hissing noise accompanies the purple streamers. For larger diameter wires, the onset purple streamers are longer and louder and develop a brighter base. For larger pipes, corona starts in the form of a full flare described in the section on wet corona below.

Smaller wires exhibit negative corona first (especially at lower frequencies). As the voltage is increased, the first phenomena observed are small reddish purple beads of visible light regularly spaced along the wire. The number of spots increases with increasing voltage. This is similar to dc or 60 Hz, but at VLF/LF the corona is considerably brighter due to the increased energy. Positive corona forms first as described above for larger wires and/or higher frequencies. However, if there are surface irregularities on the larger wires, negative corona in the form of small white spots will form at these locations, especially at small points. At VLF, these irregularities burn off fairly quickly due to the increased energy in the corona, conditioning the wires.

Wet

Falling snow appears to lead to the lowest corona onset voltage (Peek, 1929, p 202). However, for U.S. Navy applications, rainfall (spray-wet) conditions have been selected for the limiting design case for outdoor applications.

The description of dry corona phenomena at VLF/LF is consistent with that given in the literature for 60 Hz. However, there is little in the literature describing wet corona phenomena at 60 Hz. Consequently, the following detailed description of the breakdown phenomena for spray-wet conditions is based on Forestport testing. It applies whenever there is enough precipitation to form drops on the bottom of the wire, with at least an occasional drop falling away from the wire. The description and drawings given in Figures 6-7 through 6-11 are consistent with the description and drawings of wet corona phenomena at 16.5 kHz given by Larionov and Tarasova (1989).

The nature of electrical breakdown for spray-wet conditions is different than for dry conditions. Many of the breakdown phenomena observed for wet conditions do not occur for dry conditions. In general, the breakdown phenomena occur at a much lower voltage for spray-wet conditions than for dry conditions. However, when the voltage is increased to the dry breakdown level, the phenomena observed are essentially the same for both cases.

All the phenomena observed on the larger wire diameters used for spray-wet testing corresponded to positive corona. This is consistent with measured data at dc under spray-wet conditions, which shows that positive corona forms first on wires with diameters larger than 0.6 cm and negative corona forms first on smaller wires (Schukantz, 1993).

Drop Distortion

The first phenomena observed is that the drops on the bottom of the wire are constricted (squeezed) by the electrostatic force and hang down farther from the cable when the wire is energized with a significant voltage. The amount of the constriction increases with voltage. Often when the voltage is increased enough, the constriction forces the larger drops off the cable (Figure 6-7) (Richards, 1974)

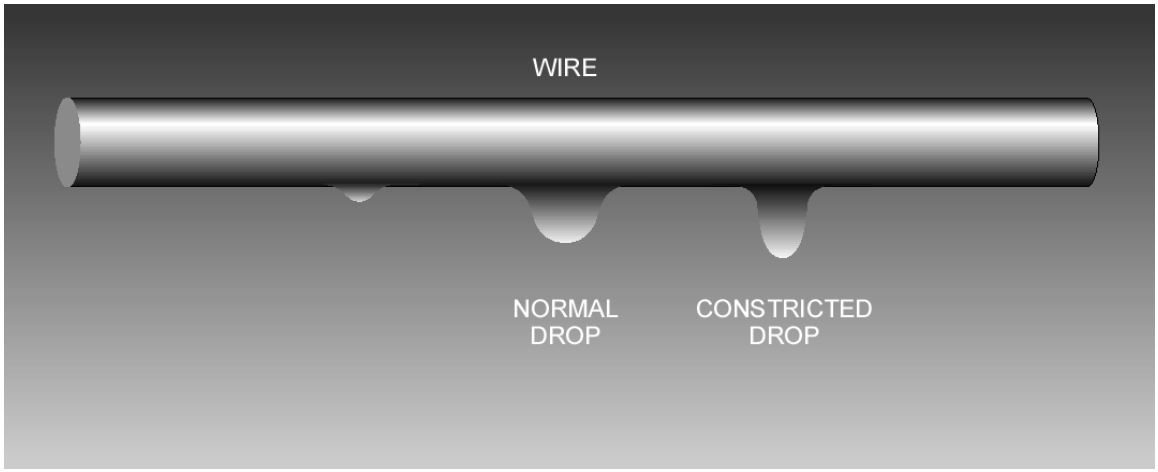

Figure 6-7. Water drops on energized wire.

Sparklers

The second phenomena observed as the voltage increases is very dim and can only be seen in the dark with dark-adapted vision. Under these conditions, small dim white intermittent flashes can be observed a short distance below the cable (approximately 0.25-inch). These flashes appear to be on both sharp ends that occur just as the drop separates. The brightest part of this corona appears on the falling drop, a short but finite distance below the separation point. This phenomenon occurs at very low levels of surface electric field (approximately 0.3 kV/cm equivalent on the surface of the wire, calculated with no water present).

As the drop starts to separate from the wire, it forms the classical teardrop shape with the pointed end toward the cable (Figure 6-8.) As separation occurs, the drop carries a charge corresponding to the applied RF voltage on the electrode at the time of separation. As the drop falls, it will rapidly reshape into a flattened spherical shape due to the combination of surface tension and aerodynamic forces. This reshaping takes some time so the drop remains teardrop-shaped for a period of time after separation. The glowing phenomenon is attributed to electrical breakdown of the air (corona) caused by the intense electric field near the pointed end of the drop. This field is due to the charge on the drop, the shape of the drop, and the charge on the wire. This field is nearly doubled when the RF voltage on the wire reverses polarity, which occurs one half RF cycle after separation. The glow is observed to appear at a distance below the separation point consistent with the distance the drop falls in one half RF cycle.

The glow only occurs for an instant on a falling drop shortly after it separates from the wire and hence appears as an intermittent flickering below the cable as water drops fall off. It also occurs for an instant on the sharp end of the portion of the water remaining on the cable (Figure 6-8). We call this phenomenon “sparklers,” and it is the first breakdown phenomenon that occurs as the voltage is increased. If there is enough precipitation to form water streamers, this glow can start somewhat down the water streamer at the point where it starts to break up into individual drops (Figure 6-9, left side). As the voltage is increased, the white glow associated with each drop grows brighter, longer, and wider but remains separated from the wire.

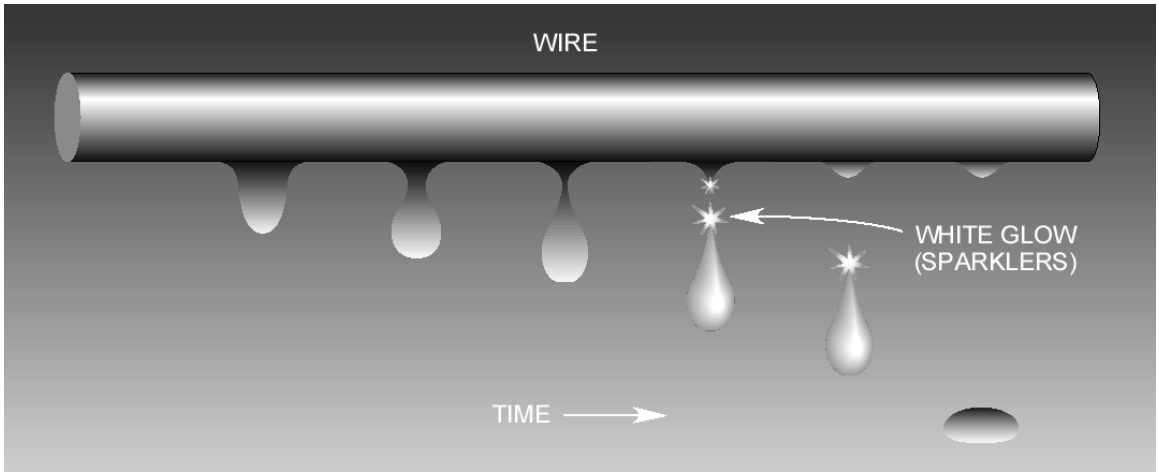

Figure 6-8. Falling drop sequence.

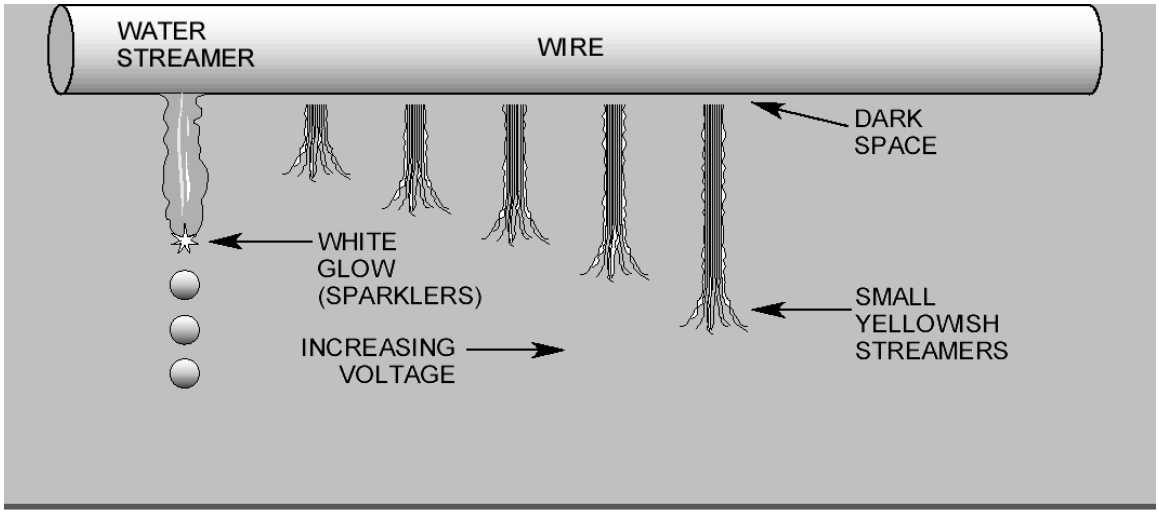

Figure 6-9. Purple streaks.

Purple Streaks

As the voltage is increased further, the sparklers grow in length. When they get to be about 0.50-inch long, they start to turn faintly purple. As the voltage is increased, these become longer and brighter purple. At this level, they are 1 to 2 inches long, still separated from the cable by about 0.25 inch and only occur when a drop falls. They also make a definite hissing or spitting noise with each falling drop. If the wire has drops hanging from it and the cable is suddenly energized at this voltage level, many of the larger drops will be forced off the wire with a definite “pfsst” sound as though the cable were spitting them off. As the voltage is increased, careful examination reveals that the lower ends of the purple streaks have miniature, slightly yellowish leaders, extending beyond the ends (see Figure 6-9).

Ghosts

As the voltage is increased further, the first stationary (self-sustaining) phenomenon observed depends on the nature of the wire. For the 1-inch stranded cable, it consisted of a small, round, dimly

white, glowing spherical body (head) located slightly below the wire, with a dark space between it and the wire. Below it there was another dark space and below that was a dimly glowing, purple, conical shaped form (skirt) (see Figure 6-10). We termed this phenomenon a "ghost," and it was only observed on the 1-inch stranded cable during the indoor rainfall rate tests. The ghosts appeared for wet conditions, independent of the rainfall rate. With only a slight increase in voltage, the ghosts turned into a self-sustaining continuous purple mini-flare described below.

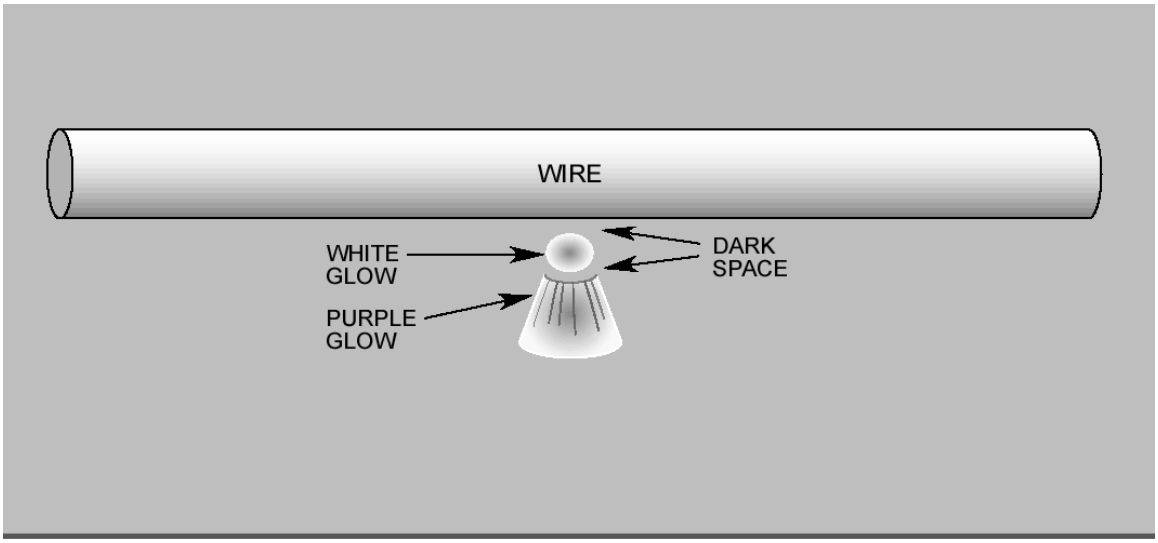

Figure 6-10. Ghost.

Purple Mini-Flares

As the voltage is increased, the intermittent purple streaks described above eventually grow longer and the starting point moves closer to the wire surface. When the voltage increases enough, the starting point appears to attach to the wire. At this level, they become continuous (although flickering slightly) and a faint, whitish purple, hot spot appears on the surface of the wire (Figure 6-11). These are termed purple mini-flares. They extend nearly straight out in the direction of the wire radius. They are usually stationary below the wire, but under certain conditions, particularly on stranded cable, they may move around somewhat and can spiral around the wire. There is a definite sizzling noise associated with the purple mini-flares and the intensity of the sound increases with voltage. This phenomenon is accompanied by the smell of ozone. Purple mini-flares are self-sustaining. Their source is on the surface of the wire and, as voltage increases, they are the first phenomena that dissipate any significant amount of power. For that reason, we used the onset of purple mini-flares to define the onset of "significant" corona for spray-wet conditions on wires. They are very similar to the purple streamers that form for dry conditions (Figure 6-6).

When the purple mini-flares first appear, they are approximately one to three wire diameters long, depending somewhat on the geometry. They are longer for larger heights of the wire. This is in part because the corona onset voltage is higher and more energy is available in the capacitor bank for the corona process. As the voltage is increased above the onset level, the mini-flares elongate and the hot spot on the surface gets brighter and whiter. As the voltage is increased further, a cylindrical stem forms, starting at the hot spot on the wire and extending perpendicular to the surface out a short distance away from the wire. The length of the mini-flares is weakly dependent on the water flow rate and is longer at the locations where a water stream forms.

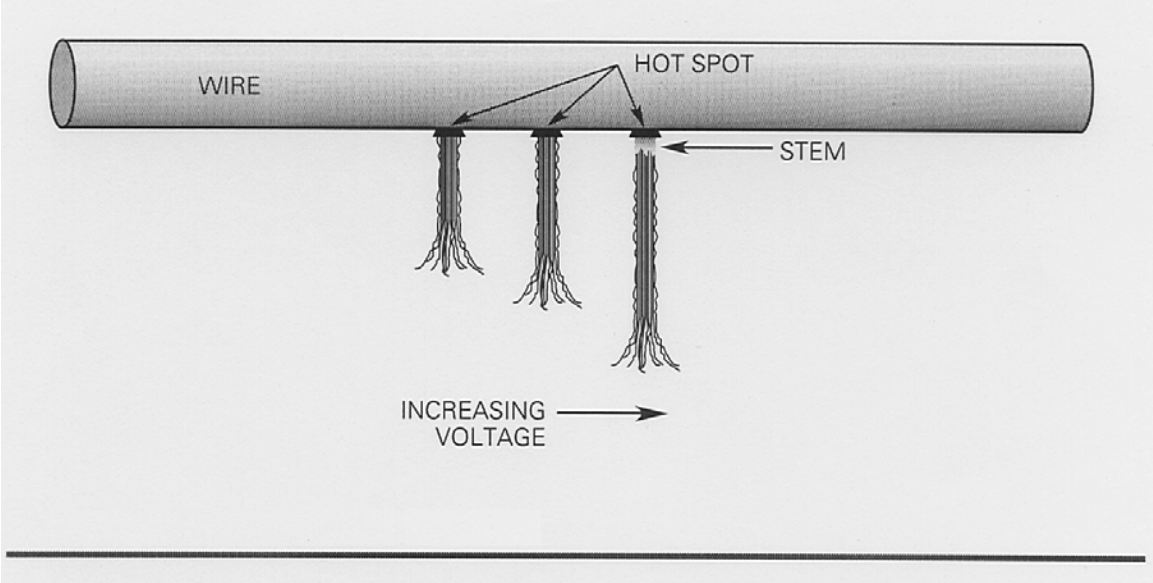

Figure 6-11. Continuous purple streamers.

Flashover

As the voltage is further increased, the next phenomenon observed depends on the geometry involved and the impedance of the high-voltage circuit. At Forestport, either a continuous discharge from one to several feet long formed, or if the plasma from this discharge reached the ground, a flashover occurred. We have termed this continuous discharge a “flare,” and it is described in the section below.

When a flashover occurs, all the energy stored in the capacitor bank is dissipated in a short time, most of it in the discharge itself. There is a white lightning-like streak from the object to ground. The path of the spark approximately follows the electric field lines, and it is accompanied by a loud bang. Figure 6-12 shows a drawing of a typical flashover path. The sound associated with flashover increases with the discharge voltage, corresponding to a greater amount of energy dumped by the capacitor bank. If the transmitter is kept running, a continuous series of flashes takes place, with accompanying bangs, occurring at a several (approximately 5 to 25) discharges per second. This is caused by the energy stored in the capacitors discharging through the circuit completed by the arc across the test object. This circuit typically rings down at a frequency in the high frequency range corresponding to the resonant frequency of the capacitor and load circuit with the load shorted out. After the capacitor bank rings down, the arc goes out, and the VLF transmitter recharges the capacitors, which then ring up at the VLF frequency, until the voltage is high enough for flashover to reoccur and the sequence starts over.

Figure 6-13 shows a picture of a flashover on an insulator. Note the irregular path of the flashover. In addition, at the bottom there are two separate paths probably resulting from two or more different flashovers that occurred within the exposure time. Note the water sprayer on the right-hand side of the figure. The water droplets from the sprayer are glowing with corona. This figure also shows a good example of purple streaks. They are forming on the water drops falling from the lowest of the three upper corona rings. Note that the purple streaks start well below the surface of the ring. On the left end of the center string of purple streaks, there is an example of one just after separation, where

there is purple on both the part of the drop that has separated from the surface as well as on the part that remains on the surface.

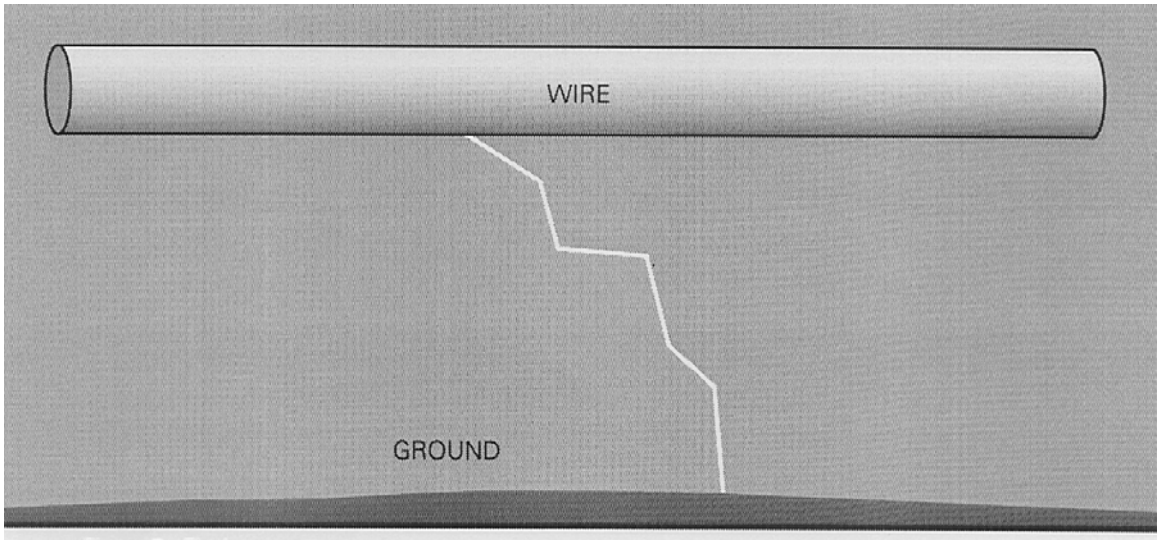

Figure 6-12. Drawing of flashover.

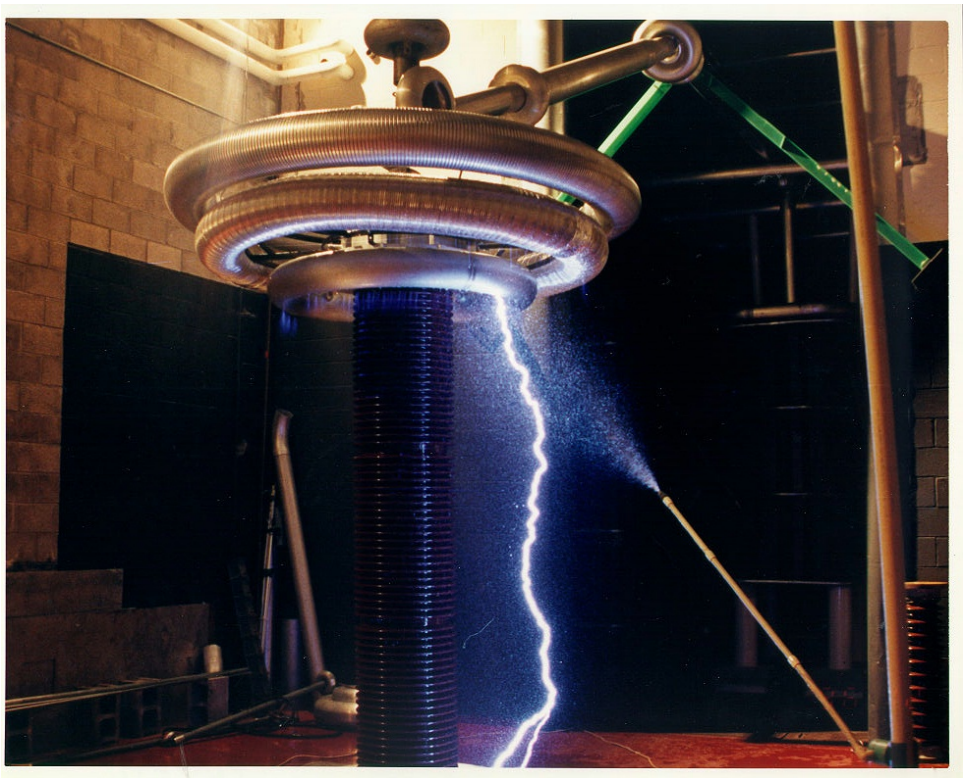

Figure 6-13. Picture of flashover.

Flares

As the voltage is increased, if flashover does not occur, a continuous discharge from one to several feet long is formed. We have termed this continuous discharge a "flare." A drawing of a flare is given in Figure 6-14. Figure 6-15 shows a picture of a flare. In Figure 6-15, the streamers are particularly visible in the dark area of the doorway. Note that the colors as seen by the human eye are not well reproduced in photographs, especially the deep purple associated with ultraviolet.

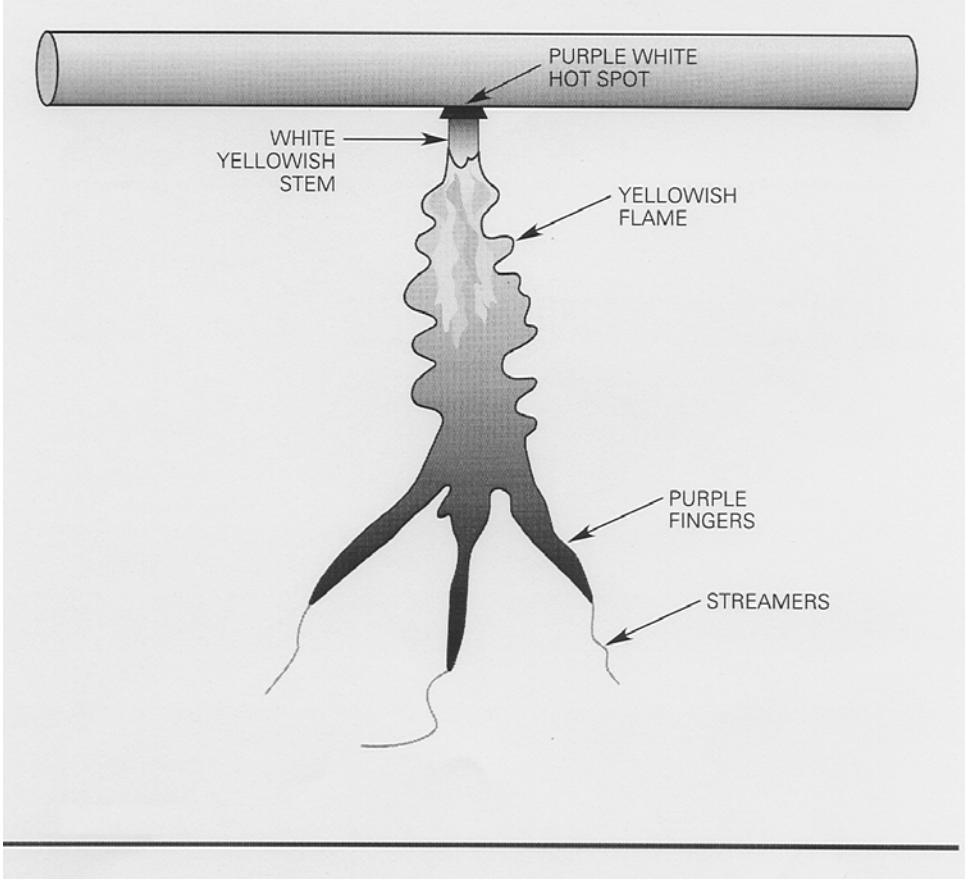

Figure 6-14. Drawing of flare.

For spray-wet conditions, both flares and flashovers usually start from the wire surface at or very near the location of the longest purple mini-flares. For the high-voltage circuit at Forestport, flares tended to form on objects with small radii of curvature that are located some distance from ground. Flashover tends to occur with objects having larger radii of curvature and when they are located closer to the ground. This is attributed to the fact that the beginning of a discharge draws considerable current, which rapidly lowers the electrode voltage due to the finite source impedance. If this voltage drops fast enough and far enough, then there will not be enough voltage available to drive the discharge all the way across the gap. Equilibrium results where the voltage level is great enough to provide the energy required by the continuous ionization in the flare but not enough to drive it across the remainder of the gap. We believe that the flare is an incomplete flashover that would continue across the gap if the RF voltage source had very low impedance. Thus, the flare phenomena depend on the circuit characteristics. However, the voltage at which flares form is

believed to be the same as the voltage at which flashover would take place with a low impedance source.

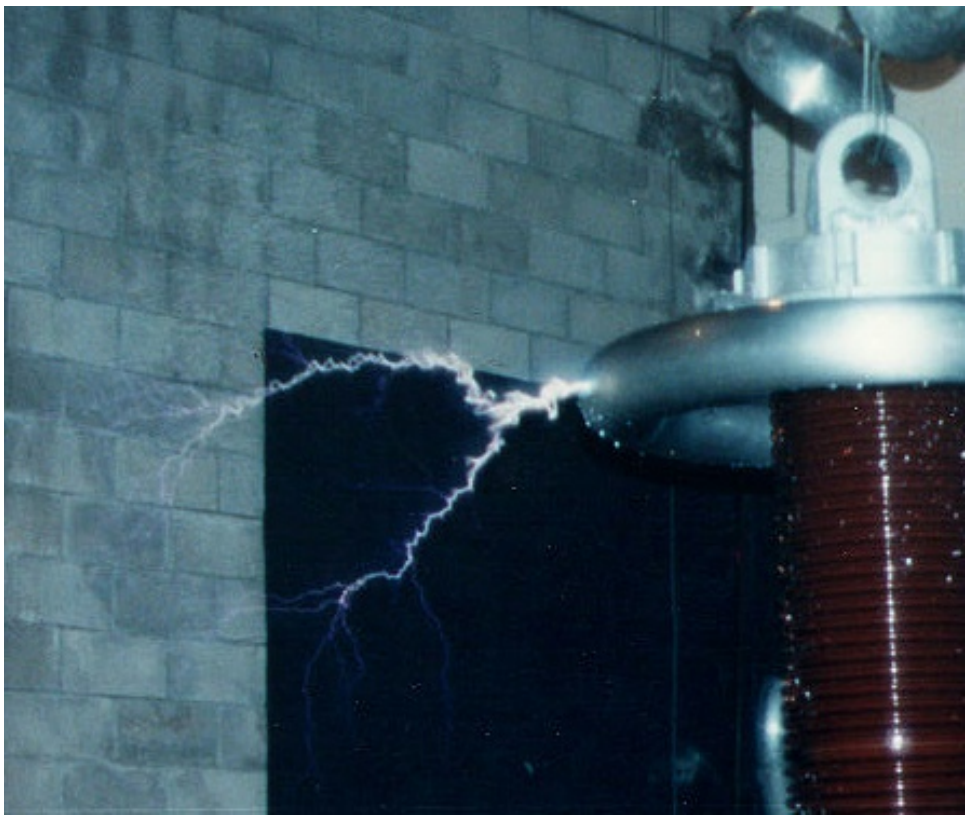

Figure 6-15. Picture of flare.

The flares originate from a bright, whitish purple region on the surface of the electrode, from which a cylindrical stem about 1 inch in diameter extends normal to the surface of the wire. At lower voltages, this stem terminates in a purple glowing discharge that has some smaller yellow streamers. As the voltage is increased, the stem lengthens somewhat and increases in diameter, but the most noticeable phenomenon is a wavy, yellow flame-like region that extends from the stem. This flame-like region can grow considerably longer, up to several feet, as the voltage is increased. It has the same appearance as the quiet arc that forms between electrodes when current is limited. The flame is usually one to several inches wide and takes a wavy path generally away from the high-voltage electrode, and usually waves around somewhat erratically. The end of the flame usually terminates in two or three fingers that are mostly purple but have flickering, yellowish white extensions that appear to be the classic streamers described in the high-voltage literature (see Figures 6-14 and 6-15). Flares are accompanied by a roaring noise, similar to a blowtorch, which increases in intensity with voltage.

If the transmitter is left on, the flare will usually move around slowly, with the source location on the wire tending to move up. The upward movement is probably due to the natural rising of the heated air around the flare. A flare will also tend to move in the direction of any wind blowing, including the air movement induced by falling water drops. Occasionally, the flare will appear to jump to another spot on the wire, or a flashover will occur from the end of the flare. Under certain conditions, flares can flicker on and off rapidly. For example, on the 1-inch stranded wire, as the

voltage was increased, flares were observed to flicker on and off briefly, starting from the location of the longer purple mini-flares.

MEASURED CORONA ONSET DATA

Data Description

Most of the corona onset data measured from 1994 on are included in Appendix 6A. The maximum surface electric field on the wire, pipe, or cable was calculated for each case as described in Chapter 4. The data from the measurements shown in the following section validated that the air density correction factor, discussed in Chapter 3, applies at VLF/LF for smooth cylinders. This correction is applied to both the surface electric field and the wire diameter. All the data for smooth cylinders have been corrected for atmospheric density. However, the data tables in the appendix give both the original and corrected data.

The reduced environmental data include both relative and absolute humidity, also given in the appendix. At power system frequencies, a humidity correction factor has been developed, which was described in Chapter 3. It is well known that at dc and power system frequencies that an increase in humidity increases the onset voltage. This is believed to be due to absorption of electrons by water vapor molecules. At VLF/LF, our measurements show just the opposite. The presence of humidity reduces the onset voltage, at least for larger wires. The amount of the reduction varies with the amount of humidity and with frequency and wire diameter. It appears that at VLF/LF there is a relationship between the wire diameter, frequency and humidity, which has not yet been worked out. For that reason, the measured data at VLF/LF have not been corrected for humidity.

The relevant data sets measured at Forestport are listed in Table 6-1 along with the frequency and the primary parameters being investigated by that set of measurements. Note that data sets taken prior the discovery of the voltage calibration error on 18 May 1993 are not included in the appendix, although some of those data were corrected and used in our analysis.

The Effect of Air Density

Several of the measurements were directed at determining the effect of air density. These measurements were taken using the horizontal inside test setup during the winters of 1996 and 1997. The setup used is shown in Figures 6-3, 6-6, and 4-15. The corona onset voltage was measured for three different values of air density using a set of test samples consisting of several smooth pipes and four samples of stranded cables.

The air density variation was accomplished by changing the temperature in the test cell. The winters at Forestport tend to be very cold. This allowed us to cool down the inside of the test cell to a temperature just above freezing, make a set of measurements, and then quickly warm it up for another set of measurements. After making a series of measurements at a cold temperature, the thermostat would be turned up and the large space heater warmed the test cell within a couple of hours. Measurements were then made at the warmer temperature. The measurements were usually made at three temperatures denoted cold, warmer, and warmest. The coldest temperature was slightly above freezing around 35^{o} F, and the warmest temperature was approximately 80^{o} F. The middle temperature was usually around 50^{o} F.

A controlled environmental chamber was not available at Forestport and changing the temperature over a given range of values was the only way to emulate density variation. There are at least two significant problems with this method. One is that the absolute humidity of the air in the test cell did

not remain constant. We had hoped that the method of starting with cold air and then rapidly warming it up would keep the absolute humidity nearly constant. Unfortunately, the warmer air rapidly absorbed moisture from the cement block walls and always had higher absolute humidity than the cold air.

Table 6-1. Corona onset data for wires, pipes, and cables measured at Forestport.

Date	Configuration	Frequency (kHz)	Effect	Included in Appendix 6A
Sept-Oct 85	Inside vertical		Frequency, diameter, slope	No
Sept 86	Inside horizontal		Frequency, diameter, slope	No
Sept 89	Outside horizontal		Corona power	No
Dec-Jan 89/90	Meter #1 blown out during flame test			No
June 92	Outside horizontal		Large diameter cables	No
14 July 92	Outside horizontal		Cable and vibration dampers	No
18 May 93	Voltage calibration error discovered			No
28 Oct 93	New calibration technique developed			No
10 Aug 94	Outside wires horizontal	27.5, 40	Repeat with new calibration and better geometry	Yes
27 Oct 94	Outside horizontal cages	27.5	Caging, corona phenomena, ons/ext, power	Yes
8 Feb 96	Inside wires horizontal	29, 53	Air density	Yes
13 May 96	Inside pipes Horizontal	29.2	Diameter, smooth – stranded	Yes
11 July 96	Outside pipe Wet & dry	27.8, 43	Diameter, freq wet – dry	Yes
10 Sep 96	Outside sloping cable & pipe	30, 43	Slope, wet – dry	Yes
22 Oct 96	Outside sloping cable & pipe		Slope	Yes
5 Feb 97	Inside horizontal 15’ lengths	29, 47	Humidity	Yes
8 Feb 97	Inside horizontal 10’ lengths	14	Air density	Yes
15 Feb 97	Inside horizontal 15’ lengths	29	Air density	Yes
18 Feb 97	Inside horizontal 15’ lengths	47	Air density	Yes

The second problem had to do with air circulation. On a couple of occasions, we made measurements with the door open in order to get the inside of the test cell cold enough. On both of these occasions, significantly lower than expected corona onset voltages were observed. The wind was blowing on those days, and probably small particles of blowing snow were to blame because after the door was closed for a while the onset voltages returned to nearly the expected values. The other example occurred on the day the 29-kHz data (15 Feb 97) was measured. On that day a thaw occurred and the door was kept open and a fan used to blow cold air in to get a relatively low temperature. These data did not behave as expected, and we believe that the fan was blowing dust off the ceiling and that the dust particles in the air reduced the corona onset voltage. Therefore, the data for 8 and 15 Feb 97 for 29 kHz probably do not reflect the true variation with atmospheric density.

These problems not withstanding, by the time we took the last set of data (47 kHz, 18 Feb 97), we had refined our method and the weather cooperated to give excellent data, which shows that the theoretical effect of density variation as outlined in Chapter 2 is valid. The 1996, 29-kHz air density data (30 kHz, 8 Feb 96) were also good and are shown below.

The data were processed using computer programs to calculate the maximum surface electric field on the test object as outlined in Chapter 4. In addition, the atmospheric environmental data were processed to obtain the air density and humidity. The raw and processed data for these measurements are shown in Appendix 6A under the dates 8 Feb 96, 8 Feb 97, 15 Feb 97, and 18 Feb 97.

The first example, for which the data is given in Figures 6-16 and 6-17, gives the critical surface electric field for corona onset at 29 kHz, measured using four smooth pipe samples at three different temperatures. The relative air density variation over this temperature range was from about 0.94 to 0.99. Figure 6-16 gives the data uncorrected for air density. It appears that the small diameter wire (1.79 cm diameter) may have been rough or had some imperfection that caused it to go into corona at a lower voltage than expected. Figure 6-17 gives the data after correction to the standard air density by adjusting both the surface electric field and the pipe diameter (Chapter 3). For this case, standard temperature and pressure (STP) was defined to be 25^{o} C and 760 mm Hg. Ignoring the anomalous data for the small wire, the curves for the three different temperatures are much closer together for the corrected case, indicating the correction is effective.

The second example, given in Figures 6-18 and 6-19, shows the measured critical surface electric field for corona onset at 47 kHz, using seven different smooth pipes. Again, note that the corrected curves (Figure 6-19) are much closer together than the uncorrected curves. In this case, the shift in the pipe diameters caused by the correction is clearly in the right direction to reduce the difference between the curves.

The third example, given in Figures 6-20 and 6-21, is for stranded cables at 47 kHz. The relative air density variation for this test was on the order of 0.95 to 1.03. In this case, the uncorrected curves are almost the same, while the corrected curves are separated. This indicates that the air density correction factor using similitude does not appear to apply at VLF/LF to stranded cables and rough surfaces. This is a somewhat surprising result for which we do not have a complete explanation at this time, although it has something to do with the frequency effect for rough surfaces.

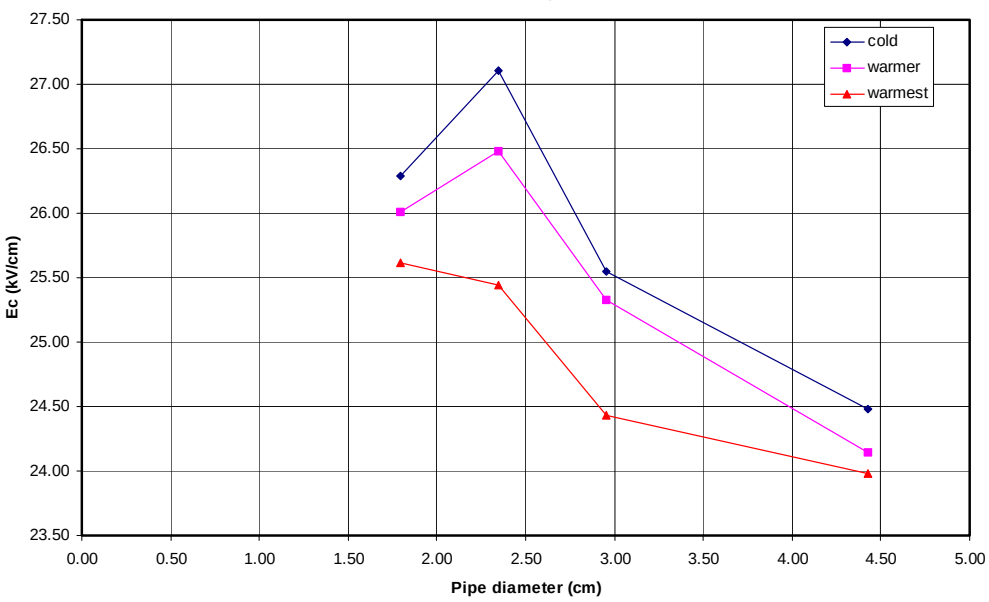

Figure 6-16. Air density, smooth pipes inside at 29 kHz, uncorrected for air density.

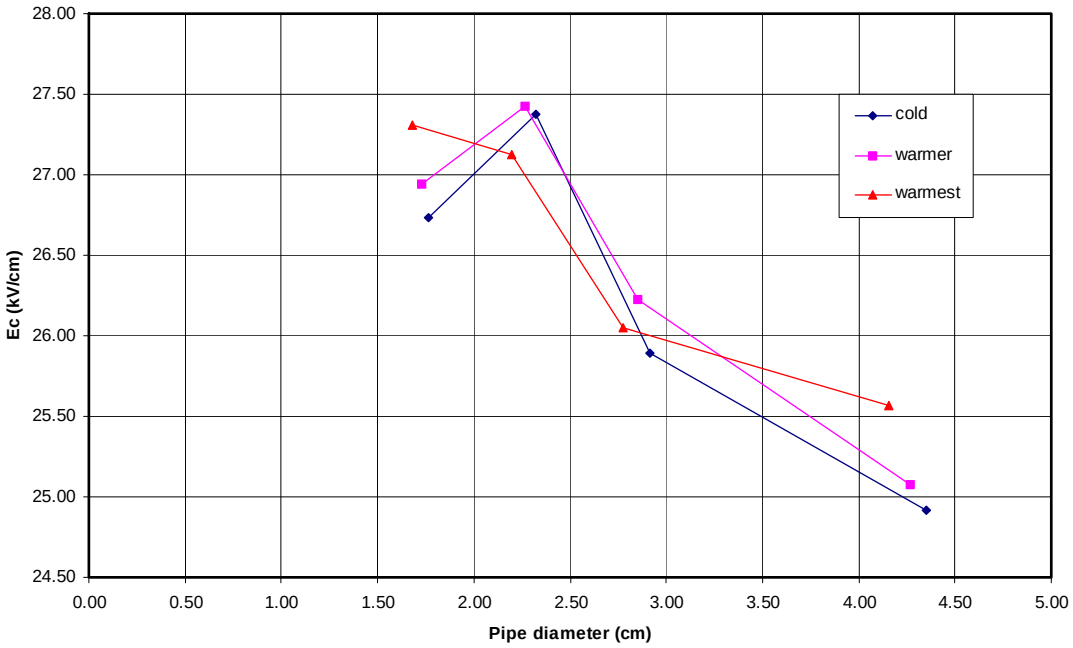

Figure 6-17. Air density, smooth pipes inside at 29 kHz, corrected for air density.

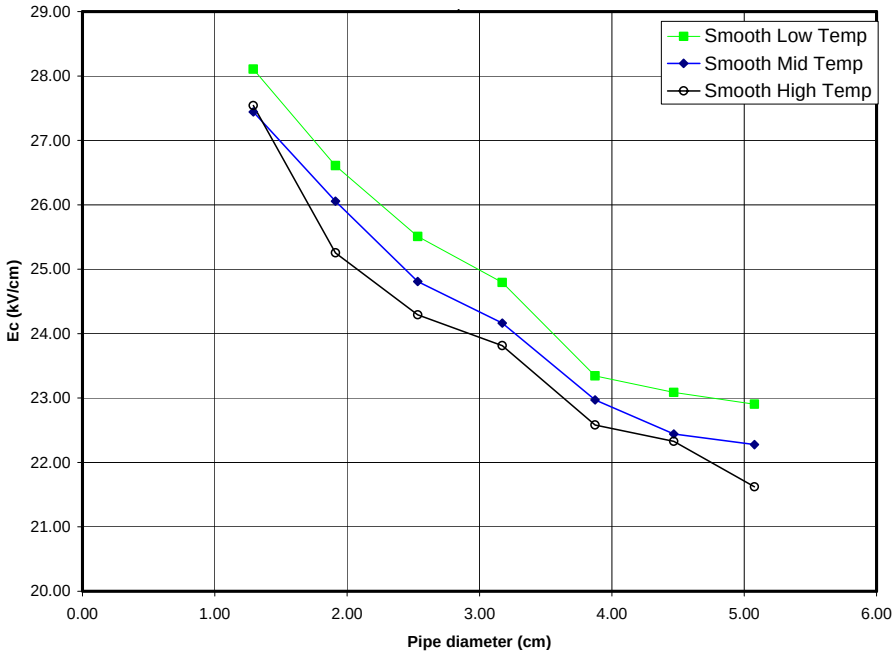

Figure 6-18. Air density, smooth pipes inside at 47 kHz, uncorrected for air density.

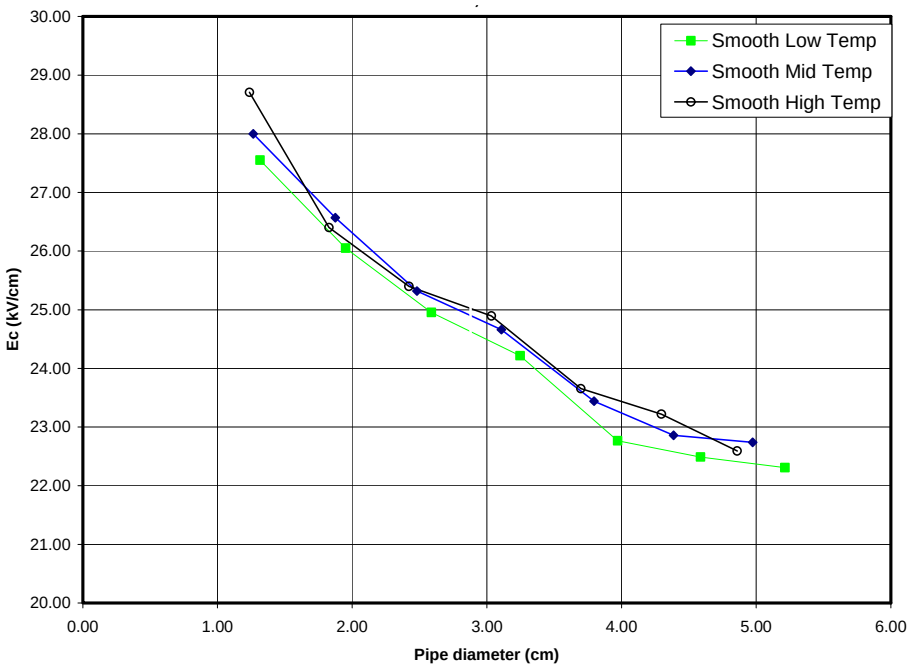

Figure 6-19. Air density, smooth pipes inside at 47 kHz, corrected for air density.

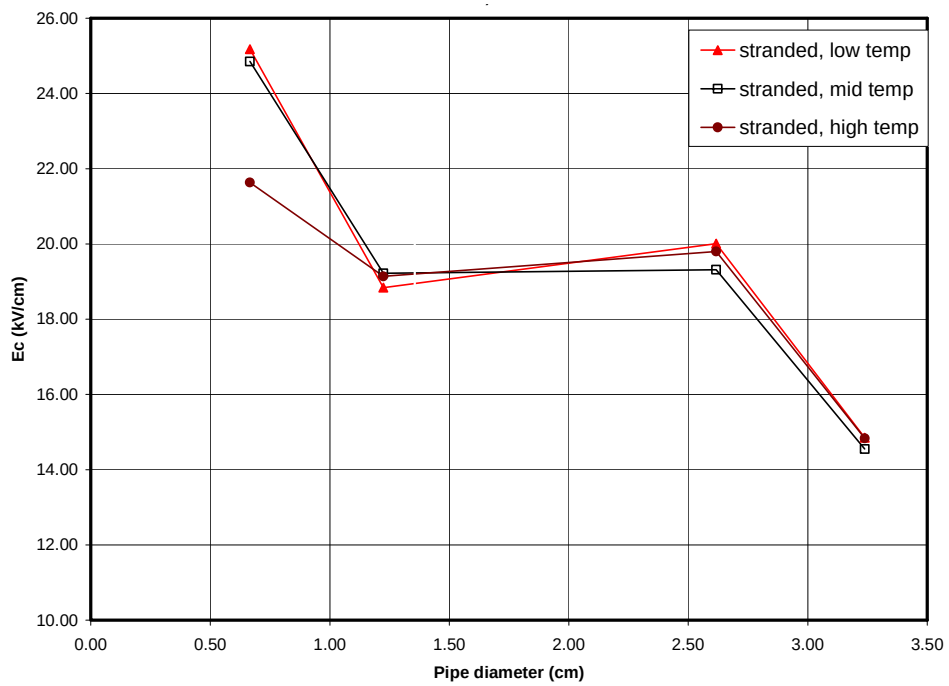

Figure 6-20. Air density, stranded cables inside at 47 kHz, uncorrected for air density.

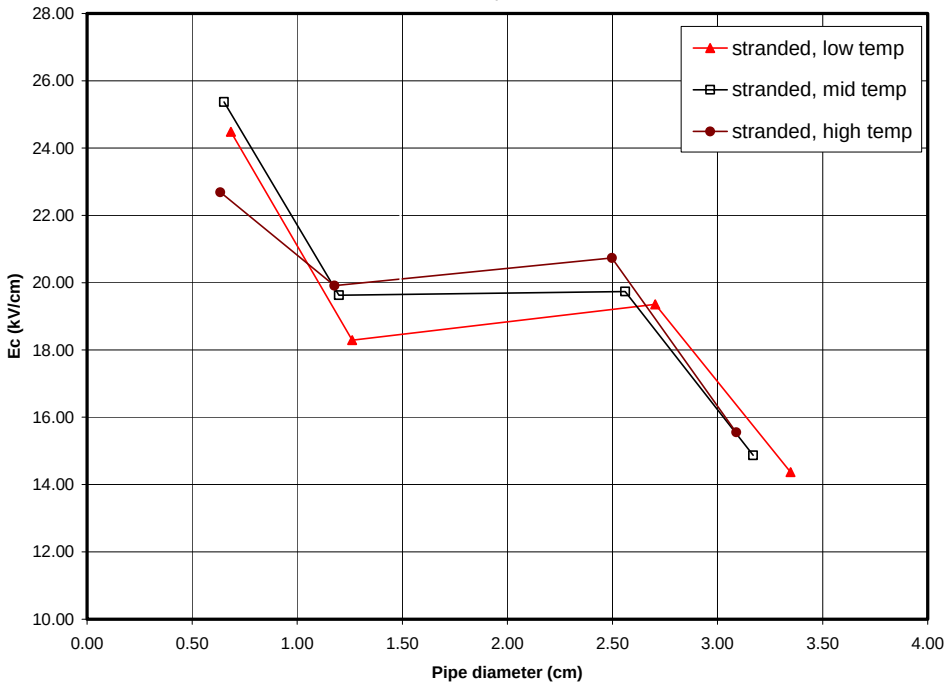

Figure 6-21. Air density, stranded cables inside at 47 kHz, corrected for air density.

Even though the data shown in Figures 6-20 and 6-21 do not show the air density effect, they are believed to be accurate because they were measured at the same time as the data for smooth pipes (Figures 6-18 and 6-19), which do show the expected air density effect. These were the last measurements taken in this series, and the experimental technique had been refined. The data indicate that the corona onset level on stranded cables has little or no variation over the range of air density achieved. Thus the air density correction factor derived in Chapter 3 does not apply to stranded cables at least over normal sea level density variations. For this reason, we did not apply it in processing the measured data for stranded cables.

Of course, air density must have an effect on the onset voltage of stranded cables, but our data indicate it has little or no effect over the small density changes achieved. We do not have an explanation for this, but we expect that for larger density variations (e.g., high altitude) the pressure variation would be more in line with the correction factor given in Chapter 3 and measurements of the air density effect on stranded cables over wider density variations are needed.

Both data sets presented for smooth pipes show that the true atmospheric density correction factor derived in Chapter 3 does apply to corona onset on smooth objects under dry conditions at VLF/LF. For that reason, we have applied the correction factor to the data for smooth pipes. This indicates that air density has less effect on the onset voltage for stranded cables, at least over normal atmospheric density variations near sea level. We do not have an explanation for this but we expect that for larger density variations (e.g., high altitude) the pressure variation would be more in line with the correction factor given in Chapter 3.

Peek developed a corona onset formula at 60 Hz for spray-wet conditions and deliberately did not include the air density effect since it was not characterized. Similarly, we do not have data for the effect of air density at VLF/LF under spray-wet conditions. However, our definition of corona onset involves the corona originating from the surface of the conductor as it does for dry conditions. Since this corona is very similar to that at onset for dry conditions, the wet corona onset data have been corrected for air density as well as the dry corona onset levels. It is not certain that air density affects wet corona onset the same as it affects the dry corona onset, and measurements of the air density effect on wet corona onset are needed.

Smooth Pipes and Wires

All the data presented in this section have been normalized to a standard temperature of 25° C and a standard atmosphere of 760 mm of Hg using the air density correction factor. (25° C was chosen because it is the temperature widely used in the power system corona literature). Appendix 6A contains detailed data sheets of the observed corona onset values and the normalization factors.

The surface electric field at corona onset for smooth pipes at 29 kHz from several data sets is shown in Figure 6-22. In addition, the curves based on the 60-Hz data of Peek (1929) and Miller (1956, 1957) are included. Comparing the upper curve for dry smooth pipes and low humidity to the 60-Hz data shows that the onset values are essentially the same at VLF and 60 Hz. The following formula fits the observed values for smooth conductors:

$$E_c = 17.25 + \frac{12}{d^{0.43}} \tag{6-1}$$

where E_c is the rms onset field in kV/cm, and
d is the wire or pipe diameter in cm.

The initial constant (17.25) is equal to 0.707 times the peak breakdown gradient for a uniform field, which is 24.4 kV/cm. The product is the rms value for E_c for a uniform field. Theoretically, E_c should approach the uniform field value for very large diameter wires. The figure indicates that this is the case. The constant in the numerator of the second term in the equation is 0.696 times the first term. This term is inversely dependent on the wire radius, and it accounts for the increased field on the wire surface required to cause breakdown for smaller diameter wires. This term arises because the field falls off more rapidly with distance from the wire surface for smaller diameter wires, and there is a minimum energy-distance product required for initiation of corona as discussed in Chapter 2.

The middle curve in Figure 6-22 shows results when the relative humidity of the air increased to about 90%. For this case, the onset field is reduced significantly, and the decrease is greater for larger wire diameters. An equation that approximately fits this case is also included in the figure. The initial constant is reduced to a value of 14.0 to account for the onset field reduction observed on the larger diameter wires. At 60 Hz, the presence of humidity normally increases the onset gradient, while the data show that the effect of humidity is the opposite at VLF/LF.

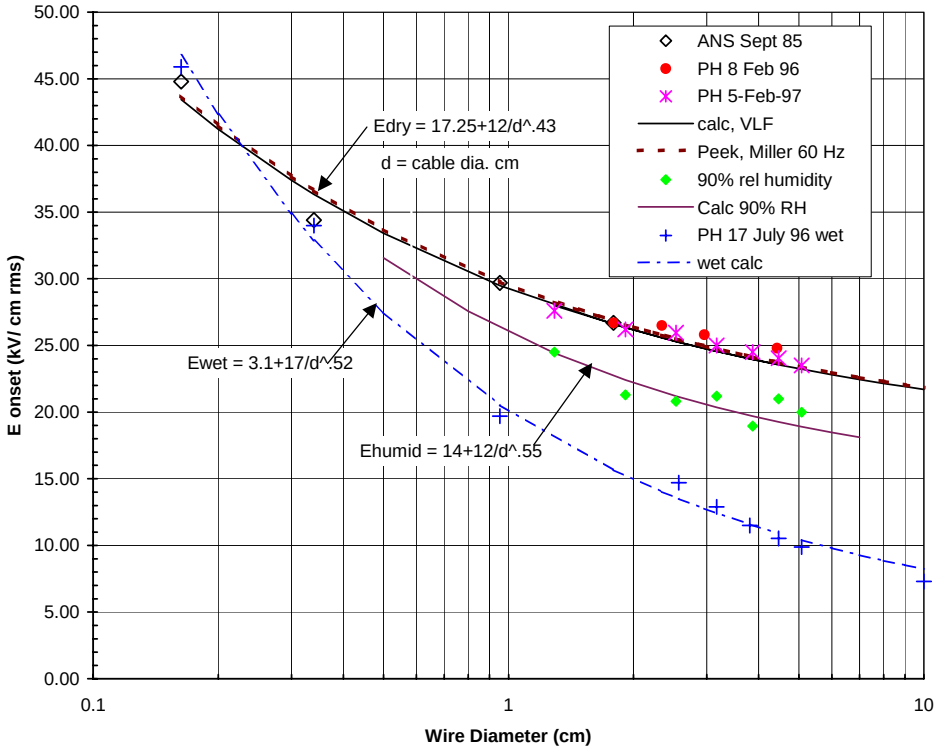

Figure 6-22. Corona onset surface field versus diameter for smooth wires at 29 kHz.

The lower curve for wet conditions shows a major reduction in the critical gradient for the larger diameter wires. However, the very small diameter wires show only a slight increase in onset gradient when wet. The asymptotic value for the larger diameters corresponds to 3.1 kV/cm rms, which is consistent with the breakdown strength of air with falling drops of water measured using widely spaced parallel plates as described in Chapter 8.

Figure 6-23 shows a similar data set for 47 kHz with the appropriate curve fit equations. The curve fit for dry, low-humidity data is nearly the same as that for the 29-kHz data. The data for high humidity show a slightly greater decrease in onset gradient for the larger diameter wires than was

found at 29 kHz. The curve for the wet corona onset shows a major reduction over the dry case for larger diameter wires, similar to the 29-kHz data. For this case, the asymptotic value for larger wires is about 3.0 kV/cm rms. The smaller diameter wires show a slight increase in onset gradient when wet similar to the 29-kHz data. We believe that there is a small decrease of corona onset fields with frequency, but the frequency effects are much smaller than the humidity effects. As a result, it is difficult to observe the frequency effect since the different frequency tests were performed at different times with different relative humidity.

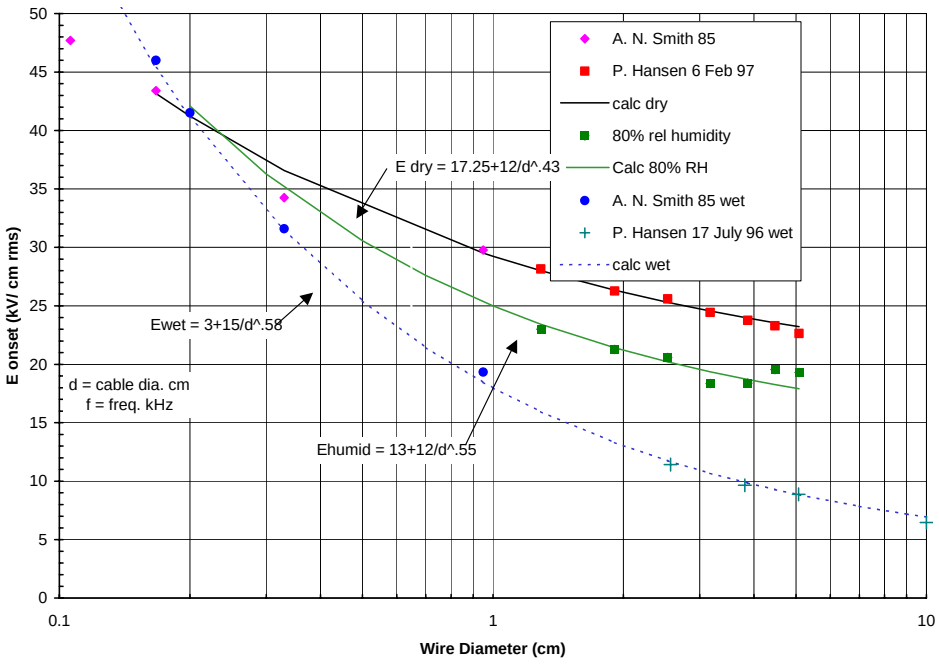

Figure 6-23. Corona onset surface field versus diameter for smooth wires at 47 kHz.

Stranded Wires and Cables

Most VLF/LF antenna configurations use stranded cables similar to the conductors used in power system systems. The maximum surface electric field on a stranded cable is greater than that on a smooth conductor of the same diameter due to the protrusion of the strands. The maximum field occurs on the outermost point of the strand farthest away from the center of the cable. The surface fields are further increased locally by contamination or wire surface roughness. It is common practice to calculate the gradients on such conductors as if they were smooth using the maximum cable diameter. The localized increase in the surface electric field reduces the voltage for corona onset and therefore reduces the apparent surface field for corona onset as calculated for a smooth conductor.

Corona onset measurements were taken for stranded cables at different times at Forestport. The processed results are plotted in Figures 6-24 and 6-25. Figure 6-24 gives the observed values of critical onset field for dry and wet conditions observed for stranded cables at 29 kHz. The dry data are representative of measurements made with the relative humidity less than 50%. The curve fit and associated formulas for these two cases are also shown in the figure, along with the curve fit for the smooth wire case.

From the figure, it is clear that the dry stranded cables exhibit a significant reduction in critical field relative to smooth wires. For dry cables around 2 centimeters in diameter, the surface electric fields at onset are 15 kV/mm for stranded cables and 26 kV/mm smooth conductors (a ratio of 0.58 to 1). On the other hand, the ratio for stranded cables under wet conditions is smaller. For a diameter of 2 centimeters, the onset fields are 12 kV/mm for stranded cables and 15 kV/mm for smooth pipes (a ratio of 0.80 to 1). For small diameter cables near 0.3 centimeter in diameter, the ratio is about 0.9 to 1.

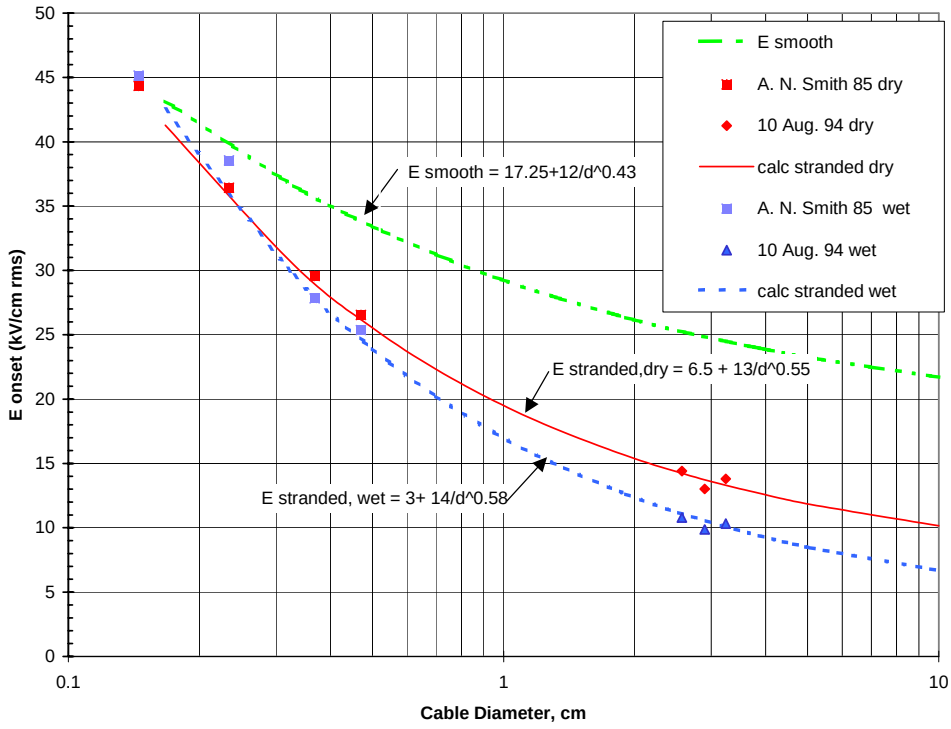

Figure 6-24. Corona onset surface fields for stranded cables at 29 kHz.

Data for stranded cables measured for both dry and wet conditions at frequencies around 43 kHz are shown in Figure 6-25 along with a curve fit for the data. The data are very similar to the 29-kHz data. The data for dry conditions exhibit significant scatter. The asymptote for large diameters is greater for these data than for the 29-kHz data. However, the spray-wet data have a slightly smaller asymptote than that for the 29-kHz data.

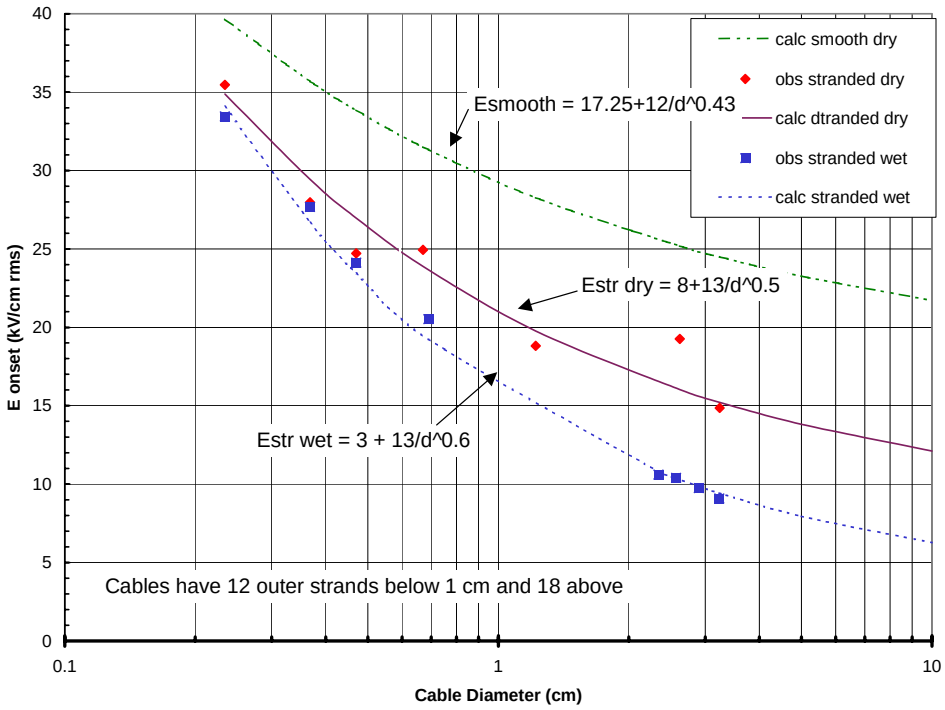

Figure 6-25. Corona onset surface fields for stranded cables at 43 kHz.

Curve Fit Equations

Curve fit equations for all of the above cases are given in Table 6-2. The equations are of the form:

$$E_c = E_\infty + \frac{K}{d^z} \tag{6-2}$$

where E_c is the critical surface field for corona onset (kV/cm),
E_∞ is the asymptotic critical field for large diameters (kV/cm),
d is the cable diameter in cm, and
z is the exponent defining the variation with diameter.

The similarity law described in Chapter 3 requires that the critical onset **voltage** remain constant when the product of relative air density and the physical size scale factor also remains constant. The equations given in Table 6-2 can be modified to explicitly include relative atmospheric density in a way that satisfies the similarity condition, as shown below.

$$E_c = \delta \cdot \left(E_\infty + \frac{K}{(\delta \cdot d)^z} \right)$$

where δ is the relative atmospheric density and the other parameters are defined in the preceding equation.

Table 6-2A. Curve fit equations for corona onset gradients on smooth pipes.

Frequency (kHz)	Condition	Equation
29	Dry	$E_c = 17.25 + \frac{12}{d^{0.43}}$
29	High humidity	$E_c = 14.0 + \frac{12}{d^{0.55}}$
29	Wet	$E_c = 3.1 + \frac{17}{d^{0.52}}$
47	Dry	$E_c = 17.25 + \frac{12}{d^{0.43}}$
47	High humidity	$E_c = 13.0 + \frac{12}{d^{0.55}}$
47	Wet	$E_c = 3.0 + \frac{15}{d^{0..58}}$

Table 6-2B. Curve fit equations for corona onset gradients on stranded cables.

Frequency (kHz)	Condition	Equation
29	Dry	$E_c = 6.5 + \frac{13}{d^{0.55}}$
29	Wet	$E_c = 3.0 + \frac{14}{d^{0..58}}$
43	Dry	$E_c = 8.0 + \frac{13}{d^{0.50}}$
43	Wet	$E_c = 3.0 + \frac{12}{d^{0.60}}$

These equations can be used for design. They also provide insight into the effects of the various parameters at VLF/LF, as described in the following sections.

Surface Roughness and Stranding Factors

It is traditional to use a surface roughness factor (m) to indicate the amount the corona onset voltage is reduced over that for a smooth cylinder (Naidu & Kamaraju, 1995, p. 30). This factor

includes the effect of stranding and other surface irregularities such as nicks, scratches, strand displacement, and surface contamination, which may be the result of handling during the manufacturing, shipping, and installation process. The factor is sometimes called the stranding factor, although strictly speaking that should apply to the effect of stranding only. The factor is defined as the ratio of the observed critical surface electric field at corona onset for a stranded cable (field calculated as if the cable were smooth) divided by the observed critical surface field at corona onset for a smooth pipe of the same diameter. The surface roughness and stranding factor is applied as follows:

$$E_c = m \cdot \left(17.25 + \frac{12}{d^{0.43}} \right) \tag{6-3}$$

where E_c is the onset gradient for a stranded conductor,
d is the wire or pipe diameter in centimeters,
m is the surface roughness factor, and
the equation in the brackets is for a smooth cylinder.

The stranding effect can be estimated by calculating the maximum surface field on a stranded conductor and dividing that into the field on a smooth conductor having the same diameter as the maximum diameter of the stranded cable. This calculation provides the inverse of the amount the fields are increased by the roughness of the stranding. This factor was calculated for typical stranding configurations using a method-of-moments electrostatic computer program and the results shown in Table 6-3.

Table 6-3. Stranding factors for typical cable configurations calculated using electrostatic computer program.

Number of Outer Strands	E_{smooth}/E_{strand} (max dia)
2	0.727
3	0.762
4	0.771
6	0.779
12	0.794
18	0.801
22	0.808

Measured stranding factors are expected to approximate those calculated; however, they are slightly larger. The measured onset fields are reduced less than the calculations indicate. This is attributed to the fact that at the maximum surface point (outer most point of a strand) the local field falls off at a rate faster than 1/r, which requires an increase in the surface field for breakdown as discussed in Chapter 2.

Miller (1957) measured this factor at 60 Hz, and although he called it the stranding factor, his measurements included the effect of both surface roughness and stranding. The results are shown in Table 6-4.

Table 6-4. Measured surface roughness factors (dry) for stranded cable (diameters 0.368 to 2.68 inches), (Miller, 1957).

Surface Condition	Range of Surface Roughness Factor
New clean	0.88 – 0.96
New as received (some surface damage)	0.53 – 0.73
Weathered	0.68 – 0.82

Note that for "new clean" conductors special care was taken to avoid and remove surface damage and contamination. This is the true stranding factor and Miller's data indicate that it is somewhat greater than that calculated by the ratio of fields. However, the "new as received" cables, which had typical surface damage and contamination, went into corona at much lower voltages, some nearly one-half the value for the equivalent smooth cylinder.

The "weathered" cables were taken out of service after 1 to 25 years. Extreme care was taken to ensure that the surface condition of these cables as tested remained unchanged from that in the field. These "weathered" cables have surface roughness factors that lie between the values for "new clean" conductors and "new as received" conductors. Miller concluded that weathering decreases the surface roughness factor over that of "new clean" conductors, probably due to deposits of oxidation and dirt. The surface roughness value for "weathered" copper conductors appeared to be near the upper value given in Table 6-4, while the aluminum conductors weathered in industrial areas were near the lower limit.

In some cases, "weathering" actually increases the corona onset voltage for cables that are installed with scratches and contamination. This is borne out by the fact that the "weathered" conductors typically had surface roughness factors greater than that of the "new as received" conductors. The increase is attributed to the fact that corona burns off surface irregularities and contamination, essentially like the conditioning effect for high-voltage electrodes. At VLF, there is considerably more energy in the corona and the conditioning of the cables takes place much more rapidly than at 60 Hz. At VLF, we found that the corona onset voltage increased after running the cables in corona for a few minutes, and after that the corona onset voltage stabilized. For this reason, our standard practice was to run the sample well into corona for a few minutes prior to measurements of corona onset.

The stranding-surface roughness factor at VLF/LF can be examined based on the Forestport VLF/LF data by taking the ratio of the curve fit equations given in Table 6-2 for stranded and smooth conditions. The stranding-surface roughness factor calculated in this way is shown in Figure 6-26.

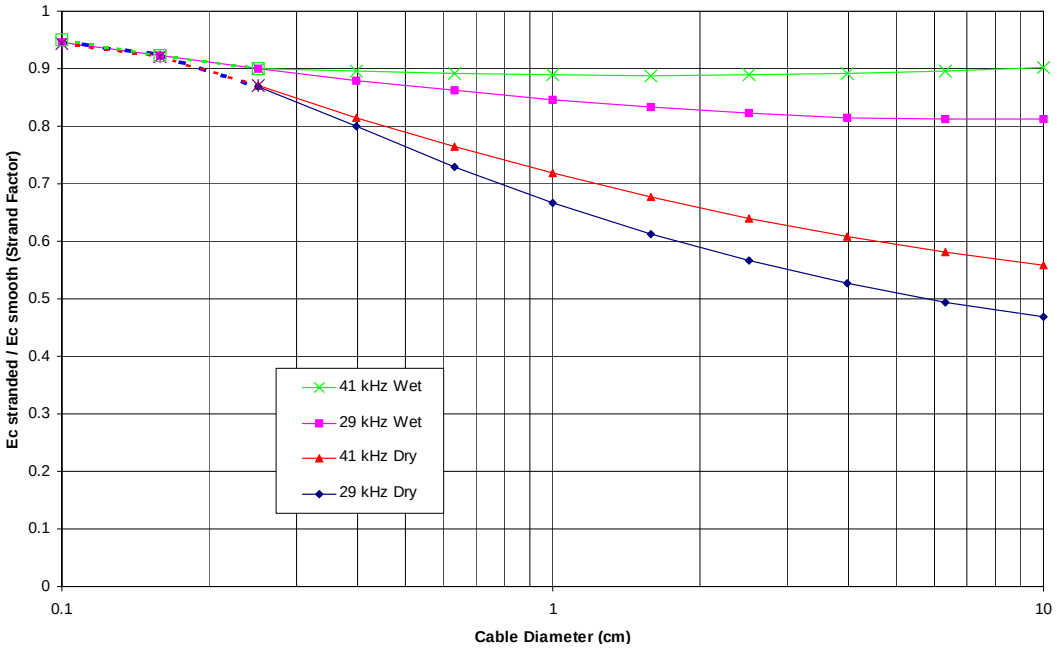

Figure 6-26. VLF/LF stranding factor.

All of the curves in the figure show that the stranding-surface roughness factor decreases with increasing wire diameter. For the dry case, the stranding-surface roughness factors vary from 0.5 at the larger diameter wires to an estimated value near 1.0 for the smaller diameter wires. Note that the values for wire diameters below 0.25 cm have been extrapolated because the calculated values in that region increased rapidly, becoming greater than 1.0, and we do not believe that to be the case. It is likely that this factor approaches 1.0 for small diameters, and the figure gives appropriate extrapolated values. The fact that the curve fit equations do not show this indicates that these formulas may need adjustment to fit better at the smaller diameters.

The stranded cables used for these tests had some surface damage, although we tried to clean them up as much as possible. The low values for the stranding-surface roughness factor shown in the figure may be partially due to the presence of this damage, corresponding to Miller's "new as received (some surface damage)" category shown in Table 6-4. Again, there is a definite tendency for this factor to be lower for the larger diameter wires.

The stranding-surface roughness factor is closer to 1 for wet conditions than for dry conditions. Again, note that this factor decreases for larger diameters.

The effect of stranding, or surface roughness, appears to be less at higher frequencies, as evidenced by the fact that the stranding factor is closer to 1 for the 41-kHz data than for the 29-Hz data. We do not have an explanation for this.

The Effect of Precipitation

The presence of falling water significantly decreases the voltage level at which corona occurs. Rainwater is a good conductor at VLF/LF frequencies. The hanging drops form protuberances on the surface of the wire. The electric field is enhanced at the outermost point of the drop. Simple electrostatic theory indicates the field at the outermost point would be enhanced by a factor of three for hemispherical drops. Actual water drops are nearly prolate spheroidal, and the field enhancement

factor is greater (Richards, 1974). One school of thought is that the reduction in corona onset voltage is due to the field enhancement, which causes corona to form on the tips of the hanging drops. However, the real explanation is not that simple since water does not emit secondary electrons and thus corona does not form on the water surface. Observations confirmed that corona does not form on the tips of the hanging water drops. The initial corona occurs for a brief instant in the air below the conductor just after a water drop separates. This corona appears to form on the sharp point on the end of the falling drop shortly after it separates from the conductor. The distance below the conductor where the corona forms is consistent with a reversal in polarity of the VLF waveform.

Rainfall deposits water on the conductor, which in turn falls off the conductor in the form of drops. If the precipitation rate is great enough, continuous water streamers form falling from the conductor. These streamers eventually break up into drops some distance away from the conductor. The surface electric field causes the water drops to contract in the direction parallel to the surface. This causes the drops to be narrower and hang down farther. As the field increases, this change in shape forces the larger drops to fall off. A given field forces all drops exceeding a certain size threshold to fall off. The stronger the field, the smaller is the threshold (Richards, 1974). When the drops fall off, there is a “pfsst” sound accompanying the corona. Thus, when a voltage is suddenly applied to a wet conductor, it appears that the high field causes the larger water drops to “spit” off.

As the voltage is increased, corona forms first as instantaneous flashes on falling drops a short distance below the conductor after they have separated from the conductor. As the voltage is increased, this corona becomes brighter and lengthens (purple streaks). The starting location of the corona moves closer to the conductor surface but does not touch it over a wide range of voltage. The corona that occurs away from the conductor is associated with falling water drops or streams. It is intermittent and moves around, following the water flow. As the voltage increases, eventually the end of the purple streak moves up to the conductor surface (purple mini-flares). This corona is continuous, self-sustained, and similar to the initial corona that forms for dry conditions, but it occurs at a considerably lower level for spray-wet conditions. The level where this continuous self-sustained corona (purple mini-flares) formed was used as the definition of wet corona onset for the wet measurements at Forestport.

Our observations indicate that these continuous self-sustaining corona streamers or flares have their source on the metal surface of the conductor and not from water drops or streamers. However, they form in close proximity to the places where the water streamers were falling, and it appears that the ultraviolet radiation from the corona on the falling drops helps to initiate the self-sustaining corona at a lower level than when dry. It is also likely that the excess humidity and microscopic water droplets near the conductor surface play a part in the reduction of the corona onset level for wet conditions.

The equations in Table 6-2 have been employed to quantify the impact of spray-wet conditions. The reduction of the critical onset field for wires, pipes, and cables under spray-wet conditions compared to dry conditions is shown in Figure 6-27. For smooth pipes about 1 inch (2.54 cm) in diameter, the reduction factor is approximately 0.5. For very small conductors, our data indicate that the presence of falling water actually increases the corona onset field (reduction factor >1), although the wire diameter at which this occurs is too small for practical antenna usage. There is a crossover point where the factor is 1.0 for wire diameters around 0.2 cm.

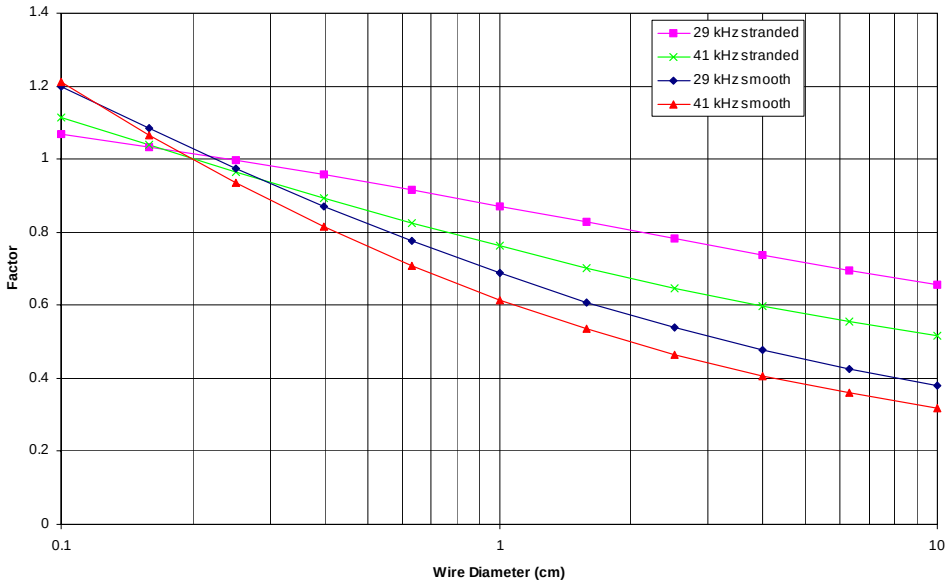

Figure 6-27. VLF/LF wet reduction factor.

One possible reason for the increase in corona onset for smaller wires with wet conditions is that surface tension allows the water to cling all around the wires. The water coating does not emit secondary electrons, hence does not support self-sustaining corona. Another possible reason is that the water coating makes the effective wire diameter larger, thereby increasing the corona onset voltage. A third possible reason is that increased humidity increases the corona onset voltage for small diameter wires as discussed in the section on humidity later in this chapter.

Examination of Figure 6-27 shows that the wet reduction factor for stranded cables is much closer to 1.0 than it is for smooth pipes. This is because the stranded cables already have built in surface perturbations, which causes corona to form on them at a much lower equivalent field than on smooth conductors without water.

Figure 6-27 indicates that the reduction in the onset field for wet conditions is more at the higher frequencies than the lower frequencies for both smooth and stranded conductors. One possible explanation for this is that there is more energy in the corona on the falling drops at higher frequencies (see Chapter 7) and hence more ultraviolet available to trigger the self-sustaining corona. Another possible explanation is that humidity causes a decrease in the corona onset voltage for larger wires at higher frequencies, which is also discussed in the section on humidity later in this chapter.

Some important conclusions regarding design follow from an examination of the data for spray-wet conditions shown in Figures 6-22 to 6-25 and the corresponding equations (also in Table 6-2). First, for pipes and cables with diameters large enough to be practical for use in large antennas, the spray-wet corona onset level is considerably reduced from that for dry conditions. Thus, the worst design case for corona free operation is spray-wet conditions. Finally, the equations for the corona onset level for spray-wet conditions are essentially the same for both smooth and stranded cables, independent of surface roughness and frequency (at least up to 50 kHz).

Rate

A special series of tests was conducted at Forestport using the inside horizontal test setup to determine the effect of the precipitation rate on corona onset fields. Rainfall rate was varied from a

very low value (sprinkles) to a relatively high value (several inches per hour). The results of these measurements indicate that the corona onset voltage is essentially independent of precipitation rate. This is true provided sufficient water is falling to allow formation of drops on the bottom of the conductor that occasionally drop off. Thus, for practical purposes, the corona onset voltage is independent of rainfall rate over a wide range of rainfall rates.

Some reduction in flashover voltage was observed at high rainfall rates when continuous water streamers formed off the high-voltage electrode, especially if they started near a high surface field point and the end of the streamer started to approach electrical ground. The continuous water streamer is a good conductor at VLF/LF frequencies, and the electric fields are enhanced as the conducting water stream nears ground. For normal rainfall rates, this condition only occurs when the electrode is within a foot or so of the ground. Most practical configurations for VLF/LF applications have larger gaps, and this condition only occurs during extreme rainfall rates (typhoon or testing with a fire hose).

Figures 6-22 and 6-25 show that the onset field for high relative humidity approaches that for spray-wet conditions. This is probably due to the fact that at high relative humidity droplets can form in the air and on the surface of the conductor causing conditions approaching dew or light rainfall.

The Effect of Slope

Most of the Navy's VLF/LF antennas have wires and cables that slope. Many of the antennas are umbrella top-loaded monopoles, which have top guys that are an active part of the antenna. The active guys have slopes around 45^{o}. The slope of the wire does not affect the onset voltage for dry conditions. However, for wet conditions, water drops form and fall off the wire differently depending on the slope of the wire. This effect was measured for both vertical and horizontal configurations inside the test facility and for horizontal and sloped configurations outside the test facility. The inside vertical configuration was described earlier in this chapter (Figures 6-4 and 6-5). The outside sloped configuration was also described earlier in this chapter (Figure 4-16). The outside test samples were 20 feet long and suspended using the winch and utility pole as described in Chapter 5. The lower end of the test sample was 10 feet above the ground. The cable slope was adjusted by changing the height of the upper end of the cable using the winch. Several samples with different diameters were measured at slopes from about 25^{o} to slightly more than 45^{o}.

The tests also examined the interaction of water with the conductors. When the conductors were vertical, the water did not drip off the wire but ran down to the end of the wire. For horizontal conductors, all the water falls off in drops or streamers. Nevertheless, for spray-wet conditions, the measured surface electric field necessary to form wet corona (as defined in Chapter 5) was found to be the same for both vertical and horizontal configurations.

When the conductor is sloping, the water both falls off in drops or streamers and runs down toward the lower end. For each condition and spray rate there was a critical slope below which the water fell off the conductor as drops and streamers, and above which all the water ran down the conductor to the end. This critical angle was on the order of 25^{o} to 30^{o} depending on the rainfall rate and whether the cable was stranded or smooth. Nevertheless, for the cases measured, the voltage for wet corona onset was independent of rainfall rate and slope to within experimental error.

The Effect of Caging or Bundling

It has long been known that putting multiple conductors in parallel cages (bundles) allows higher voltage operation without corona (Miller, 1956, Trinh et al, 1973). This is because the multiple

conductors shield one another, reducing the surface fields. Further discussion of this was given in Chapter 4, in which an approximate formula for the maximum surface electric field on a cage of wires was derived. This formula, called the complete Modified Simple Geometric Theory (MSGT) formula, namely

$$E_n = \frac{V}{n}\left\{\frac{1}{a} + \frac{n-1}{b + a/2}\right\}\left[\frac{1}{\ln(2h/a_{eqC})}\right]$$

where V is the voltage on the cage,
n is the number of conductors in the cage
a is the radius of the conductors
b is the radius of the cage,
h is the height of the cage, and
a_{eqC} is the equivalent radius for capacitance of the cage.

The equivalent radius for capacitance is the radius of a single cylindrical conductor that has the same capacitance per unit length as the cage. The formula defining the equivalent radius for capacitance is given below.

$$a_{eqC} = \left(n \cdot a \cdot b^{n-1}\right)^{1/n}$$

The equivalent radius for capacitance is greater than the radius of a single conductor but less than the cage radius b.

Miller (1956, Figure 6) indicates that the critical surface field for corona onset for wires in a cage is not the same as the critical surface field for a single wire in the cage, but equal to the critical surface field for a wire having a radius equal to the equivalent radius for capacitance of the cage a_{eqC}. This is a surprising result, and measurements made at Forestport indicate that this is not true, as discussed below.

The critical surface field for corona onset is a function of the field distribution immediately around the wire as discussed in Chapter 2. Thus, if the cage configuration materially changes the field distribution around the wires it could change the critical surface field required for the onset of corona. However, calculations show that for practical cage configurations the field distribution around the wires in a cage is essentially the same as for a single wire. This implies that the critical corona onset field for wires in a cage should be the same as that for an individual wire. The corona onset voltage is of course higher for the cage because of the reduced fields on the individual wires.

A series of measurements of corona onset for several cage configurations were made at Forestport using the outside horizontal configuration (Figures 6-1 and 6-2). The data are included in Appendix 6A with the date 27 October 94. The cages consisted of two, three, and four conductors of 1-inch stranded cable. A picture of one of the cage configurations tested is shown in Figure 6-28. Several cage diameters were tested with spacing that varied from 4 to 24 inches. Corona onset was also measured for a single 1-inch stranded cable.

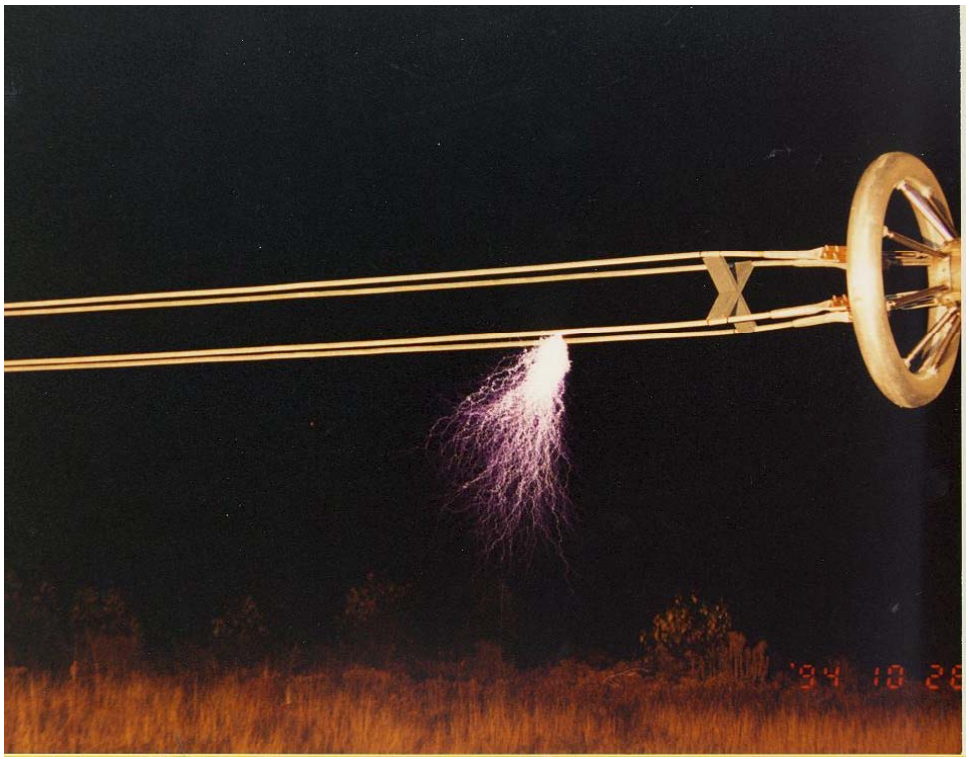

Figure 6-28. Four-wire cage, outdoor test setup.

The corona onset voltages for the cages and single cable were measured and the data reduced to obtain the critical gradient (surface electric field) for corona onset. The cages were relatively close to the ground (approximately 10 feet) for this test configuration. The field on the lowest cable was somewhat greater than on the other cables because it was closer to the ground. The fields were calculated using a two-dimensional electrostatic computer program, rather than the formula given above, in order to take this into account.

The formula works well for cages that are mounted at higher elevations, as would be the case for actual antenna or power line installations. A simplified formula, useful for practical design, which gives the optimum spacing for the wires in a cage above ground derived in Chapter 4 is repeated here. This spacing (S_{min}) is optimum in the sense that it results in the minimum surface electric field on the cage wires. S_{min} varies logarithmically with height and for $3 \leq n \leq 6$ and is given by the following normalized formula:

$$\frac{S_{min}}{a} = 10 \cdot Log\left(\frac{2h/a}{10}\right)$$

where S_{min} is the wire-to-adjacent-wire spacing in the cage,
h is the height above ground, and
a is the individual wire radius.

As an example, consider a cage constructed with wire having a 0.02-meter radius, and located at a height of 10 meters above ground. The optimum wire-to-adjacent-wire spacing in such a cage is seen to be 20 wire radii or a distance of 0.4 meters.

The processed data for the cage tests are shown in Figure 6-29. The data show that the critical field for the onset of corona on cages under wet conditions is the same as for a single cable. The data for dry conditions are similar but have considerably more variability, which is attributed to the high humidity (dew) associated with the outside measurements in the evenings.

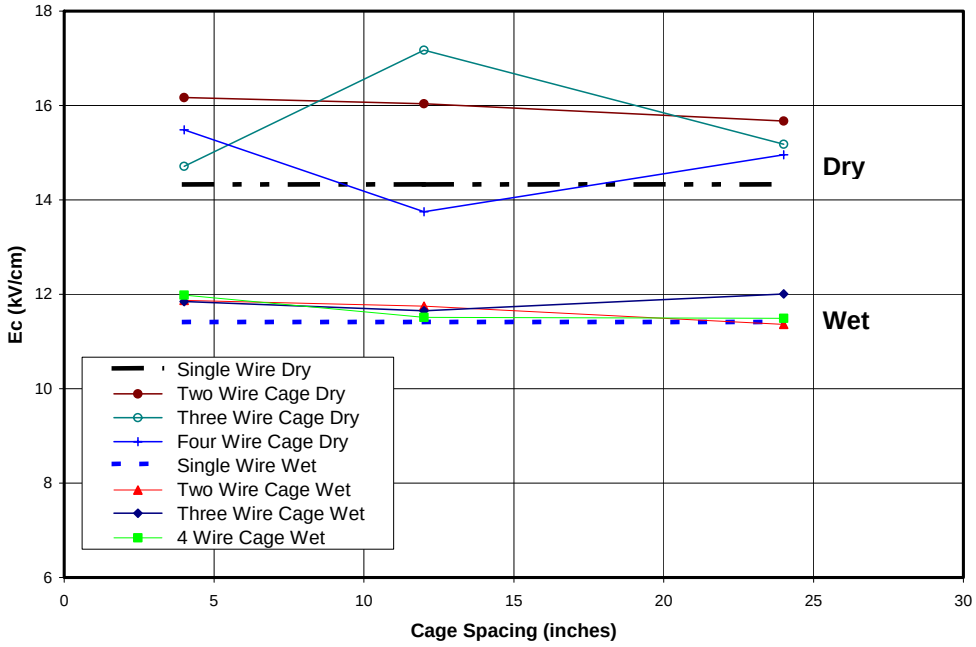

Figure 6-29. Cage data wet and dry at 27.5 kHz.

Thus, for practical cage designs, the critical field for corona onset is the same as that for a single conductor for both wet and dry conditions. The maximum field on the surface of wires in a cage configuration is considerably less than that on a single wire in the same location, as indicated by the MSGT formula given above. Thus, the corona onset voltage for a cage is considerably greater than that for a single wire.

The Effect of Frequency

Introduction

There has been considerable study of the breakdown (flashover) of uniform field gaps as a function of frequency. As frequency is increased, the peak breakdown voltage in a uniform field is the same as at dc for quite a large range of frequencies, including power system frequencies. Meek and Craggs, (1978, p. 539) state that the breakdown voltage is the same as at dc for frequencies up to the order of 1000 Hz. As the frequency is increased beyond 1000 Hz, the breakdown voltage decreases but not greatly until the frequency exceeds 100 kHz. The transition region extends over a large range of frequencies, and the starting point depends on the gap length. For example, Reukema (1928) found that there was no appreciable change in breakdown voltages between sphere gaps of up to 2.5 cm for frequencies as high as 25 kHz. From 20 to 60 kHz, the breakdown voltage is progressively reduced to about 15% below the 60-Hz value. At higher frequencies, up to 425 kHz, the breakdown voltage remained approximately constant.

Corona forms prior to flashover when the field is sufficiently non-uniform. The processes involved at corona onset are essentially the same as those that result in breakdown in a uniform field. Thus, the frequency variation of corona onset is expected to follow that for uniform field breakdown. The data presented below are consistent with this concept.

However, for non-uniform fields at dc or low frequency the voltage level required to break down the gap can greatly exceed the corona onset level and is in fact mainly a function of the total gap distance. At low frequencies, the mobility of the slower ions is such that they can move completely out of the active region within a half cycle and the breakdown phenomena is the same as at DC. However, at VLF and LF, depending on the length of the active region, the ion mobility is such that they are not all swept out of the active region within a half cycle. This leads to space charge buildup just above the initial ionization level. In non-uniform gaps, this space charge results in enhanced fields at the surface. This usually results in flashover at a much lower voltage than at low frequency.

The amount that the breakdown is reduced below the dc (or low frequency level) depends on the frequency and gap geometry. For non-uniform field gaps, there is little variation of the corona onset level with frequency up through LF. However, the breakdown (flashover) level in non-uniform field gaps can be considerably lower at VLF/LF than at 60 Hz. This is because at the higher frequencies space charge builds up, which enhances the fields and reduces the flashover voltage. Thus, there is a marked difference between the frequency variation of corona onset and the frequency variation of flashover. This difference is part of the confusion about the frequency effect at VLF/LF.

DC

Description

The appearance of positive and negative corona on wires is distinctly different. Positive corona appears as a uniform bluish-white sheath over the entire surface of the wire. Positive corona can also form individual long bright zigzag streamers. Negative corona appears as separate reddish glowing spots or small streamers at localized discrete spots distributed along the wire with the number of spots increasing with voltage.

The localization of negative corona is attributed to the effect of residual space charge. During an initial avalanche, slow-moving positive ions form near the electrode surface, enhancing the electric field. The result is that all of the secondary electrons resulting in further avalanches form in the enhanced field region. Thus, the streamers initiating electrons originate from a small local region (spot). The region beyond the cloud of positive ions has a reduced field, and a cloud of electrons tends to form there, restricting the growth of the streamers. Thus, negative corona predominantly consists of small current pulses (Trichel pulses).

For positive corona, initiating electrons are distributed over the entire ionization region. There are two types of visible corona for this case. The uniform glow on the surface is known as Hermstein glow (positive continuous glow corona) and is formed by small avalanches covering the positive surface. The second type of positive corona occurs as a long bright streamer. These long streamers consist of plasma filaments that carry their own ionization region and propagate rapidly toward the lower field region. The concentrated region of positive ions formed by these large avalanches simulates a sharp electrode extension with the associated enhanced field at the front. Further ionization in this intensified field may extend the spike and form a self-propagating streamer. These streamers result in current pulses 8 to 30 times as large as the negative corona current pulses (Qin, 1993).

The level of onset for corona is slightly different for positive and negative polarity depending on the diameter of the wire. Positive corona tends to form first (at lower voltage) for larger wires, and negative corona tends to form first for smaller wires. The presence of surface irregularities also can affect which polarity of corona forms first, with sharp irregularities tending to form negative corona first.

Measurements

Figure 6-30 contains the results of dc measurements made using a special coaxial setup shown in Figure 6-31 (Schukantz, 1993). The measurements were made with relatively small-diameter wires (0.04 cm to 1.27 cm). The measurement results for dry conditions show good agreement with the calculations of Sarma and Janischewskyj (1969). Our dc measurements indicated that negative corona formed at a slightly lower level than did positive corona for both the wet and dry cases. This is expected for the relatively small-diameter wires measured. In Figure 6-30, the slope of the positive and negative corona onset curves indicates that these curves cross over, and for larger diameter wires positive corona probably forms at a lower level than negative corona. The figure shows that this is true for the largest diameter measured (1.26 cm diameter) for both wet and dry conditions.

The appropriate formulas from Table 6-2A, labeled "Watt Formula," have also been plotted in Figure 6-30 for comparison. For dry conditions, the dc measurements correspond very well to the VLF/LF formula. For wet conditions, the VLF/LF formula is slightly above the dc positive onset curve.

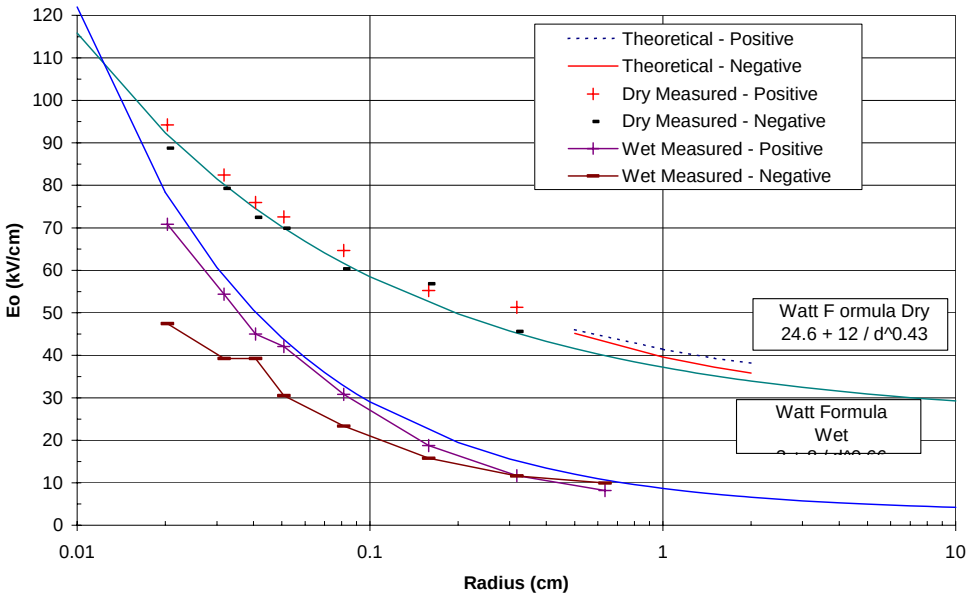

Figure 6-30. Dc corona onset measurements compared to theoretical results.

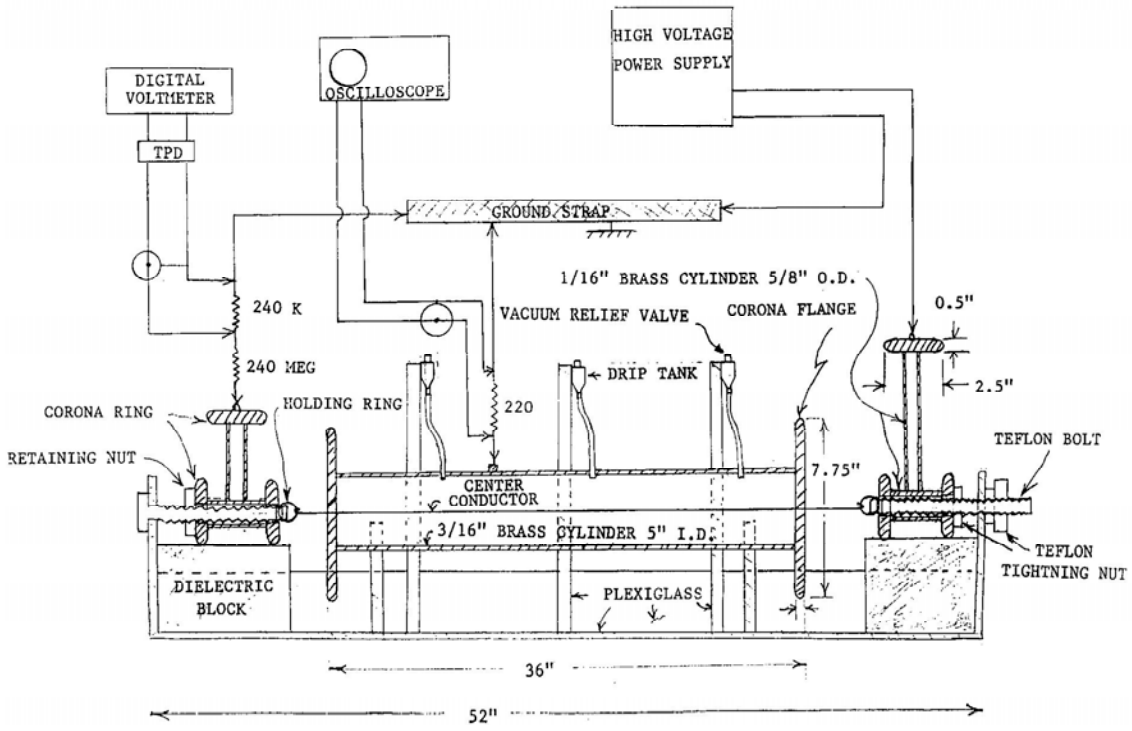

Figure 6-31. Coaxial cylinder dc corona test setup.

60 Hz

Description

The appearance of 60-Hz corona is the same as at dc, except that at 60 Hz the corona from both polarities is seen at the same time. For smaller wires, the negative corona appears first (at lower voltage), and as the voltage level is increased, positive corona appears. The opposite is true for larger diameter cylinders.

Dry Measurements

For smooth dry cylinders at 50-60 Hz, the best measurements available to us are those done by Peek (1929) and Schuman (1924). These results were discussed in Chapter 2 and are displayed in Figure 6-32. Note that there is quite a bit of scatter in Peek's 60-Hz data, while Schuman's 50-Hz data appears to be very self-consistent (i.e., forming a smooth curve). The best simple exponential curve fit to Schuman's data is given by the following formula:

$$E_c = 25.79 + \frac{18.88}{d^{.4096}} \text{ Volts peak / cm} \qquad (6\text{-}4)$$

This indicates that Schuman's data is asymptotic to a value of 25.79 kV/cm. This value is greater than the expected value of 24.4 kV/cm for dry air. At low frequency, the addition of humidity to the air increases the breakdown level, and it is likely that Schuman's data is higher than 24.4 kV/cm because of ambient humidity, which was not recorded. However, the difference could also be calibration error, as Schuman made these measurements in 1924 and the calibration was done using sphere gaps.

Schuman did not measure wires with diameters less than 0.1 cm. However, there are some 60-Hz data available for small wires from measurements made by Miller (1957) and some 50-Hz measurements (Bright, 1950), which are also shown in the Figure 6-32. A piecewise curve fit formula has been developed to fit Schuman's data along with data of Peek (1929), Miller (1957, and Bright (1950) for the smaller diameters. This curve fit (labeled "Schuman + Peek & Bright" in Figure 6-32) will be used for comparison to measured VLF/LF data.

Wet Measurements

Very little data is available for corona onset on wet smooth conductors at 60 Hz. Peek made measurements of corona onset for wet wires for only two diameters. The two data points are shown on Figure 6-33 (Peek, 1929). However, as seen in the figure, the corona onset for Peek's data at the two diameters is much below the measured corona onset at VLF/LF. This is attributed to the fact that Peek's definition of corona onset was probably different than the one used for the VLF/LF measurements. For example, corona onset defined by the first appearance of sparklers on falling drops will have a much lower onset voltage than results obtained using our definition.

Peek derives a formula that fits his two data points given below:

$$E_c = 3.1 + \frac{18}{d^{.338}}$$

Note that Peek specifically left the effect of air density out of this formula because it is not certain how air density affects the performance under spray-wet conditions. Peek's formula has also been plotted in Figure 6-33 but, as can be seen, for diameters of practical interest it is an extrapolation and therefore not useful for comparison to VLF/LF data, even if the definition of corona had been the same.

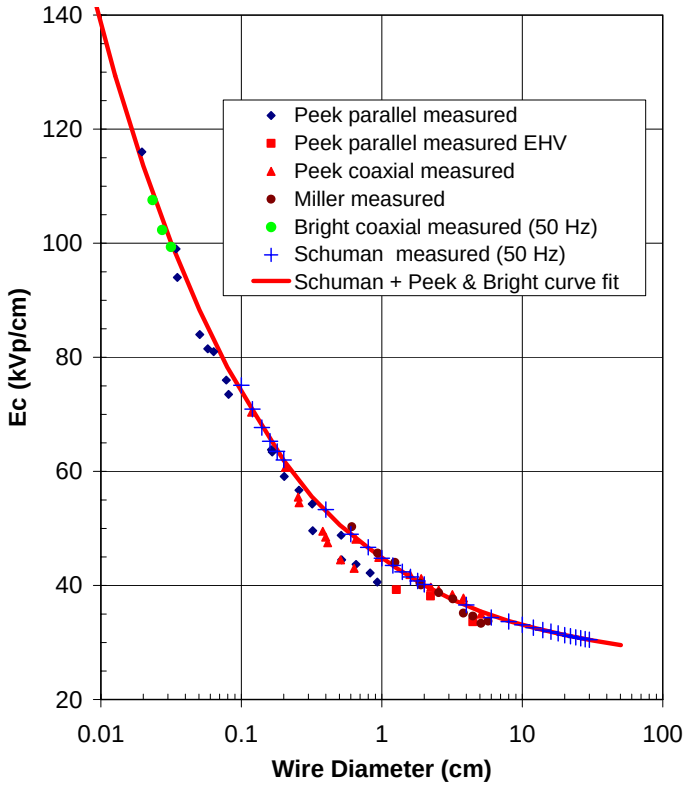

Figure 6-32. 50- and 60-Hz dry corona onset measurement comparison.

Miller (1956, 1957) made measurements of smooth dry cables and corona onset measurements for larger diameter wet stranded cables. He found that the level at which corona formed on wet stranded cables was below the corona onset level for dry stranded cables by a factor of 0.16 for cables of practical sizes larger than about 2 cm. Using this value, an estimated value of 60-Hz corona onset has been developed using Miller's data for smooth dry conductors, also shown in Figure 6-33. Note that the corona onset levels observed by Miller are also much lower than observed at VLF/LF, which may be due to a different definition for corona onset.

In summary, we do not have suitable 60-Hz corona onset data to compare with the measured VLF/LF data to determine the frequency effect for corona onset for wet cables. As an alternative, we have considered the effect observed when the frequency is shifted from VLF to LF.

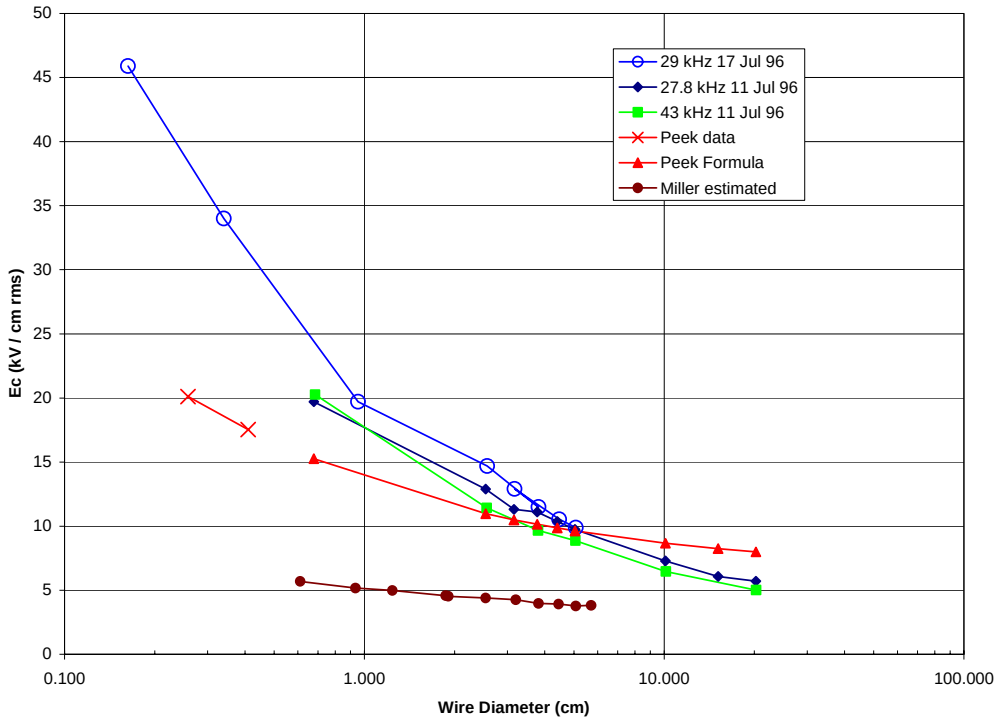

Figure 6-33. Wet corona onset measurements, smooth conductors, VLF/LF and 50–60 Hz.

VLF/LF

Background

Because of the limitations of the Forestport test cell, data is available at only a few VLF/LF frequencies. To characterize the frequency effect at VLF/LF, it is desirable to make the measurements at both VLF/LF and 60 Hz using the same test setups. Unfortunately, Forestport does not support 60-Hz measurements.

There is some past data for the corona onset level on smooth dry pipes at 60 Hz, and a comparison of the 60-Hz data to the Forestport VLF/LF data will be used to estimate the frequency effect for these conditions. There are no 60-Hz data available for the onset level for wet conditions for either smooth, stranded, or rough surfaces for comparison to our measurements.

Measurements

Smooth Dry Conductors

The Forestport data that best show the effect of frequency on the corona onset level for wires, pipes, and cables at VLF were measured using the inside horizontal configuration. Measurements for this test configuration were taken for a wide range of diameters at two or three VLF/LF frequencies.

The “corrected” corona onset data, developed from the air density experiment described earlier in this chapter, have been averaged over the measurements at the three densities. This average is plotted as a function of diameter in Figure 6-34. Also included in this figure are the 29-kHz data for the low-

humidity case. For comparison, Figure 6-34 includes both the Watt curve fit formula (Table 6-2A) for the 29-kHz (smooth dry) and the 60-Hz formula, which is the piecewise curve fit formula presented in Figure 6-32 (Schuman + Peek & Bright curve fit).

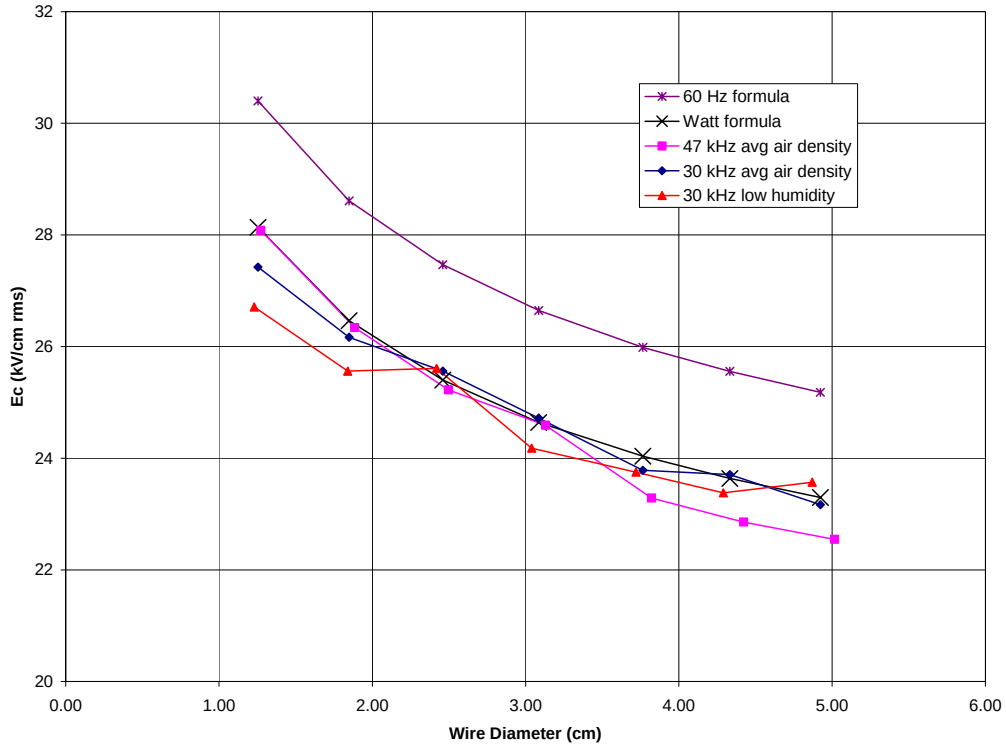

Figure 6-34. VLF/LF corona onset field level compared to formulas.

Note that the Watt formula is a good fit to the averaged "corrected" air density VLF/LF data but that both the formula and data are well below the 60-Hz curve. The available 50–60 Hz data contain some uncertainty due to the method of calibration and the fact that the humidity level was not known. However, they are the only data available for development of an estimated frequency correction factor. An estimate is given by the ratio of the corona onset level at VLF/LF using the averaged corrected air density data to the corona onset level at 50–60 Hz value using the piecewise curve fit formula for 60 Hz (Schuman + Peek & Bright). Figure 6-35 shows this correction factor. From the figure for smooth dry conductors at 29 kHz, over the range of diameters measured, the frequency correction factor is approximately 0.92 or 8% below the 60-Hz value. The frequency correction factor for 47 kHz is similar except that for wire diameters greater than about 3.1 cm it appears to drop down to 8% of the 60-Hz value.

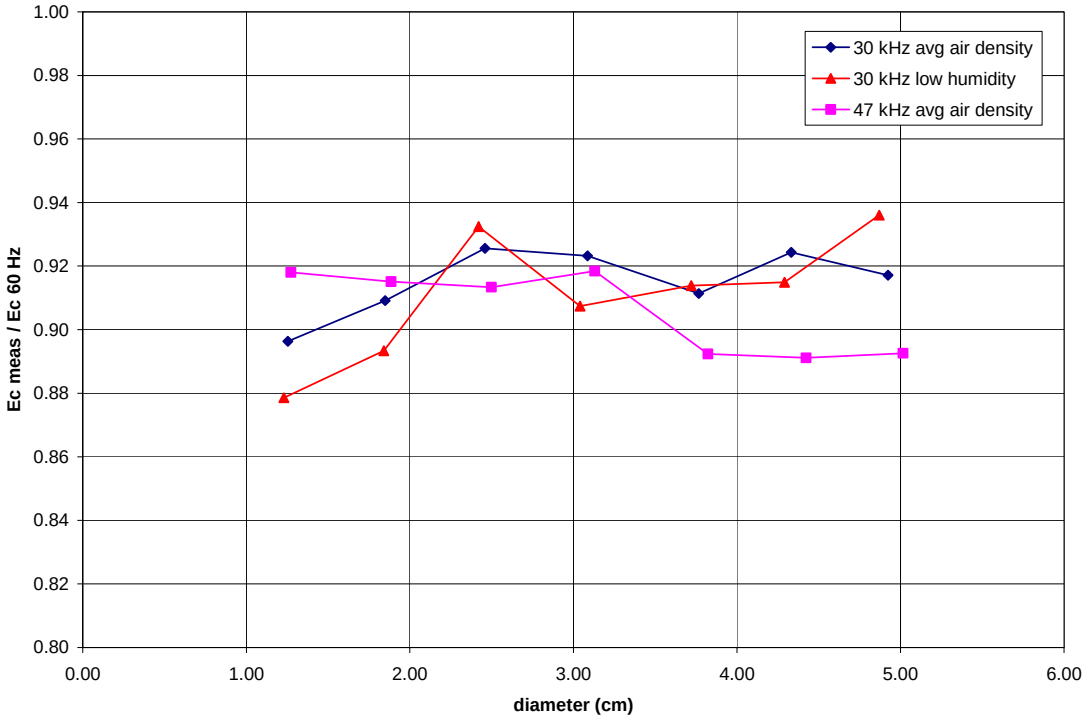

Figure 6-35. Observed frequency correction factor, smooth dry.

Smooth Wet Conductors

Corona onset for smooth conductors under wet conditions was measured using the outside test cell at frequencies of 27.8 kHz and 43 kHz. The data are shown in Figure 6-33 along with Peek's wet 60-Hz data discussed above. The figure also includes some other data taken inside at 29.0 kHz. Note that the smallest diameter conductor measured (0.68 cm) was stranded. All other conductors were smooth.

As an alternative to 60-Hz data, which is not available, the measured data for 43 kHz has been compared to the data for 27.8 kHz and the results shown in Figure 6-36. These results show that for smooth wet conductors the corona onset level at 43 kHz is 12% below the onset level at 27.8 kHz. The data given in Figure 6-36 show that the difference in corona onset level for wet stranded conductors at these two frequencies is minimal, except for the largest diameter. Some of the effect on corona onset for wet conditions is caused by humidity, which is assumed to be 100% for spray-wet conditions. As will be discussed later in this chapter, at VLF/LF humidity appears to reduce the corona onset voltage for larger diameter wires. This is opposite of the effect of humidity at 50 to 60 Hz and may be the cause of the reduction observed in the one data point for wet stranded conductors.

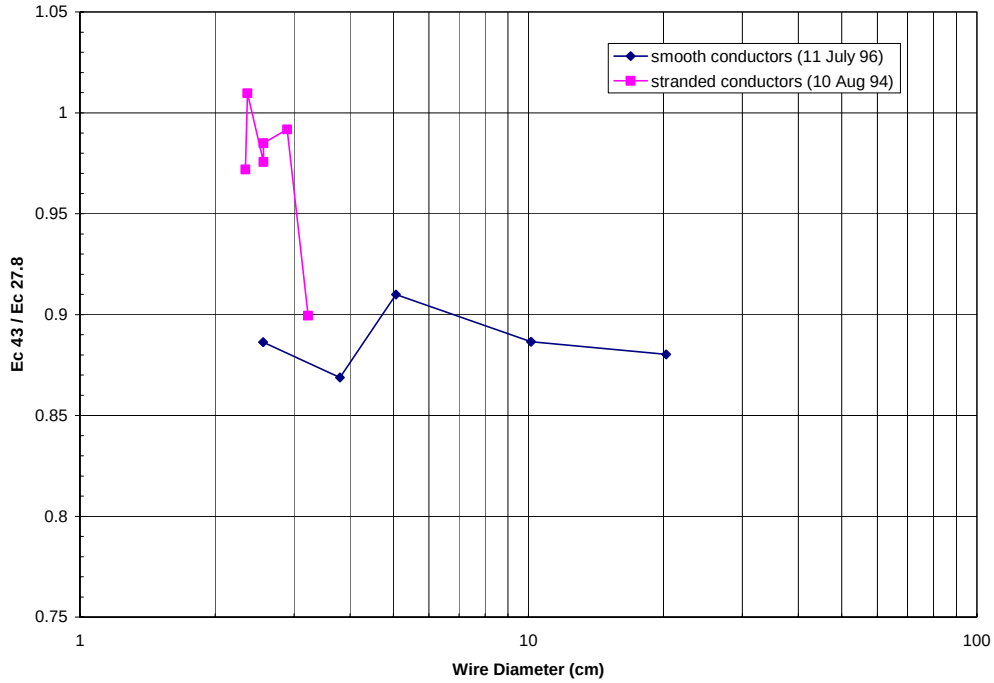

Figure 6-36. Frequency effect for smooth wet conditions.

Stranded Dry Conductors

For stranded cables, the breakdown voltage (or field) is a function of the cable stranding configuration and surface condition. The dry corona onset level for the stranded conductors taken during the air density test has been averaged at both 29 kHz and 43 kHz and is shown in Figure 6-37. Note that the since this data was taken with stranded cables it has not been corrected for air density. The figure shows that there is little, if any, difference between the corona onset levels at these two frequencies. This may be related to the fact that the air density correction factor of chapter 3 does not appear to apply to stranded cables over the range of density variations available in these measurements.

Stranded Wet Conductors

Data for wet stranded conductors are also shown in Figure 6-37. Again, these data show that there is very little difference in the corona onset level between 29 kHz and 40 kHz for the stranded cables.

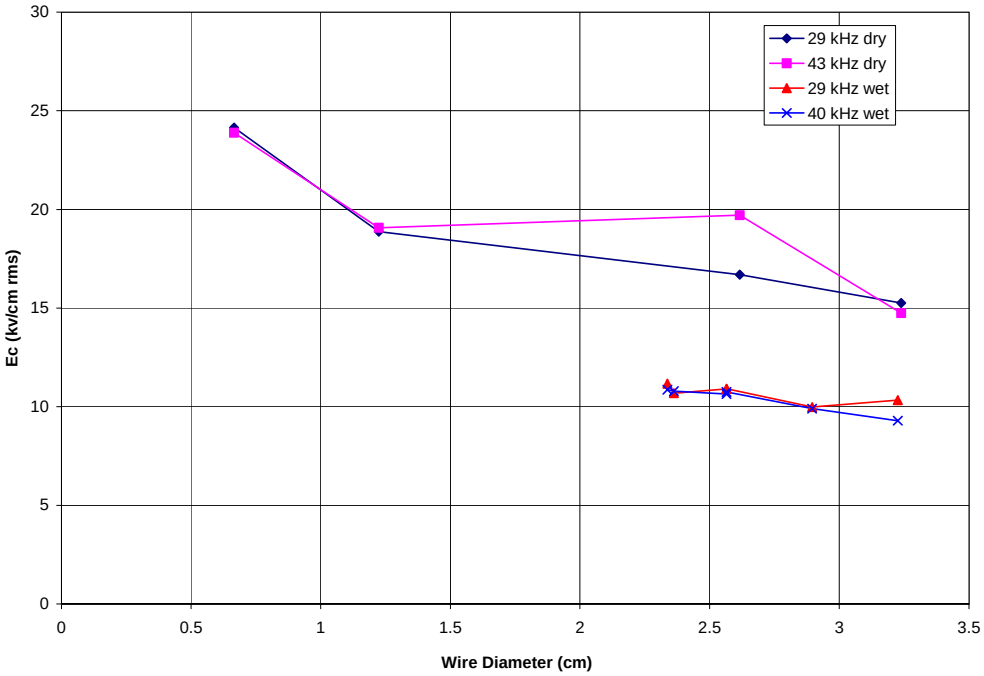

Figure 6-37. Frequency effect for stranded cables, wet and dry.

The Effect of Humidity

Introduction

The behavior of corona inception or breakdown in humid air is much more complex than for dry air. The addition of water vapor increases the humidity of the air. This changes the mixture of gases that compose atmospheric air. The difference in the gas makeup changes the individual parameters affecting breakdown. These parameters include the ionization coefficient (α), the electron attachment coefficient (η), the photon absorption coefficient (μ), and the mobility of both types of ions and electrons (V_+, V_-, and V_e). These parameters are all functions of the applied electric field, air density, and humidity. These parameters and the distribution of the electric field in the gap determine the level at which breakdown occurs and the nature of the breakdown. The presence of water vapor also changes the reactions involved with the generation of ions. This changes the makeup of the ionic species, which also results in changes to the breakdown characteristics (Poli 1985).

The net result is that changing the amount of humidity in the air changes the fundamental curve of breakdown voltage versus gap length (Paschen curve). The change is a function of the gap length. There are other effects that depend on the gap geometry and waveform, which leads to complicated behavior as a function of humidity. For example, for very small wires the corona onset voltage decreases with increased humidity, but for larger wire it increases with increased humidity (Gallo et al., 1969; Abdel-Salam, 1985).

In general, the addition of humidity increases the breakdown strength of air at low frequencies. The major mechanism for the dependence of breakdown strength on humidity involves the electron attachment rate (η). Van der Waals molecules such as O_2, N_2O, CO_2, and H_2O have greatly enhanced rates of electron attachment compared to the attachment rate with ordinary isolated single molecules (Hatano, 1986; Shahin, 1969). The interaction between the various components in the gas is

complicated and incompletely understood. The presence of water vapor seems to greatly increase the rate of the formation of negative oxygen ions, which are not stable and shed the electron with time constants less than 100 pico seconds. Though this time constant is short, the net effect of increasing humidity is to increase the absorption rate of electrons. This results in greater breakdown strength at dc and low frequency because the net ionization coefficient ($\alpha - \eta$) is reduced, increasing the field necessary to cause avalanches. However, at the same time, this process leaves an increased number of residual negative ions that can reduce breakdown strength at higher frequency because the residual charge enhances the effective local field when the polarity is reversed.

Another proposed mechanism for increased electron attachment rates involves the direct attachment of electrons to the water molecules (Banford & Tedford, 1977; Klots & Compton, 1978; Parr & Moruzzi, 1972; Kreuger, 1991, p. 85). Experiments indicate that a single water vapor molecule cannot absorb an electron. However, aggregate molecules of water $(H_2O)_n$ are thought to be very effective at forming negative ions. At moderate humidity levels and room temperature, especially where the water vapor is approaching condensation, there are likely to be large numbers of small aggregates (Elford, 1991). The negative ions formed by water aggregates are likely to have very slow drift velocities.

Kuffel indicates that increased breakdown voltage with humidity may be due to both increased electron attachment and a reduced secondary ionization coefficient due to the absorption of photons by water vapor molecules (Meek & Craggs, 1978, p. 421).

Abdel-Salam (1985) developed a method for calculating both the inception voltage and corona current as a function of voltage in humid air for a positive wire above a ground plane. He included the effect of an increasing photon absorption rate with increasing humidity, which, as Kuffel indicated, reduces secondary electrons. However, the absorbed photons also liberate electrons (photoelectrons) that are distributed throughout the ionization layer. Abdel-Saam's calculation indicates that the distribution of these photoelectrons depends strongly on gap geometry and plays a very important role in determining whether the inception voltage increases or decreases with increasing humidity. His theoretical results show increasing inception voltage with increasing humidity for large diameter wires but decreasing inception voltage with increasing humidity for smaller diameter wires. These theoretical results are in agreement with both the measurements of Gallo et al. (1969), which show decreasing corona onset voltage with increased humidity for small wires. Measurements at 60-Hz on larger wires show increased corona onset voltage with increased humidity.

Gosho and Saeki (1985) propose yet another way that humidity may affect breakdown. They propose that the surfaces of the electrodes absorb water when humidity is present and that the absorbed water somehow increases the production rate of initiating electrons from the surface.

One interesting dilemma is that most of the results reported give the effect of humidity in terms of the absolute humidity in g/m^3. This is reasonable in that it implies that the effects are tied to the constituency of the gas. However, the measurements by Gallo et al. (1969) indicate clearly that the corona phenomenon is a function of relative humidity and not absolute humidity.

Even if the exact cause is not known, it is well known that increasing humidity at dc and 60 Hz increases the breakdown level for practical gaps and wire sizes. This is reflected in the various humidity correction factor curves that have been developed (Cobine, 1958, p.183) and that are included in various high-voltage testing standards (see Chapter 3). However, at the Forestport test facility, it was observed that humidity has the opposite effect at VLF/LF, reducing the breakdown

level significantly. It follows that if humidity increases the breakdown level at 60 Hz but reduces it at VLF/LF, humidity must play a significant part in the observed frequency effect.

The section below presents the results of measurements of the effect of humidity at dc and 60 Hz gathered from the literature. This is followed by the results of VLF/LF corona onset measurements at Forestport designed to observe the effect of humidity. The Forestport measurements indicate that the effect of humidity at VLF/LF is relatively complicated and plays a large part in the frequency effect. A section follows that includes a discussion of theoretical considerations and how they relate to the observed frequency-humidity measurements; our overall formulation for these effects follows that.

DC

Dc measurements of the Townsend current have been used to determine the ionization and attachment coefficients (α and η). Measurements by Davies (1990) show that the electron attachment rate (η) increases when moisture is present. The amount of the increase is a function of the electric field, increasing rapidly with field strength. A partial explanation for this is contained in Verhaart and van der Laan (1984). They used dc measurements to determine the value of the effective ionization coefficient (α - η) as a function of humidity. They concluded that the presence of water vapor in the air effectively reduces the number of free electrons. Their measurements indicate that the mechanism for this reduction is a process that reduces the recombination rate of negative oxygen atoms. They propose that collisions with water vapor molecules convert the unstable negative oxygen ions into a more stable state, greatly reducing the rate at which the ions give back the extra electron.

The value of the field at which the effective ionization coefficient (α - η) equals zero corresponds to the fundamental breakdown strength of the gas, which is the breakdown field for a very large uniform field gap. Verhaart and van der Laan observed that the critical value for dry air is 31.8 V/cm/Torr, which corresponds to 24.16 kVp/cm at STP. The critical value observed for humid air was 34.5 V/cm/Torr, corresponding to 26.22 kVp/cm at STP. They found this to be independent of the amount of water vapor when the vapor pressure was between 0.05 and 11.25 mm Hg at 778 mm Hg total pressure. The increase when humidity is present equals 8.5%, and this is the expected value for the increase of the dc breakdown field in a large gap. The increase for smaller gaps may be less. It is somewhat surprising that this result is independent of humidity. However, as shown below, both the 60-Hz continuous wave breakdown voltage and the low-probability breakdown voltage for impulse waveforms have only a small dependence on the amount of humidity present.

The asymptotic value for breakdown across large gaps should correspond to the asymptotic value for corona onset on large cylinders. Verhaart and van der Laan (1984) indicate that this asymptote for atmospheric air (containing normal amounts of humidity) is expected to be 26.2 kVp/cm at STP as opposed to 24.4 kVp/cm for dry air. If Schuman (1924) used atmospheric air, this provides a possible explanation as to why his 60-Hz corona onset data are asymptotic to 25.8 kVp/cm instead of 24.4 kVp/cm.

Dc measurements of corona onset on wires above a ground plane have been undertaken by Gallo et al. (1969) as a function of temperature and humidity. These measurements indicate that for very thin wires the inception voltage decreases significantly with increasing humidity for both positive and negative polarity. They also made an extensive set of corona current versus voltage measurements and found that the variation with humidity follows relative humidity and not absolute humidity. They attribute this to the greatly reduced mobility of the positive ions when they combine with the polar water molecules, known as hydration. This process is most important for positive corona (Shahin, 1969). For negative corona, they speculate that the free electrons may be subject to hydration and absorbed to form negative ions.

Gallo et al (1969) also made observations of the uniformity of the corona along the wire as a function of humidity and found that the both the appearance and the uniformity of the corona was affected by the humidity. The changes were most closely correlated with relative humidity.

For thicker wires, it is well known that the corona inception voltage at dc and 60 Hz increases with increasing humidity. Abdel-Salam (1985) calculated corona onset with positive polarity for both thin and thick wires as a function of relative humidity. The calculations showed a significant reduction in the onset voltage with increased humidity for thin wires. For example, at 88% relative humidity the calculated inception voltage was less than 75% of the calculated value for dry air. This is in agreement with the measurements of Gallo et al. (1969). For the larger (1-inch) diameter wire, the calculated curve shows a nearly linear increase with humidity. The slope of the calculated curve for the larger diameter wire agrees well with the measured breakdown in small gaps at 60 Hz (Kuffel and Zaengle, 1984**,** p. 104)

Gosho and Saeki (1985) made dc measurements using a negative point plane geometry. The point had a very small radius (0.08 m). They found that the pre-breakdown current increased significantly with increased humidity. This result is consistent with the results of (Gallo et al.) for small diameter wires. Gosho and Saeki measured the statistical time lag for flashover and found that it was considerably reduced by humidity. They also note that with increasing humidity, the Trichel pulse frequency increased and the onset level for continuous corona was reduced. They attribute their results to increased electron emission from the electrode surface due to absorbed water vapor. They note that the increase in humidity is equivalent to that of providing external irradiation.

Impulse Breakdown

The effect of humidity on breakdown for transients depends on the definition of breakdown, the waveform, and the gap. The test standards define waveforms such as lightning and switching transients in terms of their rise and fall times. The standard correction factors for impulses are specified for V_{50} (the peak voltage that will break down the gap 50% of the time) for various waveforms. Gap geometry does have an affect, but it is not a strong function of gap length (Cobine, 1958, p. 182).

Cobine (1958) reports the results of the early development of correction curves for the effect of humidity. He states that the correction factor depends on the nature of the gap and on the presence of insulating material in the field, such as the flashover path of an insulator. For surge or impulse waves, the correction factor depends on the wave shape and the observed time lag of breakdown (Curtis, 1928). Cobine gives a set of correction curves for the various conditions. These are referenced to a correction factor of 1 at “standard humidity,” which is taken to be a water vapor partial pressure of 0.6085 inches Hg. This corresponds to 1.54 cm Hg and a relative humidity of 47.7% at STP (20° C) or 64.7% at STP (25 ° C). The correction factors vary $\pm$ 8% or more with humidity, depending on the gap configuration and waveform. All of the correction factors given by Cobine show increasing breakdown strength with increasing humidity.

Several experiments involving humidity variation were conducted at the University of Swansea in Wales. These experiments were performed in a specially constructed chamber 1.2 meters internal diameter and 3 meters in height with a closed-loop control system that allowed the humidity in the chamber to be adjusted to maintain the dew point constant to within 0.1° C (Davies et al, 1989). This chamber allowed the environmental conditions to be much more closely controlled than in the normal high-voltage laboratory. Tests with this chamber have smaller confidence intervals than experienced in open laboratory tests.

Many tests were done using this chamber with the temperature near 20° C, which limits the maximum absolute humidity to about 17 g/m^3. These tests indicated that the 50% breakdown voltage for impulse waveforms increased nearly linearly with absolute humidity. These tests were then repeated at 30° C, which allowed a maximum humidity of approximately 30 g/m^3, and the linearity was found to extend to the higher humidity levels (Figure 6-38). The 1989 data were taken using a positive polarity switching impulse waveform (100/2500 μs) applied to a 5-cm diameter sphere 20 cm above a ground plane. These measurements, taken at 30° C, have a rate of voltage increase that is approximately 1.8% per g/m^3 increase in humidity referred to the standard humidity of 11 g/m^3. Davies et al. (1989) found the slope of their data to be about twice that of the CEA/IEC standard (1989, 1994) humidity correction factor for switching impulses.

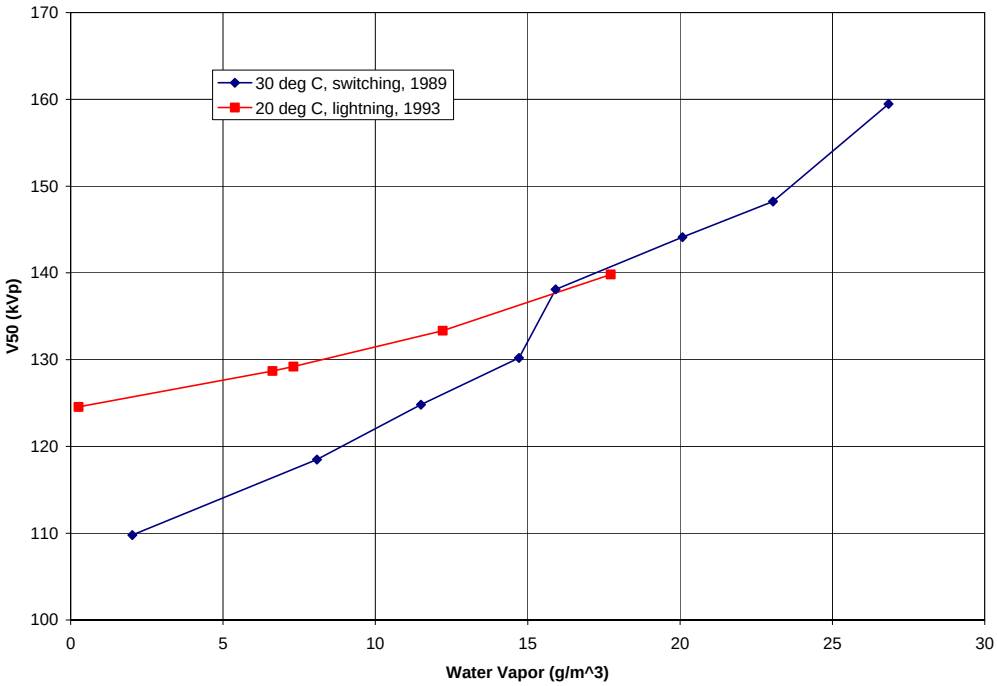

Figure 6-38. The effect of humidity on the breakdown strength of air for impulse waveforms (after Davies et al. 1989).

In a different test, Davies et al. (1991) measured the 50% breakdown voltage for positive polarity switching impulses at temperatures near 20° C and found the increase rate to be 0.98% per g/m^3. This compares favorably to both the IEC standard and positive polarity switching transient measurements using a 20-cm rod-plane gap by Soetjipto et al. (1987) that gave an increase of 1.06% per g/m^3. The difference between these two measurements is not explained, and it may be due to differences in gap geometry or waveform.

Later, using a new chamber, they measured the breakdown voltage for a positive lightning impulse (0.88/45 μs) applied to a 2-cm rod with a hemispherical end cap located 20 cm above a ground plane (Davies et al., 1991). These tests were done with the temperature near 20° C. The data for V_{50} with the lightning impulse are shown in Figure 6-38, and have a slope of approximately 0.69% per g/m^3. This indicates that the slope of the breakdown level versus humidity is a function of the waveform, being greater for pulses with faster rise times.

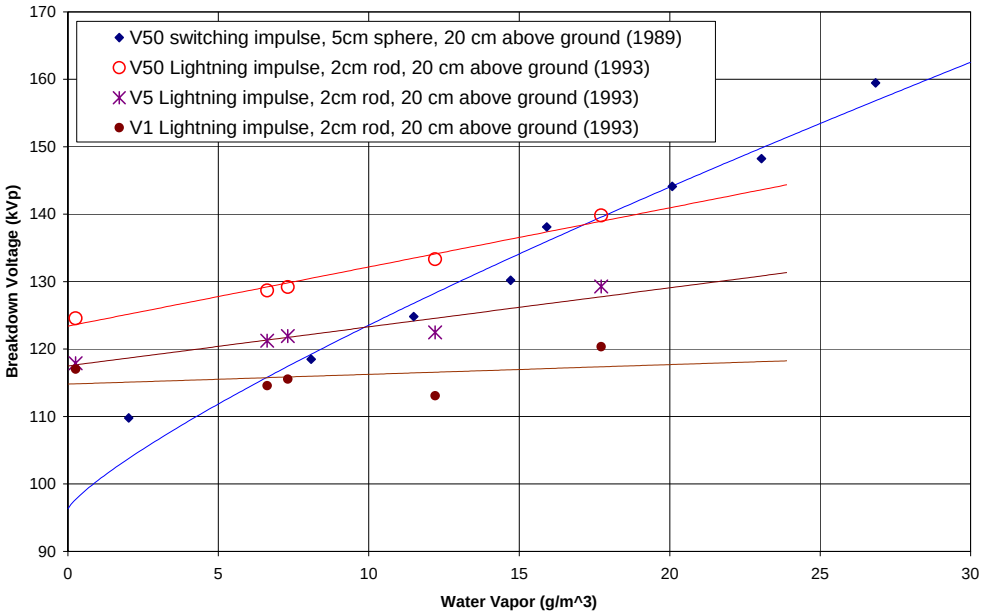

Figure 6-39. The effect of humidity on the breakdown strength of air for transient waveforms as a function of probability level (after Davies et al. 1991).

Davies et al. (1991) also measured probability levels other than 50% and found that the slope versus humidity level decreases with decreasing probability level. Their data for 1%, 5%, and 50% probability of breakdown are shown on Figure 6-39. The slope of the curve fit to the 1% breakdown level has a slope of 0.11% per g/m^3, which is on the order of that measured at 60 Hz (see 60-Hz section below). It should be noted that the variability of the measurements of low-probability breakdown is high (much greater than for the 50% measurements), so the confidence level of the estimated slope is reduced.

The low-probability of breakdown level for pulses corresponds more nearly to the withstand level for CW signals. Davies et al. (1991) observed that the low probability of breakdown voltage is almost independent of humidity as long as the humidity is above a minimal level. This is consistent with the findings of Verhaart and van der Laan (1984) mentioned above. The corresponding mean field strength at withstand found by Davies et al was 5.03 kV/cm, which agrees with the nationally recognized withstand level of 5.0 kV/cm associated with positive streamer propagation for dry conditions.

Meek and Craggs (1978) report the results of several investigations into the effect of humidity on impulse breakdown. On page 640, they give a curve of humidity correction factors for dc and power-frequency voltages and for impulse voltages. On page 642, they report on several experiments involving the effect of humidity. One of these experiments involving rod-plane and rod-rod gaps between 20 and 80 cm long used lightning and switching transients of both polarities. The results of these measurements indicate that the humidity correction factor does not change much with gap length. The breakdown for positive polarity was found to be more affected by humidity than for negative polarity. In addition, switching-impulse breakdown was found to be more affected by humidity than dc and power frequencies. Another finding showed that if humidity effects were measured in an enclosed system, errors occurred due to the effects of residual discharge products, which typically reduce the onset voltage for breakdown.

Poli (1985) provides a very interesting set of measurements designed to examine the effect of humidity on corona formation for impulses. The test setup was a positive polarity rod-plane gap consisting of a 2-cm diameter rod with a hemispherical end cap located 40 cm above the ground plane. The relative frequency of corona formation and the statistical time lag to corona formation were measured for three levels of humidity. The corona onset voltage is represented by the extrapolated zero-probability corona inception voltage and is given in Table 6-5 below. Note that the corona inception voltage does increase with increasing humidity consistent with the measurements for dc, 60-Hz, and low-probability impulse breakdown. However, the slope inferred from Poli's data is only 0.06% per g/m^3; about one-fourth of that observed for the dc and 60-Hz breakdown measurements. In addition, Poli found that the statistical time lag for corona formation increased with humidity. This is in contrast to Gosho and Saeki (1985) who found that the statistical time lag for impulse flashover was greatly reduced with increased humidity. However, both of these authors find the production of initiator electrons to increase with increased humidity.

Table 6-5. Corona onset for 2-cm rod-plane gap 40-cm above-ground positive polarity impulses (after Poli, 1985).

Humidity (g/m^3)	Threshold Voltage V_s (kVp)	Ratio $V_s/71$
7.5	71.18	1.0026
13.5	71.34	1.0048
19.5	71.68	1.0095

60 Hz

Cobine (1958, p. 182) reports that Frank made measurements of the effect of humidity on corona formation and found that the initiation voltage increased by about 3.5% when the relative humidity increased from 0 to 100%. The increase was essentially linear with humidity and nearly independent of electrode shape and gap length.

Kuffel and Zaengle (1984, pp. 103-105) include a discussion of the effect of humidity on the breakdown level at 60 Hz. Kuffel made measurements using sphere gaps sized between 2 and 25 cm diameter at various spacings. He found no uniform dependency for the change in breakdown voltage with gap length. This is not surprising since the addition of humidity changes the gas constituents and hence the Paschen curve of breakdown voltage versus gap length. This implies that the change in the breakdown voltage for the new gas mixture can be different for each gap length. Kuffel's measurements at 60 Hz indicated that for a given humidity the breakdown voltage increased with gap length up to a certain critical length, where it peaked. The breakdown voltage then decreased for larger gaps. This introduces the very important concept of a critical gap, which is discussed in a later section.

For a given gap length, Kuffel found that the rate of increase in breakdown voltage was always greatest between 0 to 4 mm Hg humidity and was less for humidity larger than 4 mm Hg. The breakdown voltage increased approximately linearly from 4 mm Hg to 17 mm Hg as long as the gap spacing was less than that having the maximum breakdown voltage. There was less linearity for larger gaps.

The humidity above is given in terms of the vapor pressure p_v in mm Hg. The absolute humidity h_a in g/m^3 can be calculated from the following formula:

$$h_a = p_v \frac{288.8}{273 + t}$$

where t is the temperature in degrees C.

At 20° C, the factor 288/(273 + t) is equal to 1.02 so that at STP(20) the value of the absolute humidity in g/m^3 is only 2% greater than the vapor pressure in mm Hg.

Figure 6-40 shows Kuffel's results for the largest diameter spheres (25 cm) at 1-cm spacing, which approximates a uniform field gap. Kuffel gives the following conclusions for breakdown at dc and 60 Hz from his measurements:

1. The breakdown voltage increases with the partial pressure of water vapor.
2. The total voltage change for a given humidity change increases with gap length.
3. The humidity effect increases with the size of the spheres and is largest for uniform field electrodes.

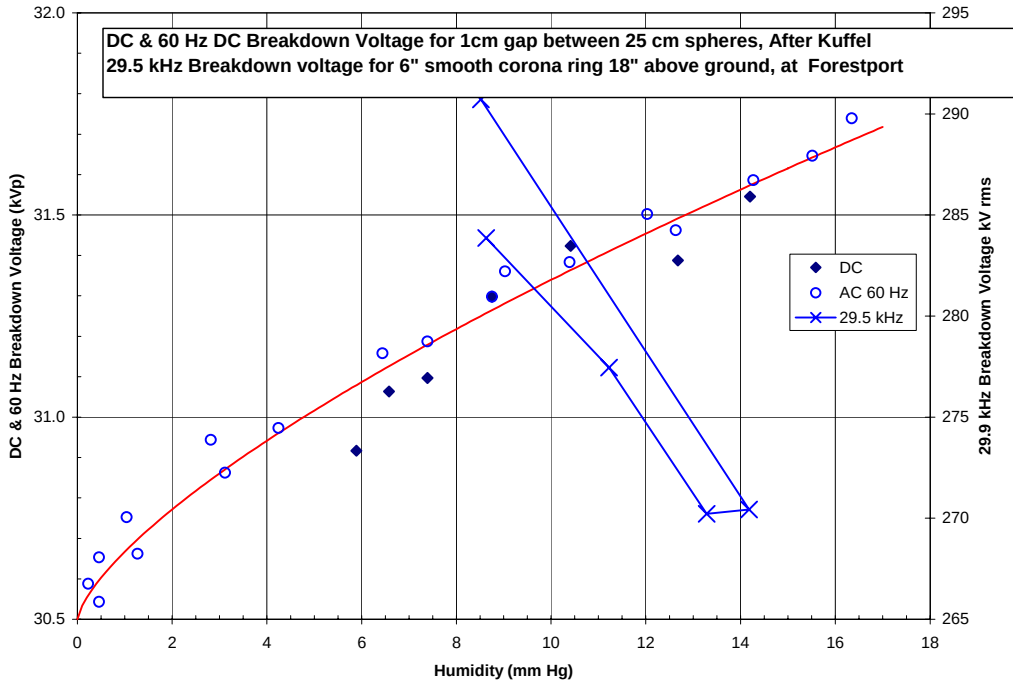

Figure 6-40. 60-Hz breakdown as a function of humidity (after Kuffel & Zaengle, 1984).

Kuffel indicates that all of these effects can be explained by Townsend's theory and the fact that the water vapor present in the air absorbs electrons and thereby changes the effective ionization coefficient (α - η), which is integrated over the distribution of the electric field within the gap.

There are other observations confirming that the presence of water vapor increases the breakdown level at dc and 60 Hz (Kuffel, 1961 a & b; Standring et al., 1963). They present breakdown data between spheres for various levels of humidity. The largest sphere diameters (100 cm) at the largest

spacing (50 cm) exhibited the largest change. Within the humidity range of 4 to 17 g/m^3 (relative humidity 25 to 95% at 20° C), the relative increase of breakdown voltage observed was linear between 0.2 to 0.35% per g/m^3. Kuffel concludes that at 60 Hz the humidity effect is unlikely to exceed 2 or 3% over the range of humidity normally encountered in the laboratory environment and only needs to be taken into account for either very high or very low humidity. This finding is also consistent with the discussion of Meek and Craggs (1978, p. 544), which shows a maximum variation of 4% with humidity for gaps of 1 to 3 cm in length.

These findings are also consistent with the findings of Davies et al. (1991) for low-probability impulse breakdown and the findings of Verhaart and van der Laan (1984) that the breakdown strength of air containing water vapor is approximately independent of the humidity. However, it does not seem to be consistent with their finding that the fundamental breakdown strength of air is approximately 8% greater than the breakdown strength of dry air when humidity is present. The difference may be due to the fact that the 60-Hz measurements were taken with relatively small gaps and the measurements of Verhaart and van der Laan with a very large gap.

For the case of highly non-uniform fields, where corona forms prior to breakdown, there are some conflicting data. For example, Meek and Craggs (1978, p. 421) describe several different tests involving highly non-uniform field gaps. These tests indicated that the presence of humidity changes the character of the corona, reducing its stability and extent. This is consistent with the observations of Gallo et al. (1960). In some of these cases, the rule of increasing sparkover voltage with increasing humidity was not followed. For example, for smaller diameter wires, this was the case with the data of Gallo et al.

Meek and Craggs (1978, p. 421) also report conflicting data from measurements using rod-plane and rod-rod gaps of various lengths. For these tests, the effect of humidity was markedly different depending on whether breakdown occurred prior to the formation of corona, or developed from either a pulsed form of corona or a continuous glow corona. The breakdown level with no corona preceding it followed the rule of approximately 0.23% per g/m^3 increase with humidity. The breakdown voltage showed a marked increase with humidity when the breakdown occurred from pulsed corona. In contrast, the breakdown voltage decreased with increasing humidity when breakdown occurred from continuous-glow corona humidity (Meek & Craggs, 1978, p. 613). The type of corona that preceded breakdown depended on the geometry of the gap and the humidity.

Other VLF and RF Measurements

Sometimes switching transients on power lines have components in the VLF/LF range or higher. These transients, called oscillatory switching impulse voltages (OSIV), are pulses consisting of exponentially damped sine waves. There have been some experimental investigations on the breakdown of gaps with this type of high-voltage transient. Some of these investigations indicate that the breakdown strength for OSIV is lower than that for standard switching impulse voltages (SSIV) (Couper et al., 1988).

Bharadwaj and Prabhakar (1996) measured the effect of the variation of humidity on the breakdown characteristics of a gap when exposed to both unidirectional and bi-directional high-voltage sine wave pulses with frequencies in the VLF range (4.2, 10, and 20 kHz). The temperature used for these measurements was 40° C, the humidity range was from 14.1 to 36 g/m^{3,} and the gap length was varied from 8 to 30 cm. They found some unusual things. First of all, the bi-directional OSIV breakdown occurred at significantly lower values than unidirectional OSIV. In addition, they found that breakdown often occurred on the second or subsequent peaks of the sine wave where the voltage was much lower than on the first peak. This indicates that the mechanism of breakdown for

OSIV is different than for SSIV. Both of these phenomena are consistent with the proposition that space charge buildup occurs with a time constant such that it lowers the breakdown voltage for VLF/LF sinusoidal waveforms. They also found that for bi-directional waveforms of 10 kHz and above, the breakdown level increased rapidly with humidity for low levels of humidity, but when the humidity was greater than 28 g/m^3 the rate of increase reduced. The amount of reduction depends on gap length, and for the shorter gaps the breakdown level actually reduced with increasing humidity for frequencies of 10 kHz and above.

A similar investigation using transient RF pulses in the HF range was undertaken by Australian investigators following the observation of "pluming" on a high-power HF transmitting antenna located at Darwin (Plumb et al., 1984 a & b). The description of the pluming closely resembles flares (see description of corona in this chapter). In their investigation, they found that the corona onset level at HF was approximately the same as at dc. They made measurements with increased humidity and found that the presence of humidity reduced the onset level by approximately 1%, which is consistent with the results reported by Cobine (1958, p. 182).

All the measurements of Plumb et al used RF pulses varying from 10 to 300 μs. They found that the breakdown voltage decreased as the pulse length was increased from 10 to 100 μs. Beyond 100 μs, no decrease was observed for pulse lengths up to 300 μs. They saw an increase in corona onset level with humidity for these relatively short pulses, while for CW waveforms at our VLF/LF test facility we see a decrease in corona onset level with humidity. This is consistent with the proposition that the breakdown level at VLF/LF is lowered due to the buildup of space charge but that the time constant for the charge buildup is longer than one cycle at VLF/LF.

Another interesting result from Plumb et al was that for 10-μs pulses the breakdown voltage decreased when the gap had previously been repeatedly broken down with 100-μs pulses. This was no longer true for 10-μs pulses. They attribute this phenomena to the formation of new species such as NO, NO_2, etc., which requires 100 μs or more. The relatively long time constant for the formation of these new species may also explain some of the reduction in onset levels observed at VLF/LF.

Forestport VLF/LF Measurements

Corona Ring Test

At Forestport, we often observed that the breakdown voltage for dry conditions on a given test sample was reduced if the humidity was high, particularly if there was still water laying on the floor from a previous wet test. For this reason, we suspected that increased humidity lowers the corona onset or breakdown voltage at VLF/LF. This is the opposite of the effect of humidity at 50/60 Hz. A preliminary investigation was done in February 1995 using a 6-inch minor diameter toroidal corona ring positioned horizontally 18 inches above the ground. This was our first attempt at measuring the humidity effect. The data for the ring at 29.5 kHz, shown in Figure 6-41, confirmed that humidity decreases the critical voltage at VLF. These data were measured using a horizontal corona ring, but because it has a large minor diameter the correction factor developed is considered to be a good estimate of the asymptotic value for large diameter wires and cables.

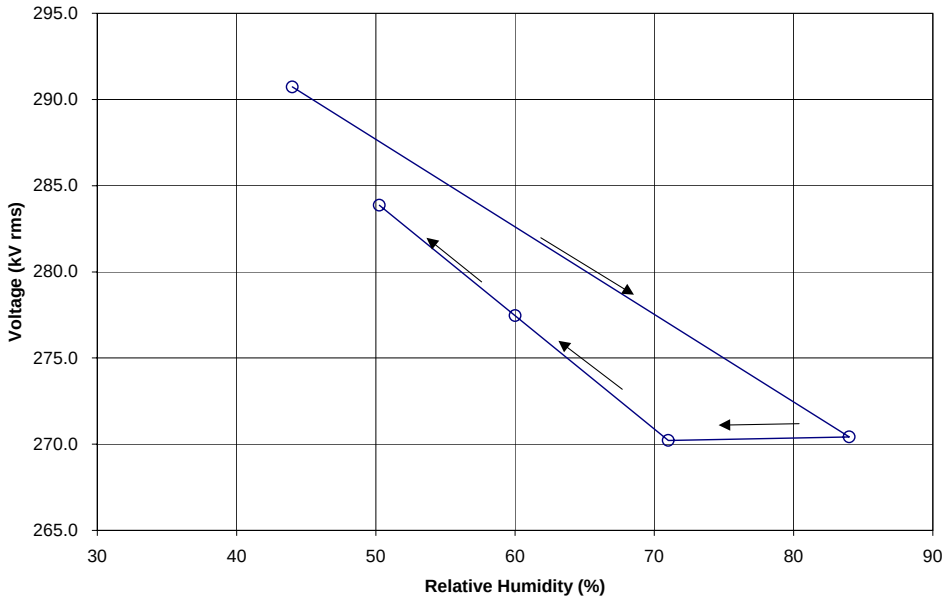

Figure 6-41. Humidity test, 6-inch toroid at 29 kHz.

The test procedure consisted of first measuring the dry flashover/flare voltage for the ring in ambient conditions. Then the humidifiers were turned on and the humidity was increased to approximately 90%. The humidifiers were turned off and the dry flashover/flare voltage measured again. Following that measurement the roll-up door was opened for a few minutes to exchange some of the humid inside air for the dryer outside air. The door was closed and the dry flashover/flare measured again. This was repeated two more times for a total of five data points. The arrows in Figure 6-41 indicate the order of the measurements.

There is a hysteresis like effect in the 29.5-kHz data, which is attributed to the measurements being taken before humidity equilibrium was established. There are at least two processes involving time constants that must settle to reach equilibrium. These are the mixing of the dry outside air with the inside humid air and the amount of water absorbed on the surface of the electrode. It is likely that if enough time is taken to allow the humidity processes to come to equilibrium that the data points would define a single curve.

The flashover/flare data for these tests were also plotted in Figure 6-40 for comparison to the dc and 60-Hz data of Kuffel. Note that the slope of the curve for the 29.5-kHz data is strongly negative compared to the positive slope of the curves for dc and 60-Hz data.

Proposed Asymptotic Correction Factor

The humidity correction factors defined in the various test standards are normalized to the standard humidity, 11 g/m^3, so that they are equal to 1 at standard humidity (Kuffel & Zaengle, 1984). The standards all define the humidity correction factor such that it is proportional to breakdown level. Since breakdown level increases with increasing humidity, the correction factor is positive (CF > 1.0) when the humidity is above the standard level and negative (CF < 1.0) when the humidity is below the standard level. However, in order to compare VLF/LF data to the 60-Hz data, we have defined a different humidity correction factor that is normalized to zero humidity (dry air). This correction

factor is defined to be the ratio of the breakdown voltage for air at a given humidity to the breakdown voltage of dry air (zero humidity).

Data normalized in this way are shown in Figure 6-42. Shown in the figure are the normalized curves of the switching impulse data by Davies et al. (1991) and the 60-Hz data after Kuffel (1961 b). These curves begin at 1.0 for dry air and increase above that as the humidity level increases. The curve for 60 Hz has a value of 1.5% at the standard humidity level (11 g/m^3).

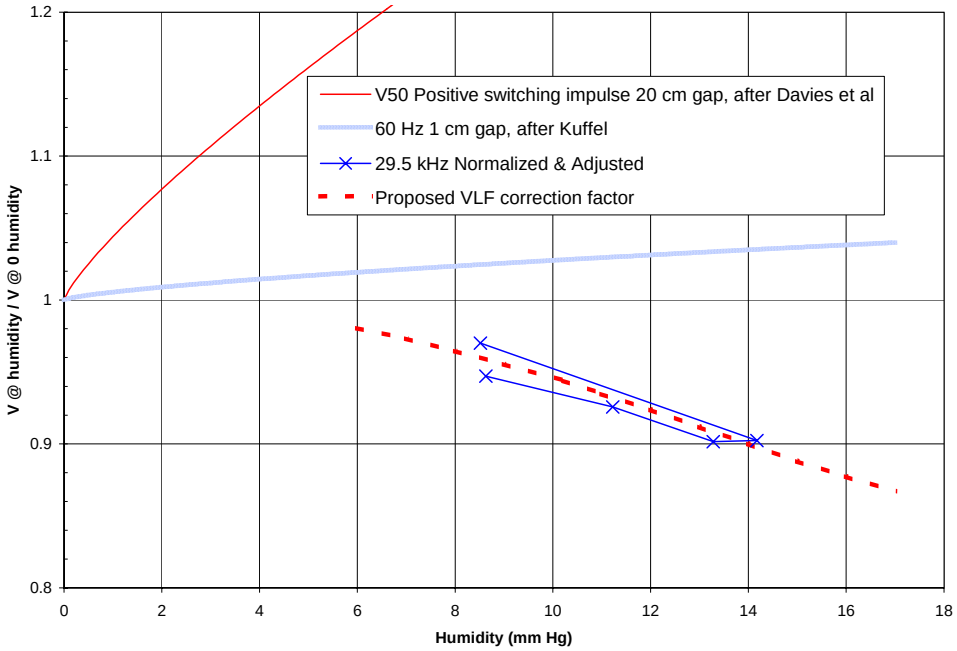

Figure 6-42. Proposed VLF humidity correction factor.

Figure 6-42 also includes the normalized 29.5-kHz data measured at Forestport using a 6-inch ring. Measurements at zero humidity could not be done at Forestport, and the data were normalized to the estimated value at zero humidity so that it could be plotted on the same scale. The estimate was based on the assumption that the breakdown level at 29.5 kHz for zero humidity is nearly the same as it is at 60 Hz. The process involved first normalizing the breakdown voltage data as a function of humidity by the largest value. A curve, labeled "proposed correction factor" was fit to this normalized data. This curve was then adjusted down so that the value of the curve extrapolated to zero humidity was approximately 1.0 (see Figure 6-42).

The humidity correction factor is a function of both the wire diameter and frequency. The proposed correction factor curve given in Figure 6-42 was developed using data for a 6-inch minor diameter corona ring. Thus, it approximates the correction factor for a very large diameter wire. In lieu of better data, we propose that it be used as an estimate of the asymptotic correction factor for large diameter wires at 30 kHz. The difference between the 60-Hz curve and the proposed VLF curve in the mid-humidity range agrees with the 8% frequency correction factor observed for larger wires in dry atmospheric air (see frequency effect section above).

The figure shows that the effect of humidity at VLF is very different than it is at 60 Hz. At 60 Hz, the slope of the breakdown voltage versus humidity curve is positive, while at VLF the slope is

negative. This implies that the humidity correction factor is frequency dependent. The humidity correction factor for different wire sizes can be seen as a family of curves, parametric in wire diameter, plotted on the same scales as Figure 6-42. The proposed correction factor in the figure is an estimate of the asymptotic curve for large wires at 29 kHz.

There are no data for the VLF humidity correction factor curve at low humidity levels and further measurements are needed to define it. The breakdown level for dry air is needed to determine the left-hand end of the curves. These data are not yet available. By definition, the humidity correction factor at zero humidity will be 1.0. At VLF, it seems likely that for large diameter wires when the humidity increases the correction factor will always be below 1.0. For smaller diameter wires, it is likely that as humidity increases the humidity correction factor will increase following the 60-Hz correction factor for a ways, then curving back down below 1.0. The reason the humidity correction factor follows the 60-Hz curves for low humidity is that the small wires have a small equivalent gap, which reduces the frequency effect. If the gap is small enough, the breakdown level approaches the 60-Hz values. We next present limited data at VLF/LF that indicates that this is the case.

Note that the asymptotic value for large wires should also be equal to the asymptotic value for large gaps. There are no data available yet for the breakdown strength of air in a uniform field gap as a function of gap length and humidity at VLF/LF. These data need to be measured in order to develop a complete understanding of the humidity effect at these frequencies. Similarly, extensive measurements of corona onset levels as a function of wire diameter and humidity at VLF/LF are needed. Limited data of this type developed at Forestport is shown in the next section.

Wire, Pipe, and Cable Measurements

The variation of corona onset voltage with humidity was tested at Forestport using the inside horizontal test setup. These measurements were performed during the winter when the ambient humidity is very low. We used four humidifiers inside the test cell to increase the humidity (Figure 6-43). Two of the humidifiers can be seen on tripods in the background of Figure 6-3. The last tests at Forestport prior to closing that site were the humidity tests in February 1997 following preliminary tests in 1995 and 1996.

Figure 6-43. Humidifier.

The 1997 humidity tests were done during the winter during cold weather where the outside air is quite dry. The procedure was as follows. First, the large roll-up door was opened for approximately ½ hour and the test cell filled with cold dry outside air. This air was then brought to room temperature (70° F) using a heater. The resulting humidity in the test cell was 20% to 30%, depending on the atmospheric conditions. Corona onset voltages were then measured for the complete set of horizontal samples at that humidity on two frequencies (approximately 29 kHz and 47 kHz). Following these measurements, the humidifiers were turned on and the humidity increased to about 50%, and another set of corona onset voltages were taken. This was repeated again to reach a humidity of about 90%.

Data were taken for both 29 kHz and 47 kHz at the three humidity levels (low, mid, and high). The target humidity levels were 30%, 50%, and 90% relative humidity. Accurate humidity control is difficult in an open test cell such as at Forestport, and the humidity ranges achieved for these tests were from 24% to 37% for the low humidity range, from 52.5% to 58% for the mid humidity range, and from 85% to 90% for the high humidity range. In addition a limited set of data was taken at 14 kHz for mid (54%) and high humidity (78%).

The measured data at 14 kHz are contained in the data set for 8 February 1997 (Appendix 6A) and were the last data taken at Forestport. The data for 29 kHz and 47 kHz are contained in the data set for 5 February 1997 (Appendix 6A). These data are plotted versus wire diameter in Figures 6-44 to 6-46. The data for smooth pipes have been corrected for air density (STP 25° C); the data for the stranded cables have not been corrected. The original data for the smooth samples at 29 kHz and 47 kHz have been plotted versus relative humidity in Figures 6-47 and 6-48. The shape of the curves is similar when plotted versus absolute humidity.

In each of these data sets, the general trend is that the critical surface field for corona onset decreases with increasing humidity. There is a moderate decrease from low to mid humidity, and there is a larger decrease from mid to high humidity. However, for the smallest diameter wires, both smooth and stranded, all the low to mid humidity level measurements are the opposite of this trend, with the exception of the data for smooth conductors at 47 kHz.

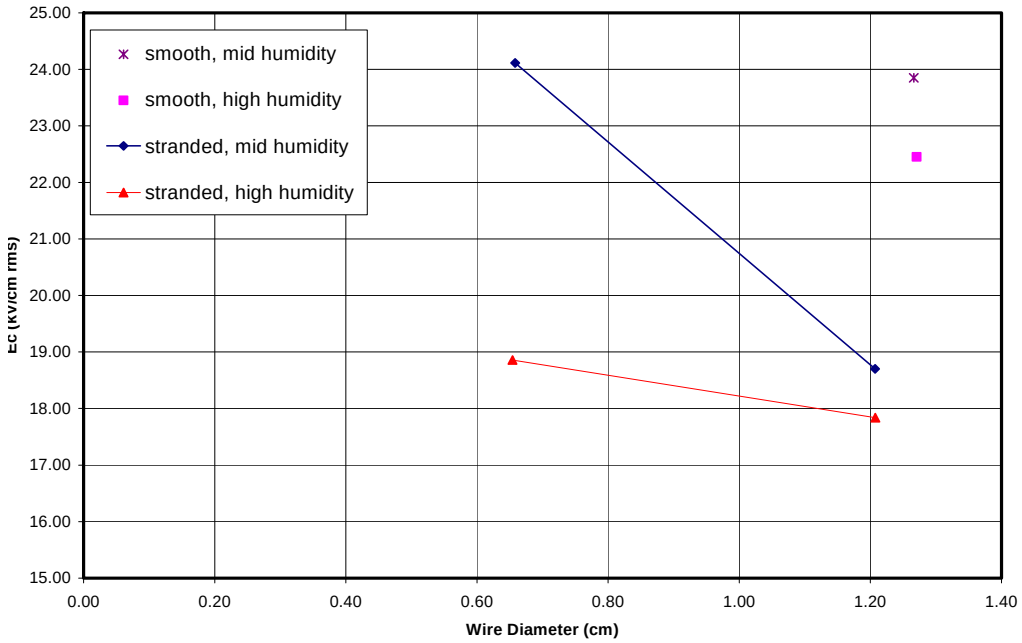

Figure 6-44. Humidity test data at 14 kHz.

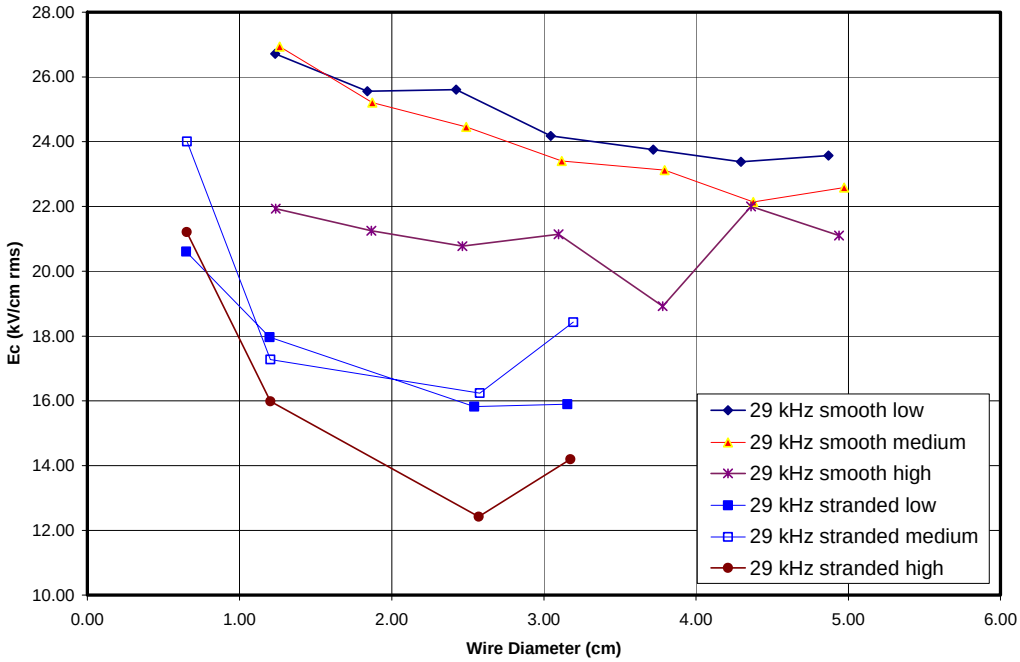

Figure 6-45. Humidity test data at 29 kHz.

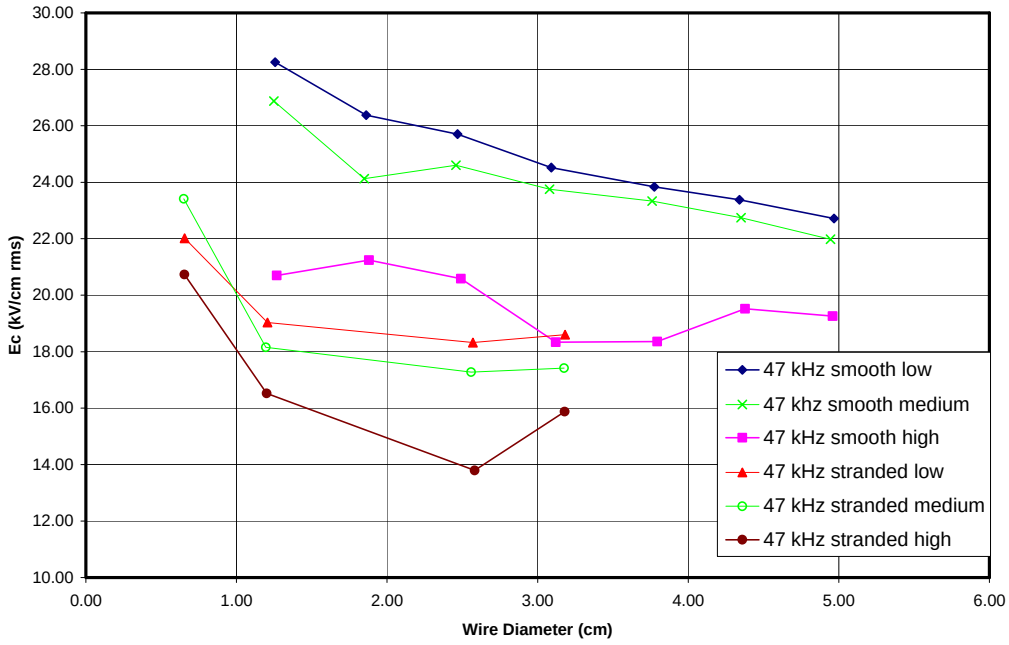

Figure 6-46. Humidity test data at 47 kHz.

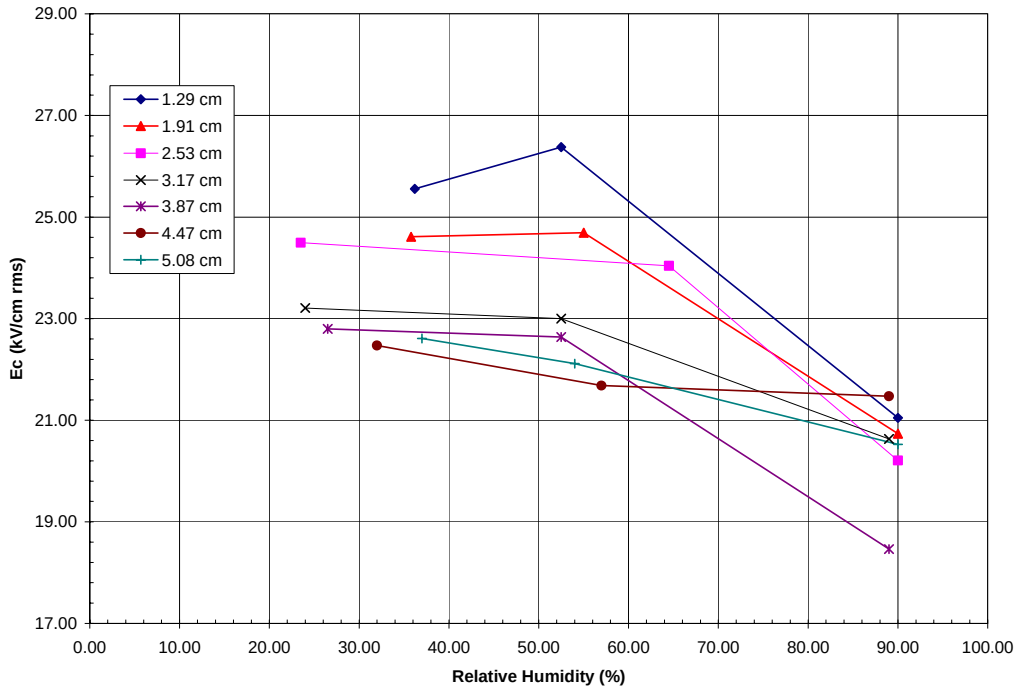

Figure 6-47. Corona onset field for various wire sizes versus relative humidity, 29 kHz.

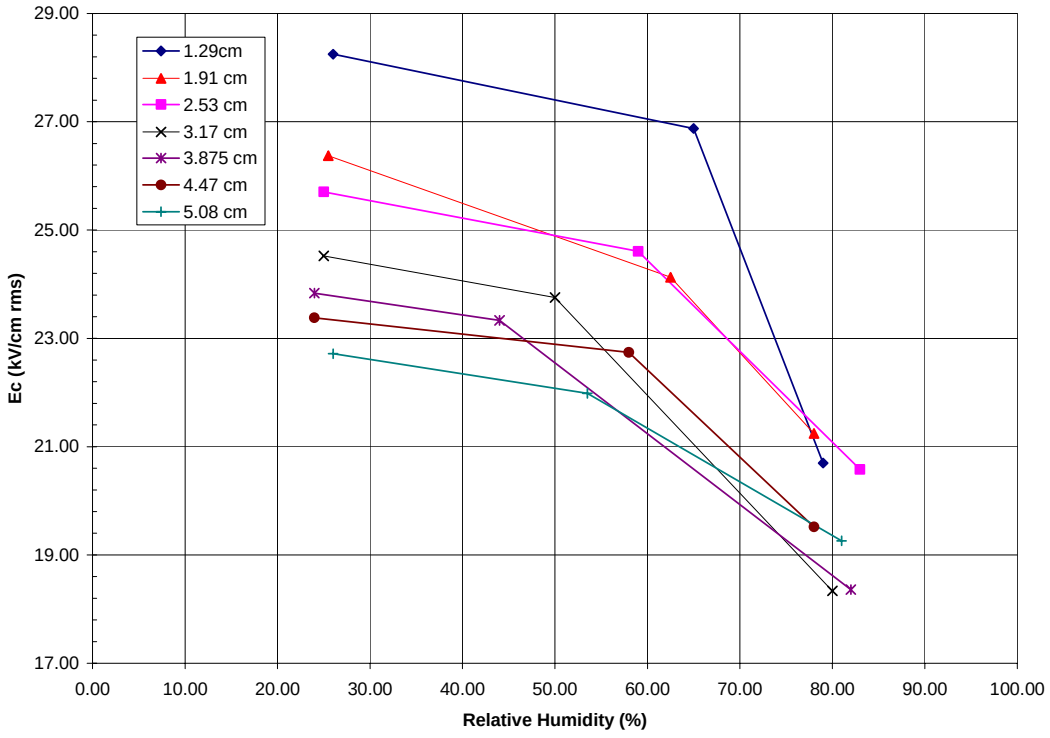

Figure 6-48. Corona onset field for various wire sizes versus relative humidity, 47 kHz.

There is more variability for the high-humidity measurements than for low-humidity measurements for both the smooth and stranded wires. This is also reported to be the case for high relative humidity measurements at 60 Hz and is attributed to the fact that at high relative humidity water vapor starts to form droplets. In addition, when the relative humidity is high, water begins to condense on the surface of the conductor. These are random processes that increase the variability of the measurements.

The corona onset field data for different humidity levels for smooth pipes at 29 kHz and 47 kHz have been normalized by the appropriate formula for smooth pipes from Table 6-2A. The results are shown in Figure 6-49 and 6-50 plotted as correction factors. The curve of the normalized average from the air density tests is also included in these plots. Note that the average value for corona onset during the air density tests corresponds closely to the value at low humidity for both frequencies. The corona onset value at mid humidity was reduced below that by about 5%. The value for corona onset at high humidity varied considerably but was reduced by more than 10% and sometimes more than 25%.

Examination of Figure 6-47 for 29 kHz and 6-48 for 30 kHz indicates the following:

First, the slope of the curves between the low and mid humidity value changes in a regular manner with wire diameter. For the smallest wire, this slope is positive and it decreases with increasing wire diameter becoming negative and eventually appears to approach an asymptotic limit for the larger wires.

The data for 47 kHz (Figure 6-48) are different in that the slope between low and mid humidity is approximately the same negative value for all the diameters measured, including the smallest diameter wire.

For both the 29- kHz data and the 47-kHz data, the slope of the curves between mid- and high-humidity levels is strongly negative.

A qualitative explanation of these effects has been developed and is presented in a following section (see Combined Effects).

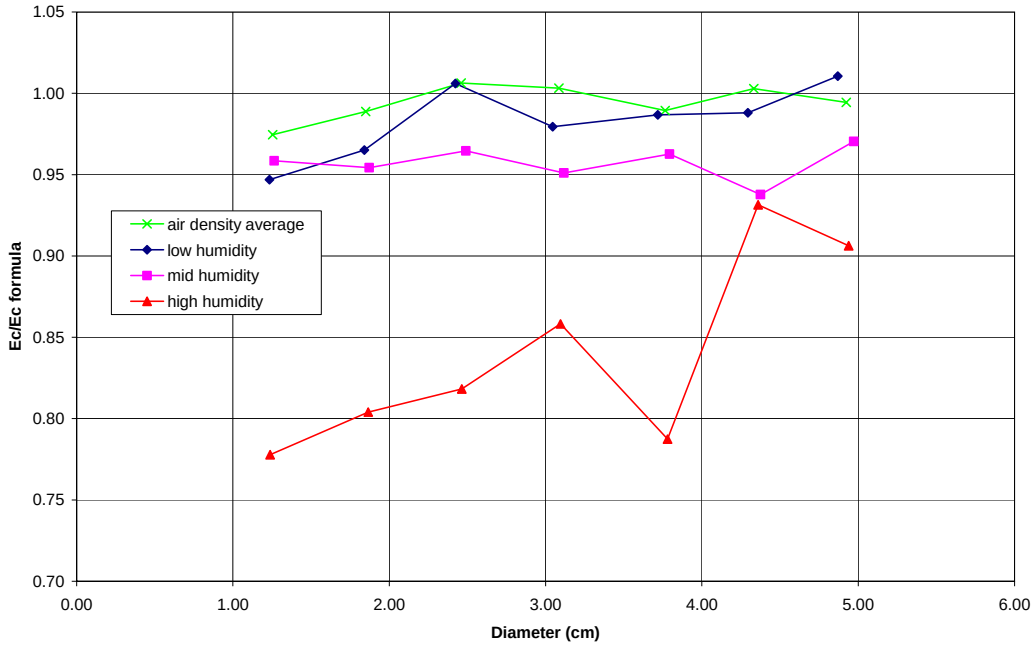

Figure 6-49. Measured humidity correction factor, 29 kHz.

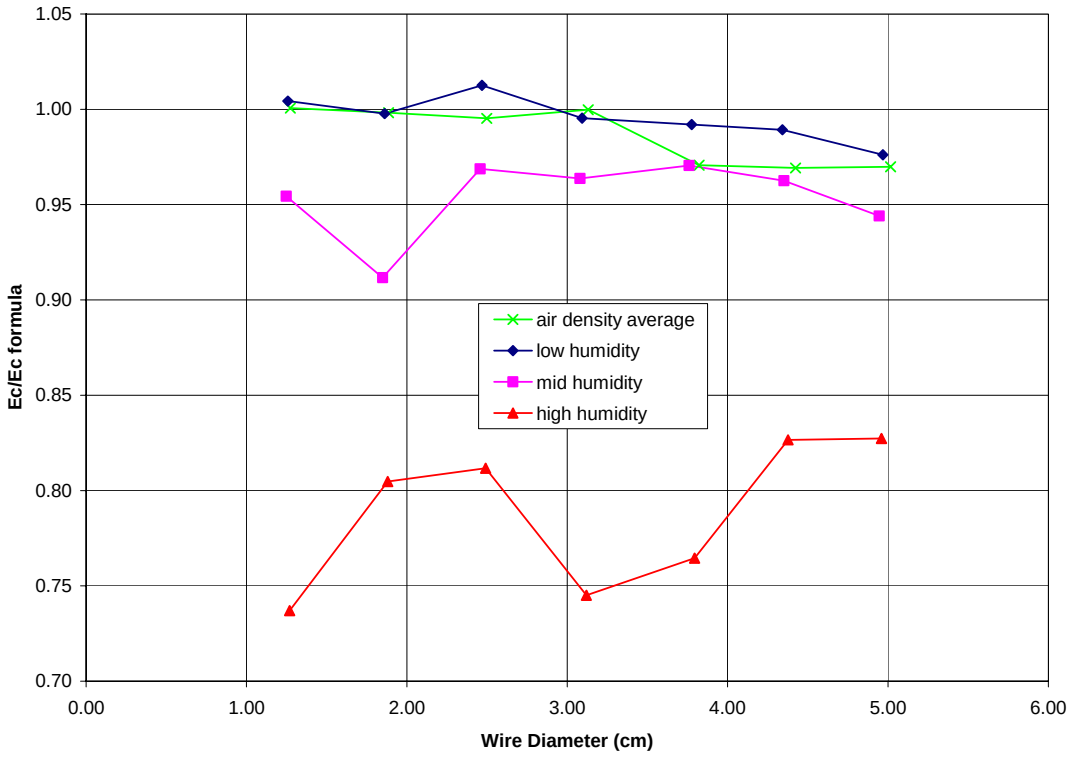

Figure 6-50. Measured humidity correction factor, 47 kHz.

The Effect of Impurities

The atmosphere contains significant amounts of dust, pollen, and spores. In some locations, salts and other chemical pollutants are significant. At higher latitudes, small particles of wind-blown snow

can have a significant effect on high-voltage performance. The concentration of the various atmospheric particles varies greatly with time and geographic location, with diameters from 0.1 to 10 μm. In some cases, the particles, which may also include insects, play an important role in corona formation and frequency effects. The impurities can have an effect both in the air and when they are deposited on the surface of the object under test. There is little quantitative data on the effect of airborne impurities on corona onset levels.

The deposition of the impurities on the surface of insulators is called contamination. The effect of contamination on breakdown levels for insulators has been investigated extensively at power system frequencies. There has been a limited amount of investigation into the effect of surface contamination on corona onset voltages on wires. Peek (1929, p. 76) shows some data on the 60-Hz visual corona level with oil, water, and dirt deposited on the surface of the conductor. These data indicate that water lowers the onset level the most.

In general, impurities and contamination significantly reduce breakdown level. LaForest (1968) states that in 1956 Newell and Warburton (1956) discovered that fair weather corona was caused by airborne substances such as insects, dust, pollen, spider webs, vegetation, leaf particles, bird droppings and other non-metallic materials. Previously, damage to the surface of the conductors had erroneously been supposed to be the cause (Comber, et. al., 1982, p.180). Some effort has been expended to quantize this effect at power line frequencies (Newell and Warburton, 1956, 1957). One interesting thing discovered is that more of the airborne sources are present during the summer months with the largest amount present during the month of August.

The mechanism for the reduction in corona onset voltage when airborne impurities are present is explained as follows. Corona discharge is initiated when airborne dielectric particles pass near the surface of the conductor. Corona initiation usually happens before the particle contacts the surface. This is caused by the induced dipole charge on the dielectric particle, which enhances the field between it and the conductor. If the enhanced field is large enough, it will result in discharge. When the particle touches the conductor (or the discharge reaches it connecting it to the conductor), it assumes the same charge as the conductor. Since like charges repel, it then rapidly drifts away. This explains the observation that under the right conditions less snow sticks to energized transmission lines (Comber, et al., 1982, p.180).

The dielectric constant of dust can be large, particularly when it has absorbed water. For particles on the surface of the conductor, the field is concentrated on the tip protruding out from the surface. Materials with high dielectric constants are drawn into high electric field areas independent of polarity, even if the field is oscillating. Thus, floating particles can be drawn toward particles on the surface, where they often stick together forming larger protrusions (Kreuger, 1991, vol II, p. 88). As a protrusion grows the field is more concentrated at the tip, which reduces the breakdown level.

Kuffel and Zaengle (1984, pp. 107–109) discuss measurements of the time to breakdown for various gaps with different conditions of air carrying dust. These measurements indicate that the time to breakdown is increased considerably by moving air and even more by filtering the air. This is consistent with the breakdown voltage being reduced by the presence of floating dust particles. The effect of dust on the breakdown level at dc is greater than it is at 60 Hz (Kreuger, 1991, vol. I, p. 146).

For practical outdoor applications, the spray-wet condition associated with falling rain is essentially the worst case, with the possible exception of falling snow. Peek (1929, p**.** 202) indicates that he observed corona losses during falling snow that were greater than for rainfall. The increased losses were attributed to the corona onset voltage being reduced while snow is falling. He states that

"the effect of snow is greater than any other storm condition." At Forestport, corona onset measurements were made on cables that had been iced (see Figure 6-51). The result of these measurements showed that the corona onset voltage for iced conditions is essentially the same as for spray-wet conditions. We did not make measurements for snowfall conditions.

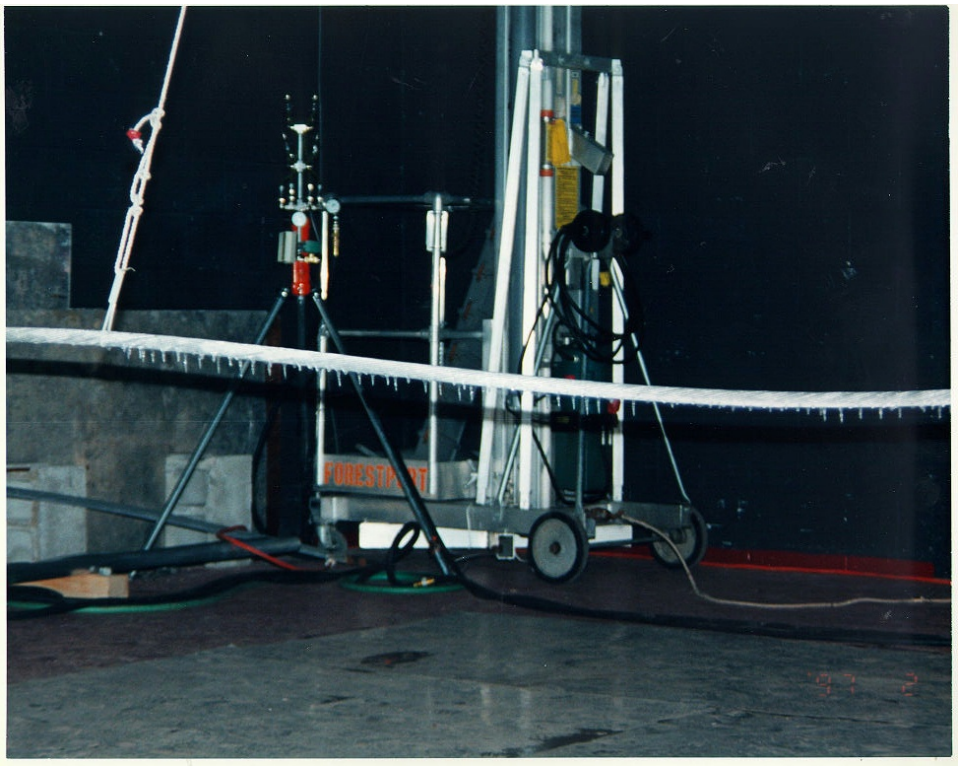

Figure 6-51. Frozen cable.

The presence of impurities and contamination significantly reduce the breakdown voltage. For adequate design, safety factors must be used to take this into account. This is obviously true for outdoor applications, but it also required for indoor applications where dust, insects, or condensation are not normally present but can occur over the course of time. Breakdown can be especially damaging if the materials used are flammable, as is often the case for indoor high-voltage hardware. For this reason, it is standard practice to periodically clean indoor high-voltage equipment to reduce contamination.

For outdoor application, falling rain or snowfall is the worst case. High-voltage hardware designed for outdoor use is usually not flammable. Since the design of outdoor high-voltage components must take rainfall into account, there is usually no need to use an additional safety factor for impurities.

COMBINED EFFECTS

From the data presented in the section on the humidity effect, it is clear that the corona onset level is a function of both frequency and humidity and that the effects of both frequency and humidity are functions of wire diameter. This section brings together our observations of the effect of frequency and humidity with results reported in the literature and with theoretical considerations to provide a qualitative explanation for the effects in the VLF/LF range. Unfortunately, the data available are not

adequate to provide a complete quantitative description; however, the data areadequate to give quantitative indications for designs using safety factors.

Critical Frequency

Gaps

Many investigators have reported that for breakdown of air in uniform field gaps for any given frequency there is a critical gap length below which the breakdown voltage is independent of the frequency (Muller, 1934). For longer gaps at that frequency, the breakdown voltage is reduced over the low-frequency level. Two values of the critical gap length observed by Muller are given in Meek and Craggs (1978, p. 690), as 0.45 cm at 110 kHz and 0.09 cm at 995 kHz. The explanation given for the critical gap length (as a function of frequency) is that the length of the gap is just long enough so that the slower positive ions do not move out of the gap within one half cycle. Thus, a space charge buildup occurs with the corresponding field enhancement and reduction of the breakdown voltage. For shorter gaps, the ions are swept out of the gap within a half-cycle and no space charge buildup can occur.

The existence of a critical gap length for a fixed frequency implies that for a fixed gap length there is a frequency below which the breakdown voltage is independent of frequency and above which the breakdown voltage is reduced. This is called the critical frequency and is a function of the gap length. The two data points from Muller have been plotted on Figure 6-52 as critical frequency versus gap length.

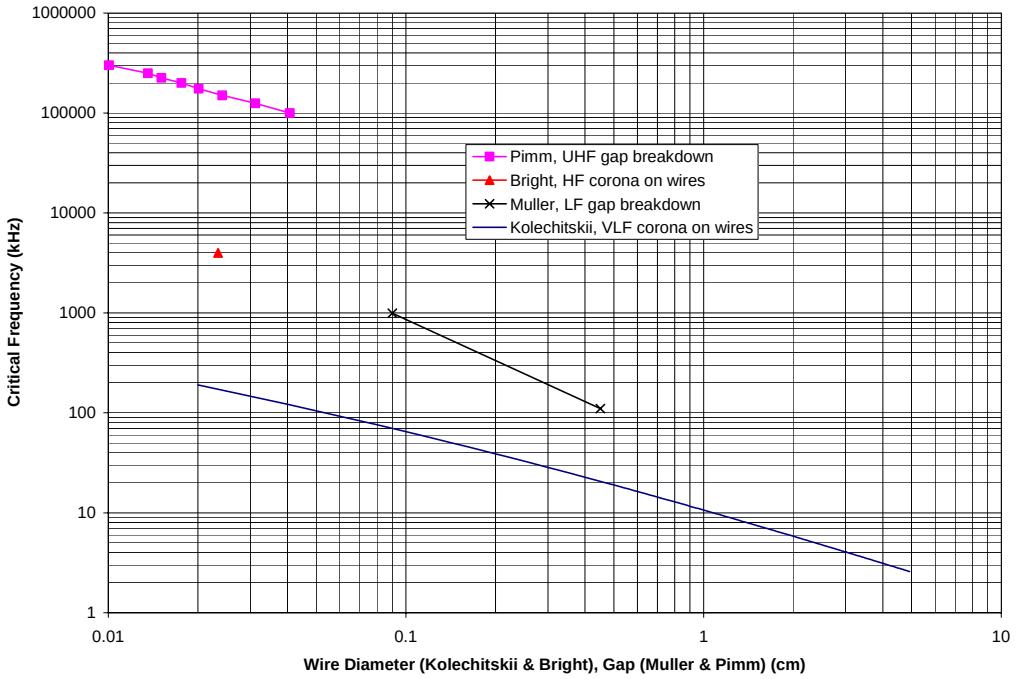

Figure 6-52. Critical frequency after Kolechitskii (1967), Pim (1949), and Bright (1950).

There is an analogue between breakdown in a gap and corona onset on a cylinder. When breakdown occurs around a cylinder, corona forms first in the high field region near the cylinder. Chapter 2 includes a discussion about the processes involved with the formation of corona around a

cylinder. There is an active region around the cylinder where ionization occurs (See Figure 2-11). The thickness of this active region is analogous to gap length for a uniform field gap. Consequently, for a given size wire, one might expect that there is a critical frequency below which the onset voltage does not vary with frequency and above which the onset voltage is reduced. Kolechitskii's experimental results confirm this.

VLF/LF Corona on Wires: Kolechitskii

Kolechitskii (1967) made extensive well-instrumented measurements of corona on wires at frequencies between 10 and 100 kHz, with a few measurements at higher frequencies. He also made measurements at 50 Hz using the same test setup. Corona onset was determined by monitoring the waveform of the current flowing through the gap and noting when corona current pulses started to flow. At VLF/LF, the glow of the corona jacket at onset was observed to be much brighter than at 50 Hz and corresponded with corona current initiation. "So at high frequencies the corona onset voltages can be determined quite reliably from the glow around the conductor." This was also found to be true at the Forestport HVTF.

Several interesting findings of Kolechitskii are described below:

1. The onset voltage is practically independent of frequency up to 67 kHz, and Peek's formula applies for clean smooth dry conductors. However, his data show a decrease in the critical surface electric field for VLF/LF of up to 5% from that at 50 Hz, depending on frequency and wire diameter. The difference was greater for larger wire diameters and lower frequencies. Some of the reduction was attributed to surface irregularities due to imperfect grinding. It was also observed that contamination such as dust or oil deposits decrease the onset voltage by 10 to 15%.
2. The corona extinction voltage at VLF/LF was lower than at 50 Hz and the difference was greater at higher frequencies. The fact that the corona extinction level is lower than the onset level is attributed to the fact that the corona heats the air, reducing the air density (Van Brunt, 1994). This is consistent with Kolechitskii's observations and the fact that power dissipated in corona is proportional to frequency (Chapter 7).
3. There is a difference in the visible nature of the corona at onset, and correspondingly the corona current waveform, as frequency increases. The phenomena can be divided into a low-frequency effect, a high-frequency effect, and a transition region. It is important to note that the frequency where this transition takes place is a function of the wire diameter, starting at lower frequency for larger wires.
    a. In the low-frequency effect region, the corona appears as a thin sheath near the wire, corresponding to the corona observed at dc for negative polarity (negative corona). When the voltage and current waveforms are examined, it is observed that the corona current flows for a small portion of the cycle near the peak of the negative half-cycle.
    b. In the high-frequency effect region, the initial corona consists of individual or clusters of thin branching channels having a length much greater than the wire diameter. These correspond to positive corona streamers observed at dc (positive corona). In this case, examination of the voltage and current waveforms indicate that the corona current flows for a small portion of the cycle just after the positive going zero crossing. These channels or clusters have an intact base on the wire and are spaced along the wire a distance somewhat greater than their length. They also tend to move about, around, and along the wire.

c. In the transition region between the low-frequency region and the high-frequency region, both types of corona can be seen to some degree.

The explanation for these effects is as follows. Well below the critical frequency the negative onset voltage has a magnitude less than the positive onset voltage and corona first starts to appear near the peak of the negative half-cycle. The corona observed in this case is similar to the corona observed with negative dc voltages.

When the frequency is well above the critical frequency, the residual negative ions from the dark Townsend currents during the negative half-cycle cause the field to be enhanced when the voltage goes positive, causing positive corona to appear first.

There is a transition region where the frequency is such that both positive and negative corona appear to some extent. In this region, both negative and positive corona currents flow. The positive corona currents start to flow near the peak of the positive cycle. As the frequency is increased, this point moves toward the zero crossing. When it reaches the zero crossing, only positive corona appears. This marks the critical frequency and the transition to the high-frequency region.

4. Kolechitskii empirically determined a critical frequency, dependent on wire size, that defines the start of the high-frequency region, given by

$$f_{cr} = \frac{7.56}{r + .298 \cdot \sqrt{r}} \quad \text{kHz} \ ,$$

where r is the wire diameter in centimeters.

A plot of Kolechitskii's formula for critical frequency versus wire diameter is included in Figure 6-52. Note that a wire with a diameter of 1 cm has a critical frequency of 10 kHz. This means that in the VLF/LF band most practical wire sizes will be operating above the critical frequency, i.e., in the high-frequency region.

Kolechitskii also determined that in the high-frequency region the corona region around the wire was at a distinctly higher temperature than in the low-frequency region.

HF Corona on Wires: Bright

A similar critical frequency effect can be seen in corona onset data measured by Bright (1950). These data include measured corona onset voltages for three small wires (0.316 mm, 0.274 mm, and 0.234 mm) at 60 Hz and five frequencies ranging from 1.6 MHz to 9.4 MHz. The onset voltage for Bright's data has been normalized to the 60-Hz value and plotted in Figure 6-53. Note that at 1.5 MHz the onset level he measured was 88% to 90% of that at 60 Hz. This is very similar to the level we measured at VLF, although for larger wires. His data show a transition region between 3 MHz and 4 MHz for all three wire sizes. Above the transition region, the corona onset voltage drops to approximately 75% of the 60-Hz value. Assuming the critical frequency is the high end of the transition region, per Kolechitskii's observation, the critical frequency for the 0.326-mm diameter wire is approximately 4 MHz. This point has been plotted in Figure 6-52 for comparison with Kolechitskii's formula and Muller's measured data.

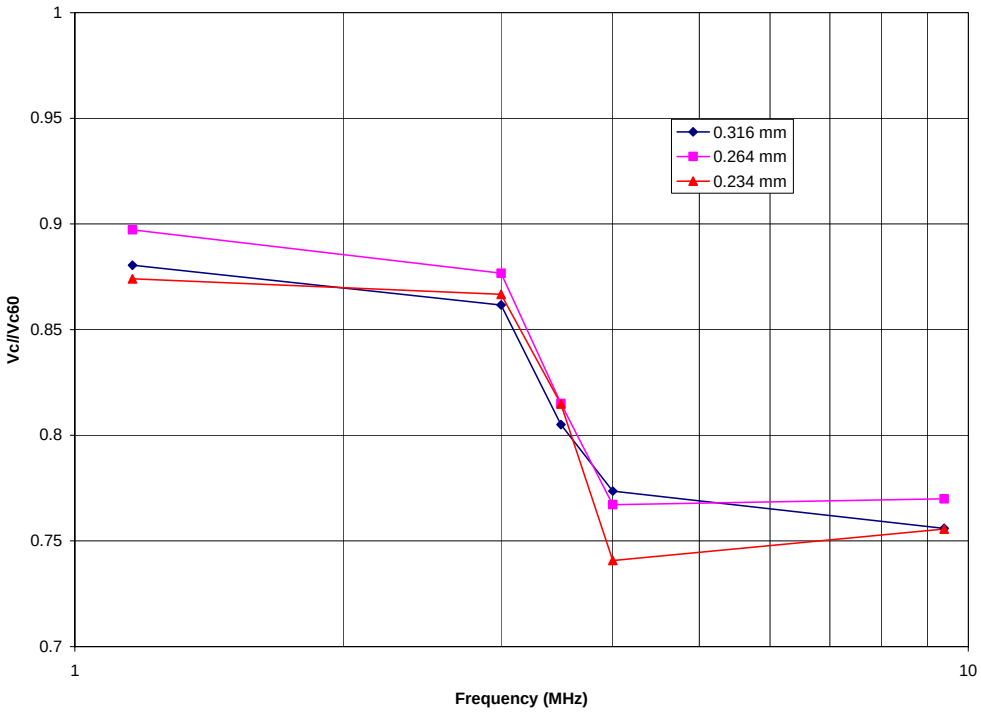

Figure 6-53. Corona onset frequency correction factor at HF (Bright, 1950).

UHF Breakdown of Gaps: Pim

Pim (1949) describes measurements of the breakdown characteristics of air in parallel plate gaps, at frequencies between 100 and 300 MHz. In these measurements, the gap was varied up to a length of 1-mm, and the pressure was varied from 50 Torr to 1000 Torr. Pim found that as the gap length increased the breakdown voltage followed a smooth curve, increasing until a critical gap length was reached, when for further increases in the gap length there is a decrease in the breakdown voltage. As the gap length is increased further, eventually the breakdown voltage starts to increase again. The critical gap length, where the discontinuity occurs, depends on the frequency.

Pim (1949) developed a family of curves of the breakdown voltage versus gap length for air at atmospheric pressure, parametric in frequency, for frequencies between 100 MHz and 300 MHz (Meek & Craggs, 1978, figure 8-7, p. 607). Included in this figure is a curve for 50 Hz. Pim's data show that when the gap is less than the critical length, the breakdown voltages is independent of frequency, and the measurements at every frequency form a single curve approximately 10% below the value for 50 Hz. As the gap is increased beyond the critical length, the breakdown strength falls rapidly. This occurs at a different gap length for each frequency, and the curve separates from the single curve when the gap reaches the critical length for that frequency. As the gap is increased well above the critical length, the breakdown voltage starts to increase again. With further increase, the separate curves come back together, forming a single curve approximately 40% below the 50-Hz value. Note that similarity does not hold for gaps operating in the region where the curves have separated.

The critical gap length measured by Pim depends on frequency. Again, the concept of the critical gap length can be inverted to define a critical frequency as a function of gap length. The values of the

critical frequency versus gap length have been determined from Pim's family of curves for air at one atmosphere and have been plotted in Figure 6-52.

Pim explains this phenomenon on the basis of the velocity of an electron avalanche traveling across the gap and reaching the opposite side just as the electric field is reversing its direction. The e^n electrons from the first avalanche propagate back across the gap arriving with e^{2n} electrons, etc. Thus, when the gap length and frequency are such that an electron avalanche propagates across the gap in something like one-fourth cycle, a discontinuity in the breakdown characteristics of the gap can be expected because the avalanche suddenly grows across effectively twice the gap distance. In addition, because of the double growth avalanche, the residual ion density in the gap is increased, and the external electric field required to create an ion density sufficient to initiate a spark is reduced.

Critical Frequency Summary

Direct comparison of the critical frequency data for corona onset and gap breakdown is incorrect because, as discussed in Chapter 2, the equivalent gap length for wires is not equal to the wire diameter but depends on the corona onset gradient and the wire diameter. In Chapter 2, a formula was developed for the thickness of the active region around a wire. We have used this formula to convert the independent variable of the corona onset curves for wires (Kolechitskii (1967) and Bright (1950) from wire diameter to equivalent gap. These new curves are plotted in Figure 6-54. When plotted versus equivalent gap length, the curve based on Kolechitskii's formula has the same slope as Muller's data but is considerably lower. In addition, the single data point due to Bright appears to be on an extension of Muller's curve. Together they define a second curve parallel to Kolechitskii's but higher. Finally, Pim's data has similar slope to the other two curves but is considerably higher than either.

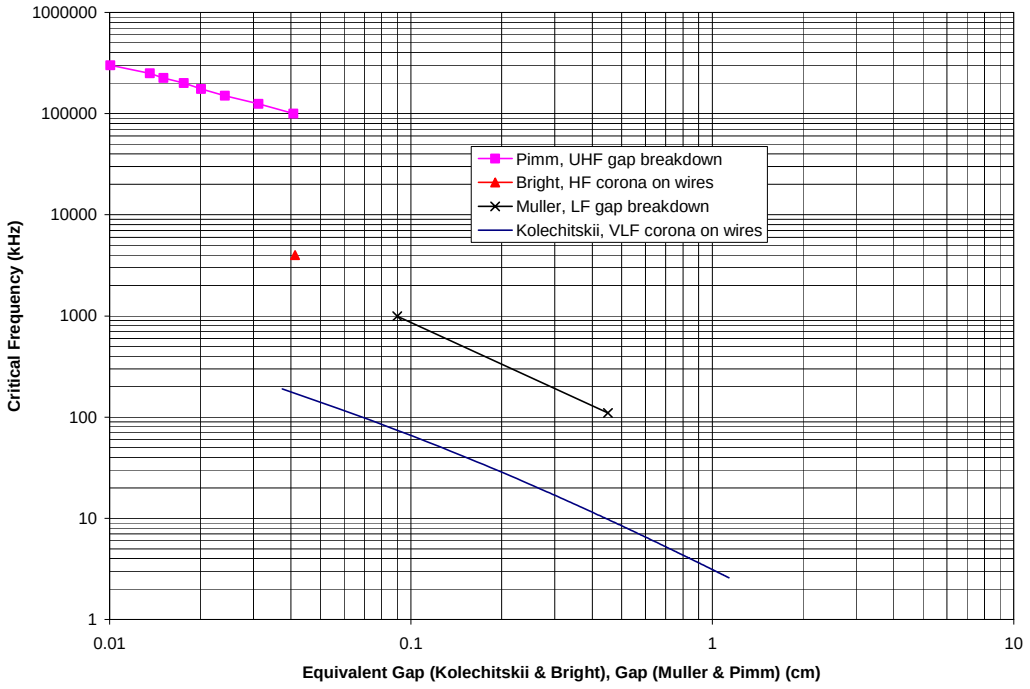

Figure 6-54. Critical frequency versus equivalent gap.

There appears to be three distinctly different sets of critical frequencies. This is attributed to the action of the three distinctly different sets of charged carriers (negative ions, positive ions, and electrons). Each critical frequency involves a resonant effect whereby the mobility of the charge carriers puts space charge in a location that enhances the field at the time when the voltage reverses.

The critical frequency associated with the lowest curve (Kolechitskii) is attributed to the presence of negative ions, their lifetime, and drift rate. This is indicated by the fact that the critical frequency occurs at the point where corona currents flow at the positive going zero crossing. The next higher curve is the combination of the two curves labeled Muller and Bright. This critical frequency associated with this curve is attributed to the presence of positive ions, their lifetime, and drift rate. This is consistent with Muller's explanation that the critical gap corresponds roughly to the length at which positive ions are expected to accumulate in the gap (Meek & Craggs, 1978, p. 690). The critical frequency associated with the upper curve (Pim, 1949) is attributed to the buildup of electrons and is associated with the electrons crossing the gap in one half cycle.

It seems likely that the critical frequency phenomena for wires discovered by Kolechitskii is analogous to the critical frequency for breakdown in gaps described in Meek and Craggs (1978, Chapter 8). The simple explanation for this phenomenon involves the buildup of space charge from residual ionization of the pre-ignition avalanches. In uniform field gaps, high-frequency phenomena occur when the gap length and frequency are such that ions cannot move out of the gap before the waveform reverses. Similarly, for wires the high-frequency phenomena occur when the active region around the wire (Chapter 2) is large enough that the ions cannot move out before waveform reversal. The active region is larger for larger diameter wires. This is discussed in more detail in the next section.

Pulsating Corona

For both positive and negative electrodes in air and other electronegative gases, the pre-breakdown current occurs as regular impulses. The pulses in negative corona were discovered by Trichel and Kipp in Loeb's laboratory in 1936 (Raizer, 1991, p. 350; Loeb, 1939, sections 8 & 9) and are called Trichel pulses. The pulse repetition rate is a function of voltage. The initial rate is quite low, and as the voltage increases the pulse magnitude remains essentially the same but the repetition rate increases, reaching 1 MHz (Raizer, 1991, p. 351). Above this level, the Trichel pulses are replaced with continuous current corresponding to steady-state self-sustained corona. For low-level positive corona, intermittent pulses can form at low rates on the order of 10 kHz. At higher levels, positive corona forms a "continuous" glow. Later, Hermstein showed experimentally that negative ions influence the formation of the positive glow in air, which is sometimes called "Hermstein glow." Both Trichel and Hermstein failed to note that the "continuous" positive glow actually pulses very rapidly with initial repetition rates on the order of 1 MHz (Morrow, 1997). Morrow provides a theoretical explanation of this effect and indicates it was not really studied until 1970. All of the impulses associated with these phenomena have very fast rise times and are the source of radio noise that can be emitted by any high-voltage system such as power transmission lines, VLF/LF transmitting antennas, or high-voltage power supplies.

For positive conductors, as the voltage is increased, the initial corona current flows in intermittent pulses and continues in this mode over a fairly wide range of voltage. Eventually a voltage is reached where the corona becomes continuous. These pulses, known as flashing corona, are sometimes called pre-inception streamers. The repetition rate for these streamers is low at both ends of the voltage range where they occur and reaches a few kilohertz near the center. However, as previously stated, the positive "continuous" glow actually pulses at repetition rates on the order of 1 MHz. Morrow

(1997) notes that the presence of humidity reduces the frequency of the positive glow pulses. For negative conductors, the initial pulse repetition rate is very low and increases with voltage up to approximately 1 MHz. The accepted explanation for these phenomena is given below.

For positive electrodes, the breakdown is due to accelerating electrons that are drawn into the breakdown channel. The channel remains contained and has a filamentary appearance. Because they stay contained, the positive filaments tend to propagate faster and farther into the gap than negative corona does. These filaments consist of avalanches of electrons that move rapidly toward the positive conductor where they are neutralized. They leave behind a space charge consisting of positive ions. This space charge reduces the field around the positive conductor, cutting off further avalanches until the space charge drifts out of the active region (Morrow, 1997).

For negative corona, the process is more complicated. The initiation of breakdown around a negative electrode starts with the acceleration of residual electrons by the electric field. These electrons are moving away from the electrode. When the field is strong enough, the accelerated electrons have enough energy to ionize gas molecules, releasing more electrons, which are also accelerated. This process leads to an electron avalanche. As discussed in Chapter 2, secondary electrons are liberated from the electrode by collision from the positive ions and from ultraviolet radiation. This process produces a negative streamer in about 10^{-9} seconds. The electrons in this streamer slow down as they move farther from the electrode. They tend to diffuse due to the repulsive Coulomb force and rapidly attach to electronegative molecules such as oxygen.

Positive ions are left behind by the avalanches, which drift toward the electrode. A cloud of negative ions forms in the region away from the electrode where the field is lower and the avalanches stop. The negative space charge weakens the field between it and the negative conductor to the point where the formation of avalanches is suppressed. The positive ions drift toward the negatively charged conductor and are neutralized. The negative ions are eliminated by either dissociation or by moving well out of the active region. As the ions are eliminated, the field is restored and the process starts over.

Negative corona Trichel pulses do not form in electronegative gases such as argon or nitrogen because the electrons are rapidly absorbed and the negative space charge corresponding to the cloud of electrons at the end of an avalanche cannot form. The slow-moving negative space charge corresponding to these electrons is required to cut off the pulses, thus forming the individual Trichel pulses. The electronegative characteristic causes the field level for the formation of avalanches to be greater. In this case, the space charge from the remaining positive ions near the conductor enhances the field, and when an avalanche forms it leads directly to self-sustained breakdown.

Corona Current Waveforms

For ac excitation, there is an interaction between alternating voltages on the electrode and the time constants of the corona pulse phenomena. If the frequency of the excitation is well below the corona pulse repetition rate, the corona formation is the same as dc or 60 Hz. As the frequency of excitation approaches the corona pulse repetition rate, there is an interaction with the residual space charge that reduces the corona onset level corresponding to the high-frequency region observed by Kolechitskii. Figure 6-55 (Smith, 1963) shows measured current and voltage waveforms at two VLF frequencies that illustrate this. The waveforms on the left side of Figure 6-55 were measured on a small diameter wire and correspond to operation at a frequency below the critical frequency. In this case, the onset phenomena is essentially the same as at dc or 60 Hz. Examination of the top waveform, taken when the voltage was just above the onset level, shows that the negative corona currents (Trichel pulses) start to flow at a point in the negative half-cycle when the voltage reaches the corona onset level.

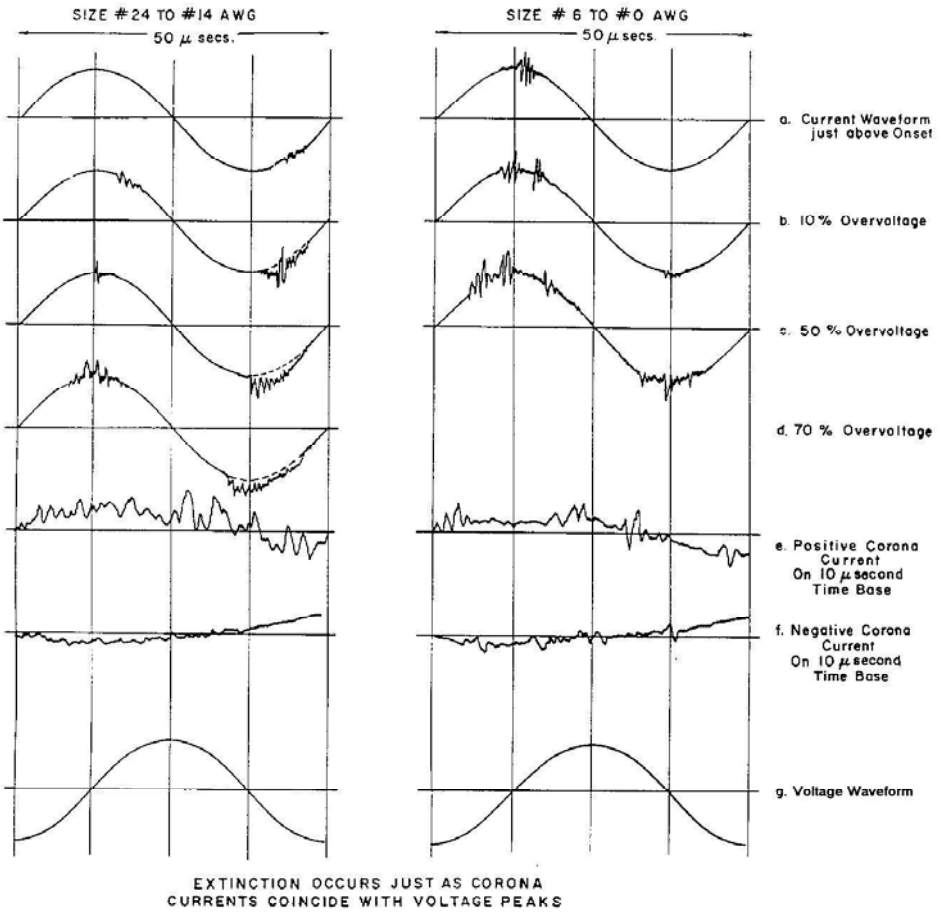

Figure 6-55. Voltage and current waveforms at VLF (after Smith, 1965).

The right side of Figure 6-55 shows the waveforms measured using a large wire and corresponds to operation at a frequency above the critical frequency. The top waveform occurred when the voltage was just above the onset level. This waveform shows positive corona currents (pulses) starting immediately after the voltage crosses from negative to positive. This is attributed to field enhancement from negative space charge due to slow moving negative ions. The same type of phenomena is seen at 60 Hz on insulated wires when there is a split in the insulation (Van Brunt, 1994). In this case, the negative charge required to enhance the field on polarity reversal accumulates on the surface of the dielectric (Van Brunt, 1994, p. 771).

The current waveforms above the critical frequency are consistent with the concept that negative space charge developed from pre-discharge avalanches enhances the field on the positive going zero crossing. The fact that this does not happen when the frequency is below the critical frequency is consistent with the idea that the time constants associated with this negative space charge are involved in determining the frequency behavior.

There is a definite change in the appearance of the corona for frequencies below and above the critical frequency. Below the critical frequency, the corona is a rather uniform reddish-white brush discharge that likely corresponds to negative corona. Above the critical frequency, the corona appears to go directly to bluish-white flares extending out from the wire surface, corresponding more

to positive corona (Kolechitski, 1967). This is consistent with the polarity at which the corona currents flow.

Relationship to Critical Frequency

The phenomenon of regular Trichel pulses occurs for both dc and during the appropriate half-cycle for low-frequency ac. As described above, these pulses are cut off by the presence of space charge that reduces the electric field on the electrode surface. Consider a voltage that reverses at a frequency on the order of the Trichel pulse frequency. Trichel pulses occur during the negative half-cycle when the voltage is great enough. Each Trichel pulse is cut off by the formation of a large negative space charge. If the polarity of the electrode is reversed to positive just at that time, the space charge will greatly enhance the field. This results in self-sustained breakdown at a lower level than for dc or 60 Hz.

We propose that the critical frequency is such that polarity reverses at just the right time to provide maximum field enhancement. The frequency at which this happens depends on the time constants associated with the space charge buildup.

The amount of time that it takes to build up the space charge depends on the distribution of the field in the gap, the mobility of positive and negative ions, their lifetimes and the mobility of the free electrons. A quantitative explanation of this phenomenon is not yet available. Any theory must include the dynamics of electrons and both the positive and negative ions and will be further complicated if humidity, aerosols, and micro-droplets are included. Nevertheless, the resulting concept is quite simple. As discussed in Chapter 2, some ionization takes place at levels below the onset of self-sustained corona discharge. This ionization leads to free electrons, which move relatively quickly and heavier ions that are much slower. As the frequency is increased, it eventually reaches a value where the ions cannot be cleared from the active region in a half-cycle. The result is a space charge buildup. This space charge dissipates by dispersion and recombination. However, if the polarity reverses at the right time the surface field is enhanced greatly, resulting in self-sustained corona at a voltage less than for dc or 60 Hz.

There appears to be at least three distinct processes that result in this phenomenon, each having different time constants and a different associated critical frequency. The three different curves of critical frequency shown in Figure 6-54 are attributed to each of these processes. For example, the time constant for the negative ions seems to be the longest, and the lowest critical frequency curve in Figure 6-54 is associated with them. This corresponds to the critical frequency involved with corona processes for practical size wires at VLF/LF.

The time constant for positive glow corona impulses is shorter, as the initial pulses occur at repetition rates of 1 MHz or more. For this reason, the middle curve of critical frequency is attributed to the effect of the positive ions. This is the next highest critical frequency and the one that occurs with small wires at high frequency (Bright, 1950).

Finally, the velocity of electron avalanches is greatest implying that the breakdown due to electron avalanches has the shortest time constant. The top curve in Figure 6-54 is attributed to the effect of electron avalanches because it has the highest critical frequency. This critical frequency effect was measured using small gaps at UHF (Pim, 1949), but it is likely that the same effect will occur for corona onset on small wires.

At frequencies less than either of the higher two critical frequencies, the breakdown strength of air is approximately 10% below that for dc or 60 Hz. In the region of the critical frequency, it appears to

be less than that, and it seems likely that as frequency increases well above the critical frequency, the breakdown level increases somewhat and stabilizes at that level.

Note that humidity affects these time constants because the frequency of the Trichel pulses is reduced by the presence of humidity (Morrow, 1997). Based on the qualitative theory given above, this implies that the critical frequency is reduced by the presence of humidity. This is consistent with the measurements at Forestport. Kuffel's measurements at 60 Hz are also consistent with this in that they showed that for a fixed gap the breakdown voltage increases with increasing humidity up to a maximum and then decreases as the humidity is increased further (Kuffel & Zangel, 1984**,** p. 103).

The conclusion is that in the VLF/LF band for a given wire of practical size and a given atmosphere, there is a critical frequency below which the corona onset level is independent of frequency and equal to the dc/60-Hz value. Above this frequency, the onset level is reduced. There is a transition region where the correction factor decreases from 1 to a minimum between 5 and 15% less than 1. The critical frequency is a function of wire diameter and humidity and possibly other parameters such as rainfall, impurities, and surface condition. The variation of this critical frequency is not well understood.

The reduction in breakdown level for frequencies above the critical frequency at VLF/LF is attributed to the buildup of space charge from slow-moving negative ions in the active ionization region around the wire. The smaller the size of the active region (equivalent gap), the higher the frequency required to enable the buildup. The equivalent gap is monotonically related to wire diameter (Chapter 2), and at least for VLF/LF frequencies there is a wire size below which the equivalent gap is too small to allow charge buildup, and hence the breakdown level approaches that for 60 Hz.

Application to Measured Data

Frequency Effect

A first cut at a frequency correction factor is given by the formulas developed to fit the measured corona onset data for wires at VLF and 60 Hz. (For practical purposes, the corona onset levels for 50 and 60 Hz are the same.) The curve shown in Figure 6-56 was developed by taking the ratio of the formula for the critical surface field for corona onset at VLF (29 kHz smooth wires, Table 6-2A) to the critical surface field for corona onset at 60 Hz (curve fit to Schuman + Peek & Bright, Figure 6-32). The 60-Hz and VLF values used for this ratio are those for air with approximately the same amount of humidity.

This ratio, plotted in Figure 6-56, indicates that for larger wires the VLF corona onset field stabilizes at a level approximately 7% below that for 60 Hz. Smaller wires have a higher critical frequency. Thus, when the wire is small enough, the operating frequency will be below the critical frequency, and this ratio is expected to approach 1. However, as the wire diameter is reduced, the calculated ratio based on our curve fit formulas crosses 1 and takes on values greater than 1.

The formulas do not asymptotically give the appropriate result for small diameter wires. This probably is a consequence of extrapolation of results to small diameters. For this reason, the curve in Figure 6-56 is labeled "proposed frequency correction factor (30 kHz)." The correction factor equals 1 for small wires (where the calculated curve exceeds 1) and fits the calculated curve for larger wires. The correction factor is consistent with the measured data shown in Figure 6-35. The factor shows a transition region from low-frequency behavior to high-frequency behavior for a wire diameter

between 0.03 cm and 0.4 cm. This is consistent with Kolechitskii's formula, which gives a critical frequency of 30 kHz for a wire diameter of 0.39 cm (Figure 6-52).

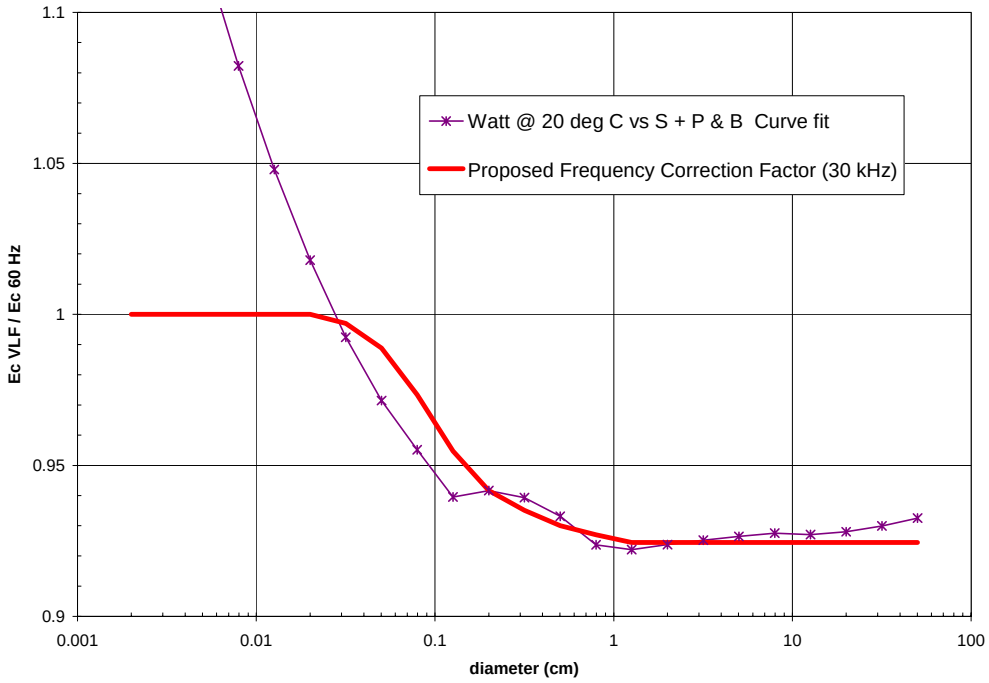

Figure 6-56. Calculated and proposed frequency correction factor for 30 kHz.

The data suggest that there is a critical frequency for a given wire size above which the corona onset level is reduced by a given amount below that for dc or 60 Hz. For frequencies below the critical frequency, there is a transition region where the amount of reduction becomes less and eventually approaches that for dc or 60 Hz. The critical frequency is directly related to wire diameter being larger for larger diameters.

Humidity Effect

Forestport data indicate that humidity affects the fundamental breakdown strength of the air, and increases in humidity lowers the critical frequency. This is consistent with negative ions becoming less mobile with increasing humidity, thus increasing the time constant for their decay. This explains the complex behavior observed in the humidity measurements.

It is clear that for a wire energized at a frequency well below the critical frequency, the effect of humidity is the same as that for dc or 60 Hz. Figure 6-40 (Kuffel's dc and 60-Hz data) shows that for this case the breakdown level increases with increased humidity. However, our data show that at VLF/LF, when the frequency is well above the transition region defined by Kolechitskii, the effect of increased humidity is to reduce the breakdown level. In addition, the breakdown level approaches the wet breakdown level as the relative humidity approaches 100%.

Examination of Figure 6-47 (29.5 kHz) illustrates the effect of changing humidity. The 1.29-cm-diameter wire was operating below critical frequency for both the low and mid humidity levels, and the breakdown level increased when the humidity increased from low to mid level. When the

humidity was increased to the high level, the critical frequency was lowered enough to reverse this effect and reduce the breakdown level.

For larger wire diameters, the critical frequency is lower, and the transition between these two effects occurs at a lower humidity level. This is illustrated in Figure 6-47 for the next larger diameter wire (1.91 cm) where the increase in breakdown strength between low and mid level humidity is small. This is attributed to the fact that the critical frequency for this larger wire is lower (closer to the operating frequency). The increased humidity increases the fundamental breakdown strength of the air but, at the same time, this is being countered by the decreasing critical frequency now approaching the operating frequency. The net effect is that there is almost no change in the breakdown level as the humidity increases.

Figure 6-47 shows that increased humidity decreases the breakdown strength for wires having diameter 2.53 cm or greater. This is because the operating frequency (30 kHz) is above the critical frequency for these larger wires, even for the low-humidity case. Note that 47 kHz is above the critical frequency for all the wires, including the two smaller wires. Thus, all of these curves show a decreasing breakdown voltage with increased humidity (Figure 6-48).

The detailed shape of the curves of breakdown versus humidity is not revealed since there are measurements at only three values of humidity. It appears that in the low- to mid-humidity region the decrease in the breakdown level is linear and the slope increasing slowly with diameter, approaching a constant value for the larger wires. This is indicated by Figures 6-57 and 6-58, which present the same data normalized to the value measured at low humidity. The asymptotic behavior is particularly evident in Figure 6-58, provided the 1.91-cm-diameter wire data are ignored. It should be kept in mind when examining the curves that the high humidity measurements exhibit considerable variability due to the effect of micro-droplets in the air and on the surface.

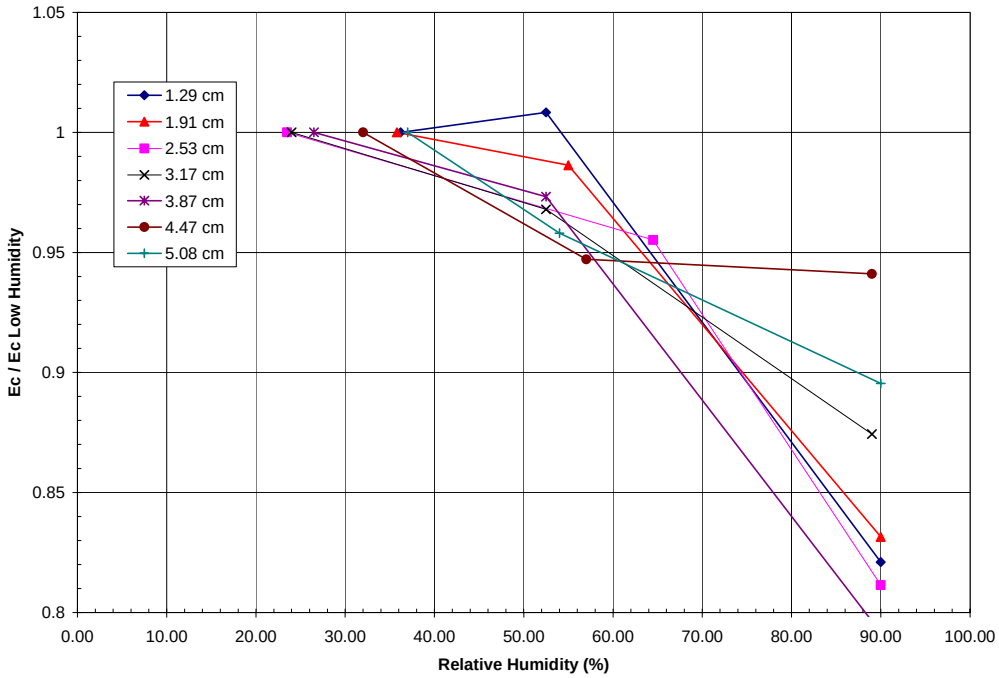

Figure 6-57. Onset field normalized to low-humidity value, 29 kHz.

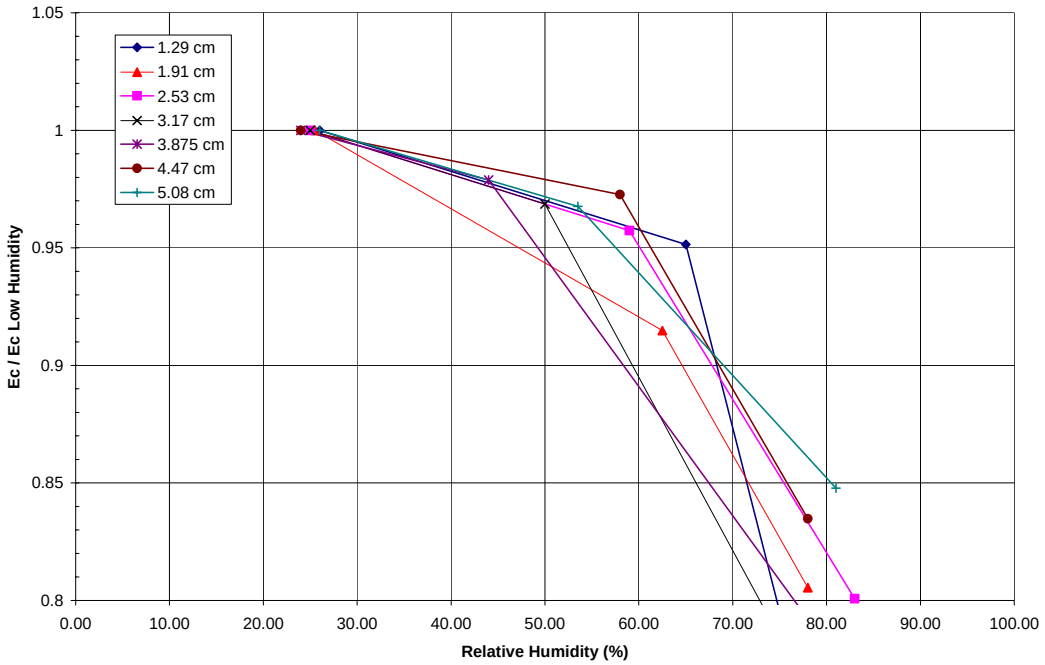

Figure 6-58. Onset field normalized to low-humidity value, 47 kHz.

From Figure 6-57, for 29 kHz the asymptotic value for the slope at large diameters is approximately −0.22%/(% relative humidity). The value of the slope from Figure 6-58 for 47 kHz is approximately −0.11%/(% relative humidity). Comparison of these figures indicates that the 47-kHz data decreases at a slower rate than the 29-kHz data. This seems contradictory but may be because at 47 kHz, the low-humidity point has already been reduced due to operation in or above the transition region.

In summary, the humidity correction factor is negative, linear, and approximately equal to −0.20% (% relative humidity) (at STP 25) for wires operating above the critical frequency. The slope will be less negative when the operating frequency is in the transition region, and the slope will be positive equal to that measured at 60 Hz when the operating frequency is below the transition region.

The critical gradient approaches that for wet conditions as relative humidity increases for all three cases. The linear region extends to relative humidity levels of 80% to 85% when the operating frequency is above the critical frequency. Conglomerated water molecules decreases the breakdown strength at a greater rate so the slope goes much more negative as the humidity approaches 90% and eventually ends at or near the wet breakdown level for 100% humidity.

Figure 6-59 gives a proposed set of curves for the effect of humidity on breakdown level. There are three curves showing the proposed effect for (1) a small wire operating well below the critical frequency, (2) a medium wire operating just below the transition region, and (3) a large wire operating above the critical frequency. The top curve (corresponding to case #1) is similar to Kuffel's 60-Hz correction factor, which has increasing breakdown strength with humidity. The middle curve (corresponding to case #2) represents the VLF measurements for the wires having diameters of 1.91 cm and 2.53 cm at 29.5 kHz from Figure 6-47, which is based on measurements that exhibit little variation with humidity. The bottom curve (corresponding to case #3) represents VLF measurements on the larger diameter wires and the 6-inch diameter toroidal corona ring, which have decreasing breakdown strength with humidity.

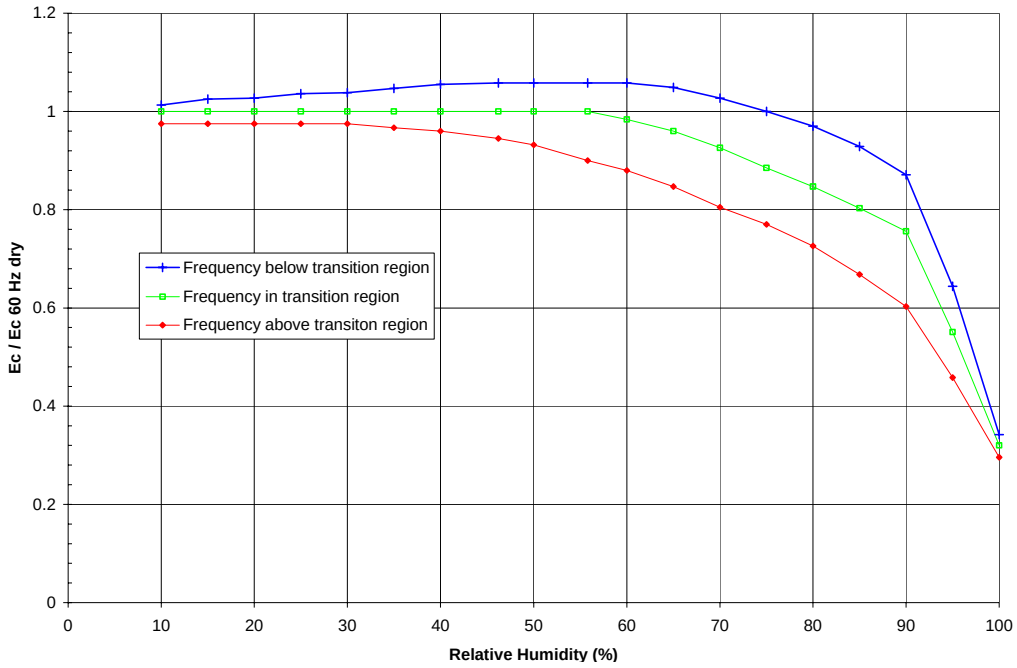

Figure 6-59. Proposed humidity correction factor.

These curves are based on the limited data and the above rationale. We cannot estimate the relationship between critical frequency, humidity, and wire diameter, or the size of the transition region. Determination of these relationships will require carefully controlled measurements over a wide range of frequencies. There is enough data to estimate the magnitude of the humidity effect on corona onset level. The curves in Figure 6-59 fit both our VLF/LF measurements and the dc and 60-Hz measurements in the appropriate regions.

Note that the curves in Figure 6-59 are plotted in terms of the ratio of E_c at VLF/LF as a function of humidity divided by E_c at 60 Hz for dry air. By normalizing to the low-frequency value for dry air, the curves include the effect of humidity. For example, the curve for the frequency of operation below the transition region (#1) shows the increase in breakdown level with increasing humidity as observed at 60 Hz. The curve for the wire operating above the transition region (#3) shows an approximately linearly decreasing breakdown level until 90% relative humidity is approached. The curve for the wire operating in the transition region (#2) shows almost no change in breakdown strength until higher humidity levels. This is because the increase in the fundamental breakdown strength of air due to increased humidity is countered by the decrease in the critical frequency. All of the curves show the breakdown level decreasing drastically and approaching the value for wet conditions as the humidity approaches 100%.

Combined Humidity, Frequency, and Diameter

The correction factor plotted versus humidity in Figure 6-59 can be alternatively plotted versus frequency as shown in Figure 6-60. This figure gives a plot of the frequency correction factor for three different cases of humidity (low, mid, and high). Again, the plots are normalized to the low-frequency breakdown strength for dry air to show the effect of humidity. The low-frequency parts of the three curves in Figure 6-60 agree with 60-Hz results. The low-humidity curve is only slightly above the value for dry air in this region. The mid-humidity case is above that, and the high-humidity case has the highest value in this region. The order of the three curves is inverted with

the high-humidity curve being the lowest at the higher frequencies. The transition region starts at a lower frequency with increasing humidity, which reflects reduction of critical frequency by humidity. The curves do not quantify the relationship between critical frequency, diameter, and humidity. Nevertheless, the magnitude of the correction factor is supported by data.

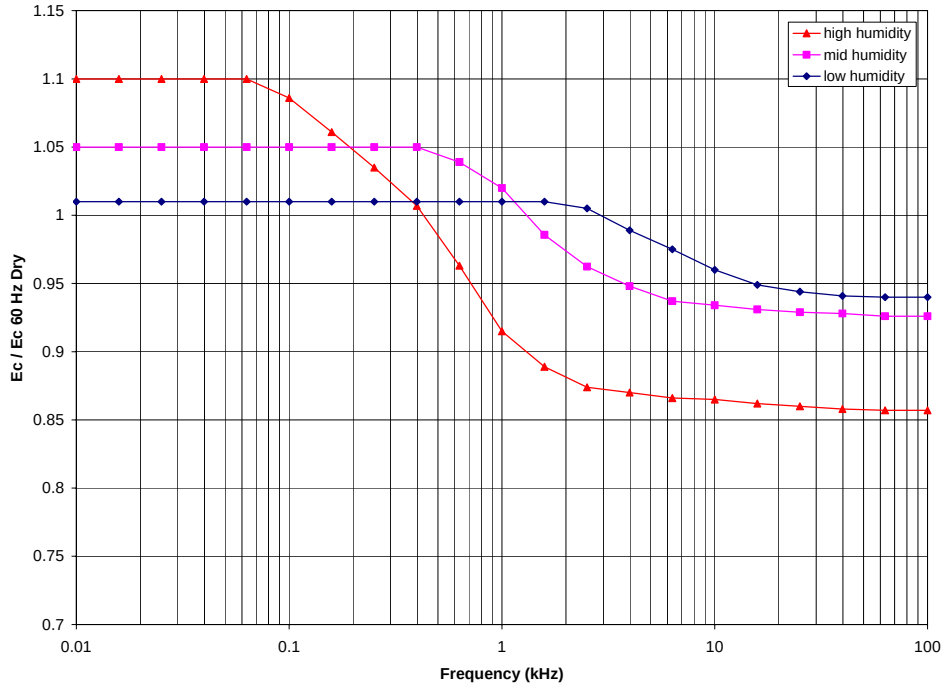

Figure 6-60. Proposed frequency correction factor combined with humidity.

GENERAL CORONA ONSET FORMULAS FOR VLF/LF

General formulas are presented in this section for the critical field level for corona onset on wires and cables at VLF/LF that include the effect of humidity, frequency, air density, and wire diameter. These equations have been developed by modification of the equations previously given in Table 6-2. The equations account for both wet and dry conditions. For wet conditions, the factor of 110% is used for the relative humidity.

The general equation for the critical surface field for corona onset on smooth conductors in the VLF range is

$$E_c = A \cdot (1 - 0.6 \cdot (RH/100)^3) \cdot (0.9 + 0.095/(f/30 + 1)) + B \cdot (1 + RH/600)/d^x$$

where E_c is the critical gradient in kV/cm rms,
$A = 17.25$,
$B = 12.0$,
$x = 0.5$,
RH = relative humidity in %,
f = frequency, kHz, and
d = pipe diameter in cm.

Figure 6-61 shows that this equation provides an excellent fit to the measured data.

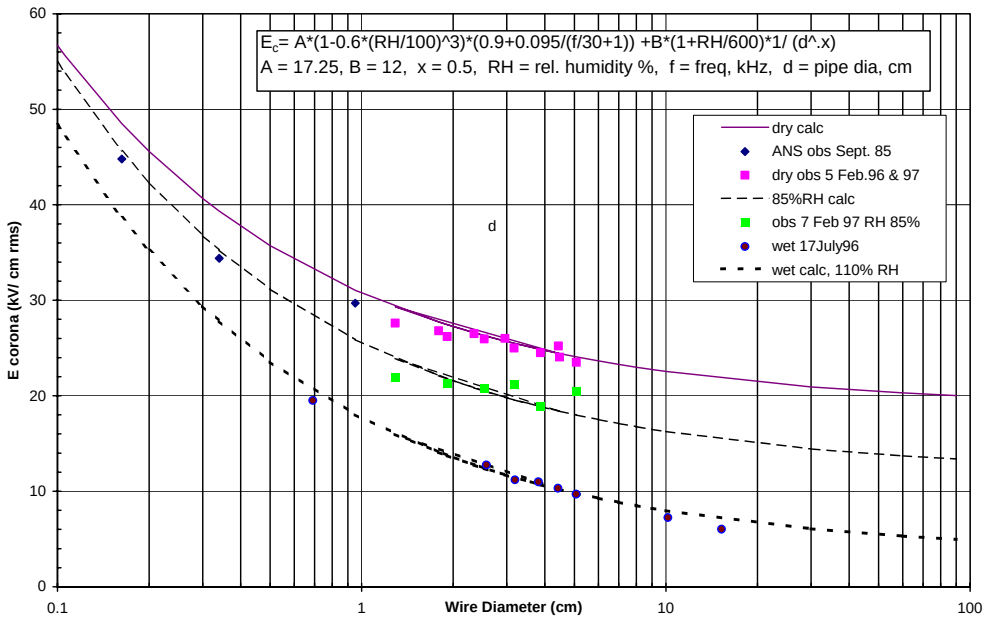

Figure 6-61. General formula for corona onset gradient versus diameter and frequency, smooth, comparison to 29-kHz data.

The general equation for the critical surface field for corona onset on stranded cables in the VLF range, given below, is the same except for including the stranding factor K_{str}.

$$E_c = A \cdot K_{str} \cdot (1 - 0.6 \cdot (RH/100)^3) \cdot (0.9 + 0.095/(f/30+1)) + B \cdot (1 + RH/600)/d^x$$

Figure 6-62 shows that this equation is also an excellent fit to the measured data for stranded cables. The stranding factor used (K_{str}) in Figure 2-24 was 0.5, which applies to the large wires. The equation for the smooth case is the same as the equation for the stranded case except that $K_{str} = 1$.

Figures 6-61 and 6-62 show that a single equation provides an excellent design tool that includes the effects of diameter, frequency, relative humidity, stranding, and wet or dry conditions.

DESIGN DATA

In this section, design data are presented in the form of the voltage allowable on a wire, pipe, or cable. Three environmental conditions are considered: dry clean indoor air, humid indoor air, and outdoor conditions including rain. The voltages are derived for corona-free operation. The onset of corona has been defined earlier in this chapter for wet conditions and corresponds to the beginning of significant power dissipation.

The formulas for the critical surface electric field for corona onset in Table 6-2 have been combined with the formula for the surface electric field on a single long wire above ground to derive the allowable voltage for corona-free operation. These curves are provided to provide a basic understanding of the magnitudes of the voltages involved. However, the best approach for more complicated geometry is to use electrostatic computer programs to calculate the surface electric fields and apply the corona onset fields based on the formulas of Table 6-2.

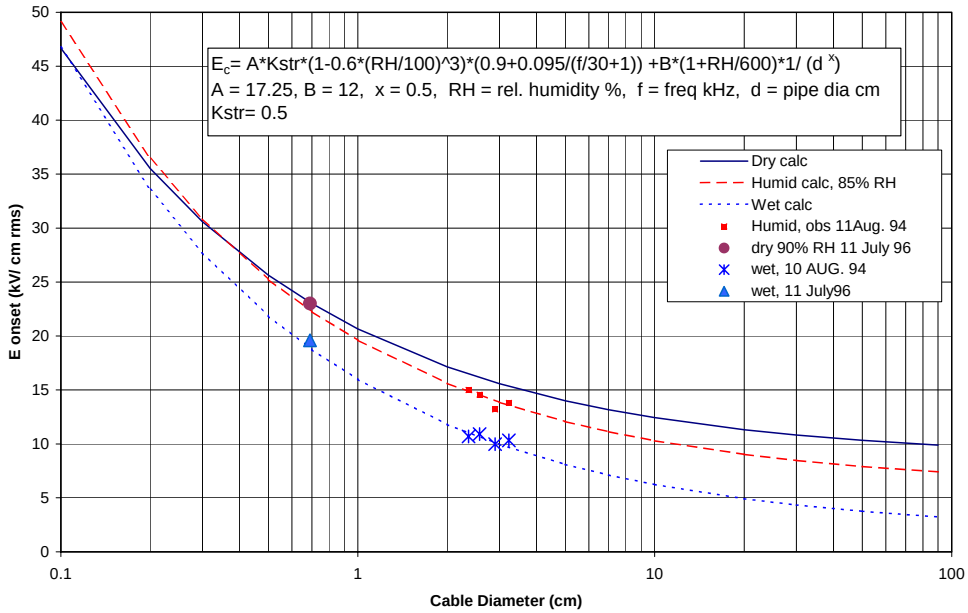

Figure 6-62. General formula for corona onset gradient versus diameter and frequency, stranded, comparison to 29-kHz data.

The curves presented here do not include a safety factor because it would depend strongly on the situation involved. For example, if the configuration involves indoor dry, clean conditions and materials such as Litz wire which can burn, then a significant safety factor (100%) is suggested to account for unusual conditions of dirt, humidity, or condensation. If the configuration involves outdoor situations, where the worst case is spray-wet, and the materials are not flammable, then a smaller safety factor is required (25%). There are cases where some corona during inclement conditions would be acceptable, and for this case it may be that no safety factor is required.

At typical VLF stations, indoor bus connections are made by the use of smooth pipes. Figure 6-63 gives the maximum operating voltages as a function of pipe diameter at 1, 2, 4, and 10 meters above, or spaced from, a grounded conducting surface. These voltages are based on long wire formulas. Practical design should account for end effects. For example, the gradient (surface field) at the ends of pipes increases to about twice the value for an infinite long wire. This effect can be reduced with the use of corona rings at or near the ends of the pipes. It is also important to note that the design of the connections used is very important. Sharp edges on connecting flanges can significantly reduce the corona free operating voltage of a pipe.

Figure 6-64 gives similar results for stranded cables operating in typical rain conditions. The safe, (corona onset) voltage is seen, as expected, to be much lower than for the same diameter smooth dry pipe conditions. Safe operating voltages for stranded cables with dry conditions can be calculated using the formulas given in Table 6-2B. However, the critical gradient for wet conditions is less than for dry and since outside cables must be capable of wet (rain conditions) operation. Figure 6-64 gives the practical limiting condition for outdoor operation.

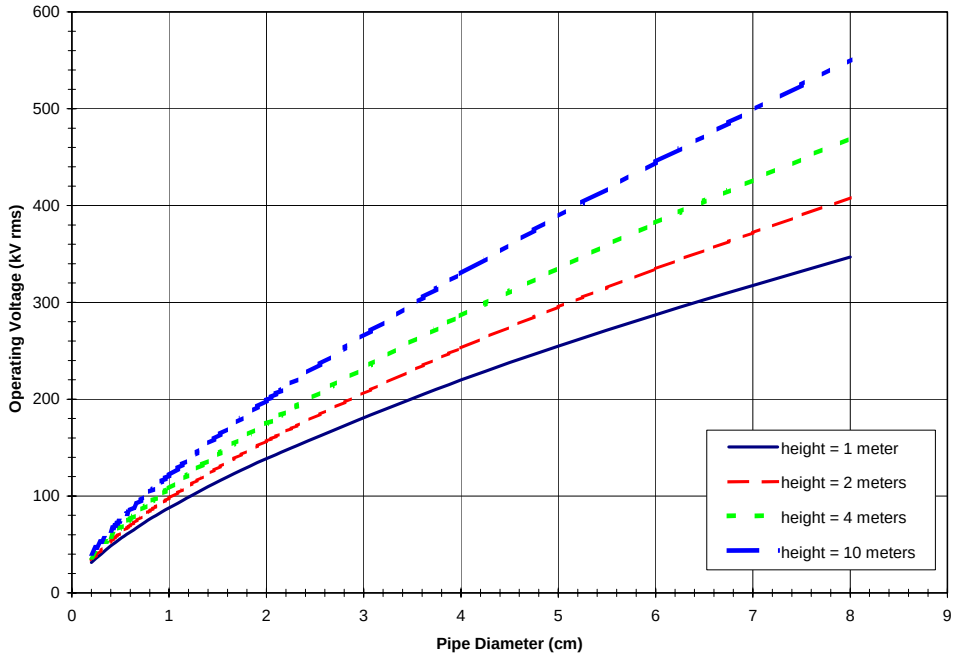

Figure 6-63. Design voltage for smooth pipes, clean and dry.

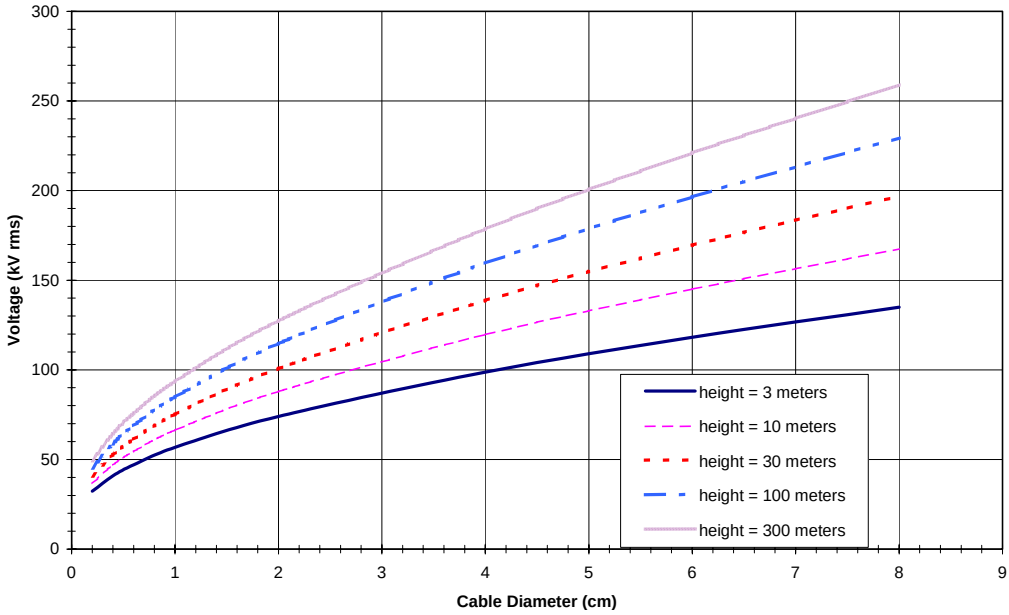

Figure 6-64. Design voltage for stranded cables, outside wet.

Appendix 6A Corona Onset Data for Wires, Pipes, and Cables

This appendix contains the data measured at Forestport regarding corona onset at VLF and LF. The data sets are catalogued by a file date, usually the data when the measurements in that file took place. The file date is not necessarily the date for all of the measurements in that file as some of the files contain data measured on different days. The list of data files and the data they contain is given in the table below.

Data Set No.	Date	Page	Configuration	Freq kHz	Effect
1	10 Aug 94	6A-2	Outside wires horizontal	27.5, 40	Repeat with new calibration and better geometry
2	27 Oct 94	6A-5	Outside horizontal cages	27.5	Caging, corona phenomena, ons/ext, power
3	8 Feb 96	6A-8	Inside wires horizontal	29, 53	Air density
4	13 May 96	6A-11	Inside pipes horizontal	29.2	Diameter, smooth – stranded
5	11 July 96	6A-13	Outside pipe wet & dry	27.8, 43	Diameter, freq wet – dry
6	10 Sep 96	6A-18	Outside sloping cable & pipe	30, 43	Slope, wet – dry
7	5 Feb 97	6A-21	Inside horizontal 15’ lengths	29, 47	Humidity
8	8 Feb 97	6A-27	Inside horizontal 10’ lengths	14	Air density
9	15 Feb 97	6A-31	Inside horizontal 15’ lengths	29	Air density
10	18 Feb 97	6A-36	Inside horizontal 15’ lengths	47	Air density

The data sheets from these files are printed in the form of spreadsheets. They contain the raw measured data as well as the processed data. The measured corona onset voltage is given along with the calculated electric field and the corresponding measured wire diameter. The environmental parameters are given as well as the electric field and wire diameter corrected for atmospheric density. The file catalogue date is in the upper left-hand corner cell of each spreadsheet.

1. 10 AUG 94

10 Aug 94	Outside wires horizontal	27.5, 40 kHz	Repeat with new calibration and better geometry

10-Aug-94

Outside Cables Above Ground (Good Geometry)
Measurements Done on 11 Aug
27 kHz

Night tests Outside --- means nearly 100% Humidity

Frequency 27.5 kHz
k meter 1

dry conditions

cables	diameter cm	height to center cm	Temp Deg C	RH %	Bp mm Hg	Water % moles	Relative density	Vavg kV rms	K geom	Corrected for meter & geom E kV/cm	Density diameter cm	Correction E kV/cm
Al smooth	2.34	292.00	13.3	89.00	730	1.39377	1.0000	116.2	1.00	16.07	2.34	16.07
Cuholcore	2.36	292.01	10.6	98.00	731	1.277429	1.0101	109.7	1.00	15.03	2.39	14.88
Alumoweld	2.57	295.29	10.6	98.00	731	1.277429	1.0101	114.0	1.00	14.56	2.59	14.41
gavanize	2.57	292.75	13.3	89.00	730	1.39377	1.0000	119.2	1.00	15.24	2.57	15.24
Cuweld	2.90	294.82	10.6	98.00	731	1.277429	1.0101	114.0	1.00	13.17	2.92	13.04
Al	3.23	294.98	13.3	89.00	730	1.39377	1.0000	130.7	1.00	13.81	3.23	13.81

wet conditions

cables	diameter cm	height to center cm	Temp Deg C	RH %	Bp mm Hg	Water % moles	Relative density	Vavg kV rms	K geom	Corrected for meter & geom E kV/cm	Density diameter cm	Correction E kV/cm
Al smooth	2.34	292.00	13.3	89.00	730	1.39377	1.0000	80.8	1.00	11.17	2.34	11.17
Cuholcore	2.36	292.01	10.6	98.00	731	1.277429	1.0101	78.0	1.00	10.69	2.39	10.58
Alumoweld	2.57	295.29	10.6	98.00	731	1.277429	1.0101	85.4	1.00	10.90	2.59	10.80
gavanize	2.57	292.75	13.3	89.00	730	1.39377	1.0000	85.3	1.00	10.91	2.57	10.91
Cuweld	2.90	294.82	10.6	98.00	731	1.277429	1.0101	86.4	1.00	9.98	2.92	9.88
Al	3.23	294.98	13.3	89.00	730	1.39377	1.0000	97.8	1.00	10.33	3.23	10.33

10-Aug-94

Outside Cables Above Ground (Good Geometry)
Measurements Done on 11 Aug
40 kHz

Night tests Outside --- means nearly 100% Humidity
Frequency 40.7 kHz
k meter 1

Dry conditions

cables	diameter cm	height to center cm	Temp Deg C	RH %	Bp mm Hg	Water % moles	Relative density	Vavg kV rms	K geom	Corrected for meter & geom E kV/cm	Density diameter cm	Correction E kV/cm
Al smooth	2.34	291.36	7.2	100.00	730	1.04105	1.0218	112.2	1.00	15.52	2.39	15.19
Cuhholcore	2.36	295.19	10.6	98.00	730	1.277873	1.0098	96.3	1.00	13.17	2.39	13.04
Alumoweld	2.57	292.75	7.8	99.00	731	1.069755	1.0205	92.4	1.00	11.82	2.62	11.58
Galvanized	2.57	288.30	7.8	99.00	731	1.069755	1.0205	107.0	1.00	13.72	2.62	13.44
Cuweld	2.90	291.01	9.4	96.00	731	1.161644	1.0141	109.7	1.00	12.70	2.94	12.52
Al	3.23	291.81	7.2	100.00	730	1.04105	1.0218	113.4	1.00	12.00	3.30	11.74

Spray wet conditions

cables	diameter cm	height to center cm	Temp Deg C	RH %	Bp mm Hg	Water % moles	Relative density	Vavg kV rms	K geom	Corrected for meter & geom E kV/cm	Density diameter cm	Correction E kV/cm
Al smooth	2.34	291.36	7.2	100.00	730	1.04105	1.0218	78.5	1.00	10.86	2.39	10.63
Cuholcore	2.36	295.19	10.6	98.00	730	1.277873	1.0098	78.9	1.00	10.79	2.39	10.69
Alumoweld	2.57	292.75	7.8	99.00	731	1.069755	1.0205	83.2	1.00	10.64	2.62	10.43
Galvanized	2.57	288.30	7.8	99.00	731	1.069755	1.0205	83.8	1.00	10.74	2.62	10.53
Cuweld	2.90	291.01	9.4	97.00	731	1.173745	1.0141	85.5	1.00	9.90	2.94	9.76
Al	3.23	291.81	7.2	100.00	730	1.04105	1.0218	87.8	1.00	9.29	3.30	9.09

2. 27 OCT 94

27 Oct 94	Outside horizontal cages	27.5 kHz	Caging, corona phenomena, ons/ext, power

27-Oct-94

Outside Cables Above Ground (Geoff Dann Cage Measurements)
Measurements Done on 26 Oct
27 kHz

k meter 1

Night tests Outside --- means nearly 100% Humidity

Frequency 27 kHz

		Dry conditions					Corrected For Meter and Geometry					
n Cage	Separation inches	Electro E max 1/in	Electro E max 1/cm	corona Inception kV	corona Extinction kV	k Geom	corona Inception kv/in	corona Extinction kV/in	Corona Inception kV/cm	corona Extinction kV/cm	CI/CE	
1	0	0.3220	0.1268	113.0	100.0	0.9938	36.2	32.0	14.2	12.6	1.13	
2	4	0.2350	0.0925	173.0	152.0	1.0101	41.1	36.1	16.2	14.2	1.138158	
2	12	0.2320	0.0913	172.0	149.0	1.0209	40.7	35.3	16.0	13.9	1.154362	
2	24	0.2420	0.0953	160.0	136.0	1.0280	39.8	33.8	15.7	13.3	1.176471	
3	4	0.1940	0.0764	190.0	162.0	1.0137	37.4	31.9	14.7	12.5	1.17284	
3	12	0.1890	0.0744	224.0	177.0	1.0303	43.6	34.5	17.2	13.6	1.265537	
3	24	0.2030	0.0799	182.0	168.0	1.0435	38.6	35.6	15.2	14.0	1.083333	
4	4	0.1680	0.0661	230.0	181.0	1.0179	39.3	31.0	15.5	12.2	1.270718	
4	12	0.1610	0.0634	209.0	186.0	1.0378	34.9	31.1	13.7	12.2	1.123656	Avg
4	24	0.1770	0.0697	203.0	184.0	1.0572	38.0	34.4	15.0	13.6	1.103261	1.161834

27-Oct-94 Spray Wet Conditions Corrected For Meter and Geometry

Cage	Separation inches	Electro E max 1/in	Electro E max 1/cm	corona Inception kV	corona Extinction kV	k Geom	corona Inception kv/in	corona Extinction kV/in	Corona Inception kV/cm	corona Extinction kV/cm	CI/CE	
single	0	0.3220	0.1268	90.0	88.0	0.9938	28.8	28.2	11.3	11.1	1.022727	
2 X 4"	4	0.2350	0.0925	127.0	107.0	1.0101	30.1	25.4	11.9	10.0	1.186916	
2 X 12"	12	0.2320	0.0913	126.0	117.0	1.0209	29.8	27.7	11.7	10.9	1.076923	
2 X 24"	24	0.2420	0.0953	116.0	105.0	1.0280	28.9	26.1	11.4	10.3	1.104762	
3 X 4"	4	0.1940	0.0764	153.0	137.0	1.0137	30.1	26.9	11.8	10.6	1.116788	
3X 12"	12	0.1890	0.0744	152.0	138.0	1.0303	29.6	26.9	11.7	10.6	1.101449	
3 X 24"	24	0.2030	0.0799	144.0	134.0	1.0435	30.5	28.4	12.0	11.2	1.074627	
4 X 4"	4	0.1680	0.0661	178.0	142.0	1.0179	30.4	24.3	12.0	9.6	1.253521	
4 X 12"	12	0.1610	0.0634	175.0	161.0	1.0378	29.2	26.9	11.5	10.6	1.086957	Avg
4 X 24"	24	0.1770	0.0697	156.0	141.0	1.0572	29.2	26.4	11.5	10.4	1.106383	1.113105

3. 8 FEB 96

8 Feb 96	Inside wires horizontal	29, 53 kHz	Air density

Morning Tests, Cold 29 kHz

Pipes	Frequency 29.31 k meter diameter cm	kHz height to center cm	Temp Deg C	RH %	Bp mm Hg	Water g/m^3	Relative density	Vavg kV rms	K geom	Corrected for meter & geom E kV/cm	Density diameter cm	Correction E kV/cm
small	1.79	88.21	14.0	54.00	720	6.5	0.9834	132.8	0.9281	26.29	1.76	26.73
medium	2.34	88.48	12.0	57.00	720	6.1	0.9903	167.5	0.9393	27.11	2.32	27.37
large	2.96	88.79	13.0	51.00	720	5.8	0.9865	188.6	0.9429	25.54	2.92	25.89
X-large	4.43	89.53	14.0	51.00	719	6.1	0.9827	244.6	0.9500	24.48	4.35	24.91

Afternoon Tests, Warmer

Pipes	Frequency 29 diameter cm	kHz height to center cm	Temp Deg C	RH %	Bp mm Hg	Water g/m^3	Relative density	Vavg kV rms	K geom	Corrected for meter & geom E kV/cm	Density diameter cm	Correction E kV/cm
X-large	4.43	89.53	19.0	46.00	717	7.5	0.9629	241.2	0.9500	24.14	4.27	25.07
large	2.96	88.79	18.0	46.00	717	7.0	0.9658	187.0	0.9429	25.33	2.86	26.22
medium	2.34	88.48	18.0	46.00	717	7.0	0.9655	163.6	0.9393	26.48	2.26	27.42
small	1.79	88.21	18.0	46.00	717	7.0	0.9655	131.4	0.9281	26.01	1.73	26.94

Afternoon Tests, Warmer

Pipes	Frequency 29 diameter cm	kHz height to center cm	Temp Deg C	RH %	Bp mm Hg	Water g/m^3	Relative density	Vavg kV rms	K geom	Corrected for meter & geom E kV/cm	Density diameter cm	Correction E kV/cm
small	1.79	88.21	26.0	40.00	715	9.70	0.9380	129.4	0.9281	25.62	1.68	27.31
medium	2.34	88.48	26.0	40.00	715	9.70	0.9380	157.2	0.9393	25.44	2.20	27.12
large	2.96	88.79	26.0	40.00	715	9.70	0.9380	180.4	0.9429	24.43	2.77	26.05
X-large	4.43	89.53	26.0	40.00	715	9.70	0.9380	239.6	0.9500	23.98	4.16	25.57

08-Feb-96 Air Density Correction Factor Measurements Inside, Smooth Pipes above ground Page 1 of 2

Morning Tests, Cold 52 kHz

Frequency 52.4 kHz

k meter 1 Dry Conditions

Pipes	diameter cm	height to center cm	Temp Deg C	RH %	Bp mm Hg	Water g/m^3	Relative density	Vavg kV rms	K geom	Corrected for meter & geom E kV/cm	Corrected for Density diameter cm	Corrected for Density E kV/cm
X-large	4.43	89.53	14.0	51	719.3	6.1	1.0	241.4	0.94999	24.16	4.35	24.45
large	2.96	88.79	12.5	52	719.6	5.7	1.0	189	0.942926	25.60	2.92	25.90
medium	2.34	88.48	12.0	59	720.1	6.3	1.0	164.7	0.939277	26.66	2.32	26.97
small	1.79	88.21	13.0	72.5	719.8	8.2	1.0	137.8	0.928058	27.28	1.77	27.60

Afternoon Tests, Warmer

Frequency 52.7 kHz Dry Conditions

Pipes	diameter cm	height to center cm	Temp Deg C	RH %	Bp mm Hg	Water g/m^3	Relative density	Vavg kV rms	K geom	Corrected for meter & geom E kV/cm	Corrected for Density diameter cm	Corrected for Density E kV/cm
small	1.79	88.21	22.0	45	716.5	8.7	1.0	130.1	0.928058	25.76	1.71	26.06
medium	2.34	88.48	18.0	46.5	716.8	7.1	1.0	163.8	0.939277	26.51	2.26	26.82
large	2.96	88.79	18.0	46	716.8	7.0	1.0	187.8	0.942926	25.44	2.86	25.74
X-large	4.43	89.53	19.0	48	719.8	7.8	1.0	232.8	0.94999	23.30	4.28	23.58

08-Feb-96 Page 2 of 2

Afternoon Tests, Even Warmer Dry Conditons

Frequency 53 kHz

Pipes	diameter cm	height to center cm	Temp Deg C	RH %	Bp mm Hg	Water g/m^3	Relative density	Vavg kV rms	K geom	Corrected for meter & geom E kV/cm	Density Correction diameter cm	Density Correction E kV/cm
small	1.79	88.21	25.0	40.00	1016	9.2	0.9	130.17	0.928058	25.77	1.69	27.39
medium	2.34	88.48	25.0	40.00	1016	9.2	0.9	152	0.939277	24.60	2.21	26.14
large	2.96	88.79	25.0	40.00	1016	9.2	0.9	180.6	0.942926	24.46	2.78	25.99
X-large	4.43	89.53	25.0	40.00	1016	9.2	0.9	226.2	0.94999	22.64	4.17	24.07

4. 13 MAY 96

13 May 96	Inside pipes horizontal	29.2 kHz	Diameter, smooth – stranded

13-May-96

Horizontal Rod Tests
Inside, Smooth Pipes & 1 Cable Above Ground
Note Rods are 10 ft long, Cable is 15.5ft long
30 kHz

Morning Tests

Tests actually done on 14 may

Frequency 29.2 kHz
k meter 1

Pipes	diameter cm	height to center cm	Temp Deg C	RH %	Bp mm Hg	Water % moles	Relative density	Vavg kV rms	K geom	Corrected for meter & geom E kV/cm	Density Correction diameter cm	Density Correction E kV/cm
Dry Flare												
stranded	2.67	88.65	19.4	52.00	733	1.20	0.98	126.3	0.9412	18.50	2.62	18.82
Wet Corona Inception												
stranded	2.67	88.65	19.4	52.00	733	1.20	0.98	92.4	0.9412	13.53	2.62	13.77
small	1.79	88.21	19.4	60.00	733	1.38	0.98	73.2	0.9281	14.49	1.76	14.74
medium	2.34	88.48	19.4	60.00	733	1.38	0.98	81.9	0.9393	13.25	2.30	13.49
large	2.96	88.79	19.4	60.00	733	1.38	0.98	89.3	0.9429	12.09	2.90	12.31
x-large	4.43	89.53	19.4	60.00	733	1.38	0.98	104.2	0.9500	10.43	4.35	10.62

13-May-96 14-May-96

Horizontal Rod Tests
Inside, Smooth Pipes& 1 cable above ground
52 kHz

Afternoon Tests
Tests actually done on 14 May

Frequency 52 kHz

Pipes	diameter cm	to center cm	Temp Deg C	RH %	Bp mm Hg	Water % moles	Relative density	Vavg kV rms	K geom	& geom E kV/cm	Density Correction diameter cm	Density Correction E kV/cm
Wet Corona Inception												
x-large	4.43	87.31	21.7	54.00	733	1.43	0.97	79.2	0.9429	7.92	4.32	8.12
large	2.96	87.31	21.7	54.00	733	1.43	0.97	78.3	0.9393	10.60	2.88	10.88
medium	2.34	88.48	21.7	54.00	733	1.43	0.97	72.6	0.9500	11.88	2.29	12.19
small	1.79	88.21	21.7	54.00	733	1.43	0.97	64.8	0.9281	12.83	1.75	13.16

5. 11 JULY 96

11 July 96	Outside pipe wet & dry	27.8, 43 kHz	Diameter, freq wet – dry

11-Jul-96 Outside, Pipes Above Ground Also Includes July 17 Data

July 11, 1996 - Corona Inception 28 kHz

Night tests Outside --- implies at or nearly 100% Humidity

Frequency 27.8 kHz
k meter 1

Dry conditions

Pipes	diameter cm	height to center cm	Temp Deg C	RH %	Bp mm Hg	Water g/m^3	Relative density	Vavg kV rms	K geom	Corrected for meter & geom E kV/cm	Density Correction diameter cm	Density Correction E kV/cm
8"	20.32	312.42	12.8	90.00	732	10.03	1.0040		1.00		20.40	
6"	15.24	311.15	12.8	90.00	732	10.03	1.0040		1.00		15.30	
4"	10.16	310.52	13.3	88.00	732	10.15	1.0021		1.00		10.18	
2"	5.07	311.78	13.3	88.00	732	10.15	1.0021	279.5	1.00	20.18	5.09	20.13
1.74"	4.42	307.34	13.3	88.00	732	10.15	1.0021	243.7	1.00	19.74	4.43	19.70
1.5"	3.83	313.06	12.8	86.00	732	9.58	1.0037	240.8	1.00	21.87	3.84	21.79
1.25"	3.19	312.74	12.8	86.00	732	9.58	1.0037	204.4	1.00	21.58	3.20	21.50
1"	2.57	313.07	12.8	86.00	732	9.58	1.0037	178.2	1.00	22.53	2.57	22.45
.27 " strand	0.69	305.14	15.6	92.00	728	12.16	0.9895	59.8	1.00	23.34	0.68	23.58

17-Jul-96 Corona Inception for smaller Diameters, Flare Inception for larger (see below)

Night tests Outside --- implies at or nearly 100% Humidity

Frequency 28 kHz

Spray Wet

Pipes	diameter cm	height to center cm	Temp Deg C	RH %	Bp mm Hg	Water g/m^3	Relative density	Vavg kV rms	K geom	Corrected for meter & geom E kV/cm	Density Correction diameter cm	Density Correction E kV/cm
.27" strand	0.69	312.13	15.6	92.00	728	12.16	0.9895	50.2	1.00	19.51	0.68	19.71
1"	2.57	313.07	15.6	92.00	728	12.16	0.9895	100.9	1.00	12.75	2.54	12.89
1.25"	3.19	309.57	15.6	92.00	728	12.16	0.9895	105.9	1.00	11.20	3.15	11.32
1.5"	3.81	310.52	15.6	92.00	728	12.16	0.9895	120.4	1.00	10.99	3.77	11.11
1.74"	4.42	310.18	15.6	92.00	733	12.16	0.9964	127.8	1.00	10.33	4.40	10.37
2"	5.07	310.51	14.4	90.00	728	11.11	0.9937	134.1	1.00	9.69	5.04	9.75
4"	10.16	313.06	14.4	90.00	728	11.11	0.9937	174.2	1.00	7.24	10.10	7.29
6"	15.24	312.42	14.4	90.00	728	11.11	0.9937	197.6	1.00	6.03	15.14	6.07

11-Jul-96
17-Jul-96 Flare Inception

Night tests Outside --- implies at or nearly 100% Humidity

Pipes	Frequency 28 Spray Wet diameter cm	kHz height to center cm	Temp Deg C	RH %	Bp mm Hg	Water g/m^3	Relative density	Vavg kV rms	K geom	Corrected for meter & geom E kV/cm	Density Correction diameter cm	Density Correction E kV/cm
.27" strand	0.69	312.13	15.6	92.00	728	12.16	0.9895	113.3	1.00	44.08	0.68	44.55
1"	2.57	313.07	15.6	92.00	728	12.16	0.9895	115.3	1.00	14.58	2.54	14.73
1.25"	3.19	309.57	15.6	92.00	728	12.16	0.9895	121.0	1.00	12.80	3.15	12.94
1.5"	3.81	310.52	15.6	92.00	728	12.16	0.9895	125.1	1.00	11.42	3.77	11.54
1.74"	4.42	310.18	15.6	92.00	733	12.16	0.9964	129.7	1.00	10.49	4.40	10.53
2"	5.07	310.51	14.4	90.00	728	11.11	0.9937	136.0	1.00	9.82	5.04	9.88
4"	10.16	313.06	14.4	90.00	728	11.11	0.9937	174.2	1.00	7.24	10.10	7.29
6"	15.24	312.42	14.4	90.00	728	11.11	0.9937	197.6	1.00	6.03	15.14	6.07
8"	20.32	313.69	13.9	94.00	728	11.22	0.9956	229.8	1.00	5.67	20.23	5.70

11-Jul-96 Outside, Cables Above Ground Also Includes July 17 Data

July 11, 1996 - Corona Inception 43 kHz
Night tests Outside --- implies at or nearly 100% Humidity
Frequency 43 kHz
k meter 1

Dry conditions

cables	diameter cm	height to center cm	Temp Deg C	RH %	Bp mm Hg	Water g/m^3	Relative Density	Vavg kV rms	K geom	Corrected & geom E kV/cm	Density Correction diameter cm	Density Correction E kV/cm
1"	2.57	313.07	12.2	87.00	732	9.37	1.0056	168.0	1.00	21.24	2.58	21.13
1.5"	3.81	312.42	12.2	87.00	732	9.37	1.0056	213.2	1.00	19.44	3.83	19.33
2"	5.07	313.05	11.1	88.00	732	8.84	1.0096	276.6	1.00	19.95	5.12	19.76
4"	10.16	314.33	11.1	88.00	732	8.84	1.0096	282.4	1.00	11.73	10.26	11.62

17-Jul-96 Corona Inception for smaller Diameters, Flare Inception for larger (see below)
Night tests Outside --- implies at or nearly 100% Humidity
Frequency 42 kHz

cables	Spray Wet diameter cm	height to center cm	Temp Deg C	RH %	Bp mm Hg	Water g/m^3	Relative Density	Vavg kV rms	K geom	Corrected for meter & geom E kV/cm	Density Correction diameter cm	Density Correction E kV/cm
8"	20.32	313.69	13.3	96.00	728	11.07	0.9976	202.7	1.00	5.00	20.27	5.02
4"	10.16	313.69	13.3	96.00	728	11.07	0.9976	155.1	1.00	6.44	10.14	6.46
2"	5.07	311.78	13.3	96.00	728	11.07	0.9976	122.6	1.00	8.85	5.06	8.87
1.5"	3.81	315.60	13.3	96.00	728	11.07	0.9976	105.8	1.00	9.63	3.80	9.65
1"	2.57	310.53	13.3	96.00	728	11.07	0.9976	90.0	1.00	11.40	2.56	11.42
.27" strand	0.69	317.21	12.8	94.00	728	10.48	0.9995	52.2	1.00	20.26	0.69	20.27

11-Jul-96
17-Jul-96 Flare Inception
Night tests Outside --- implies at or nearly 100% Humidity

Frequency	42	kHz								Corrected for meter & geom	Density Correction	
	Spray Wet diameter	height to center	Temp	RH	Bp	Water	Relative	Vavg		E	diameter	E
cables	cm	cm	Deg C	%	mm Hg	g/m^3	Density	kV rms	K geom	kV/cm	cm	kV/cm
=====	=====	=====	=====	=====	=====	=====	=====	=====	=====	=====	=====	=====
8"	20.32	313.69	13.3	96.00	728	11.07	0.9976	202.7	1.00	5.00	20.27	5.02
4"	10.16	313.69	13.3	96.00	728	11.07	0.9976	155.1	1.00	6.44	10.14	6.46
2"	5.07	311.78	13.3	96.00	728	11.07	0.9976	122.6	1.00	8.85	5.06	8.87
1.5"	3.81	315.60	13.3	96.00	728	11.07	0.9976	111.2	1.00	10.12	3.80	10.14
1"	2.57	310.53	13.3	96.00	728	11.07	0.9976	99.2	1.00	12.56	2.56	12.59
.27" strand	0.69	317.21	12.8	94.00	728	10.48	0.9995		1.00		0.69	

6. 10 SEP 96

10 Sep 96	Outside sloping cable & pipe	30, 43 kHz	Slope, wet – dry

10-Sep-96 Sloping Pipe Measurements Outside Pipes at 30 degree Angle to Ground

30 kHz Data

Frequency 29.189 kHz Night Tests Outside, implies at or nearly 100 % relative humidity
k meter 1

Dry Corona or Flare Inception

Pipes	diameter cm	height to center cm	Temp Deg C	RH %	Bp mm Hg	Water g/m^3	Relative Density	Vavg kV rms	K geom	Corrected for meter & geom E kV/cm	Density Correction diameter cm	Density Correction E kV/cm
1/4" strand	0.69	457.54	14.4	92.50	725	11.42	0.9895	62.4	0.9234	21.32	0.68	21.54
1" strand	2.57	458.48	7.1	94.43	725	7.34	1.0144	120.6	0.9630	13.81	2.60	13.62
1/2 stainless	1.27	457.84	10.0	94.00	725	8.80	1.0040	122.0	0.9485	25.09	1.28	24.99
3/4 stainless	1.91	458.15	8.0	94.30	725	7.77	1.0112	144.6	0.9556	21.16	1.93	20.93
1"	2.57	458.48	14.4	94.00	725	11.61	0.9895	164.3	0.9630	18.82	2.54	19.02
1.25"	3.18	458.79	13.9	94.00	726	11.22	0.9918	136.8	0.9697	13.19	3.15	13.29
1.5"	3.81	459.11	16.7	92.00	724	13.00	0.9802	143.0	0.9737	11.88	3.73	12.12

Wet Corona or flare inception

Pipes	diameter cm	height to center cm	Temp Deg C	RH %	Bp mm Hg	Water g/m^3	Relative Density	Vavg kV rms	K geom	Corrected for meter & geom E kV/cm	Density Correction diameter cm	Density Correction E kV/cm
1/4" strand	0.69	457.54	14.4	92.50	725	11.42	0.9895	62.8	0.9234	21.45	0.68	21.68
1" strand	2.57	458.48	6.7	94.50	725	7.14	1.0160	117.3	0.9630	13.44	2.61	13.23
1/2 stainless	1.27	457.84	9.3	94.10	725	8.44	1.0064	81.4	0.9485	16.74	1.28	16.63
3/4 stainless	1.91	458.15	7.6	94.37	725	7.55	1.0128	92.8	0.9556	13.58	1.93	13.41
1"	2.57	458.48	14.4	92.50	725	11.42	0.9895	101.2	0.9630	11.59	2.54	11.72
1.25"	3.18	458.79	13.9	94.00	726	11.22	0.9918	111.9	0.9697	10.79	3.15	10.87
1.5"	3.81	459.11	16.7	92.00	724	13.00	0.9802	132.6	0.9737	11.02	3.73	11.24
1.74"	4.42	459.41	14.4	100.00	724	12.35	0.9878	138.7	0.9773	10.22	4.37	10.35
2"	5.08	459.74	13.9	100.00	724	11.93	0.9897	147.5	0.9806	9.72	5.03	9.82
4"	10.16	462.28	12.8	100.00	724	11.14	0.9936	194.8	0.9979	7.43	10.09	7.48

10-Sep-96 Sloping Pipe Measurements Outside Pipes at 30 degree Angle to Ground

Measurements actually done on 11 & 12 Sept 43 kHz Data

Night Tests Outside, implies at or nearly 100 % relative humidity

Frequency 43.164 kHz

k meter 1

Dry Corona or Flare Inception

Pipes	diameter cm	height to center cm	Temp Deg C	RH %	Bp mm Hg	Water g/m^3	Relative Density	Vavg kV rms	K geom	Corrected for meter & geom E kV/cm	Density Correction diameter cm	Density Correction E kV/cm
1/4" std	0.69	457.54	15.0	100.00	724	12.77	0.9859	61.4	0.9234	20.97	0.68	21.27
1" std	2.57	458.48	17.8	80.00	722	12.08	0.9731	137.7	0.9630	15.78	2.50	16.21
1/2 stainless	1.27	457.84	4.4	95.00	725	6.20	1.0245	110.6	0.9485	22.74	1.30	22.20
3/4 stainless	1.91	458.15	3.9	94.00	725	5.91	1.0265	143.2	0.9556	20.96	1.96	20.42
1"	2.57	458.48	15.0	100.00	724	12.77	0.9859	171.0	0.9630	19.59	2.53	19.87
1.25"	3.18	458.79	15.0	100.00	724	12.77	0.9859	170.1	0.9697	16.40	3.13	16.63

Wet Corona or flare inception

Pipes	diameter cm	height to center cm	Temp Deg C	RH %	Bp mm Hg	Water g/m^3	Relative Density	Vavg kV rms	K geom	Corrected for meter & geom E kV/cm	Density Correction diameter cm	Density Correction E kV/cm
1/4" std	0.69	457.54	15.0	100.00	724	12.77	0.9859	58.7	0.9234	20.04	0.68	20.33
1" std	2.57	458.48	17.8	80.00	722	12.08	0.9731	109.3	0.9630	12.52	2.50	12.87
1/2 stainless	1.27	457.84	4.4	95.00	725	6.20	1.0245	76.8	0.9485	15.79	1.30	15.42
3/4 stainless	1.91	458.15	3.9	94.00	725	5.91	1.0265	87.5	0.9556	12.81	1.96	12.48
1"	2.57	458.48	15.0	100.00	724	12.77	0.9859	100.0	0.9556	11.37	2.53	11.53
1.25"	3.18	458.79	15.0	100.00	724	12.77	0.9859	109.3	0.9697	10.53	3.13	10.68
1.5"	3.81	459.11	17.8	80.00	722	12.08	0.9731	129.8	0.9737	10.78	3.71	11.08
1.74"	4.42	459.41	16.1	82.00	722	11.20	0.9794	134.7	0.9773	9.93	4.33	10.14
2"	5.08	459.74	16.1	82.00	722	11.20	0.9794	147.3	0.9806	9.71	4.98	9.91
4"	10.16	462.28	16.1	82.00	722	11.20	0.9794	183.7	0.9979	7.01	9.95	7.16

7. 5 FEB 97

5 Feb 97	Inside horizontal 15’ lengths	29, 47 kHz	Humidity

05-Feb-97 Humidity Correction Factor Inside, Smooth Pipes Above Ground

Wed Morning warm inside raining outside 29 kHz Low Humidity

Frequency 29.3 kHz
k meter 1

smooth pipes	diameter cm	height to center cm	Temp Deg C	RH %	Bp mm Hg	Water g/m^3	Relative Density	Vavg kV rms	K geom	Corrected for meter & geom E kV/cm	Density Correction diameter cm	Density Correction E kV/cm
1/2" ss	1.29	78.85	18.3	36.20	722	7.41	0.96	93.8	0.9588	25.55	1.23	26.71
3/4" ss	1.91	82.46	18.7	35.80	722	6.53	0.96	124.5	0.9619	24.61	1.84	25.56
1" Al	2.53	85.97	24.2	23.50	722	4.81	0.96	155.7	0.9642	24.49	2.42	25.61
1.25" Al	3.17	87.39	20.5	24.00	722	4.64	0.96	176.0	0.9656	23.21	3.04	24.18
1.5" Al	3.87	87.84	21.1	26.50	722	5.12	0.96	201.2	0.9679	22.80	3.72	23.75
1.75" Al	4.47	88.83	18.5	32.00	722	6.01	0.96	220.9	0.9697	22.47	4.29	23.38
2" Al	5.08	89.44	17.4	37.00	722	7.15	0.96	244.4	0.9714	22.61	4.87	23.57

05-Feb-97 Afternoon Tests

29 kHz Low Humidity
Stranded Dry

Stranded Cables	diameter cm	height to center cm	Temp Deg C	RH %	Bp mm Hg	Water g/m^3	Relative Density	Vavg kV rms	K geom	Corrected for meter & geom E kV/cm	Density Correction diameter cm	Density Correction E kV/cm
1/4" galv	0.67	85.83	16.9	35.50	721	5.08	0.98	44.7	0.9541	20.61	0.65	21.13
1/2" galv	1.22	82.81	16.1	35.50	721	4.85	0.98	63.8	0.9583	17.97	1.20	18.36
1" Al	2.62	69.91	18.1	27.00	721	4.14	0.97	98.4	0.9645	15.82	2.54	16.28
1-1/4" Al	3.24	74.72	17.3	31.00	721	4.56	0.97	118.0	0.9658	15.90	3.15	16.32

05-Feb-97 Humidity Correction Factor Inside, Smooth Pipes Above Ground
Frequency 29.5 kHz 29 kHz medium humidity
07-Feb-97

smooth pipes	diameter cm	height to center cm	Temp Deg C	RH %	Bp mm Hg	Water g/m^3	Relative Density	Vavg kV rms	K geom	Corrected for meter & geom E kV/cm	Density Correction diameter cm	Density Correction E kV/cm
1/2" ss	1.29	89.85	16.8	52.50	729	8.52	0.98	99.2	0.9588	26.38	1.26	26.94
3/4" ss	1.91	82.76	16.9	55.00	729	8.93	0.98	125.0	0.9619	24.69	1.87	25.21
1" Al	2.53	85.97	18.1	64.50	729	9.87	0.98	152.8	0.9642	24.04	2.49	24.46
1.25" Al	3.17	87.29	18.9	52.50	729	8.03	0.98	174.4	0.9656	23.00	3.12	23.41
1.5" Al	3.87	87.24	18.6	52.50	729	8.52	0.98	199.4	0.9679	22.64	3.79	23.12
1.75" Al	4.47	88.53	18.5	57.00	729	9.25	0.98	213.0	0.9697	21.68	4.38	22.14
2" Al	5.08	88.84	17.4	54.00	729	8.77	0.98	238.6	0.9714	22.11	4.97	22.58

07-Feb-97 Morning Tests 29 kHz Medium humidity Stranded Dry

Stranded Cables	diameter cm	height to center cm	Temp Deg C	RH %	Bp mm Hg	Water g/m^3	Relative Density	Vavg kV rms	K geom	Corrected for meter & geom E kV/cm	Density Correction diameter cm	Density Correction E kV/cm
1/4" galv	0.67	84.93	17.4	54.00	729	7.99	0.98	52.0	0.9541	24.01	0.66	24.38
1/2" galv	1.22	83.21	17.8	57.00	729	8.64	0.98	61.4	0.9583	17.27	1.20	17.58
1" Al	2.62	74.91	17.1	56.00	729	8.10	0.99	102.6	0.9645	16.24	2.58	16.48
1-1/4" Al	3.24	73.82	16.9	58.00	729	8.30	0.99	136.4	0.9658	18.43	3.19	18.69

05-Feb-97 Humidity Correction Factor Inside, Smooth Pipes Above Ground

Frequency 29.5 kHz 29 kHz High humidity
07-Feb-97

smooth pipes	diameter cm	height to center cm	Temp Deg C	RH %	Bp mm Hg	Water g/m^3	Relative Density	Vavg kV rms	K geom	Corrected for meter & geom E kV/cm	Density Correction diameter cm	Density Correction E kV/cm
1/2" ss	1.29	80.85	21.3	90.00	729	20.64	0.96	77.6	0.9588	21.04	1.24	21.93
3/4" ss	1.91	82.86	18.4	90.00	729	15.49	0.98	105.0	0.9619	20.74	1.87	21.25
1" Al	2.53	85.17	17.8	90.00	729	16.42	0.97	128.2	0.9642	20.21	2.46	20.78
1.25" Al	3.17	86.69	17.8	89.00	729	15.32	0.98	156.2	0.9656	20.63	3.10	21.14
1.5" Al	3.87	87.44	17.2	89.00	729	15.32	0.98	162.7	0.9679	18.46	3.78	18.92
1.75" Al	4.47	88.33	16.9	89.00	729	15.32	0.98	210.8	0.9697	21.47	4.36	22.00
2" Al	5.08	89.14	20.1	90.00	729	16.42	0.97	221.7	0.9714	20.53	4.94	21.11

07-Feb-97 Afternoon Tests 29 kHz High humidity Stranded Dry

Stranded Cables	diameter cm	height to center cm	Temp Deg C	RH %	Bp mm Hg	Water g/m^3	Relative Density	Vavg kV rms	K geom	Corrected for meter & geom E kV/cm	Density Correction diameter cm	Density Correction E kV/cm
1/4" galv	0.67	85.53	18.2	87.00	729	13.44	0.98	46.0	0.9541	21.21	0.65	21.59
1/2" galv	1.22	83.11	18.1	85.00	729	13.09	0.98	56.8	0.9583	15.98	1.20	16.27
1" Al	2.62	87.21	18.0	85.00	729	13.01	0.98	81.2	0.9645	12.42	2.57	12.64
1-1/4" Al	3.24	73.62	19.0	83.00	730	13.47	0.98	105.0	0.9658	14.20	3.17	14.49

05-Feb-97 Humidity Correction Factor Inside, Smooth Pipes Above Ground

Wed Morning warm inside raining outside 47 kHz Low Humidity

Frequency 47 kHz

k meter 1

smooth pipes	diameter cm	height to center cm	Temp Deg C	RH %	Bp mm Hg	Water g/m^3	Relative Density	Vavg kV rms	K geom	Corrected for meter & geom E kV/cm	Density Correction diameter cm	Density Correction E kV/cm
1/2" ss	1.29	80.55	16.7	26.00	728	4.48	0.97	101.4	0.9588	27.52	1.26	28.25
3/4" ss	1.91	83.16	17.2	25.50	728	4.39	0.97	130.2	0.9619	25.69	1.86	26.37
1" Al	2.53	84.97	17.7	25.00	728	4.30	0.97	158.8	0.9642	25.05	2.47	25.70
1.25" Al	3.17	86.49	17.8	25.00	728	4.30	0.97	180.8	0.9656	23.90	3.09	24.52
1.5" Al	3.87	87.24	17.2	24.00	728	4.13	0.97	204.6	0.9679	23.23	3.77	23.84
1.75" Al	4.47	88.33	17.0	24.00	728	4.38	0.97	223.0	0.9697	22.72	4.34	23.38
2" Al	5.08	88.74	16.7	26.00	729	4.22	0.98	239.8	0.9714	22.23	4.97	22.72

05-Feb-97 47 kHz Low Humidity Stranded Dry

Stranded Cables	diameter cm	height to center cm	Temp Deg C	RH %	Bp mm Hg	Water g/m^3	Relative Density	Vavg kV rms	K geom	Corrected for meter & geom E kV/cm	Density Correction diameter cm	Density Correction E kV/cm
1/4" galv	0.67	86.13	16.9	24.00	728	3.44	0.99	47.8	0.9541	22.02	0.66	22.34
1/2" galv	1.22	82.81	16.9	26.00	728	3.74	0.99	67.6	0.9583	19.04	1.21	19.32
1" Al	2.62	81.51	17.8	24.50	728	3.70	0.98	118.0	0.9645	18.32	2.57	18.65
1-1/4" Al	3.24	74.52	17.4	25.00	728	3.70	0.98	138.0	0.9658	18.60	3.18	18.93

05-Feb-97 Humidity Correction Factor Inside, Smooth Pipes Above Ground

Thurs Afternoon, Cloudy and cold 47 kHz Medium Humidity

Frequency 06-Feb-97 smooth pipes	47 diameter cm	kHz height to center cm	Temp Deg C	RH %	Bp mm Hg	Water g/m^3	Relative density	Vavg kV rms	K geom	Corrected for meter & geom E kV/cm	Density Correction diameter cm	Density Correction E kV/cm
1/2" ss	1.29	80.75	18.7	65.00	727	12.57	0.97	95.8	0.9588	25.99	1.25	26.88
3/4" ss	1.91	82.96	17.1	62.50	728	12.08	0.97	118.2	0.9619	23.34	1.85	24.13
1" Al	2.53	84.57	17.3	59.00	727	10.77	0.97	151.2	0.9642	23.87	2.46	24.61
1.25" Al	3.17	86.39	17.7	50.00	728	9.12	0.97	174.4	0.9656	23.05	3.08	23.75
1.5" Al	3.87	87.14	18.3	44.00	728	8.03	0.97	199.4	0.9679	22.64	3.76	23.33
1.75" Al	4.47	88.93	18.3	58.00	728	9.99	0.97	217.8	0.9697	22.15	4.35	22.74
2" Al	5.08	88.54	18.5	53.50	728	9.21	0.97	230.8	0.9714	21.41	4.94	21.98

06-Feb-97 Afternoon Tests 47 kHz Medium Humidity Stranded Dry

Stranded Cables	diameter cm	height to center cm	Temp Deg C	RH %	Bp mm Hg	Water g/m^3	Relative density	Vavg kV rms	K geom	Corrected for meter & geom E kV/cm	Density Correction diameter cm	Density Correction E kV/cm
1/4" galv	0.67	85.83	19.2	53.00	728	8.69	0.98	50.8	0.9541	23.41	0.65	23.97
1/2" galv	1.22	82.41	19.3	50.00	728	8.28	0.98	64.4	0.9583	18.15	1.19	18.60
1" Al	2.62	82.51	18.9	54.00	728	8.71	0.98	111.6	0.9645	17.28	2.56	17.68
1-1/4" Al	3.24	86.32	18.0	62.00	728	9.49	0.98	133.8	0.9658	17.42	3.18	17.76

8. 8 FEB 97

8 Feb 97	Inside horizontal 10’ lengths	14 kHz	Air density

08-Feb-97 Humidity Correction Factor Inside, Smooth Pipes Above Ground

Sat Morn, Sunny & cold, frost on trees 47 kHz High Humidity

Frequency	47	kHz								Corrected for meter & geom	Density Correction	
smooth pipes	diameter cm	height to center cm	Temp Deg C	RH %	Bp mm Hg	Water g/m^3	Relative density	Vavg kV rms	K geom	E kV/cm	diameter cm	E kV/cm
1/2" ss	1.29	80.75	17.4	79.00	732	12.83	0.98	75.0	0.9588	20.34	1.27	20.70
3/4" ss	1.91	82.96	16.9	78.00	732	12.66	0.98	105.8	0.9619	20.89	1.88	21.24
1" Al	2.53	85.87	17.6	83.00	732	13.47	0.98	128.6	0.9642	20.24	2.49	20.58
1.25" Al	3.17	86.99	18.2	80.00	732	12.99	0.98	136.6	0.9656	18.03	3.12	18.33
1.5" Al	3.87	87.44	17.8	82.00	732	14.12	0.98	158.5	0.9679	17.99	3.79	18.36
1.75" Al	4.47	88.33	18.7	78.00	732	13.43	0.98	187.7	0.9697	19.12	4.38	19.52
2" Al	5.08	89.24	18.1	81.00	732	14.78	0.98	203.2	0.9714	18.81	4.96	19.26

06-Feb-97 Afternoon Tests 47 kHz High Humidity Stranded Dry

Stranded Cables	diameter cm	height to center cm	Temp Deg C	RH %	Bp mm Hg	Water g/m^3	Relative density	Vavg kV rms	K geom	Corrected for meter & geom E kV/cm	Density Correction diameter cm	E kV/cm
1/4" galv	0.67	85.93	19.0	84.00	732	13.64	0.98	44.4	0.9541	20.73	0.65	21.08
1/2" galv	1.22	82.81	19.7	80.00	732	13.51	0.98	58.7	0.9583	16.52	1.20	16.84
1" Al	2.62	72.81	18.1	84.00	733	12.90	0.99	86.6	0.9645	13.80	2.58	13.98
1-1/4" Al	3.24	70.92	19.6	84.00	733	14.09	0.98	116.3	0.9658	15.87	3.18	16.17

8-Feb-97 Humidity Correction Factor Inside, Smooth Pipes Above Ground

Saturday Morning 14 kHz Low Humidity Not Done

08-Feb-97 Humidity Correction Factor Inside, Smooth Pipes Above Ground

Sat Afternoon, Sunny just thawing 14 kHz Medium Humidity

Frequency 14 kHz

smooth pipes	diameter cm	height to center cm	Temp Deg C	RH %	Bp mm Hg	Water g/m^3	Relative Density	Vavg kV rms	K geom	Corrected for meter & geom E kV/cm	Density Correction diameter cm	Density Correction E kV/cm
1/2" ss	1.29	20.95	15.2	54.00	731	8.77	0.98	61.1	1.0000	23.40	1.27	23.85

????? Afternoon Tests 14 kHz Medium Humidity Stranded Dry

Stranded Cables	diameter cm	height to center cm	Temp Deg C	RH %	Bp mm Hg	Water g/m^3	Relative Density	Vavg kV rms	K geom	Corrected for meter & geom E kV/cm	Density Correction diameter cm	Density Correction E kV/cm
1/4" galv	0.67	40.73	16.7	50.00	731	7.06	0.99	43.8	1.0000	24.12	0.66	24.38
1/2" galv	1.22	39.41	17.6	50.00	731	7.48	0.99	54.8	1.0000	18.70	1.21	18.97

08-Feb-97 Humidity Correction Factor Inside, Smooth Pipes Above Ground

Sat Morn, Sunny & cold, frost on trees 14 kHz High Humidity

Frequency 47 kHz

smooth pipes	diameter cm	height to center cm	Temp Deg C	RH %	Bp mm Hg	Water g/m^3	Relative Density	Vavg kV rms	K geom	corrected for meter & geom E kV/cm	Density Correction diameter cm	Density Correction E kV/cm
1/2" ss	1.29	19.75	16.3	78.00	731	11.93	0.98	56.8	1.0000	22.11	1.27	22.45
3/4" ss	1.91	22.66	16.6	78.00	731	12.66	0.98	>63	1.0000	#VALUE!	1.88	#VALUE!

08-Feb-97 Saturday Morning just before Pizza

Stranded Dry 14 kHz Medium Humidity

Stranded Cables	diameter cm	height to center cm	Temp Deg C	RH %	Bp mm Hg	Water g/m^3	Relative Density	Vavg kV rms	K geom	for meter & geom E kV/cm	Density Correction diameter cm	Density Correction E kV/cm
1/4" galv	0.67	166.12	18.6	84.00	731	13.28	0.98	43.3	1.0000	18.86	0.65	19.18
1/2" galv	1.22	39.51	17.6	80.00	731	11.96	0.99	52.3	1.0000	17.84	1.21	18.09

9. 15 FEB 97

15 Feb 97	Inside horizontal 15’ lengths	29 kHz	Air density

15-Feb-97 Air Density Correction Factor Inside, Smooth Pipes Above Ground

29 kHz Low Temperature

Saturday Morning, Cold, cloudy, with some wind and blowing snow outside

k meter 1 Frequency 29.3 kHz

smooth pipes	diameter cm	height to center cm	Temp Deg C	RH %	Bp mm Hg	Water g/m^3	Relative Density	Vavg kV rms	K geom	Corrected for meter & geom E kV/cm	Density Correction diameter cm	Density Correction E kV/cm
1/2" ss	1.29	81.15	1.9	49.00	723	2.69	1.03	100.6	0.9588	27.26	1.33	26.45
3/4" ss	1.91	83.46	1.3	52.00	723	2.75	1.03	123.2	0.9619	24.29	1.97	23.51
1" Al	2.53	85.47	1.4	58.00	723	3.09	1.03	155.0	0.9642	24.42	2.62	23.64
1.25" Al	3.17	86.29	4.0	49.00	723	3.11	1.02	185.0	0.9656	24.46	3.25	23.91
1.5" Al	3.87	87.94	4.8	47.00	723	3.14	1.02	203.4	0.9679	23.05	3.95	22.59
1.75" Al	4.47	88.53	5.6	44.00	723	3.09	1.02	224.4	0.9697	22.84	4.55	22.44
2" Al	5.08	89.24	5.3	46.00	723	3.17	1.02	238.8	0.9714	22.11	5.17	21.70

15-Feb-97 Morning Tests 29 kHz Low Temp Stranded Dry

Stranded Cables	diameter cm	height to center cm	Temp Deg C	RH %	Bp mm Hg	Water g/m^3	Relative Density	Vavg kV rms	K geom	Corrected for meter & geom E kV/cm	Density Correction diameter cm	Density Correction E kV/cm
1/4" galv	0.67	83.83	4.5	49.00	723	3.21	1.0261	55.2	0.9541	25.54	0.68	24.89
1/2" galv	1.22	82.31	4.3	49.00	723	3.16	1.0270	61.8	0.9583	17.42	1.26	16.96
1" Al	2.62	74.81	3.8	50.00	723	3.12	1.0289	100.8	0.9645	15.96	2.69	15.51
1-1/4" Al	3.24	70.42	4.1	50.00	723	3.18	1.0275	115.0	0.9658	15.72	3.33	15.30

15-Feb-97 Air Density Correction Factor Inside, Smooth Pipes Above Ground

Sat Afternoon, Cloudy just freezing slight snow 29 kHz Mid temperature

Frequency	29	kHz								Corrected for meter & geom	Density Correction	
smooth pipes	diameter cm	height to center cm	Temp Deg C	RH %	Bp mm Hg	Water g/m^3	Relative Density	Vavg kV rms	K geom	E kV/cm	diameter cm	E kV/cm
1/2" ss	1.29	81.45	17.2	32.00	722	4.66	0.98	101.8	0.9588	27.57	1.26	28.24
3/4" ss	1.91	82.96	17.2	30.00	722	4.38	0.98	127.2	0.9619	25.11	1.87	25.73
1" Al	2.53	85.07	16.6	33.00	722	4.65	0.98	160.4	0.9642	25.29	2.48	25.86
1.25" Al	3.17	86.19	16.9	34.00	723	4.87	0.98	183.2	0.9656	24.23	3.10	24.79
1.5" Al	3.87	87.04	17.4	33.00	722	4.87	0.98	205.6	0.9679	23.36	3.78	23.94
1.75" Al	4.47	88.13	18.2	31.50	723	4.87	0.97	225.8	0.9697	23.01	4.35	23.65
2" Al	5.08	89.14	18.4	27.00	723	4.24	0.97	241.6	0.9714	22.37	4.94	23.01

06-Feb-97 Afternoon Tests 29 kHz Medium Humidity Stranded Dry

Stranded Cables	diameter cm	height to center cm	Temp Deg C	RH %	Bp mm Hg	Water g/m^3	Relative Density	Vavg kV rms	K geom	Corrected for meter & geom E kV/cm	Density Correction diameter cm	E kV/cm
1/4" galv	0.67	85.83	17.3	28.00	723	4.12	0.9796	53.6	0.9541	24.70	0.65	25.22
1/2" galv	1.22	82.21	16.7	32.00	723	4.52	0.9816	70.2	0.9583	19.79	1.20	20.17
1" Al	2.62	74.21	17.1	32.00	722	4.63	0.9799	102.6	0.9645	16.27	2.56	16.61
1-1/4" Al	3.24	70.42	18.1	28.00	723	4.30	0.9770	113.6	0.9658	15.53	3.16	15.89

15-Feb-97 Air Density Correction Factor Inside, Smooth Pipes Above Ground

Sat Morn, Sunny & cold, frost on trees 29 kHz High Temperature

Frequency smooth pipes	29 diameter cm	kHz height to center cm	Temp Deg C	RH %	Bp mm Hg	Water g/m^3	Relative Density	Vavg kV rms	K geom	Corrected for meter & geom E kV/cm	Density Correction diameter cm	Density Correction E kV/cm
1/2" ss	1.29	81.45	27.4	17.00	723	4.45	0.94	96.5	0.9588	26.13	1.22	27.70
3/4" ss	1.91	82.86	31.6	12.00	723	3.94	0.93	128.4	0.9619	25.36	1.78	27.25
1" Al	2.53	85.07	28.5	17.00	723	4.73	0.94	155.6	0.9642	24.54	2.38	26.10
1.25" Al	3.17	86.19	26.8	18.50	723	4.69	0.95	180.7	0.9656	23.90	3.00	25.28
1.5" Al	3.87	86.94	26.8	19.00	723	4.83	0.95	201.8	0.9679	22.93	3.66	24.26
1.75" Al	4.47	88.23	28.4	16.00	723	4.44	0.94	224.6	0.9697	22.88	4.20	24.34
2" Al	5.08	88.74	28.2	8.00	723	2.19	0.94	241.8	0.9714	22.42	4.78	23.81

15-Feb-97 29 kHz High Temp Stranded Dry

Stranded Cables	diameter cm	height to center cm	Temp Deg C	RH %	Bp mm Hg	Water g/m^3	Relative Density	Vavg kV rms	K geom	Corrected for meter & geom E kV/cm	Density Correction diameter cm	Density Correction E kV/cm
1/4" galv	0.67	166.12	28.2	19.00	723	5.20	0.9444	52.8	0.9541	21.97	0.63	23.26
1/2" galv	1.22	82.41	27.3	20.00	723	5.22	0.9470	67.6	0.9583	19.05	1.16	20.12
1" Al	2.62	77.51	26.7	21.00	723	5.29	0.9491	109.3	0.9645	17.17	2.48	18.09
1-1/4" Al	3.24	73.52	26.7	20.00	723	5.03	0.9492	109.2	0.9658	14.76	3.07	15.55

15-Feb-97 Air Density Correction Factor Inside, Smooth Pipes Above Ground

Wed Morning Last Day 29 kHz Low Temp Repeat

Frequency 29 kHz										Corrected for meter & geom E	Density Correction	
19-Feb-97 smooth pipes	diameter cm	height to center cm	Temp Deg C	RH %	Bp mm Hg	Water g/m^3	Relative Density	Vavg kV rms	K geom	kV/cm	diameter cm	E kV/cm
1/2" ss	1.29	80.30	11.8	32.00	723	3.35	1.00	96.5	0.9588	26.20	1.28	26.33
3/4" ss	1.91	82.20	11.8	37.00	723	3.89	1.00	128.4	0.9619	25.40	1.90	25.52
1" Al	2.53	84.30	11.9	36.50	723	3.86	0.99	155.6	0.9642	24.59	2.52	24.72
1.25" Al	3.17	84.99	11.8	38.50	723	4.03	1.00	180.7	0.9656	23.98	3.16	24.09
1.5" Al	3.87	85.19	11.7	37.00	723	3.86	1.00	201.8	0.9679	23.04	3.86	23.15
1.75" Al	4.47	86.00	11.7	38.00	723	3.95	1.00	224.6	0.9697	23.03	4.45	23.13
2" Al	5.08	86.31	11.8	38.00	723	3.98	1.00	241.8	0.9714	22.58	5.06	22.68

19-Feb-97 Wed morning of last test day 29 kHz Low temp repeat Stranded Dry

Stranded Cables	diameter cm	height to center cm	Temp Deg C	RH %	Bp mm Hg	Water g/m^3	Relative Density	Vavg kV rms	K geom	Corrected for meter & geom E kV/cm	Density Correction diameter cm	E kV/cm
1/4" galv	0.67	84.51	11.5	38.00	723	3.91	1.0005	52.8	0.9541	24.40	0.67	24.38
1/2" galv	1.22	79.10	11.3	37.50	723	3.81	1.0013	67.6	0.9583	19.20	1.23	19.17
1" Al	2.62	73.71	11.4	37.00	723	3.78	1.0010	109.3	0.9645	17.37	2.62	17.35
1-1/4" Al	3.24	68.61	11.4	37.00	723	3.79	1.0008	109.2	0.9658	15.02	3.24	15.01

10. 18 FEB 97

18 Feb 97	Inside horizontal 15’ lengths	47 kHz	Air density

18-Feb-97

Air Density Correction Factor
Inside, Smooth Pipes Above Ground
47 kHz Low Temperature

Monday Morning, Cloudy and calm, appears to be warming
Frequency 47.0 kHz kHz
k meter 1

smooth pipes	diameter cm	height to center cm	Temp Deg C	RH %	Bp mm Hg	Water g/m^3	Relative density	Vavg kV rms	K geom	Corrected for meter & geom E kV/cm	Density Correction diameter cm	Density Correction E kV/cm
1/2" ss	1.29	82.35	6.8	37.50	728	2.85	1.02	104.0	0.9588	28.11	1.32	27.55
3/4" ss	1.91	83.06	6.4	38.50	728	2.87	1.02	134.8	0.9619	26.61	1.95	26.05
1" Al	2.53	85.17	6.2	39.00	728	2.86	1.02	161.8	0.9642	25.51	2.59	24.95
1.25" Al	3.17	86.39	5.9	39.00	728	2.80	1.02	187.6	0.9656	24.79	3.25	24.22
1.5" Al	3.87	86.84	5.4	40.00	728	2.79	1.03	205.4	0.9679	23.35	3.97	22.77
1.75" Al	4.47	87.93	5.1	41.00	728	2.80	1.03	226.4	0.9697	23.09	4.59	22.49
2" Al	5.08	88.64	5.1	41.00	728	2.80	1.03	247.0	0.9714	22.90	5.21	22.31

18-Feb-97

Morning Tests
47 kHz Low Temp
Stranded Dry

Stranded Cables	diameter cm	height to center cm	Temp Deg C	RH %	Bp mm Hg	Water g/m^3	Relative density	Vavg kV rms	K geom	Corrected for meter & geom E kV/cm	Density Correction diameter cm	Density Correction E kV/cm
¼" galv	0.67	85.53	4.8	41.70	728	2.78	1.03	54.6	0.9541	25.18	0.68	24.48
½" galv	1.22	84.81	4.3	41.00	728	2.66	1.03	67.2	0.9583	18.84	1.26	18.29
1" Al	2.62	70.41	3.3	44.00	728	2.67	1.03	124.6	0.9645	20.01	2.70	19.36
1-1/4" Al	3.24	72.92	3.3	44.00	728	2.67	1.03	109.6	0.9658	14.85	3.35	14.37

18-Feb-97 Air Density Correction Factor
Inside, Smooth Pipes Above Ground
47 kHz Mid temperature

Monday Afternoon, Cloudy, hazy sunshine with some south wind, definitely warming
Frequency 47 kHz

smooth pipes	diameter cm	height to center cm	Temp Deg C	RH %	Bp mm Hg	Water g/m^3	Relative density	Vavg kV rms	K geom	Corrected for meter & geom E kV/cm	Density Correction diameter cm	Density Correction E kV/cm
½" ss	1.29	81.75	17.6	31.00	726	4.63	0.98	101.4	0.9588	27.44	1.26	28.00
¾" ss	1.91	83.06	17.3	30.00	726	4.41	0.98	132.0	0.9619	26.06	1.87	26.57
1" Al	2.53	84.97	17.5	29.00	726	4.31	0.98	157.3	0.9642	24.81	2.48	25.32
1.25" Al	3.17	86.29	17.6	28.00	726	4.19	0.98	182.7	0.9656	24.16	3.11	24.66
1.5" Al	3.87	86.94	17.6	29.00	726	4.32	0.98	202.2	0.9679	22.97	3.80	23.44
1.75" Al	4.47	88.33	16.9	31.00	726	4.45	0.98	220.3	0.9697	22.44	4.39	22.86
2" Al	5.08	89.44	17.6	30.50	726	4.54	0.98	240.8	0.9714	22.28	4.97	22.74

18-Feb-97 Afternoon Tests
47 kHz Mid Temperature
Stranded Dry

Stranded Cables	diameter cm	height to center cm	Temp Deg C	RH %	Bp mm Hg	Water g/m^3	Relative density	Vavg kV rms	K geom	Corrected for meter & geom E kV/cm	Density Correction diameter cm	Density Correction E kV/cm
¼" galv	0.67	84.63	17.5	30.50	726	4.53	0.98	53.8	0.9541	24.85	0.65	25.37
½" galv	1.22	79.91	17.6	31.00	726	4.62	0.98	67.8	0.9583	19.22	1.20	19.63
1" Al	2.62	70.21	17.6	32.00	725	4.78	0.98	120.3	0.9645	19.32	2.56	19.74
1-1/4" Al	3.24	72.42	17.6	32.00	725	4.77	0.98	107.2	0.9658	14.55	3.17	14.87

18-Feb-97 Air Density Correction Factor
Inside, Smooth Pipes Above Ground
47 kHz High Temperature

Monday Afternoon, cloudy, hazy sunshine, south wind, warming
Frequency 47 kHz

smooth pipes	diameter cm	height to center cm	Temp Deg C	RH %	Bp mm Hg	Water g/m^3	Relative density	Vavg kV rms	K geom	Corrected for meter & geom E kV/cm	Density Correction diameter cm	Density Correction E kV/cm
1/2" ss	1.29	81.45	22.9	28.00	724	5.72	0.96	101.7	0.9588	27.54	1.24	28.71
3/4" ss	1.91	83.26	23.8	27.50	724	5.90	0.96	128.0	0.9619	25.25	1.83	26.40
1" Al	2.53	84.47	23.9	22.00	724	4.74	0.96	153.8	0.9642	24.29	2.42	25.40
1.25" Al	3.17	86.49	23.9	27.00	724	5.83	0.96	180.2	0.9656	23.81	3.03	24.90
1.5" Al	3.87	87.04	24.6	25.00	725	5.61	0.95	198.8	0.9679	22.58	3.70	23.65
1.75" Al	4.47	88.33	22.5	29.00	725	5.77	0.96	219.2	0.9697	22.33	4.30	23.22
2" Al	5.08	89.34	23.9	27.00	725	5.82	0.96	233.7	0.9714	21.62	4.86	22.59

18-Feb-97 Saturday Afternoon
47 kHz High Temperature
Stranded Dry

Stranded Cables	diameter cm	height to center cm	Temp Deg C	RH %	Bp mm Hg	Water g/m^3	Relative density	Vavg kV rms	K geom	Corrected for meter & geom E kV/cm	Density Correction diameter cm	Density Correction E kV/cm
1/4" galv	0.67	166.12	25.0	27.00	725	6.19	0.95	52.0	0.9541	21.63	0.63	22.69
1/2" galv	1.22	79.21	22.6	27.00	725	5.41	0.96	67.4	0.9583	19.14	1.18	19.91
1" Al	2.62	70.11	24.6	25.00	725	5.61	0.95	123.2	0.9645	19.80	2.50	20.74
1-1/4" Al	3.24	71.62	24.9	22.00	725	5.01	0.95	109.0	0.9658	14.84	3.09	15.55

CHAPTER 7 POWER LOSS IN CORONA

BACKGROUND

Early during the development of the electric power industry, it was discovered that significant amounts of power could be lost in corona on high-voltage transmission lines. The early designers wanted quantitative formulas for corona power dissipation to use in the design process because economics is the driving force of power transmission system design. This resulted in experimental programs to measure corona power at 60 Hz. Harding (1924 a & b) made such measurements at Purdue University while Ryan and Henline (1924) did the same at Stanford University. Since that time, there have been many corona power measurements at 60 Hz. As a result, the magnitude of power dissipated in corona at power system frequencies is well known. This information is used for designing power systems that have low lifetime cost. At these frequencies, it is often the case that minimum cost is realized by operating with some corona on the transmission lines during inclement weather, especially in rural areas and at high elevations. This is because elimination of corona requires larger diameter conductors, and the lifetime cost of the larger conductors, including the cost of capital, is more than the cost of the power lost through occasional corona.

High-powered radio transmitting systems in the VLF through HF range were being developed at the same time that high-voltage transmission lines were being developed. This led to the study of corona phenomena at radio frequencies to develop design data for high-power transmitting antennas. Ryan and Marx (1915) describe some of the results of these early RF measurements.

Measurements at power system frequencies indicate that corona power is approximately proportional to frequency. There are no extensive measurements of corona power at RF frequencies available. However, Peek (1929, p. 211) reports a single measurement at 100 kHz. The power measured by Peek agrees approximately with the postulate that corona power is proportional to frequency in that the corona power measured at 100 kHz was about 1000 times greater than the corona power at 60 Hz for the same conditions.

Due to the lack of data, the U.S. Navy began a program in the 1980s at the Forestport HVTF to measure the power dissipated in corona at VLF/LF. Part of the motivation for this program was to examine the utility of operating high-power antennas in corona. At the time, some thought that operation in corona would enable an antenna to radiate more power. It was also thought that operation in corona had the potential to increase intrinsic antenna bandwidth since corona increases the effective capacitance of the antenna, thereby reducing its Q. It turns out that this technique might be useful for ELF antennas, but it is not practical at VLF/LF because of the large amount of power dissipated in corona at VLF/LF.

In 1989, the measurement program at Forestport was extended to include the corona power dissipated per unit length of wire and cable. Watt and Hansen (1992) reported the results of these measurements. Additional measurements have been carried out at the Forestport facility since that time, including tests between 8 February 1996 and 15 February 1997. The results of some of these tests are included in this chapter, and have been used to develop curves and design formulas. The results indicate that corona power is proportional to frequency, and at VLF/LF sufficient power is dissipated in corona so that most, and preferably all, of the components should be operated corona free, even during inclement weather.

CORONA POWER LOSS FORMULAS

Introduction

One objective of the corona power measurement program was to develop formulas for calculating corona power losses that could be used for analysis of existing and future VLF/LF designs. The development of these formulas was indirect, starting with available 60-Hz formulas and guided by empirical results. Many tests were conducted with smooth and stranded wires of different sizes at frequencies in the VLF/LF band. The majority of the tests were done with the wire above and parallel to ground at several different heights. However, there were some tests using a coaxial configuration and one with a slanted wire.

The first step was to fit these data to the 60-Hz equation modified by a factor K_1 which was considered to be a function of frequency, wire diameter, stranded or smooth and wire surface condition. For each test configuration K_1 has a fixed value. The modified equation fits the data well as will be shown in the sections below. The variable for the 60 Hz formula is voltage and the equation is useful for 60-Hz applications because the voltage along the line can be measured or calculated. However, for VLF/LF applications the voltage distribution on the antenna cannot be measured and is difficult to calculate. The surface electric field (gradient) on the conductors can be calculated for VLF/LF antennas and the corona power loss formula needs to be in terms of the surface electric field for this application.

The variable for the 60-Hz equation can be changed to surface electric field but in this form the equation has explicit height dependence. There are sound theoretical arguments that this equation should not have height dependence and for this reason we concluded that this formula is incorrect and needed to be modified. This conclusion was supported by the empirical results in that for the range of heights of the tests, the term given by K_1 times the explicit height dependence factor was more nearly constant than K_1 by itself. This led to the concept of replacing both factors by a single factor K_3, which is also expected to be a function of frequency, surface condition, wire diameter etc. The results of many tests with different test wires, frequencies, and conditions showed that K_3 was less dependent on these parameters than expected. The result is a simple equation that can be used to predict VLF/LF corona power loss with sufficient accuracy to support antenna design. The subsections that follow trace the chronological development of the corona loss equations for VLF/LF. Our development starts with the original Ryan and Henline formulation and shows how their results were modified to fit VLF/LF applications.

60-Hz Formulas

The development of the corona power loss formulas started with an initial effort at 60 Hz (Ryan and Henline, 1924). Their measurements of corona power involved the use of an early version of an oscilloscope, which was used to generate a Lassajous figure of voltage versus charge as shown in Figure 7-1. They observed that when the peak voltage was less than the corona onset voltage, the pattern generated is a line segment that corresponds to the charge being in phase with the voltage. Current is the time derivative of charge; therefore in-phase charge means out-of-phase (orthogonal) current. When the voltage and charge form a line segment, the current and voltage are orthogonal and no power is dissipated. This is illustrated by curve I in Figure 7-1.

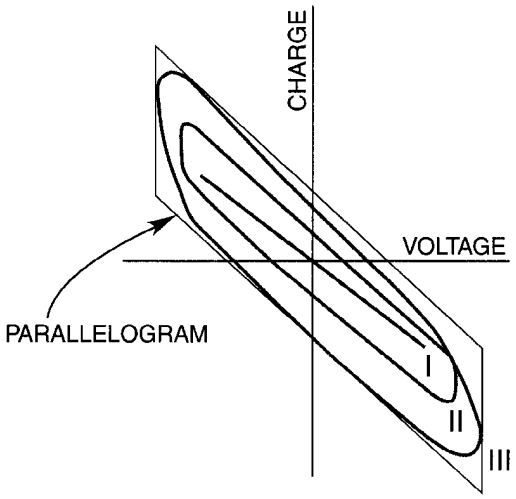

Figure 7-1. Charge – voltage diagram after Ryan and Henline.

The power dissipated per cycle is proportional to the area contained within a voltage-charge Lassajous pattern similar to a hysteresis loop. This is because the portion of the charge moving perpendicular to the voltage axis corresponds to current that is in-phase with the voltage, resulting in power dissipation. Curve II of Figure 7-1 was taken with the peak voltage somewhat above the corona onset level, and curve III was taken with the peak voltage approximately 20% greater than curve II. Curve I represents a case with no power dissipated, while curves II and III represent cases with power dissipation.

Ryan and Henline made many measurements for various conditions and determined that (1) peak voltage was of dominating importance in the corona loss-voltage relationship and (2) the power lost in corona from a high-voltage transmission line is approximately the product of the voltage in excess of the corona onset voltage and line charging current. This led them to hypothesize a hysteresis character for corona losses. Analysis of the voltage-charge diagrams revealed that the charge lags behind the corresponding voltage by an approximately constant amount and that the energy dissipated per cycle is proportional to the product of the crest voltage and the difference between the voltage peaks and the onset voltage.

Based on their observations, and assuming a parallelogram for the voltage–charge diagram (see Figure 7-1), they developed an empirical formula for the power dissipated in corona.

$$P_{corona} = 4 \cdot f \cdot C \cdot V \cdot \left(V - V_{on}\right) \tag{7-1}$$

where P_{corona} is the corona power in watts after corona onset,
f is the frequency in Hz,
C is the total capacitance of the wire in Farads,
V is the peak voltage in volts, and
V_{on} is the corona onset peak voltage in volts.

This formula indicates that the corona power is a function of the voltage on the wire times the difference between the voltage on the wire and the corona onset voltage.

The leading term ($4 \cdot f \cdot C \cdot V$) approximates the charging current. The voltage difference (V-V_{on}) represents that portion of the voltage that is in phase with the charging current. In effect, the phase angle between the total voltage and the charging current is contained in this term and not explicitly stated. Corona power is zero when the voltage is less than the onset voltage (i.e., (V- V_{on}) < 0). Ryan and Henline used the convention that the corona power equation is multiplied by a unit step function U(V_{on}), not shown in equation 7-1, and this convention is also used in the development of our formulas below. This convention should not lead to confusion since negative power cannot exist.

From Figure 7-1, it is clear that a parallelogram overestimates the area contained within the hysteresis loop. Thus, the original Ryan and Henline corona power formula (Equation 7-1) overestimates the power in corona. Nevertheless, it provides curves that provide a good match to the variation of corona power with voltage and frequency.

Ryan and Henline developed an alternate formula through physical reasoning. They assumed a purely resistive plasma sheath surrounding the conductor. The assumption of pure resistance is good for dense plasma as long as the thickness is much smaller than the wavelength, which is the case for VLF/LF. They also assumed that the sheath completely surrounds the conductor and that all the charging current flows through the sheath. Further, they assumed the charging current is the same as the displacement current that would flow away from the conductor if there were no corona. One final assumption is that the voltage drop across the resistive sheath is equal to the difference between the actual voltage and the onset voltage. In this case, the power is simply given by

$$P_{corona} = 2 \cdot \pi \cdot f \cdot C \cdot V \cdot \left(V - V_{on}\right) \tag{7-2}$$

where the voltages are given as rms values.

Equation 7-2 can be interpreted as follows. The total displacement current flowing through the resistive sheath is equal to the first term $I_D = (2 \cdot \pi \cdot f \cdot C \cdot V)$. The second term ($V$-$V_0$) represents the voltage drop across the resistive sheath. The dissipated power is calculated by $P = V\, I\, cos(\theta)$. However, since the sheath is assumed resistive, the voltage drop and current are in-phase, so $cos(\theta) = 1$ and need not be included in the equation.

Although not mentioned by Ryan and Henline, equation (7-2) can be obtained from equation (7-1). The approach is to take Equation 7-1 and convert the voltage units to rms with a leading factor 8. Then, as an approximation to account for the real versus the idealized parallelogram, the factor 8 is reduced by 27% and made equal to 2·π (6.28). The factor $2 \cdot \pi \cdot f$ is the radian frequency, ω, which completes the conversion of Equation 7-1 to Equation 7-2.

Ryan and Henline reformulated their equations (7-1 and 7-2) in terms of the total capacitance of the wire, C, and the total power dissipated by the wire. The resulting equations can be converted to give power per unit length by dividing both sides of the equation by the sample length, l, as follows.

$$P_{cl} = \frac{P_{corona}}{l} = \omega \cdot C_l \cdot V \cdot \left(V - V_{on}\right) \text{ Watts/m} \tag{7-3}$$

where P_{cl} is the corona power per unit length and
C_l is the capacitance per unit length.

The factor $\omega \cdot C_l$ is the inverse of the capacitive reactance per unit length of the wire. The voltage on the wire times this factor is equal to the displacement current per unit length leaving the wire:

$$\omega \cdot C_l \cdot V = \frac{V}{X_{C_l}} = I_{Dl}$$

where ω is the radian frequency ($2 \cdot \pi \cdot f$),
f is the frequency in Hz,
V is the voltage on the wire,
C_l is the capacitance per unit length of the wire,
X_{cl} is the capacitive reactance per unit length, and
I_{Dl} is the displacement current per unit length leaving the wire.

Note that the magnitude of the displacement current can also be calculated from the electric field on the surface of the wire:

$$I_{Dl} = 2 \cdot \pi \cdot a \cdot \omega \cdot \varepsilon_0 \cdot E$$

As previously mentioned, Ryan and Henline's second formulation assumed a sheath of corona around the wire having a voltage drop across the sheath of ΔV. The corona sheath is assumed to be purely resistive so the voltage drop is in phase with the current. For this case, the product of voltage drop and current gives power dissipated in the sheath.

$$P_{cl} = I_{Dl} \cdot \Delta V \quad \text{Watts/meter} \tag{7-4}$$

Ryan and Henline postulated that the voltage drop across the sheath is equal to V-V_{on}, and the equation for power lost in that sheath becomes:

$$P_{cl} = I_{Dl} \cdot \Delta V = I_{Dl} \cdot (V - V_{on})$$

This is equivalent to Equation 7-3.

VLF Formulas

The dense plasma of corona at atmospheric pressure acts like a purely resistive medium. Current flowing in the plasma dissipates power in a manner similar to hysteresis as discussed above. There are at least two differences that occur between the corona observations at power system frequencies and VLF/LF.

First, at 60 Hz the corona appears as a uniform sheath around the wire or cable. However, at VLF/LF, except on very small wires, the corona occurs in staggered mini-flares. This is the phenomenon observed for operation above the critical frequency (see Chapter 6). In this case, only a portion of the total charging current that flows out along the wire goes through the resistance of the plasma.

Second, just above the inception level, corona currents only flow during part of a cycle. At power system frequencies, the corona current begins to flow when the voltage waveform is near the maximum, although the start does shift away from the maximum as the voltage increases above onset. On the other hand, at VLF/LF Smith (1963) shows that for larger wires corona starts near the current maximum, i.e., at the voltage minimum. This implies that the proportion of the total charging current per cycle flowing through the corona is less at VLF/LF than at 60 Hz.

Modified Ryan and Henline Formula

Both of the effects discussed above reduce the proportion (one spatially and the other temporally) of the total charging current flowing in the plasma, thereby reducing the power lost in corona. To

take this into account we have modified the Ryan and Henline equation by adding a factor K_1 ($0 \leq K_1 \leq 1$) to obtain:

$$P_{corona} = K_1 \cdot \omega \cdot C \cdot V \cdot (V - V_{on}) \tag{7-5}$$

Given in terms of power density, this equation becomes

$$P_{cl} = \frac{P_{corona}}{l} = K_1 \cdot \omega \cdot C_l \cdot V \cdot (V - V_{on}) \tag{7-6}$$

This can be converted to a function of the surface electric field along the wire using the following identities:

$$q_l = C_l \cdot V$$

$$E = \frac{q_l}{2 \cdot \pi \cdot \varepsilon_0 \cdot a}$$

where q_l is the charge density along the wire,
ε_0 is the permittivity of free space, and
a is the wire radius.

Making the appropriate substitutions into Equation 7-6 yields

$$P_{cl} = K_1 \cdot (2 \cdot \pi \cdot \varepsilon_0 \cdot a)^2 \cdot \omega \cdot \frac{E}{C_l} \cdot (E - E_{on}) \tag{7-7}$$

where E is the surface electric field along the wire and
E_{on} is the critical electric field for corona onset on the wire.

It should be pointed out that the conversion of voltage to surface electric field assumes that the existence of corona does not affect the surface electric field. This is not strictly true, but it will be shown that the resulting equation is still useful.

These equations can be applied to both a coaxial configuration and a wire above ground. For the case of concentric cylinders (coaxial), the capacitance per unit length is given by

$$C_l = \frac{2 \cdot \pi \cdot \varepsilon_0}{\ln(D / d)}$$

where D is the diameter of the outer cylinder and
d is the diameter of the inner cylinder ($d = 2a$).

Substituting this into Equation 7-7 gives the following:

$$P_{cl} = \frac{K_1}{2} \cdot \omega \cdot \pi \cdot \varepsilon_0 \cdot d^2 \cdot \ln(D / d) \cdot E \cdot (E - E_{on}) \tag{7-8}$$

Substituting for ε_0 and converting the units to frequency in kHz, d in cm, and E_s and E_0 in kV/cm gives the following:

$$P_{cl} = K_1 \cdot (\pi / 36) \cdot f \cdot d^2 \cdot \ln(D / d) \cdot E \cdot (E - E_{on}) \tag{7-9}$$

where f is in kHz,
D and d are in cm, and
E and E_{on} are in kV/cm.

The formula for a wire above ground is the same as Equation 7-9 except the log term becomes $\ln(4h/d)$ where h is the height of the wire above ground ($h >> d$):

$$P_{cl} = K_1 \cdot (\pi / 36) \cdot f \cdot d^2 \cdot \ln(4 \cdot h / d) \cdot E \cdot (E - E_{on}) \tag{7-10}$$

where f is in kHz,
h and d are in cm, and
E and E_{on} are in kV/cm.

Note that Equations 7-9 and 7-10 are formulated in terms of electric field and contain a term having logarithmic height variation. The height variation is inconsistent with the concept of corona being driven by the electric field very near the wire surface and contained within a thin region close to the wire, especially at and just above onset, as discussed in Chapter 2. The measurements reported in Chapter 6 show that for test configurations of interest the corona onset field (not voltage) is independent of height. When formulated in terms of electric field, all corona phenomena should be independent of the height of the wire above ground, as long as the wire height is sufficient to obtain a nearly uniform field around the wire.

For a fixed value of K_1 equations 7-9 and 7-10 contain height variation. This height dependence implies that the original equations of Ryan and Henline are incorrect. However, for 60 Hz applications there is not much error numerically when using the equations because the height dependence is logarithmic. For the equations to be height independent the height variation would have to be compensated for by introducing the inverse variation into K_1, an unnecessary complication.

The following two sections outline the development of a simple empirical formula useful for VLF/LF applications. This formula is a combination of the modified Ryan and Henline formula and the theoretical formula derived in the section below and introduces a new test dependent factor K_3. This factor replaces the combination of K_1 and the height dependent factor in the equations. Thus for a given test configuration, the value of K_1 determined with the modified Ryan and Henline formula also determines the value of K_3 used in the new formula.

Theoretical Formula

In an attempt to determine the variation of corona power with electric field, a theoretical formula was derived using assumptions similar to those of Ryan and Henline combined with the plasma thickness formula developed in Chapter 2. The assumptions are (1) the displacement current leaving the wire is unaffected by the plasma sheath, (2) the plasma sheath is purely resistive, and (3) the voltage drop across that sheath is given by the integral of the electric field from the surface of the wire to the edge of the sheath.

For these assumptions, corona power is given by Equation 7-4, repeated below for convenience,

$$P_{cl} = I_{Dl} \cdot \Delta V \tag{7-4}$$

where P_{cl} is the corona power per unit length (Watts/m),
I_{Dl} is the magnitude of the displacement current leaving the wire (amps/m), and
ΔV is the voltage drop across the plasma sheath (volts).

The magnitude of the displacement current is given by $I_{Dl} = 2 \cdot \pi \cdot a \cdot \omega \cdot \varepsilon_o \cdot E_a$, where E_a is the surface field on the wire, calculated without considering the effect of corona.

The voltage drop across the plasma sheath is determined by integrating the electric field from the wire surface out to the edge of the active region. A formula for radius of the active region is given below (see the end of Chapter 2).

$$r_a = \frac{E_a \cdot a}{E_0}$$

where r_a is the radius of the active region,
E_a is the surface field on the wire,
a is the radius of the wire, and
E_0 is the uniform field breakdown level for similar conditions.

The formula above applies only when the surface electric field is greater than the corona onset level, E_{on}. Note that E_0 is the breakdown field for in a uniform field gap (parallel plates) with similar conditions and is a function of atmospheric conditions (density, wet, dry) and frequency. As indicated in Chapter 6, E_0 is equal to the asymptotic breakdown field for large wires and is the leading term in the equations for the value of the critical field at corona onset.

The electric field around the wire is given by the following formula:

$$E = \frac{E_a \cdot a}{r}$$

where E_a is the field on the surface of the wire ($r = a$).

Integrating the electric field between the radius a and r_a gives the voltage drop across the active region:

$$\Delta V = \int_a^{r_a} \frac{E_a \cdot a}{r} \cdot dr = E_a \cdot a \cdot \ln(r)\Big|_a^{r_a}$$

$$\Delta V = E_a \cdot a \cdot \{\ln(r_a) - \ln(a)\}$$

$$\Delta V = E_a \cdot a \cdot \ln(\frac{r_a}{a})$$

Substituting for r_a gives $\Delta V = E_a \cdot a \cdot \ln(\frac{E_a}{E_0})$.

Note that ΔV is the surface electric field times the radius of the wire adjusted by the log of the amount the surface field is above the uniform gap breakdown field.

Substituting these results into the previous formula for corona power results in a new formula for corona power.

$$P_{cl} = I_{Dl} \cdot \Delta V = 2 \cdot \pi \cdot a^2 \cdot \omega \cdot \varepsilon_o \cdot E_a^2 \cdot \ln(\frac{E_a}{E_0}) \quad \text{for } E_a > E_0 \tag{7-11}$$

This formula is consistent with the proposition that corona power is a function only of the local fields around the wire and not height above ground. It also indicates direct dependence on wire radius squared resulting from the variation of the thickness of the active region with wire diameter and the variation of displacement current with wire diameter.

The critical onset field for finite-sized wires, E_{on} is significantly greater than the asymptotic value for large wires, E_0 (see Chapter 6). Thus the above formula over estimates corona power when the

surface field is equal to the onset field. This problem can be addressed by replacing E_0 with E_{on}, or more correctly, with the effective onset field E_{one}, discussed later, and introducing a factor K_2. However, even with these changes the formula does not predict corona power variation above onset as well as the modified Ryan and Henline equation. As a result, a different, empirical, corona power formula was developed and is described in the next section.

Empirical Corona Power Formula

The proposed formula is empirical in that it is not completely based on theory. It includes a combination of aspects of both the Ryan and Henline formula and the theoretical formula derived in the section above, including variation with radius squared. It does have the feature that corona power is a function only of the electric field in the vicinity of the wire and is independent of the height above ground. The resulting formula is given below, and it is the recommended formula for estimation of the power dissipated in corona on wires at VLF/LF.

Assume that the voltage drop is proportional to the factor $\Delta V = (E_a - E_{on})\cdot d$, where $d = 2\cdot a$ is the diameter of the wire. Modifying Equation 7-4 by including a factor K_3 and substituting the relationship for ΔV gives:

$$P_{cl} = K_3 \cdot I_{Dl} \cdot \Delta V$$

$$P_{cl} = K_3 \cdot \pi \cdot \omega \cdot \varepsilon_o \cdot E_a \cdot (E_a - E_{on}) \cdot d^2 \qquad (7\text{-}12)$$

The factor K_3 includes both the effect of K_1, the amount of active surface on the wire, and K_2 the proportionality factor for the voltage ΔV. This equation is similar to Equations 7-9 and 7-10 except the height variation that was included in the logarithmic term has been eliminated. For a particular wire configuration, K_3 can be directly related to the factor K_1 as follows:

$$K_3 = \frac{K_1}{2} \cdot \ln(4h/d) \qquad (7\text{-}13)$$

for a wire above ground and

$$K_3 = \frac{K_1}{2} \cdot \ln(D/d) \qquad (7\text{-}14)$$

for a wire inside cylinder of diameter D.

The section below describes the measurements of corona power. These measurements were processed and fitted to the equations by adjusting the value of K_3 for each measurement configuration and condition. The values of K_3 so determined are used in the empirical (recommended) equation (7-12) to estimate corona power, as discussed in the section on K_3 below. Note some of the data were fit to the modified Ryan and Henline equations. For this case K_1 was determined and then converted to K_3 by using the above equations.

TEST CELL CONFIGURATIONS

Corona power measurements were carried out at Forestport in 1989, using both horizontal and vertical test samples consisting of wires, cables, and pipes. These samples were tested for both dry and spray-wet conditions.

The vertical test cell consisted of a grounded cylinder made up of hardware cloth with the energized sample placed at the center. A description of this test cell is given in Chapter 6, with a

diagram shown in Figure 6-4. The outer diameter of the coaxial cell was 3.2 meters, and its height was 3.6 meters. The test sample was 1.98 meters long. During the 1985 tests, the shield ring at the upper end of the sample was 0.61 meters in diameter and was made of aluminum pipe 0.15 meters in diameter. The lower end had a similar ring plus a larger 0.8- by 0.2-meter ring immediately below it. For the 1989 tests the double rings at the top and bottom were each replaced with single smaller 0.36- by 0.064-meter ring. Figure 7-2 shows a picture of the vertical test cell taken during the 1989 tests with the #8 stranded wire well into corona.

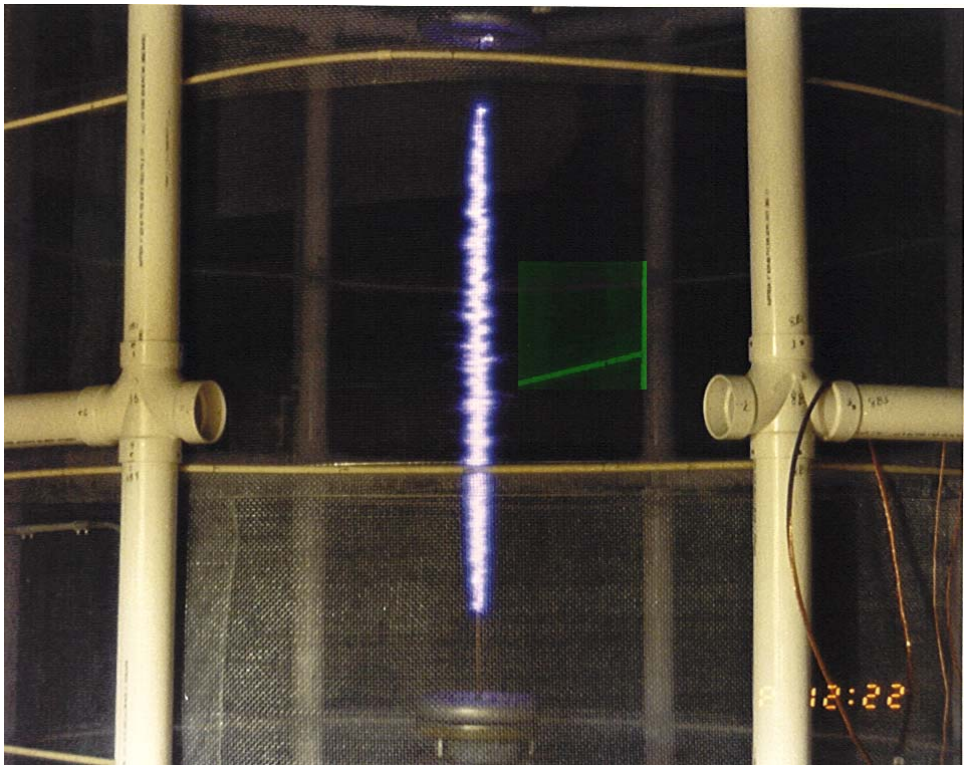

Figure 7-2. Forestport vertical test cell with #8 wire well into corona.

For horizontal tests, the outside test configuration was used for the corona power tests that took place in 1989. This test configuration is described in Chapter 6 and illustrated in Figures 6-1 and 6-2. The samples were 20 feet (6.1 m) long and 8 to 10 feet (2.4 – 3.05 m) above the ground plane. For these tests, the electrical ground under the samples was made up of 4-foot by 8-foot aluminum sheets shown in Figure 6-1. There was also a 30-foot by 30-foot extension to the ground system made from wire mesh hardware cloth, which was not in place at the time of the picture. Figure 7-3 shows the horizontal outside test setup at night with the sample well into corona.

The corona loss per meter length of line is relatively small at power system frequencies and it is necessary to use rather long lines for measurement of corona power. For long lines, the end effects are small and can be ignored in the derivation of loss per unit length of line. We were able to use short lines for the VLF and LF measurements because the losses are significantly larger. However, the end effects become more important with short lines and their effect must be included when interpreting the measurement results. Toroidal-shaped corona rings were placed at both ends of the test sample to keep the end connections from going into corona. These rings were kept small so that they would not significantly shield the wire in an attempt to keep the field along the sample as

uniform as possible. This reduces the uncertainty in the magnitude of the surface electric field at the center of the wire and simplifies interpretation of the results.

The field along the samples was estimated using computer programs for both the vertical and horizontal test cells. These results showed that the field is not truly uniform for either test setup. For both setups, the surface electric field varied from a maximum near the sample center to minimums near the both ends due to shielding from the corona rings. For the horizontal case, the sample was long enough so that the magnitude of the surface field at the center of the wire was the same as that for an infinite length wire. This was not true for the vertical test cell.

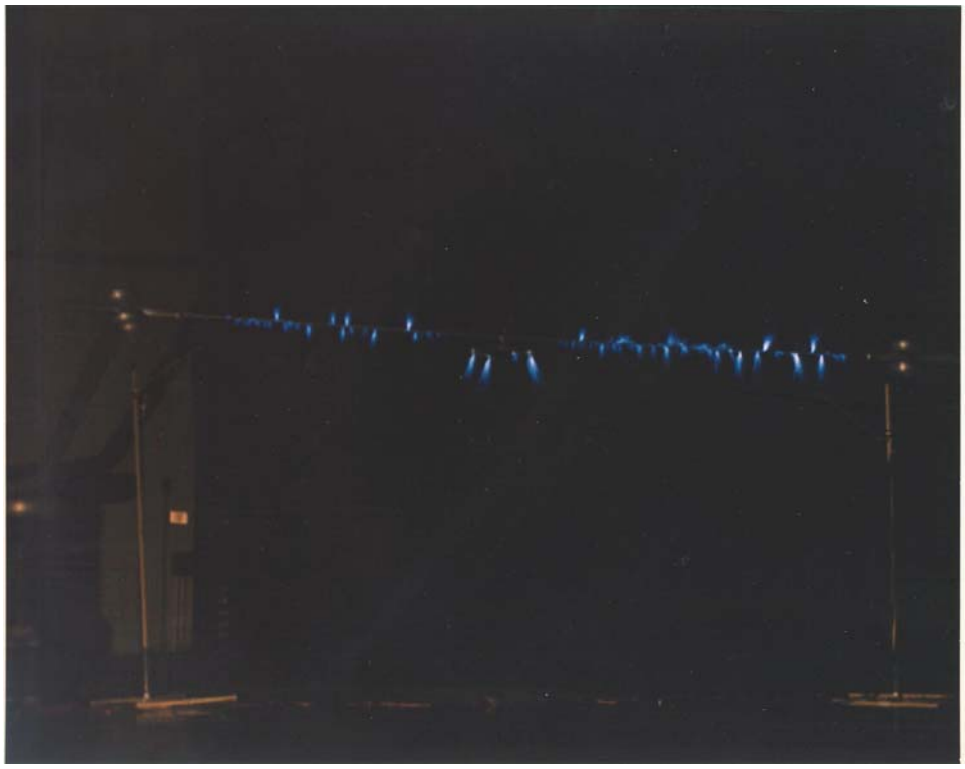

Figure 7-3. Outside horizontal test cell in corona.

The calibration of the test cells was checked using a measurement method based on neon bulbs. The neon bulbs are attached to small plates mounted on either side of a thin dielectric slab, which acts as an antenna. These lights were mounted with tape at several points along one of the larger diameter test samples. The surface electric field on the sample is proportional to the voltage on the test sample. The antenna portion of the neon bulb device picks up a voltage proportional to the surface electric field, which is imposed across the neon bulb. As the voltage on the sample increases, the voltage across the neon bulb increases, eventually igniting the bulb (at approximately 67 volts).

The bulb devices were calibrated by determining the voltage at which they ignited when placed at the center of the horizontal test sample. The calibration depends upon knowing the relationship between the voltage and the field at the center of the horizontal wire, which is determined by calculation. Following calibration, the bulbs were placed at several locations along the test sample, the voltage increased, and the firing voltage for each one was recorded. The firing voltages at each point were converted to surface electric field using the calibration data. This data was taken in both the vertical and horizontal test cells. The lower two curves in Figure 7-4 show the voltage at which

the neon bulbs turned on, after correction for small differences in the turn-on field of the different sensors. The relative field strength at any point is inversely proportional to the voltage at which the neon bulb fired. This is because it takes more voltage on the wire to ignite the neon bulbs when the field is low. The upper two curves in Figure 7-4 give the ratio of the surface electric field strength along the wire to the theoretical calculated field strength at the center. The end points for both curves are obtained by extrapolation.

Figure 7-4 shows that for the horizontal test cell the fields on the 20-foot test wire approach the calculated value except within about 4 feet of the ends. However, for the vertical test cell, even with the smaller rings the field does not reach the calculated value anywhere along the test sample. The field near the center was about 6% below that calculated for an infinite coaxial geometry and was further reduced near the end corona rings. The difference in corona onset voltage measured in the vertical and horizontal test cells was also about 6%.

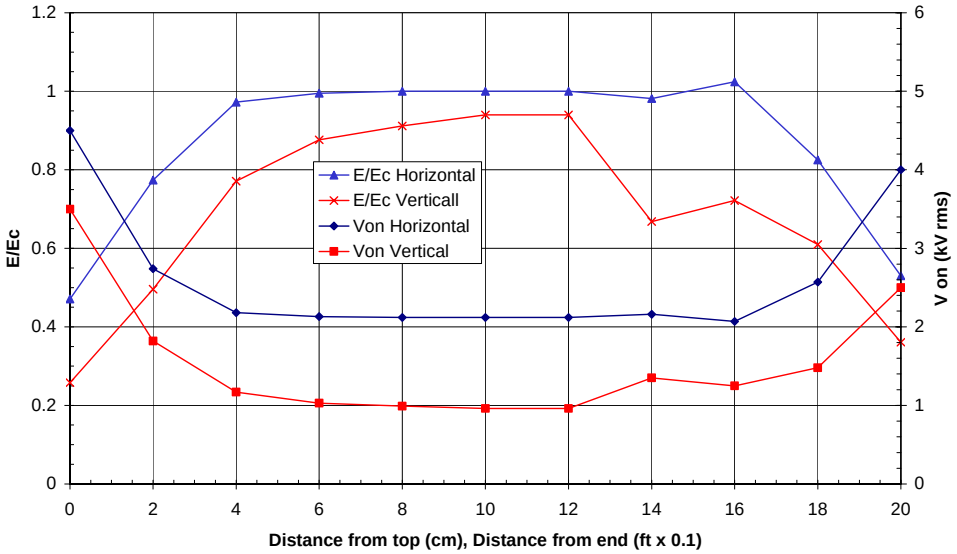

Figure 7-4. Vertical and horizontal test cell neon bulb calibration data.

The reduced field strength at the center of the vertical test cell is due to the relatively short cell and sample length and the corona rings used at the ends. A correction factor for the maximum field in the vertical test cell was developed by averaging the estimates of the three different calibration techniques: (1) comparison of the onset voltages for the vertical and horizontal test cell, (2) the two-dimensional (2-D) electrostatic computer code, and (3) surface electric field measurements using the neon bulbs as calibrated in the horizontal configuration. For the 1985 measurements, the field at the center of the vertical test cell was 0.9 times the value calculated for an infinite coaxial configuration. The configuration used in 1989 had smaller rings, and this factor was 0.94.

EFFECTIVE LENGTH

Since the test samples are relatively short, the end effects can have a significant effect on power density calculations. In both of the test cells, the surface field is a maximum at the center and falls off toward the ends. Therefore, the amount of the sample in corona varies as a function of voltage. At or slightly above corona onset only a small portion of the wire near the center will be in corona. At higher voltages more of the wire will be in corona but the center region will have surface field

strength well above onset, while away from the center the field strength will be less. Thus, the most intense corona will be at the sample center, and the intensity will be reduced with distance away from the center (see Figure 7-2). As a result, the power dissipated along the wire will not be uniform. The effective length must be determined to convert the total corona power measurements to power per unit length.

The estimation of the effective length was based on the modified Ryan and Henline equations, which have the same voltage and field variation as the recommended equation, 7-12. The effective length estimated in this way is consistent with both the modified Ryan and Henline and the empirical equations. The modified Ryan and Henline Equations 7-6 and 7-7 used for this analysis are repeated below.

$$P_{cl} = K_1 \cdot \omega \cdot C_l \cdot V \cdot \left(V - V_{on}\right) \quad \text{Watts/m} \tag{7-6}$$

$$P_{cl} = K_1 \cdot (2 \cdot \pi \cdot \varepsilon_0 \cdot a)^2 \cdot \omega \cdot \frac{E}{C_l} \cdot (E - E_{on}) \tag{7-7}$$

The corona onset voltage is a parameter measured during the tests. However, because of the previously discussed variation of the electric field along the test sample, the onset voltage in Equation 7-6 is a function of position along the wire. Equation 7-7 has an advantage in that the surface electric field at onset (E_{on}) is constant along the wire.

The effective length is defined as the length of a wire, having uniform surface electric field equal to the field at the center of the test sample, which dissipates the same amount of power as the original sample with the non-uniform field. The method used to determine the effective length is based on Equation 7-7, although the same results can be obtained from Equation 7-6, with added complications. The approach used is to numerically integrate the function $E \cdot (E\text{-}E_{on})/C_l$ along the wire. This integral is set equal to the integral over a length of wire with a uniform field equal to the field at the center of the sample wire. The effective length is the length of wire required to make the second integral equal to the first integral as follows:

$$\int_0^l \frac{E(l)}{C_l(l)} \cdot \left(E(l) - E_{on}\right) \cdot dl = \int_0^{l_e} \frac{E_c}{C_{lc}} \cdot \left(E_c - E_{on}\right) \cdot dl = \frac{l_e \cdot E_c}{C_{lc}} \cdot \left(E_c - E_{on}\right)$$

where $E(l)$ is the actual surface field along the sample,
E_o is the onset gradient,
E_c is the gradient at the center of the sample,
$C_l(l)$ is the capacitance per unit length along the sample,
l is the length of the sample, and
l_e is the equivalent length of wire in corona.

Note that E and C_l vary along the length of the wire, while E_{on} is constant. The integral can be evaluated by taking advantage of the fact that E and C_l have the same variation with position:

$$E = F(l) \cdot E_c$$

$$C_l = F(l) \cdot C_{lc}$$

where E_c is the surface electric field at the center of the wire,
C_{lc} is the capacitance per unit length at the center of the wire, and
$F(l)$ gives the variation in field strength and capacitance along the wire.

This variation in both the field strength and capacitance is given by $F(l)$ as shown by plots of E/E_c in Figure 7-4 for the vertical and horizontal test cells.

Substituting the above expressions for E and C_1 into Equation 7-7 and solving for the effective length, gives the following.

$$l_e = \frac{1}{(E_c - E_{on})}\int_0^l (E_c \cdot F(l) - E_{on}) \cdot dl = \frac{1}{\left(\frac{E_c}{E_{on}} - 1\right)} \cdot \int_0^l \left(\frac{E_c}{E_{on}} \cdot F(l) - 1\right) \cdot dl$$

A computer program was written to numerically integrate this function and calculate the effective length. The results of these calculations are given as a function V/V_{on} (same as E/E_{on}) for both the vertical and horizontal test cells in Figure 7-5. Note that at onset the effective length is small, but as voltage increases, it becomes asymptotic to a value somewhat less than the sample wire length. A curve-fitting program was used to generate simple analytic representations of these curves to enable processing the corona power data in terms of power dissipated per unit length of wire. Plots of the analytic representations are included in the figure.

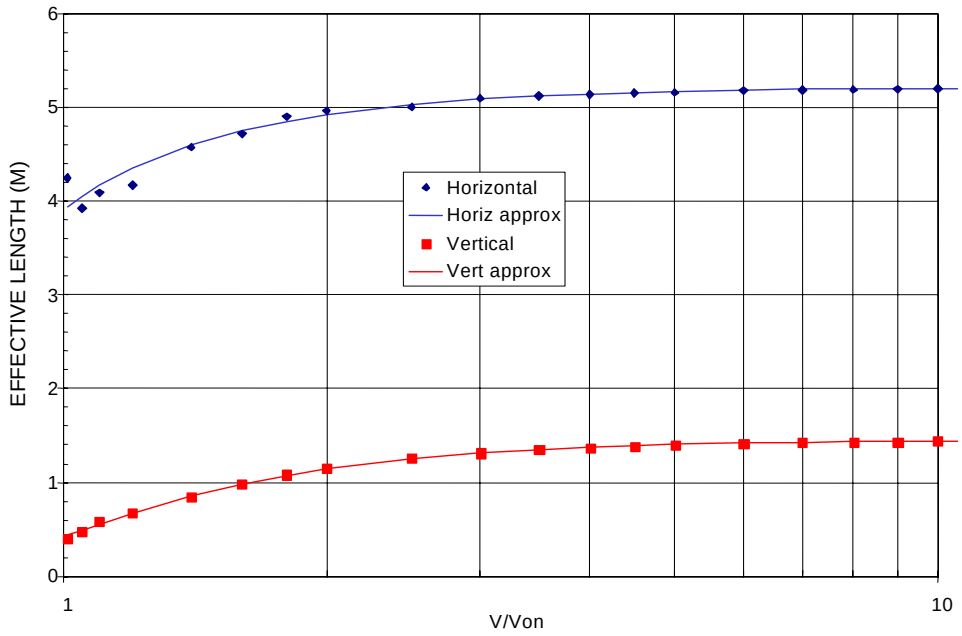

Figure 7-5. Forestport test cell estimated effective lengths.

CORONA POWER MEASUREMENT

Method

Corona power was determined from measurements of the total input power to the high voltage resonant circuit. The technique involves first measuring the total input power as a function of voltage for a test configuration with no corona, such as a large diameter pipe. Then the input power is measured for a test configuration that does have corona, such as a smaller diameter wire. The power dissipated in corona is the difference between the total input power with corona and the total input power for the corona-free configuration at the same voltage.

Figure 7-6 shows a block diagram of the instrumentation used to measure the total power into the high-voltage resonant circuit. Figure 7-7 shows a picture of the power measurement equipment. The

helix house matching-transformer is shown on the left of the picture. The white lead on the left is the Litz wire feeding the resonant circuit. The current in the resonant circuit, *I*, was measured using the (green) Pearson current transformer mounted on the Litz wire. The current transformer was connected to one of four digital multi-meters (DMMs) (HP-3468A digital multi-meter) located on top of the blue shipping container shown on the right-hand side of the figure.

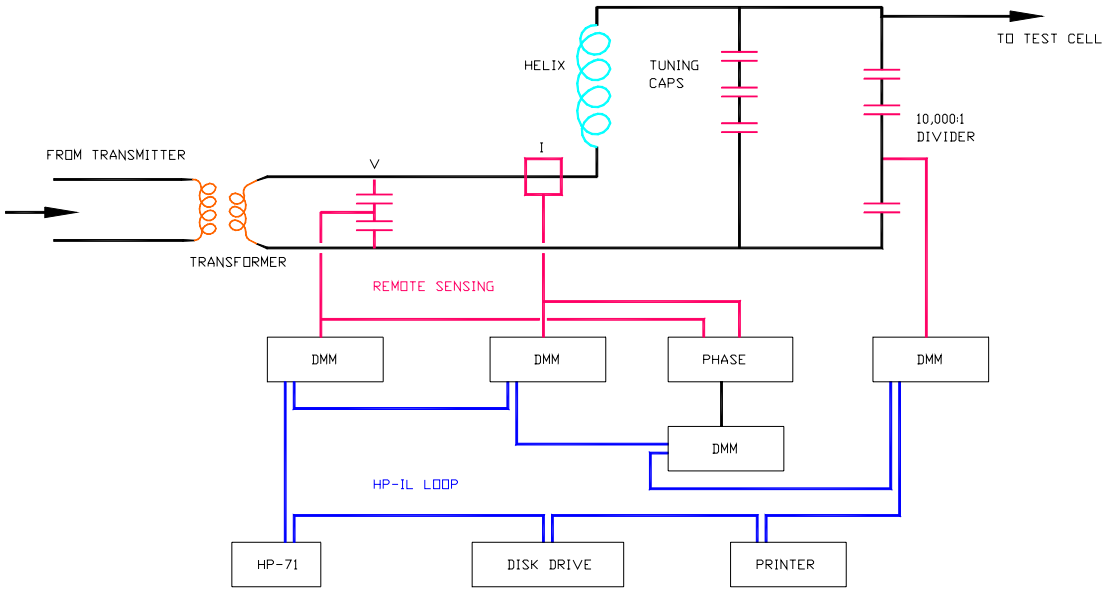

Figure 7-6. Corona power test instrumentation block diagram, Forestport, 1989.

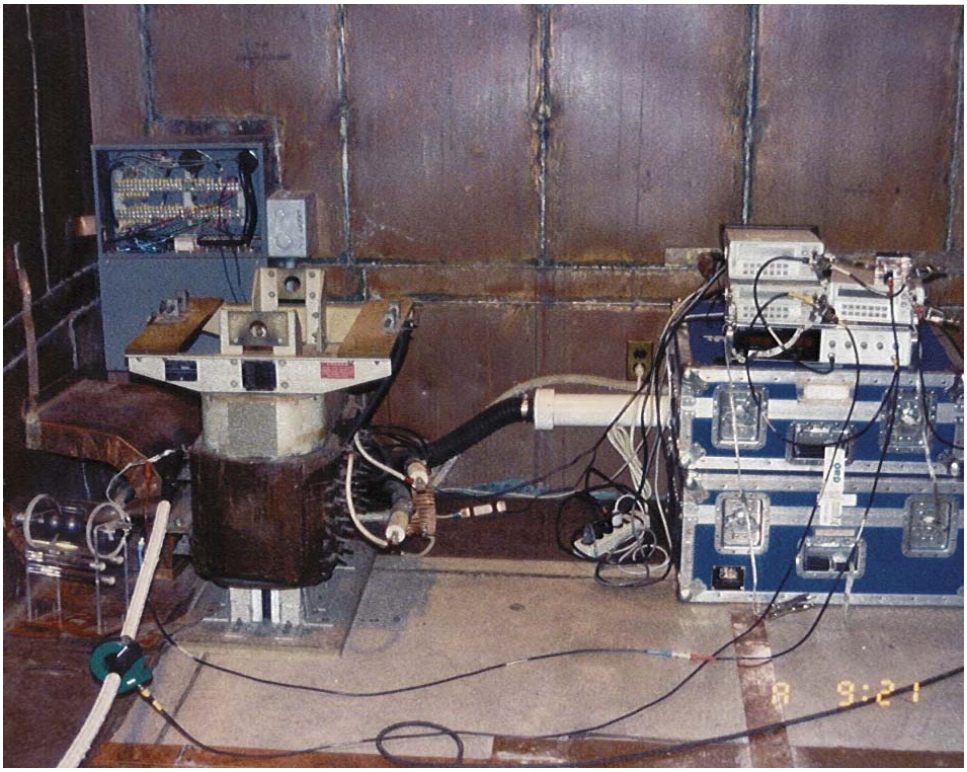

Figure 7-7. Forestport power measurement equipment.

The voltage, V, at the transformer output was measured using a 100:1 capacitive divider, connected to another DMM. The phase between the voltage and current was measured using the HP Gain-Phase meter shown, which provided a dc output proportional to phase. This dc signal was connected to a third DMM. A fourth DMM was connected to the 10,000:1 divider connected to the high voltage on the test object (not shown).

The outputs of the four DMMs were fed to an HP-71 computer using an HPIL link to route the signal approximately 50 feet into the observation room. The HPIL link worked well even in the high field environment of the helix house. The computer was connected to a printer and the measured data were periodically printed to produce a real-time readout. The data were also stored on a floppy disk for later processing. The calibration of the 10,000:1 high-voltage divider requires considerable care and is further described in Chapter 5.

Using this test setup, the circuit input power is calculated by the standard method:

$$P_{in} = V \cdot I \cdot \cos(\theta)$$

where V is the voltage measured at the transformer,
I is the current measured at the transformer, and
θ is the phase angle between voltage and current.

This power includes the losses in all the circuit components including the capacitors, the inductor (helix), and the insulators. The magnitude of the impedance (V/I) was plotted versus this phase angle as the circuit was tuned using the variometer. The magnitude of the impedance was a minimum at a phase angle of approximately -4^{o}, indicating a phase error in the voltage divider system (Figure 7-8). This phase error was subtracted out as part of the input power calculation.

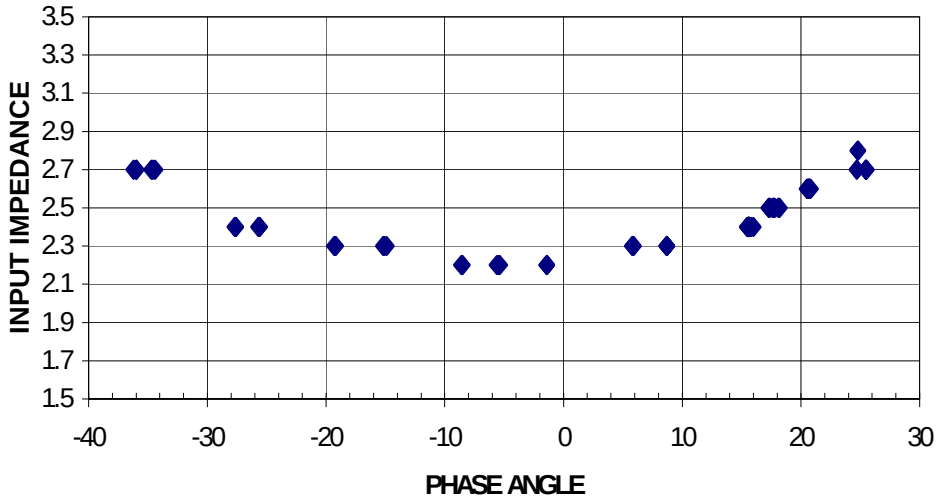

Figure 7-8. Forestport corona power test, phase calibration.

Calibration Measurements

The corona power is the difference between the power into the circuit at a given voltage with no corona present and the input power to the circuit, at the same voltage, with the test object in corona.

The corona-free circuit power was measured using a large diameter pipe in place of the test sample. The diameter of the pipe was large enough to be corona free at the maximum measurement voltage. Using the pipe in place of the sample ensured that all the high-voltage components, including insulators, were energized during the calibration. This is necessary because the insulators dissipate power, especially when wet. The circuit power versus voltage, with no corona, was measured first and then subtracted from the power into the circuit at the same voltage, with the test sample in place.

A calibration run was made prior to each set of measurements. This consisted of measuring the total power into the circuit versus high voltage over the range of voltage levels to be used later for corona power measurements. During wet tests, it was impossible to keep the insulators completely dry, and the power dissipated in them must be accounted for as well. During the outdoor tests, the wind sometimes changes during a test series, and the wetness of the insulators changes from that during the calibration run. This resulted in increased variability of experiment results for outdoor wet tests.

Figure 7-9 shows a typical plot of observed power losses for the vertical test cell. The test circuit power loss appears to vary according to the formula $P_{loss} = K \cdot V^{(2.03)}$. The value of K is dependent on frequency and the amount of inductance and capacitance in the circuit. For the Forestport test cell, nominal values are $K = 0.276$ at 29.5 kHz, and $K = 0.098$ at 57.4 kHz (for V in kV rms).

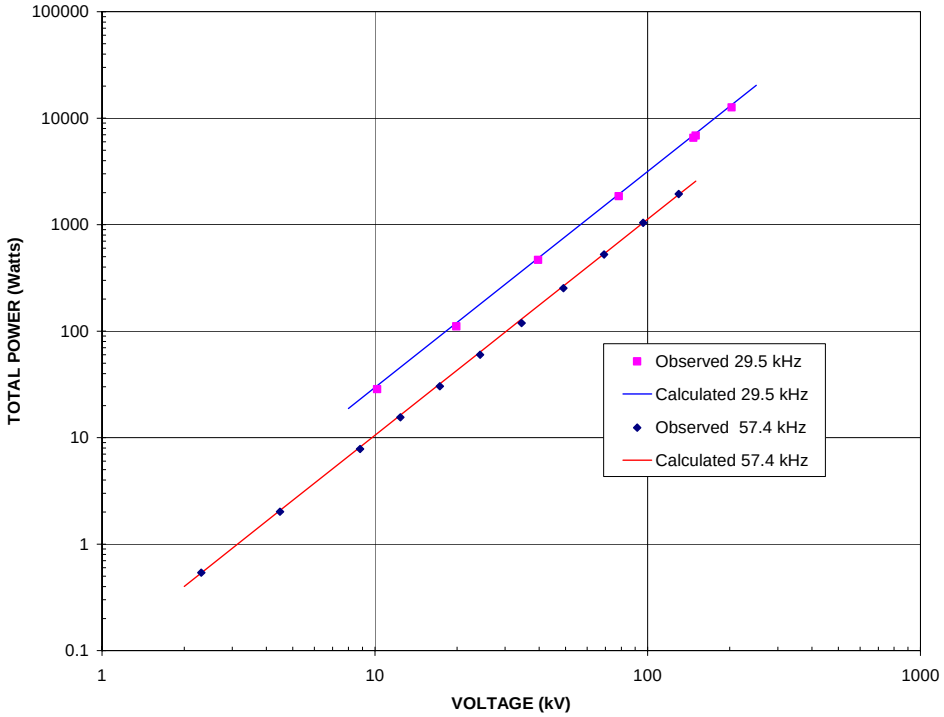

Figure 7-9. Vertical test cell power calibration data.

Corona power was determined by subtracting the test cell power calculated by the above formula from the measured total input power. At voltages below corona onset, there should be no corona power. Sometimes it appeared that the circuit losses varied between the time of the calibration run and the corona tests, which led to non-zero values of corona power at low voltage. For those data sets, we compensated by adjusting the value of *K* slightly (a few percent at most) to force the low-voltage values of corona power to zero. The exponent 2.03 was kept the same.

The horizontal test cell was calibrated in a similar manner.

The technique normally used to maintain resonance of the high-voltage circuit involved adjusting frequency to track changes in resonance. When corona forms, it effectively increases the electrical size of the conducting object involved, thereby adding capacitance, which changes the resonant frequency of the circuit. Operation at higher voltages for any length of time resulted in the capacitors warming up, changing their capacitance slightly, which also changed the resonant frequency. It was determined that the power measurements were more stable and repeatable if calibrated and measured at exactly the same frequency. To accomplish this, resonance was maintained by tuning the circuit with a small variometer instead of changing the test frequency.

MEASUREMENTS

Configurations Tested

Corona power versus voltage was measured using several different samples in both the vertical and horizontal test cells for both wet and dry conditions and with three frequencies in the VLF/LF band. During the 1989 campaign, a rather extensive set of corona power measurements was taken. Tables 7-1 and 7-2 list the samples and conditions used during the test period. Note that the frequencies are

listed as F1, F2, and F3 corresponding to the low-, medium- and high-frequency for each test. The frequencies in each range were not all the same because the capacitance of the test setup and samples varied. For the horizontal test cell, F1 was about 18 kHz, F2 was 27 to 28 kHz, and F3 was about 48 kHz. For the vertical test cell, there were no measurements at F1, F2 was 28 to 29 kHz, and F3 was about 57 kHz. Note that the diameter of the vertical test cell was always 3.2 meters. The height for each of the horizontal tests is given in Table 2 below.

Table 7-1. 1989 corona power vertical test samples (D = 3.2 meters).

		F1		F2		F3	
Sample	Diameter (cm)	Wet	Dry	Wet	Dry	Wet	Dry
3/8” rod	0.952				x		X
#8 smooth	0.33				x	x	X
#8 stranded	0.368			x	x	x	X
#18 smooth	0.368				x		X
Cage, 2 x #8 strand	S = 10			x	x	x	X

Table 7-2. 1989 corona power horizontal test samples (wire height in meters).

		f1		f2		f3	
Sample	Diameter (cm)	Wet	Dry	Wet	Dry	Wet	Dry
Cage, 2 x 1” strand	D = 2.57 S = 61			3.2	3.2		
1” smooth	2.54	2.4	2.4	2.4	2.4	2.4	2.4
1” stranded Al*	2.57	2.65	2.65	2.65	2.65	2.65	2.65
#6 stranded Cu	0.470	2.4	2.4	2.4	2.4	2.4	2.4
#8 stranded Cu	0.368	2.4	2.4	2.4	2.4	2.4	2.4
#10 stranded Cu	0.234	2.4	2.4	2.4	2.4	2.4	2.4
#18 stranded Cu	0.145	2.4	2.4	2.4	2.4	2.4	2.4

` * Dixon, 2002

Power Measurements

Figure 7-10 shows a typical data set and the processed results for the horizontal 1.01-inch diameter stranded cable two-wire cage, spray-wet, operating at 27 kHz. The curve labeled “Input Power” is the total power into the test cell with the test sample in place. The curve labeled “System Power” is the best-fit curve for the power into the circuit measured with a large diameter test sample that did not go into corona (calibration data). The curve labeled “Corona Power,” is the difference between these two curves, and corresponds to the power dissipated in corona.

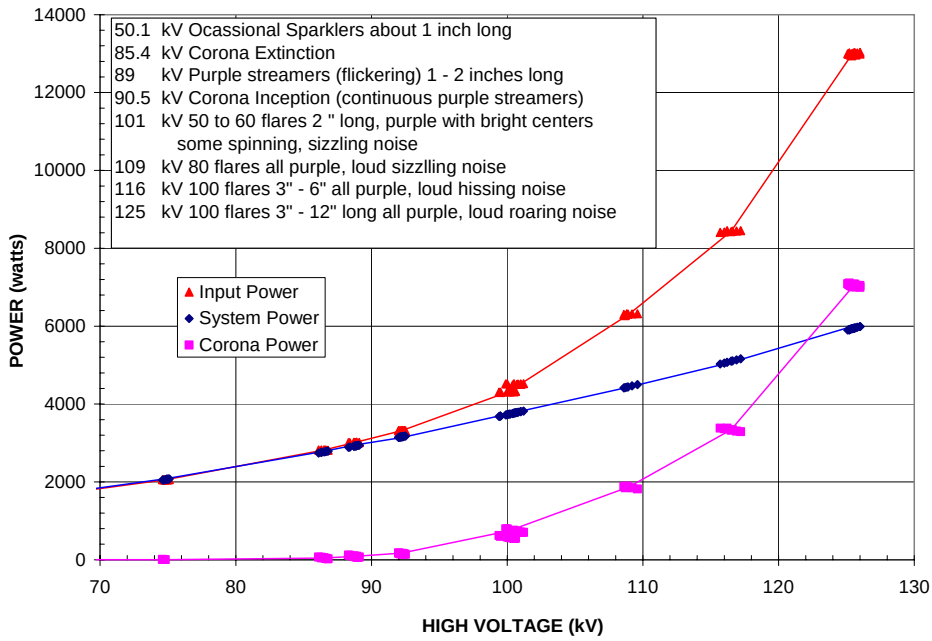

Figure 7-10. Corona power for the 1.01-inch stranded two-wire cage, spray-wet at 27 kHz.

For spray-wet conditions, there are several corona-like phenomena that occur as the voltage is increased (see Chapter 6 for detailed descriptions of these phenomena). The phenomena and voltage at which they occurred for this sample are listed in Figure 7-10. As the voltage is increased, the first phenomenon is corona on falling water drops (sparklers) that can only be seen in the dark with a dark-adapted eye. The next phenomena are flickering purple streaks that arise from falling water drops or streams. Further increases in voltage leads to continuous purple streaks, termed purple mini-flares that arise from a bright hot spot on the wire. The purple mini-flares that form under wet conditions are similar to the purple streamers that mark corona onset for dry conditions. As the voltage increased, more purple mini-flares formed, until at the highest test voltage there were approximately 100 of them, some as long as 1 foot.

A second example of measurements using the same cable setup and frequency but for dry conditions is shown in Figure 7-11. In this case, instead of continuously increasing corona, there is a sharp threshold between no corona and the formation of small mini-flares. For dry conditions, it does not have to be dark to determine corona onset because the mini-flares give off a distinct audible buzzing sound and are often dimly visible in daylight. The phenomena observed for dry conditions as the voltage increases are listed on the figure. The onset voltage was 113 kV, and corona power increased very rapidly with voltage above that level. As the voltage increased, more of the cable became active in corona and there were more flares. The flares become longer and spaced farther apart as the voltage is increased. These flares dissipate considerable power. For the example shown in Figure 7-11 at the highest voltage tested, 130.4 kV, there were nine flares dissipating slightly more than 8 kW (approximately 1 kW per flare).

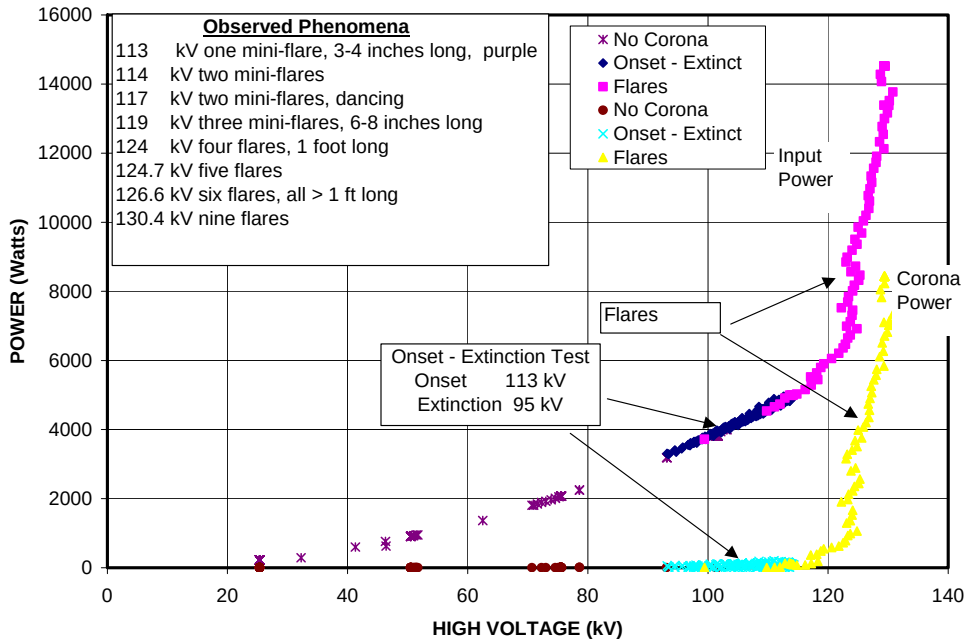

Figure 7-11. Corona power data for 1.01-inch stranded two-wire cage, dry at 27 kHz.

Onset – Extinction

Description

For both wet and dry corona, there is a hysteresis effect that takes place between the onset and extinction levels. A detailed look at what happens between onset and extinction for dry conditions is shown in Figure 7-12, which is an expansion of the data shown in Figure 7-11. The direction of the voltage change is indicated in the figure by the numbered arrows. The voltage starts well below the onset level, and there is little or no corona power as the voltage increases towards the onset level. Purple mini-flares ignite when the onset voltage (113 kV) is reached and the corona power increases to about 175 watts. Once these mini-flares ignite, they remain even when the voltage is decreased until the voltage reaches the extinction level. For the data shown in Figure 7-12, the voltage was decreased following ignition and the corona power fell, approximately linearly with voltage, until the extinction level of 95 kV was reached. Ignition of the purple mini-flares is easy to detect when there is little or no wind. However, during windy conditions it is much more difficult to determine the ignition point. This is attributed to the wind blowing away the space charge around the wire changing the onset level.

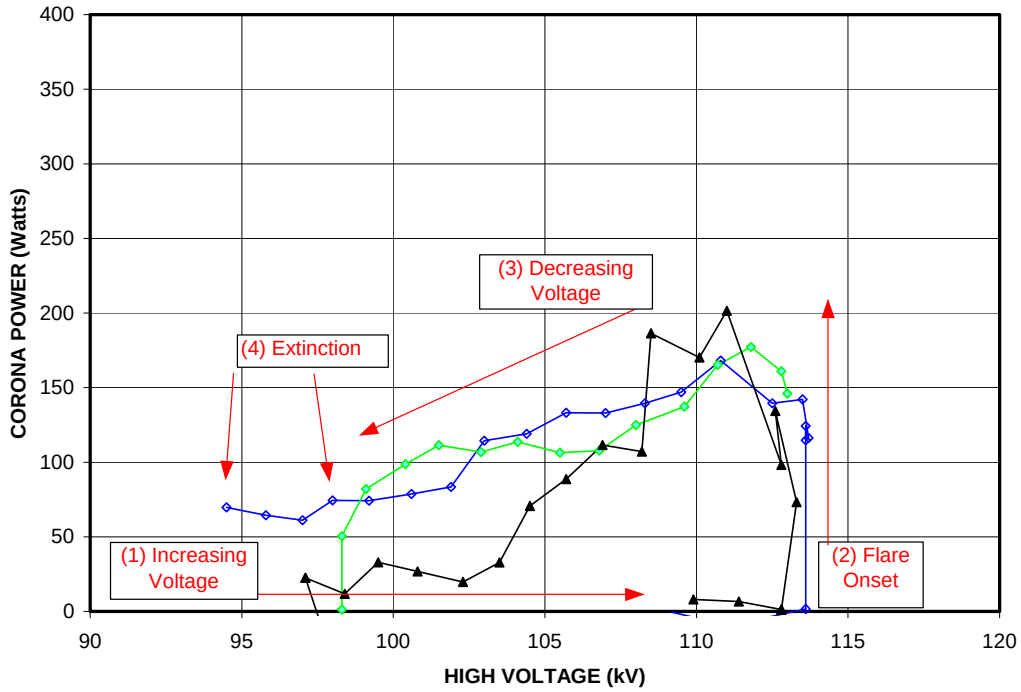

Figure 7-12. Corona power at onset, 1.01-inch stranded two-wire cage, dry, 27 kHz.

An example of hysteresis phenomena for wet conditions is shown in Figure 7-13, which is an expansion of the data shown in Figure 7-10. On the average what occurs is as follows. Below about 90.5 kV, there is very little corona power corresponding to the corona on the drops. At 90.5 kV, the purple mini-flares ignite and the corona power increases to about 100 watts. Following ignition, the voltage was decreased. The corona power correspondingly decreased, approximately linearly with voltage, until the purple mini-flares extinguished at around 85 kV. For the specific example shown in Figure 7-13, the ignition occurred at 92.5 kV with power levels shown that range from 140 to 180 watts (right set of vertical squares). The other two sets of squares represent conditions as the voltage is decreased towards extinction.

A second example showing measurements of the power dissipated between the onset and extinction levels for wet conditions is shown in Figure 7-14. These data were also taken using the two-wire cage of 1.01-inch cables. In this figure corona power and voltage are plotted versus time (sample number). The voltage was increased until the purple mini-flares occurred, and then decreased again until they went out. This was repeated several times as a part of the averaging method used to obtain onset and extinction voltages (Chapter 5). Note that the breakdown process is statistical in nature and each cycle is slightly different.

Examining the right-hand half of Figure 7-14 (samples 300–380) shows that when the voltage is below the ignition level of the purple mini-flares, the corona power is small. When the voltage reached the onset level for purple mini-flares, the corona power suddenly increases. The voltage was decreased after that and the corona power decreased slowly until the extinction level was reached. The last two cycles are a good illustration of this process. Note that the power is small, but not zero, when the voltage was below the ignition level for the purple mini-flares. This power is dissipated in the non-stationary purple streaks and corona on water drops.

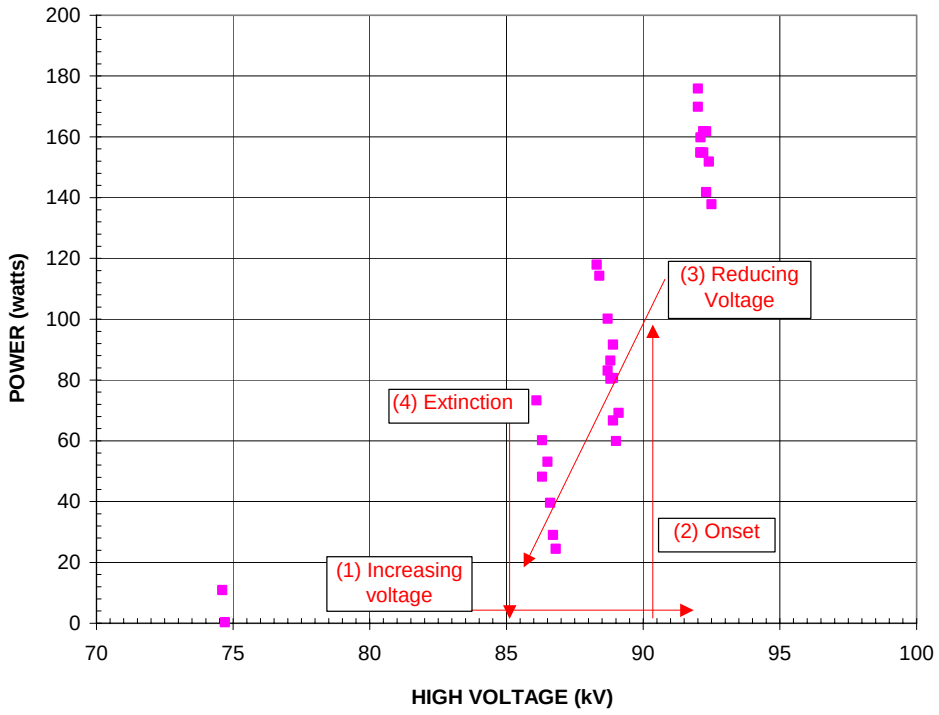

Figure 7-13. Corona power at onset, 1.01-inch stranded, two-wire cage, wet, 27 kHz.

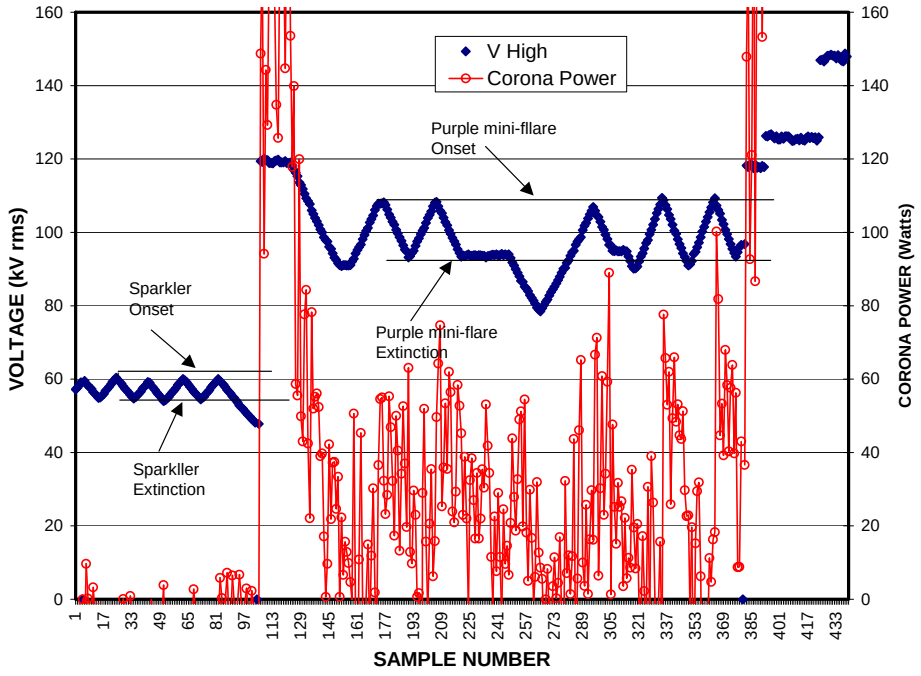

Figure 7-14. Wet corona voltage and power data in the vicinity of onset.

On the left side of Figure 7-14, there is a similar section of data taken around the level of sparkler onset and extinction. Note that the voltage where this occurs is much below the ignition level for purple mini-flares, and that there is very little power dissipated. In fact, the power dissipated was within the noise level of the measurement system, which is why there sometimes appears to be more power dissipated when the sparklers have gone out.

Wet Onset Definition

For spray-wet conditions, the threshold of corona onset is not distinct as it is for dry conditions, and it is necessary to choose a definition for corona onset that is consistent with the objective of developing design criteria for VLF/LF high-voltage systems. For these systems, it is desirable to operate at as high a voltage as possible without dissipating much power through corona or damaging the system components. A second consideration is that the corona onset definition has to be based on a repeatable phenomenon that can be easily measured.

The corona that forms on water drops does no damage and dissipates so little power that it could not be reliably measured with the test setup at Forestport. It follows that water-drop corona is acceptable in an operational antenna system. The non-stationary purple streaks dissipate more power but still not enough to be consequential, and they do no damage. Their presence is also acceptable for an operational antenna. Also, they are not suitable as a good definition of corona onset because they grow continuously out of sparklers as voltage increases, and as a consequence it is difficult to determine when they first appear. In contrast, it is relatively easy to determine the level at which continuous purple mini-flares start (unless it's windy). They arise from a bright spot on the wire, and they are similar to the purple streamers that mark dry corona onset. They dissipate measurable amounts of power and the bright spot on the hardware can cause damage over time. For these reasons, the voltage at which these purple mini-flares appear was chosen to define wet corona onset. Below this level, there is some corona power, but it was often below the threshold of the measurement system.

Using the ignition of the purple mini-flares as the definition of wet corona onset, the onset voltage for the 1.01-inch two-wire cage of Figure 7-10 was 90.5 kV rms, although, as shown in the figure, there is a slight amount of corona power dissipated below that level.

Formula

Neither the empirical formula, Equation 7-12 nor the modified Ryan and Henline formulas, Equations 7-6 and 7-7, are accurate around the level of onset, because at onset the term (V-V_{on}) or (E-E_{on}) forces the calculated power at onset to be zero, not the value that suddenly occurs at onset. Thus, at onset, and immediately above onset, the formula gives values of power dissipated that are too small. For this region, we propose to further modify the formulas by replacing the onset levels in the last term with the effective onset level. The formulas become,

$$P_{cl} = \frac{P_{coron}}{l} = K_1 \cdot \omega \cdot C_{_l} \cdot V \cdot (V - V_{one}) \tag{7-15}$$

$$P_{cl} = K_1 \cdot (2 \cdot \pi \cdot \varepsilon_0 \cdot a)^2 \cdot \omega \cdot \frac{E}{C_l} \cdot (E - E_{one}) \tag{7-16}$$

$$P_{cl} = K_3 \cdot 2 \cdot \pi \cdot a \cdot \varepsilon_o \cdot \omega \cdot E \cdot (E - E_{oe}) \cdot d \tag{7-17}$$

where V_{one} is the effective onset voltage, and
E_{one} is the effective onset surface field.

The values of V_{one} and E_{one} that fit the data are slightly less than the actual onset levels but well above the extinction levels. The data for the 1.01-inch stranded two-wire cage data are consistent with the equivalent onset level being 0.65% less than onset for both the dry and spray-wet conditions at 27 kHz, shown in the section on Corona Power below.

As previously mentioned these formulas are multiplied by implicit unit step functions, $U(V_{on})$ or $U(E_{on})$ according to the convention of Ryan and Henline. The use of these unit step functions and values of V_{one} or E_{one} slightly less than V_{on} or E_{on} enables the formulas to reproduce the effect of the sudden jump in power that occurs when the voltage reaches the onset level. The effect seen when reducing the power level from above onset can be reproduced by changing the formula by replacing the unit step functions with $U(V_e)$ and $U(E_e)$ respectively, and using a different (much smaller) value of K_1 or K_3.

Curve Fitting

Curve fitting involves fitting the measured data with one of the equations. The parameters that can be adjusted are the equivalent onset voltage or field and the factor K_1, K_2, or K_3 depending upon the equation. By adjusting these parameters, formulas were obtained which provided reasonably good fits to the collected data. The empirical equation, with the associated factor K_3, is the one we settled on as being the best. Some of the curve fitting results that follow were done using the modified Ryan and Henline equations with the factor K_1. In that case the equivalent value of K_3 is usually included, with the exception of the two-wire cage data.

The wet 1.01-inch stranded two-wire cage (24-inch separation) wet 27-kHz data shown in Figure 7-10 has been fitted using Equation 7-15, shown plotted in Figure 7-15. Note that the modified Ryan and Henline equation gives an excellent fit between extinction and onset when using the extinction voltage in the last term and with a value of $K_1 = 0.03$. In Figure 7-15, the solid line corresponds to using a unit step function of the onset voltage $\{U(V_{on})\}$, while the dashed line corresponds to using a unit step function of the extinction voltage $\{U(V_e)\}$.

The data from Figure 7-10, corona power for the wet 1.01-inch two-wire cage, are presented with a logarithmic scale in Figure 7-16. Two separate equations are required to fit these data; one shown as a solid line for the data between onset and extinction and a solid line for the data above onset. The data between onset and extinction are well fitted by Equation 7-15 with the parameters given in the previous paragraph. The dashed curve shown in Figure 7-15 has been re-plotted as the solid curve fitting the lower voltage data in Figure 7-16. As the voltage increased above onset, the curve fit required using Equation 7-5, which has onset voltage as the last term, and a value of $K_1 = 0.15$, as shown in the figure. From these data, it is clear that the slope of power versus voltage is steeper above onset than below onset.

Similarly, the data for the dry 1.01-inch two-wire cage in the vicinity of onset and extinction have been curve fitted using Equation 7-15, as shown in Figure 7-17 plotted with a logarithmic scale. Between onset and extinction, an excellent curve fit is obtained using the extinction voltage in the last term of the equation, and with a factor of $K_1 = 0.007$. Several onset and extinction runs are included in this figure to illustrate the statistical nature of the process. The curve fit approximates an average of these runs. Above onset the curve fit using an equivalent onset voltage, V_{one}, slightly less than that measured and $K_1 = 0.07$ results in a good fit up to almost 125 kV. Above that level, large flares developed, and a good fit to that portion of the data can be obtained with an equivalent onset voltage of 116 kV and $K_1 = 0.38$. For the two-wire cage the displacement current was calculated using the equivalent radius for capacitance, a_{eqC}, (Chapter 4). One problem with the cage data is that

sometimes (typically low level) only one wire was in corona and at other times (typically higher levels) both wires went into corona.

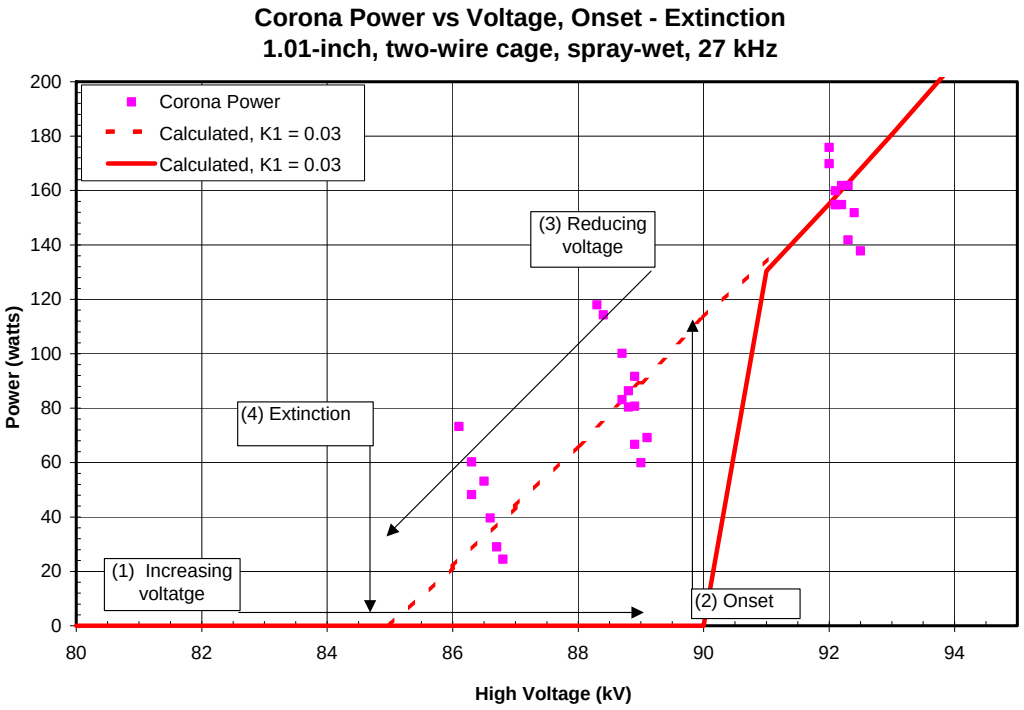

Figure 7-15. Corona power between onset and extinction for 1.01-inch, two-wire cage, spray-wet at 27 kHz.

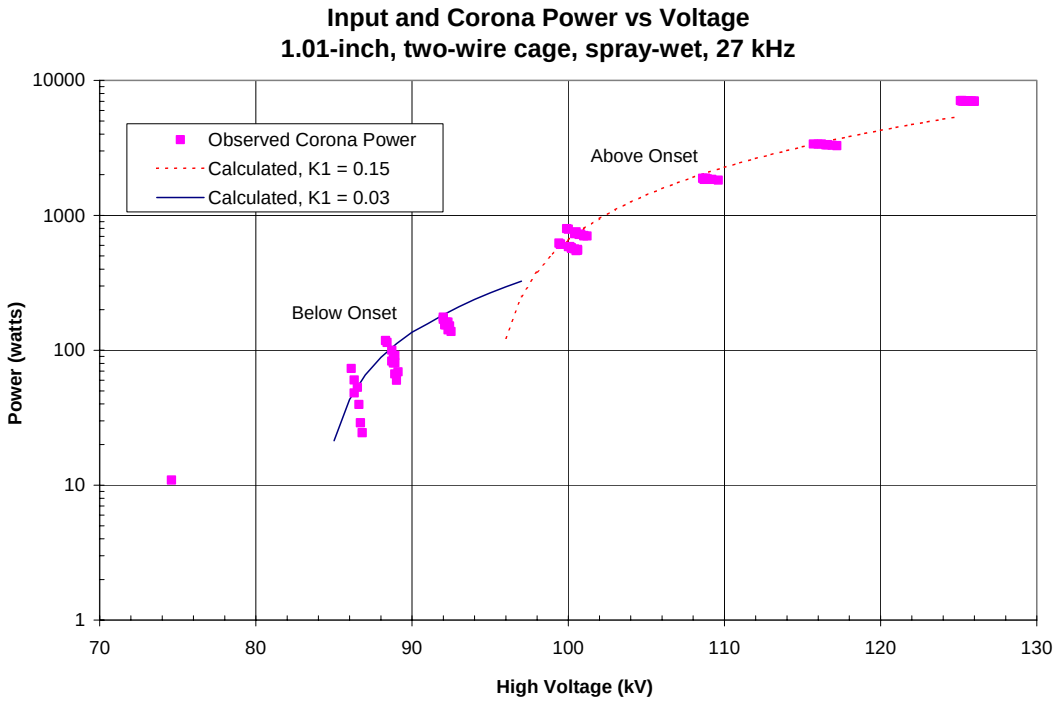

Figure 7-16. Equation fit for horizontal 1.01-inch stranded two-wire cage, wet at 27 kHz.

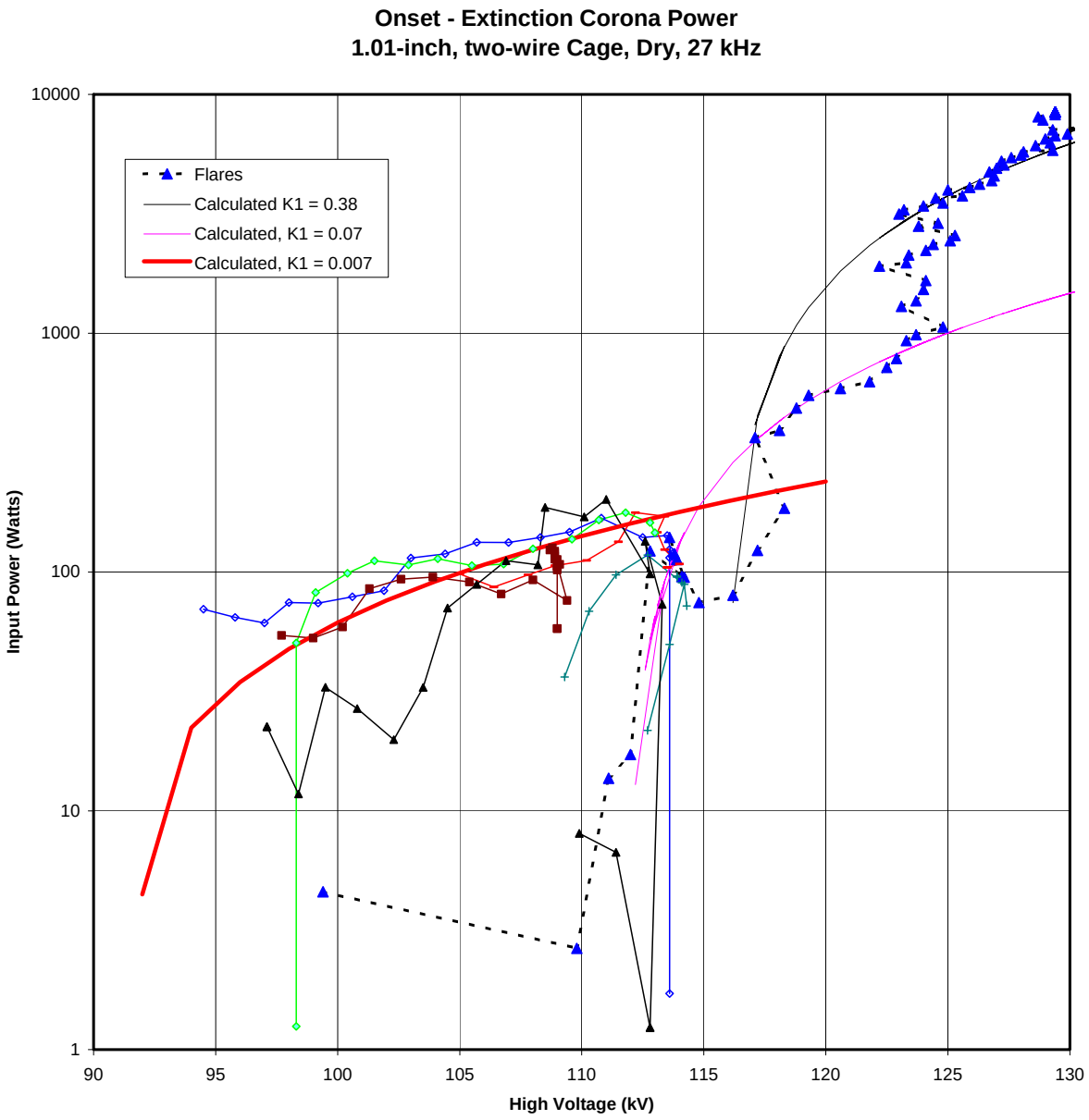

Figure 7-17. Curve fit for horizontal 1.01-inch, stranded two-wire cage, dry at 27 kHz.

For both wet and dry cases, there are different regions corresponding to different corona phenomena. In each region the data can be fit with Equation 7-6 by using different values for the equivalent onset voltage and K_1. As the voltage increases the points where changes in the equation are required to fit the data are correlated with changes in the observed phenomena. The value of K_1 for the region below onset is small, where the corona is dim. It is nearly an order of magnitude greater for the region immediately above onset. It increases again at a higher voltage level, corresponding to the region where flares form.

Power Density

Power density is determined by dividing measured total power by the effective wire length. The effective wire length is a function of the amount that the voltage is above the onset level as previously discussed (see Figure 7-5). The effective wire length was calculated for each case by using the analytic representations described above. An example of processed data is shown in Figure 7-18 for a #8 smooth dry wire at 29.4 kHz in the vertical test cell. In this figure, two different sets of measurements are shown (Data files COR 9-10 and COR 20). The data from these measurements are similar except the onset voltage was somewhat greater for the COR 20 data. The curves have been fit to the COR 9-10 data.

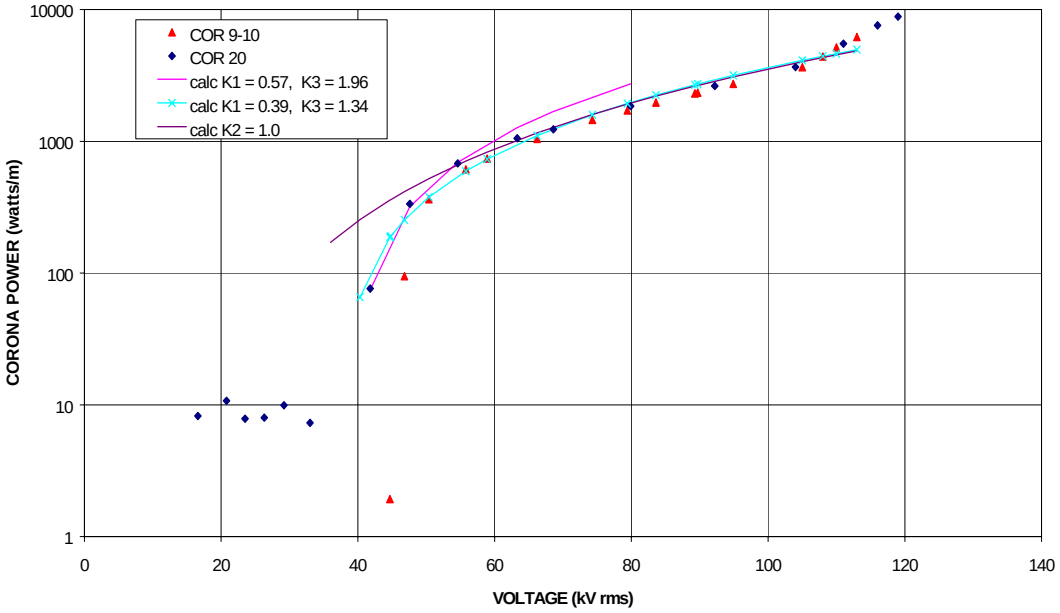

Figure 7-18. #8 smooth dry vertical at 29.4 kHz and formula comparison.

Two different curves generated by the modified Ryan and Henline formula for cylindrical geometry, Equation 7-15, are shown in the figure denoted in the legend by calc $K_3 = 1.96$, and calc $K_3 = 1.34$. The curve with $K_3 = 1.96$ fits better at and just above onset, but the curve with $K_3 = 1.34$ was selected as a better fit to all the measurements. The equation fits the data fairly well with this value of K_3 except that the measured power density just above onset increased slightly faster than the calculated values. One possible reason for this is that the estimated effective wire length may be too small in the vicinity of onset.

At a level slightly above 100 kV, the nature of the corona changes from many mini-flares to a few large lightning-like flares. In Figure 7-18, it can be seen that above this level the corona power increases more rapidly than predicted by the equation. This change was not observed with the horizontal test cell until much higher voltages were reached. The transition to large flares in the vertical test cell at lower voltages is attributed to the close proximity of the test wire to the grounded outer cage, which results in enhanced field strengths near the wire when significant ionization is present. The indoor conditions (no wind) for the vertical test cell allow the buildup of ionization products within the cell. In this case, the enhanced field strength does not fall off from the wire as

rapidly as for the horizontal wire geometry where the ground potential is further away and even slight wind will disperse the ionization products.

Comparison of Formulas

Figure 7-18 contains plots of all three equations, the modified Ryan and Henline with the factor K_1, the theoretical equation with the factor K_2, and the empirical equation with the factor K_3. Note that the curves generated by the modified Ryan and Henline formula ($K_1 = 0.57$ and $K_1 = 0.39$) are the same as the curves generated by the empirical equation (7-12) with $K_3 = 1.96$ and $K_3 = 1.34$, respectively.

The theoretical curve with $K_2 = 1.0$ is shown in the figure for comparison. This curve is a good fit well above onset giving credibility to the theory. However, this formula gives too much corona power in the vicinity of onset. This can be partially corrected by adjusting K_2 and E_{one}, but even with these adjustments the empirical formula fits the data better and is therefore the formula of choice for curve fitting.

Vertical – Horizontal Comparison

Figure 7-19 shows the observed and calculated power densities as a function of surface electric field for a #8 stranded wire in both the vertical and horizontal test cells at 28 kHz. For both cases, the observed and calculated values agree fairly well up to about 50 kV/cm. Note that above 80 kV/cm the vertical data show a sudden increase in slope, similar to the data in Figure 7-18. This is the result of the large flares, which occur at lower voltage in the vertical test cell than the horizontal test cell. This is attributed to residual ionization within the coaxial geometry of the vertical test cell. For the horizontal case shown at high surface field levels, the observed power was less than the calculated value.

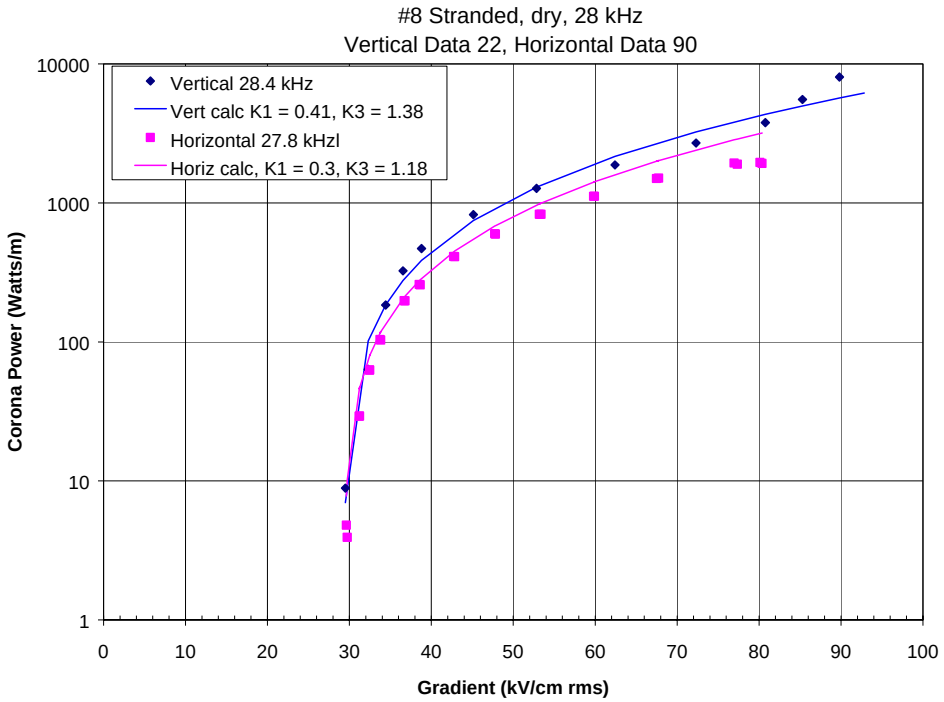

Figure 7-19. #8 stranded wire dry, vertical and horizontal at 28 kHz.

Note that at the lower voltage levels the power for both vertical and horizontal cases is nearly the same. However, as the voltage increases the power for the vertical case is somewhat larger. This can be attributed to the fact that the field falls off uniformly around the wire in the vertical case resulting in the formation corona all around the wire involving more of the surface area (Figure 7-2). The factor K_1 (and hence K_3) includes the proportion of the wire area in corona and this could explain why K_1 (K_3) is larger for the vertical case. However, as previously mentioned the modified Ryan and Henline equations using K_1 contain height (or D for the cylindrical case) dependence, which accounts for part of the difference. Note that the values of K_3 for the vertical and horizontal case are closer together than the values of K_1, providing further validation for the empirical formula based on the height independence proposition.

Stranded – Smooth Comparison

Data for the smooth and stranded #8 wires under dry conditions for the vertical test cell at 28–29 kHz are shown in Figures 7-18 and 7-19. For the smooth wires and stranded wires the values determined for K_3 were 1.34 and 1.38 respectively. This indicates that at least for smaller diameter wires K_3 is not strongly dependent upon the wire being smooth or stranded.

Since K_3 includes the proportion of the surface area involved in corona, the value of K_3 depends on surface condition, especially for smooth wires. This is because only the roughened portion of the surface goes into corona first, not the entire surface. We were reasonably careful with our samples to remove any obvious roughness. However, the wire surfaces were not polished or specially prepared. As a result, the surface roughness varies between samples. Roughness over a portion of the surface reduces the onset voltage in that region. At voltages just above onset, only the rough area is involved in corona, resulting in a smaller value for K_3. As the voltage increases, eventually the undamaged area goes into corona resulting in an apparent increase in the value of K_3.

Frequency Comparison

Figure 7-20 shows an example of data taken using the #8 stranded wire in the horizontal cell with dry conditions at two frequencies, 17.9 and 27.8 kHz. There is good agreement between the observed data and values calculated using the fit. The values of K_3 are similar but a little larger for the lower frequency.

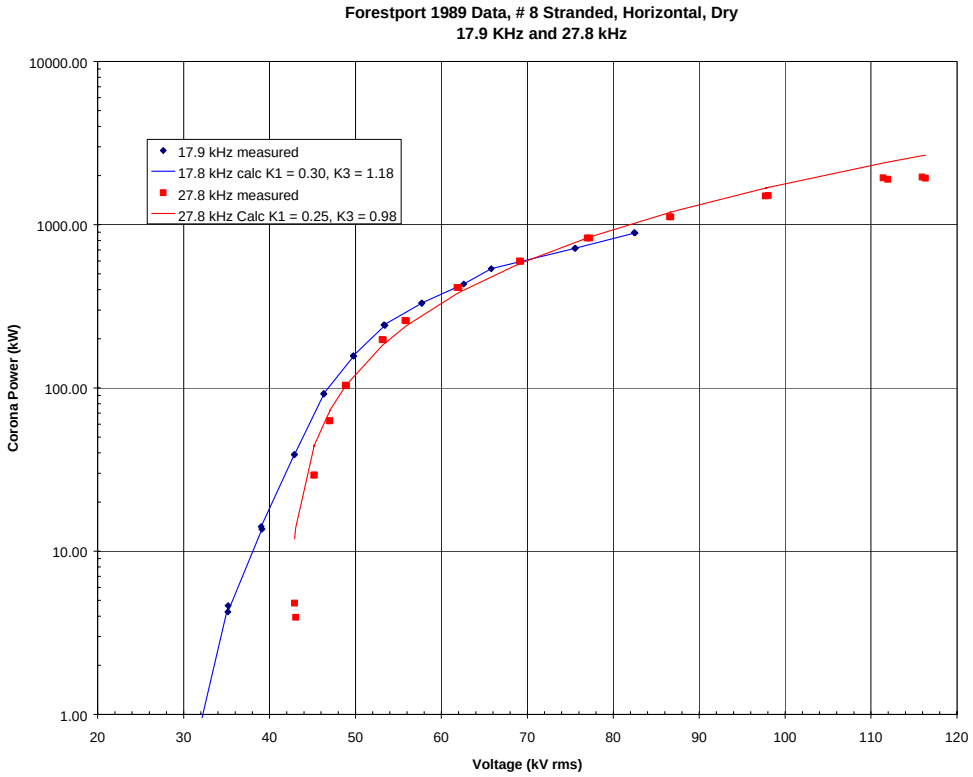

Figure 7-20. Horizontal #8 stranded wire dry at two frequencies.

For fixed environmental conditions, the onset voltage should remain constant or decrease slightly with increasing frequency. However, for the data shown in Figure 7-20, the onset level for 27.8 kHz was greater than that for 17.9 kHz. This is attributed to the fact that the measurements were made outside at night, and environmental conditions varied during an evening's test. For dry tests, changing humidity, and particularly the formation of dew, changed the onset voltage for different test runs and explains the apparent anomaly in onset voltage for this data set.

The difference in onset voltage resulted in more power being dissipated at 17.9 kHz than at 27.8 kHz over a range of voltages immediately above onset. However, the slope of the 27.8-kHz data was greater than that at 17.8 kHz, which agrees with the expected frequency dependence, and as the voltage was increased the power dissipated at 27.8 kHz eventually exceeded that at 17.9 kHz. Consequently, even for cases where the onset voltage was affected by moisture, there is good agreement between the observed data and values calculated using our formula.

Figure 7-21 shows the total corona power dissipated using the #6 stranded wire (0.47-cm diameter) dry in the horizontal test cell for three different frequencies. For these data, the onset value at 17.9 kHz is again less than that at 27.8 kHz, but like the data above the slope of the curves increases with frequency.

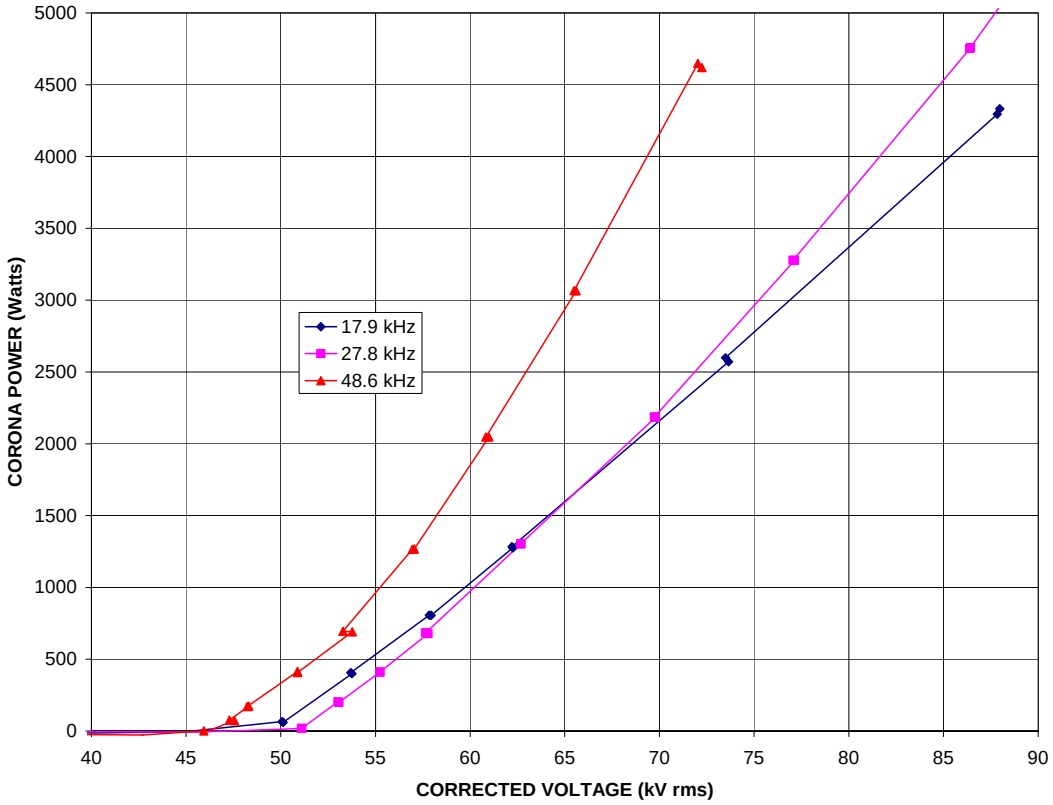

Figure 7-21. Corona power for #6 stranded wire dry, horizontal, at three frequencies.

These data have been plotted in terms of power density in Figure 7-22, along with the appropriate curve fit. For the data shown the value of K_3 decreased with increasing frequency.

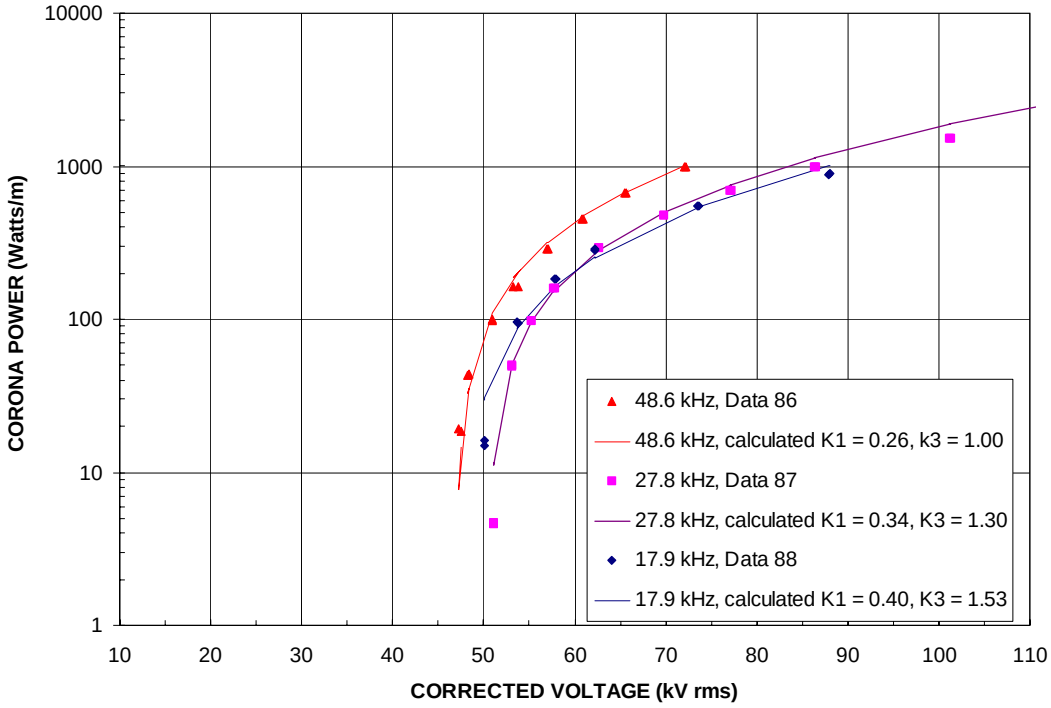

Figure 7-22. Corona power density for #6 stranded wire horizontal, dry, at three frequencies.

Diameter Comparison

Corona power versus surface electric field is plotted in Figure 7-23 for three sizes of stranded wire (#18, #8, and #6) in the horizontal test cell, spray wet at 28 kHz. The data is well fit with our equation by using values of K_3 equal to 1.23, 0.95, and 0.95 respectively. Some dependence on diameter and frequency was expected because of the critical frequency effect described in Chapter 6.

Again for this data set the expected decrease of onset surface field with wire diameter was not observed, in that the #6 wire went into corona at a slightly greater field level than the smaller #8 wire. This indicates that surface roughness is likely the reason for both the low onset voltage and low value of K_1 for the #8 sample, which could obscure the effect of frequency for this data set.

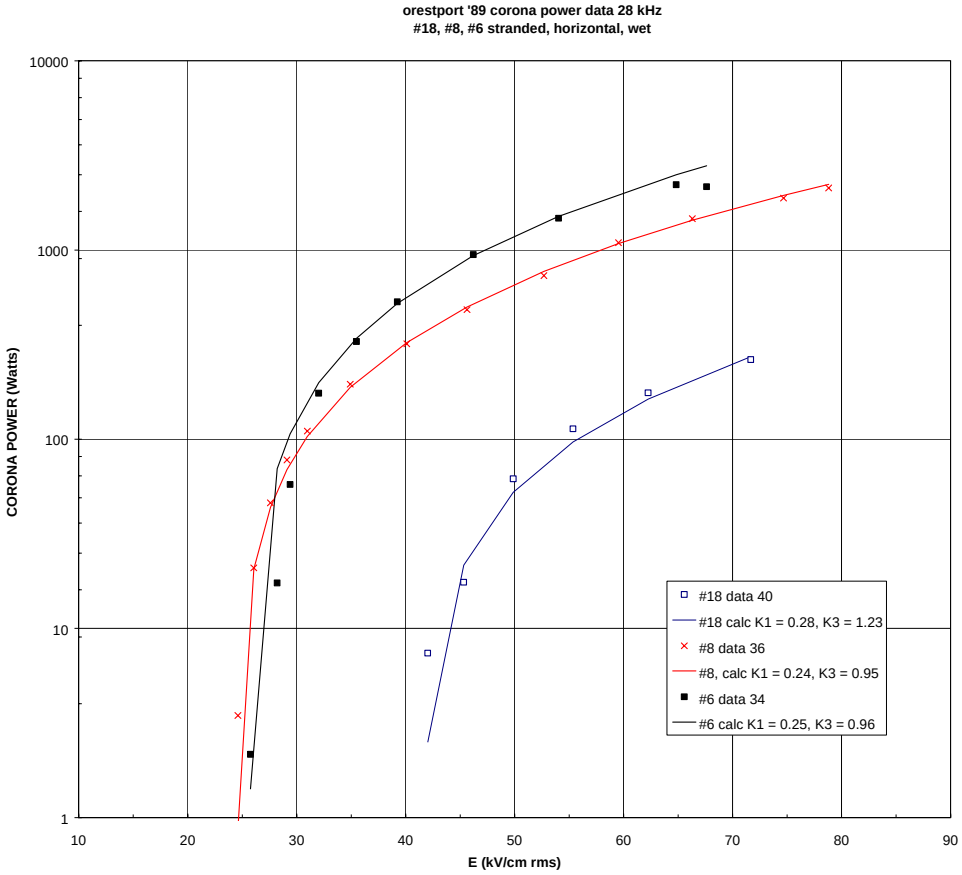

Figure 7-23. Corona power versus electric field for three wire sizes at 28 kHz.

Wet and Dry Comparison

Measured corona power data for a 1.01-inch stranded horizontal cable with dry conditions at 27.8 kHz is shown in Figure 7-24. The data for same wire with wet conditions is shown in Figure 7-25, along with the curve fitted to the dry data (K_3 = 1.70). The onset level for wet conditions (9.8 kV/cm) is less than for dry conditions (13.6 kV/cm) as expected. The curve for wet corona power starts at a lower gradient and increases at a slower rate than the curve for dry conditions. Eventually, somewhere above the dry onset level, the wet curve merges with the dry curve. This is consistent with our observation that as the voltage increases the wet corona phenomena eventually become very similar to those for dry conditions, corresponding to the region where the curves merge.

Figures 7-26 and 7-27 are for the other two frequencies and show both the wet data and fitted curves for both the wet and dry data. Note that the value of K_3 for wet conditions is considerably less than it is for dry conditions. These figures also contain an average curve developed by using the average of the wet and dry onset and K_3 values in the equation. It can be seen from the figures that the empirical equation fits the wet data in the region above onset but not over the entire voltage range. A reasonable fit for wet conditions is obtained by a piecewise continuous approximation consisting of three sections. The sections are: (1) the wet curve, (2) the average curve, and (3) the dry curve. As voltage increases wet corona power is given first by the wet curve up until it intersects the intermediate curve. Above that point it is given by the intermediate curve until that intersects the dry

curve. Above that point wet corona power is essentially the same as for dry conditions and is given by the dry curve. As seen in the figures the piecewise linear function is a good approximation for wet corona power but can be above or below the actual value.

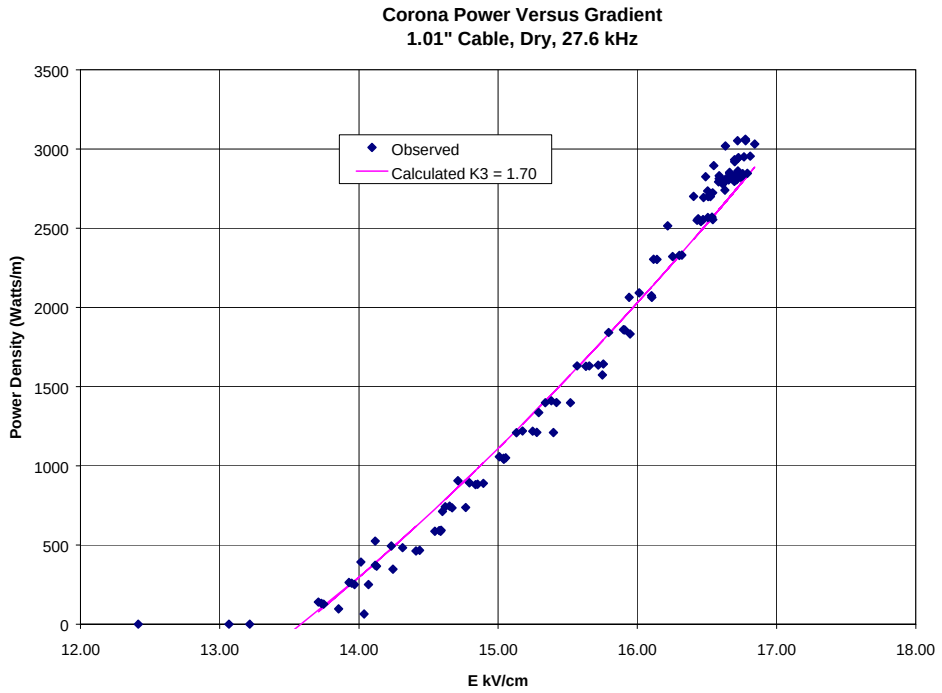

Figure 7-24. Corona power for 1.01-inch stranded Aluminum cable, dry at 27.6 kHz.

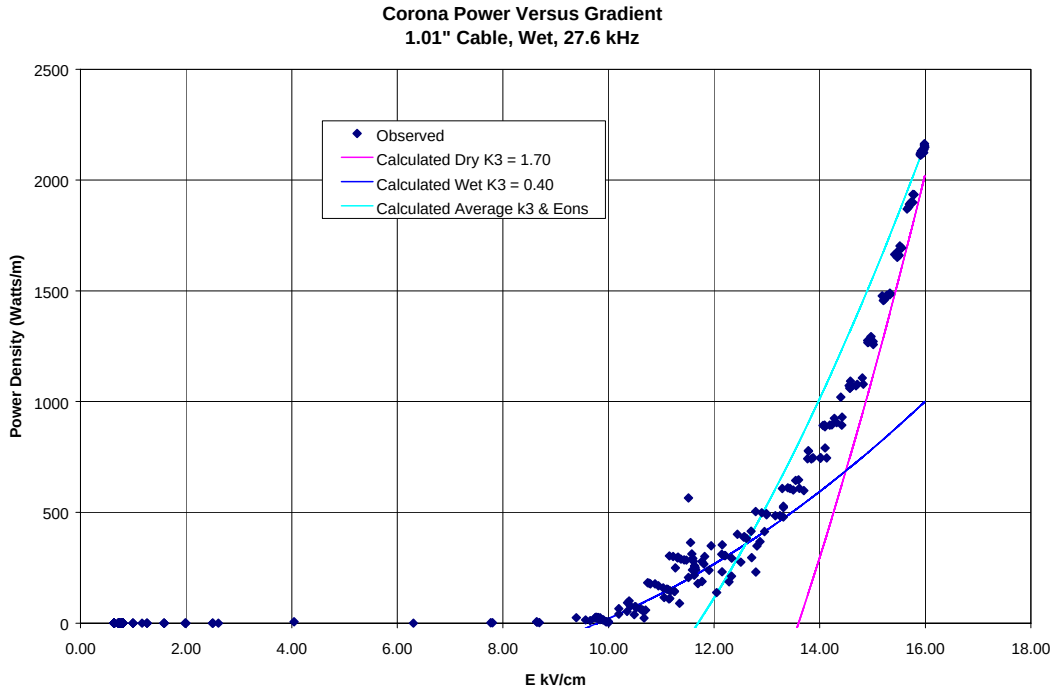

Figure 7-25. Corona power for 1.01-inch stranded Aluminum cable, wet at 27.6 kHz.

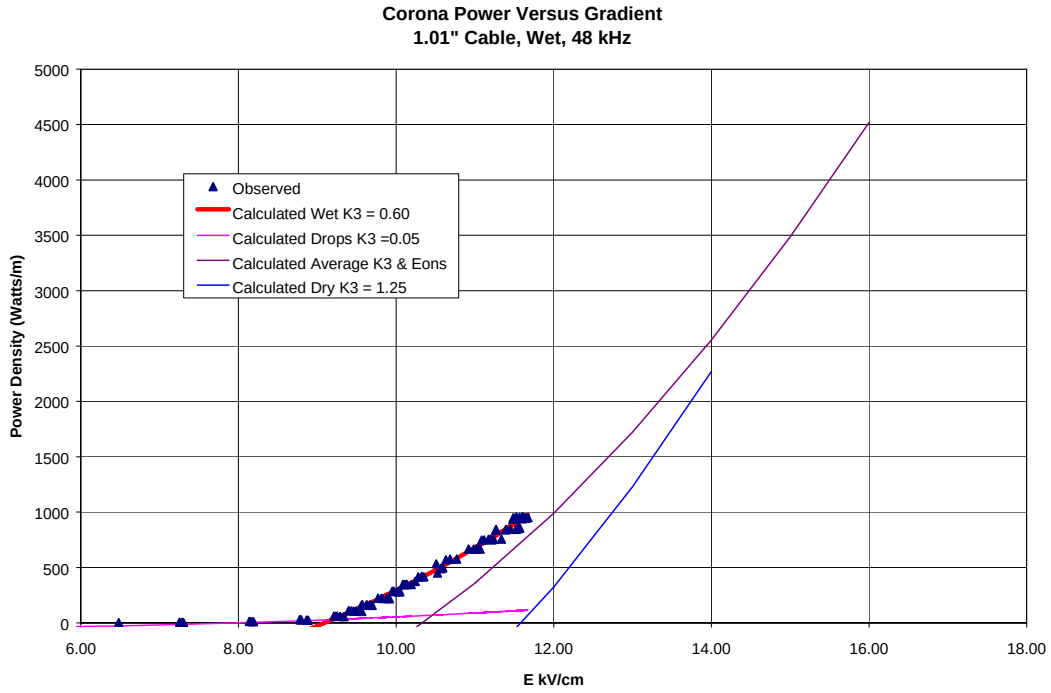

Figure 7-26. Corona power for 1.01-inch stranded aluminum cable at 48 kHz.

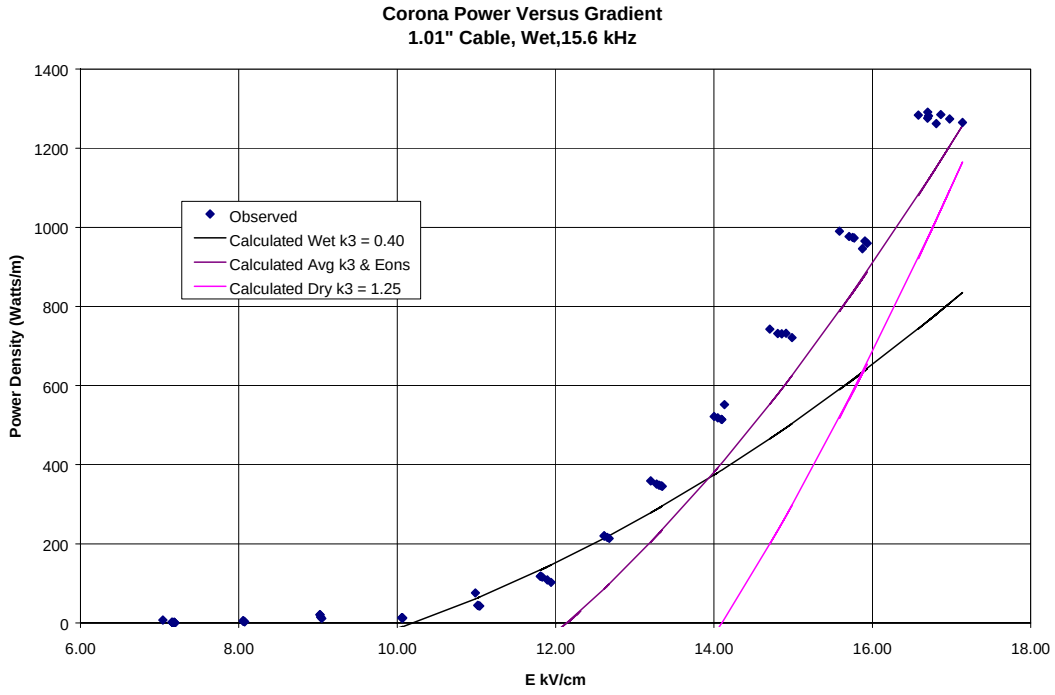

Figure 7-27. Corona power for 1.01-inch stranded aluminum cable at 15.6 kHz.

For each case with wet conditions there is a small amount of corona power that starts at a much lower level, not easily seen with the scales chosen for the plots. This corresponds to corona on the drops and streamers (moving mini-flares). Thus for wet conditions there are essentially three major regions of corona: (1) corona on drops and moving mini-flares, (2) wet corona, primarily the stationary purple mini-flares, and (3) corona similar to dry conditions, primarily flares. A curve has been fit to the corona power on the drops in Figure 7-26 at 48 kHz. The value of K_3 is very small for this phenomenon. As previously discussed we have chosen to ignore the corona on drops since it causes no harm. Also this low-level data is less accurate because the corona power is derived as the difference of two large numbers and there is more uncertainty in the effective length of the sample at low levels.

Corona power data for both dry and spray-wet conditions are shown in Figure 7-28 for the #8 stranded horizontal wire. The curves are similar to that for the larger wire in that wet corona power starts at a lower gradient, increases less rapidly than for dry conditions and eventually merges with the curve for dry conditions. Note this data also shows low level power corresponding to corona on drops but this is not easily seen with the scale chosen.

There are some notable differences between the data for the #8 wire and that for the 1-inch stranded cable. First note that for smaller diameter wires the wet and dry corona onset levels are nearer to each other (see Figure 6-24). For #8 wires the wet onset level is approaching the dry onset level. It appears that as the two onset levels become closer the value of K_3 for wet conditions becomes larger. For the case shown in Figure 7-28, K_3 is only slightly less than for wet conditions. Another difference is that the value of K_3 for the #8 wire with dry conditions is considerably less than that for the 1-inch cable. This suggests that the value of K_3 for dry conditions decreases with diameter. Conversely, for wet conditions, the value of K_3 is considerably greater for the smaller wire. This suggests that the value of K_3 for wet conditions is a strong function of the difference between the wet and dry onset levels. For smaller wires the wet and dry onset levels become closer together and it appears that the corresponding values of K_3 do the same.

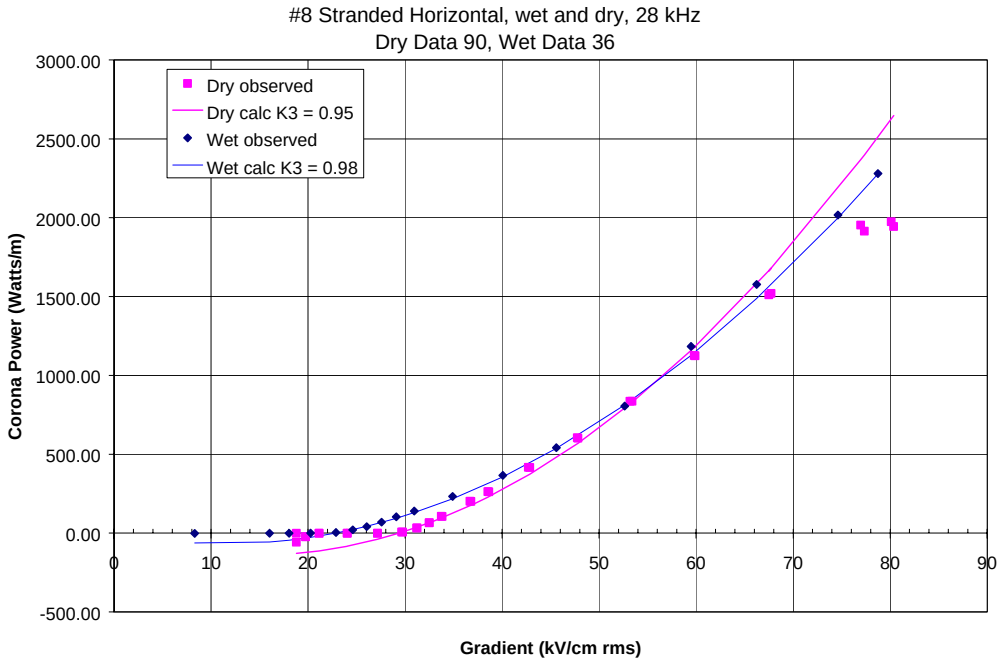

Figure 7-28. Corona power for #8 stranded wire horizontal, wet and dry.

The Effect of Wind

The data for the 1-inch stranded cable was taken with a gusty wind of 15 to 20 miles per hour. Wind increases the onset voltage by blowing away the space charge from around the conductor. This affect is variable due to the nature of the wind and the flow around the cable. The result is illustrated in Figure 7-29 below, which is the dry corona power data for 48 kHz. In this figure the groups of data points correspond to a fixed transmitter power level with 1-dB increments. The figure shows that at a fixed transmitter power level the corona power varied in a regular way so as to move downward as the voltage moved upward. The reduction in power corresponds to the wind variably increasing the onset gradient, which decreases the corona power. The result is a family of corona power curves with different onset gradients. Two of these are shown in the figure both having $K_3 = 1.25$. From the figure it is seen that some of the time the wind increased the onset gradient from 9.6 kV/cm up to almost 13 kV/cm. The change in onset gradient is attributed to the wind blowing away the initial charge buildup and also to changing atmospheric density around the wire due to the wind variation.

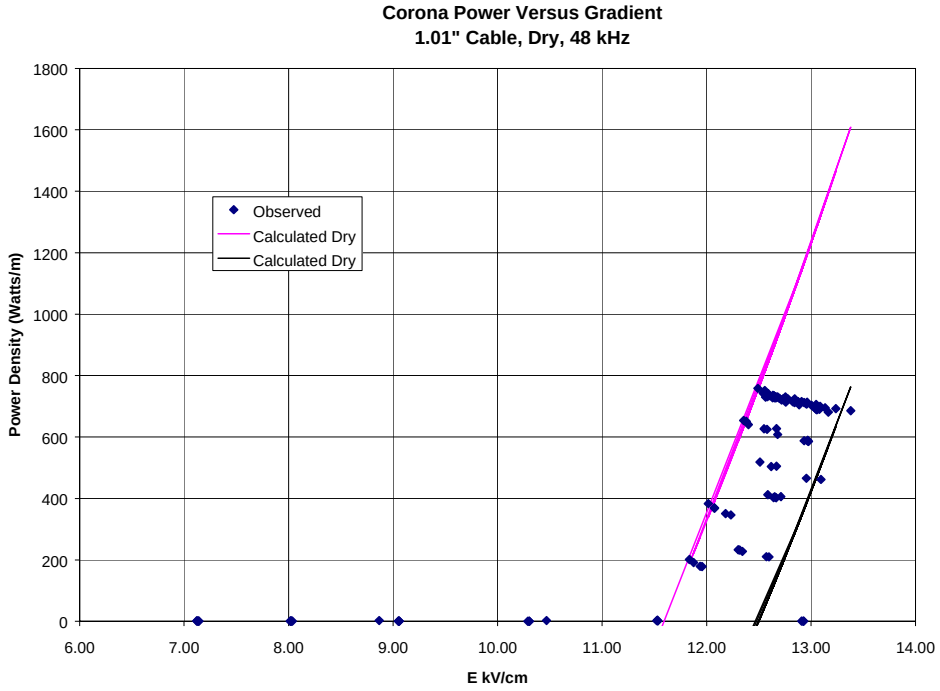

Figure 7-29. Corona power for 1.01-inch stranded aluminum cable, dry at 48 kHz.

Discussion of the K_3 Factor

The measured data have been processed to obtain the values of K_3 as shown in Table 7-3 below. Note that all the values of K_3 lie between 0 and 2, with most of them somewhat above 1.0. It is important to understand that K_3 is not exactly determined. Rather it is obtained by curve fitting without a strict criterion for the best fit. Nevertheless, based on the data presented above, it is clear that VLF and LF corona power follows the form of the empirical equation (and the modified Ryan and Henline equations). These equations include the parameter K_3 (K_1) and the equivalent onset or extinction gradient (voltage). The factor K_1 includes both the proportion of the surface in corona and any phase shift in the displacement current. At 60 Hz, the Ryan and Henline data indicate this factor

is 1.0, but our data show that at VLF/LF it is much smaller, being approximately 0.25 and never greater than 0.5. This indicates that K_1 and hence K_3 is a function of frequency over the range from 60 Hz to VLF/LF.

The frequency variation of corona power between 60 Hz and VLF/LF is probably related to the critical frequency effect (Chapter 6). Below the critical frequency, the wire is nearly uniformly covered with a thin plasma sheath. Above the critical frequency, corona starts with small flares that extend farther away from the wire than the plasma sheath but which are spaced out along the wire. Thus, above the critical frequency less of the wire surface is actively involved in corona. This is because the flares shield a portion of the wire close to themselves, reducing the field in that area.

For dry conditions, the critical frequency is a function of wire diameter being lower for larger diameter wires. Thus for dry conditions, K_1 might be expected to increase with decreasing frequency for fixed wire diameter. Similarly, for fixed frequency, K_1 might be expected to increase with decreasing wire diameter. There is no data on critical frequency effects for wet conditions.

Unlike K_1, it is difficult to give a direct physical meaning to K_3 because it originates as a factor in an empirical equation. However, since it is linearly related to K_1, it includes the variation with the percent of active area, although weighted by the conversion factors of Equations 7-13 and 7-14. Thus K_3 will have the same frequency variation as K_1. The expected frequency effect would tend to give a larger value for K_3 for lower frequency and/or smaller diameter. The individual data set for #6 wires as shown in Figure 7-22 has the opposite variation, for which we have no explanation. However, one way of looking at the data overall is to examine the average values of K_3 as a function of frequency. Table 7-3 contains a row with the average of K_3 over diameter at each frequency. The averages are nearly the same for each frequency, which is evidence for little or no frequency variation of K_3 over the VLF/LF band.

The values of K_3 observed for dry conditions have been plotted versus diameter in Figure 7-30. The horizontal data shown exhibit some scatter with points falling between 1.0 and 1.5. For dry conditions they show that K_3 is larger for larger diameter cables, approximately 1.5 for the 1-inch cable and reducing to just above 1.0 for the smallest diameter wires.

Also note that for dry conditions K_3 was larger for the vertical case than the horizontal case. There are two possible explanations for this effect. First, the field is uniform around the wire in the vertical case. The horizontal test setup was fairly close to the ground, and the field around the wire is slightly less uniform than for a wire much higher above ground. Thus, the percentage of active area is somewhat reduced for horizontal wires close to ground. However, calculation of the field on the wires indicates this factor is small at the height of our horizontal test cell (10 feet) and probably not the reason for this effect.

Table 7-3. K3 data.

Freq kHz	17.9	27.8	48.7	17.9	27.8	48.7
Wire Dia	Horizontal Wet			Horizontal Dry		
	F1	F2	F3	F1	F2	F3
1.01" std	0.33	0.40	0.60	1.25	1.70	1.25
1" sm	0.27	0.36	0.45	X	1.48	1.48
#6 std	1.07	0.96	0.99	1.53	1.30	0.99
#8 std	1.10	0.94	1.08	1.18	0.98	1.06
#10 std	1.00	0.92	1.19	1.17	1.04	1.17
#18 std	1.05	1.23	1.14	1.23	1.09	1.14
Avg	0.80	0.80	0.91	1.27	1.27	1.18
Freq kHz		29.4	57.4		29.4	57.4
	Vertical Wet			Vertical Dry		
	F1	F2	F3	F1	F2	F3
3/8" sm	-	-	-	-	1.45	1.02
#8 sm	-	-	1.13	-	1.96	1.65
#8 std	-	0.98	1.08	-	1.39	1.39
#18 sm	-	-	-	-	1.81	1.81
Avg	-	0.98	1.11	-	1.65	1.47

X - anomalous data.

The second possible explanation has to do with the residual ionization in the indoor cylindrical vertical test cell. Residual ionization increases the displacement current, which would significantly increase the power, especially at levels above onset. The residual ionization would be greater for dry conditions because for spray-wet conditions the water and the air movement resulting from the spray significantly reduces residual ionization. This would explain why K_3 for wet conditions was essentially the same for the vertical and horizontal measurements, discussed below. For these reasons, the residual ionization is considered the most likely explanation for the larger values of K_3 observed for vertical dry conditions. Under normal outside conditions on an antenna, residual ionization cannot build up as much as it did in the indoor vertical cage; thus, the value of K_3 expected in practice would be closer to the values observed for the horizontal case. For this reason the vertical dry data have been ignored in the development of the recommended values for K_3.

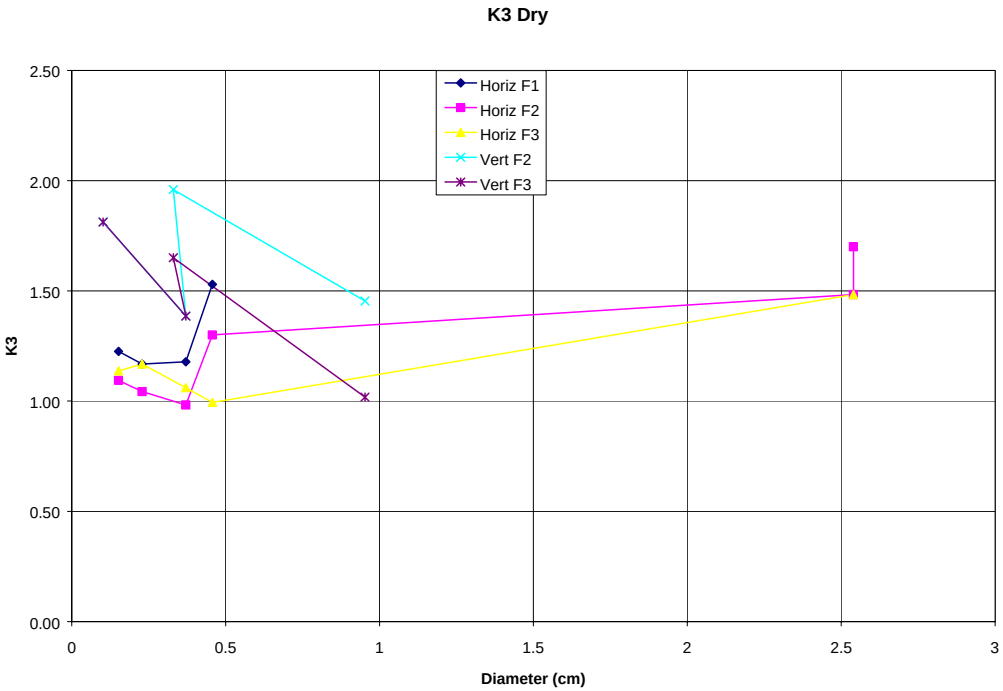

Figure 7-30. K_3 versus wire diameter, dry.

The values of K_3 obtained for wet conditions have been plotted versus diameter in Figure 7-31. For small wet wires the value of K_3 is only slightly less than it is for dry conditions. Also note that the results for vertical and horizontal orientation were essentially the same. The biggest difference is that the value of K_3 for large diameter wires is much less than for dry conditions or smaller wires. Thus for wet conditions the diameter dependence of K_3 is the opposite from that for dry conditions. For 1-inch diameter wires K_3 for wet conditions is 0.4 increasing to around 1.1 for smaller wires.

The percentage of active surface area will be reduced at onset if the surface is rough or damaged. This is true for both wet and dry conditions. The reason is that only the rough areas go into corona first, which results in less active surface area. As the voltage increases, more of the area goes into corona, until eventually the active area becomes the same as for the undamaged case. Thus, for rough surface condition the onset level is lowered and K_3 will be reduced at and immediately above onset. As the voltage increases more of the surface goes into corona and K_3 increases, eventually becoming equal to the normal value. This effect is expected to be greater for smooth than for stranded conductors. Also note that at the voltages well above onset K_3 will increase corresponding to the formation of large flares.

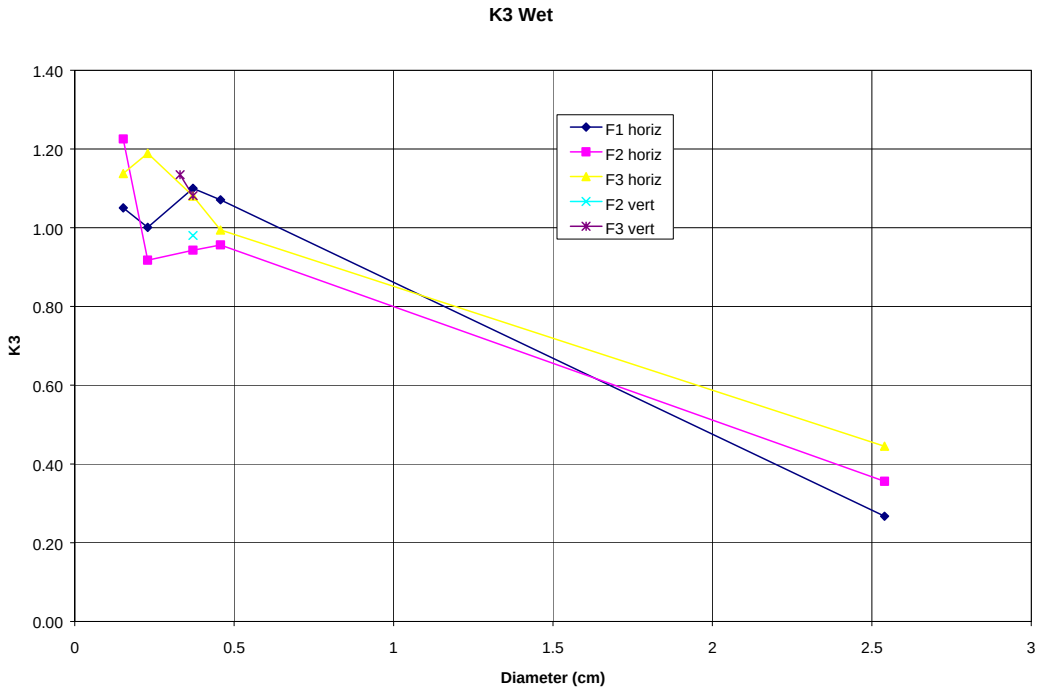

Figure 7-31. K_3 versus wire diameter, wet.

CORONA POWER

The empirical equation, 7-12, with the value of K_3 as determined above can be used to develop a quantitative understanding of the power dissipated by corona. Equation 7-12 can be formulated in terms of the relative amount the operating voltage (field) is above the onset voltage (field). When the relative amount (percentage factor) that the operating electric field is above the corona onset, voltage is given by δ, then the operating field is given by;

$$E = E_{on} \cdot (1 + \delta)$$

where E is the surface electric field on the wire,

E_{on} is the surface electric field at onset and
δ is the relative amount the voltage is above the onset voltage.

Since the electric field and voltage are directly related, the same equation applies to the operating voltage V.

$$V = V_{on} \cdot (1 + \delta)$$

Substituting into Equation 7-12 gives

$$P_{cl} = k_3 \cdot \pi \cdot \cdot \omega \cdot \varepsilon_o \cdot E_o^2 \cdot \delta \cdot (1 + \delta) \cdot d^2$$

This equation shows that just above onset, when δ is small, corona power is proportional to δ. It also shows that corona power is proportional to the onset field squared. Onset field is a function of wire diameter (Figures 6-61 and 6-62), being smaller for larger diameter wires. This relationship is

approximately inversely proportional to the square root of wire diameter. The second power of wire diameter is included in the equation; thus the overall variation is approximately proportional to the 3/2 power of wire diameter. The equation also indicates corona power is directly proportional to frequency.

The above equation can be rewritten using convenient units as follows:

$$P_{cl} = k_3 \cdot \frac{2 \cdot \pi}{9} \cdot a_{cm}^2 \cdot f_{kHz} \cdot E_{on \cdot kV\,/\,cm}^2 \cdot \delta \cdot (1 + \delta) \tag{7-18}$$

This equation has been used to calculate the corona power per unit length dissipated on an infinite wire above and parallel to ground at 0.65% over-voltage for both smooth and stranded wires with dry and wet conditions at frequencies of 60 Hz, 30 kHz, and 60 kHz. The results are plotted in Figure 7-32 for smooth wires and Figure 7-33 for stranded wires.

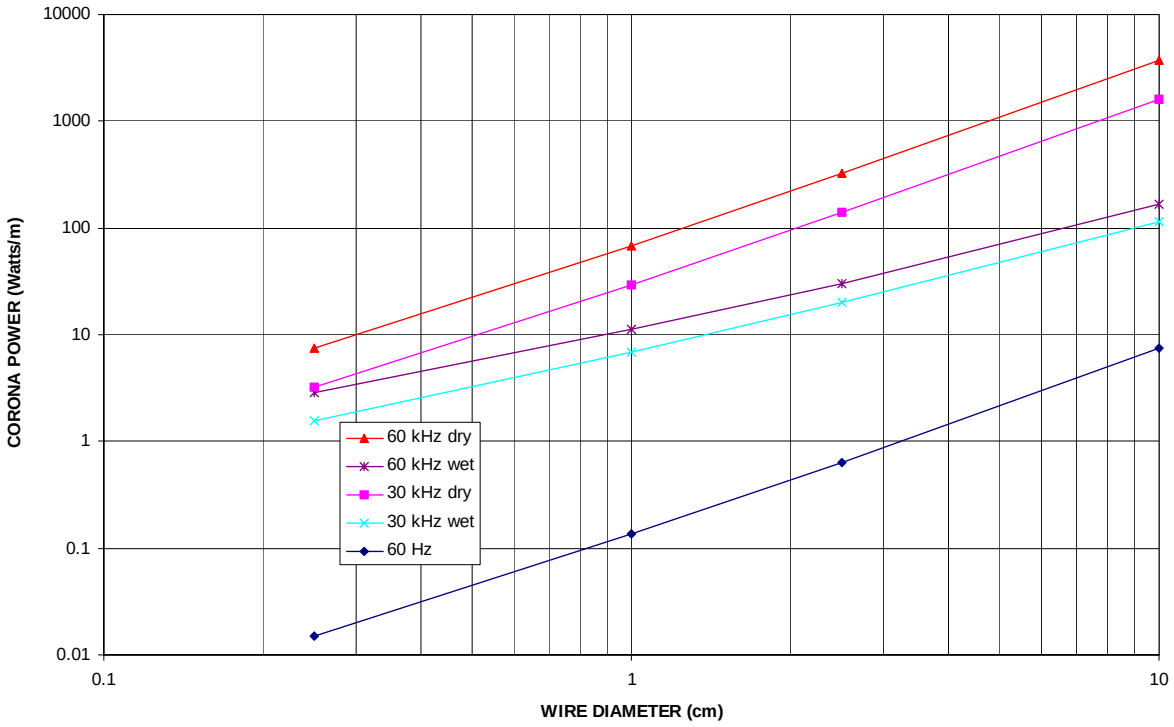

Figure 7-32. Calculated corona power density for smooth wires (0.65% over-voltage).

The 60-Hz values of E_{on} and V_{on} used to develop the plots were based on Equation 6-4 (Schuman's data). For stranded dry data at 60 Hz, a surface roughness factor of 0.7 was assumed. For 60 Hz a value of K_3 equal to 2.0 was used to account for the greater active surface area at 60 Hz. No data were plotted for wet conditions at 60 Hz because we do not have a formula for E_{on} for that case.

The VLF values for E_{on} used to develop the corona power for these figures were based on the equations in Table 6-2A. Since the variation of K_3 with diameter is not known for intermediate diameters, we have chosen to use K_3 = 1.0 for both the dry and wet VLF/LF data in these plots. The results taken from the chart should be adjusted accordingly. For example, the curve is accurate for small wet wires but for wet wires around 1-inch diameter the power should be reduced by a factor of 0.4. Similarly for dry wires the curves are accurate for small wires but for wires with diameter around

1-inch they should be increased by a factor of 1.5. The results shown in the figure apply to a long wire well above the ground, assuming the voltage is uniform along the wire. The results do not apply to the regions near the wire ends as the charge buildup there increases the field.

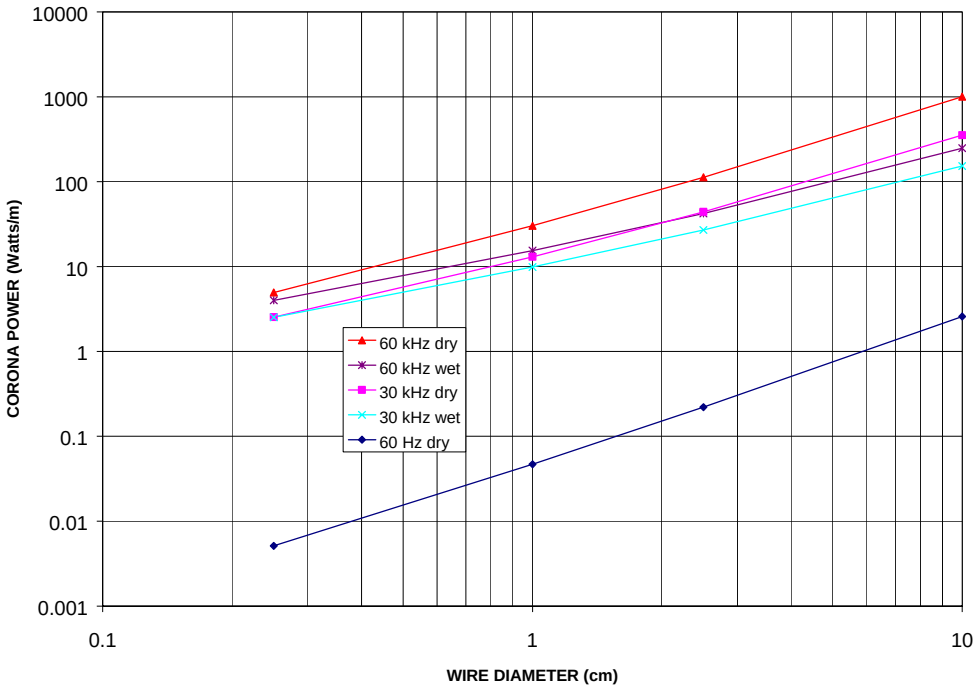

Figure 7-33. Calculated corona power density for stranded wires (0.65% over-voltage).

The value of 0.65% over-voltage was selected because it reproduces the corona power density at onset for the 1.01-inch two-wire cage at 29.0 kHz with a single wire in corona. In Figure 7-12, the initial corona power at onset was about 175 watts for the dry case or 43.8 watts/m for the 4-meter equivalent length test sample. Figure 7-33 indicates that the calculated corona power density with 0.65% over-voltage for a dry stranded 1-inch cable is 44.1 watts/m.

Similarly, Figure 7-14 shows that at the same frequency with wet conditions the corona power at onset was 110 watts, corresponding to a corona power density of 27.5 watts/m. The calculated corona power density for that case with a 0.65% over-voltage is 27.0 watts/m (from Figure 7-33).

Thus, at onset the initial corona power at 29 kHz corresponds to that calculated using a 0.65% over-voltage, which amounts to using an E_{one} (E onset equivalent) that is reduced by 0.65% from E_{on}. Thus, Figures 7-29 and 7-30 give the estimated corona power density at onset.

These figures make it clear that there is considerable power dissipated in corona at VLF/LF. Since corona power is proportional to frequency the corona power at 60 kHz is about 1,000 times more than at 60 Hz. Also, note that corona power increases with wire diameter. As an example, a smooth dry 1-inch (2.54 cm) diameter wire at 60 kHz dissipates 322 watts/m at onset.

The dependence of corona power at levels above onset is shown in Figure 7-34. In this figure, corona power normalized to the value at onset (0.65% over-voltage) is plotted versus percentage over-voltage. For the range plotted (up to 20%), corona power is proportional to over-voltage to a power slightly greater than 1.0. At 20% over-voltage, the corona power is 36.7 times that at onset. As the percentage over-voltage becomes greater, the rate of increase becoming asymptotic to over-

voltage squared. For example, when the voltage is 1.5 times the onset voltage (50% over-voltage) the corona power is 115 times that at onset (not shown on the figure). For the case of a 1-inch dry conductor at 60 kHz, that would equal 15.9 kW per meter.

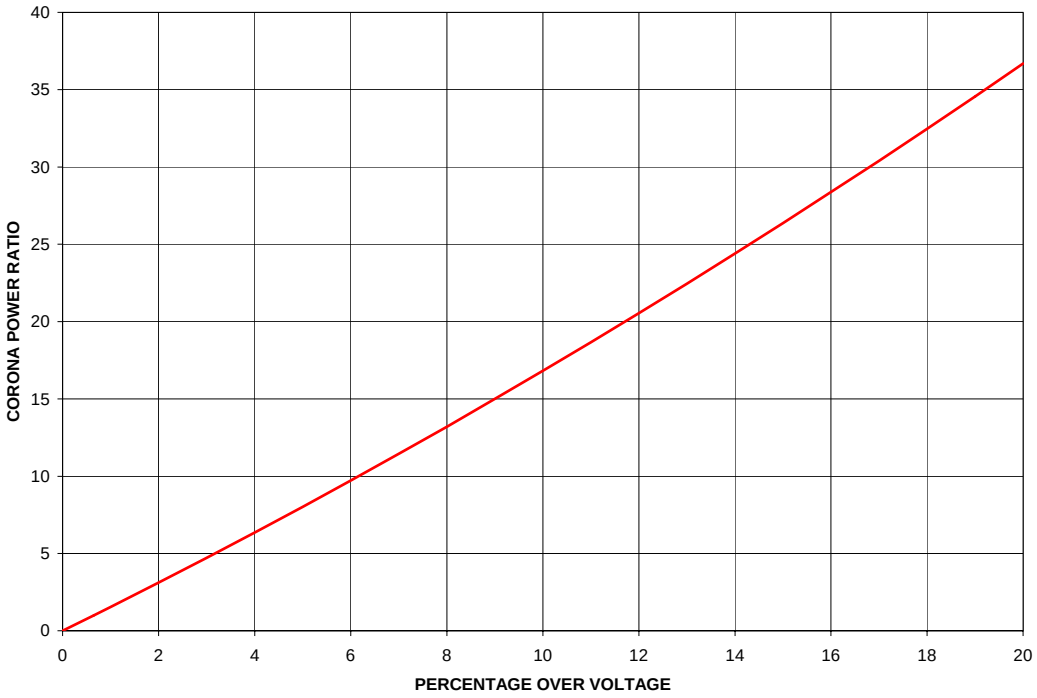

Figure 7-34. Corona power as a function of percentage over-voltage.

CONCLUSIONS

One conclusion from these studies is that large amounts of power are consumed in VLF and LF corona when the voltage is much above the corona onset level. As an example, a 1.01-inch stranded cable operating at 27 kHz with spray-wet conditions has a calculated corona power of 454 watts per meter when the voltage is 10% above onset. VLF/LF antennas are constructed from extensive lengths of conductors operated at high voltage. Operation in corona would dissipate extensive amounts of power and should be avoided on VLF/LF antennas. For example, the Navy's Jim Creek VLF antenna consists of 10 spans that run across a valley between two mountains. There are several miles of conductor in the antenna, and if even a small percentage of the conductor was in corona, it could easily dissipate the entire amount of power available from the transmitter. Tests at Jim Creek where the antenna was operated in corona confirmed this, in that as transmitter power was increased above the corona formation point almost all the increased power went into the corona.

A second conclusion is that the empirical equation, 7-12 (or the equivalent 7-18), can be used to estimate the amount of power dissipated by corona at VLF/LF. This equation for power is based on the simple concept of multiplying the displacement current times the voltage drop across the resistive corona sheath around the wire. It includes an empirically determined constant K_3. This equation has a couple of advantages over the 60-Hz formulation of Ryan and Henline. First of all it is entirely in terms of the surface electric field, which facilitates its use for VLF/LF antenna analysis. Secondly it does not have explicit height dependence and is therefore consistent with the theory of breakdown presented in Chapter 2.

In application the onset gradient E_{on} is replaced by the equivalent onset gradient, E_{one}, determined as 0.65% below the onset gradient as given in Chapter 6 (Figures 6-22-25 or the formulas in Table 6-2). Multiplying the equation by a unit step function of the actual onset gradient $U(E_{on})$ duplicates the threshold effect for corona power. The values of K_3 to be used depend upon wire diameter and wet or dry conditions as described below.

For dry conditions, the recommended value of K_3 is 1.5 for 1-inch diameter cable and it reduces to 1.2 for small diameter cables (#6, #8, #18) (see Figure 7-30 horizontal data). We have no data for intermediate diameters and linear variation between these diameters is assumed.

For wet conditions, the recommended value of K_3 is 0.4 for 1-inch diameter cable and it increases to 1.1 for small diameter cables (see figure 7-31). Again, we have no data for intermediate diameters and linear variation between these diameters is assumed.

For wet conditions, the same equation for corona power is used but with different values of onset gradient, E_{on}, and K_3 in three regions to make a piecewise continuous function. In the first region, just above onset, the onset gradients are taken from Chapter 6 but reduced by 0.65% and the value of K_3 is for wet conditions (Figure 7-31).

In the second region, the values used in the equation are average of the wet and dry values for E_{on} and K_3. The first region ends and the second region begins when the corona powers for the wet and average equations are equal.

In the third region, the values used in the equation are the dry values for E_{on} and K_3. Similarly the second region ends and the third region begins when the corona powers for the average and dry equations are equal.

The corona power equations, 7-12 and 7-18, which are equivalent, are repeated below. The values to be used for E_{on} and K_3 are summarized in Table 7-4. MKS units are used in Equation 7-12.

$$P_{cl} = K_3 \cdot \pi \cdot \omega \cdot \varepsilon_o \cdot E_a \cdot (E_a - E_{on}) \cdot d^2 \tag{7-12}$$

Where P_{cl} is the corona power per unit length,

K_3 is a factor taken from the table below,

ω is the radian frequency,

ε_0 is the permittivity of free space,

E_a is the field on the surface of the conductor,

E_{on} is the critical field on the surface of the conductor for corona onset, and

d is the diameter of the conductor.

$$P_{cl} = k_3 \cdot \frac{2 \cdot \pi}{9} \cdot a_{cm}^2 \cdot f_{kHz} \cdot E_{on \cdot kV/cm}^2 \cdot \delta \cdot (1 + \delta) \tag{7-18}$$

Where P_{cl} is the corona power in watts per meter,

K_3 is a factor taken from the table below,

a_{cm} is the conductor radius in cm,

f_{kHz} is the frequency in kHz, and

δ is the ratio of the surface field to the onset surface field.

Table 7-4. Parameters for Corona Power Equations 7-12 and 7-18.

For dry conditions use the equations with the parameters specified below. For wet conditions the use the same equations but make a piecewise continuous function in three regions with different parameters in each region as specified below.		
Condition	E_{on} is a function of diameter taken from Figures 6-22-25 or the formulas in Table 6-2 modified as specified below.	K_3 (from formula) a = radius in cm formulas valid for $0 \leq a \leq 2.5$ cm
Dry	$E_{on\ dry}$ *(1-.0065)	$K_3 = 1.15*a + 0.185$
Wet region 1	$E_{on\ wet}$ *(1-.0065)	$K_3 = 1.18*a - 0.314$
Wet region 2	Average of $E_{on\ dry}$ & $E_{on\ wet}$	$K_3 = 1.165*a - 0.065$
Wet region 3	$E_{on\ dry}$	$K_3 = 1.15*a + 0.185$

Note that the empirical data do not show any definitive frequency variation of K_3 with frequency over the VLF/LF range. They also do not indicate any significant difference in K_3 for smooth or stranded conductors. However, there was considerable scatter in the observed values of K_3, which might obscure small variations. Both the value of E_{on} and K_3 depend on surface condition of the sample. The empirical equation with K_3 as given above is useful for purposes of engineering design at VLF/LF, but to get exact results for a particular situation the true values for K_3 and E_{on} must be determined.

CHAPTER 8 PARALLEL PLATES, RINGS, RODS AND SPHERES

INTRODUCTION

This chapter presents the results of measurements of the breakdown level for both wet and dry conditions using parallel plates, toroids (rings), vertical rods with hemispherical end caps, and one case of a sphere. These configurations are embodied in some way in most high-voltage apparatus. The objective of the measurements was to provide empirical data for design curves that can be used to design VLF/LF high-voltage hardware.

The test configurations were chosen because they are simple representations of typical components of high-voltage hardware. For example, the optimum design for a Base Insulator Assembly (BIA) is a uniform field in the center region of the insulator. The parallel-plate experiment determined the breakdown level for a uniform field in air for both dry and wet conditions at VLF/LF. The parallel-plate test with wet conditions revealed some unusual visual phenomena that we believe were previously unknown. Some of these phenomena in modified form occur for wet conditions on other shapes such as with rings, rods, and spheres. For these configurations, the phenomena are always transitory but identifiable because they had been observed in a more stable form during the parallel-plate tests.

Corona rings (toroids) are often used in high-voltage applications. As such, they are positioned at various angles with respect to other objects and to ground. In particular, they are often positioned with the plane of the ring either parallel to ground or perpendicular to ground. There is little quantitative information in the literature on the breakdown of corona rings at 60 Hz, especially for wet conditions, and none at VLF/LF. For this reason, a series of breakdown measurements at VLF were undertaken using both vertical and horizontal corona rings.

Rods with hemispherical end caps and spheres are often used as protective devices (spark gaps) in high-voltage designs. Kotter (1983) gives some breakdown data for rod gaps at VLF and concludes that the breakdown voltages are essentially the same for dry and wet conditions. With this exception, there is little information about breakdown of these devices for wet conditions at VLF. Hence, a series of breakdown measurements were taken using rods with hemispherical end caps.

During 1987, an extensive set of measurements was undertaken at Forestport to determine the flashover, or flare voltage, for a set of linear tubular insulators of different lengths with different size corona rings (Dann, 1987). The corona rings were mounted from the ends of the insulators such that the planes of the rings were parallel. The position of the rings along the insulators axis was adjustable. For each insulator, measurements were taken with the corona rings set in various positions to determine the optimum location of the corona rings.

As a part of one of the earliest design projects undertaken at the HVTF, these data were processed to determine the surface electric field on the corona rings at breakdown. The processed data indicated that the critical gradient (surface field) on the ring at breakdown was nearly independent of ring height. This critical field was plotted versus the minor diameter of the corona ring (Dann & Hansen, 1990). The plot revealed there was a relationship similar to the well-known curve for the corona onset critical field on cylinders (Chapter 6).

The resulting curve was used successfully for insulator design and applies when the corona rings are oriented parallel to each other or to ground. However, later as part of the process of designing a horizontal feed-through bushing, we discovered that for wet conditions this curve overestimates the

breakdown voltages for rings oriented with the plane of the ring perpendicular to the ground. This led to a series of tests designed to more accurately quantify the high-voltage performance of corona rings.

During 1995, a special series of measurements were taken using corona rings of different sizes to develop more accurate empirical design data for high-voltage applications at VLF/LF. This series of measurements used both rings with the plane of the ring parallel to the ground and perpendicular to the ground (vertical ring). At the same time, a set of measurements was taken for vertical rods with hemispherical end caps and one sphere.

This chapter documents the breakdown measurements taken at Forestport using parallel plates, vertical rods with hemispherical end caps and a sphere at the end of the rod, and vertical and horizontal rings. For each configuration, a series of measurements of breakdown voltage were taken at several heights. These measurements were processed to determine the surface field at breakdown using the computer techniques discussed in Chapter 4. The results have been analyzed, and design curves are presented with some theoretical discussion of the measurements. Unlike the results given in Chapter 6 for wires pipes and cables, there are few similar results for rings at power system frequencies in the literature.

This chapter also includes the results of measurements of the breakdown of parallel plates with and without an insulator present and also the minimum current required to sustain an arc across a gap at VLF/LF.

PARALLEL PLATES

For many types of insulators, including BIAs, the optimum design results in a uniform field between the high-voltage electrode and ground. This corresponds to the classic parallel-plate geometry used for testing breakdown strength of gases. However, for application to VLF/LF antennas, the most important breakdown strength involves spray-wet conditions, corresponding to wind-driven rain. There is little information in the literature quantifying the breakdown strength of air under these conditions. In an attempt to determine this important parameter at VLF/LF, a set of tests was undertaken using a parallel-plate setup. Tests were done in August 1984 and repeated again in March 1995 after a calibration error in the high-voltage measurement procedure was corrected.

Three types of tests were performed for parallel-plate configurations. The objective of the first type of test was to determine the effect of dripping water on the breakdown voltage when an insulator was in place. For this test, a single post insulator was set in the center of the parallel plate setup, and the underside of the top plate was sprayed from beneath with a fine stream of water. This resulted in the insulator being wet and the air between the plates being filled with drops from the spray and from drops falling from the top plate.

The objective of the second test was to determine the effect of the dripping water without the presence of the insulator. The test configuration was the same except that the center post insulator was removed.

The purpose of the third test was twofold: (1) to explore the effect of water streamers on breakdown strength and (2) to measure the breakdown strength of air at VLF in the presence of dripping water. High-voltage testing had shown that flashover for wet conditions usually occurs where water flowing off the object forms streams (streamers). In order to investigate the effect of streamers and drops, the parallel plate configuration was modified to allow a single fine stream of water to pass through the center of the high-voltage plate to a grounded plate below.

Test Configuration 1: Parallel Plates with Insulator

This test was only performed once in 1984 and was designed to measure the surface-gradient limit on a petticoated insulator. The test configuration is illustrated in Figure 8-1 and pictured in Figure 8-2. These tests were performed with a single 7-inch long insulator placed in the center of the circular top plate. The insulator was not an optimum design in that the ends were unglazed and there were sharp threads in the porcelain near the ends of the unglazed region (see blowup in Figure 8-1). Also, the petticoats were small and the insulator had a hole through the center. A water nozzle was used to spray the insulator and the underside of the top plate. The nozzle was arranged so that the water did not wet the 2-inch minor diameter corona ring that bounded the upper plate.

The results of the tests are somewhat surprising in that it appears that for both dry and spray-wet conditions the flashover level is not limited by the insulator. Although the insulator itself was not the best, the configuration was optimal for test purposes in the sense that the parallel plates resulted in a nearly uniform field. Also, the use of the flat-plate flush against the insulator end eliminates the field concentration caused by an endcap. This is especially critical at the triple interface point where porcelain, air, and conductor meet.

Even though the flashover level did not appear to be limited by the presence of the insulator, another phenomenon was observed, involving the insulator that did limit the operating voltage for spray-wet conditions. This consisted of a hot orange-yellow flame, or arc, on the insulator surface that appeared when the voltage approached flashover voltage. The flame started in the region of the sharp threads and extended to the petticoated region. The fact that the flame started in the area of the sharp threads indicates that the level at which it starts involves the details of insulator shape.

The phenomena observed during the parallel plate with insulator test are listed below in order of occurrence with increasing voltage:

1. Flickers of light on drops just as they fall from the upper plate, just barely visible as dim white flashes to the dark-adapted eye. These are easier to see with binoculars.
2. Flashes from drops as they leave the upper plate, generally bluish or purple. They form about ½ inch below the upper plate. It appears as if the drips have several tails (3 or 4) going into corona and repelling each other slightly.
3. Bluish spot of corona appear in the area of upper threads of insulator. This is probably because of the field enhancement due to the very fine threads that have sharp points.
4. The bluish spot of corona grows to form a series of vertical bluish purple lines on the area of the upper threads. This corona appears to heat the insulator only slightly and was deemed non-detrimental to the insulator. Also, this corona would not occur at this level on an insulator with no threads.
5. Purple streaks on the drops falling from the upper plate not particularly near to the insulator body, similar to the flashes but longer. They appear to be a continuous but slightly jagged line that extends downward. The length of these purple streaks varies somewhat when the voltage is fixed, but their average length increases as the voltage increases.

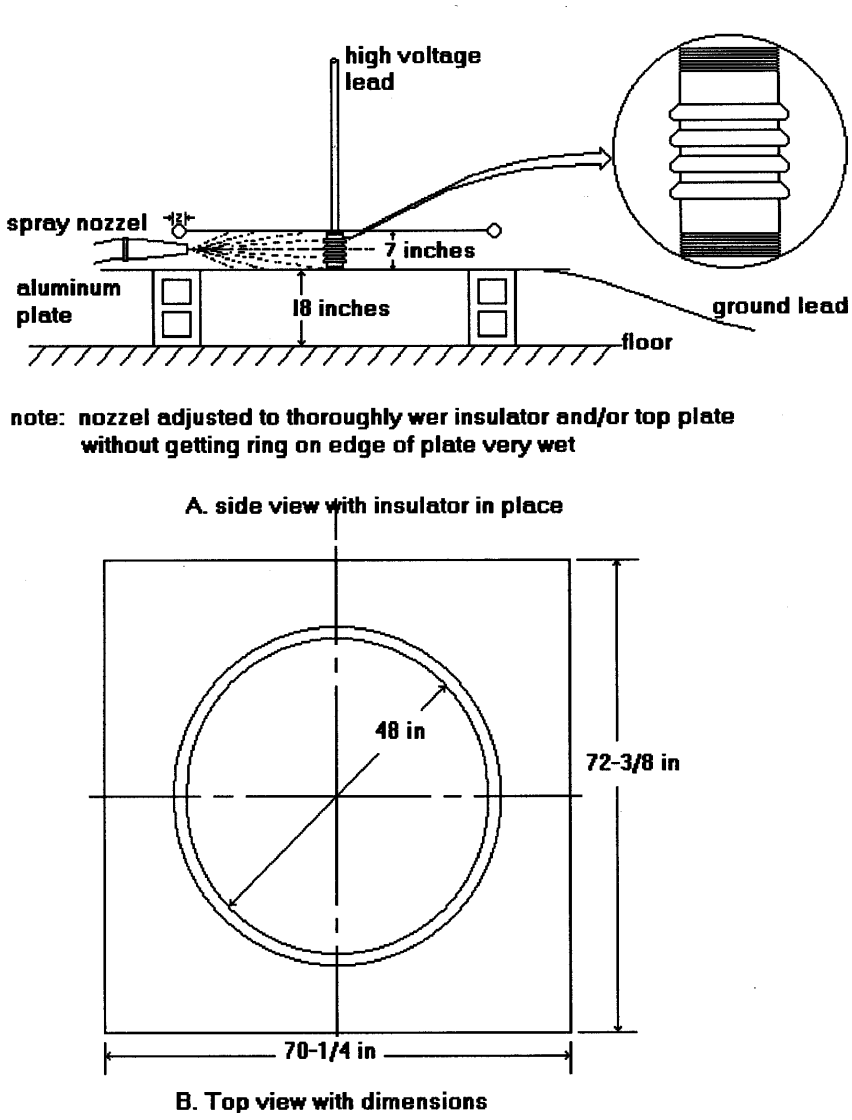

Figure 8-1. Drawing of parallel-plate test setup with single insulator.

6. Surface flame or arc forming on the insulator body. An orange-yellow flame forms between the blue glow on the upper threads and the top of the petticoats. This flame has the appearance of an arc. It is stable and it actually flows across the space between the tips of the petticoats. This phenomenon is unacceptable for operation because the arc is very hot, and any contact with the insulator would lead to localized heating that will crack or even melt or burn the insulator. The orange-yellow flame on the surface of an insulator cannot be allowed for VLF/LF insulator designs because it will eventually destroy the insulator. However, the level at which this phenomenon occurs is a function of the insulator shape. The level will be higher for insulators used in operational VLF/LF installations since they do not have threads and the petticoats are much wider and larger in extent.
7. Flashover. The location of the flashover varied between the flame on the insulator surface and flares on falling drops not necessarily near the insulator body. The flashovers were split

approximately evenly between these two processes, indicating that the flashover limit for the wet insulator was essentially the same as for the gap alone in the presence of falling water drops.

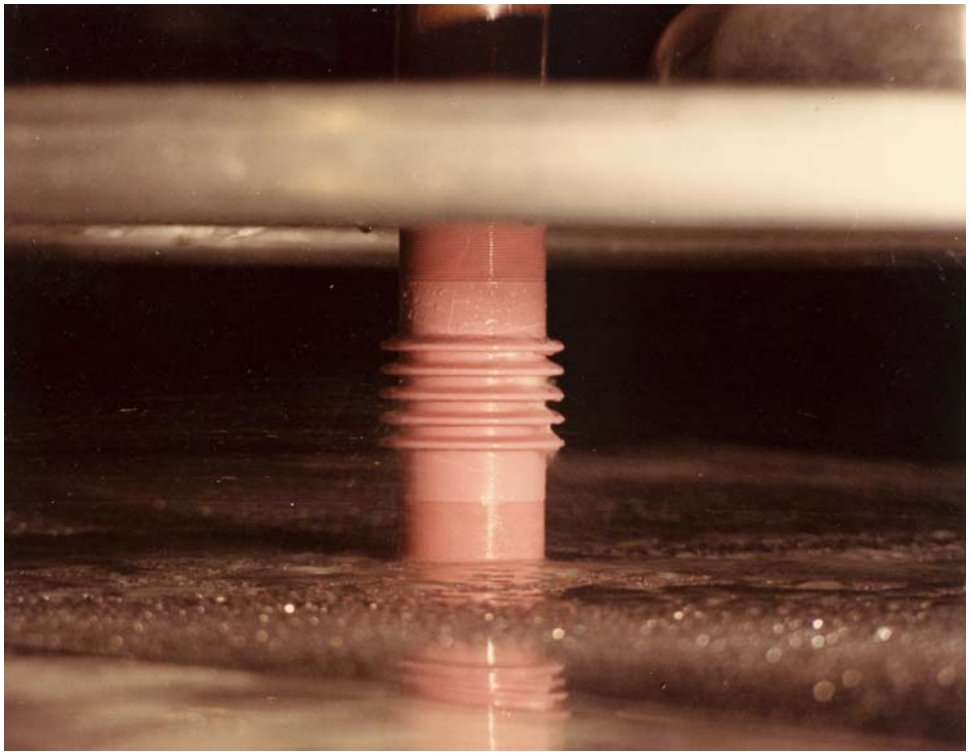

Figure 8-2. Picture of parallel plate setup with single insulator.

Table 8-1 summarizes the observed voltage levels corresponding to these phenomena.

Table 8-1. Test 1, Parallel plates insulator in place 7-inch separation (voltages in rms).

A. Dry, f = 28.933 kHz, all numbers are the average of five readings.			
Corona Inception	90.3 kV~	5.08 kV/cm	
Corona	87.9 kV	4.94 kV/cm	
Extinction	113 kV*	6.36 kV/cm	
Flashover			
~ Corona formed between threads in the middle of the lower threaded section.* Flashovers were between plates away from insulator. There was one possible flashover inside the insulator, but this could not be verified and was not recorded.			
B. Wet			
Corona Inception	14.34 kV	0.807 kV/cm	Falling water drops just after they start
Corona Extinction	14.3 kV	0.804 kV/cm	
	17 kV	0.956 kV/cm	Occasional falling drops. Drops go into corona for first 1/3 of way down.
	30 kV	1.69 kV/cm	Frequent falling drops in corona from plates and insulator petticoats.
	45 kV	2.53 kV/cm	3-inch streamers form associated with drops falling from upper plate.
Corona inception on insulator body	49 kV	2.76 kV/cm	Purple vertical lines crossing upper threaded section.
Corona extinction	30 kV	1.69 kV/cm	Vertical lines disappeared, single spot remains.
	26.5 kV	1.49 kV/cm	Single spot extinguished.
Flashover	51 kV **	2.87 kV/cm	First on streamers associated with water drops falling from plate, then from an orange streamer on the surface of insulator bridging petticoat gaps stopping for a while at bottom petticoat, then flashing.
** Flashover 10 times at this level about equally distributed between drops and insulator. Further attempts at flashover testing were aborted because the insulator became wet inside and afterwards flashed inside at a much lower level.			

Note that while attempting to take a series of flashover readings to average, the insulator flashed over inside. The test setup was disassembled and water was discovered within the insulator. The insulator was warm to touch, but not hot. This was attributed to either heating of the water, the surface flame, or the internal flashover.

Test Configuration 2: Parallel Plates with Spray from Beneath

This test configuration (Figure 8-3) had the same geometry as test 1 except the insulator was removed. The object of the test was to determine the limit of high-voltage breakdown at VLF for air under spray-wet conditions. This test was also only performed in 1984.

The following phenomena were observed with increasing voltage:

1. Flickers on falling drops just as they separated from the upper plate, just barely visible as white light to the dark-adapted eye. This corresponds to sparklers as defined in Chapter 6.
2. Flashes from drops as they leave the upper plate, generally bluish or purple, forming 1/2 inch or so below the upper plate. Sometimes it appears as if the drops have several tails (3 or 4) going into corona and repelling each other slightly. These correspond to the intermittent purple streaks described in Chapter 6.
3. Longer purple streaks forming on the drops falling from the upper plate. They start similar to the flashes, slightly below the plate, and extend downward a distance that grows with increasing voltage.
4. As the voltage increases, the purple streaks eventually reach the ground resulting in flashover.

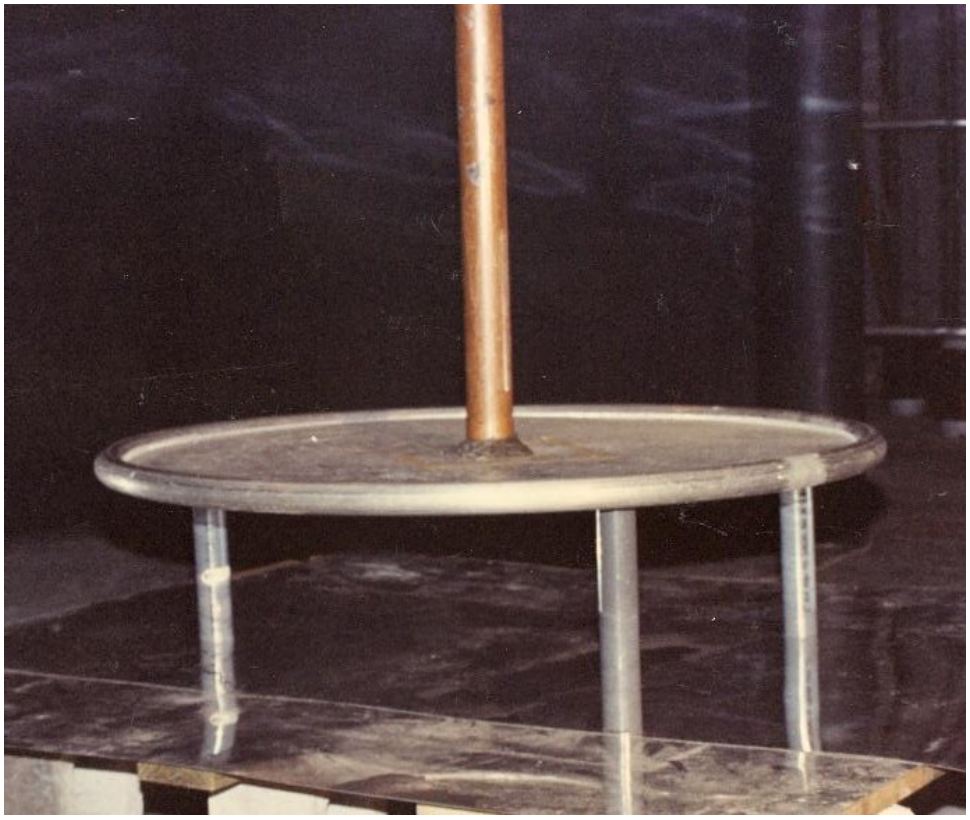

Figure 8-3. Parallel plate test setup without insulator.

Figure 8-4 is a picture showing many purple streaks and a single flashover. The nozzle and water spray can be seen near the bottom of the picture, lighted by illumination from the flashover.

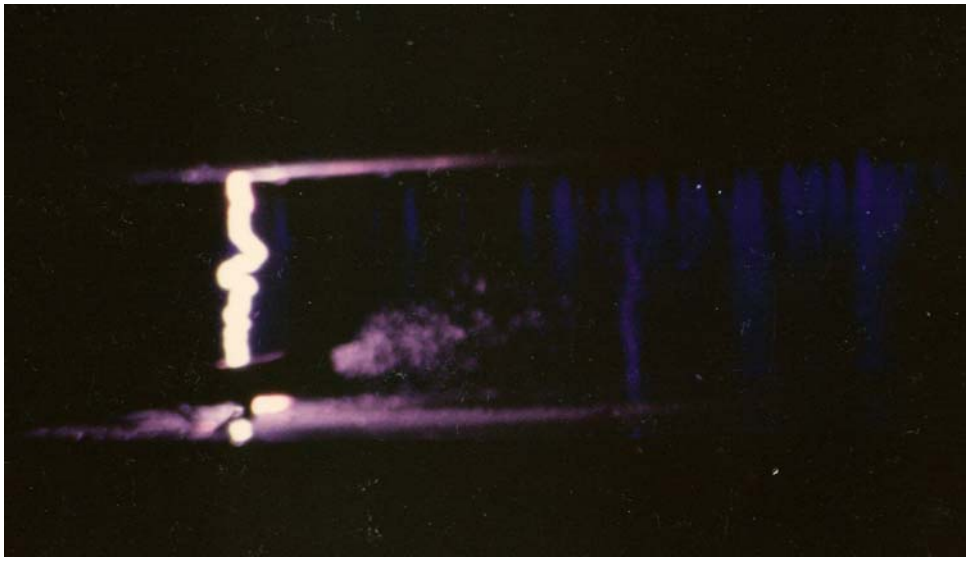

Figure 8-4. Parallel plate setup with spray nozzle showing blue streaks and flashover.

The test results are summarized in Table 8-2. The flashover voltage for these conditions was essentially the same as with the insulator present. This is somewhat surprising in that it appears that the surface gradient on the insulator is not the limiting parameter for flashover under spray-wet conditions.

Table 8-2. Test 1, Parallel plates, no insulator, spray from beneath 7-inch separation (voltages in rms).

Wet, f = 28.9 kHz			
Corona Inception	14.4 kV	0.810 kV/cm	Falling water drops just after they start
Purple Streaks	23.5 kV	1.33 kV/cm	Occasional purple streaks 1-inch long, starting 1-inch below the top plate.
	28 kV	1.57 kV/cm	Occasional purple streaks 2 inches long.
	29 kV	1.63 kV/cm	Occasional purple streaks 4 inches long.
	36 kV	2.25 kV/cm	One or more 4-inch purple streak at all times.
Flashes on bottom	40 kV	2.25 kV/cm	Little pinpoints of light from the splashes of water on the bottom plate.
Corona on spray	45 kV	2.53 kV/cm	Water spray in corona at the nozzle.
	46 kV	2.59 kV/cm	Flashover to nozzle (moved nozzle).
Purple streaks	>46 kV	> 2.59 kV/cm	Longest purple streaks go almost all the way to ground, encased in a glow about 1-inch diameter.
Flashover	51.4 kV	2.89 kV/cm	Average of 5 flashovers.

Test Configuration 3: Parallel Plates with Single Water Stream

The purpose of this test was twofold: (1) to explore the effect of water streamers on breakdown strength and (2) to measure the breakdown strength of air at VLF with dripping water. This test was originally done in 1994 with parallel-plate spacing of 7 and 14 inches and later in March of 1995 with parallel-plate spacing of 7, 14, and 21 inches. The tests were all performed for frequencies near 29 kHz.

For this test, the parallel-plate test setup was modified by loading the top plate with water held by the corona ring around the edge of the plate. A fine hole (pin-hole) was punched through the center of the plate to let a single stream of waterfall onto the flat ground plate beneath (Figures 8-5 and 8-6). The water flow rate varied depending on the amount of water in the reservoir on top of the plate.

With no voltage present, the water streamer appeared as follows. When the reservoir was full, a smooth stream of water exited the hole and seemed to be continuous from the top plate to the bottom plate, and it had the appearance of laminar flow from the top most of the way down. As the water supply depleted, the flow rate slowed and there appeared an identifiable transition region where the water stream changed from laminar to turbulent flow. As the flow rate slowed further, the transition point moved up the stream. At slower rates, the stream appeared to break up into individual drops below the transition point. These drops fell straight down. As the flow rate slowed more, the streamer would break up into drops at a point closer and closer to the top plate. When the reservoir was nearly empty, groups of drops and finally only single drops would drip from the hole.

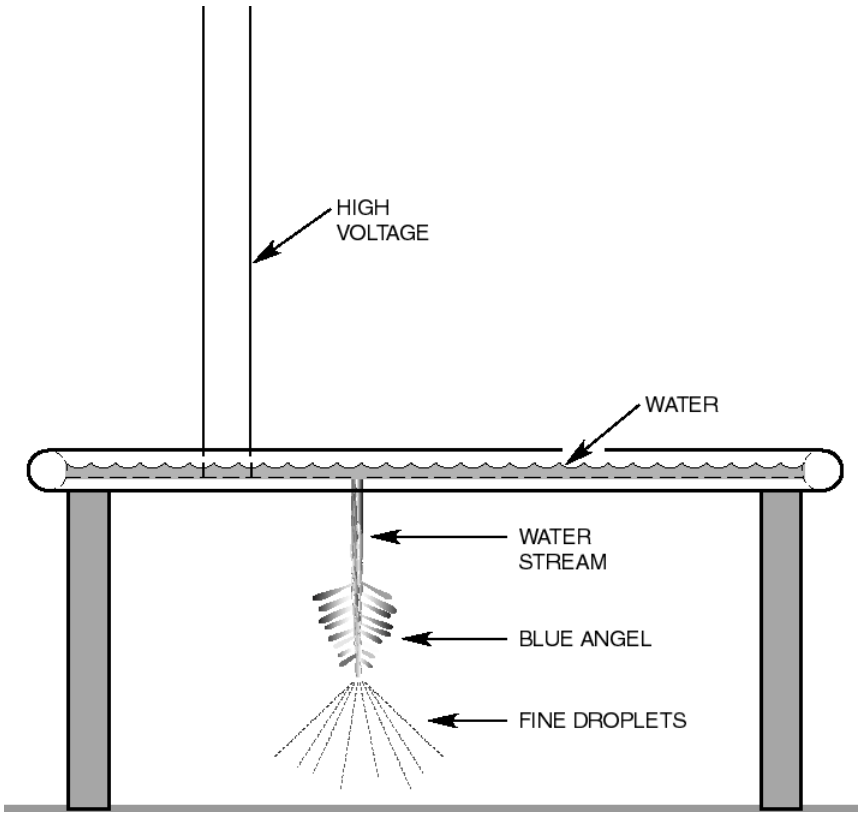

Figure 8-5. Parallel plate showing water stream.

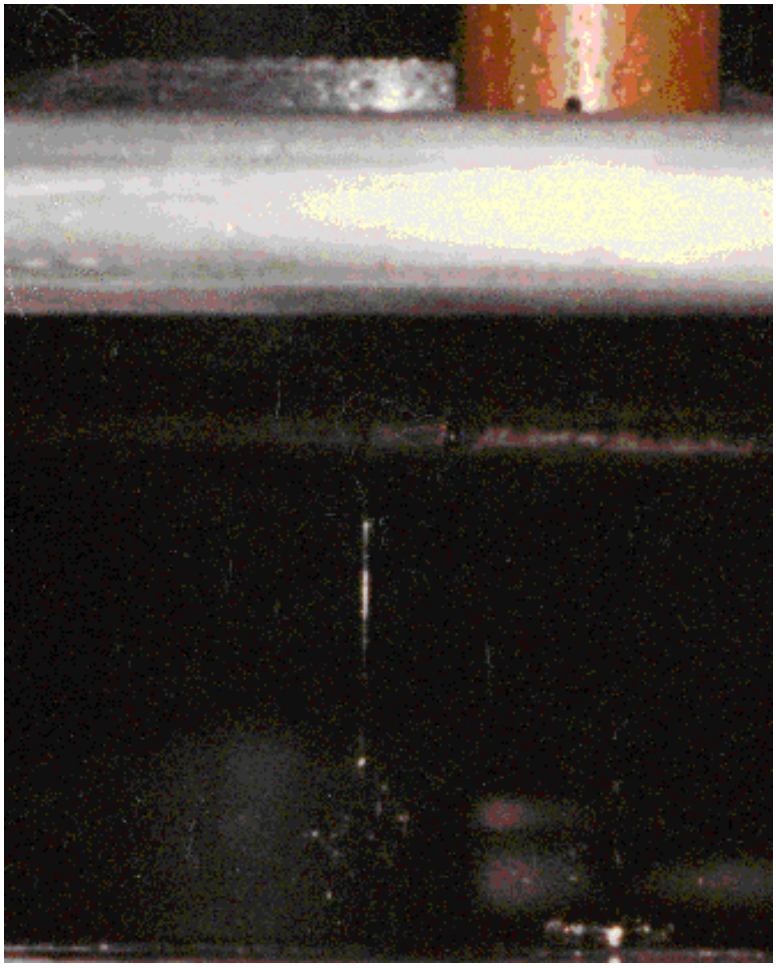

Figure 8-6. Parallel-plate picture of water stream showing laminar flow and breakup.

Application of voltage changed the behavior of the water stream tending to make the water stream thinner and causing the laminar flow region to become longer and to occur at much lower flow rates than before the voltage was applied. High voltage levels gave rise to some very unusual phenomena. These phenomena were stable in the parallel-plate configuration and easy to observe. The observed phenomena, listed below, were a function of both water flow rate and voltage. The major headings in the list below follow the sequence from greater to lesser flow rates, corresponding to the reservoir emptying. Under each heading, the phenomena are listed with increasing voltage.

Single Continuous Stream (Greatest Flow Rate)

This flow rate corresponded to the reservoir being full. The phenomena observed for this case followed the applied voltage and appeared to be controllable. With no voltage, there was a smooth steady stream that was laminar on the upper portion, having a transition to turbulent flow in the mid-portion. When the voltage was applied, it could be seen in lighted conditions that the stream became noticeably thinner and the transition region moved down. When the voltage increased enough, the stream appeared to be laminar for the entire extent to the bottom plate. The picture in Figure 8-6 was taken with the voltage on and shows the laminar flow region extending down several inches from the top plate.

No corona was apparent at low voltages even in the dark. As voltage was increased, the transition region from laminar to turbulent flow, which appeared to be about 2 to 3 inches in length, was enveloped in a shroud of purple corona. This corona did not appear to affect the water stream in any way. It first appeared about ½ inch below the upper plate. There was no sound associated with the corona. As the voltage increased, it clearly had the form of a cone and looked rather like a Christmas tree suspended in space. The position of the surface of the cone appeared to shimmer slightly and we named the cone the Blue Angel. Beneath the Blue Angel, the water column broke up into fine drops that dispersed rather than falling straight down. The breakup of the water column can be seen in Figure 8-6.

The Blue Angel is depicted in Figure 8-5 and pictured in Figure 8-7. As the voltage increased, the Blue Angel moved down the column. The position of the cone on the water column could be adjusted by controlling the voltage. However, it tended to move up the column as the flow rate decreased.

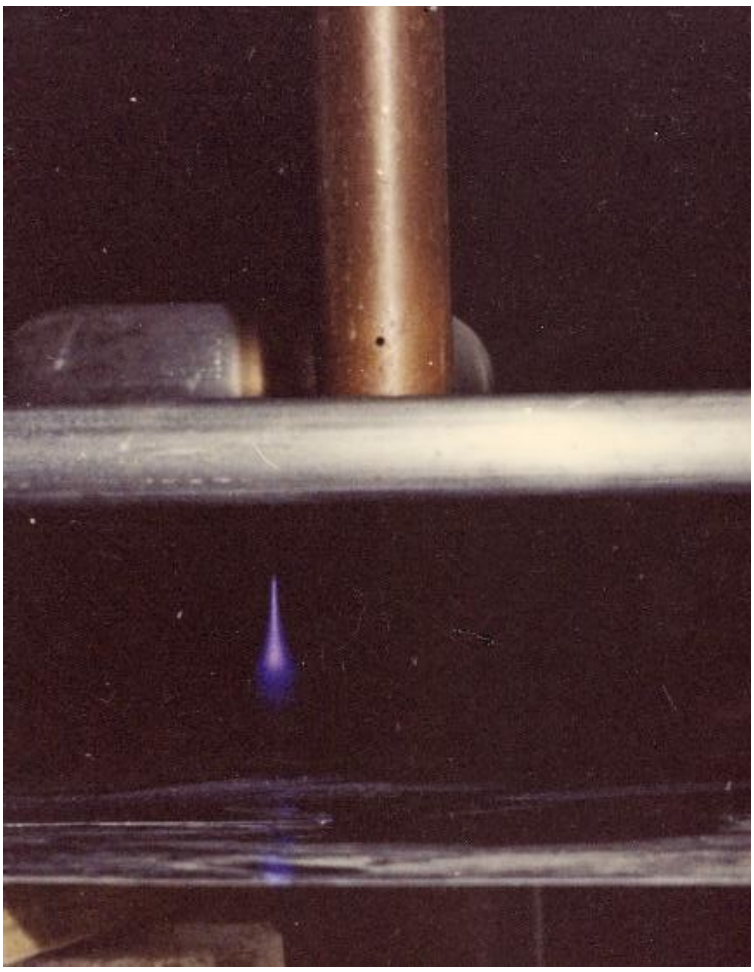

Figure 8-7. Parallel-plate test setup showing Blue Angel.

The Blue Angel apparently forms in the region where the water flow changes from laminar to turbulent. The water flow rate and the applied voltage affect the location of this region. The effect of voltage is due to the dielectric force on the water from the electric field, with possibly some contribution from the magnetostrictive force due to the current flowing in the water column, both of which tend to constrict the water column. Thus application of the high voltage constricts the water column,

causing the laminar/turbulent transition to move down the column. The laminar/turbulent transition is marked by a blue glow around the column (glow discharge), and below that the corona spreads slightly in a cone (Blue Angel). Close inspection with binoculars revealed that this glow and cone is due to tiny drops of water being shed by the stream. These drops are repulsed from the main stream by the electrostatic force, forming a cone.

Occasionally, water dripped from a leak in the top plate about 3 inches away from the water stream. When such a drop was in flight, it appeared to repulse the stream. The Blue Angel seemed to disappear when the drop pushed the water stream away. The stream returned to normal once the drop splashed on the bottom. There was audible corona associated with the drop hitting the bottom.

The location of the glow moved down the column as the voltage increased. The voltage could be increased to the point where the glowing column reached the bottom plate. When this happened, little legs of bright purple formed around the outside edge of the bottom of the cone. These purple legs wiggled around, giving the cone the appearance of dancing.

Further increasing the voltage caused the glow to move down further, eventually disappearing. At that point, the water stream was continuous, apparently laminar for the whole extent between the top and bottom plate. For this condition, the voltage could be increased well above the level at which flashover occurred when the stream was not continuous or if falling drops were present. This is attributed to the fact that the continuous water column acts like a resistor, uniformly grading the field between the plates.

For this condition, RF current flows through the water stream, heating the water as it falls. This was evidenced by steam that arose from the puddle formed on the grounded plate. The water starts being heated when it exits the hole in the top plate, and is heated continuously as it falls. The temperature is greatest at the bottom of the column. This temperature depends on many variables, including the amount of water in the column, the length of time it takes to fall to the bottom plate, the RF current, and the conductivity of the water. The power dissipated in the stream was estimated assuming a column with 1/8-inch diameter and water resistivity of 200 Ohm-meters as measured for the Forestport water system. At 55 kV, the 7-inch-long column dissipated 650 watts, and at 110 kV the 14-inch-long column dissipated 1315 watts.

At this level, occasional drops falling from the top surface formed the purple tube of corona that we called purple streaks, which caused an audible hissing sound. Flashover occurred just after the drop hits the bottom. Flashover only occurred when a drop fell. The stream remained steady even when a flashover occurred.

As the voltage is increased further, the heating increases and eventually a level is reached where the water in the column boils away just before it hits the bottom plate. Once this happens, there are a few discharges that occur in the bottom inch or so of the column, followed by complete breakdown (flashover) across the gap, accompanied by a loud discharge. The flashover completely disrupts the water stream and flashovers occur continuously across the plates until the voltage is reduced or removed and the water stream becomes stable again.

Intermediate Flow Rates

At intermediate flow rates, there was a visible point within the water stream where it changed from laminar to turbulent flow. Farther down in the turbulent flow region, the water stream appeared to break up into individual drops. The application of voltage noticeably decreased the diameter of the water streamer and increased the length of the laminar flow region.

As the voltage increased, the Blue Angel formed in the transition region between the laminar and turbulent flow. The location where the turbulent flow breaks into individual drops was somewhat below the laminar/turbulent transition. As the voltage increased, the drops would appear to repel each other and would fall away from the stream in trajectories that formed the somewhat conical-shaped region. Some distance beneath the Blue Angel, the water stream would dissipate. At lower flow rates, the drops form just under the Blue Angel, and the water stream disperses in a cone of very fine drops as shown in Figures 8-5, 8-6, and 8-7.

Slow Flow Rates with Only Single Drops

When the reservoir level was low, a single drop or groups of drops would fall. The rate at which the drops fell varied from a few per second to several seconds between drops. For conditions where the drop rate was relatively rapid, or there were groups of drops with no voltage, the application of voltage changed the drops into a thin laminar stream exiting from the hole. Then after a short fall (1 to 3 inches) the laminar stream became turbulent and broke up into drops. The length of the laminar flow section increased with voltage. Further increase in voltage would result in the Blue Angel at the transition region as well as the other phenomena described in the section above on intermediate flow rates.

For relatively slow drip rates (approximately 1 or 2 per second), application of the voltage was observed to constrict hanging drops so that they got thinner and longer, but there was not enough water to form a stream. The phenomena observed are described below. The phenomena were essentially the same as observed when the parallel plates were sprayed from beneath. (See also Chapter 6, Figures 6-8 to 6-11).

Drop Constriction

With increasing voltage, the first phenomenon observed was the constriction of the hanging drops. Next were dim flashes of white light starting a slight distance below the top plate. The distance corresponds approximately to the distance the drop would fall in ½ cycle. These flashes get brighter and move closer to the top plate with increased voltage. We termed this phenomenon “sparklers” (see Chapter 6.). Careful observation indicated that there were sometimes flashes on both the falling drop and the remainder of the drop left on the top plate.

Purple Streaks

As the voltage is increased further, the sparklers grow in length. When they get to be about ½-inch long, they start to turn faintly purple. As the voltage is increased, these become longer and brighter purple. These are called purple streaks and only occur when a drop falls. At the level where they are 1 to 2 inches long, the top of the purple streaks are still separated from the top plate by about one-quarter inch. There are many purple streaks shown in Figure 8-4 (taken while using the spray nozzle). The bottom end of the purple streaks move toward ground at a rate that can be observed by the naked eye. The purple streak appears to be a tail behind the falling drops. There is a definite hissing or spitting noise with each falling drop. Sometimes, when the top plate has a hanging drop and the voltage is turned on suddenly, the drop will appear to be forced off the top plate with a definite “pfsst” sound as though spit off the plate. As the voltage is increased, the streaks get longer and longer. Careful observation revealed that the bottoms of the purple streaks have miniature, slightly yellowish leaders, extending beyond their ends (see Figure 6-9).

Flashover

When the voltage is further increased, the purple streaks become longer and longer approaching the bottom plate. At voltages near flashover, the purple streak formed by the drop falling would terminate in a glowing cone of partial discharge at the bottom. There is a threshold voltage below which the purple streaks approach the bottom plate and the cone forms, and above which flashover occurs with each falling drop. Flashover is accompanied by a bright flash and loud bang. When the voltage exceeds the threshold, flashover occurs with each falling drop but does not occur except when a drop falls. Each falling drop is accompanied by the bright flash and loud bang associated with flashover.

Flashover from a single drop is pictured in Figure 8-8, and a time exposure for several flashovers is shown in Figure 8-9. In lighted conditions, it was clear that the drop stays together all the way to the bottom plate, with the purple streak appearing behind the drop. When the drop hits bottom, there immediately follows the bright white flashover and accompanying loud bang.

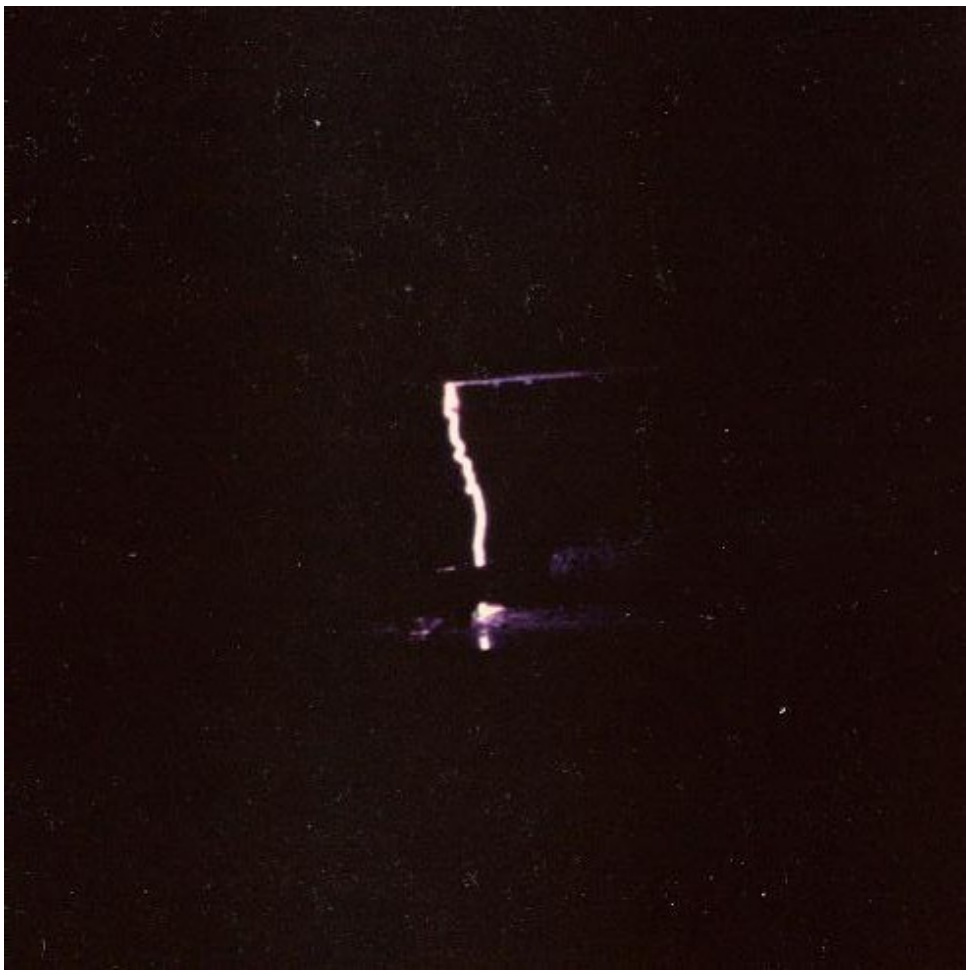

Figure 8-8. Parallel-plate test setup showing flashover on a single drop.

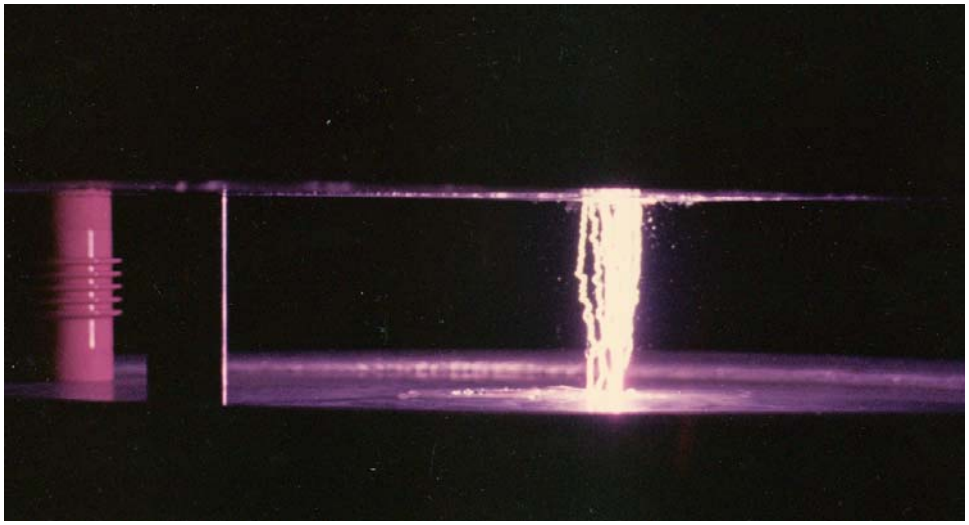

Figure 8-9. Parallel-plate test setup with multiple flashovers.

The voltage at which each of these phenomena occurred is given in Tables 8-3 and 8-4.

Table 8-3. Parallel-plate test with 14-inch spacing. (Excerpt from logbook 15 March 1995)

Voltage kV	Field kV/cm	Description
0	0	4-5 drops per second.
78	2.19	Turns into a stream, laminar flow, for 1 inch then comes to a point and tries to form a cone (purple) followed by only small drops (mist).
90	2.53	The laminar stream is 2 inches long, then the cone is wider.
100	2.81	The laminar flow part is now 4 inches long and the cone starts to glow and oscillate, fine mist below the cone.
118	3.32	The laminar stream goes down 2 inches smooth and clear. The next 2 inches is faintly glowing blue around the outside of the stream. Below that the blue cone appears 1 inch long and ½ inch wide.
140	3.94	Flashover.
0	0	Thin continuous stream.
93	2.62	Purple glow in the lower part of the stream, 2 inches long and 2 inches above ground plane.
131	3.68	Cone leaped to the top, broke up and then flashover.
0	0	Heavy continuous stream, turbulent flow.
96	2.70	Stream smoother.
107	3.01	Steam rising.
129	3.63	Stream starts glowing.
137	3.85	Multiple violent flashovers.

Table 8-4. Parallel plate test with 21-inch spacing. (Excerpt from logbook 15 March 1995)

Voltage (kV)	Field kV/cm	Description
0	0	Laminar flow.
170	3.19	Some flashes off rings at first, then they stopped.
186	3.49	Steam forms at bottom of water column.
197	3.69	Column starts to break up occasionally in the bottom inch. Then with a slight increase in voltage the bottom inch starts to flash over, followed by disruption of the stream and flashover across the entire gap. The column is definitely smoother when the voltage is on.
0	0	Groups of drops.
150	2.81	Goes laminar but in spurts corresponding the original groups of drops. Spreads out about 3 inches below the plate and then goes into a small cone.
0	0	Approximately 4 drops per second.
113	2.12	Laminar flow.
>113	>2.12	Blue Angel forms on the water stream, a short distance below the top plate.

Breakdown Strength of Air with Falling Drops

A series of tests was performed to determine breakdown voltage when only single falling drops were present. These tests were carried out for three plate separation distances (7, 14, and 21 inches). For these tests, water level was set quite low so that even with the high voltage only single drops fell through the hole in the upper plate. These tests were done using the standard flashover measurement technique described in Chapter 5 and the results are given in Table 8-5.

Table 8-5. Parallel plate breakdown level when single falling drops were present.

Plate Separation (inches)	Breakdown Voltage (kV) Corrected to STP (25° C)	Electric Field Strength (kV/cm)
7	53.4	3.00
14	112.6	3.17
21	171.0	3.21

The data in Table 8-5 were generated using the parallel-plate configuration with the water adjusted so that only individual falling drops were present. When more water was present a column of water formed part way across the gap and the breakdown level was more variable, sometimes a little more and sometimes a little less than that given in Table 8-5. When the configuration was changed to spray onto the bottom of the top plate, the breakdown level was also variable, but when drops were falling from the top plate, the breakdown voltage was essentially the same as given in Table 8-5.

The data in Table 8-5 indicate a tendency for the breakdown strength to increase with plate separation. There is no theory for the breakdown strength of air when falling water drops are present. The theory for dry air (Chapter 2) indicates that the breakdown strength for parallel plates decreases, asymptotically approaching a constant value of 17.1 kV/cm rms (24.4 kV/cm peak) as the separation increases. The data presented above indicate that for wet conditions the opposite is true, as breakdown strength increases towards an asymptotic limit for large spacing. For spray-wet conditions at 29 kHz, this limit is approximately 3.25 kV/cm. This value is close to the asymptotic value determined for the corona onset level on cylinders under wet conditions in Chapter 6, which was 3.1 kV/cm.

VERTICAL RODS AND SPHERE

This section gives the results of the measurements of the breakdown level for rods with hemispherical end caps above ground. One set of measurements was taken using a sphere larger than the rod. Breakdown measurements were made for each configuration at several heights for both wet and dry conditions.

Configurations

Measurements were taken using four different vertical rods with hemispherical end caps and one sphere above ground. The rods had diameters from 1 inch to 8 inches; the sphere had a diameter of 10 inches but was mounted on a 4-inch diameter rod. The test configurations are illustrated in Figures 8-10 through 8-12, with the dimensions labeled. Table 8-6 gives the values of the dimensions for these configurations.

Table 8-6. Dimensions of rod test configurations (inches).

Configuration	L	r_p	r_1	d
1” rod	*	*	*	*
3” rod	112.5	1.5717	1.486	1.5
4” rod	80.0	1.999	2.016	2.5
8” rod	105	4.018	3.99	4.99
10” sphere	96	2.049	5.092	10.00

* See Figure 8-10.

The breakdown voltage was measured for each configuration at several heights above the ground, listed in Table 8-7. The heights were measured from ground to the lowest part of the hemispherical end cap on the rod.

Table 8-7. Heights for rings, rods, and sphere measurements (inches).

6	12	18	24	30	36	48	60	72

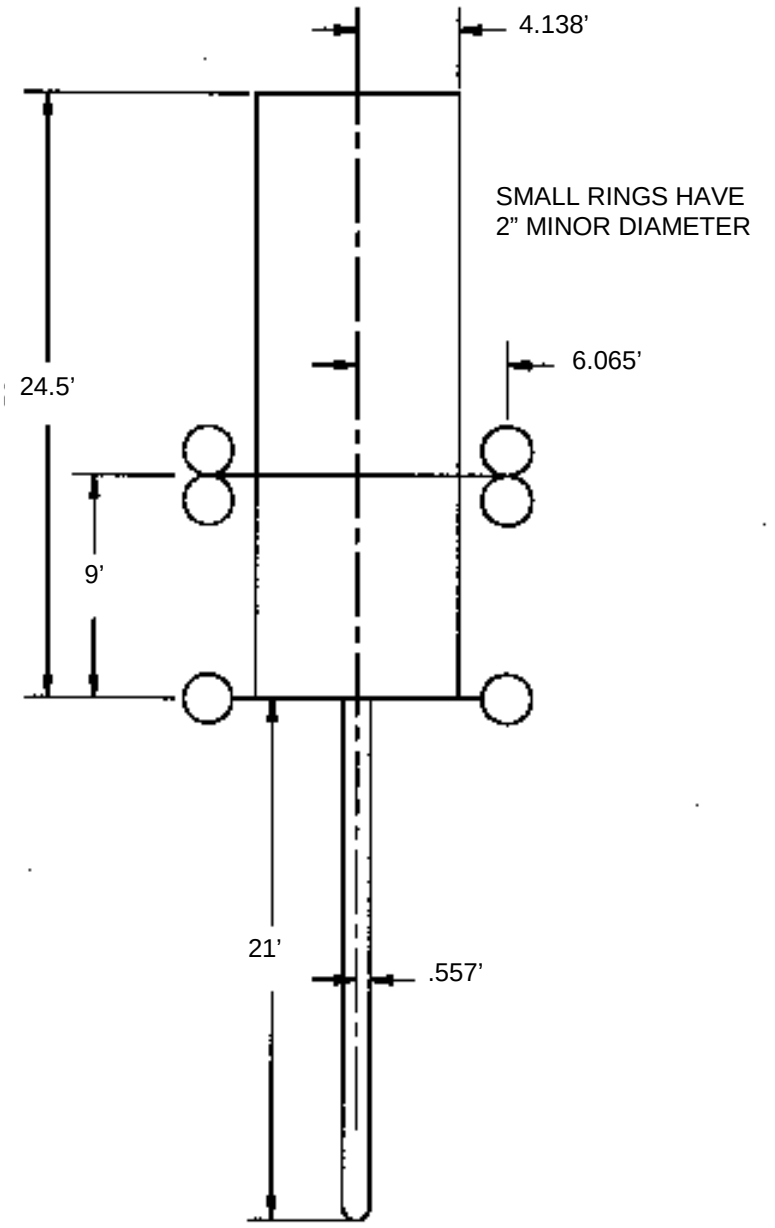

Figure 8-10. One-inch rod dimensions.

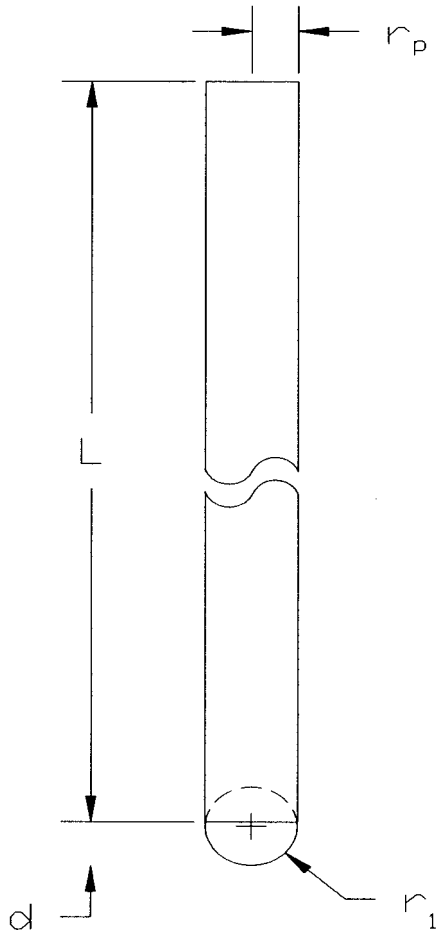

Figure 8-11. General rod configuration and dimensions.

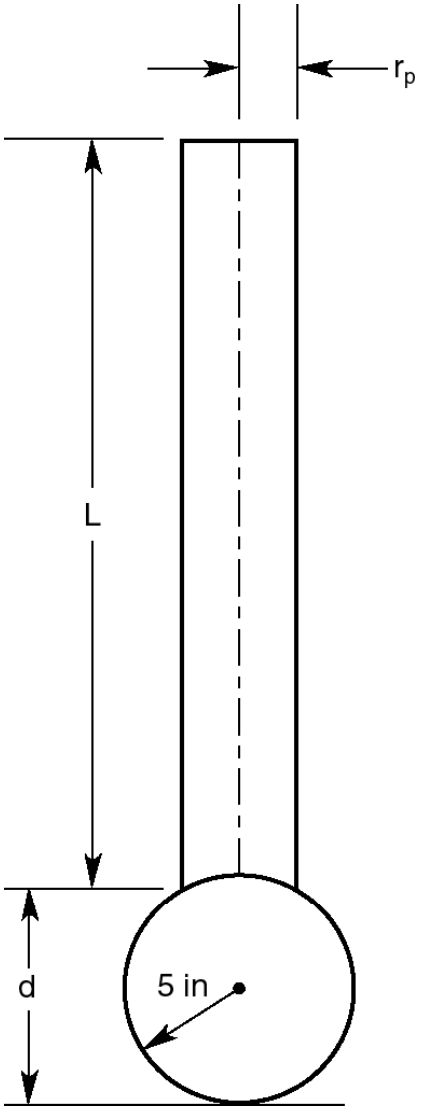

Figure 8-12. Sphere configuration and dimensions.

The rod configurations are rotationally symmetric. The surface fields were calculated using the computer program for rotationally symmetric configurations as described in Chapter 4. The maximum surface field occurs on the tip of the rod. This field normalized to one volt is called G_0 given in dimensions of 1/length. For any given voltage, the field on the tip of the rod is given by multiplying that voltage times G_0.

$$E_{max} = V \cdot G_0$$

where E_{max} is the maximum surface field (rod tip)
V is the voltage on the rod, and
G_0 is the calculated field on the rod tip for unit voltage.

A plot of the calculated values of G_0 for the four rods and the 10-inch sphere are given in Figure 8-13.

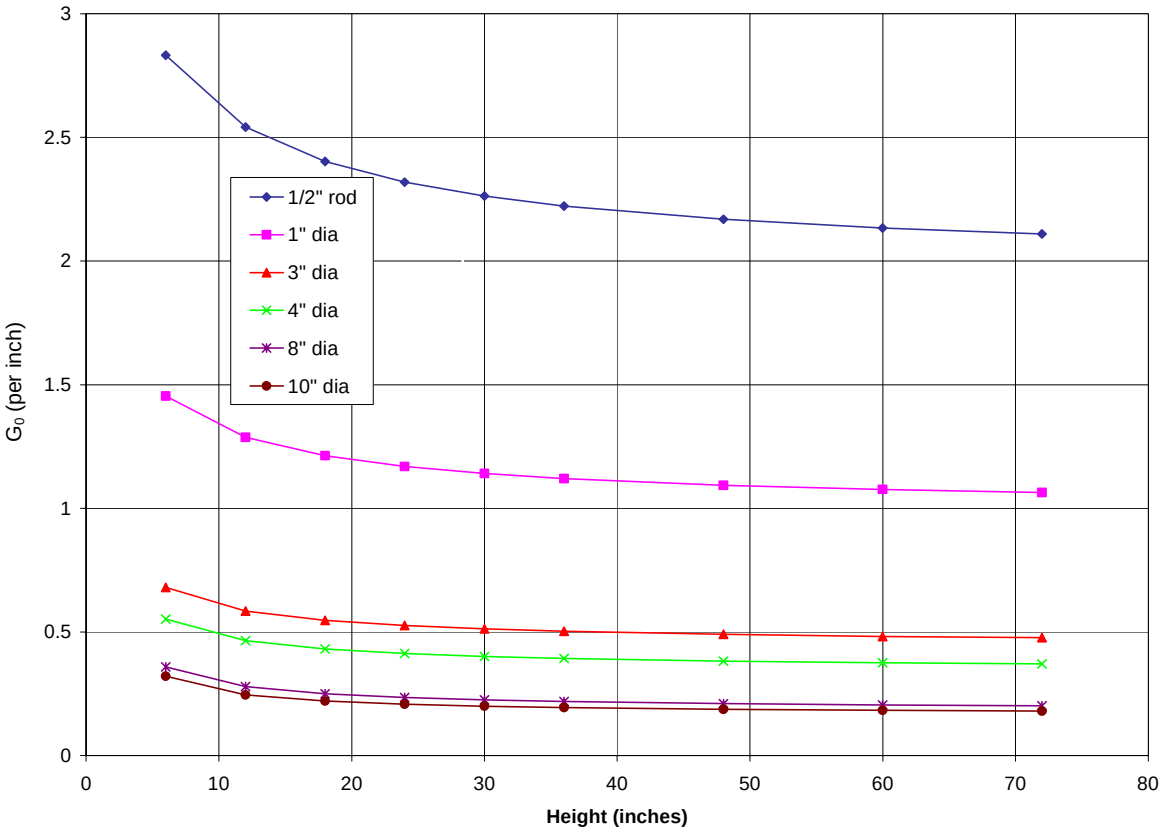

Figure 8-13. G_0 for rods.

Observed Phenomena

Dry

For dry conditions, two breakdown phenomena were observed. Either a flare formed or complete flashover occurred. No corona was observed prior to the flare or flashover. When the rod was near ground, flashover usually occurred first. When the rod was more elevated a flare, as described in Chapter 6, occurred before flashover. With the smaller rods, the flare sometimes took the form of brush corona consisting of many small flares (Figure 8-14). Brush corona formed on the smaller rods, while a single flare formed on the larger rods. Flares draw considerable power from the circuit, and they also increase the capacitance of the circuit. The increased power draws more current from the source, and the increased capacitance changes the resonant frequency of the circuit. Both of these effects tend to reduce the voltage and can limit current in the flare. A flare appears to be an incomplete flashover. However, when a flare is present, the transmitter power can be increased, and eventually flashover will occur if there is enough power available from the transmitter.

Flares only occur for non-uniform fields. For gaps with large spacing having highly non-uniform fields, a flare will form first even for a very low-impedance source. However, for gaps that are not so large, the occurrence of a flare, or flashover, depends on the source impedance, and it is likely that some of the flares observed at the HVTF would be flashovers for a low-impedance source. The flare and flashover levels were both recorded when possible, but for design purposes the limiting phenomenon is taken to be whichever occurred first.

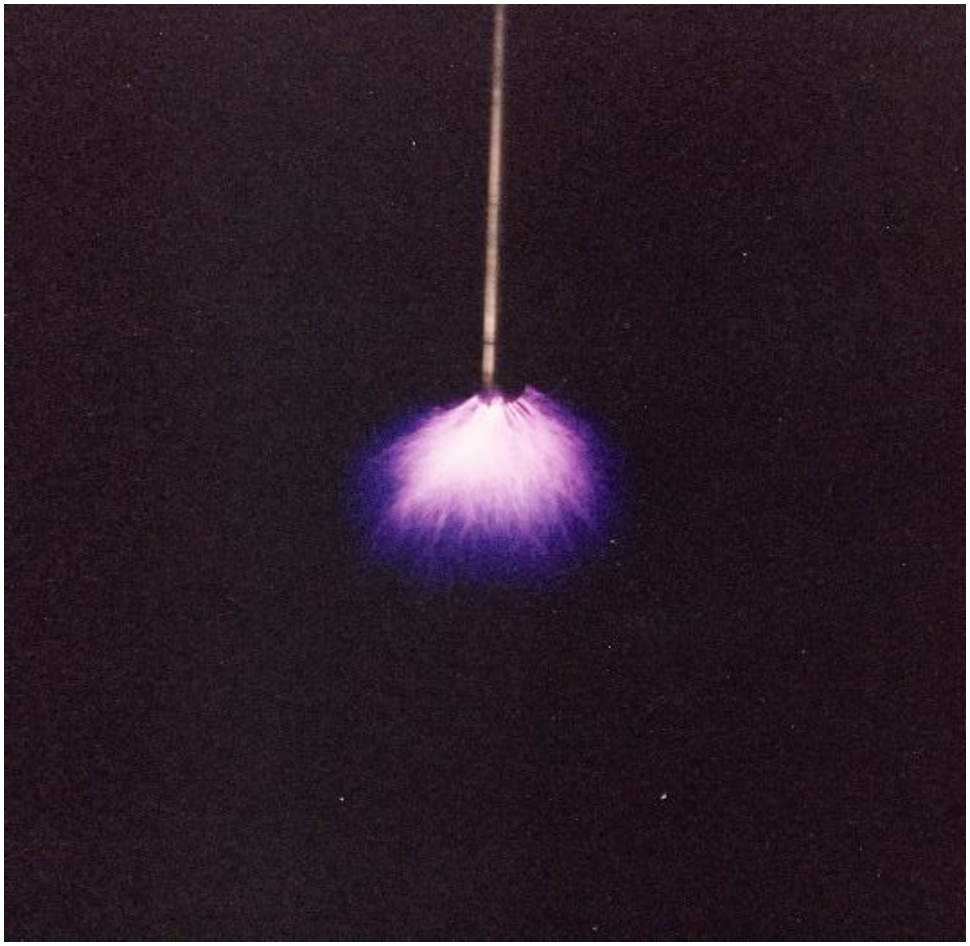

Figure 8-14. Small rod dry in brush corona.

Wet

There were two different methods used for wetting the rod. One experimental method used a reservoir within the rod. The reservoir fed a hole at the center of the hemispherical end cap. A stopcock was used to allow adjustment of the water flow rate. The other method of wetting the rods was to spray the rod externally in the area around the tip simulating windblown rainfall.

For wet conditions, there were many different phenomena observed. Some of them are similar to those described above in the parallel-plate discussion and in Chapter 6. These include drop distortion, sparklers, purple streaks, purple mini-flares, full flares, and flashover. As for dry conditions, flashover occurred first when the rod tip was close to ground, and a flare occurred first when the rod was higher. Flashover, or flare, whichever occurred at the lowest voltage, was used as the limiting phenomena for developing the design curves. However, the primary phenomena used for delimiting the performance for wet conditions is what we called mini-flare inception, which corresponds closely to the criteria used for wet-corona onset on wires as defined in Chapter 6. Wet flare inception was defined as the point when the purple streak on the water drops, or streamers, moved up to the surface, attached themselves to the rod and a white hot spot formed on the surface, i.e., purple mini-flares. This corresponds to self-sustaining corona.

Internal Water

There were some interesting phenomena observed for the setup with the water exiting through the hole at the center of the rod. They were similar to the phenomena observed with the parallel plates. Figures 8-15 and 8-16 illustrate the phenomena that occurred without voltage as function of water rate. Figure 8-15 shows individual drops falling at very low flow rates. Figure 8-16A shows the stream exiting the rod at a moderate flow rate. For this flow rate, the stream is initially laminar and transitions from laminar to turbulent flow at some distance below the rod. Some distance below the transition, the stream breaks up into individual drops. Figure 8-16B shows the long smooth, apparently laminar, stream that formed at higher flow rates.

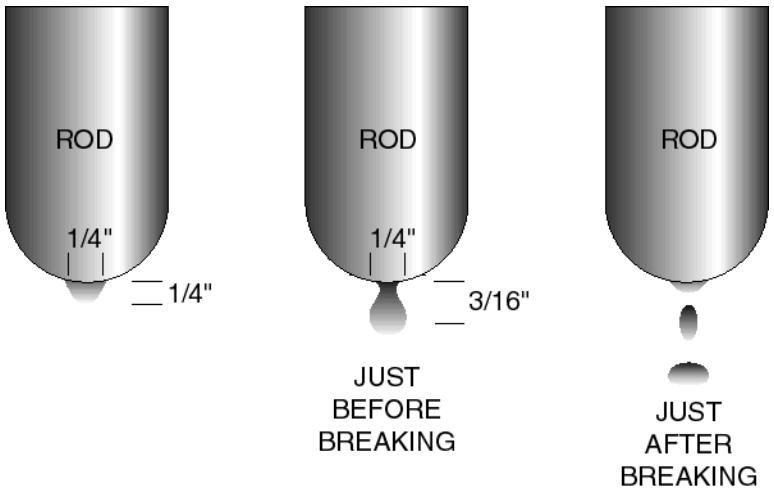

Figure 8-15. Water drops falling off the end of the rod.

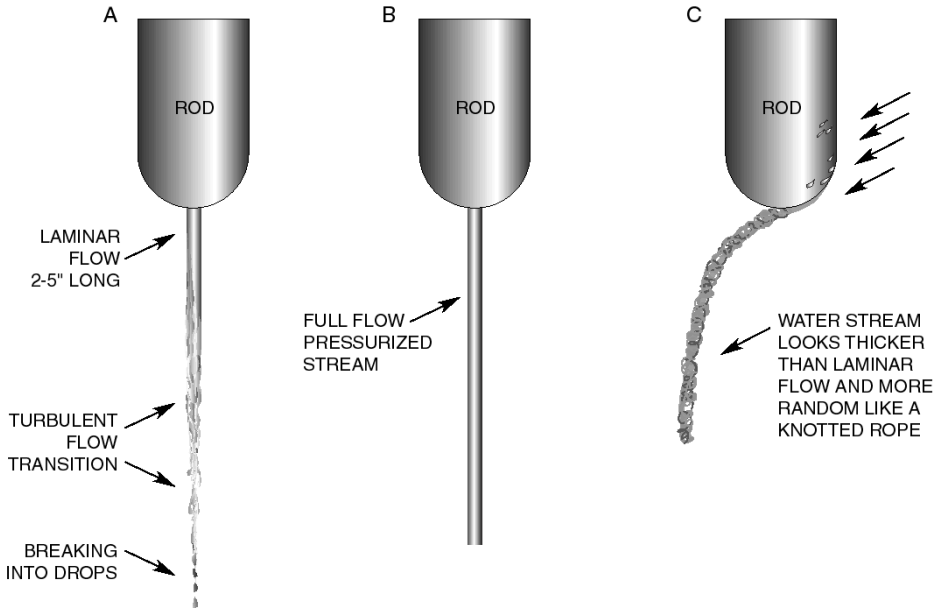

Figure 8-16. Water falling off rod with internal and external water sources.

When high voltage was applied, these phenomena changed depending upon the flow rate. As in the parallel plate test, the application of high voltage tends to constrict the water drops or stream, increasing the length of laminar flow. Sometimes, when only drops were present, the application of voltage would result in a thin laminar stream for some distance below the rod. Also, the drops that formed below the laminar-turbulent transition were smaller when the voltage was applied. The constrictive force increased with voltage holding the laminar flow region together longer. Table 8-8 lists the water phenomena before and after the application of voltage.

Table 8-8. Water phenomena observed before and after application of high-voltage with the water exiting hole in rod center.

Before Application of Voltage	After Application of Voltage (same flow rate)
Single drops falling off at approximately 1 per second	Thin stream of laminar flow about 2 inches long before breaking up into turbulent flow and drops.
Laminar flow exiting the rod followed by a turbulent flow region and then breakup into drops	Laminar flow region becomes thinner and longer. The transition regions into turbulent flow and breakup into drops both move downward with increasing voltage.
Turbulent flow exits the rod followed by breakup into drops	Laminar flow region immediately beneath the rod. Again the transition region boundaries both move downward.
Any flow rate that becomes laminar when high voltage is applied.	With enough voltage, a “Blue Angel” forms. (See discussion below.)

The Blue Angel described in the parallel-plate section above was also observed for the rod with the internal water source. When the voltage was increased enough, a Blue Angel formed for all conditions where there was a region of laminar flow. Below the Blue Angel, the water stream broke up into a spray cone with a half-angle of approximately 20^{o}. The water drops in the cone were very fine and fell to the ground, forming a circular wetted region several inches in diameter as illustrated in Figure 8-17.

The corona around the laminar-to-turbulent transition region appears to be caused by very fine drops breaking away from the surface of the water stream. The drops are charged, and the charged water stream repulses them. The fine drops from the top have farther to fall than the drops from near the bottom, giving the Christmas-tree shape. The spray cone consists of small drops, which form at the bottom of the Blue Angel where the laminar flow region breaks up. These drops repulse each other, resulting in the spray cone.

As with the parallel plate configuration, the distance downstream where these phenomena occurred varied with voltage and flow rate. As the voltage increases, the laminar flow region moves down and the Blue Angel moves downstream. Similarly, increased water flow rate causes the Blue Angel to move downstream and results in a reduction in the spray cone angle. The water drops in the spray cone appear to be larger for increased flow rates.

As the voltage was increased further, either a flare formed or flashover occurred. The flare started from the metal surface of the rod and made a definite hissing sound. A small flare on the 1-inch rod with an internal water source is pictured in Figure 8-18. The flare emanates from a source on the surface, which glows brightly with a whitish purple, sometimes yellow color and appears to be very

hot. When the flare forms, it affects the water stream by repelling it as shown in the figure. With the internal water source, the water stream and flare are fairly stable, and the Blue Angel and spray cone can be readily observed. For the larger rods the flare did not form until a higher voltage was reached, and they were larger, similar to those shown in Figures 6-14 and 6-15, and made a roaring sound.

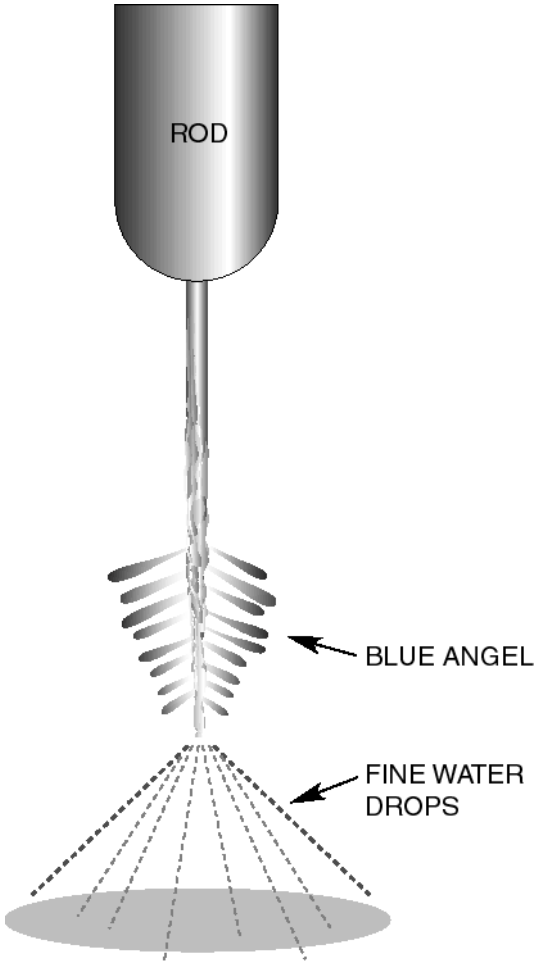

Figure 8-17. Drawing of rod with internal water source showing stream and Blue Angel.

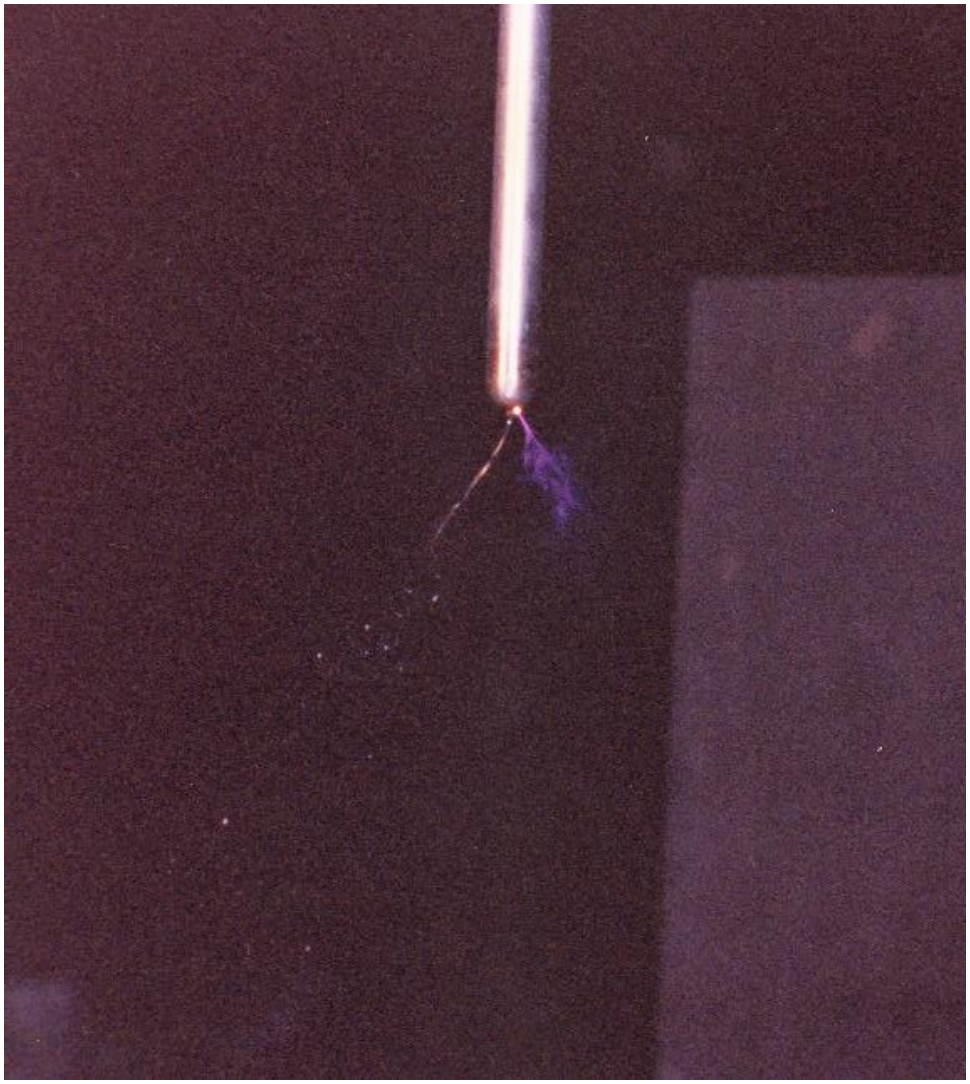

Figure 8-18. One-inch rod with internal water source exhibiting Blue Angel and a flare.

External Spray

Most of the rod measurements were made with external spray, corresponding to outdoor applications. For this case, the water does not run smoothly off the end of the rod, and there were some additional interesting phenomena. The water forms turbulent streamers that run off the bottom of the rod slightly to one side (Figure 8-16C). The location where the stream falls off varies and moves around randomly, although it depends somewhat on the amount and direction of spray. The stream falling off the rod is thicker than it is for laminar flow, and the surface has a rough irregular appearance similar to a knotted rope. The application of voltage did not appear to affect the thickness or exit position of the stream.

As the voltage was increased, purple streaks formed from falling drops and eventually moved up to the surface of the rod and formed a hot spot. This is similar to the definition of wet corona onset for cylinders that was used in Chapter 6 and in this chapter to define self-sustaining corona (flare onset) for the rods under spray-wet conditions. For all cases with external spray, a Blue Angel would form

about 2 inches away from the rod (Figure 8-19) when the voltage was increased enough. With external spray, the drops that formed when the water stream breaks up were larger and formed a coarser water cone (Figure 8-20). The unpredictable motion of the water stream causes the Blue Angel and spray cone to be intermittent and difficult to observe. Nevertheless, by knowing what to look for, it can be seen with careful observation.

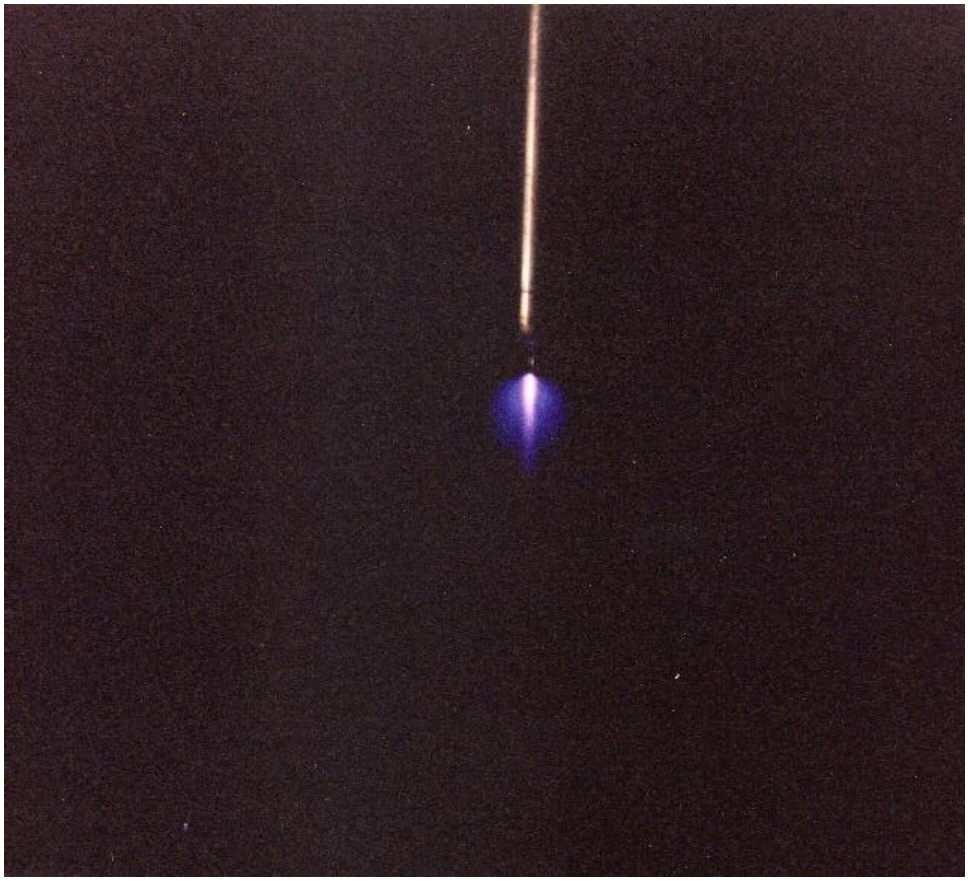

Figure 8-19. Picture of rod with external spray showing Blue Angel.

As the voltage increased further, either a flare formed or flashover occurred. The flares seem to start within the water stream or from falling water drops and then jump to the metal surface. The flares for external spray are essentially the same as for the internal water source except that the positions of the flare and water stream move around rapidly. The flare repels the water stream as shown in Figures 8-18 and 8-21. Larger rods gave rise to larger flares. The flare has a single stem that emanates from a hot spot on the metal surface. The stem has a lighter bluish-purple color and then breaks up into several jagged fingers. As the voltage is increased, the stem grows longer and the fingers reach out farther. The location of the stem and the position of the fingers move about unpredictably. The fingers reach out, following the field lines towards ground. As the voltage increases, they reach closer to ground. Flashover occurs when they reach within about 4 inches of ground. When the flare forms first, the water seems to have very little to do with flashover except that it causes the flare to start at a lower voltage. Once the flare forms, it dictates flashover for the cases that were examined.

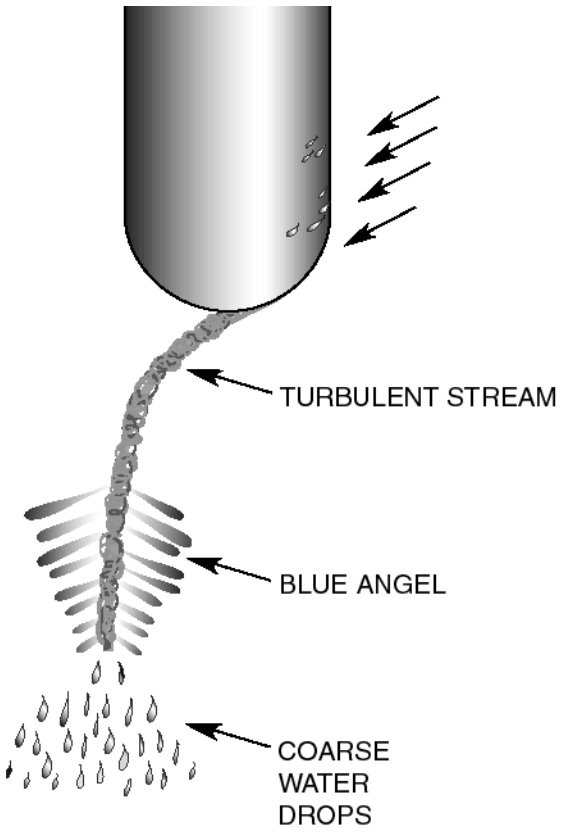

Figure 8-20. Drawing of rod with external spray showing Blue Angel.

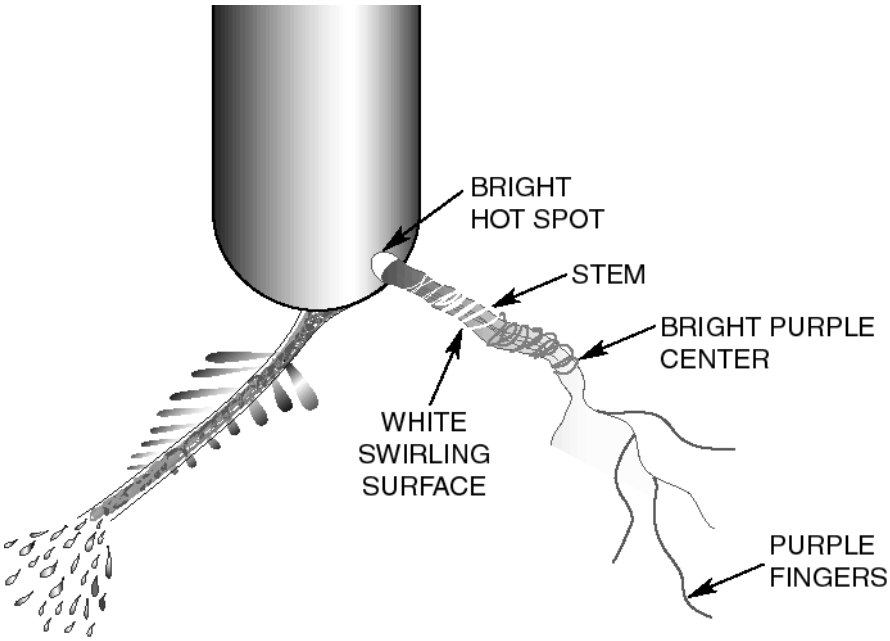

Figure 8-21. Drawing of rod with external spray showing Blue Angel and a flare.

The larger objects (8-inch pipe and 10-inch sphere) collect more water, which changes the water phenomena slightly. The phenomena described below occurred to some extent with one sprayer but were easier to see when the water came from sprayers on two sides. The water flowing off the rod (or sphere) forms a conical-shaped blob at the bottom of the rod. The water then forms one main stream and a few smaller streams that fall off the tip of the cone. These streams are turbulent, with an appearance similar to that described above for the external spray condition. The main stream falls nearly straight down, but the smaller streams fall obliquely (Figure 8-22A). When the voltage increases to near flashover, each turbulent stream breaks up into a spray cone, but with much larger drops than for laminar flow streams. The Blue Angel forms around the smaller streams as shown in Figure 8-22B. Occasionally drops fall off the rod, flashing purple as they fall. These sometimes initiate flares or flashovers, which repulses the water formation below the rod, also shown in the figure.

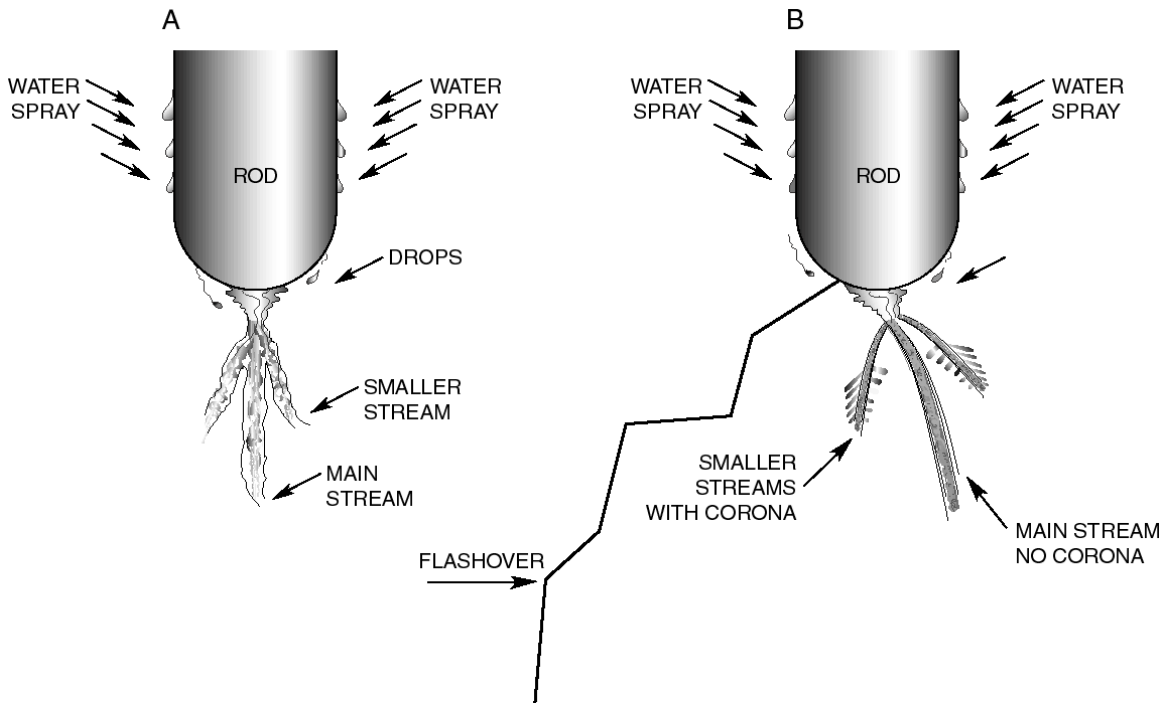

Figure 8-22. Drawing of phenomena on larger rods with heavy external spray.

Measured Data

The measured data for the vertical rods and the one sphere both dry and wet are included in the Chapter 8 data file as Excel spreadsheets named "vertrods3," "vertrods30," and "vertrods48." For each configuration, the breakdown voltage was measured as described in Chapter 5 using an average of at least five measurements. The voltages were then corrected to STP (25^{o} C). These voltages were then used with the computer-calculated gradients to determine the critical value of the field (*Ec*) on the rod tip at breakdown. The data for critical gradients presented in this chapter have all been corrected for air density.

Dry

Rods and spheres are often used as protective devices. The formation of a flare is not very useful for protection. Thus, the diameter and spacing of the rods should be selected such that flashover

occurs before a flare forms. For intermediate gap lengths, the formation of a flare is probably a function of the source impedance and may be different for different installations. For a very powerful (low impedance) source, such as would be the case for most VLF/LF stations, the flare condition as measured at Forestport could be a flashover. For that reason, it was decided to use the condition of flashover or flare (whichever came first) to define breakdown for dry conditions.

When a flare formed first, the transmitter could be turned up enough to cause flashover when there was enough available power. Figure 8-23 shows an example of the measured breakdown voltage for dry conditions at 29.8 kHz. The measured points are marked with open or filled symbols. The filled symbols represent configurations for which flashover occurred first and mark the flashover voltage. The open symbols represent configurations for which a flare occurred before flashover and mark the flare formation voltage.

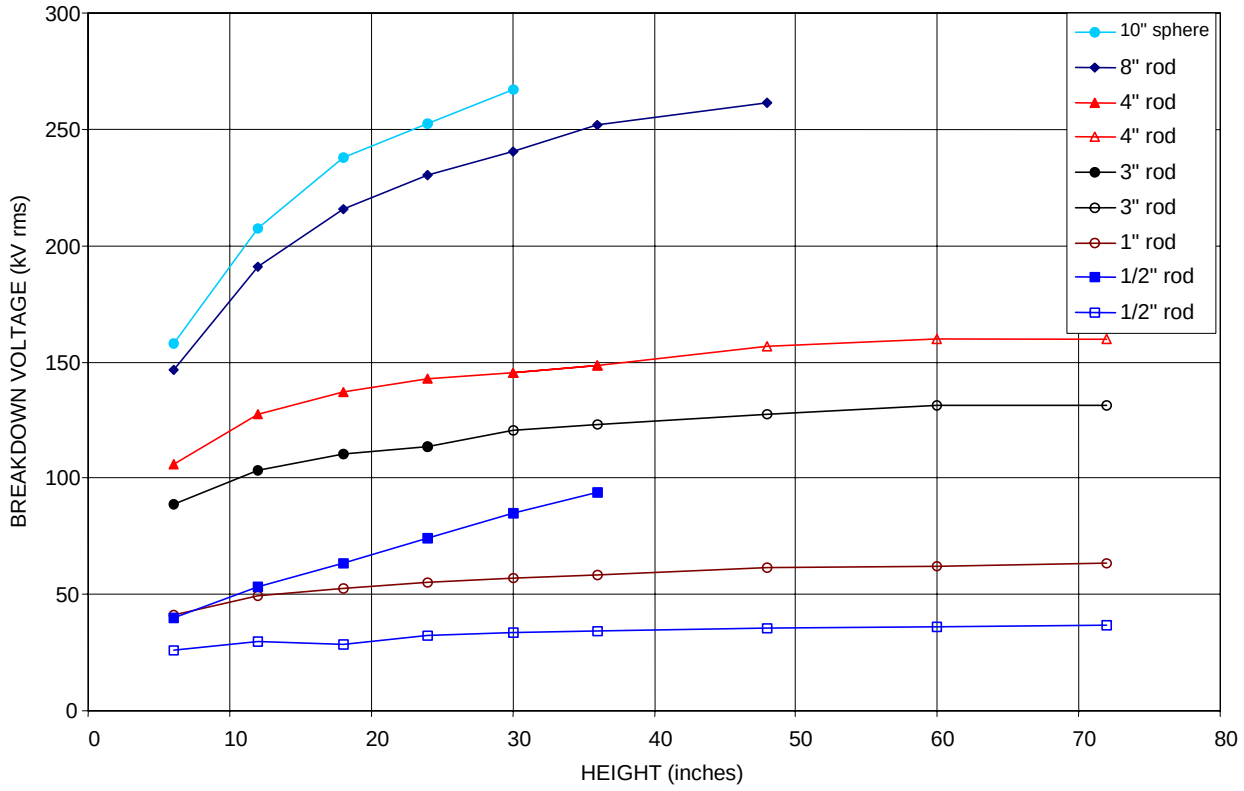

Figure 8-23. Vertical rod, dry breakdown voltages at 29.8 kHz (for ½-inch rod, closed symbols for flashover, open symbols for flares).

When the rod is relatively close to the ground relative to rod diameter, flashover occurs first (lower voltage). It is seen from the figure that flashover occurred first for the 10-inch sphere and the 8-inch rod at all heights tested. Note that there was not enough voltage available at Forestport to flash over the 10-inch sphere when the spacing was greater than 30 inches or the 8-inch rod when the spacing was greater than 48 inches. For the 3-inch and 4-inch rods, flashover occurred first for closer spacing, but a flare formed first for larger spacing. For the ½-inch and 1-inch diameter rods, a flare always formed before flashover. Flashover measurements are included in the figure for the ½-inch rod. They were obtained by increasing the transmitter power beyond the point where a flare formed until

flashover occurred. This was not done for every configuration; usually only the flare or flashover voltage, whichever came first, was recorded.

The voltages measured were corrected to STP (25°C) using the air-density correction factor as discussed in Chapter 6. The corrected voltages are converted to the gradient (surface field) on the end of the rod by multiplying by G_o. Figure 8-24 shows the critical gradients for dry conditions for the ½-inch rod at both 29.8 kHz and 48.9 kHz. Note that the surface field for the onset of flares is nearly independent of height, while the apparent surface field at flashover is nearly a linear function of height. The term apparent surface field is used for flashover in the case of the ½-inch rod because flashover always occurred at a voltage higher than the onset of a flare. The plasma in the flare is a conductor, which changes the field around the rod. Residual ionization from the flare also affects the fields around the rod. The calculated (apparent) field does not take these effects into account.

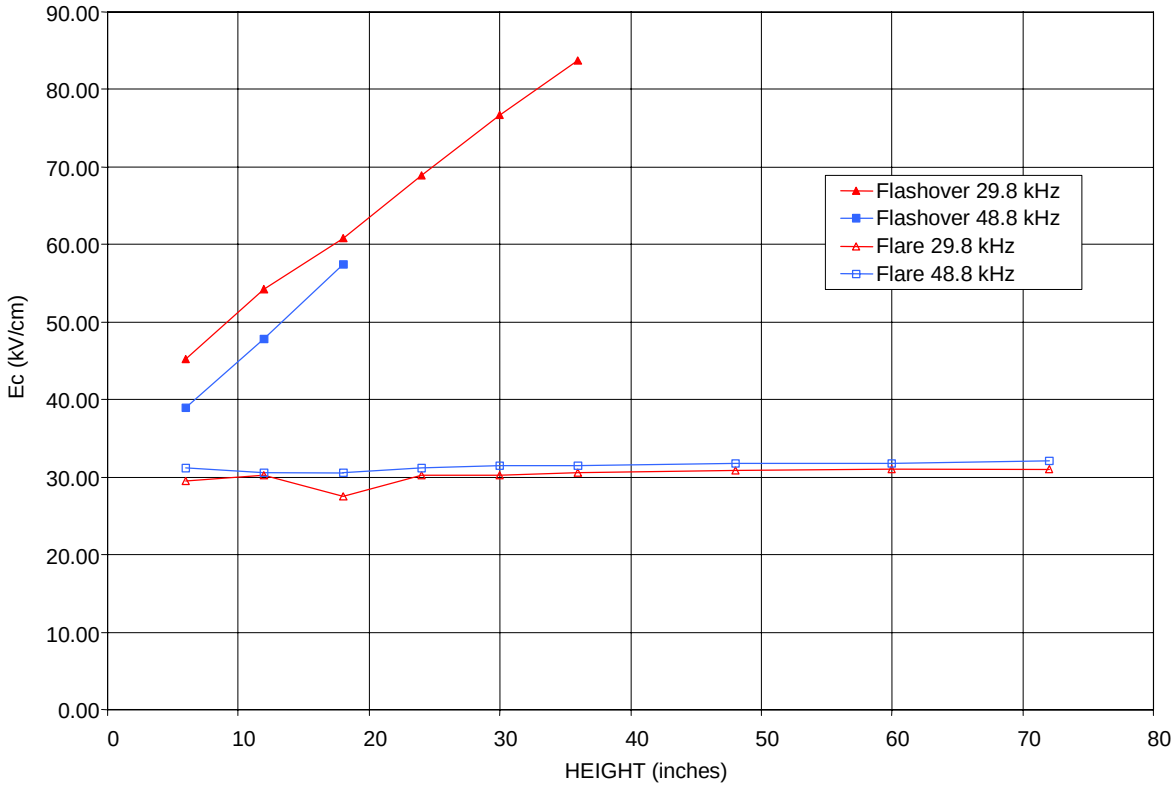

Figure 8-24. Half-inch rod, dry flashover and flare gradients.

The curves of flashover/flare gradient for the two frequencies are shown in Figure 8-25 and 8-26. In both of these sets of curves, the gradients are nearly constant showing a slight increase with height. Both figures show some statistical variation that is an inevitable part of high-voltage breakdown measurements.

The average breakdown gradient for the dry condition has been calculated for each rod diameter at both frequencies using the data of Figures 8-25 and 8-26. This is called the critical gradient and has been plotted versus diameter in Figure 8-27. Note that these curves show a decreasing breakdown gradient versus diameter and are similar to the corona onset curves for wires and cylinders given in Chapter 6. The frequency effect is apparent in that the curve for 48.8 kHz is about 5% below that for

29.8 kHz, except for the ½-inch rod dry. The fact that the flare gradient for the ½-inch dry rod for 29.8 kHz is greater than the flare gradient for 48.8 kHz is clearly shown in the original data of Figure 8-24. This seems to be anomalous and may be the result of measurement error. However, it may be the result of the humidity effect because, as discussed in Chapter 6, for small radius objects the presence of humidity can increase the breakdown strength at low frequencies but reduce it at higher frequencies. Note that the flashover gradient for 29.8 kHz was above the flashover gradient for 48.8 kHz.

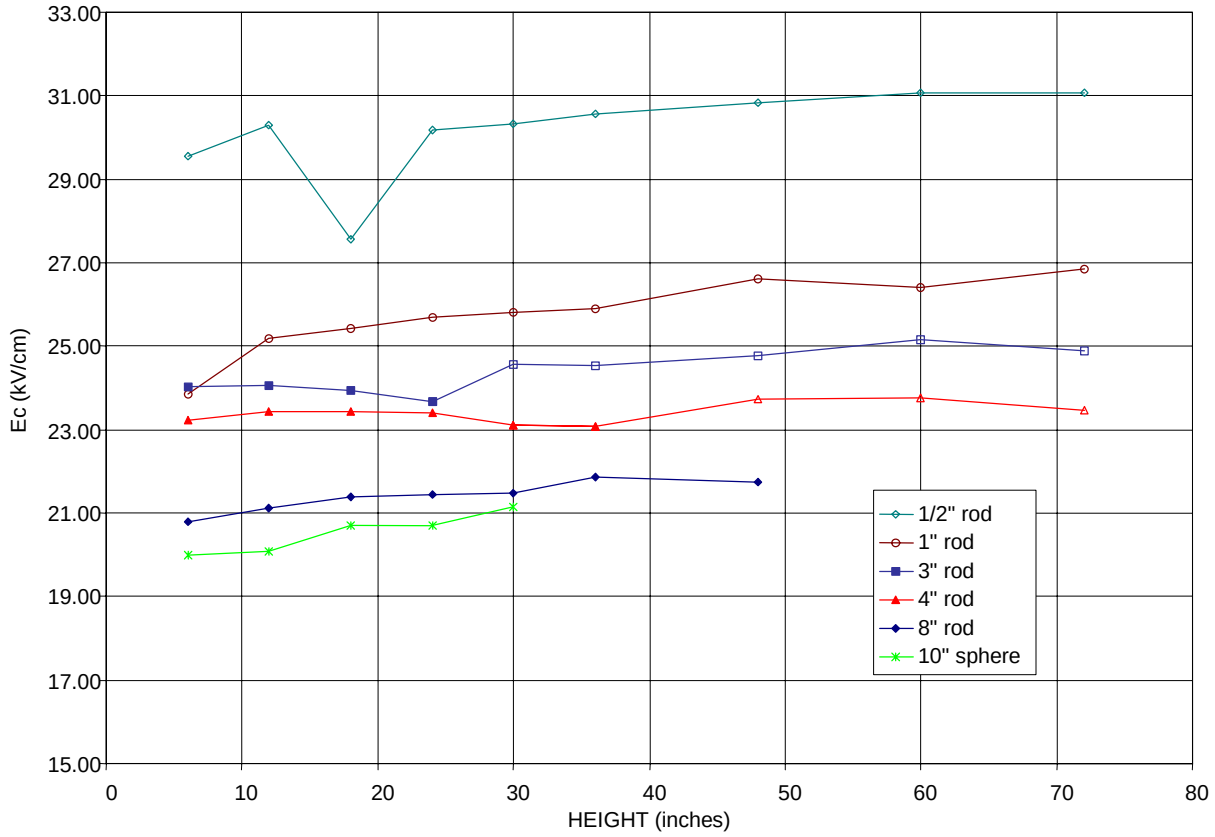

Figure 8-25. Dry vertical rods, flashover/flare gradients versus height at 29.8 kHz.

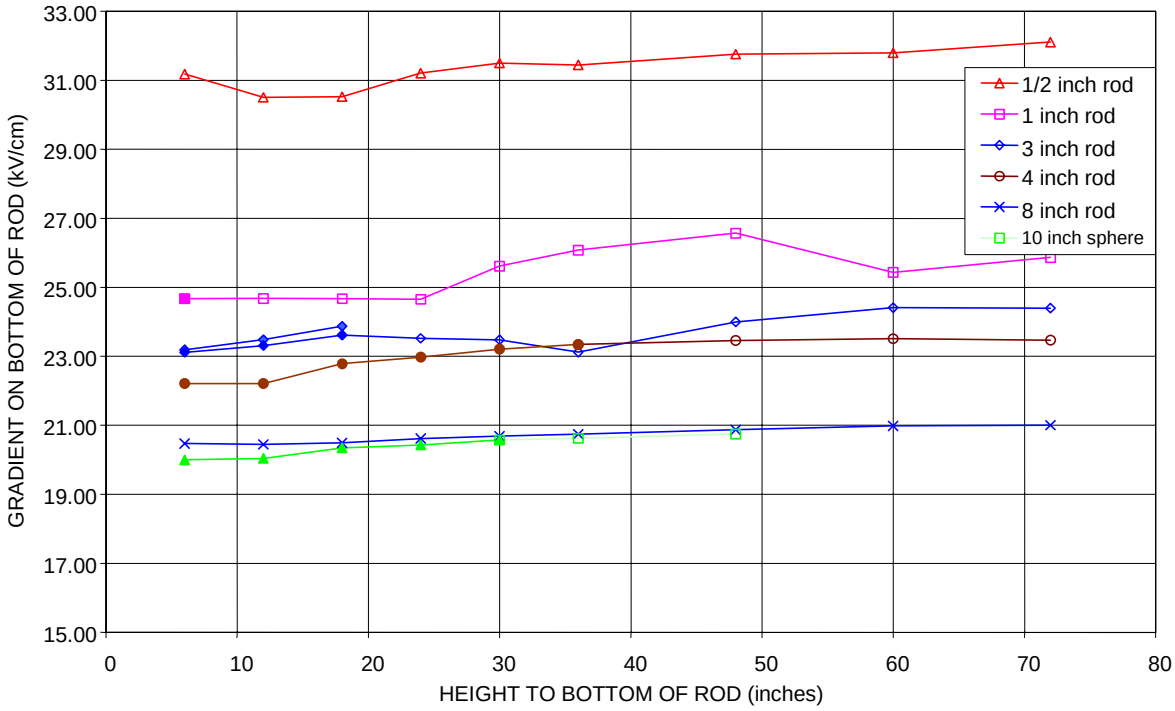

Figure 8-26. Dry vertical rods, flashover/flare gradients versus height at 48.8 kHz.

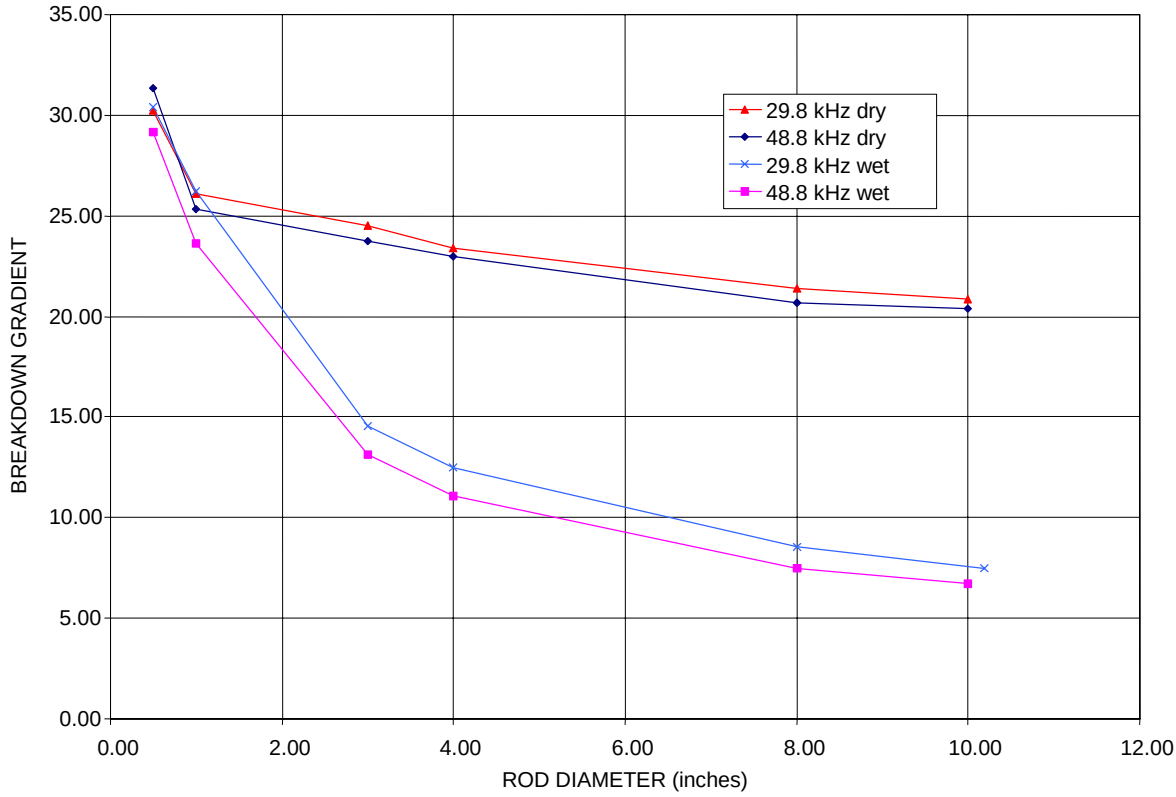

Figure 8-27. Vertical rods average breakdown gradient versus diameter.

Gap Factor

The curves of dry flashover/flare gradient versus height given in Figures 8-25 and 8-26 have been normalized by the average of each curve and plotted in Figure 8-28 for 29.8 kHz and Figure 8-29 for 48.8 kHz. For each frequency all of the data have been averaged point by point and the resulting "average" curve is also shown. The average curves for both frequencies are very similar and have been plotted together in Figure 8-30. An average of the curves for each frequency has also been included and can be used as a "gap factor." The gap factor curve (dry average curve of Figure 8-30) is nearly linear with height. Note that the gap factor is 1.0 at a height of 30 inches. Thus the average curves for the breakdown gradient of dry rods versus diameter given in Figure 8-27 apply exactly for a height of 30 inches. The gap factor is used to adjust the breakdown gradient for larger or smaller gaps. For dry conditions, the breakdown gradient is about 2% greater when the gap is 72 inches and 2% less when the gap is 6 inches. Breakdown voltage has a statistical component and an indication of its variability for dry conditions is given by the normalized data shown in Figures 8-28 and 8-29.

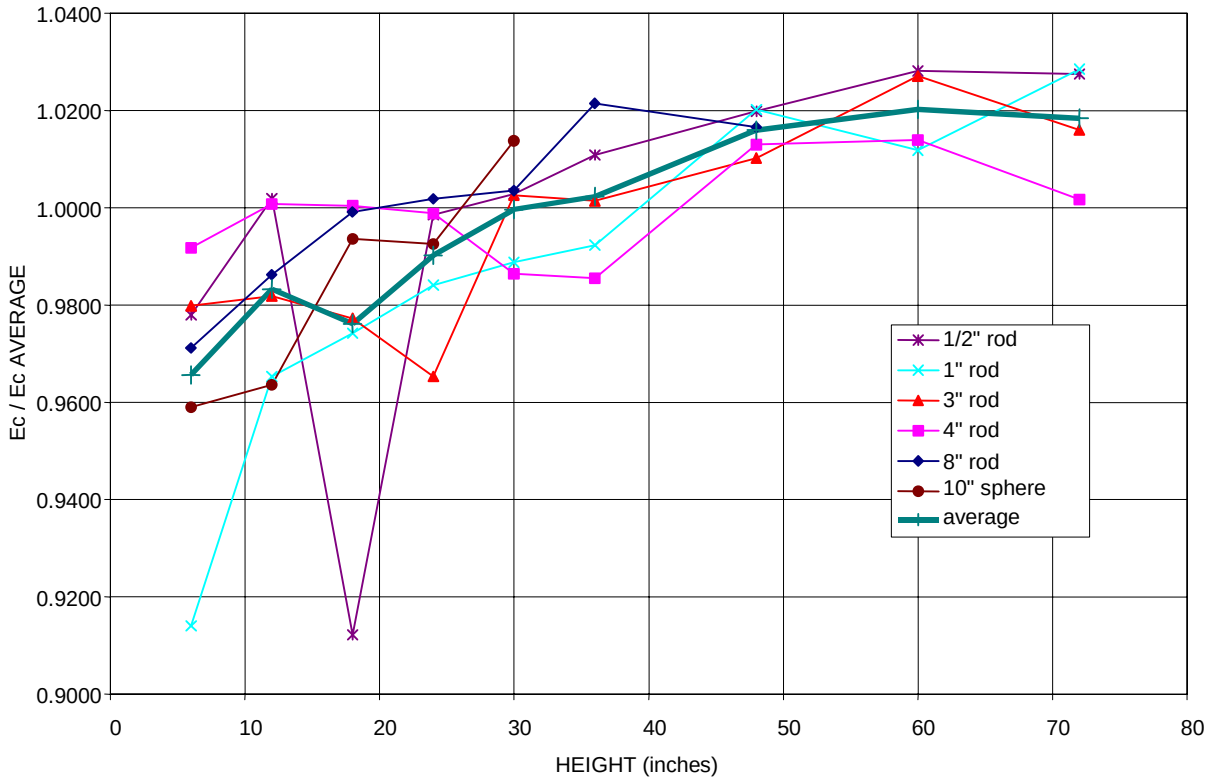

Figure 8-28. Dry rods at 29.8 kHz, gap factor.

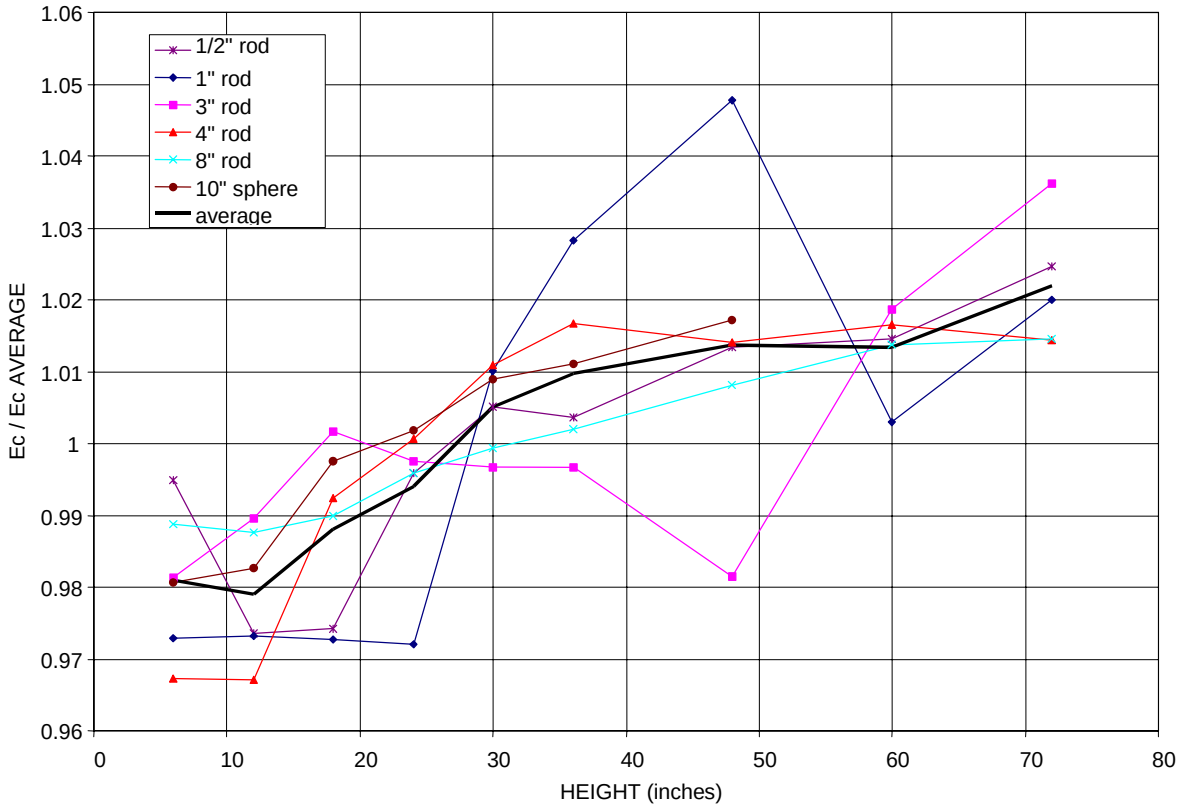

Figure 8-29. Dry rods at 48.8 kHz, gap factor.

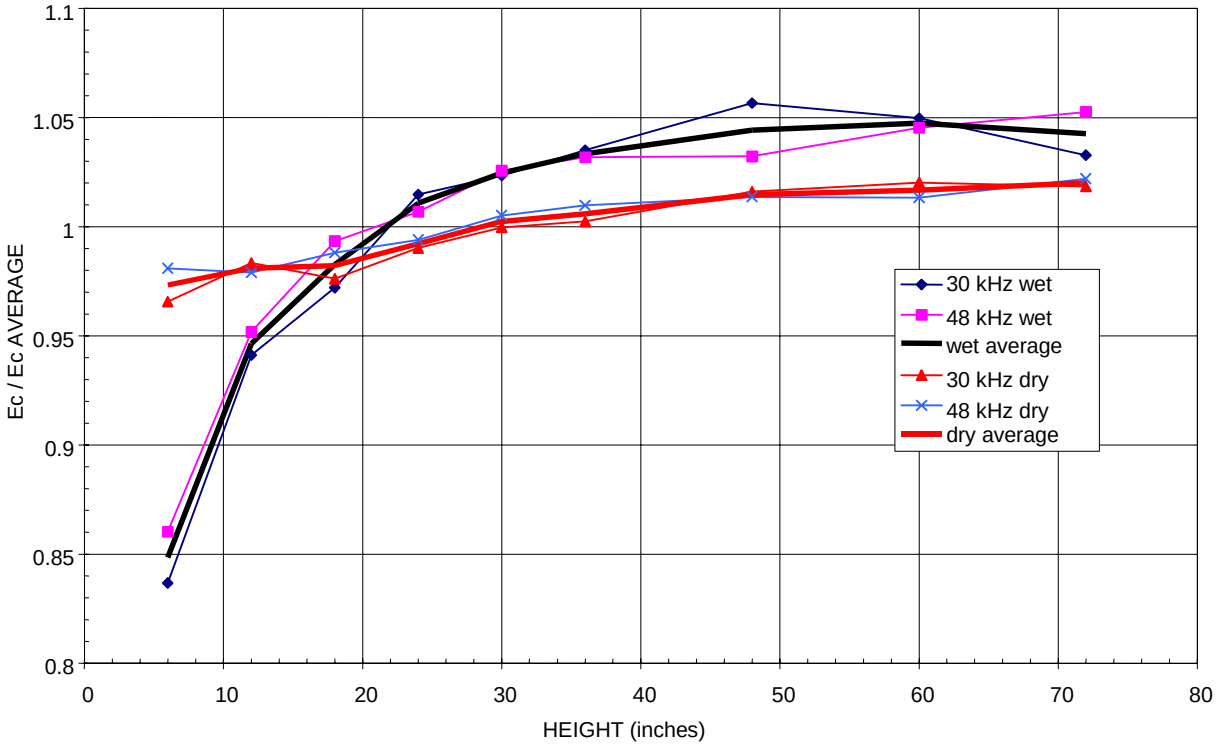

Figure 8-30. Vertical rod combined wet and dry gap factor.

Wet

For wet conditions, the breakdown phenomena are more complicated than for dry conditions and several different phenomena appear as the voltage is increased. However, when the voltage becomes high enough, the breakdown phenomenon are the same as those for dry conditions, either the formation of a flare or flashover. As for dry conditions, when a flare formed first the transmitter could be turned up to cause flashover when enough power was available. With the ½-inch and 1-inch diameter rods, a flare always formed before flashover for either wet or dry conditions. The flashover voltage was measured for the ½-inch rod wet for 29.8 kHz and 49.8 kHz, and the apparent gradient on the rod at flashover is shown in Figure 8-31. The apparent gradient at flashover for dry conditions is shown also. Note that the wet and dry flashover gradients for each frequency are nearly the same. Note also that the wet flashover gradients for 49.8 kHz are approximately 10% less than the wet flashover gradients for 29.8 kHz.

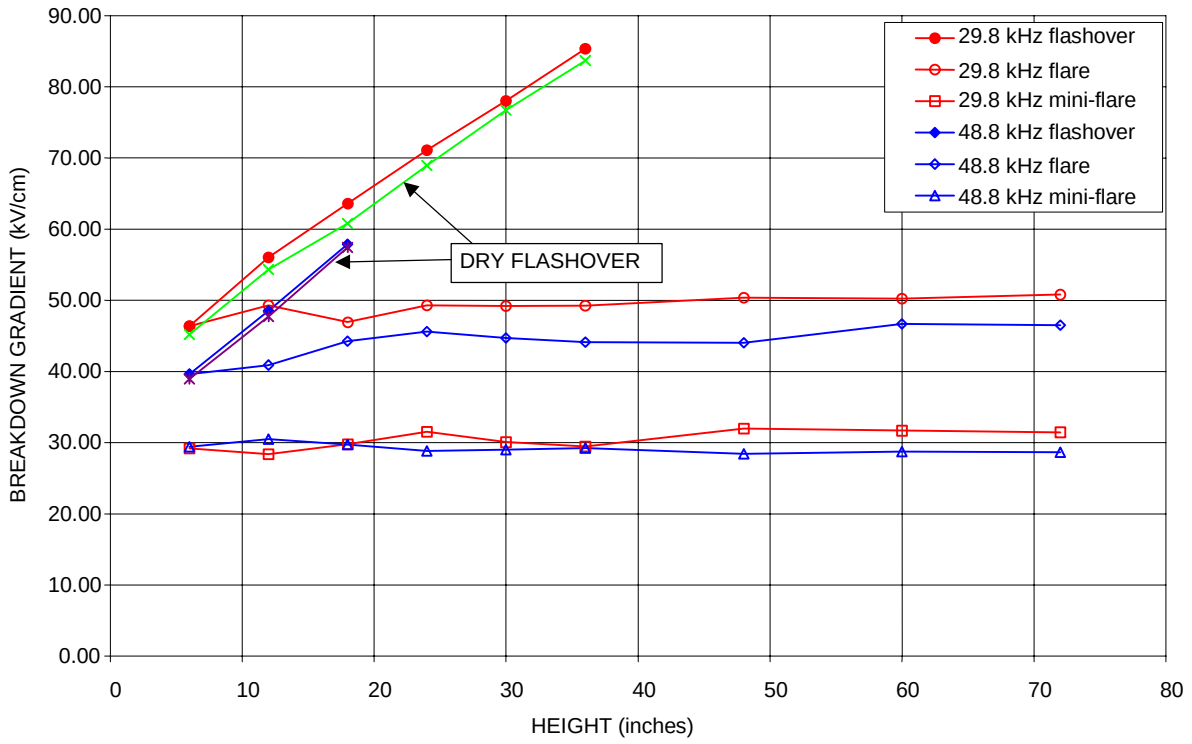

Figure 8-31. Half-inch rod wet breakdown gradients.

Wet flashover and dry flashover voltages are nearly the same for small diameter rods at VLF/LF for which corona formation precedes flashover (as previously noted by Kotter [1983]). This was purported to be a desirable characteristic for protective devices used outdoors. Unfortunately, the data show that for wet conditions the small diameter rods will flare at voltages much less than flashover. The flare is not desirable for many reasons, including the fact that it may become a flashover depending on the source impedance. Also, the flashover time for rods is longer than for uniform field gaps, and so rods do not protect as well against transients with fast rise times. Thus, rods may not be the best protective devices for outside use.

There was a third phenomenon observed and measured for wet conditions, the formation of purple mini-flares on the rod. This corresponded to the top of the purple streaks moving up and attaching

themselves to the surface of the rod, where a white hot-spot formed. This phenomenon is the same as the definition used for wet corona onset on cylinders in Chapter 6. The onset of this phenomenon is distinct. It can be measured as discussed in Chapters 6 and 7 and corresponds to the start of the dissipation of significant amounts of power. The curves for the onset of mini-flares using the ½-inch rod are included in Figure 8-31. They lie below the flare or flashover level and are nearly constant with height. The onset of a purple mini-flare is the definition of wet breakdown used for the remainder of the wet rod measurements.

As in the case of the dry rod measurements, the breakdown voltages were corrected for air density and converted to the gradient on the rod tip. The measured breakdown gradients for the purple mini-flares on rods for spray-wet conditions at the two frequencies tested are shown in Figures 8-32 and 8-33. Again the measured points are marked with open or filled symbols. The filled symbols represent configurations for which flashover occurred first, and the open symbols represent configurations for which mini-flares occurred first. As in the case of dry conditions, flashover occurred first when the rod was close to the ground relative to the rod diameter. These curves are similar to the curves for dry conditions and show that the critical gradient is nearly constant, slightly increasing with height. The rate of increase with height is slightly greater for the wet curves than for the dry curves. These figures also show some statistical variation, which is an inevitable part of the high-voltage breakdown process.

The average breakdown gradient for the wet condition has been calculated for each rod diameter at the two frequencies measured using the data of Figures 8-32 and 8-33. This gradient is shown plotted versus diameter in Figure 8-27. Note that the curves shown in Figure 8-27 show decreasing breakdown gradient with diameter and are similar to the corona onset curves for cylinders shown in Chapter 6. The frequency effect is apparent in that the curve for wet conditions at 48.8 kHz is about 10% below that for 29.8 kHz, including the case of the ½-inch rod. This is about twice the difference for dry conditions and may be in part due to humidity, since humidity for wet conditions is essentially 100%.

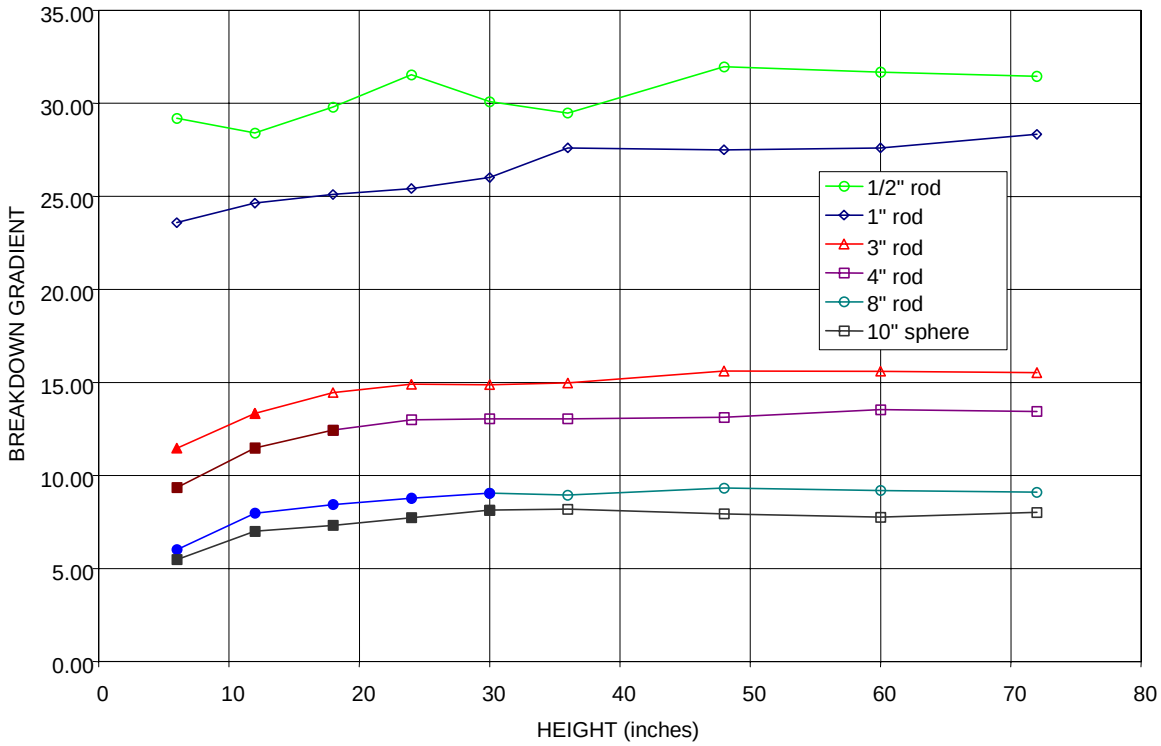

Figure 8-32. Wet vertical rods, mini-flare breakdown gradient at 29.8 kHz.

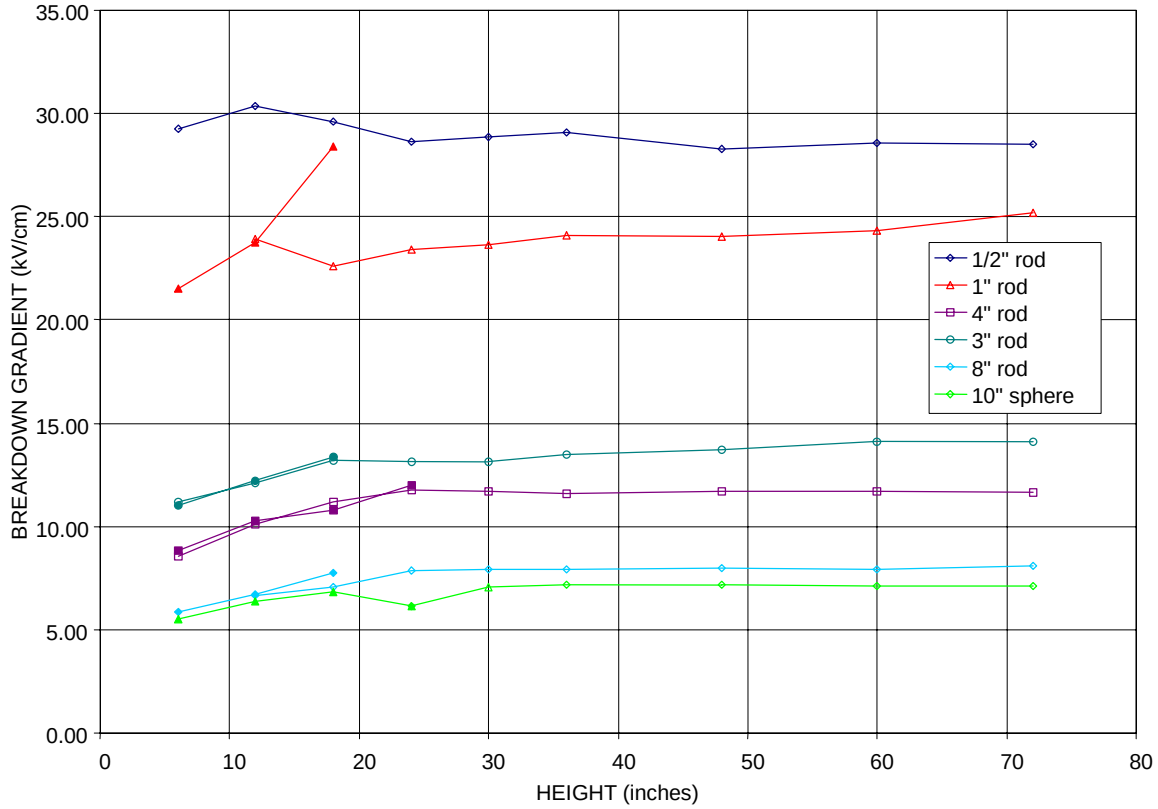

Figure 8-33. Wet vertical rods, mini-flare breakdown gradient at 48.8 kHz.

Gap Factor

The curves of wet breakdown gradient versus height shown in Figures 8-32 and 8-33 have been normalized by the average of each curve and plotted in Figure 8-34 for 29.8 kHz and Figure 8-35 for 48.8 kHz. All of the normalized curves have been averaged point by point and the resulting "average" curves are also shown in the figures. The average curves for both frequencies, wet and dry, have been plotted in Figure 8-30. Note that the wet curves for the two frequencies are very similar. An average of the curves for both frequencies, wet and dry, is also given and is intended to be used as a "gap factor" to adjust the breakdown gradient for larger or smaller gaps. The wet-gap factor is 1.0 at a height of 22 inches. Thus, the average curves for the breakdown gradient of wet rods versus diameter given in Figure 8-27 apply to a height of 22 inches. The gap factor is used to adjust the breakdown gradient for gaps that are larger or smaller than 22 inches.

Comparison of the wet and dry gap factor curves (average curves) in Figure 8-30 indicates that for wet conditions the variation with gap length (height) is greater than it is for dry conditions. For wet conditions, the breakdown gradient decreases significantly when the gap is less than 22 inches, and the slope increases rapidly as the gap gets smaller. Water is a good conductor at VLF/LF. Thus, the water falling off the rod decreases the effective gap and is probably the cause of this decrease. This effect may depend somewhat on the rate of the water falling, but we do not have data to quantify this effect. For separations greater than 22 inches, the slope of the wet gap factor decreases, and the gap factor asymptotically approaches a value of 4.5%. The statistical variation for wet conditions is somewhat greater than that for dry conditions as can be seen from Figures 8-34 and 8-35.

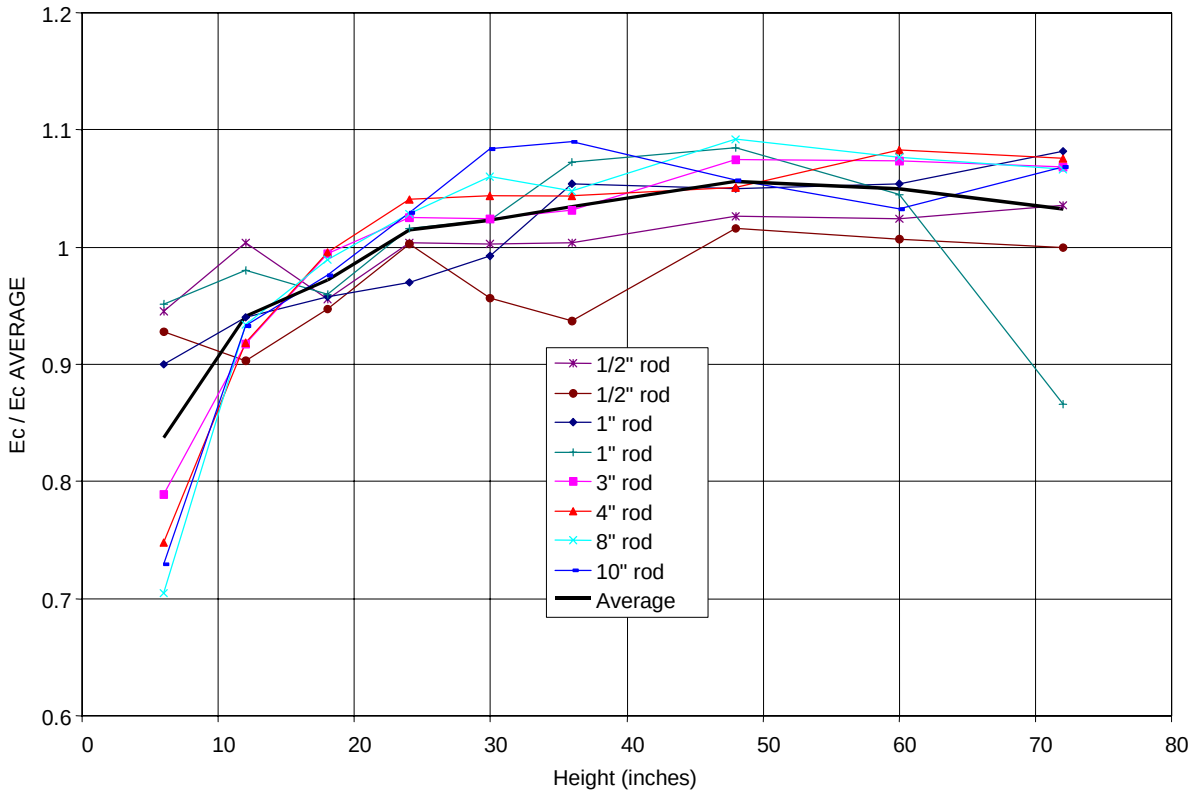

Figure 8-34. Wet rods gap factor at 29.8 kHz.

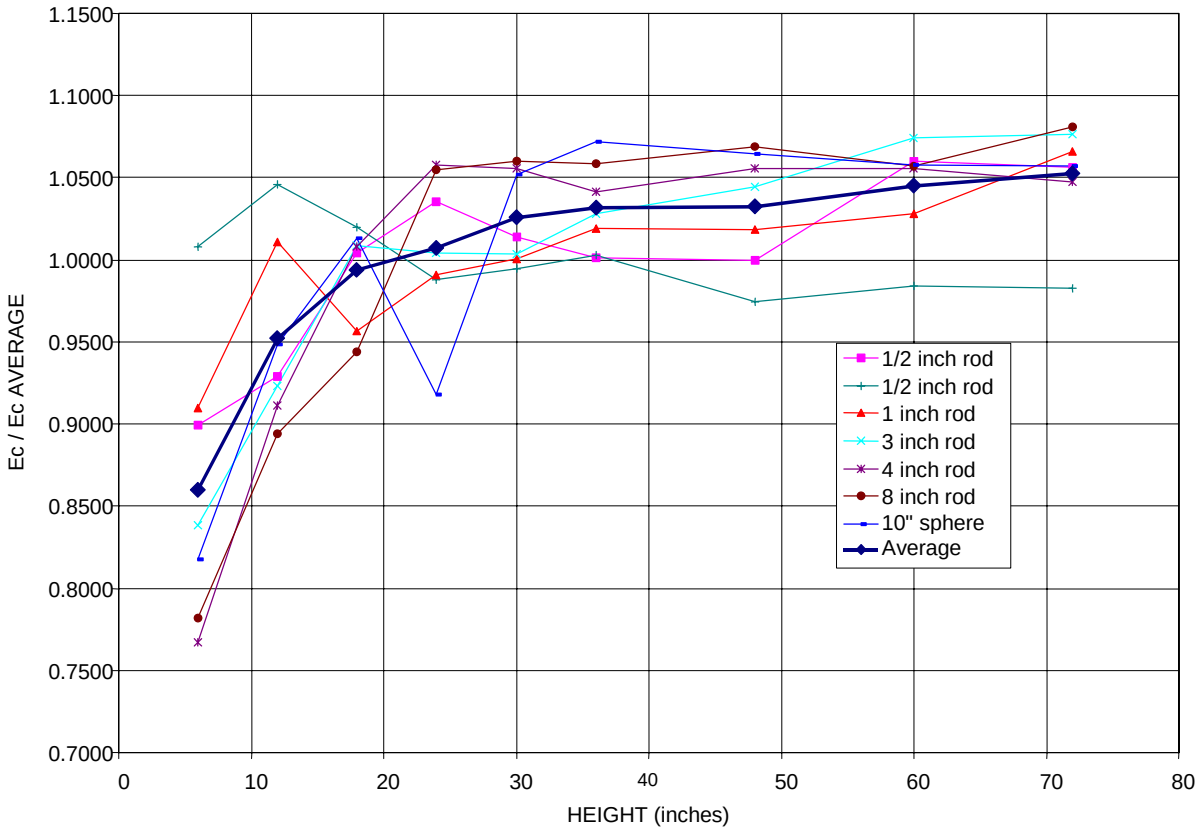

Figure 8-35. Wet rods gap factor at 48.8 kHz.

Design

Figure 8-23 showed the measured dry breakdown voltages, both flashover and flare for vertical rods above a ground plane for 29.9 kHz at STP (25°C). The breakdown voltages for 48.8 kHz are approximately 5% less than those for 29.9 kHz as indicated in Figure 8-24. The curves in Figure 8-23 give an indication of the flashover voltages for rods as a function of height and can be used for analysis and design. However, we have developed a better design - analysis approach based on the critical gradients determined from the measurements. This approach has general application to configurations with different size rods, different spacing, and other than flat ground planes.

This approach involves the use of Figure 8-27 to determine the critical gradient for the rod of interest. The curves in this figure can be interpolated to obtain values for rod diameters other than those plotted. Note that the curves are based on the average critical gradient over a range of heights. For dry conditions the curves of Figure 8-27 correspond to a gap spacing of 30 inches, and the curves for wet conditions correspond to a gap spacing of 22 inches. After determining the average critical gradient the appropriate gap factor in Figure 8-30 is used to adjust to other spacing. The normalized gradient G_0 on the rod tip is calculated for the configuration in question (Chapter 4). Given the normalized gradient on the rod, G_0, and the critical gradient for that configuration, E_c, the breakdown voltage is determined by

$$V_c = \frac{E_c}{G_0} \quad .$$

VERTICAL AND HORIZONTAL RINGS

Breakdown measurements were performed using elevated corona rings (toroids) at Forestport during May 1994, January 1995, and March 1995. All of these data were taken for frequencies near 30 kHz. The rings used for most of these measurements were made from smooth aluminum, but a few measurements were done using 6-inch and 8-inch rings made from corrugated flexible pipe. Corrugated rings were tested because they were often used for testing trial insulator assemblies and we needed to determine the difference in performance between a corrugated ring assembly and a final assembly with smooth rings.

Test Configurations

Measurements were taken using five different size rings having minor diameters from 1 inch to 8 inches. The test configurations for the horizontal and vertical rings are illustrated in Figures 8-36 and 8-37. Table 8-9 lists the dimensions for both ring configurations.

Table 8-9. Dimensions of ring test configurations. See Figures 8-36 and 8-37.

Configuration	*L* (feet)	r_p (in)	r_1 (in)	r_2 (in)	$(r_1+r_2)/r_2$
1” ring	8	2.049	7.688	0.5	16.4
2” ring	8	2.049	5.34	1.025	6.2
3” ring	8	2.049	3.595	1.5	3.4
6” ring	8	2.049	9.0	3.0	4.0
8” ring	8	2.049	12.0	4.0	4.0

Both the vertical and horizontal rings measurements were taken at the same heights above ground at the rod measurements listed in Table 8-7. The heights were measured from ground to the lowest part of the ring (Figure 8-38).

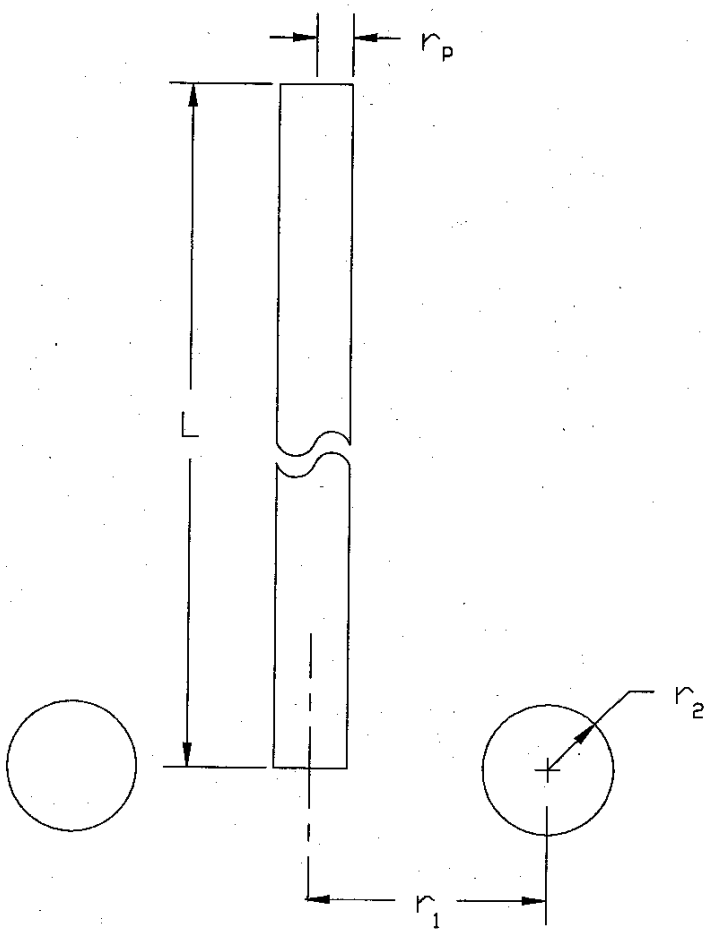

Figure 8-36. Horizontal ring test configuration and dimensions.

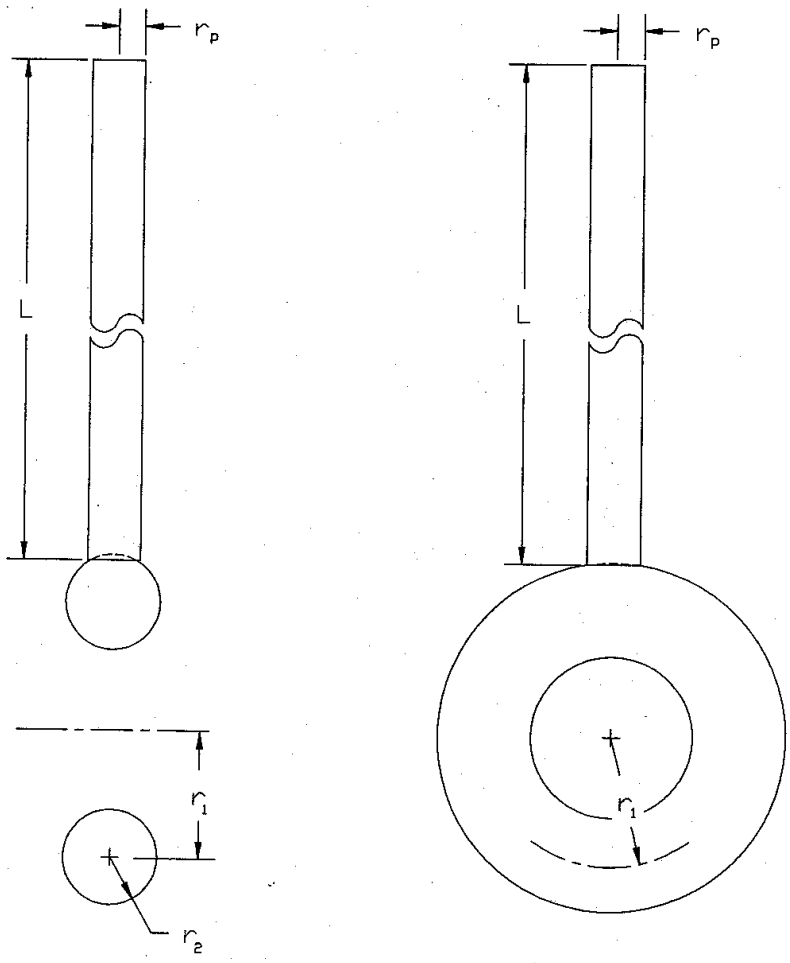

Figure 8-37. Vertical ring test configuration and dimensions.

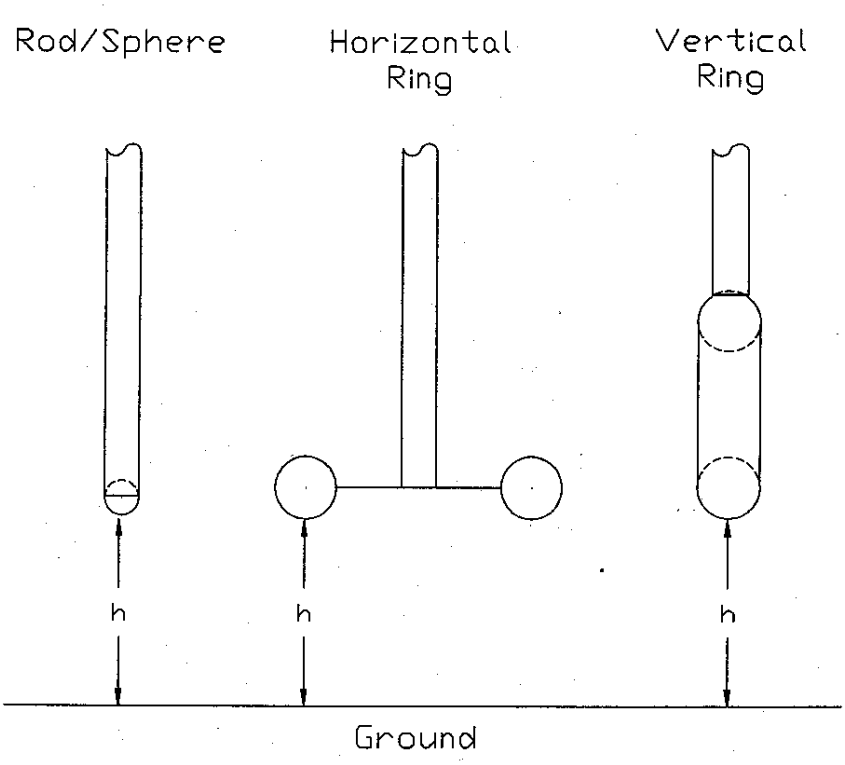

Figure 8-38. Height measurement for rods and rings.

Observed Phenomena

Dry Conditions

The phenomena observed for dry conditions for both the vertical and horizontal rings were the same as described in the section above on the rod measurements.

Wet Conditions

External spray was the only wet condition used for the ring measurements. For vertical rings under wet conditions, the water all runs off the bottom of the ring, and the phenomena were essentially the same as for the vertical rods with external spray described in the above section on rod measurements. However, when the rings are horizontal, the water runs off the ring at many locations around the ring, and the Blue Angel and spray cone are normally not seen. The observed phenomena for horizontal rings are mostly like those described in Chapter 6 for horizontal cylinders under spray-wet conditions.

Gradient Calculations

The normalized gradients G_o have been calculated for each ring configuration. The dimensions of G_o are per cm and the actual gradient (field on the surface of the ring) is determined by multiplying G_o by the voltage.

Horizontal Rings

The horizontal ring configuration is rotationally symmetric, and the surface fields were calculated using the computer program for rotationally symmetric geometry as described in Chapter 4. For horizontal rings, the location of the maximum surface field point depends on the height above ground and the rod configuration. For a ring above ground, the maximum surface field lies somewhere between the outermost edge of the ring and the bottom of the ring. If the ring were suspended in free space, without the supporting pipe, the maximum field point is on the outer edge of the ring. However, as the ring is lowered toward ground, the maximum field point moves around the ring surface toward ground. When the ring is just above ground, the maximum field is on the bottom of the ring.

The pipe suspending the ring somewhat influences the position of the maximum surface field. The pipe is at the same voltage as the ring and tends to move the location of the maximum field slightly away from the pipe (i.e., around the ring towards the bottom). The pipe also provides some shielding, thereby reducing the magnitude of the maximum field. Thus, to accurately determine the breakdown gradient from the measurements, it was necessary to calculate the maximum surface field as a function of height for each ring, including the effect of the support rod.

For wet conditions, the position where breakdown (flare or flashover) started always appeared to be close to the bottom of the ring near where a water streamer flowed off the ring. For this reason, we decided to try processing the data for wet conditions using the gradient on the bottom of the rings as well as the maximum gradient. The calculated maximum and bottom gradients normalized to 1 volt (G_0) for horizontal rings are shown in Figures 8-39 to 8-43. The curves for the horizontal rings maximum and bottom gradients are designated *H*, *m* and *H*, *b*, respectively.

Vertical Rings

For the vertical rings, the maximum gradient occurs on the bottom of the ring and was the only value used to process the data. The vertical ring configurations are not rotationally symmetrical and 3-D computer programs are required to make this calculation. It is a significant effort to obtain accurate answers for 3-D configurations, and much of the effort described in Chapter 4 resulted from addressing the problem of determining gradients for vertical rings. As with the horizontal rings, the effect of the support rod was included. The normalized gradient on the bottom of the vertical rings, designated *V*, *b* is also shown in Figures 8-39 to 8-43. Note that the curves for the vertical ring gradients are not as smooth as the curves for the horizontal rings. This is an indication of the increased difficulty and decreased accuracy encountered when calculating surface fields for 3-D objects.

Measured Data

The breakdown measurements for the smooth rings with minor diameters of 1, 2, 3, 6, and 8 inches have been combined in an Excel spreadsheet titled “Ring Summary Mod4.” Both the original data and the data corrected to STP are included. The measured data for corrugated rings are included in the spreadsheet titled “HORZRINGS.” For each configuration, the breakdown voltage was measured using an average of at least five measurements. The voltages were corrected to STP (25^o C). These voltages were then used in combination with the calculated gradients to determine the critical value of the surface field (*Ec*) at breakdown (critical gradient).

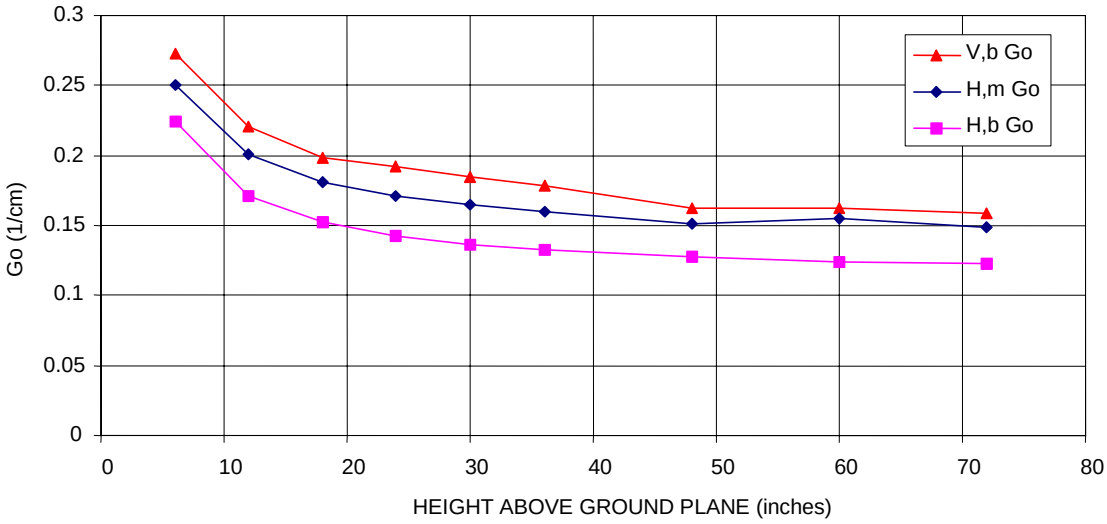

Figure 8-39. Normalized gradients for 1-inch ring with support rod.

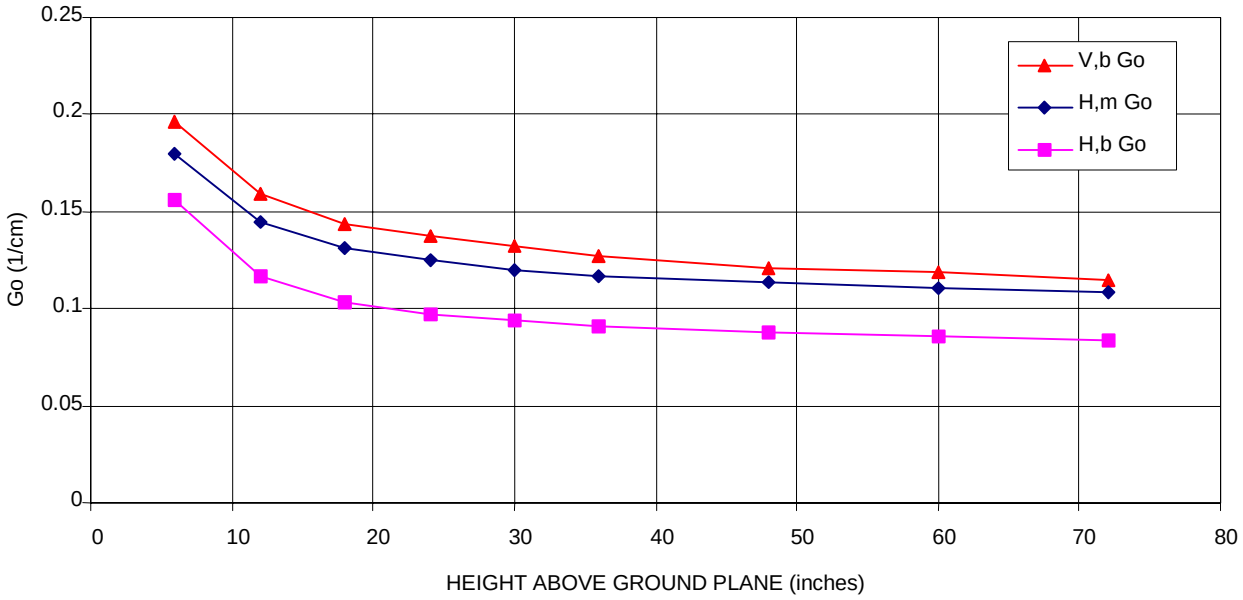

Figure 8-40. Normalized gradients for 2-inch ring with support rod.

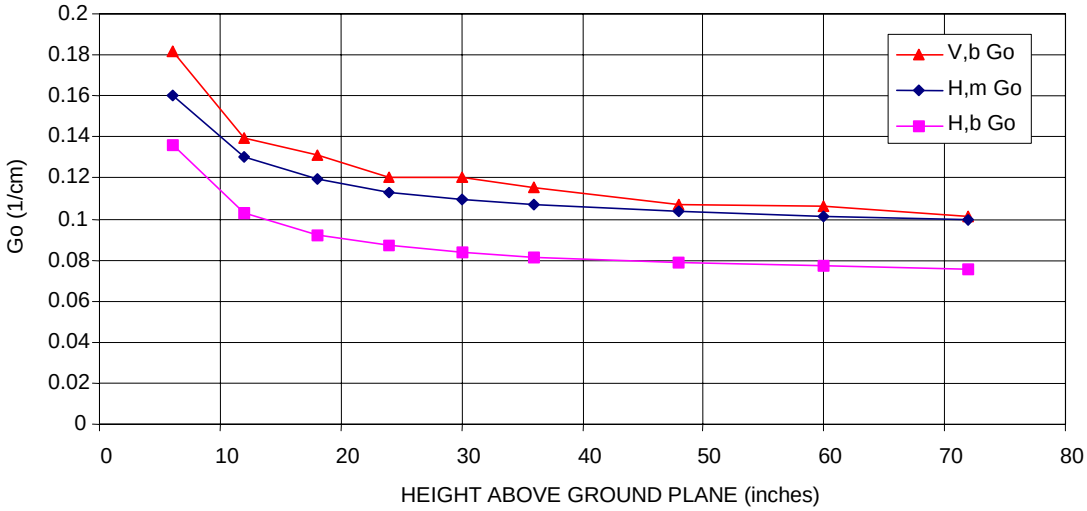

Figure 8-41. Normalized gradients for 3-inch ring with support rod.

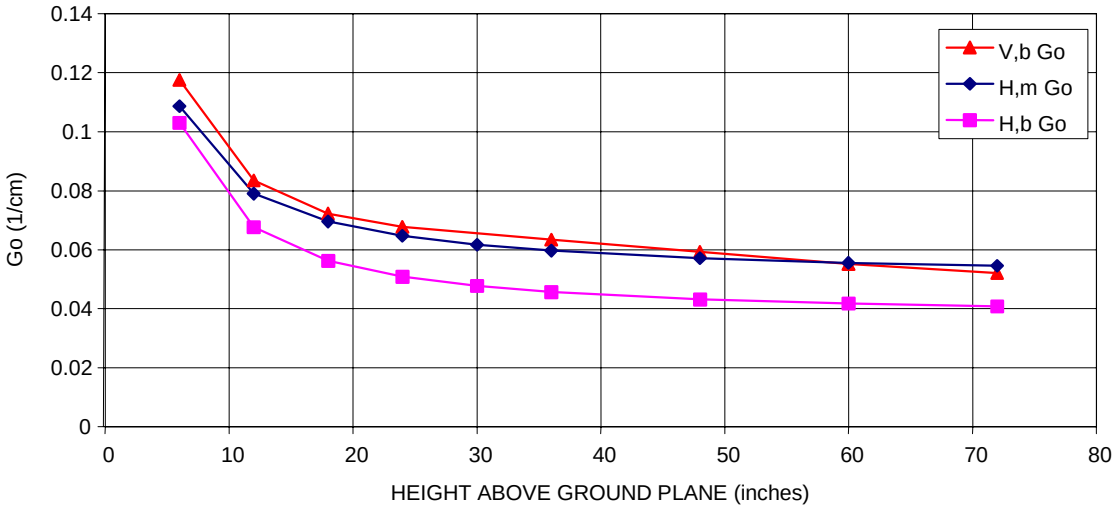

Figure 8-42. Normalized gradients for 6-inch rings with support rods.

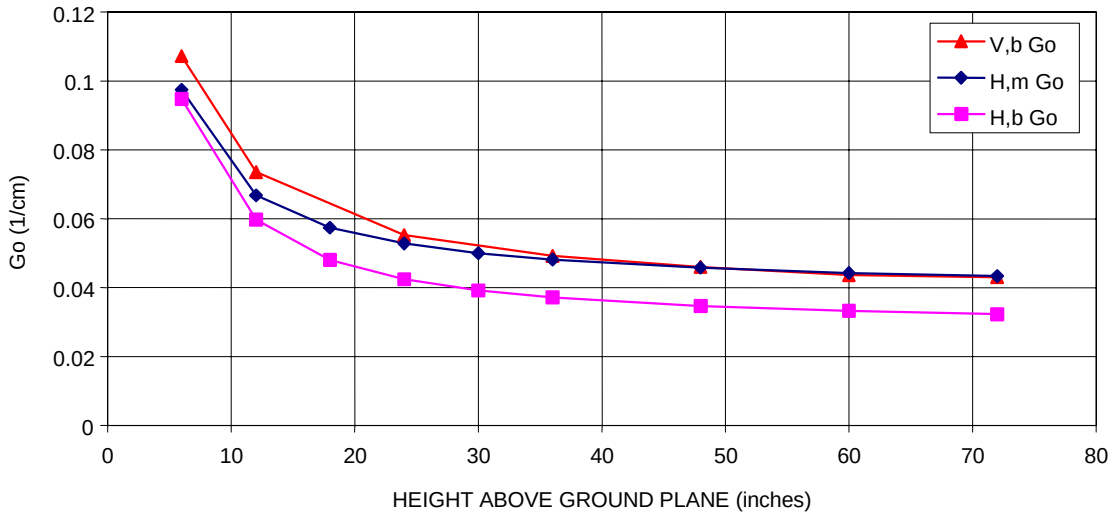

Figure 8-43. Normalized gradients for 8-inch ring with support rod.

Some typical curves generated in this way for the 6- and 8-inch rings under wet conditions are shown in Figures 8-44 and 8-45. In these figures, both the maximum and bottom gradient have been calculated. For wet conditions, the bottom breakdown gradient is nearly constant with height, while the maximum gradient is not. This is true for both ring sizes, corrugated and smooth. This indicates that for wet conditions breakdown is most closely correlated with the gradient on the bottom where the water falls off. For this reason, all of the wet horizontal ring data were processed using the bottom gradient instead of the maximum gradient.

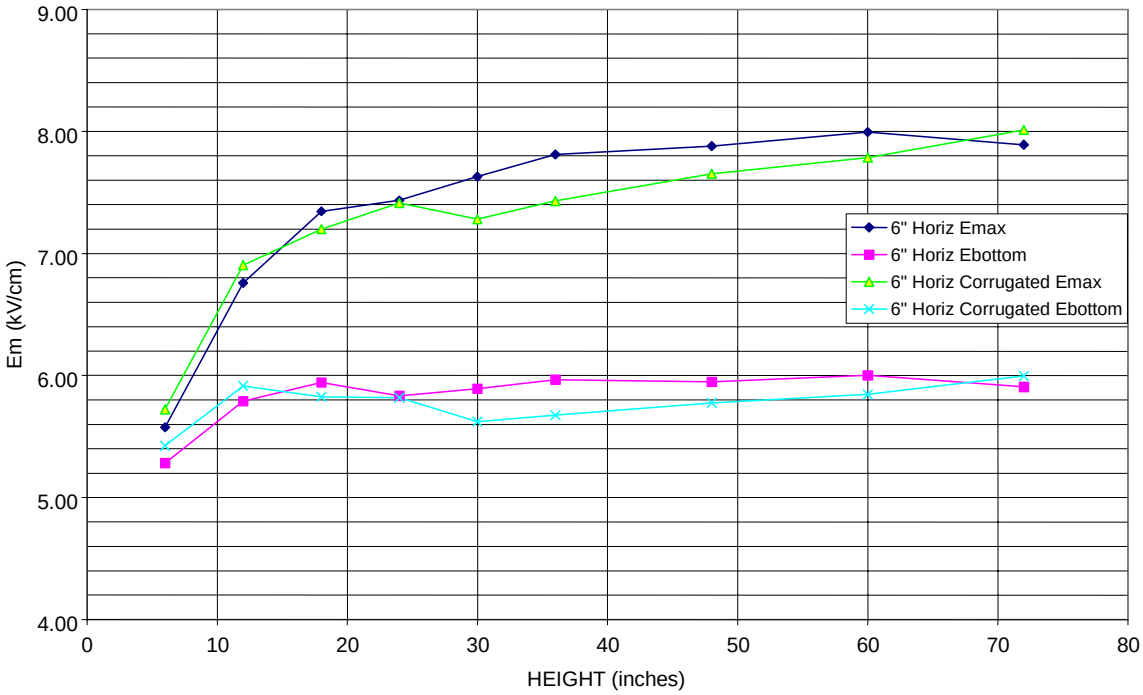

Figure 8-44. Breakdown gradients (rms) observed for wet 6-inch horizontal at 30 kHz.

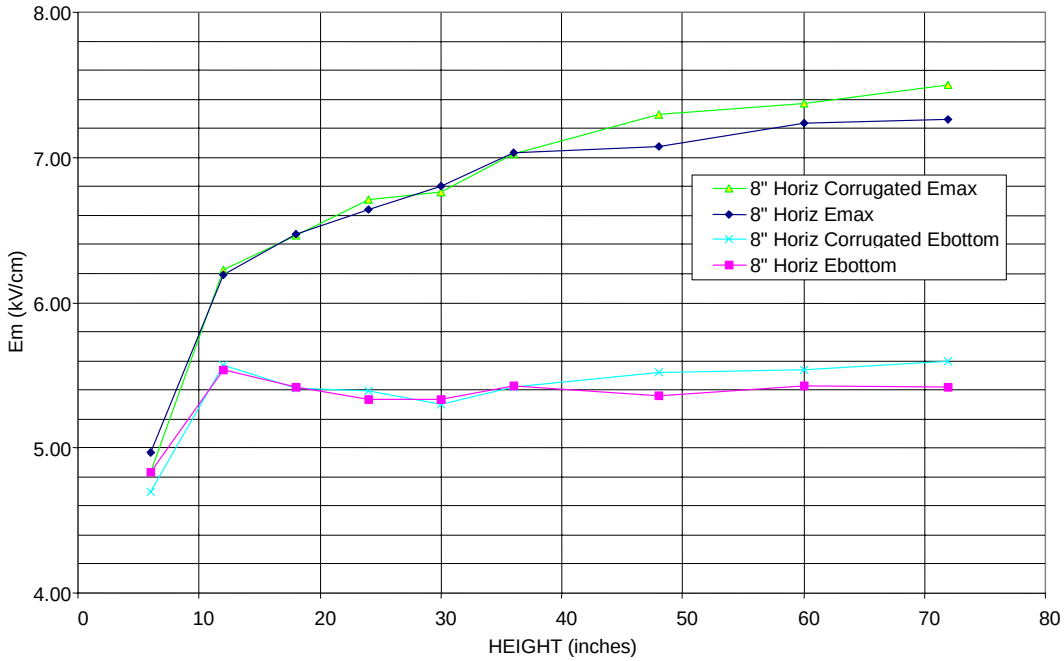

Figure 8-45. Breakdown gradient (rms) observed for wet 8-inch horizontal ring at 30 kHz.

Smooth Rings

The gradient at breakdown (critical gradient) is determined from the measured breakdown voltage and the calculated normalized gradient. Plots of the observed critical gradient for all the smooth ring data are shown in Figures 8-46 to 8-50. The curves are labeled "V" for vertical rings and "H" for horizontal rings, respectively. The maximum surface gradient is shown for both vertical and horizontal dry cases and the vertical wet case. The bottom gradient is also shown for the horizontal wet case. Note that the critical gradient for each ring is nearly constant with height, indicating the strong correlation between the surface field and breakdown.

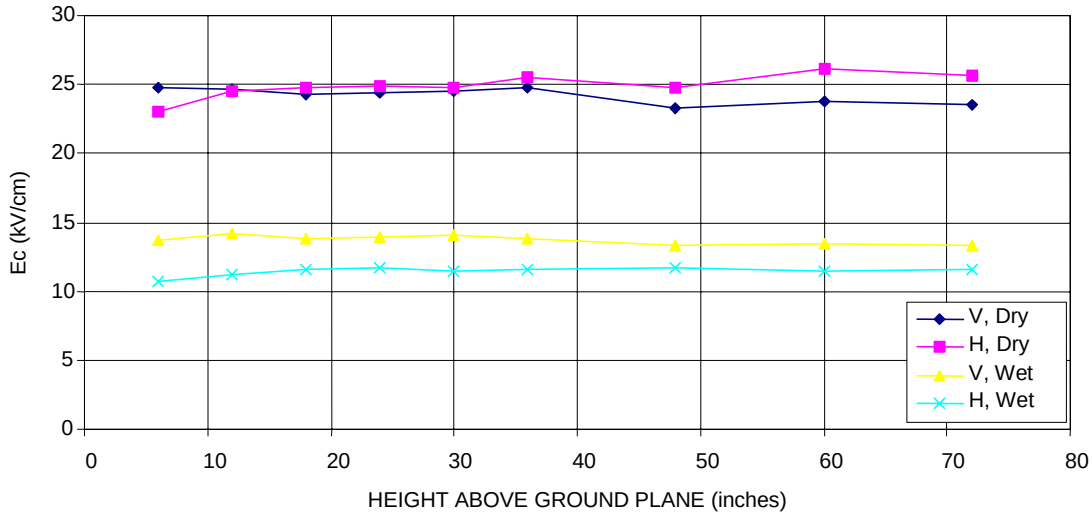

Figure 8-46. Critical gradients (rms) observed for 1-inch ring.

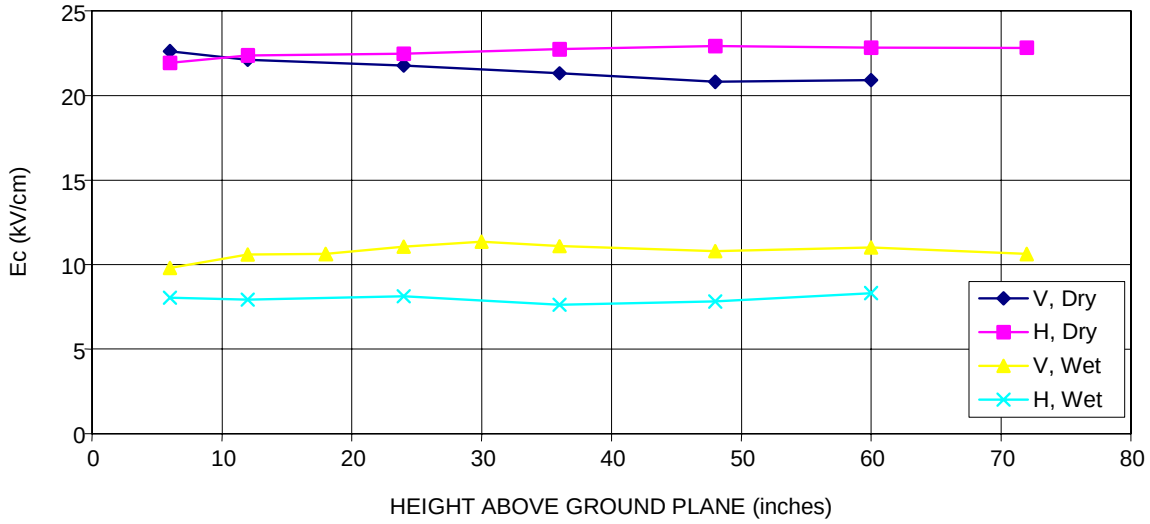

Figure 8-47. Critical gradients (rms) observed for 2-inch ring.

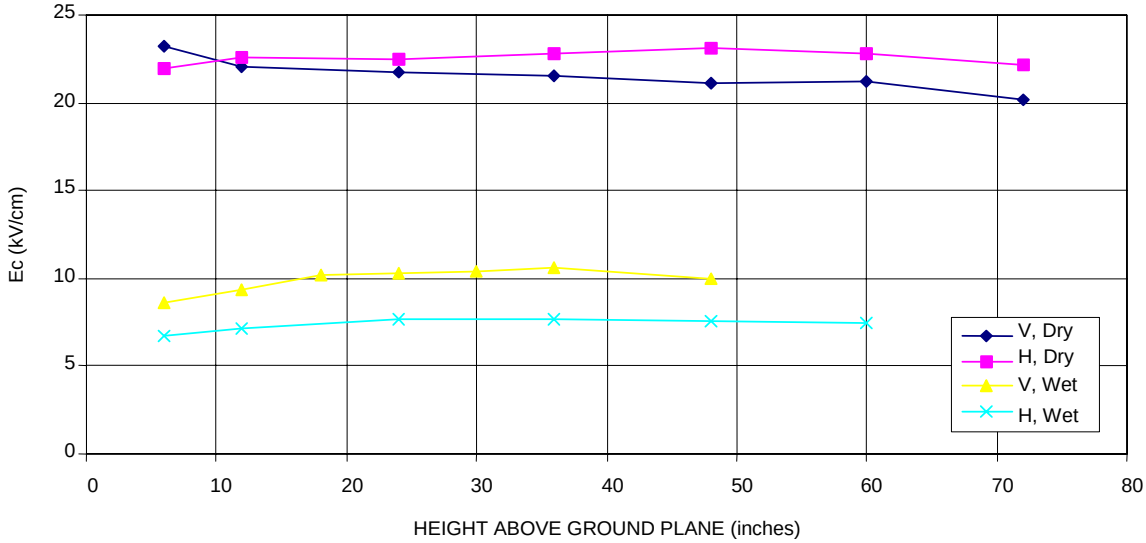

Figure 8-48. Critical gradients (rms) observed for 3-inch ring.

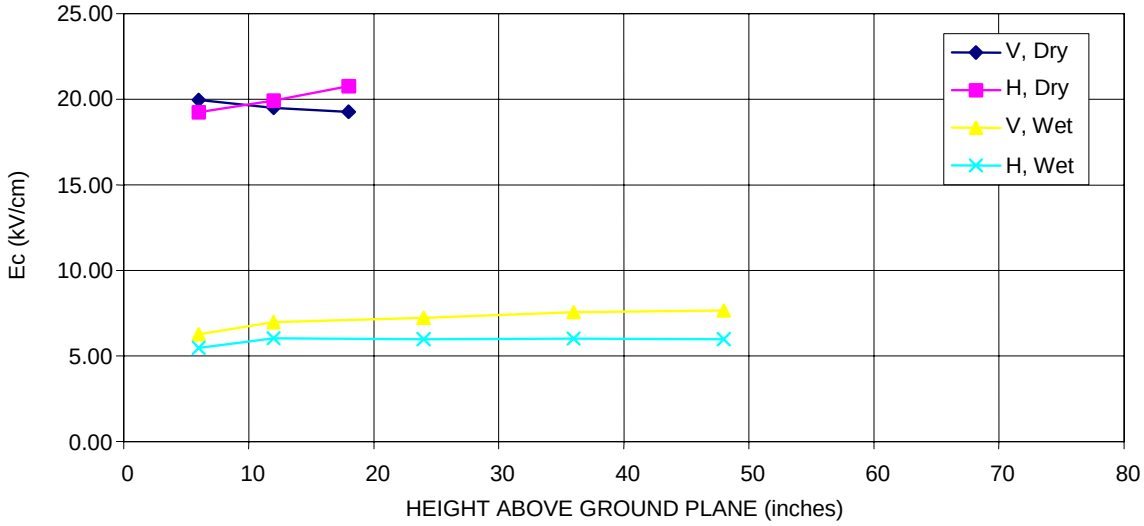

Figure 8-49. Critical gradients (rms) observed for 6-inch ring.

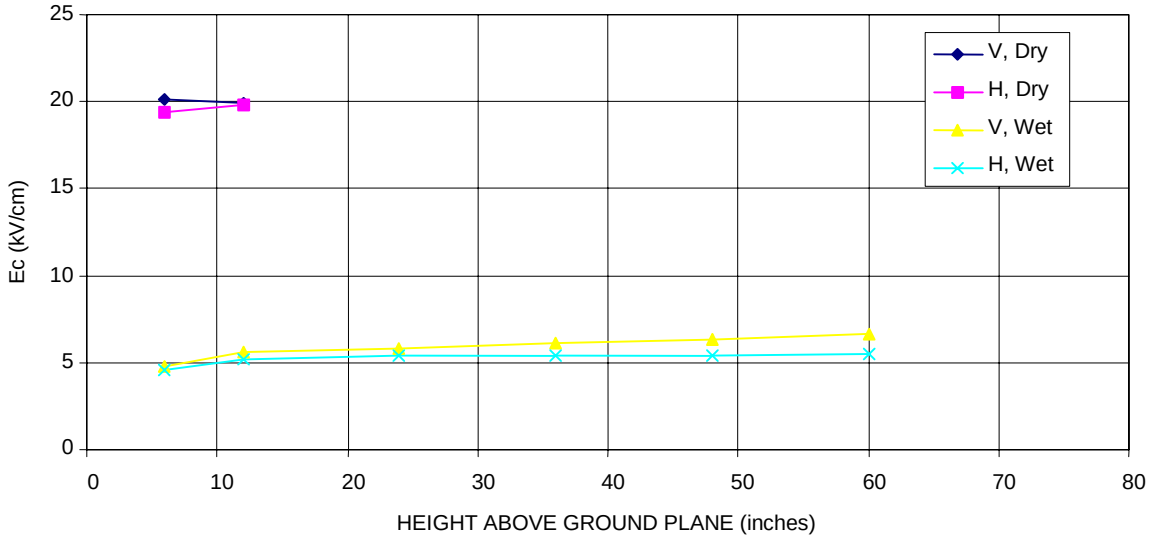

Figure 8-50. Critical gradients (rms) observed for 8-inch ring.

The breakdown gradient for each diameter ring has been averaged over height using the data from the critical gradient curves in the figures. The resulting values of critical gradient have been plotted versus ring minor diameter in Figure 8-51. These data have been corrected to STP (25° C). The correct application of the air density correction factor modifies the ring dimensions (Chapter 3), which is why the plotted points do not occur at the integer ring diameters that were measured. These curves are used in the design procedure below and are further discussed in the discussion section following the surface curvature section.

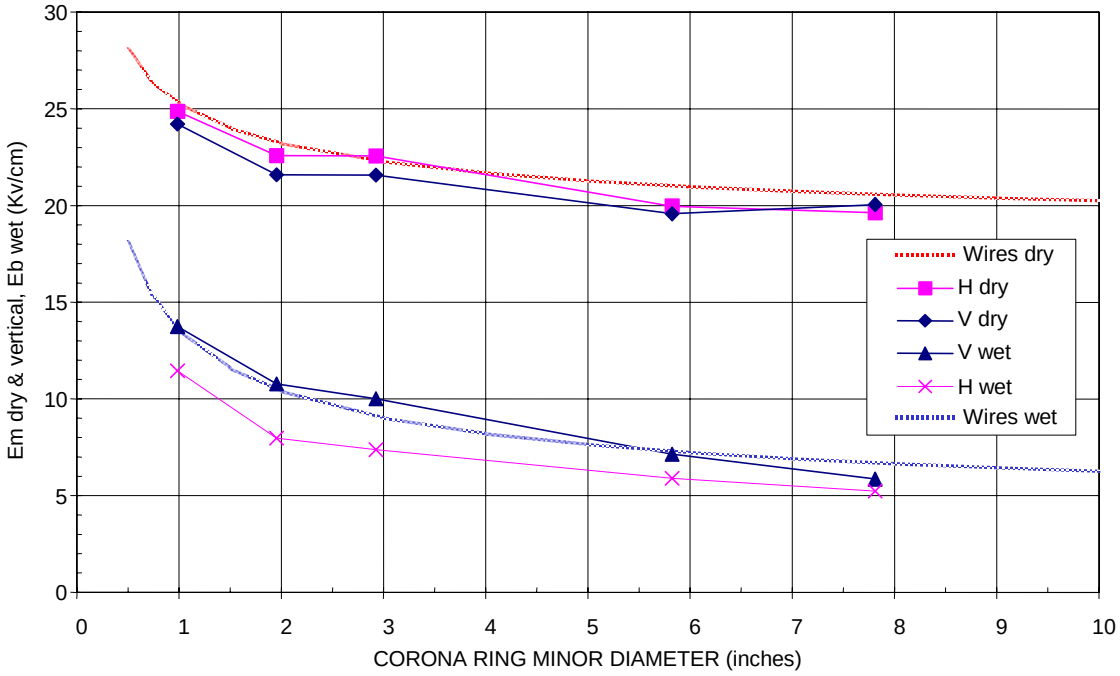

Figure 8-51. Critical gradient (rms) versus diameter for smooth rings averaged over height.

Gap Factor

The critical gradient curves in Figure 8-51 provide values that were obtained by averaging over all the heights measured. Examination of Figures 8-46 to 8-50 shows that for the wet cases there is a tendency for the critical gradient to increase with height, especially at lower heights, similar to the rod data. A gap factor has been developed for the rings in the same way as was done for the rods. The wet-ring gap factor using the measured data is shown in Figure 8-52 (curves labeled data). The figure shows that at heights of 24 inches and below the critical gradient decreases in a regular way as the gap decreases for both ring configurations. The data for vertical rings show the breakdown gradient is equal to the average (gap factor = 1.0) at a height of 17 inches and reduces smoothly to about 11% less than the average at a height of 6 inches. For the wet horizontal ring data, the critical gradient is equal to the average at a height of 13 inches and falls smoothly to about 7% below the average at a height of 6 inch. For heights of 24 inches and below, the recommended gap factor used to correct the average curves is the same as the measured data shown in the figure.

Above 24 inches, there are fewer data, and the figure indicates considerably more variability in the data. The figure shows a tendency for the vertical ring gap factor to be higher and the horizontal ring gap factor to be lower. However, the average of the vertical and horizontal gap factors is nearly constant at about 2.25%. Because of the sparse data and the variability above 24 inches, the recommended gap factor, shown in the figure, is a smooth fit between the vertical and horizontal curves below 24 inches and a constant equal to +2.25% above 24 inches. However, it should be noted that above 24 inches the uncertainty is greater with variability on the order of $\pm$2%. The curves labeled "Horizontal Factor" and "Vertical Factor" in Figure 8-52 are the recommended values used to adjust the average critical gradient versus diameter curves for wet conditions given in Figure 8-51 for different gap lengths.

The gap factor from the data for dry rings is shown in Figure 8-53. For dry conditions, the horizontal ring data shows a slight tendency for the critical gradient to increase with height, but there is no clear tendency indicated, unlike the rod measurements. The data for vertical rings show a slight trend in the opposite direction. This is unusual and is further discussed in the section following the discussion of the radius of curvature below. The magnitude of the variation with height is less for dry conditions than for wet conditions. The tendency is opposite for the horizontal and vertical rings but the average of the two is nearly unity. This seems anomalous, and for this reason a gap factor has not been developed to correct the dry-ring critical gradients.

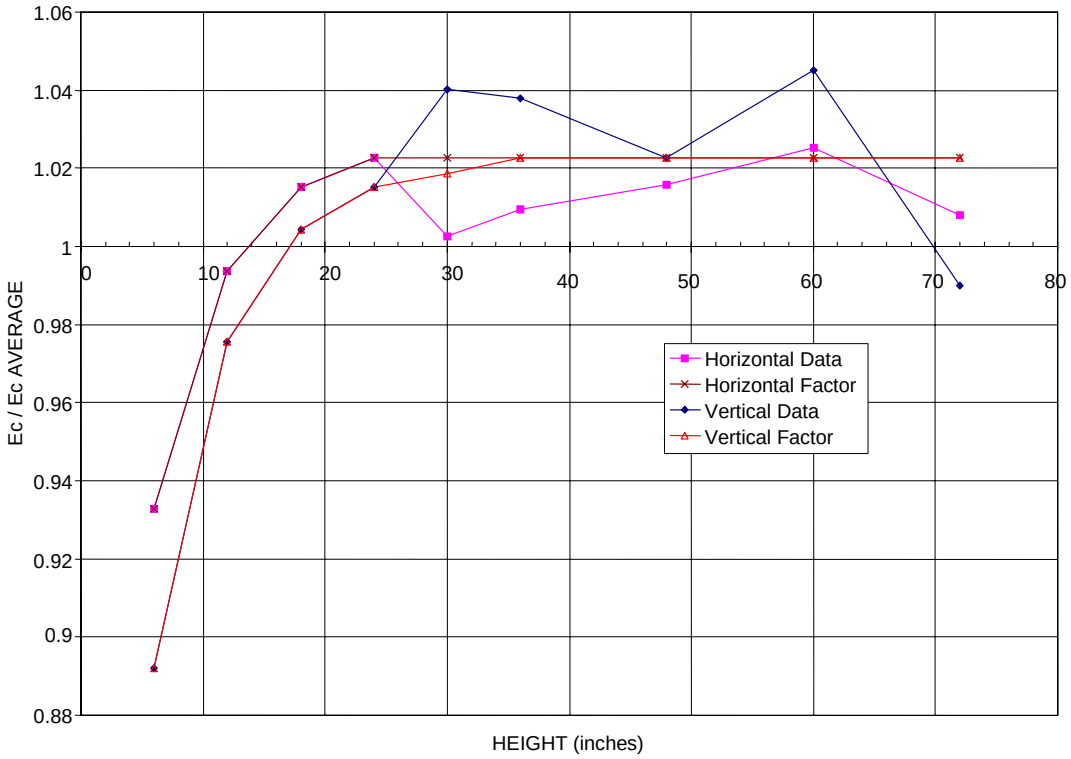

Figure 8-52. Gap factor for smooth wet rings.

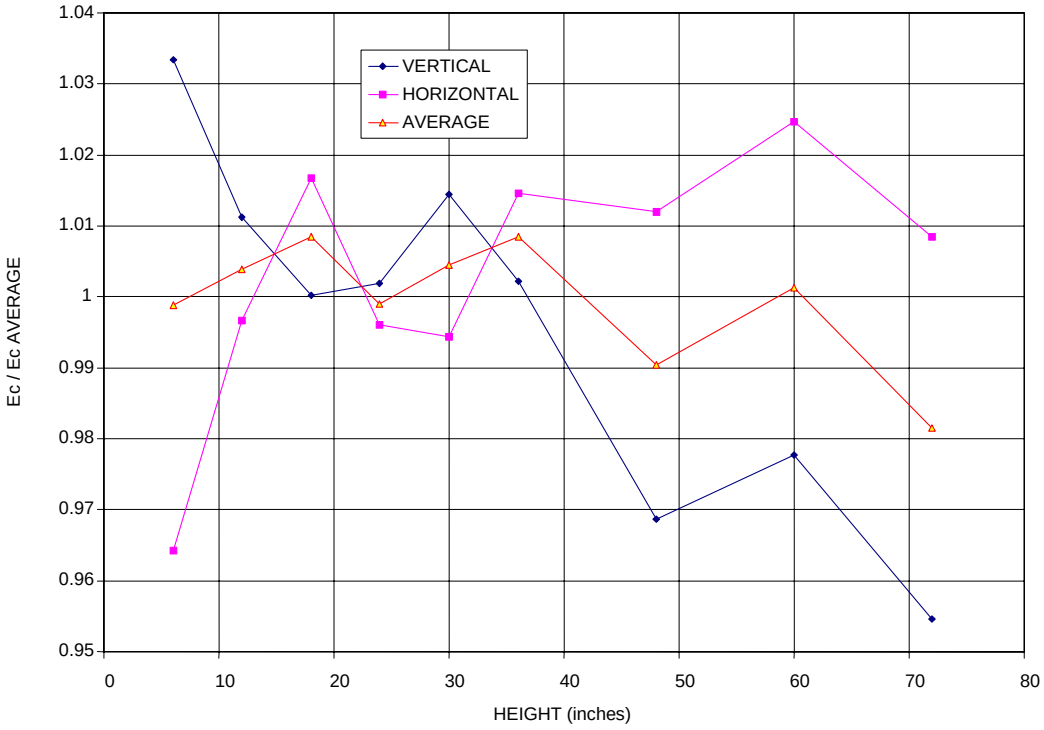

Figure 8-53. Gap factor for smooth dry rings.

Corrugated Rings

Data for the 6-inch and 8-inch minor-diameter rings made from both smooth and corrugated pipe is shown in Figures 8-44 and 8-45. Corrugated rings are made from flexible pipe that facilitates building mockups that can be changed easily. A picture of a mockup using corrugated pipe is shown in Figure 8-54. One objective of the ring tests was to determine the difference in performance between corrugated and smooth rings.

The data presented in these figures show that the breakdown gradient for spray-wet conditions is essentially the same for both the smooth and corrugated rings. This means that corrugated rings can be used as a mockup to estimate performance of an insulator assembly under spray-wet conditions.

It is interesting to note that at the largest height, the data for both ring sizes showed slightly greater breakdown gradient for corrugated rings than the smooth rings. The difference is small and may have occurred due to the unavoidable statistical variability of high-voltage breakdown measurements. However, we believe it to be real and attribute it to the fact that the water flows together more naturally and forms larger water streamers on the smooth rings. Corrugated rings tend to break up the water falling off into smaller streams and for this reason they provide a slight increase in breakdown voltage for spray-wet conditions.

For dry conditions, the opposite is true in that corrugated rings flared at a slightly lower voltage than the smooth rings.

Figure 8-54. Mockup of large corona ring using corrugated pipe.

Surface Curvature

General Case

As discussed in Chapter 2, the formation of corona is a function of the electric field on the electrode surface and in the immediate vicinity of the surface. The breakdown criterion can be related to the number of free electrons generated in the active ionization region above the surface (Olsen, et al., 1997). The number of free electrons is a function of an integral of the ionization coefficient, which is a function of the electric field, over the active region (the region where the electric field exceeds the threshold for electron avalanches). The total number of free electrons depends on the field within the active region and the thickness of the active region. Increasing the surface field increases both the rate that free electrons are generated and the thickness of the active region, thus increasing the total number of free electrons.

The field is generally a maximum on the surface and falls off away from the surface. For configurations where the field falls off rapidly, the surface field must be higher to have an active region large enough to generate the required number of electrons. For configurations where the field falls off more slowly, the active region is larger and the surface field need not be as high to generate the required number of electrons. Thus, the critical surface field for breakdown is inversely related to the rate at which the field falls off away from the surface.

In the immediate vicinity of a charged surface, the rate that the electrostatic field falls off is solely a function of surface curvature. The formulas in Table 8-10 give the electric field magnitude and its derivative as a function of the distance from the surface (δ), for a sphere, a cylinder, and a general curved surface. The radius of the sphere and the cylinder is denoted by the letter *a*.

Table 8-10. Rate of field fall-off.

Configuration	$E(\delta)$	$E'(\delta)/E_s$	$E'(0)/E_s$	$J = 1/R_s$
Sphere	$\frac{E_s \cdot a^2}{(a+\delta)^2}$	$\frac{-2 \cdot a^2}{(a+\delta)^3}$	$\frac{-2}{a}$	$\frac{2}{a}$
Cylinder	$\frac{E_s \cdot a}{(a+\delta)}$	$\frac{-a}{(a+\delta)^2}$	$\frac{-1}{a}$	$\frac{1}{a}$
General	$\frac{E_s \cdot a \cdot b}{(a+\delta)\cdot(b+\delta)}$	$\frac{-a \cdot b \cdot (a+b+2\delta)}{(a+\delta)^2 \cdot (b+\delta)^2}$	$\frac{-(a+b)}{a \cdot b}$	$\frac{(a+b)}{a \cdot b}$

The curvature *k* of a two-dimensional (2-D) curve, a curve drawn on a plane, is defined as follows.

$$k = \frac{d\phi}{dS}$$

where φ is the tangent angle of the curve and,
S is the distance along the curve.

Curvature has the dimension of inverse length. The radius of curvature, *R*, is the inverse of curvature and has the dimension of length.

$$R = \frac{1}{k}$$

For a generalized 2-D surface, a curve is defined by the intersection of the surface and a plane normal to the surface. At a point on the surface, the curvature of this curve takes on different values as the direction of the plane through the normal varies. The direction associated with the value of the curvature is the direction of the plane. The curvature can be negative or positive. As the direction varies, *k* goes through a minimum and a maximum, which are in perpendicular directions. The minimum and maximum values are known as the principal curvatures, (k_1 & k_2). There are two corresponding principal radii of curvature denoted by $R_{1,2} = 1/k_{1,2}$. In general, these are a function of position on the surface. In Table 8-10, the principle radii of curvature for the general surface are denoted by *a* and *b*.

The principal of curvatures are related to the rate of change of the area of an elementary area of the curved surface. It can be shown that the sum of the two principal curvatures is equal to the decrease of the normal derivative of an elementary area per unit area (Tai, 1997, pp. 41–42). Based on this, Tai defined a "surface curvature," *J*, as follows.

$$J = \frac{1}{R_1} + \frac{1}{R_2}$$

The inverse of J can be called the "surface radius" or "surface radius of curvature," R_s, which has units of length.

$$\frac{1}{R_s} = J = \frac{1}{R_1} + \frac{1}{R_2}$$

where R_1 and R_2 are the principle radii of curvature at a point on the surface.

The principal radii of curvature for a sphere are both equal to a. This gives a value for the surface radius, R_s, of $a/2$. A circular cylinder has two principal radii of curvature; one is equal to a and the is other infinite because it is in the direction of the cylinder axis. For this case, the surface radius is equal to a. For the generalized case in Table 8-10, the radii of curvature are a and b and the surface radius of curvature is given by

$$R_s = \frac{1}{(\frac{1}{a} + \frac{1}{b})} = \frac{a \cdot b}{a + b}$$

The above equation can be rearranged to give

$$\frac{R_s}{a} = \frac{b}{a + b}$$

which proves convenient for summarizing data. By convention, a is the smaller of the principal radii.

Figure 8-55 gives a plot of R_s normalized to a as a function of the surface aspect ratio b/a, showing that R_s/a lies between one-half and 1 ($\frac{1}{2} \leq R_s/a \leq 1$). When the aspect ratio is 1, the object is a sphere with surface radius R_s equal to $a/2$. As the aspect ratio increases, the magnitude of R_s increases. When the aspect ratio goes to infinity, the object becomes a cylinder with surface radius R_s equal to a.

It is useful to examine the rate of field decay in the immediate vicinity of the surface for the various configurations. This is given in the table by the derivative of the field in the direction normal to the surface, evaluated on the surface, and normalized by the field on the surface *E'(0)/Es*. As indicated in the table, the normalized derivative for the cylinder in the immediate vicinity of the surface is equal to $-1/a$ (that is the rate of field decay normalized to the field on the surface is inversely proportional to the radius a). Thus, the field falls off less rapidly for larger diameter cylinders and means they will have lower critical gradients. Keep in mind that even though larger diameter cylinders have lower critical gradients, they have higher critical voltages because as the radius increases the surface field reduces faster than the critical field increases (Chapter 6).

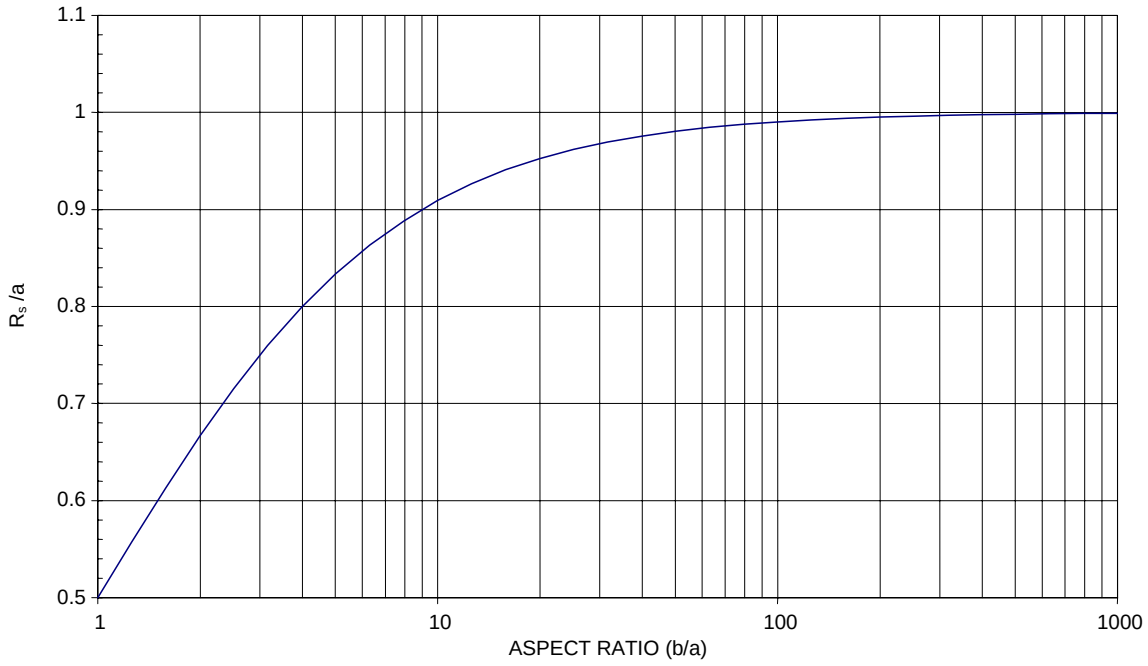

Figure 8-55. Variation of R_s with surface aspect ratio.

The normalized derivative for the sphere (see Table 8-10) is twice that for a cylinder of the same radius due to the $1/r^2$ dependence for the sphere versus $1/r$ for the cylinder. This means that in the immediate vicinity of the surface the field falls off twice as fast for the sphere as for the cylinder. Thus, the sphere is expected to have a higher critical gradient than a cylinder of the same radius.

For the generalized case of a surface with two different radii of curvature, the normalized derivative is equal to the negative of the surface curvature ($-J = -1/R_s$), as seen from the table. For this case, the field at the surface falls off at a rate greater than for a cylinder of radius a, but less than for a sphere with radius a.

The critical gradient is a function of the integral of the field normal to the surface, which is dominated by the field near the surface. To first order, the integral depends on the field and the rate of field fall-off at the surface. For this reason, different objects having the same surface radius of curvature R_s are expected to have similar critical gradients. They are not necessarily the same because even when the slopes at the surface are equal, the variation away from the surface may be different. Examples of this are illustrated by the formulas for $E(\delta)$ in Table 8-10. In the general case, the presence of other nearby conductors also affects the field variation away from the surface. Therefore, the surface radius of curvature cannot be used to define a strict equivalence between objects (Phillips, 1999). Nevertheless, it is true that all other things being equal the critical gradient for an object is inversely related to R_s. Thus, in general, changing an object to increase R_s will decrease the critical gradient (but increase the critical voltage).

Toroid

A toroid can be defined by two parameters, the minor radius a, and the major radius b, shown in Figure 8-56. The smaller principle radius is equal to $-a$ everywhere on the toroid, but the larger principle radius varies as a function of position. At the outermost edge of the toroid, point $P2$ on the figure, the larger principle radius is equal to $-b$. At the bottom of the toroid, point $P1$ on the figure, the

larger principle radius is negative infinity (also at the top). At points between *P*1 and *P*2, the larger principle radius lies between –*b* and negative infinity. The equation for the larger radius of curvature is given below using the angle around the toroid α,defined in the figure.

$$R_2 = \frac{b - a \cdot (1 + \cos(\alpha))}{\cos(\alpha)}$$

R_s as a function of α has been calculated for a set of toroid aspect ratios and is plotted in Figure 8-57. Note that on the bottom of the toroid (P1) $\alpha = 90°$ and R_s is always equal to *a* (same at the top). From the figure it can be seen that when the aspect ratio is large, R_s does not decrease much as the point on the surface moves away from *P*1 towards the edge of the toroid *P*2. However, for small aspect ratios R_s rapidly decreases as the surface point moves away from *P*1.

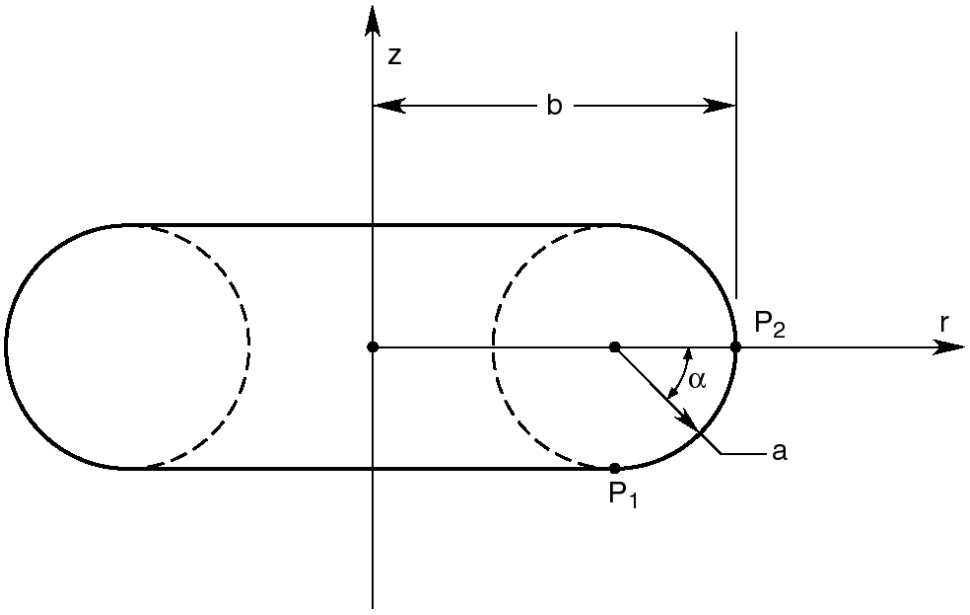

Figure 8-56. Toroidal ring parameters.

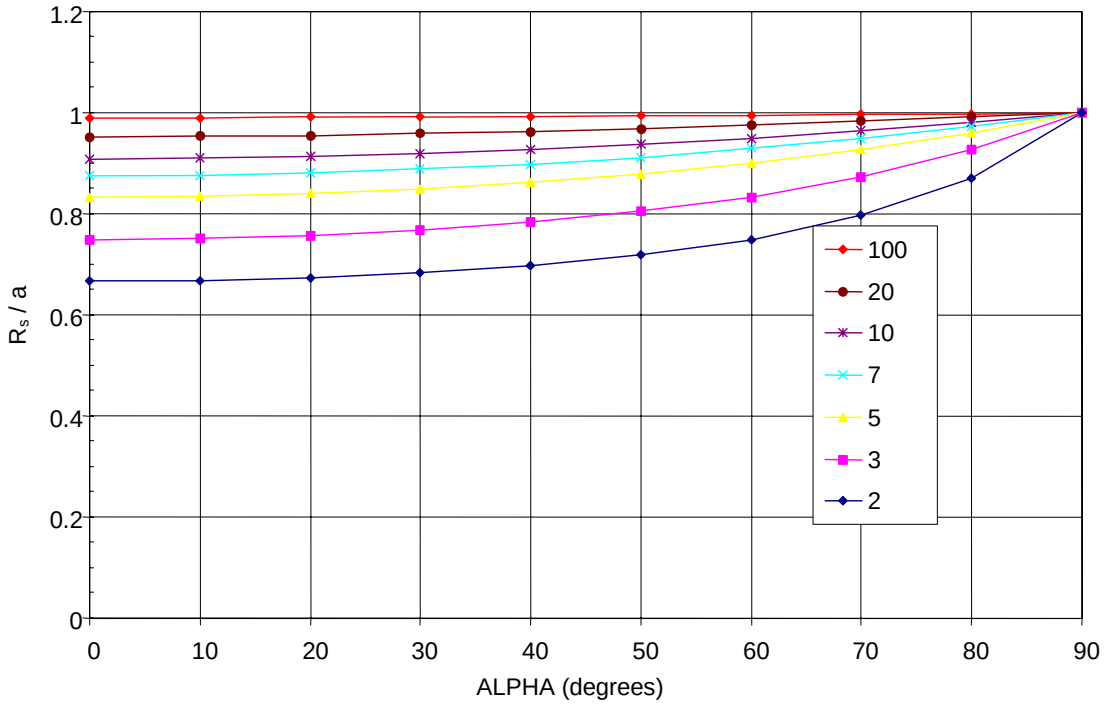

Figure 8-57. R_s/a as a function of angle around a toroid, parametric in aspect ratio.

For horizontal rings above ground, the location of the maximum field is a function of height above ground. When the ring is high, the ground has little influence and the maximum field is on the outermost edge of the ring corresponding to point *P*2 in Figure 8-56. As the ring approaches ground, the location of the maximum moves around the ring towards the bottom (*P*1 in the figure).

This is illustrated in Figure 8-58, which shows the normalized maximum and bottom gradients as a function of height for a 6-inch horizontal ring above ground (aspect ratio $b/a = 7.0$). The figure also gives the angle to the maximum field point (α). Note that at low elevations the maximum point is near the bottom of the ring ($\alpha \Rightarrow 90°$) and the maximum and bottom gradients are nearly the same. As the height increases, the maximum field point moves out towards the edge of the ring ($\alpha \Rightarrow 0°$) and there is more difference between the maximum and bottom gradients. Thus, R_s at the maximum field point decreases with height, and the critical gradient for the rings is expected to have a slightly larger value as the height increases.

As the height increases, the capacitance of the ring, and therefore the total charge on the ring, asymptotically approaches the free space value. Thomas (1954) has developed exact and approximate expressions for the capacitance of a toroidal ring in free space. Two of the approximate formulas are given below. Both formulas have been normalized to the capacitance of a sphere with radius *b*.

$$\frac{C_T}{C_S} \approx \frac{\pi \cdot b}{\ln(8 \cdot b/a)} \quad \text{For large aspect ratios } (b/a > 3.33)$$

$$\frac{C_T}{C_S} \approx 0.68 + \frac{1.07}{b/a} \quad \text{For small aspect ratios } (b/a < 3.33)$$

The relative error for the first equation is 4.5% (better than 1% if $b/a > 8.33$). The relative error for the second equation is less than 1%. Thomas notes that for small aspect ratios the capacitance of the ring is approximately 4/5th that of a sphere with radius b.

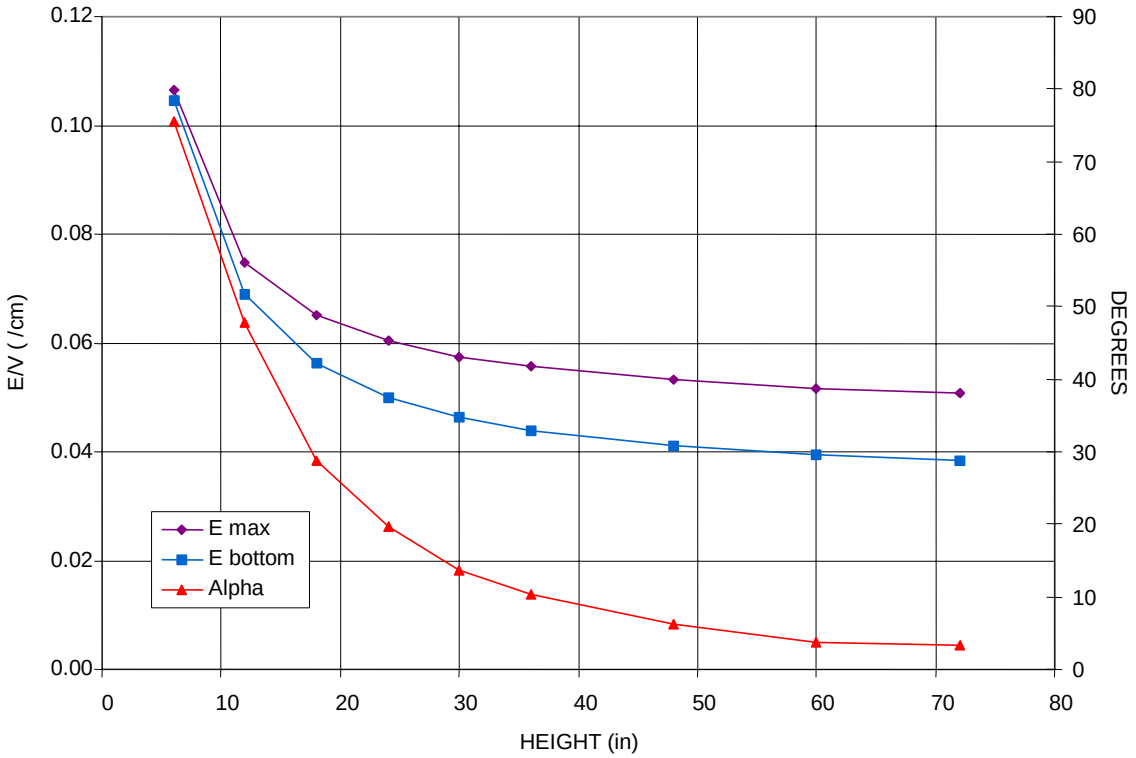

Figure 8-58. Normalized gradients on a 6-inch ring above ground including angle α.

Example Ring Aspect Ratio 7

A set of computer calculations were performed for a ring with aspect ratio 7.0 located above ground, and the results are shown Figure 8-59. The curves in the figure are normalized and can be used to determine as a function of height the maximum gradient and its location as well as the bottom gradient for any toroid having the same aspect ratio. These curves are useful for design. An example of their use is given in the design section below.

The horizontal ring data in Figure 8-59 were calculated using the 2-D computer program, and the vertical ring data were calculated using the 3-D computer program as discussed in Chapter 4. The gradients have been normalized to the gradient on a sphere in free space ($E = V/a$). The height has been normalized to the minor radius of the toroid (a in Figure 8-56). For comparison, the normalized gradient on a cylinder at the same height was determined using the exact equation derived in Chapter 4 and the results included in the figure.

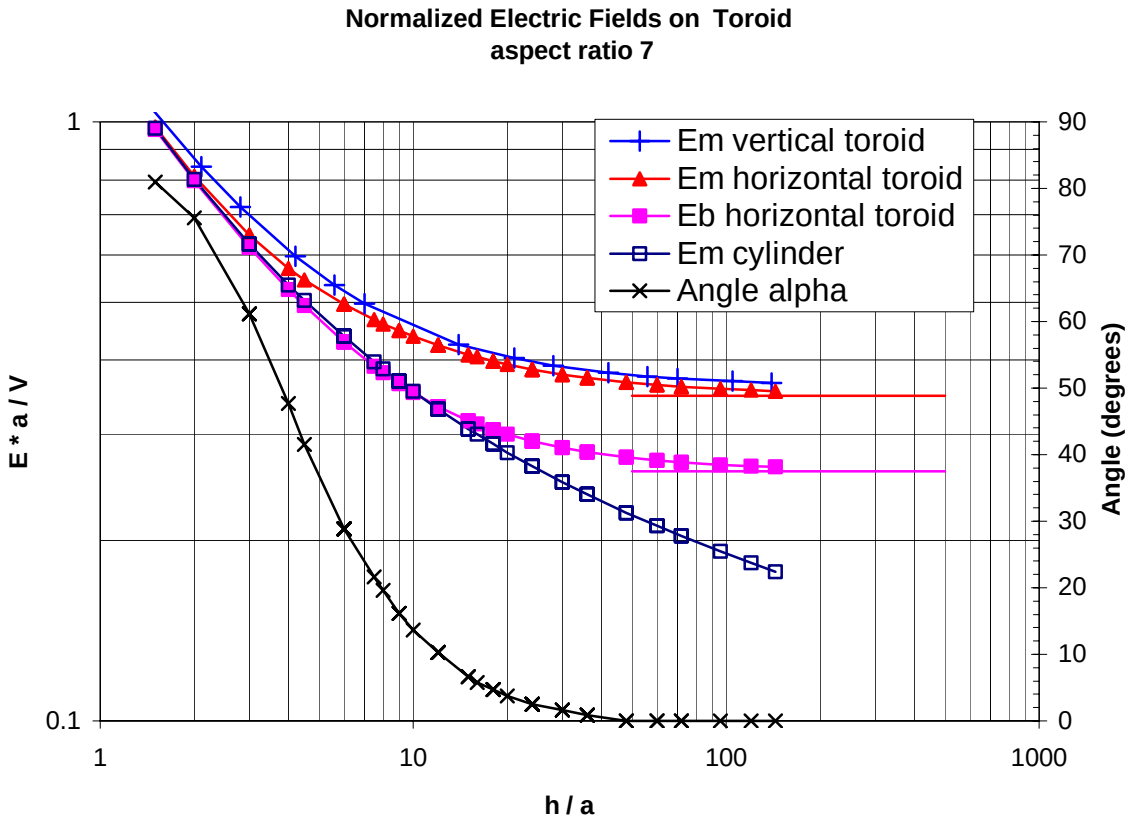

Figure 8-59. Normalized gradients for toroidal ring above ground, aspect ratio 7.0.

Figure 8-59 shows that when the ring is well above ground the maximum and bottom fields on the horizontal ring are significantly different. As the ring approaches the ground, both the maximum and bottom fields are asymptotic to the value for an infinite cylinder (radius a) at the same height. This is because the charge concentrates on the bottom side of the ring, indicated by α approaching 90°. Note the maximum field approaches the asymptote from above but the field on the bottom of the ring approaches the asymptote from below. This is attributed to the fact that the horizontal ring provides more shielding for the bottom than does a cylinder. For the case shown ($b/a = 7.0$), the field on the bottom of the ring is less than the field on the bottom of a cylinder when $h/a < 10$. The maximum departure below the field on the cylinder occurs when $b/a \cong 4.5$.

Figure 8-59 shows that for horizontal rings as the height increases above ground the location of the maximum field point moves to the outside edge ($\alpha = 0°$) and the fields on the rings asymptotically approach constant values corresponding to their values in free space. The figure shows that the maximum fields for the vertical and horizontal rings are asymptotic to the same (free space) value as height increases. The asymptotic (free space) values for rings with other aspect ratios have been calculated using the 2-D computer program and are given in Table 8-11. Note that E_{bottom} in the table was taken on the side of the ring corresponding to the bottom of the ring when horizontal. E_{max} was taken at the outside edge of the ring.

The figure also shows that the maximum field on the infinite cylinder continues to decrease as height increases unlike for the rings. This is because the cylinder is infinite. The field on the rings, which are finite, approaches an asymptotic value.

Table 8-11. Normalized free space gradients on toroidal rings.

b/a	E_{bottom}*a/V P_1 Fig. 8-56	E_{max}*a/V P_2 Fig. 8-56
2	0.460	0.663
3	0.366	0.530
5	0.293	0.408
7	0.263	0.349
10	0.235	0.303
15	0.213	0.258
20	0.199	0.235

The figure shows that as height decreases the maximum field on the vertical ring increases faster than does the maximum field on the horizontal ring. However, as the height approaches a value equal to the minor radius, the maximum field on the vertical ring comes back to approach the maximum field on the horizontal ring. To illustrate this better, Figure 8-60 gives a plot of the maximum field on the vertical ring compared to the fields on a cylinder and a sphere, all with radius a. From the plot, it is seen that when $h/a << 1$ both the curves for the cylinder and sphere are asymptotic to a straight line with slope –1 on a log-log scale. This line corresponds to the field in a parallel plate configuration of the same height ($E_m = V/h$). The maximum field for the vertical ring falls between the curves for the cylinder and sphere, and at small heights they all become asymptotic to the line with slope of –1.

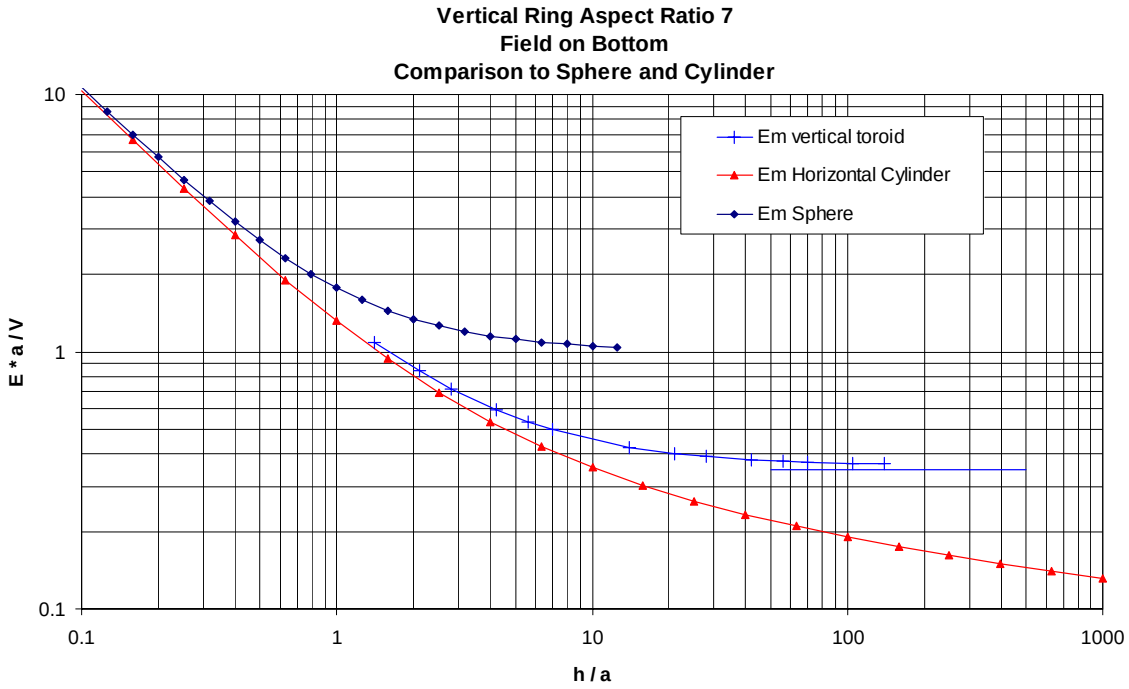

Figure 8-60. Vertical ring bottom (maximum) field compared to cylinder and sphere.

Discussion of Measured Data

The critical gradient curves shown in Figure 8-51 show the expected dependency of decreasing breakdown gradient versus ring minor-diameter. The formulas developed for cylinders at 30 kHz (Chapter 6) have been plotted on the same graph and are remarkably similar to the measured ring data. The figure shows that the dry horizontal ring data are an excellent fit to the formula for dry cylinders (curve labeled "wires dry"). Similarly, the wet vertical ring data are an excellent fit to the formula developed for wet cylinders (curve labeled "wires wet"). The vertical dry and horizontal wet data for rings are only slightly below the curves for vertical cylinders.

Based on the theoretical considerations of Chapter 2 and the discussion of surface curvature above, the critical breakdown field should be inversely related to the radius of curvature of the surface. Thus, the expectation is that the breakdown field would be greatest for the vertical ring configuration, and the data do indicate this is the case for wet conditions. However, for the case of dry rings, the data indicate the opposite in that the critical gradient for horizontal rings is slightly greater than it is for vertical rings. The reason for this is not known at this time; however, it could be due to the presence of the support pipe, ground, and/or other objects that changed the fields enough to cause this effect as discussed below. It is also possible that this is a result of error in calculating the gradients on the 3-D vertical corona rings.

The concept of the surface radius of curvature, R_s, is useful in interpreting the breakdown data for rings. The aspect ratio of the various rings used in the measurements varied considerably. The maximum aspect ratio was 16.4 for the 1-inch ring, and the minimum was 3.4 for the 3-inch ring (Table 8-12). The average of the aspect ratio for the five rings was 6.8.

The value of R_s varies with position on the ring. The maximum value is equal to the ring minor-diameter (a, or r_2) and occurs where alpha is $\pm$ 90^o (Figure 8-56). The minimum value occurs at the outside edge of the ring where alpha is 0^o. Table 8-12 also contains the calculated minimum and maximum values of R_s for the rings used for the breakdown measurements. Note that the minimum value of R_s is always less than the minor radius (a). The ratio of minimum R_s to minor radius is given in the last column. The 3-inch ring has the smallest value of this ratio (71%) because it has the smallest aspect ratio. Thus, at least for dry conditions, the critical gradient for this ring would be expected to be greater than for another ring with the same minor diameter but with a larger aspect ratio.

Table 8-12. Equivalent radius of curvature for test rings.

Ring diameter (inches)	b/a	Min R_s	(min R_s)/ a
1	16.4	0.47	0.94
2	6.2	0.86	0.84
3	3.4	1.06	0.71
6	4.0	2.25	0.75
8	4.0	3.00	0.75

The data shown in Figure 8-51 are consistent with this hypothesis in that the critical gradient for the 3-inch ring lies above a smooth curve drawn through the other points. In fact, the gradient for the 3-inch ring is only a little below that for the 2-inch ring. The most anomalous point occurred for dry conditions, where the critical gradient for the 3-inch ring was slightly greater than for the 2-inch ring. This is because breakdown for dry conditions occurs at the maximum field point, which is near the outside edge of the toroid, where R_s is a minimum. Since the 3-inch ring has a smaller minimum value of R_s due to the higher aspect ratio, for dry conditions it would be expected that it would have a corresponding increasing the critical gradient.

The critical gradients on the 3-inch ring for wet conditions were also high, as seen in the figure. This is surprising since for wet conditions breakdown seems to occur on the bottom of the ring, and the mean radius of curvature on the bottom of the ring is not a function of aspect ratio. This may indicate that the controlling gradient for the region where the water drops off may actually be slightly up on the ring.

For both the dry and wet cases, the curves are smoothed by plotting the data versus the minimum value of R_s. This indicates that the using the minimum value of R_s as an equivalent radius allows the critical gradient curves to be adjusted for differences in the aspect ratio of the toroidal rings.

The average value of the aspect ratio for the rings used to generate the curves in Figure 8-51 was 6.8. The smooth curves and formulas are a good estimate of the critical gradient for corona rings having approximately the same aspect ratio. The measured data points are good estimates for rings having aspect ratios that correspond to that of the rings measured, which are different for each minor diameter. An approximation for other aspect ratios can be obtained from the curves and formulas for the aspect ratio 6.8 by using the minimum value of R_s as an equivalent radius.

Note that data given in Figure 8-53, gap factor for dry conditions, indicate that for horizontal rings there is a tendency for the critical gradient to increase with height. In part this can be attributed to the fact that the maximum field point moves toward the outer edge of the ring, thereby increasing R_s as

the height increases. For vertical rings, there is a slight tendency for the critical field to decrease with height. This is not related to a changing value of R_s because for vertical rings the maximum field is always on the bottom. However, this could occur due to the charge becoming less uniform as the ring approaches ground. The resulting charge concentration causes the field to fall off more rapidly away from the bottom of the ring.

Figure 8-53 indicates that the critical gradient for the horizontal rings somewhat exceeds the critical gradient for the vertical rings for heights above 30 inches. This is anomalous in that it would normally be expected that the two gradients would asymptotically approach the free space value at great heights. However, in this case there was a support rod, configured differently for the vertical and horizontal cases (Figures 8-36, 8-37, 8-38). For horizontal rings, this rod affects the position of the maximum field, moving it away from the point where R_s is minimum. This may be the cause for the higher value of critical gradient for the horizontal rings. Similarly, the support rod on the vertical rings tends to concentrate the charge on the bottom of the ring, causing the field to fall faster, possibly resulting in a decreased critical surface gradient.

Design

The curves shown in Figure 8-51 form the basis of a high-voltage design procedure for toroidal rings. Formulas for the critical gradient of toroidal rings have been developed using the data presented in Figure 8-51. The formulas are given in Table 8-13 and plotted in Figure 8-61. Note that the asymptotes for the ring curves are the same as for the cylinder curves. The asymptote is 17.24 kV/cm for the dry case and 3.1 kV/cm for the wet case.

Table 8-13. Breakdown gradient (rms) formulas for toroidal rings.

Configuration	Formula
Vertical Wet	$E_c = 3.1 + 18.0/d_{cm}^{0.55}$
Horizontal Wet	$E_c = 3.1 + 14.9/d_{cm}^{0.64}$
Vertical Dry	$E_c = 17.25 + 10.9/d_{cm}^{0.51}$
Horizontal Dry	$E_c = 17.25 + 12.5/d_{cm}^{0.52}$

The approach for analysis or design of a toroidal ring configuration above ground is similar to that described in the section above on rods and in Chapter 6 for cylinders.

The first step in determining the breakdown voltage for a given configuration is to determine the normalized gradient G_0 per unit length. This can be done with a computer program as described in Chapter 4. Alternatively for rings with no support rods values of G_0 can be taken from Figure 8-59 for vertical or horizontal rings with an aspect ratio of 7.0. For vertical rings with no support structure, a good approximation to the normalized maximum field on the bottom of the ring that has been verified for aspect ratios between 5 and 10 is given by the following formula.

$$\frac{E_{\max} \cdot a}{V} = \frac{E_{\max \infty} \cdot a}{V} + \frac{1}{(h/a)}$$

where $E_{\max\infty}$ is the gradient on the outside edge of the toroid in free space taken from Table 8-11.

Estimates based on rings with no support structure give conservative results (lower than actual breakdown voltages) because the support members normally reduce the gradients. Note that for dry rings the maximum gradient is used, but for wet conditions the gradient on the ring where the water drips off is used. For horizontal rings, this would normally be the bottom. However, for outside conditions the wind may cause the water to drip off anywhere including where the gradient is maximum. For this reason, the maximum value G_0 is used for outdoor rings, especially on guy insulators hung at angles. Again, this is conservative in that it leads to lower estimated breakdown voltages.

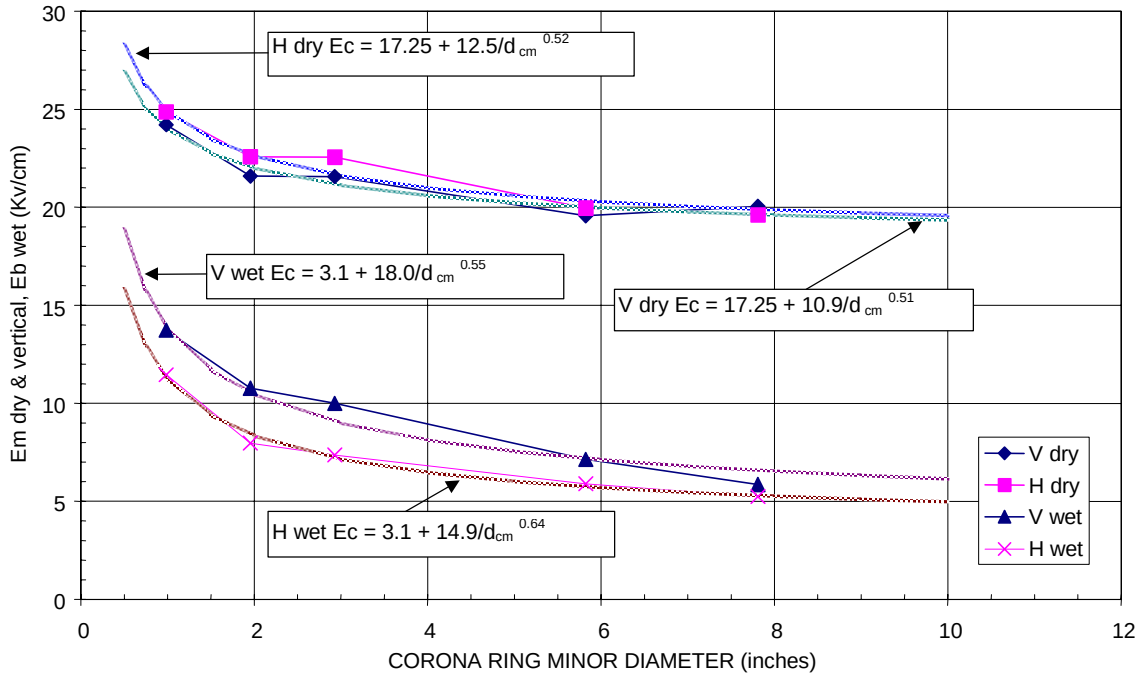

Figure 8-61. Critical gradient (rms) for toroidal rings and curve fit formulas.

The next step is to determine the critical gradient for the configuration being considered. The critical gradient for the particular size ring can be read off Figure 8-61, or the formulas in Table 8-13 can be used. The curves and formulas were developed from measurements on several rings having different aspect ratios. However, the average aspect ratio for these rings was slightly less than 7.0. If the ring aspect ratio differs significantly from this value, the critical gradient may need to be adjusted. As discussed in the section above, the critical gradient will be less for rings with larger aspect ratios and greater for rings with smaller aspect ratios. There is not enough data to quantify this effect, but when the aspect ratio is considerably different than 7.0, we recommend using the equivalent radius of curvature (converted to diameter) in the formulas to get a better estimate for the critical gradient. This critical gradient is then adjusted by the ring gap factor, but only for wet conditions.

Once the critical gradient has been determined, the breakdown voltage is determined by dividing the critical gradient by the normalized gradient.

$$V_c = \frac{E_c}{G_0}$$

Values for the breakdown (flashover-flare) voltage for dry conditions calculated in this way are shown in Figure 8-62. These voltages have been calculated for rings having an aspect ratio of 7.0 and without support members. The curves for dry conditions are plotted as pairs for the vertical and horizontal orientation of the same size ring. The breakdown voltage for vertical rings is somewhat less than for horizontal rings. This is due to the fact that for horizontal rings the maximum gradient point moves closer to the ground as the ring approaches ground, reducing the equivalent radius of curvature as discussed in the section above. As the elevation increases, the two curves tend to converge to the free space values.

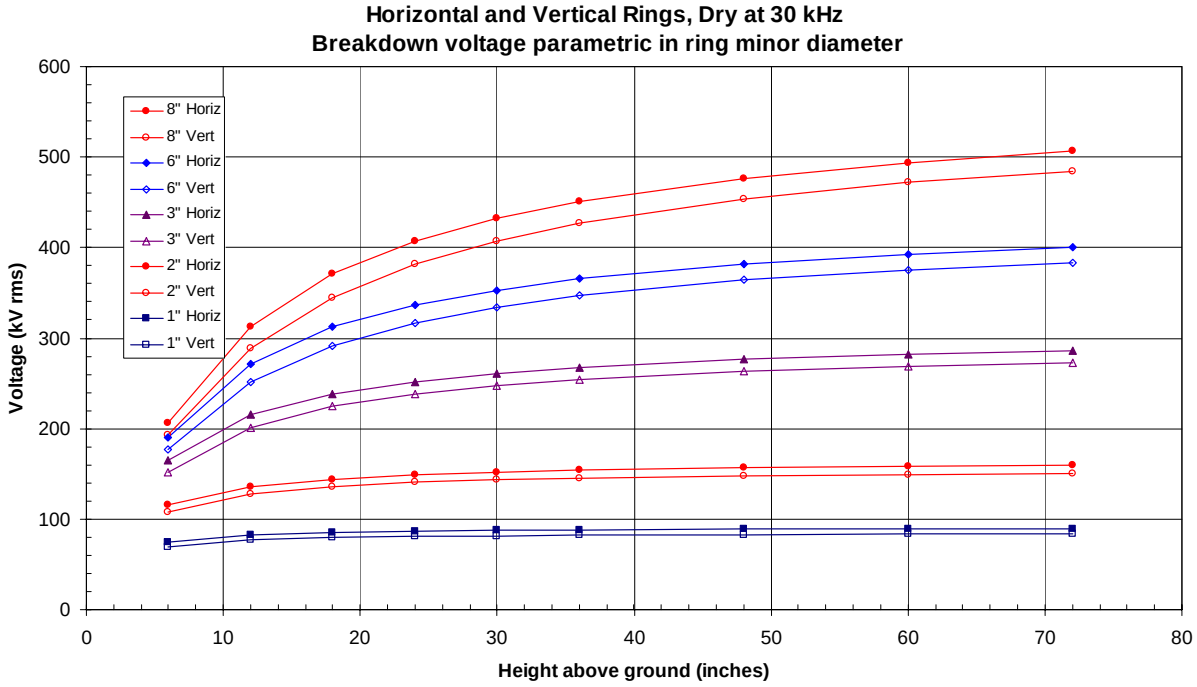

Figure 8-62. Calculated dry breakdown voltage for rings, (*b*/*a* = 7).

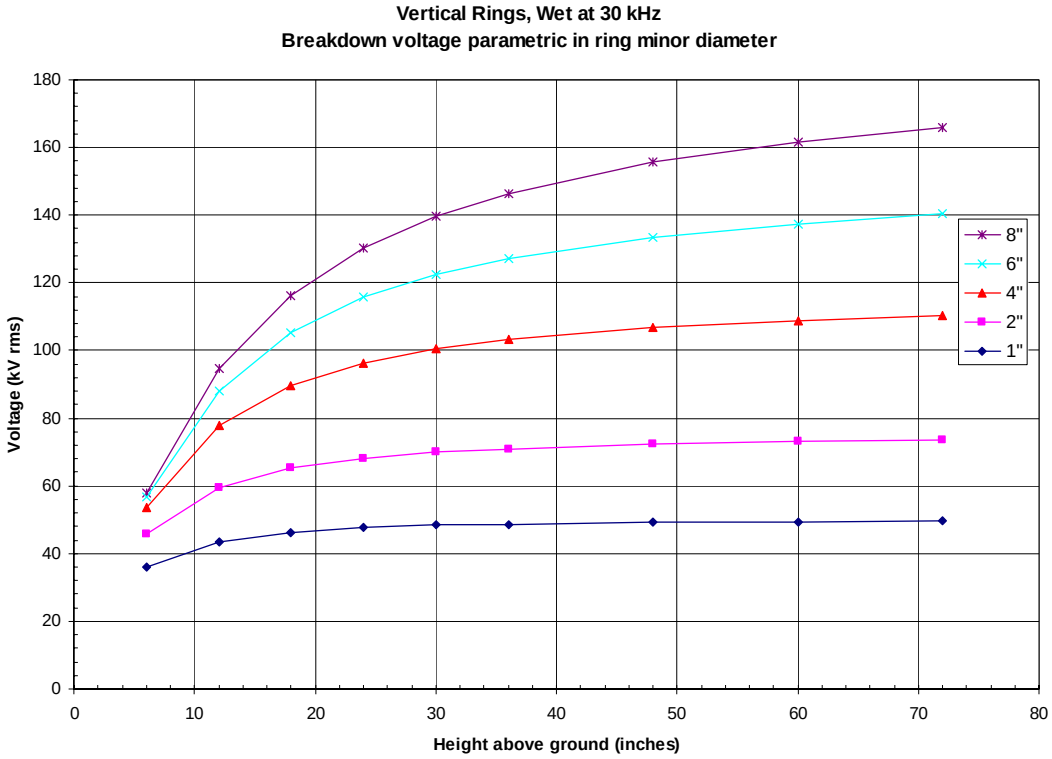

Figure 8-63. Calculated wet breakdown voltage for vertical rings, (*b*/*a* = 7).

The calculated breakdown voltage for wet conditions is shown in Figures 8-63 for vertical rings and 8-64 for horizontal rings. For wet conditions, horizontal rings have considerably greater breakdown voltage than vertical rings. This is because for wet conditions the controlling gradient is on the bottom where the water falls off. For a given voltage and height, the bottom gradient on a horizontal ring is considerably less than the bottom gradient on a vertical ring; thus the breakdown voltage is less for vertical rings.

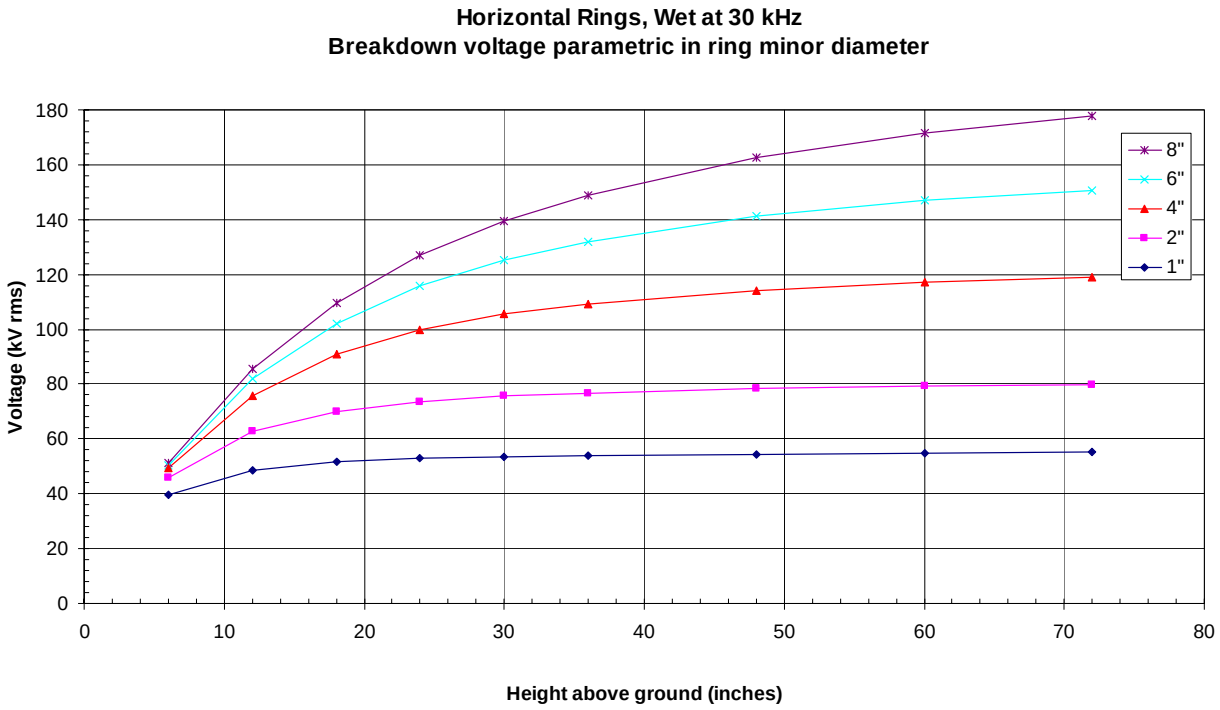

Figure 8-64. Calculated wet breakdown voltage for horizontal rings, (*b*/*a* = 7).

CONTINUOUS ARCING

For very high-voltage hardware, it is common to use more than one insulator in series to withstand the voltage. For example, VLF antennas using guyed towers often use several breakup insulators in each guy wire. For this type of configuration, it is possible for an arc to form across one of the insulators in the string without shorting out the circuit completely. In this case, the arc shorts out only one insulator and the current in the arc is carried across the remaining insulators by capacitive (displacement) current. Thus, the capacitance across the insulators that are not shorted out feeds the current in the arc. Assuming the voltage remains constant, the arc current is limited by the capacitive reactance across the insulators that are not shorted out.

A schematic diagram of this type of situation for a VLF antenna having insulated guy wires is shown in Figure 8-65. For this type of situation, an arc can be triggered across one or all of the insulators by some external cause. For example, a charged cloud overhead or direct or nearby lightning strikes can cause some or all the insulators in a guy wire to flashover. Also, dirt, insects, or other airborne foreign material, can cause a flashover at a single insulator. If an arc occurs across a single insulator in a string while transmitting the change in antenna impedance may not trigger the transmitter cut off. In that case the transmitter can continuously feed the arc and it will not extinguish until the transmitter is momentarily powered down. A picture of this phenomenon for the topload guy insulators at the Navy's VLF site in Aguada Puerto Rico is shown in Figure 8-66. In the case of the insulators at Aguada, the arc formed inside of the porcelain cones and destroyed them in a short period of time. These insulators have since been replaced.

This type of phenomena has been observed for other types of insulators operating in strings. For example, the NATO VLF site at Tavolara, an island off the East Coast of Sardinia, Italy, uses strings

of 24 fail-safe insulators placed next to each other. The insulators near the center of certain of these strings have experienced electrical damage due to sustained arcing.

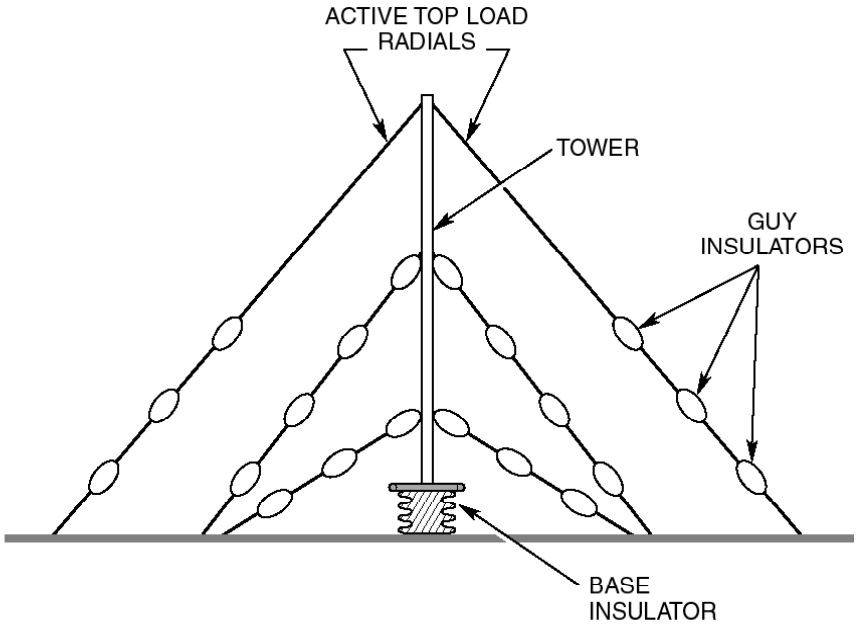

Figure 8-65. Umbrella toploaded monopole showing guy insulators.

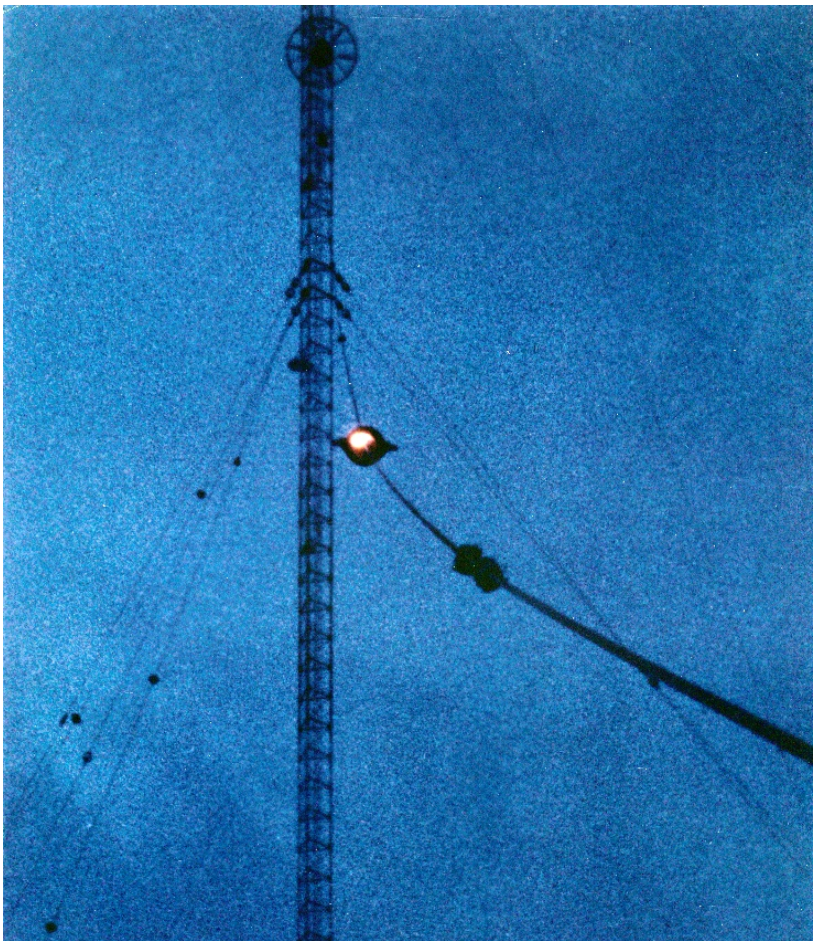

Figure 8-66. Continuous arc inside of cone insulator at Navy VLF site Puerto Rico.

An arc needs a minimum amount of current in order to be self-sustaining. The amount of current required depends on the length of the arc. A series of measurements of the minimum current required to sustain an arc were made at Forestport in conjunction with the parallel-plate measurements described above. The initial test setup consisted of a 1-inch rod passing through the parallel plate facing the end of a Racal Decca AST 8040 insulator. The second test setup consisted of two parallel plates on each side of the Racal Decca AST 8040 insulator. In this case, the 6-inch corona ring was suspended beneath the insulator. A 10-inch sphere mounted on a pneumatic actuator opposed this ring. The second test setup is illustrated in Figure 8-67 and pictured in Figure 8-68. The pneumatic cylinder was used to put the rod close to the plate to initiate the arc. Once the arc was initiated, the cylinder was then deactivated to allow the gap to reach the desired length.

As shown in the drawing, the current was measured using a Pearson current transformer, and the voltage was measured using a Jennings high-voltage voltmeter. The frequencies used for these measurements were 29 and 49 kHz. The gap was adjusted for distances from about 1-inch to a maximum of 16-inches. The procedure involved adjusting the gap to the desired length with the pneumatic cylinder deactivated. The pneumatic cylinder was then activated so that gap became small (a few inches). The transmitter was turned on, the resonant circuit tuned, and the voltage raised until the gap flashed over. The arc did not short out the high-voltage test circuit because the large insulator withstood the voltage. The capacitance between the circular plates sustained the current through the arc.

Once the arc was formed, the transmitter power was decreased slowly and the arc current and voltage monitored. Eventually, the arc extinguished and the current went to zero. The last current value read just before the arc extinguished corresponds to the minimum current required for sustaining an arc, and this value was recorded. Note that for fixed spacing the voltage across the arc increased as the arc current decreased, corresponding to the (well-known) negative resistance characteristic of an arc. The last voltage read just before the arc extinguished was the maximum, and this voltage was recorded. This voltage is plotted in Figure 8-69.

The minimum current measured just before extinguishing is plotted in Figure 8-70. Note the nearly linear dependence of the minimum current to sustain the arc on the length of the arc. The minimum current to sustain the arc is small, being less than ½-amp for the longest spacing measured. The slope at 29.5 kHz is 21.3 milliamps per inch of gap spacing. The slope at 49.3 kHz is 33.0 mA per inch of gap. It seems likely that the minimum arc sustaining current continues this frequency dependence, i.e., being less at lower frequencies and greater at higher frequencies, but we do not have data to verify this.

The design application for this concept is to ensure that each insulator has a large enough gap length such that if it were the only insulator in a string to flash over, the current that would flow through that gap would not be sustained. This design criterion is in addition to the criteria that the insulator should withstand the RF voltage imposed by the transmitting system.

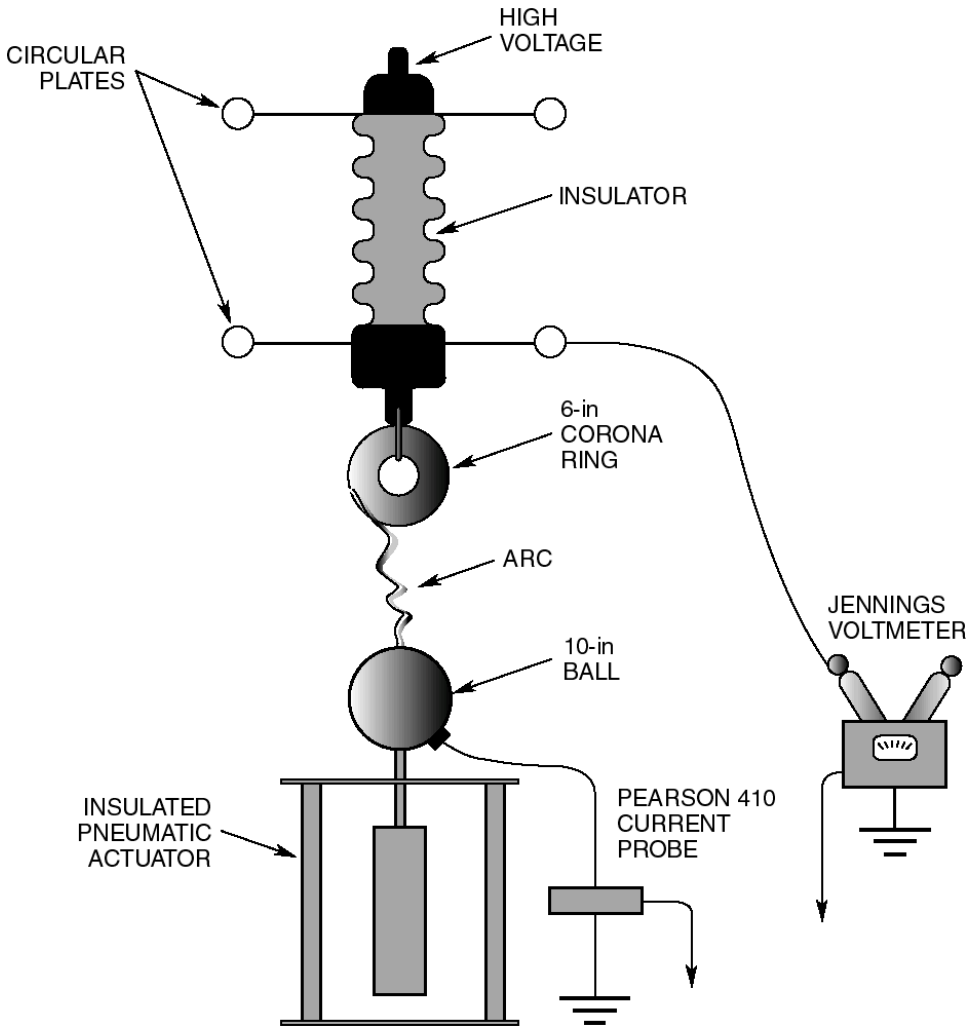

Figure 8-67. Drawing of arc current and voltage measurement setup.

Figure 8-68. Arc current and voltage measurement test setup.

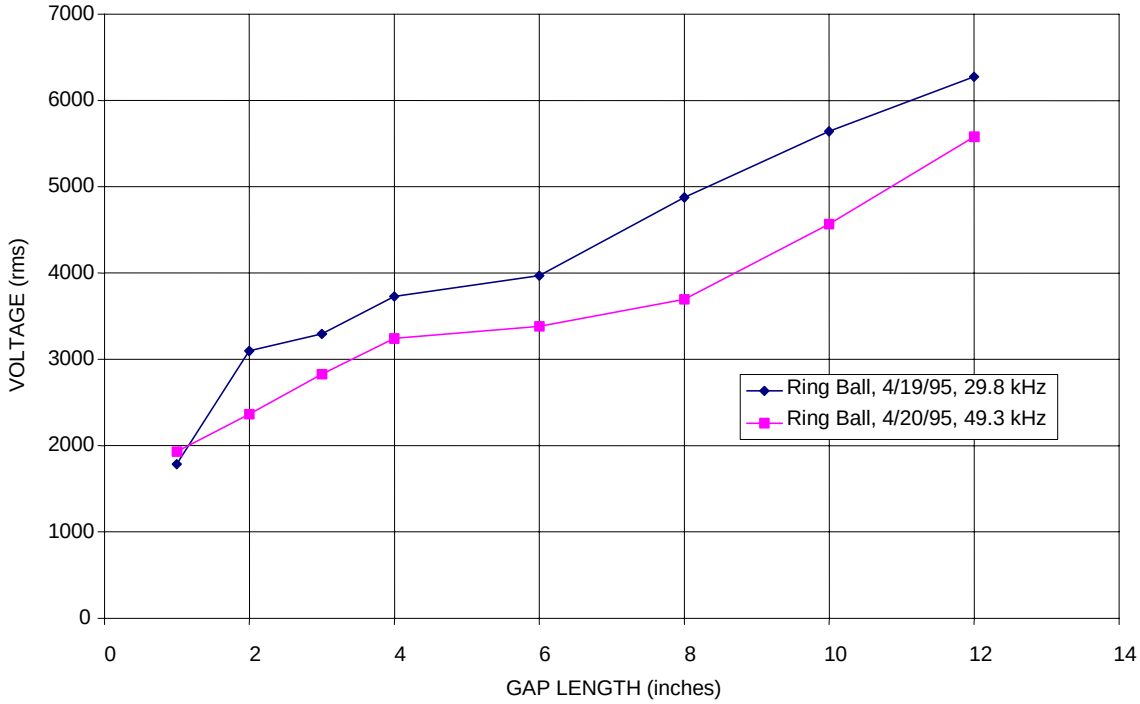

Figure 8-69. Arc extinguishing voltage.

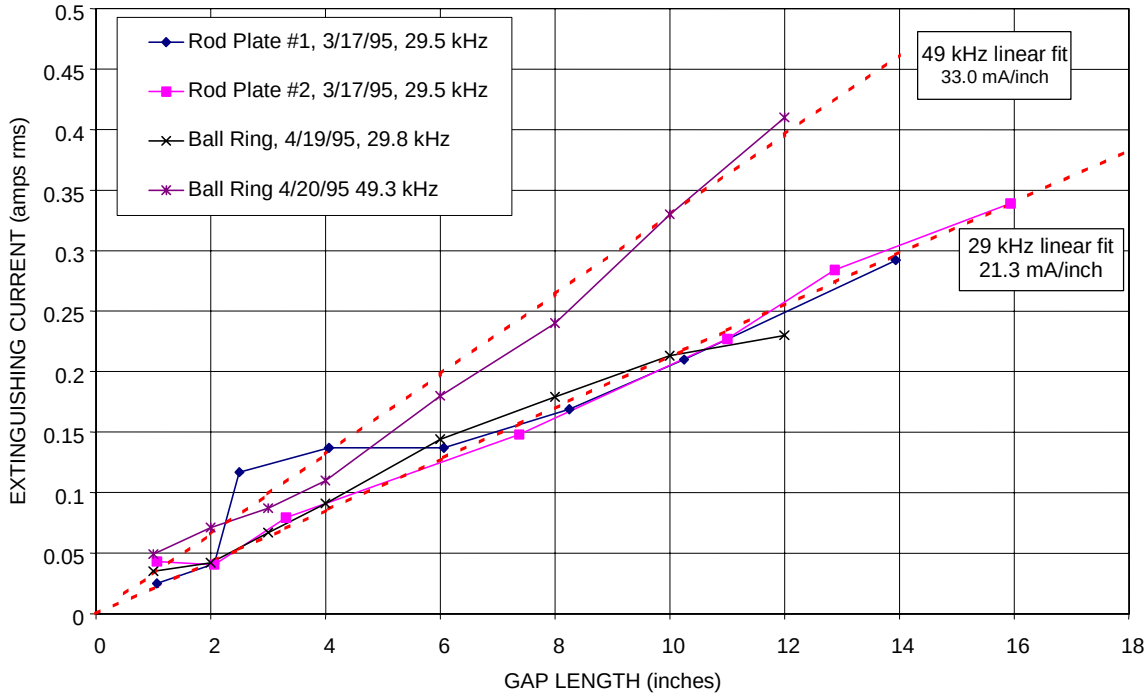

Figure 8-70. Arc extinguishing current.

References – Author Index

The page numbers in parentheses at the end of each reference list the page numbers in the book where each reference is used.

Abdel-Salam, M. 1985. "Positive Wire-to-Plane Coronas as Influenced by Atmospheric Humidity," *IEEE Transactions on Industry Applications*, vol. IA-21, no. 1, January/February 1985, pp. 35-40. (pages 1-7; 6-48, 49, 51)

Adams, G .E. 1955. "VoltageGradients on High Voltage Transmission Lines," *AIEE Transactions,* vol. 74, Pt. III, Apr. 1955, pp 5-11 (pages 4-17, 19)

Aleksandrov, G. N. 1957. "DC Corona Discharge." M. I. Kalinin Polytechnic Institute, Leningrad (pages 1-7)

Alexanderson, E. 1914. *General Electric Review*, p. 427 (page 1-8)

Algermissen. 1906. (page 1-8)

Alston, L. L. 1968. *High Voltage Technology*, Oxford University Press. (pages 2-16, 17, 18, 19, 26)

ANSI C29.1-1998. "Test Methods for Electrical Power Insulators." American National Standards Institute, Inc., 1320 Broadway, New York, NY 10018 (pages 3-8, 10, 14, 15, 16, 17; 5-1, 30, 49)

ANSI C68.1-1968 (R1973), "Techniques for Dielectric Tests." American National Standards Institute, Inc., 1320 Broadway, New York, NY 10018. Note that C68.1 has been superseded by IEEE Std 4-1995 (page 5-1)

ASHRAE. 1997. American Society of Heating Refrigeration and Air Conditioning Engineers (ASHRAE) Handbook of Fundamentals, p. 5.2. (pages 3-1, 3-6, 3-8)

Banford, H. M., and D. J. Tedford. 1977. "The use of a Photo-multiplier in the Determination of Ionization Coefficients in Gasses Stressed with a High Voltage," J. *Phys. D: Appl. Phys*., vol. 10. (pages 6-49)

Bharadwaj, Raj Mohan, and B. R. Prabhakar. 1996. "Effect of Humidity on the Breakdown of Air Gaps under Oscillatory Switching Impulse Voltage." *Conference Record of the 1996 International Symposium on Electrical Insulation*, Montreal, Quebec, Canada, (16-19 June). (page 6-56)

Bogdanova, N. B. and V. I. Popkov. 1959. Doklady Akademic Nauk SSSR 129, 314. (page 1-7)

Bogdanova, N. B. and V. I. Popkov. 1960. "Some Features of the High-Frequency Emission of a Corona Discharge," *Journal of Technical Physics* (U.S.S.R.), pp. 1090–1093. Translated from Doklady Akademic Nauk SSSR, vol. 134, no. 6, pp. 1331–1333 (Oct). (page 1-7)

Bright, A. W. 1950. "Corona and Breakdown at Frequencies up to 12 Megacycles Per Second," Brit. Elect. and Allied Ind. Res. Assoc. report, Ref L/T 229, (See Meek and Craggs, page 696). (pages 6-42, 69, 71, 72, 73, 77)

Brooks, J. L. 1982. "Memorandum of Procedure; High Voltage Tests on Commercially Available, Single Insulators. Phase 1." Naval Civil Engineering Laboratory, Technical Memorandum, (April) (page 5-44)

Brooks, J. L. 1997. "History of the High Voltage Test Facility at Forestport, New York," Professional Services Corps, Technical Report, PSC-97-003, (25 August). (page 5A-1)

Brown, W. W. 1923. "Radio Frequency Tests on Antenna Insulators." *PIRE*, pp. 495–525. (page 1-8, 5-19, 52; 5A-1)

Bruce, F. M. 1953, "Calibration of Non-uniform Field Spark Gaps for High-Voltage Measurements at Power Frequencies." *J. IEE*, vol. 100, p. 145. (pages 2-17, 20, 21)

CEA. 1991. "Dead-end/Suspension Composite Insulator for Overhead Distribution Lines." Canadian Electrical Association (CEA) Purchasing Specification LWIWG-01 (91), (Dec). (page 5-1)

CEA/IEC 60-1. 1989. "High-Voltage Test Techniques, Part 1: General Definitions and Test Requirements." International Standard, Reference number CEA/IEC 60-1. (page 5-1)

CEA/IEC 60-2. 1994. "High-Voltage Test Techniques, Part 2: Measuring Systems." International Standard, Reference number CEA/IEC 60-2. (page 5-1)

Chalmers, J. A. 1967 *Atmospheric Electricity*, Pergamon, New York, 2nd ed, Chapter 4 Ions and Nuclei, p. 86**.** (page 1-11)

Clark, E. 1932. Three Phase Multiple-Conductor Circuits, *AIEE Transactions*, vol. 51, Sept 1932. pp. 809-823 (page 4-17)

Clark, J. F. and J. H. Kraakevik. 1958. "The Fair-Weather Atmospheric Electric Potential and Its Gradient," in Recent Advances in Atmospheric Electricity, edited by L. G. Smith, Pergamon Press, New York. (page 2-7)

Clark, J. C. and H. J. Ryan. 1914. "Sphere Gap Discharge Voltages at High Frequencies." *Proceedings of the American Institute of Electrical Engineers*, vol. XXXIII, p. 937. (pages 1-8; 6-8)

Cobine, J. D. 1958. *Gaseous Conductors*, Dover Publications, New York. (pages 1-7; 2-8, 10, 12, 13, 19; 3-10; 4-2; 6-49, 51, 54, 57)

Comber, M. G., D. W. Deno and L. E. Zaffanella. 1982. "Corona Phenomena on AC Transmission Lines," Chapter 4 of EPRI 1982 (page 6-67)

Couper, I. D, A. Mejia, et al. 1988. "The Effect of Oscillator Switching Surges on Breakdown of Non-Uniform Gaps." IEEE International Conference on Properties and Application of Dielectric Materials, vol. 1, pp. 156–159. (page 6-56)

Crary, S. B. 1932. "Determination of the Disruptive Critical Voltage of a Multiple-Conductor Transmission Line" Appendix C of Clark (1932) *AIEE Transactions*, vol. 51, Sep. 1932, pp 820-821 (pages 4-21, 23)

Curtis, L. F. 1928. Phys. Rev., 31, pp. 1060-1127 (See Cobine (1958)) p. 183 (page 6-51)

Dann, G. 1987. "High Voltage LF Tests of Guyline Insulators." NCEL TM 72-87-04, (27 July) (page 8-1)

Dann, G., and P. M. Hansen. 1990. "Guyline Insulator Placement for Aguada," NCEL TM 72-90-05, (24 May) (page 8-1)

Davies, A. J., R. R. Hameed, P. Ortega, R. T. Waters, and W. T. Williams. 1989. "The Effect of Humidity on Positive-Impulse Breakdown of Rod/Plane Air Gaps," XXI International Conference on Phenomena in Ionized Gases, *Proceedings II*, 19–24 September, Ruhr – Universitat Bochum. (pages 6-51, 52)

Davies, D. K. 1990. "Measurements of Attachment Coefficients in the Presence of Ionization," in Non-equilibrium Effects in *Ion and Electron Transport*, edited by J. W. Gallagher et al., Plenum Press, New York. (page 6-50)

Davies, A. J., J. Dutton, R. Kadhim, M. Matallah, and R. T. Waters. 1991. "Switching Impulse Breakdown in Air at High Humidity Levels." XIX International Conference on Phenomena in Ionized Gasses, Contributed Papers, (13 July), University of Belgrade pp. 919-920. (pages 6-52, 53, 56, 59)

De Groot, C. J. 1924. "The High Power Station at Malabar, Java." *PIRE,* vol.12, pp 693-722 (page 1-2)

Doyle, J. R., J. J. La Forest, and T. S. Lauber, "Calculation of Electric Fields," *EPRI* 1982 Chapter 3 and Appendix 3.1 (page 4-19)

DTIC (Defense Technical Information Center). 1958. "Chronological History of U.S. Naval Communications," Accession number 142117, Available from DTIC, Cameron Station Alexandria, VA. (page 1-1)

Electro, 2003. Electrostatic computer program available from Integrated Engineering Software, see <http://www.integratedsoft.com> (page 4-25)

Elford, M. T. 1991. "The Behaviour of Low Energy Electrons in Water Vapour," in *Gaseous Electronics and Its Applications*, edited by R. W. Crompton, M. Hayashi, D. E. Boyd, T. Makabe, KTK Scientific Publishers, Tokyo, Kluwer Academic Publishers, Dordrecht, Boston, London. (page 6-49)

EPRI. 1982. Electric Power Research Institute, Transmission Line Reference Book 345 kV and Above, The Red Book. (page 2-14)

Gallo, C. F., J. E. Germanos, and J. E. Curtney. 1969. "The Effect of Humidity and Temperature Variations on the Behavior of Wire-to-Plane Coronas," *Appl. Opt*., supp. 3, pp. 111–110. (pages 6-48, 49, 50, 51, 56)

Gary, C. H., B. P. Hutzler, and J. P. Schmitt. 1972. "Peek's Law Generalization: Application to Various Field Configurations" IEEE PES Summer Conference, San Francisco, CA, July 9-14, 1972. (pages 2-17, 2-25)

Goebler, G. 1925. *Archiv fur Elektrotechnik*, vol. 14, p. 491. (page 1-8)

Gosho, Y., and M. Saeki. 1985. "Role of Water Vapor in the Breakdown of Atmospheric," Proceedings of the Eighth International Conference on Gas Discharges and Their Applications, 16–20 September, St. Catherines College, Oxford, UK, pp. 161–162. (pages 6-49, 51, 54)

Grover, F. W. 1928 "Methods, Formulas, and Tables for the Calculation of Antenna Capacity," Scientific Papers of the Bureau of Standards, no. 568 (page 4-21)

Hanselman, J. C. 1972. "Litz Wire Calculations," NOSC memo, 13 Feb, unpublished – for more information contact the author. (pages 5C-3, 4)

Hansen, P. M. 1990. “High Power Very Low Frequency/Low Frequency Transmitting Antennas,” IEEE Military Communications Conference, Monterey, California, Conference Record, vol. 3, pp. 56.5.1–56.5.6, (September) (page 5-20)

Hansen, P. M. 1992. “Optimum Design of Multi-wire Cages for High-Voltage Applications,” NRaD Technical Document 1495, NCCOSC RDT&E Division, San Diego, CA. (pages 1-8; 4-28, 30)

Harding, 1924a, “Corona Losses Between High Voltage Wires, Part I,” *Transactions American Association of Electrical Engineers AIEE*,vol. XXXI, pp. 1035-1112 (page 7-1)

Harding, 1924b, “Corona Losses Between High Voltage Wires, Part II,” *Transactions American Association of Electrical Engineer,s AIEE* XXXI, pp. 1182-1196 (page 7-1)

Hatano, Y. 1986. “Electron Attachment to Van der Waals Molecules,” *Electronic and Atomic Collisions*, edited by C. Lorents, W. E. Meyerhof, and J. R. Peterson, Elsevier Science Publishers, B.V. (page 6-48)

Hicks, W. M., *Phil Trans*, vol. 172, p. 609, 1881. (page 4-31)

Hobson, E. W. 1931. “Theory of Spherical and Ellipsoidal Harmonics,” Cambridge, Univ. Press. (page 4-31)

Houck, T. L., G. A. Westenskow, J-S. Kim, S. Eylon, E. Henestroza, S. S. Yu, and D. Vanecek. 1997. “Stacked Insulator Induction Accelerator Gaps,” *Conf. Proc., Particle Acc. Conf.,* 11–16 May, Vancouver, Canada. (page 2-18)

Howeth, I. S. 1963. *History of Communications-Electronics in the United States Navy*, U.S. Government Printing Office. (page 1-1,2)

Humphries, 1944. Page 2516 of Hodgman, C.D. and Harry N. Holmes, *Handbook of Chemistry and Physics*, 28th Edition, CRC Press, Cleveland, 1944 (page 3-11)

Hylten-Cavallius, N. 1988. *High Voltage Laboratory Planning*, Emile Haefely & Co, Basel, Switzerland, 2nd edition. (page 5-3)

IEC Publication 60-1, 1973 and 1979 Superceded by CEA/IEC 60-1: 1989 (page 3-14)

IEEE Std 4-1995, “IEEE Standard Techniques for High-Voltage Testing,” (revision of IEEE Std 4-1976), October 12, 1995. (pages 3-6, 7, 10, 14, 15, 18; 5-1, 30, 40, 49, 53)

Johnson, W. A. 2003 EIGER-S 3D, Static Developmental Code, Dr. Bill Johnson at SANDIA Laboratory, email wajohns@sandia.gov (page 4-48)

Kampschultz, J. 1930. “Air Breakdown and Arcing with Alternating Voltages at 30 and 100,000 Hertz.” *Archiv fur Elektrotechnik,* vol. 24, pp. 525–552. (page 1-9)

Kato, K. and H. Okubo. 1997. “Optimization of HVC Electrode Contour with the Highest Gaseous Insulation Performance,” *IEEE Transactions on Dielectrics and Electrical Insulation*, vol. 4, no. 6, (Dec). (page 4-3)

Klots, C. E. and R. N. Compton. 1978. “Electron Attachment to Van Der Waals Polymers of Water,” *Journal of Chemical Physics*, vol. 69, no. 4, (15 August). (page 6-49)

Kolechitskii, Y. S. 1967. “A Study of Corona at Frequencies over 10 kc/s.” Moscow Power Institute. (pages 1-7, 9; 6-9, 69, 70, 71, 73, 77)

Kotter, F. R. and A. N. Smith. 1983. “A Study of Air-Gap Breakdown at 28.5 kHz,” *IEEE Transactions on Power Apparatus and Systems*, vol. PAS-102, no. 6, June 1983, pp. 1913-1920 (pages 5-46; 8-1, 36)

Kreuger, F. H. 1991. Industrial High Voltage, vol. 1, “Electric Fields,” vol. 2, “Dielectrics,” vol. 3, “Constructions,” Delft University Press, Delft, Netherlands. (pages 1-4; 4-1; 6-49, 67)

Kucera, J., T.W. Liac, and A. .F. Rohlfs. 1970. "Atmospheric Correction Factors for High Voltage Testing," *Electra*, no. 21, 1970, pp. 74-84 (page 3-14)

Kuffel, E. 1961a. *PIEE*, 108A. p. 302. (page 6-55)

Kuffel, E. 1961b. “Influence of Humidity on the Breakdown Voltage of Sphere-Gaps and Uniform-Gaps” Institute of Electrical Engineers Paper 3322M (February). pp. 295–301. (pages 1-7; 6-55, 59)

Kuffel, E. and W. S. Zaengle. 1984. “High-Voltage Engineering.” Pergamon Press. (pages 6-51, 55, 58, 67, 78)

LaForest, J. J. 1968. “Seasonal Variation of Fair-Weather Radio Noise,” *IEEE Transactions on Power Apparatus and Systems* PAS-87, pp.198-931, Apr. 1968 (page 6-67)

LaPort, E. 1952. *Radio Antenna Engineering*, McGraw Hill (page 5-2)

Larionov, V. P., and T. N. Tarasova. 1989. “High Frequency Corona Discharge Peculiarities on Water Drops.” XIX International Conference on Phenomena in Ionized Gasses, University of Belgrade, July. (page 6-10)

Lassen, H. 1931. *Archiv fur Elektrotechnik*, vol 15, p. 322. (page 1-9)

Law, P. 1985. “Shipboard Antennas,” ARTECECH (page 1-1)

Llewellyn-Jones, F. 1957. *Ionization and Breakdown in Gasses*. Methuen, London. (page 1-7)

Loeb, L. B. 1927. *The Kinetic Theory of Gasses*. McGraw-Hill, New York, reprinted by Dover 1961 (pages 1-6, 2-12)

Loeb, L. B. 1939. Fundamental Processes of Electrical Discharge in Gases. John Wiley and Sons, New York. (page 1-6)

Loeb, L. B. and J M. Meek. 1941. *The Mechanism of the Electric Spark*. Oxford University Press. (pages 1-6; 2-18)

Loeb, L. B. 1961. *Basic Processes of Gaseous Electronics*. University of California Press. (page 1-6)

Loeb, L. B. 1965. *Electrical Coronas – Their Basic Physical Mechanisms*. University of California Press. (page 1-6)

Lorraine, P. and D. R. Corson. 1970. *Electromagnetic Fields and Wave,* Freeman, San Francisco, (page 4-6)

Lyubimov. 1983. The Memoirs Of Coulomb – The Beginning of Modern Electromagnetism (Russian), History and Methodology of the Natural Sciences XXX (Moscow, 1983, 101-129), referenced in <<http://www-gap.dcs.st-and.ac.uk/~history/Mathematicians/Coulomb.html>> (page 1-6)

MacDonald, A. D. 1966. *Microwave Breakdown in Gasses*. Wiley, 201 pages. (pages 1-11; 2-6)

Meek, J. M. and J. D. Craggs. 1978. *Electrical Breakdown of Gases*. Oxford University Press. (pages 1-7, 8, 9; 2-18; 6-38, 49, 53, 56, 69, 72, 74)

Meszaros, Anges. 1977. "On the Size Distribution of Atmospheric Aerosol Particles of Different Composition, *Atmospheric Environment*, vol. 11 pp. 1076-1081, (page 3-3)

Miller, C. E. 1956. "Mathematical Prediction of Radio and Corona Characteristics of Smooth Bundled Conductors." *AIEE Transactions Paper*, no. 56–520, Oct 1956, p. 1029. (pages 1-8; 4-17, 19, 21, 24; 6-24, 35, 36, 43)

Miller, C. E. 1957. "The Calculation of Radio and Corona Characteristics of Transmission Conductors." *AIEE Transactions on Transmission and Distribution*, Paper, no. 57-165 AIEE Winter General Meeting, New York, (21–25 January). (pages 6-24, 30, 31, 42, 43)

Morgan, V. T. and R. Morrow. 1978. "Effect of Variation of Power Frequency on the Corona Characteristics of a Heated Cylinder in a Radial Electric Field," IEE Publication 165, pp. 85-7, IEE Conference Liverpool, UK 11-14 Sep 1978 (page 1-7)

Morrow, R. 1997. "The Theory of Positive Glow Corona." *J. Phys D: Appl. Phys*., no. 30, pp. 3099–3114. (pages 6-74, 75)

Morse, P. M. and H. Feshback, 1953. *Methods of Theoretical Physics, (Part II)*, McGraw Hill ISBN: 007043316X, pp. 1184-1185 (page 4-23)

Muller, F. 1934. *Arch. Elektrotech.,* vol. 28, 561. (page 6-73), See Meek & Craggs (1978) p. 691 (page 6-69)

Naidu, M. S., and V. Kamaraju. 1995. *High Voltage Engineering*. Second edition, McGraw-Hill. (pages 2-14; 6-29)

Newell, H. H. and F. W. Warburton, 1956. "Variations in Radio and TV Interference from Transmission Lines," *AIEE Transactions on Power Apparatus and Systems*, vol. 75 pp. 420-426, June 1956 (page 6-67)

Newell, H. H., T. W. Liao, and F. W. Warburton. 1967. "Corona and Radio Interference Caused by Particles on or Near EHV Conductors: I - Fair Weather," *IEEE Transactions on Power Apparatus and Systems*, vol. PAS-86, pp. 1375-1383, November 1967 (page 6-67)

Okubo, H., T. Otsuka, K. Kato, N. Hayakawa, and M. Hikita. 1997. "Electric Field Optimization of High Voltage Electrode Based on Neural Network." *IEEE Transactions on Dielectrics and Electrical Insulation,* vol. 12, no. (4 November). (page 4-3)

Olsen, R. G., D. B. Phillips, and P. D. Pedrow. 1997. "Extrapolation of a Corona Streamer Onset Criterion to General Convex Conductor Surfaces," 10th International Symposium on High Voltage Engineering, Montreal, Quebec, Canada, (25–29 August). (pages 1-11; 2-17; 4-47; 8-54)

Olsen, R. G. and B. O. Stimpson. 1988. "Predicting VHF/UHF Electromagnetic Noise from Corona on Power-Line Conductors." *IEEE Transactions on Electromagnetic Compatibility*, vol. 30, no. 1, (February). (page 1-11)

Papoular, 1965. *Electric Phenomena in Gases,* Iliffe Book Ltd. London. (pages 2-8, 2-15)

Parr, J. E. and J. L. Moruzzi. 1972. “Electron Attachment in Water Vapour and Ammonia.” J. *Phys. D: Appl. Phys*., vol. 5. (page 6-49)

Paschen, F., Wied. Ann., 37, 69, 1889, (page 2-4)

Peek, F. W. 1911. “The Law of Corona and the Dielectric Strength of Air-I.” *AIEE Transactions*, vol. 30, pp. 1889–1988. (page 1-7)

Peek, F. W. 1922. “The Insulation of High Voltage Transmission Lines, Conception of a Million Volt Line,” *G. E. Review*, vol. 25, no. 2, (February). (pages 1-7, 2-21)

Peek, F. W. 1927. “The Law of Corona and the Dielectric Strength of Air-IV.” *AIEE Transactions*, p. 1009–1024. (pages 1-7, 2-21)

Peek, F. W. 1929. *Dielectric Phenomena in High-Voltage Engineering*, 3rd Edition, McGraw-Hill. (pages 1-7, 8, 10; 2-21, 22; 6-9, 10, 24, 41, 42, 67; 7-1)

Phillips, D. B. 1999. “Corona Onset as a Design Optimization Criterion for High Voltage Hardware,” Ph.D. Thesis Washington State University. (page 8-58)

Pierce, E. T. 1958. “Some Topics in Atmospheric Electricity” Recent Advances in Atmospheric Electricity (*Proc. Sec. Conf. Atmospheric Electricity*, Portsmouth, NH. Edited by L. G. Smith) pp. 5-16, Pergamon Press, 547, 578. (page 2-7)

Pim. 1949. *Proc IEE*, 96, Part III, 117 (See Meek & Craggs p 697) (page 1-11; 6-69)

Plessow, R. and W. Pfeiffer. 1987. “Influence of the Frequency on the Partial Discharge Inception Voltage,” (page 1-11)

Plumb, I. C., D. C. Cook, S. C. Hayden. 1984a. “Laboratory Investigations of Pulsed RF Plasmas Relevant to CW Arc Pluming at High-Power Aerials. Pt. 1: Critical Breakdown under Pulsed RF Conditions.” *PIEE*, vol. 131, Pt. A, no. 3 (May). (page 6-57)

Plumb, I. C., D. C. Cook, S. C. Hayden. 1984a. “Laboratory Investigations of Pulsed RF Plasmas Relevant to CW Arc Pluming at High-Power Aerials. Pt. 2: Relevance of Scale-Model Studies Based on Pulsed RF Techniques.” *PIEE*, vol. 131, Pt. A, no. 3 (May). (page 6-57)

Poli, E. 1985. “Positive Corona Inception Under Variable Humidity Conditions.” *Proceedings of the Eighth International Conference on Gas Discharges & Their Applica*tions, (16–20 September), St. Catherines College, Oxford, UK, pp. 593–596. (pages 6-48, 54)

Qin, Bai-Lin. 1993. “High Voltage dc Bipolar Corona Via Particle-in-Cell Simulation,” Washington State Ph.D. Dissertation, August 1993 (page 6-39)

Raether, H. 1964. Electron Avalanches and Breakdown in Gasses, Butterworth, London. **(**page 2-11)

Raizer, Y. P. 1991. *Gas Discharge Physics,* Springer-Verlag (pages 2-8, 11, 13, 15, 16, 17, 18, 25; 6-74)

Reukema, L. E. 1928. “The Relationship Between Frequency and Spark Over Voltage in a Sphere Gap Voltmeter.” Transactions American Institute of Electrical Engineers, vol. 47, p. 38. (pages 1-9; 6-38)

Richards, C. N. 1974. “A Study of Insulator Breakdown Under Navy Antenna HV RF Conditions.” Final Report CR 75.001, SAIC (March). (pages 6-10, 33)

Rizk, F. A. M. 1992. “Critical Switching Impulse Strength of Long Air Gaps: Modeling of Air Density Effects.” *IEEE Transactions on Power Delivery*, vol. 7, no. 3 (July). (page 3-14)

Ryan, H. J. and R. G. Marx. 1915. “Sustained Radio Frequency High Voltage Discharges,” PIRE V3, pp. 349-370 (pages 1-8; 7-1)

Ryan, H. J. and H. H. Henline, 1924. “The Hysteresis Characteristics of Corona Formation.” *AIEE Transactions*, (Oct.), pp. 1118–1124. (pages 1-8; 7-1, 2)

Rogowski, see Cobine, 1958, p. 177 (page 4-2)

Sarma, M. P. and W. Janischewskyj. 1969. “Steady State Analysis of the Ionization Layer.” *Proc. IEE*, vol. 116, no. 1 (January), p. 161–166. (pages 2-15, 16, 17, 23; 6-40)

Schroder, G. A. 1961. Messung der statischen Durchbruchfeldstarke in Raumluft in einen homogenen Feld bei Abstanden von 2…9 cm. Zeitschrift f. angew. *Physik*, 13, p. 296-303. (page 2-25).

Schuman, W. O. 1924. Elektrische Durchbruch - Fildstarke Von Gasen, Theoretische Grundlagen und Awendung, Springer-Verlag, Berlin. (pages 1-8, 2-22; 6-14, 50)

Schukantz, J. A. 1993. “DC Coaxial Cylinder Corona Measurements, Naval Command, Control And Ocean Surveillance Center, Research and Development Test and Evaluation Division, EM Technology & Systems Branch, Code 824, San Diego, CA Technical Report (pages 6-9, 10, 40)

Sears, F. W. and M. W. Zemansky. 1955. *University Physics.* Second Edition, Addison Wesley Publishers. (page 3-6, 3-7)

Seward, E. W. 1939. “The Electric Strength of Air at High Frequencies,” *JIEE,* vol. 84, pp. 288-292, Feb 1939 (page 1-9)

Schelkunoff, Sergi A. and Harald T. Friis, 1952. “Antennas Theory and Practice,” John Wiley (page 4-21)

Shahin, M. M. 1969. “Nature of Charge Carriers in Negative Coronas.” *Appl. Opt.*, suppl. 3, pp. 106–109. (pages 6-48, 50)

Shost, H. 1962. “Durchschlagspannungen in Luft (760 Torr) im Homogenen Field (7 bis 30 cm Abstand). Zeitschrift f. agnew. *Physik,* 14, p. 620-627 (page 2-25).

Smith, J. H. and W. E. Gustafson. 1961. “Study of VLF Corona,” U.S. Navy Electronics Laboratory Research Report no. 1044, 4 May 1961 (page 1-9)

Smith, A. N. 1963. “VLF Corona Discharge Study and Its Application to a Transmitting Monopole,” DECO Interim Report no. 34-S-2 Volume 1, 16 Sept 1963. (pages 1-9, 6-9, 75, 76)

Smith, A. N. 1973. “Insulator and Capacitor Tests Carried Out at NRTF Luallualei Feb 1973.” NELC TN 2391 (June 1973) (pages 1-3, 5A-1)

Smith, A. N. 1980. “Air Force & Navy VLF/LF High Voltage Test Facility Upgrade.” Electrospace Systems, Inc. Technical Report (August) (pages 1-4; 5A-2)

Smith, A. N. 1981. “Tunable 300 kV Air Capacitor for Forestport VLF/LF High Voltage Test Facility.” Electrospace Systems Inc., (3 Oct) (pages 1-4; 5-19)

Smith, A. N. 1982. “High Voltage Radio Frequency Test Facility Requirements.” Electrospace Systems, Inc., Technical Report (10 Sep) (pages 1-4; 5-3; 5A-1)

Smith, A. N. 1985. “Measured Corona Inception/Extinction Levels.” Electrospace Systems Inc., Report B. SD 85-098. (page 4-23)

Smith, A. N. 1986. “Forestport High Voltage Test Facility Plan.” Electrospace Systems, Inc., Technical Report (Final) (29 Oct). (pages 1-4, 11; 5A-2)

Soetjipto, S., G. Riquel, and B. Hutzler. 1987. *Proc V Int Symp on High Voltage Engineering*, Braunschweig, Paper 11.02. (page 6-52)

Standring, W.G., D. H. Browning, R. C. Hughes, and W. J. Roberts. 1963. “Effect of Humidity on Flashover of Air-Gaps Under Alternating (50 c/s) and Impulse (1/ 50us) voltages,” *PIEE* 110, pp. 1077–1081. (page 6-55)

Stoletow, J. D. 1890. *Physique*, 9, p. 468. (page 2-13)

Tai, Chen-To. 1997. Generalized Vector and Dyadic Analysis: Applied Mathematics in Field Theory. Second Edition, IEEE Press. (page 8-56)

Temoshok, 1948. “Relative Surface Voltage Gradients of Grouped Conductors,” *AIEE Transactions,* vol. 67, pp. 1583-1591 (page 4-17)

Thomas, T. S. E. 1954. “The Capacitance of an Anchor Ring.” *Australian Journal of Physics*, vol. 7, pp. 347–351. (pages 4-31; 8-60)

Townsend, J. S. 1915. *Electricity in Gases*, Oxford University Press. (page 2-9)

Trinh, N. G., P. S. Maruvada, and B. Poirier. 1973. “A Comparative Study of the Corona Performance of Conductor Bundles for 1200 kV Transmission Lines.” Paper T 73 439-7, IEEE Power Engineering Society. (May), p. 940–949. (pages 1-8, 6-35)

Trichel, 1938. *Phys. Rev.* 54, pp. 1078-1084 (page 2-11)

Valley, S. L. (Editor) “Handbook of Geophysics and Space Environment,” Air Force Cambridge Research Laboratories, McGraw Hill (page 3-12)

Van Brunt, R. J. 1994. “Physics and Chemistry of Partial Discharge and Corona: Recent Advances and Future Challenges.” *IEEE Transactions on Dielectrics and Electrical Insulation*, vol. 1, no. 5, (October), pp. 761–784. (pages 6-70, 76)

Verhaart, H. F. A., and P. C. T. Van der Laan. 1984. “The Influence of Water Vapor on Avalanches in Air,” *Journal of Applied Physics*, vol. 55, no. 9, (May). (pages 6-50, 53, 56)

Watt, A. D. 1962. “Vlf Corona” - High Performance Reliable VLF Component of the Naval Advanced Communications System – Interim Report no. 34-R-4k, Deco Electronics, Inc., 22 March 1962 (page 1-9)

Watt, A. D. 1967. *VLF Radio Engineering*, Pergamon Press, Oxford. (page 2-7; 5C-1, 4; 6-9)

Watt, A. D. and P. M. Hansen. 1992. “VLF/LF Corona Investigation,” NRaD TD 2266, May 1992 (pages 1-11; 7-1)

Whitehead, J. B. and W. S. Gorton. 1914. “The Electrical Strength of Air, the Influence of Frequency.” *AIEE Transactions*, p. 951–972. (pages 1-8; 2-24; 6-8)

Zaengle, W. S. and H. U. Nyffengger. 1974. “Critical Field Strength for Cylindrical Conductors in Air: An Extension of Peek’s Formula.” Third International Conference on Gas Discharges, September 74, pp. 302–305. (page 2-25)

Bibliography

Abdel-Salam, M., H. Anis, A. El-Morshedy, R. Radwan. *High-Voltage Engineering, Theory and Practice.* Marcel Dekker Inc., 2001

Aleksandrov, G. N. "Initial Stages of Negative Point Corona." Polytechnic Institute, Leningrad 17, June 1956

Aleksandrov, G. N. "Physical Conditions for the Formation of an Alternating Current Corona Discharge." Polytechnic Institute, Leningrad, 27 May 1955

Alexander, P. P. "Calorimetric Study of the Arc." *Thomson Research Laboratory of the General Electric*, Jan. 1930

Allibone, T. E., D. Dring, and N. L. Allen. "Impulse Corona Development." *IEE Pul*. 165, 1978

Altshuler, S. and C. E. Wood, "Investigation of AC Corona Power Loss for Vertical ELF Antennas." *Physical Science Interest*, 15 Jan. 1987

Crompton, R. W., M. Hayashi, and D. E. Boyd. *Gaseous Electronics and its Applications*. Advances in Solid State Technology. Tokyo: KTK Scientific and Dordrecht: Kluwer Academic, 1991

Attwood, S.S., W. G. Dow, and W. Krausnick. "Reignition of Metallic A-C. Arcs in Air." *IEEE Transactions*, March 1931

Barthold, L.O., e. al. "Electromagnetic of Overhead Transmission Lines Practical Problems, Safeguards, and Methods of Calculations." *IEEE Transmission and IEEE Power Engineering Society*, 11 May 1973

Bazelyan, E. M. and Yu. P. Raizer. *Spark Discharge*. New York: CRC Press, 1997

Bouwers, A. and P. G. Cath "Maximum Electric Field Strength for Several Simple Electrode Configurations." *Philip's Technical Review,* vol. VI, no. IX, 1940

Boylett, F. D. A. and J. S. T. Looms. "Effects of Discharge Products Upon Corona Discharge and Spark Breakdown Voltage." *PROC/IEE*, vol. 110, no. XII, Dec. 1963

Brooks, J. L. "Effects of VLF/LF High Voltage on Standard Wires." Naval Civil Engineering Laboratory, Technical Memorandum, 20 Oct. 1992

Burning, A. M., D. G. Kasture, and H. E. Ascher. "Absolute vs. Comparative End-of-Life." *IEEE Transactions on Dielectrics and Electrical Insulation.*vol. III, no. IV, Aug. 1996

Carrara, F. G. and L. Thione. "Switching Surge Strength of Large Air Gaps: A Physical Approach." *IEEE Transactions on Power Apparatus and Systems*, vol. PAS-95, no. II, May 1975

Carroll, J. S. and R. J. Harris. "Space Charge that Surrounds a Conductor in Corona at 60 Cycles." Transactions A.I.E.E., 1926

Chowdhuri, P. A. K. Mishra, P. M. Martin, and B. W. McConnell. "Effects of Nonstandard Lighting Voltage Waveshapes on the Impulse Strength of Short Air Gaps." *IEEE Transactions on Power Delivery*, vol. IX, no. IV, Oct. 1994

Clade, J. J. and Gary, C. H. " Predetermination of Corona Losses Under Rain: Influence of Rain Intensity and Utilization of a Universal Chart." *IEEE Transactions on Power Apparatus and Systems,* vol. PAS-98, no. VI, Nov. 1969

Comber, M. G. and L. E. Zaffanella, L.E. "Use of Single-Phase Overhead Test Line and Test Cages to Evaluate the Corona Effects of EHV and YHV Transmission Lines." *IEEE Power Engineering Society,* April 1973

Correia de Barros, M. T. and C. de Jesus. "Wide Bandwidth Modeling of Corona on High Voltage Transmission Lines." IEEE, 1944

Davenport, O. A. *Antenna Breakdown.* Mexico State University, 30 May 1960

De Jesus, C. "Modeling of Corona Dynamics for Surge Propagation." *IEEE Transaction on Power Delivery*, vol. IX, no. III, July 1994

Deno, D. W. *Conductive and Insulated Tether Tests for Pacific-Sierra Research.* High Voltage Transmission Research Facility, 19 July 1985

Devins, J. C. and A. H. Sharbaugh. *Fundamental Nature of Electrical Breakdown*. New York: C-M Technical Publications Feb. 1961

Dow, W. G., S. S. Attwood, and G. S. Timoshenko. "Probe Measurements and Potential Distributions in Copper A-C Arcs." *IEEE Transactions,* June 1933

Faraday, M., "Experimental Researches in Electricity," vol. I, Dover, New York, 1965

Farzaneh, M. and J. F. Drapeau. 1995. "AC Flashover Performance of Insulators Covered with Artificial Ice." *IEEE Transactions on Power Delivery*, vol. 10, no. 2, (April)

Farzaneh, M. and L. C. Phan. "Vibrations of High Voltage Conductors Induced by Corona from Water Drips or Hanging Metal Points." *IEEE Transaction on Power Apparatus and Systems*, vol. PAS-103, no. IX, Sep.1984

Fink, D. G., Standard Handbook for Electrical Engineers. New York: Mc-Graw-Hill 1978

Fletcher, N. H., *The Physics of Rainclouds*, Cambridge University Press, 1966

Fofana, I. and A. Beroual. "Predictive Model of the Positive Discharge in Long Air Gaps Under Pure and Oscillating Impulse Shapes." IOP Publishing, 1997

Ghosh, P. S. and Chatterjee, N. "Arc Propagation Over Electrolytic Surfaces Under Power Frequency Voltage." *IEEE Transactions in Dielectric and Electrical Insulation*, vol. III, no. IV, Aug. 1996

Goldman, A., E. O. Selim, and R. T. Waters. "Current Distribution in the Negative Corona Discharge in Air." *IEE Publications,* no. 165, 1978

Goelian, N.; P. Lalande, A. Bondiou-Clergerie, G. L. Bacchiega, A. Gazzani, I. And Gallimberti. "A Simplified Model for the Simulation of Positive-Spark Development in Long Air Gaps." IOP Publishing, 1997

Grover, F. *Inductance Calculations: Working Formulas and Tables*. Dover Publications, Inc., New York, 1946.

Guillier, J. F. and M. Rioual. “Damping Model of Traveling Waves by Corona Effect Along Extra High Voltage Three Phase Lines.” *IEEE Transactions on Power Delivery*, vol. X, no. IV, Oct. 1995

Guile, A. E. “Protection of High-Voltage Insulators from Power-Arc Damage.” Institute of Electrical Engineers, no. 3289 S, July 1960

Harding, C. F. “Corona Losses Between Wires.” *Transactions A*. IEEE, Oct. 1924

Harrison, M. A. and R. Geballe. “Simultaneous Measurement of Ionization and Attachment Coefficients.” *The Physical Review*, vol. 91, no. I, 1 July 1953

Harting, R. “Electric Fields Along a Post Insulator: AC-Measurements and Calculations.” *IEEE Transactions on Power Delivery*, vol. IX, no. II, April 1994

Jog, M.A., I. M. Cohen, and P. S. Ayyaswamy, P.S. “Breakdown of a Wire-to-Plane Discharge: Transient Effects.” American Institute of Physics, Aug. 1991

Kirkman, J. R. and J. A. Charlmers, J.A. “Point Discharge from an Isolated Point.” *Journal of Atmospheric and Terrestrial Physics*, vol. X 11 Jan. 1957

Kleiner, Johnson, McMurray, and Suzuki. “Electrical Surge Arrestor (ESA) Models for Electromagnetics Pulse Analysis.” *IEEE Transactions on Nuclear Power*, vol. NS-24, no. VI, Dec. 1977

Kulikovsky, A. A. “Positive Streamer Between Parallel Plate Electrodes in Atmospheric Pressure Air.” *J. Phys. D: Appl. Phys*., vol. 30, 1997

Kunhardt, E. E. and H. L. Lawrence (ed.). *Electrical Breakdown and Discharge in Gases*. New York & London: Plenum Press, 1982

Lambeth, P. J. and D. H. Nguyen. “Air Clearances for Electrical Railways: A Study of the Breakdown Voltage of Rod-Plane Gaps in a Variety of Atmospheric Conditions.” *IEEE Transactions on Power Apparatus and Systems*, vol. PAS-104, no. X, Oct. 1985

Landers, W. “Distribution of Electrons and Ion in a Corona Discharge.” *PROC IEE*, vol. 125, no. IX, Oct. 1978

Large, M. I. “Radio Interference Produced by Corona Discharge.” *Journal of Atmospheric and Terrestrial Physics*, vol. X, 31 Jan. 1957

Large, M. I. and E. T. Pierce. “Dependence of Point-Discharge Currents on Wind as Examined by a New Experimental Approach.” *Journal of Atmospheric and Terrestrial Physics*, vol. X, 18 Dec. 1956

Lide, D. R. *CRC Handbook of Chemistry and Physics.* Boca Raton, London, New York, Washington, D.C. CRC Press 2002

Menemenlis, C., G. Carrara, and P. J. Lambeth. “Application of Insulators to Withstand Switching Surges in Substations, Part I: Switching Impulse Insulator Strength.” *IEEE Transaction on Power Delivery*, vol. IV, no. I, Jan. 1989

Menemenlis, C. and G. Harbec. “Coefficient of Variation of the Positive-Impulse Breakdown of Long Air-Gaps.” *IEEE Power System Engineering*, 21 May 1973

Metwally, I. A. “Factors Affecting Corona on Twin-point Gaps Under DC and AC HV.” *IEEE Transactions on Dielectrics and Electrical Insulation*, vol. III, Aug. 1996

Morrow, R. and J. J. Lowke. “Streamer Propagation in Air.” IOP Publications, 1997

O’Neal, J. B. Jr. “Substation Noise at Distribution-Line Communication Frequencies.” *IEEE Transactions on Electromagnetic Compatibility*, 1988

Osswald, F., M. Roumie, G. Frick, and B. Heusch. “High Voltage Insulating Structures for Accelerators.” *IEEE Transactions on Dielectric and Electrical Insulation*, vol. III, no. II, April 1996

Palva, V. “Research on Long Air Gap Discharge at Les Renardiere,” *Electra,* no. 35, July 1974

Pansini, A. J. and K. D. Smalling. *High Voltage Power Equipment Engineering*, Fairmont Press, 1994

Parekh, H., Salama, M.M.A., and Srivastava, K.D. “Calculation of Corona Onset and Breakdown Voltages in Shot Point-to-Point Plane Air Gaps.” American Institute of Physics, 1978

Pedrow, P. D. and Q. Y. Wang. “Influence of Load Current on Bipolar DC Corona.” *IEEE Transactions on Power Delivery*, vol. IIX, no. III, July 1993

Pitt, C. J., “Final Report, Completed Project for VLF Communication System Insulator Tests,” CONSULTEC, Inc., Technical Report, 18 Sep. 1972

Podporkin, G. V. 1995. “Calculating the Switching Surge Critical-Flashover Voltage of Phase-to-Ground and Phase-to-Phase Bundle Conductor Gaps.” *IEEE Transactions on Power Delivery*, vol. 10, no. 1 (Jan)

Pokorny, W. C., R. H. Schlomann, and H. C. Barnes. “Investigation of Corona Effects from Wet Bundle Conductors for Application to UHV Configurations.” *IEEE Transactions Power Apparatus and Systems,* vol. 91, 1972

Reid, R. Corona and Partial Discharge Detection by the Charge-Release Method. Hipotronics, 1975

Richards, J. A., F. W. Sears, M. R. Wehr, M. W. Zemansky. *Modern University Physics*, Addison-Wessley, 1960

Rickard, D. A., R. T. Waters, J. and Dupuy. *Frequency Effects in Alternating Current Corona.* New York: Plenum Press, 1991

Rizk, F. A. M. “Influence of Rain on Switching Impulse Sparkover Voltage of Large-Electrode Air Gaps.” *IEEE Transactions on Power Apparatus and Systems*, vol. PAS-95, no. 4 July/Aug. 1976

Rizk, F. A. M. “Model for Switching Impulse Leader Inception and Breakdown of Long Air-Gaps.” *IEEE Transactions on Power Delivery,* vol. IV no. I, Jan. 1989

Rizk, F.A.M. “Model of Lighting Incidence to Tall Structures Part I: Theory.” *IEEE Transactions on Power Delivery*, vol.IX, no. I, Jan. 1994

Rizk, F. A. M. “Model of Lighting Incidence to Tall Structures Part II: Theory.” *IEEE Transactions on Power Delivery,* vol. IX, no. I, Jan. 1994

Rizk, F. A. M. “Switching Impulse Strength of Air Insulation: Leader Inception Criterion.” *IEEE Transactions on Power Delivery,* vol. IV, no. IV, Oct. 1989

Rosich, R. K., M. D. Rymes, and F. J. Eriksen. “Models of Lighting Channel Impedance.” *Electro Magnetic Applications*, IEEE, 1981

Schneider, K. H. and K. H. Weck. “Parameters Influencing the Gap Factor.” *Electra*, no. 35, July 1974

Schneider, K. H. “Positive Discharges in Long Air Gaps at Les Renardieres.” *Electra,* no. 53, July 1977

Slepian, J. “Extinction of a Long A-C Arc.” *Transactions A*. IEEE, April 1930

Starr, W. T. “Corona Properties of Insulating Materials.” *Electrical Manufacturing*, June 1956

Suzuki, T., K. Miyake, and T. Hara. “Breakdown Process in Rod-to-Plane Gaps with DC Voltages.” *IEEE Transaction on Industry Applications*, vol. Ia-21, no. I, Jan./Feb. 1985

Taylor, E. R. Jr., V. L. Chartier, V.L., and D. N. Rice. “Audible Noise and Visual Corona from HV and EHV Transmission Lines and Substation Conductors-Laboratory Tests.” *IEEE Transactions on Power Apparatus and Systems*, vol. PAS-88, no. IV, May 1969

Thanh, L. C. “Distribution of Electric Fields in a Rod to Plane Gap at the Onset of Negative Corona.” *PROC. IEE*, vol. 126, no. III, March 1979

Thornhill, W. T. and E. W. Beasley. “Influence of Corona Formation Upon the Design of High Voltage Apparatus.” *Marconi Review*, 1948

Trinh, N. G. and J. B. Jordan. “Modes of Corona Discharges in Air.” *IEEE Transactions on Power Apparatus and Systems*, vol. PAS-87, no. IV, May 1968

Trybus, Chodorow, Endsley, and Bridge. “Spark Gap Breakdown at EMP Threat Level Rates of Voltage Rise.” *IEEE Transactions on Nuclear Science*, vol. NS-26, Dec. 1979

Vlastos, E. “Breakdown of Air in the Nonhomogeneous Field.” *PROC. IEE*, vol. 113, no. IV, May 1966

Wilkins, R. “Corona Loss Tests on the 202-Mile 60-Cycle.” *Transactions A*. IEE. Oct. 1924

About the Authors

Peder M. Hansen graduated from the University of Michigan with a Ph.D. in electrical engineering in 1970. He immediately went to work at the Naval Electronics Laboratory Center in San Diego, which has changed names several times and is now known as SSC San Diego. He has been involved with many R&D programs primarily involved with the development of U.S. Navy communications systems. His primary area of expertise is electromagnetics, with specialization in antennas and propagation. His areas of work include: electrically small antennas, especially over lossy ground, ionospheric propagation, covert sounder aided HF communications, broadband shipboard HF communications, EHF shipboard communications, HF adaptive array antennas, using VLF/LF for tunnel detection, VLF/LF propagation, and VLF/LF transmitting antenna design, especially high voltage/high current issues. He has published numerous technical reports, several technical papers, and holds several patents. He lives in San Diego and still works at SSC San Diego.

Arthur D. Watt graduated from Purdue University with a degree in electrical engineering. During World War II, he served as an officer in the U.S. Navy, and after working at the Naval Research Laboratory he joined the staff of the National Bureau of Standards in Boulder, Colorado, where he worked on many R&D projects in the field of radio communication systems. He formed the Boulder branch of Deco Electronics, which later became the Georesearch Laboratory of Westinghouse. His fields of work include: radio propagation, antennas, transmitters, receivers, system studies, natural resource assessments, earth sciences, environmental management, geophysical prospecting, solar energy, ocean thermal energy conversion, and the design and construction of specialized electronic equipment. He was an adjunct professor at the Colorado School of Mines and is the author of the book *VLF Radio Engineering* and numerous technical reports and papers in scientific journals. He recently received the John Alvin Pierce award from the International Navigation Association for his contributions to the field of Omega and VLF navigation. He is retired and lives on his ranch in Molina, Colorado.

Peder Hansen at South Pole, January 2003.

Don Watt enjoying himself near his former home in Florence, OR.
Picture by Kirk Hansen.